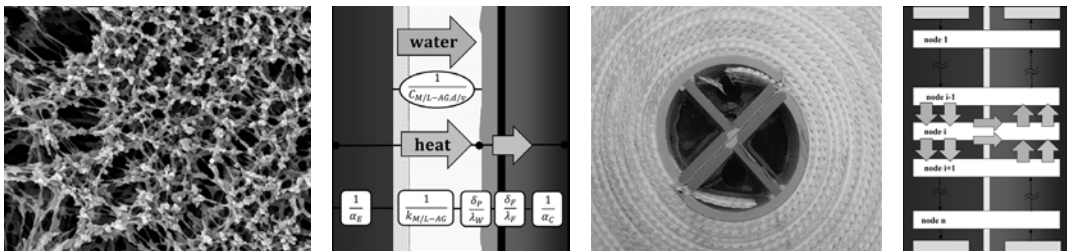


Daniel Winter

Membrane Distillation

A Thermodynamic, Technological and Economic Analysis



Membrane Distillation - a Thermodynamic, Technological and Economic Analysis

Dissertation

submitted to the

Department of Mechanical and Process Engineering

of the

University of Kaiserslautern, Germany

for the attainment of the academic degree of

Doktor-Ingenieur (Dr.-Ing.)

by

Dipl.-Ing. Daniel Winter

born in Filderstadt, Germany

2014

Research performed at the

Fraunhofer Institute for Solar Energy Systems

Freiburg im Breisgau, Germany

Dissertation for the attainment of the academic degree of Doktor-Ingenieur (Dr.-Ing.), approved by the Department of Mechanical and Process Engineering of the University of Kaiserslautern, Germany.

Date of examination: April 24th, 2015

Dean: Prof. Dr.-Ing. Christian Schindler
Department of Mechanical and Process Engineering
University of Kaiserslautern, Germany

First supervisor: Prof. Dr.-Ing. Siegfried Ripperger
Institute for Mechanical Process Engineering
University of Kaiserslautern, Germany

Second supervisor: Prof. Dr. rer. nat. Volker Wittwer
University of Freiburg, Germany
Fraunhofer Institute for Solar Energy Systems

Schriftenreihe der Reiner Lemoine-Stiftung

Daniel Winter

Membrane Distillation

A Thermodynamic, Technological and Economic Analysis

D 386 (Diss. Technische Universität Kaiserslautern)

Shaker Verlag
Aachen 2015

Bibliographic information published by the Deutsche Nationalbibliothek

The Deutsche Nationalbibliothek lists this publication in the Deutsche Nationalbibliografie; detailed bibliographic data are available in the Internet at <http://dnb.d-nb.de>.

Zugl.: Kaiserslautern, TU, Diss., 2015

Copyright Shaker Verlag 2015

All rights reserved. No part of this publication may be reproduced, stored in a retrieval system, or transmitted, in any form or by any means, electronic, mechanical, photocopying, recording or otherwise, without the prior permission of the publishers.

Printed in Germany.

ISBN 978-3-8440-3706-7

ISSN 2193-7575

Shaker Verlag GmbH • P.O. BOX 101818 • D-52018 Aachen

Phone: 0049/2407/9596-0 • Telefax: 0049/2407/9596-9

Internet: www.shaker.de • e-mail: info@shaker.de

Abstract

Global desalination capacity has increased during the past decades to alleviate water scarcity in regions with a mismatch between water availability and demand. The recent desalination market relies almost exclusively on non-sustainable, industrial-scale processes which do not provide a solution to prevent water scarcity in rural areas. The development of small-scale, self-sufficient and environmentally friendly desalination systems is considered to be one of the key challenges to sustainably overcome water scarcity.

Thermally driven Membrane Distillation (MD) has been identified as a promising approach for decentralised desalination. However, MD has not yet reached successful commercialisation, as it still requires scientific research in the fields of material, module and system development. High potential for improvement is associated with adapted membrane module design meeting custom project requirements. Comprehensive MD design methods, tools and universal design suggestions are not yet available.

This thesis presents comprehensive methods for MD process and module evaluation which may also be applied for techno-economic module and system optimisation based on arbitrary optimisation criteria. The methods refer to the context of desalination, but their general validity also allows application to related MD separation problems.

The derivation of the presented method is based on extensive experimental and numerical analysis of the fundamental MD phenomenology in coupled heat and mass transfer. The approach includes a comparative discussion on different MD process configurations, known as Direct Contact Membrane Distillation (DCMD), Permeate Gap Membrane Distillation (PGMD) and Air Gap Membrane Distillation (AGMD). The experimental equipment involves a lab test cell with a membrane surface of $150 \times 250 \text{ mm}^2$. The role of the key material properties for channel spacers, membranes, backing structures and gap spacers is quantified and discussed. Furthermore, the process sensitivity to operational parameters such as temperature, flow rate, salinity and state of deaeration is analysed.

The results are then transferred from the level of fundamental process phenomenology to the scale of application, considering full-scale module flow channels. The performance of the MD modules is characterised and discussed on the basis of key performance parameters such as output capacity, flux, thermal efficiency and thermal as well as electrical energy consumption. In order to validate the numerical models, different DCMD, PGMD and AGMD module prototypes with membrane surface areas of 5 to 15 m^2 were fabricated and characterised. Theoretical and experimental studies specifically address the strongly interlinked process sensitivities to MD concept, channel design and operational conditions. Purely theoretical studies provide suggestions on membrane selection and the role of potential material improvements. Wide-range parametric field studies demonstrate the fundamental thermodynamic limitations imposed for the different MD processes.

The technological discussion of MD modules is followed by an economic evaluation of the different MD concepts in the context of small-scale desalination applications. A comprehensive cost model

is suggested for the estimation of water unit costs, to be used as an integral quantitative measure for module and system comparison and as an optimisation criterion. The implementation of a generic parameter optimisation program allows the derivation of adapted module design specifications by performing automated iterative techno-economic optimisation, performed for selected scenarios as examples. A comparative presentation of the results indicates the suitability of the different module concepts, the expected key cost positions and economic feasibility.

Kurzfassung

Die weltweit installierte Entsalzungskapazität wurde in den letzten Jahrzehnten massiv ausgebaut, um Wassermangel in betroffenen Regionen zu begegnen. Derzeit werden fast ausschließlich Entsalzungsanlagen im industriellen Maßstab eingesetzt, welche jedoch kein Lösungsansatz für den ländlichen Raum darstellen. Daher wird die Entwicklung von kleinen, dezentralen Entsalzungssystemen als besonders wichtige Herausforderung auf dem Weg zu einer flächendeckenden Trinkwasserversorgung angesehen.

Der thermisch betriebene Membrandestillationsprozess (MD) gilt hierfür als aussichtsreicher Technologieansatz. Dennoch konnte sich die MD bis heute nicht kommerziell durchsetzen und weiterhin ist Entwicklungsarbeit in den Bereichen Materialien, Module und System zu leisten. Ein besonders hohes Verbesserungspotential wird der anwendungsorientierten Entwicklung von Membranmodulen zugeschrieben. Umfassende Gestaltungsmethoden, -werkzeuge und -richtlinien sind hierfür bisher nicht verfügbar.

In dieser Arbeit werden Methoden zur MD Prozess- und Modulbewertung erarbeitet, welche schließlich zur techno-ökonomischen Modul- und Systemoptimierung auf Basis verschiedener Optimierungskriterien angewendet werden können. Zwar werden die Methoden hier im Kontext der Entsalzung dargestellt, doch erlaubt deren Allgemeingültigkeit grundsätzlich auch Anwendung bei verwandten MD Separationsproblemen.

Die dargestellten Methoden beruhen auf umfangreichen experimentellen und theoretischen Untersuchungen zum gekoppelten Wärme- und Stofftransport in der MD. Eine zentrales Element der Arbeit stellt die vergleichende Betrachtung von Direkt Kontakt MD (DCMD), Permeat Spalt MD (PGMD) und Luft Spalt MD (AGMD) dar. Die Experimente werden mit einer Testzelle durchgeführt, welche eine Membranfläche von $15 \times 25 \text{ cm}^2$ bereitstellt. Die Einflüsse der wichtigsten Materialparameter zu Kanal-Stützgeweben, Membranen, Trägerstrukturen und Spaltgrößen werden quantifiziert und diskutiert. Zudem wird eine vergleichende Sensitivitätsanalyse zum Einfluss von Betriebsbedingungen wie Temperatur, Strömungsgeschwindigkeit, Salzgehalt und Entgasungszustand durchgeführt.

Die Ergebnisse werden weiterführend auf Strömungskanäle im Anwendungsmaßstab überführt. Die Leistungsfähigkeit der MD-Module wird anhand von allgemeingültigen Bewertungsgrößen evaluiert, welche Produktdurchsatz, Flux, thermische Effizienz und sowohl thermischen als auch elektrischen Energiebedarf beschreiben. Zur Modellvalidierung werden unterschiedliche DCMD,

PGMD und AGMD Module mit Membranflächen von 5 bis 15 m² hergestellt und charakterisiert. Die experimentellen und theoretischen Untersuchungen adressieren insbesondere die gekoppelten Sensitivitäten bezüglich MD Konzept, Kanalgestaltung und Betriebsbedingungen. Mittels Modellrechnungen werden Empfehlungen für eine angepasste Materialauswahl ausgearbeitet und das Potential möglicher Materialverbesserungen ermittelt. Die thermodynamischen Grenzen der verschiedenen MD Konfigurationen werden durch Ergebnisse umfangreicher Parameterfeldstudien deutlich.

Der technologische Teil der Arbeit wird ergänzt durch eine wirtschaftliche Bewertung der MD Verfahren am Beispiel kleiner Entsalzungsanlagen. Ein Kostenmodell zur Abschätzung der Wassergestehungskosten wird vorgestellt, welche dann als Vergleichsgröße zur Modul- und Systembewertung sowie auch als Optimierungskriterium dienen. Die Implementierung eines Parameteroptimierers erlaubt eine automatisierte, iterative techno-ökonomische Optimierung von Modulgestaltungsgrößen, welche exemplarisch für ausgewählte Szenarien durchgeführt wird. Die entsprechenden Ergebnisse geben Hinweise auf die Eignung der verschiedenen MD Verfahrensvarianten, die Verteilung der Kosten sowie die Wirtschaftlichkeit.

Table of Contents

1	Introduction	1
1.1	Motivation	1
1.2	Outline of Thesis	3
1.2.1	Challenges and Objectives	3
1.2.2	Structure and Scientific Approach	5
2	Membrane Distillation	7
2.1	Basic Concept	7
2.2	Process Configurations	9
2.2.1	Direct Contact Membrane Distillation	10
2.2.2	Permeate Gap Membrane Distillation	11
2.2.3	Air Gap Membrane Distillation	12
2.2.4	Sweeping Gas Membrane Distillation	14
2.2.5	Vacuum Membrane Distillation	14
2.2.6	Osmotic Membrane Distillation	16
2.3	Heat Recovery Strategies	17
2.3.1	Sensible Heat Recovery	18
2.3.2	Latent Heat Recovery	18
2.4	Membranes	19
2.5	Membrane Modules	24
2.5.1	Module Design Concepts	25
2.5.2	Performance Parameters for Membrane Distillation Modules	29
2.5.3	Commercial Membrane Distillation Module Developments	29
2.6	Advances in Membrane Distillation	32
2.7	Potential Fields of Application	33
3	Process Analysis	37
3.1	Fundamentals and Model Development	37
3.1.1	Transmembrane Mass Transfer	38
3.1.2	Transmembrane Heat Transfer	46
3.1.3	Heat Transfer in the Hydraulic Boundary Layers	49
3.1.4	Mass Transfer in the Hydraulic Boundary Layers	53
3.1.5	Integrated Modelling of Membranes on Backing Structures	55
3.2	Node Models for Theoretical Process Evaluation	61

3.2.1	Direct Contact Channel Configuration	62
3.2.2	Permeate Gap Channel Configuration	63
3.2.3	Air Gap Channel Configuration	66
3.3	Experimental Approach	68
3.3.1	Laboratory Cell Design and Test Rig	68
3.3.2	Testing Conditions and Evaluation of Performance Parameters	70
3.3.3	Uncertainty of Measurement and Error Propagation	71
3.3.4	Materials for Experimental Evaluation	74
3.4	Results and Model Validation	76
3.4.1	Spacers - Enhanced Heat Transfer in the Flow Channels	77
3.4.2	Membranes - An Analysis Based on Different Membrane Structures	81
3.4.3	Laminates - Membranes on Backing Structures	96
3.4.4	Extended Channel Configurations - The Gap Variants	104
3.4.5	A Comparative Evaluation of Different Process Configurations	116
4	Module Analysis	129
4.1	Multi-Node Models for Theoretical Module Evaluation	129
4.1.1	Direct Contact Module Configuration	131
4.1.2	Permeate Gap Module Configuration	135
4.1.3	Air Gap Module Configuration	138
4.1.4	Evaluation of the Module Performance Parameters	139
4.1.5	Simulation Settings	144
4.2	Experimental Approach	146
4.2.1	Test Rig for Module Characterisation	146
4.2.2	Testing Conditions and Evaluation of Performance Parameters	148
4.2.3	Uncertainty of Measurement and Error Propagation	150
4.2.4	Full-Scale Module Prototypes for Experimental Evaluation	153
4.3	Results and Model Validation	156
4.3.1	General Aspects of Membrane Distillation Module Operation	156
4.3.2	Specific Aspects of Direct Contact Module Operation	178
4.3.3	Specific Aspects of Permeate Gap Module Operation	183
4.3.4	Specific Aspects of Air Gap Module Operation	187
4.3.5	A Comparative Evaluation of Different Module Configurations	196
4.3.6	Selection of an Optimal Membrane	204
4.3.7	Performance Potential using Advanced Materials	211
4.3.8	Parametric Field Studies	219
5	Economic Evaluation	229
5.1	Cost Model Development	229
5.1.1	Investment Costs	230
5.1.2	Operational Costs	237
5.2	Results and Discussion	243

5.2.1	An Analysis of the Investment Costs	243
5.2.2	A Sensitivity Analysis on the Unit Costs of Water	244
5.2.3	Design of Waste-Heat Driven Plants	249
5.2.4	Techno-Economic Module Optimisation	250
6	Conclusion	265
6.1	Summary	265
6.2	Recommendations for Further Research	275
	Appendix	277
A	Commercial Desalination Technologies	277
B	Physical Properties of Salt Water	284
C	Ionic Composition of Salt Water	287
D	Spacers - Enhanced Heat Transfer in the Flow Channels	288
E	Laminates - Membranes on Backing Structures	289
F	Uncertainty of Measurement and Error Propagation	290
G	General Aspects of Membrane Distillation Module Operation	292
H	Specific Aspects of Air Gap Module Operation	293
I	Selection of an Optimal Membrane	294
J	Parametric Field Studies	296
	Nomenclature	298
	Literature	305
	Publications	305
	Bibliography	307
	Curriculum Vitae	323
	Acknowledgements	325

1 Introduction

1.1 Motivation

On July 28th 2010, the human right to water and sanitation was explicitly recognised by the General Assembly of the United Nations by resolution 64/292 [1]. The resolution is not effectual according to international law, but it draws attention to one of the most important challenges for the coming decades. According to the WHO / UNICEF Joint Monitoring Programme for water supply and sanitation, 770 million people did not use an improved source for drinking-water in 2011, including 185 million who relied on surface water to meet their daily drinking-water needs. More than 80% of the population without access to an improved drinking-water source lived in rural areas [2].

The issue of water scarcity will principally be intensified in the coming decades by depletion of renewable and fossil aquifers, intrusion of salt water into overstressed fresh water aquifers, pollution of available fresh water resources and consequences of climate change. An increased water demand is predicted especially in the developing world due to exponential growth of the population, increase of individual demand, industrialisation, tourism and excessive use of water for agriculture to supply local and global markets. Fresh water availability and demand is subjected to a major locational and seasonal mismatch. Especially arid and semi-arid regions in northern Africa, south-western Asia and swathes of central Asia are affected by an increase in physical water scarcity [3]. The lack of water already causes local, national and international conflicts today. Projects and work groups such as “UN-Water” or “NATO Science for Peace Programme“ have been set up in order to develop road maps and concepts for sustainable water management, especially for arid regions with increasing water demand. The activities include socio-economic as well as technological approaches, wherein the production of fresh water by water treatment techniques such as disinfection, filtration and desalination is considered an inherent part.

Successful implementation of a technological approach mainly depends on the availability of infrastructure, energy and interest in financing. During the past decades, desalination capacity has increased tremendously based on technological ability, high demand and economic sustainability. The Global Water Intelligence database DesalData has been accessed to derive some numbers and trends on the recent desalination market [4]. The global online capacity increased from 7 mio. $\text{m}^3 \text{d}^{-1}$ desalinated water in 2000 to 61 mio. $\text{m}^3 \text{d}^{-1}$ in 2014. Additionally considering recently contracted capacities, the global capacity is almost 70 mio. $\text{m}^3 \text{d}^{-1}$. The global capacity

is subdivided among three technologies that hold more than 95% of the market share. The respective market shares of the established desalination processes are 17% and 8% for thermally driven Multi-Stage Flash (MSF) and Multi-Effect Distillation (MED) and 70% for electrically driven Reverse Osmosis (RO). A brief introduction to these key technologies is provided in Appendix A.

About the half of the global capacity is produced by desalination plants with capacities greater than 50 000 m³ per day, while only 3.5% of the global capacity originates from small scale plants with a capacity lower than 1 000 m³ per day [4]. Recent desalination may therefore be considered highly industrialised, characterised by a central plant structure that requires reliable infrastructure for energy and water distribution as well as financial strength. Countries as Saudi Arabia, United Arab Emirates, USA and Spain are therefore the main producers of desalinated water in terms of capacity. Fresh water supply in some regions strongly relies on water desalination. In Saudi Arabia, the amount of water provided by desalination is already double the available natural renewable resources and current water supply is satisfied to 84% by exploitation of non-renewable groundwater resources. In the United Arab Emirates, almost all domestic and industrial water supplies rely on desalination [4].

Increasing desalination activities may significantly reduce water scarcity. However, since desalination is realised by energy-intensive processes, the supply strategies require integral consideration of both water and energy. The required energy originates almost exclusively from non-renewable energy sources, so today's established desalination approach does not represent a sustainable solution. The excessive application of desalination also causes considerable environmental impact. Applying the proposed emissions that have been derived for the individual technological approaches to the respective global capacities [5], the accumulated CO₂ emissions recently caused by desalination are estimated to be about 730 000 t per day. Besides the emission of greenhouse gases and other air pollutants, the environmental concerns revolve around concentrate and chemical discharges into the sea. The concentrate discharge mainly affects the mixing zone by saline loads, thermal loads and potential turbidity and sedimentation. Moreover, daily chemical discharges¹ have been estimated to amount to 30 t of disinfectants, 110 t of antiscalants and 400 kg of copper from corrosion [6]. Further concerns address impingement and entrainment of marine organisms at large open intake systems as well as construction-related impacts on the coast line. Eventually, the problem of water scarcity changes into a problem of energy consumption and impact on the marine environment [6].

Significant cost for energy and additives and tightened legal regulations obviously motivate the development of improved desalination processes and systems with respect to energy efficiency and pretreatment. Politically motivated research agendas strongly target sustainable water management, in which a key role is given to the application of renewable energy sources to desalination and the development of robust desalination approaches that do not rely on chemical pretreatment. The central approach of the recent desalination market mainly addresses urban areas and does not provide a solution for water scarcity in rural areas. Since renewable energy supply does not require comprehensive infrastructure, it is perfectly suited especially for decentralised

¹Considering the Arabian Gulf, the Red Sea and the Mediterranean Sea, over 70% of the global desalination capacity is located [6]

small scale applications. Small scale desalination systems with a renewable energy supply often provide the only but also the most economic option for supplying fresh water in rural areas. The high availability of solar irradiation of up to $8 \text{ kWh (m}^2 \text{ d)}^{-1}$ in arid and semi-arid zones matches the local water demand and offers a great potential for decentralised water treatment. It is important to note that especially the established thermal desalination technologies may not be efficiently downscaled for decentralised applications. The fluctuating availability generally associated with renewable energy supplies is a further issue to be considered. The necessity of research and development of small scale desalination systems is derived from this perspective, especially concerning robust and efficient processes that are feasible for operation with a fluctuating energy supply.

Technical feasibility may be proven by scientific research and development that also contributes to improved economic feasibility. Unlike established industrial desalination, the economic feasibility of small scale decentralised systems may differ significantly depending on local conditions such as energy costs and water price. Socioeconomic aspects may well decide whether a technological approach finds acceptance and success. It is important to note that the development of small scale sustainable desalination technologies is only one aspect of the overall solution needed to overcome water scarcity in a thirsty world.

1.2 Outline of Thesis

1.2.1 Challenges and Objectives

Thermally driven Membrane Distillation (MD) has been identified as a promising approach for decentralised desalination that is suitable for utilisation of low grade waste heat or fluctuating renewable energy supplies [7, 8]. The membrane based MD process is considered to be quite robust with respect to fouling and scaling and may therefore be feasible for operation with minimised pretreatment, especially with respect to chemical additives. High thermodynamic efficiency has been proven for small scale applications, allowing the implementation of energy-efficient containerised systems of reasonable costs. A detailed technology review on MD is provided in Chapter 2. The Fraunhofer Institute for Solar Energy Systems (ISE) has been working on the development of self-sufficient, solar thermally driven MD systems since 2001. Several field test systems have been built, commissioned and monitored within the framework of the EU FP5 and FP7 programmes [8–11]. Recent activities at Fraunhofer ISE have focused on the optimisation of the key component, the MD membrane module.

However, MD has not yet reached successful commercialisation, as it still requires scientific research in the fields of material, module and system development. High potential for improvement is still associated with adapted module design responding to local factors such as availability and quality of raw water and energy. As an example, high potential is attributed to the MD approach

for low-temperature operation or for the treatment of highly concentrated brines, with different design requirements to be met. A systematic adaptation of the module geometrical design and material selection with respect to specific technical and economic project requirements is essential in order to achieve optimal module performance and economic feasibility. Comprehensive design methods, tools and universal design suggestions are not yet available. Most of the scientific work presented on MD focuses on phenomenological aspects, material characterisation and feasibility studies in lab-scale approaches. Different process variants are considered, but the literature does not provide standard methods or comprehensive comparative evaluation. The results from lab-scale experiments may not be used directly for argumentation in the context of full-scale application. Comprehensive methods satisfactorily linking fundamental research to full-scale module development have not been reviewed. The selection of key materials such as membranes has not yet been sufficiently clarified, especially with regard to the potential for full-scale module and system performance. Only a few publications present studies of full-scale module performance, but they seldom provide adequate thermodynamic discussion. Even though MD is a thermally driven process, an appreciable amount of electrical energy is required for pumping and deaeration. However, integral evaluation and discussion of electrical loads is hardly mentioned. Pertinent literature almost completely lacks transparent techno-economic evaluation. It is obvious that targeted module optimisation needs to integrally consider fundamental phenomenological aspects, material selection, module concept and design as well as system integration, operational strategy and costs.

The scope of this thesis bridges the gap from fundamental research to full-scale module development. A focus is placed on the thermodynamic evaluation of MD performance rather than on practical aspects such as fouling, scaling or pretreatment. The objective is the development of a model-based method suitable for comprehensive evaluation and comparison of different MD concepts varying in the scale of application, considering key performance parameters such as output capacity, flux and thermal as well as electrical energy consumption and eventually costs. The method should support the identification of an optimal custom module design for a specific application based on arbitrary optimisation criteria. Since MD offers attractive characteristics for a wide variety of applications, the method and model should be universally valid to support MD module development also in the context of applications other than seawater desalination. Great experimental effort for complex and expensive prototype fabrication and characterisation is to be minimised in order to accelerate future developments. The model should include a high level of physical detail, so that the role of specific material properties, geometrical module design and operational strategies is reflected. Quantitative information on performance obtained for specific configurations or material selections, that might either be known from pertinent literature or from lab-scale experiments, should be reliably transferable to a full-scale module and system context. In this case, full-scale module optimisation can be efficiently supported by lab-scale experiments.

Eventually, the desired method should give a transparent recommendation for the estimation of product unit costs that provides a comparable measure and indication of economic feasibility. However, due to individual potential project conditions and target applications, this thesis does

not claim to provide a conclusive evaluation of the economic feasibility for MD.

1.2.2 Structure and Scientific Approach

The development of a comprehensive method according to the objectives stated in Sec. 1.2.1 is accomplished by a three-level approach, starting from MD fundamental phenomenology in Chapter 3, widening the scope to full-scale MD modules in Chapter 4, and finally considering economic aspects in the context of small scale MD desalination systems in Chapter 5.

The first-level approach provides the derivation of a comprehensive fundamental understanding of thermodynamic MD phenomenology including qualitative and quantitative discussion of the influencing parameters. The section covers the theoretical fundamentals and the derivation of quasi-stationary one-dimensional models for all MD configurations to be considered. This first-level model approach, also denoted "discrete single-node model", targets the prediction of the coupled heat and mass transfer phenomena with a high level of physical detail, but is valid only for a local channel position. The model approach is adopted from pertinent literature and extended as necessary. A lab-cell test facility is designed that specifically addresses the respective single-node model limitations. Extensive experimental work is carried out with different channel configurations in order to derive suitable model parametrisation and prove model validity over a wide range of operating conditions. The role of the key material properties for channel spacers, membranes, backing structures and gap spacers is quantified and discussed step by step by subsequently increasing channel complexity. A comparative evaluation and discussion of different MD channel configurations based on experimental results and model predictions concludes the chapter on MD process analysis.

The second-level approach provides the transformation of the different single-node models into multi-node models, valid for the evaluation of complete flow channels in full-scale MD modules. A detailed derivation of the module performance parameters is given. Full-scale module prototypes with different conceptual, geometrical and material specifications are fabricated, referring to the specifications studied within the process analysis chapter. A module test facility is used for extensive experimental prototype characterisation. The multi-node models are strictly parametrised according to the results of the previous process analysis and validated in the context of full-scale modules. General aspects of MD full-scale module operation are analysed and discussed based on an exemplary channel configuration. Specific aspects regarding the operation of different basic module types are discussed individually for all tested channel configurations. Similarly to the process analysis chapter, a comparative evaluation of the thermodynamic performance obtained with the different MD module types is provided. Subsequently, purely theoretical studies complete the scientific discussion on MD modules, specifically addressing aspects of membrane selection and the role of potential material improvements. Wide range parametric field studies comprehensively demonstrate the fundamental thermodynamic limitations applicable to the

different MD processes.

The third-level approach addresses the economic evaluation of the different MD concepts in the context of small-scale desalination applications. A comprehensive cost model is proposed for the estimation of water unit costs to be used as an integral quantitative measure for system comparison and as an optimisation criterion. The investment cost model is specifically adapted for the evaluation of MD desalination systems considering the expected key cost positions such as pretreatment, deaeration, MD modules, heat exchangers and other system components. Further consideration is given to economy of scale. Operational costs include financing, energy costs, chemicals, membrane exchange, maintenance, labour and insurance. The sensitivity of the water unit costs with respect to selected aspects in module and system design is demonstrated. The implementation of a generic parameter optimisation program allows the derivation of adapted module design specifications by performing automated iterative techno-economic optimisation. The optimisation method is applied to selected scenarios covering potential MD desalination projects as examples. A comparative presentation of the results indicates the suitability of the different module concepts, the expected key cost positions and economic feasibility.

2 Membrane Distillation

A detailed overview and discussion of important technological aspects of membrane distillation technology and the respective state-of-the-art is provided in the following chapter. At first, the conceptual background to the process, the available process configurations and basic heat recovery strategies are presented. Subsequently, attention is paid to aspects regarding implementation, covering different topics concerning membrane and module design. The membrane distillation process is then classified according to the potential fields of application, indicating the specific advantages of membrane distillation compared to alternative approaches. The fundamental applicability of the membrane distillation approach for various separation problems is illustrated by experimental studies that have been reviewed from pertinent literature.

The comprehensive technology review is also used to indicate the selected topics, concepts and materials that are specifically addressed by the author's own studies as presented in the following chapters of this thesis.

2.1 Basic Concept

Membrane Distillation (MD) is a thermally driven, membrane-based separation process that is primarily suited to the treatment of aqueous feed solutions. A hydrophobic, highly porous membrane separates the feed solution from the permeate. At least the feed solution is in direct contact with the membrane surface but it must not penetrate the dry membrane pore volume. A liquid-vapour interface is thus formed, as schematically illustrated in Fig. 2.1(a). If a vapour pressure gradient is established across the membrane, volatile compounds of the feed solution evaporate and the vapour molecules are forced through the membrane pores from the feed to the permeate side. Depending on the feed composition, the permeating vapour may either consist of a single or of multiple components. The selective characteristic of the MD process relies on the membrane's impermeability with respect to the liquid feed, while vapours pass the porous membrane structure. If the absolute pressure difference from the liquid phase to the vapour phase $\Delta\hat{p}_{(l)-(g)}$ is sufficiently low, the liquid phase cannot penetrate the membrane pores due to surface tension, even though the single molecules are considerably smaller than the membrane pores. A schematic illustration of this phenomenon, also known as capillary depression at a hydrophobic membrane pore, is provided in Fig. 2.1(b).

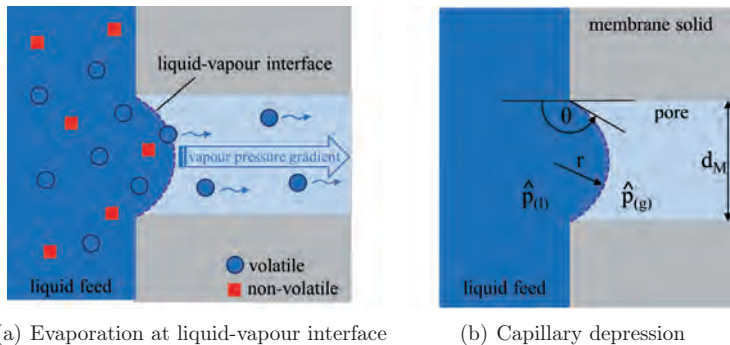


Figure 2.1: Basic functional phenomena of the membrane distillation process

At a certain pressure difference $\Delta\hat{p}_{(l)-(g)}$, the surface tension cannot maintain the liquid-vapour interface and the liquid feed penetrates the membrane pore volume. This characteristic pressure is referred to as the liquid entry pressure (*LEP*). It is obvious that the pressures in MD systems must not exceed the *LEP* in order to remain the separative functionality of the membrane. The essential non-wetting criteria is formulated in Eq. 2.1.

$$\Delta\hat{p}_{(l)-(g)} \stackrel{!}{<} LEP \quad (2.1)$$

The Young-Laplace theory describes the correlation of pressure, surface tension and surface curvature of fluids. For an ideal cylindrical pore geometry, the *LEP* may be directly derived from the Young-Laplace equation, considering the membrane pore diameter d_M , the surface tension of the liquid phase $\sigma_{(l)}$ and the contact angle θ that develops between the fluid and the membrane [12]. Since membrane wetting will first occur at the widest pore, the maximal pore size of a membrane material is considered. However, due to the complex geometrical characteristics of real pore systems, modified equations are suggested, e.g. by introducing a pore form factor $0 \leq B \leq 1$ [13]. From Eq. 2.2, it becomes obvious that a small maximal pore size, a large contact angle and a high surface tension of the feed solution generally support a reliable MD process.

$$LEP = \frac{4 B \sigma_{(l)} \cos(\theta)}{d_{M,\max}} \quad (2.2)$$

If the vapour pressure curve indicates adequate volatility of the species that is to be separated from a feed solution, the fundamental applicability of the MD process for the specific separation problem has to be verified by the essential non-wetting criterion. It is important to note that the feed composition could have a significant influence on the fluid surface tension. While inorganic substances usually have a minor effect on the hydrophobic feature, the liquid surface tension is significantly reduced in solutions containing organic substances [14–17]. Specifically tensides are considered to be very critical within MD feed solutions [18]. Due to their asymmetric hydrophobic-hydrophilic structure, tenside molecules are displaced from the interior of the aqueous phase to its interfacial surface. Thus already small amounts of tensides influence

the interfacial properties of the fluids and significantly reduce the surface tension of an aqueous solution [12].

As for any evaporative process, the transmembrane mass transfer in MD is always accompanied by enormous transmembrane heat transfer. The minimum heat transfer results from the latent heat of evaporation of the permeating species that are extracted on the evaporator side, transferred through the membrane and then released on the condenser side. However, depending on the process configuration, the channel arrangement and the membrane properties, conductive heat transfer may additionally contribute to the overall heat transfer. The heat transfer by conductive phenomena does not contribute to the mass transfer and is therefore considered to be undesirable thermal loss.

2.2 Process Configurations

A vapour pressure gradient across the membrane acts as the process driving force in any MD configuration. However, this driving force may be established in different ways. While the feed solution is always in direct contact with the membrane surface, defining the respective vapour pressure at the feed side liquid-vapour interface, the following basic approaches are used in order to create a vapour pressure gradient towards the permeate side:

- Application of a lower temperature on a permeate side liquid-vapour interface
- Application of a stripping solution on the permeate side liquid-vapour interface
- Application of a sweeping gas on the permeate side of the membrane
- Application of a vacuum on the permeate side of the membrane

The different approaches for establishing the driving force and other process requirements led to the development of various channel configurations that are widely used as classification criteria within MD technology. The most common configurations utilise a temperature difference as the driving force, while alternative approaches are considered rather exotic. The following sections provide an introduction and description of the different MD configurations and their specific features.

It should be noted that this thesis includes comprehensive comparative studies of the classic MD configurations that are illustrated in Fig. 2.2, while the alternative approaches of Fig. 2.3 will not find further consideration.

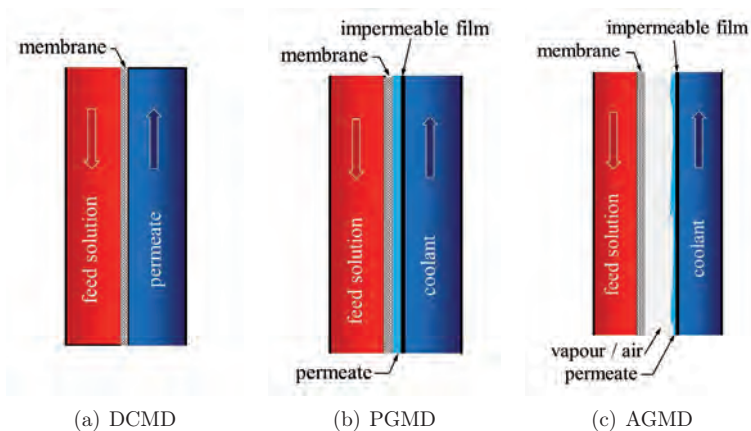


Figure 2.2: Common MD configurations driven by a temperature difference

2.2.1 Direct Contact Membrane Distillation

Direct Contact Membrane Distillation (DCMD) is the simplest MD configuration concerning the channel arrangement, which is illustrated in Fig. 2.2(a). The membrane is in direct contact with the feed solution and the permeate, while the driving vapour pressure gradient is usually induced by a temperature difference from the feed side to the permeate side. Consequently, the feed solution must have higher temperature than the permeate in order to achieve a positive driving force. For a continuous process design, the feed solution is heated and the permeate is cooled in external heat exchangers and then actively circulated parallel to the membrane. The volatile compounds of the feed solution evaporate at the feed side liquid-vapour interface, pass the membrane in the gaseous phase and condense at the cooler liquid-vapour interface on the permeate side of the membrane. Based on the phase change phenomena, the feed side is usually referred to as the evaporator side, while the permeate side is referred to as the condenser side. In DCMD, the permeate acts as a coolant, so permeate recirculation is required and the product has to be extracted outside the membrane module at any position of the cooling loop e.g. by a level drain.

In a specific variant of DCMD, the driving force is established by means of a concentration difference instead of a temperature difference. This variant involves quite specific characteristics and is therefore introduced separately in Sec. 2.2.6.

As in any evaporative process, the latent heat of evaporation is removed from the surface of evaporation and subsequently expelled at the surface of condensation. As a result, the temperature at the evaporator side liquid-vapour interface is lower than the evaporator bulk stream temperature while the temperature at the condenser side liquid-vapour interface is higher than the condenser bulk stream temperature. This effect, also known as “temperature polarisation”, significantly reduces the process driving force and may be controlled by the hydrodynamic conditions in the flow channels. The DCMD channel configuration introduces low overall heat and mass transfer

resistance compared to more complex channel configurations, thus allowing the generation of high fluxes. However, the thin membrane layer provides low resistance with respect to conductive heat transfer. Consequently, a significant amount of conductive heat transfer contributes to the overall heat transfer in DCMD.

The mass transfer within the membrane pores mainly refers to diffusive phenomena that are predominantly restricted by collisions with stagnant air molecules and the solid membrane structure. In order to reduce the mass transfer resistance, deaeration of the membrane pores has been considered as a promising approach for enhancing DCMD performance [19–21]. The membrane is indirectly deaerated by deaerating the feed solution with a vacuum system before applying it to the MD module. This enhanced configuration may therefore be referred to as vacuum-enhanced DCMD or V-DCMD. It is important to note that in V-DCMD, the vacuum system is applied for feed deaeration only, not for establishing the driving force that is still solely generated by the temperature gradient. In the V-DCMD process, the absolute pressure in the deaerated membrane pores is lower than for the case of aerated operation, which increases the absolute pressure difference from the liquid phase to the gaseous phase. Thus, the role of the limiting *LEP* and the risk of pore wetting becomes more crucial for deaerated operation compared to MD configurations that operate under aerated conditions. It is obvious that the maximal permissible hydraulic pressure on the feed side is reduced accordingly.

2.2.2 Permeate Gap Membrane Distillation

Permeate Gap Membrane Distillation (PGMD) is closely related to DCMD, since also in this configuration both sides of the membrane are in direct contact with the respective liquid fluids and the driving force is established by means of a temperature difference. As illustrated in Fig. 2.2(b), a third channel is introduced by an additional impermeable film that is located on the permeate side of the membrane. Since the permeate outlet is located at the highest module position, the gap between the membrane and the impermeable film fills with permeate during operation and is therefore referred to as the permeate gap (PG) or liquid gap (LG). A significant advantage of the PGMD configuration is the separation of permeate from the cooling fluid, which allows the use of any liquid as the coolant, e.g. cold feed solution, or the integration of the module into an existing cooling loop. The product is directly extracted from the membrane module without coming into contact with any other system components except the permeate channel, which helps to maintain high product quality over time. Furthermore, the permeate quality may be directly monitored without prior mixing within a capacious permeate stream, offering the option of fast response to quality changes and more precise leakage detection in the context of multi-module systems. Since the permeate loses its thermal function as a coolant, the hydraulic handling of the permeate is reduced to a minimum, which could be very valuable especially in the context of aggressive or hazardous permeates.

The presence of the permeate gap and the impermeable film introduces additional heat transfer resistances, which lead to a reduction of the effective temperature difference across the membrane.

It is obvious that the design of PGMD modules aims for thin permeate gaps and thin films in order to minimise the respective heat transfer resistances. However, the maximal flux in a PGMD module can never reach the maximal value from a comparable DCMD module. As for DCMD, a significant amount of conductive heat transfer contributes to the overall heat transfer in PGMD. Similarly to the V-DCMD process, also a PGMD process may be enhanced by membrane deaeration due to reduced diffusive mass transfer resistance [22]. This enhanced configuration may therefore be referred to as vacuum enhanced PGMD or V-PGMD. Also for V-PGMD, special attention has to be paid to the limiting *LEP* and the increased risk of pore wetting compared to aerated PGMD operation.

It is worth mentioning that the concept of PGMD may be applied for an alternative but closely related channel arrangement. By exchanging the membrane and film positions, the feed is separated from the heating fluid instead of the permeate from the coolant. This alternative operational mode could be denoted as Feed Gap Membrane Distillation (FGMD). FGMD allows the application of a separate heating fluid and consequently direct integration of the MD module into an existing heating loop. Since the feed solution loses its thermal function as a heating fluid, the hydraulic handling of the feed reduces to a minimum, which could be very valuable especially in the context of aggressive or hazardous feed solutions. If the brine is considered to be a valuable product, this configuration helps to maintain high brine quality and enables direct monitoring of the brine quality.

The conceptual ideas of PGMD and FGMD could be integrated into an extended channel arrangement, combining the advantages and disadvantages of both channel configurations. Such a combined channel arrangement has been discussed in the context of MD process integration into heat exchangers (MDHX) [23, 24].

2.2.3 Air Gap Membrane Distillation

The channel configuration in Air Gap Membrane Distillation (AGMD) is illustrated in Fig. 2.2(c). Similar to the PGMD channel configuration, the permeate is separated from the coolant by an impermeable film next to the membrane on the permeate side. Driven by a temperature difference, the volatile compounds of the feed solution evaporate at the feed side liquid-vapour interface, pass the membrane and the air gap in the gaseous phase and condense at the liquid-vapour interface on the cooled surface of the impermeable film. After condensation, gravity forces the liquid permeate to trickle towards the bottom of the air gap. In order to prevent the air gap from filling up with liquid, the permeate is extracted at the bottom of the membrane module. In AGMD, the permeate has no contact with the backsurface of the membrane, thus allowing the separation of compounds with low surface tension such as alcohols from dilute aqueous solutions [17, 25, 26]. The principle advantages given by the separation of the permeate from the coolant have already been discussed in the context of PGMD and may be summarised as the independent choice of a cooling fluid, minimised permeate handling, minimised contact of the

permeate with other system components and access for effective permeate quality monitoring. It is worth mentioning that the AGMD channel arrangement may also be extended by a feed side impermeable film for the introduction of an additional feed gap, as discussed for PGMD. In AGMD, the air gap is about two orders of magnitude wider than the membrane itself and thus dominates the transfer resistances. Consequently, the AGMD process shows rather low sensitivity with respect to the membrane and the film material properties. The thermal insulation between the feed side and the permeate side is greatly increased by the wide gap, compared to the configurations where only the thin membrane acts as the insulating layer. The potential reduction of conductive heat losses is one of the major argument given in favour of introducing an air gap. However, the air gap also introduces enormous additional resistance with respect to the desired mass transfer, so flux is also significantly reduced by the introduction of an air gap. To optimise the mass transfer rate in AGMD, the air gap is usually designed to be as thin as possible, always considering the limiting requirement of avoiding any direct permeate contact with the backsurface of the membrane. In order to reduce the dominant diffusive mass transfer resistance caused by stagnant air within the air gap, the air gap may directly be accessed by a vacuum system for deaeration [27]. This enhanced configuration may therefore be referred to as vacuum-enhanced AGMD or V-AGMD. It is important to note that in V-AGMD, the vacuum pressure in the gap is limited by the vapour pressure and does not contribute to the process driving force that is still solely generated by the temperature gradient. Also for V-AGMD, special attention has to be paid to the limiting *LEP* and the increased risk of pore wetting compared to aerated AGMD operation.

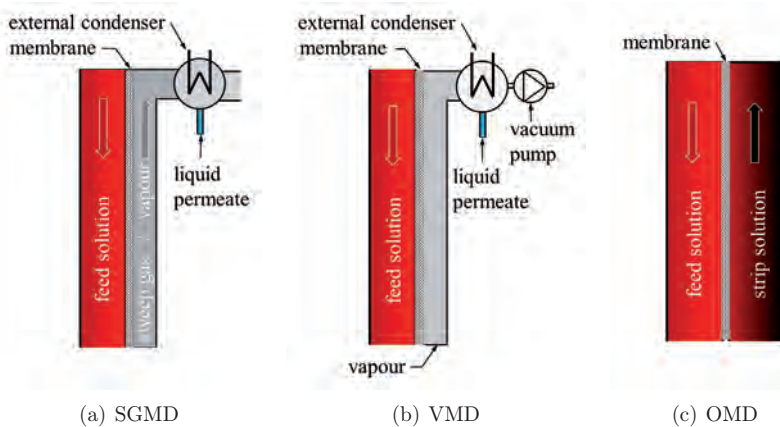


Figure 2.3: MD configurations driven by approaches other than a temperature difference

2.2.4 Sweeping Gas Membrane Distillation

The Sweeping Gas Membrane Distillation (SGMD) configuration, illustrated in Fig. 2.3(a), implements a two-channel configuration. The feed solution is circulated parallel to the membrane in the evaporator channel and establishes a liquid-vapour interface at the feed side of the membrane. A cold inert sweep gas is introduced into the flow channel on the permeate side of the membrane by forced convection, which is generated by means of a compressor. A vapour pressure gradient develops depending on the temperature difference from the feed solution to the sweep gas and the vapour content of the sweep gas. The volatile compounds evaporate at the liquid-vapour interface on the feed side, pass the membrane and get swept out of the module by the sweep gas stream while remaining in the gaseous phase. Due to the low thermal capacity of the gas stream, a significant gain in temperature is observed for the sweep gas during convection through the module based on the absorption of the warm vapour and conductive heat transfer from the warm membrane surface. The rapid convergence of the sweep gas temperature to the almost constant feed temperature limits the SGMD flux performance. High sweep gas flow velocities and short flow channels therefore benefit SGMD flux performance [28]. The vapour condensation and subsequent permeate extraction takes place in a condenser located outside of the module. Similarly to the AGMD configuration, the liquid permeate has no direct contact with the back of the membrane, so SGMD is suitable for the separation of compounds with low surface tension such as alcohols from aqueous solutions [29, 30].

The gas introduces an insulating feature which allows operation with reduced conductive heat losses compared to a DCMD channel configuration [31]. Due to limited heat transfer characteristics on the gas side compared to the feed side, temperature polarisation on the gas side by far dominates the overall temperature polarisation, also calling for high sweep gas velocities [28]. However, the sweep gas velocity is limited by the pressure loss within the sweep gas channel, which must not exceed the hydraulic pressure on the feed side of the membrane.

In order to reduce the temperature gain of the sweep gas, a cold surface for gas cooling may be introduced, similar to an AGMD channel configuration [32, 33]. For this alternative channel configuration, also referred to as thermostatic SGMD, the vapour partially condenses on the cold surface inside the module, which imposes additional constraints on module design. Other than by a temperature gradient, a driving force may also be established by simply using a dry strip gas that is enriched with vapour from the saturated liquid-vapour interface while passing the open membrane pores in the flow channel, e.g. for the application of air humidification [34].

2.2.5 Vacuum Membrane Distillation

The Vacuum Membrane Distillation (VMD) configuration, illustrated in Fig. 2.3(b), considers a two-channel arrangement quite similar to that of SGMD. The feed solution is circulated parallel to the membrane in the evaporator channel and establishes a liquid-vapour interface at the feed side

of the membrane. The flow channel on the permeate side of the membrane is designed as a dead-end channel, providing only one access point at which vacuum is applied by means of a vacuum pump. A vapour pressure difference is established by continuously evacuating the permeate side of the membrane to a pressure explicitly below the vapour pressure of the compounds that are to be removed from the feed. These compounds evaporate at the feed-side liquid-vapour interface, pass the membrane and stream towards the module exit point while remaining in the gaseous phase. Besides the vapours, the pressure gradient also removes non-condensable gases from the module. The vapour condensation and subsequent permeate extraction takes place in a condenser located outside of the module. Any remaining vapours and non-condensable gases are released through the vacuum system. Similarly to the AGMD configuration, the permeate has no direct contact with the back of the membrane, so VMD is suitable for the separation of compounds with low surface tension such as alcohols from diluted aqueous solutions [35, 36]. The driving force in VMD is adjustable independently of the feed temperature condition by active control of the vacuum pressure. A reasonable pressure gradient may be established also for low temperatures, which is an important feature considering the treatment of thermally sensitive solutions such as solutions with aromas or pharmaceutical compounds [37, 38].

It is important to note that the absolute pressure difference from the liquid phase to the gaseous phase increases, if vacuum is applied to the membrane pores. Thus, the role of the limiting *LEP* and the risk of pore wetting becomes more crucial for VMD compared to MD configurations that operate at atmospheric pressures. It is obvious that the maximal permissible hydraulic pressure on the feed side reduces accordingly. A beneficial effect of the vacuum conditions within the membrane pore volume and the permeate side flow channel is the absence of stagnant gases such as air that principally inhibit vapour transport. Furthermore, only one hydraulic boundary layer is limiting the heat transfer within the module. Low heat transfer resistance, low mass transfer resistance and high driving force are distinctive characteristics of the VMD configuration which is therefore considered the most powerful configuration with respect to potential flux [39]. The conductive heat losses in a VMD module are minimal, since no transmembrane temperature gradient is present. The thermal energy requirement almost reduces solely to the latent heat of evaporation. However, besides the thermal energy requirement, extensive use of the vacuum pump is essential and needs to be taken into consideration for a comprehensive energy evaluation.

Even though extremely high performance characteristics may be achieved with the VMD configuration, the practical relevance is considered to be limited. Most of the experimental work that has been published on VMD reports of laboratory scale test systems with small membrane samples and comparatively strong vacuum pumps. An effective permeate recovery requires condenser temperatures much lower than the ambient temperatures, so most of the VMD lab test systems include liquid nitrogen cold traps as condensers [39–41]. This approach does not seem reasonable for full-scale applications. Another factor hindering attractive full-scale VMD module design is the specific volume of vapours that significantly increases under vacuum conditions, demanding wide flow channels for internal vapour transport. However, laboratory scale VMD platforms may be efficiently used for membrane characterisation, since the VMD process is limited more than others by the membrane characteristics and is consequently quite sensitive to the respective

parameters. Furthermore, the VMD configuration offers advantageous features for the extraction of volatile organic compounds (VOCs) from dilute aqueous solutions, since the driving force may be adjusted independently of temperature conditions. Almost pure VOC flux is achieved if the absolute pressure on the permeate side is set below VOC vapour pressure but slightly above the actual water vapour pressure, thus completely avoiding a driving force for the water vapour [36].

2.2.6 Osmotic Membrane Distillation

Osmotic Membrane Distillation (OMD) is fundamentally configured identically to a standard DCMD channel set-up, implying an evaporator channel that is separated from the condenser channel by a hydrophobic, highly porous membrane. The feed solution is circulated parallel to the membrane in the evaporator channel and establishes a liquid-vapour interface at the feed side of the membrane. The vapour pressure gradient is established by means of a hygroscopic strip solution, typically a concentrated brine, which is applied on the permeate side of the membrane. If the strip solution exhibits lower vapour pressure than the feed solution, the volatile compounds evaporate at the liquid-vapour interface, pass the membrane pores and absorb into the strip solution. Since the permeate is absorbed by the strip solution, OMD is usually applied for the concentration of valuable solutions by the extraction of water rather than for the extraction of a valuable permeate. It is important to note that the strip solution is continuously diluted by the permeate during OMD operation, so the strip solution needs to be recovered in a separate recycling process in order to retain its essential hypertonic characteristic [42]. Since the OMD process can be performed under low temperature conditions, it is specifically attractive for the concentration of thermally sensitive feed solutions such as solutions with aromas or pharmaceutical compounds [42].

As in any MD process, the latent heat of evaporation is removed from the surface of evaporation and the temperature decreases at the liquid-vapour interface on the feed side. The latent heat is rejected at the surface of condensation and the temperature increases at the liquid-vapour interface on the permeate side. Consequently a negative transmembrane temperature gradient develops even though isothermal conditions are applied within the bulk liquid phases [43]. The negative temperature gradient reduces the positive vapour pressure gradient, but establishes a driving force for conductive heat transfer through the membrane in the opposite direction to the vapour flux. The required heat of evaporation is therefore directly recovered through the membrane during an OMD process. High thermal conductivity reduces the negative temperature gradient and therefore improves the process efficiency. It is important to note that the desired membrane property requirement regarding thermal conductivity is opposite to the desired characteristics in conventional MD processes that generally benefit from membranes with low thermal conductivity. Since the OMD driving force directly refers to the interfacial concentration of the strip solution, the process is considered to be more sensitive with respect to concentration polarisation phenomena than conventional MD processes [44].

It is worth mentioning that the basic idea of the OMD process may also be applied in a com-

bined DCMD-OMD process. In this variant, a temperature gradient is applied additionally to the permeate side strip solution, which results in an enhanced overall driving force [45].

2.3 Heat Recovery Strategies

In MD processes, an enormous amount of heat is transferred through the membrane, mainly as latent heat but partially also from conductive heat transfer. The minimum heat requirement in the evaporator channel is given by the latent heat of evaporation that is essentially required for the desired phase change and consequently for permeate production. Considering such an ideal case for an MD water separation process, the thermal energy requirement in the evaporator channel would be about 655 kWh per ton of permeate¹. In a real MD process, conductive transmembrane heat losses also need to be taken into consideration, resulting in an even higher energy requirement ($>655 \text{ kWh t}^{-1}$). If the required thermal energy is produced exclusively for the MD process or a limited resource of available heat is utilised, the thermal energy has a certain value and thermal process efficiency becomes a crucial MD process specification defining its competitiveness and economic feasibility. Therefore, the relevance of heat recovery in MD had already been identified in the early stage of MD development [46–48]. The basic heat recovery concepts usually considered in MD may be categorised according to two principal approaches that are closely related to those established in conventional thermal desalination technologies. The sensible heat recovery concept, illustrated in Fig. 2.4(a), is similar to the MSF approach, while the latent heat recovery concept, illustrated in Fig. 2.4(b), is similar to the MED approach. It is worth mentioning that the heat recovery concepts reduce the potentially required cooling demand at the same time.

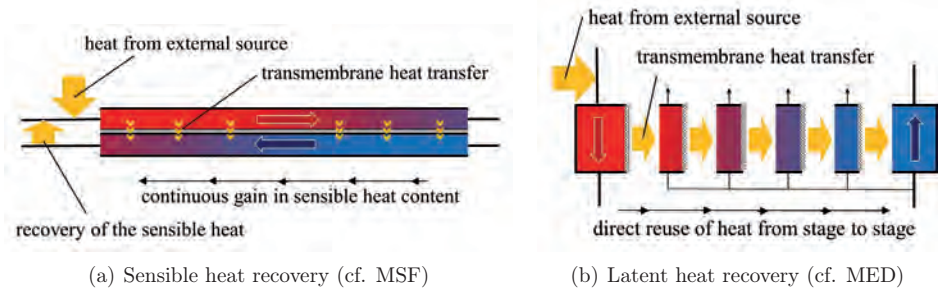


Figure 2.4: Basic heat recovery concepts suitable for MD applications.

¹A latent heat of 655 kWh per ton corresponds to a mean temperature level of about 60 °C.

2.3.1 Sensible Heat Recovery

For a sensible heat recovery approach, cold fluid is introduced into the condenser channel acting as a coolant. While circulating through the condenser channel, the coolant gains heat from the evaporator channel. The temperature of the coolant continuously increases until it leaves the condenser flow channel at a higher temperature. The heat that has been transferred through the membrane in the form of latent heat and conduction is stored within the coolant in the form of sensible heat. This sensible heat may partially be recovered by pre-heating a colder feed stream before applying heat from an external source. It is obvious that the temperature at the condenser outlet must exceed the temperature of the feed stream for heat recovery to be possible². The potential for heat recovery depends on the temperature difference between the condenser outlet and the cold feed stream, so a high temperature level at the condenser outlet is desired. The sensible heat recovery concept is applicable for DCMD, PGMD and AGMD. A large membrane transfer surface area fundamentally favours effective heat recovery. Long module flow channels that may either be constructed within a single module or by a series connection of multiple modules are characteristic for an implemented sensible heat recovery concept. In the related MSF approach, a high number of discrete stages would be comparable to long membrane module flow channels. Due to the continuous temperature profile along the module flow channels, this sensible heat recovery concept has also been denoted as an “infinite-stage flash” approach [46]. The sensible heat recovery concept is simple to implement, robust and offers high heat recovery performance at low system complexity. A major drawback is the high pumping effort for the essential circulation of the warm fluid in the long flow channels.

In DCMD, the condenser channel is operated with permeate and a heat exchanger must be applied to transfer the sensible heat from the warm permeate to the cold feed. In PGMD and AGMD, an impermeable film separates the permeate from the coolant and the condenser channel may be operated directly with the feed solution. In this variant, the pre-heating of the feed takes place within the condenser flow channel and no additional recovery heat exchanger is required. In VMD and SGMD, the temperature level of the external condenser is usually significantly lower than that of the feed solution, which obviates the implementation of a heat recovery concept.

It should be noted that this thesis covers a comprehensive evaluation of the MD process with and without heat recovery. If heat recovery is applied, the implementation is exclusively based on the concept of sensible heat recovery.

2.3.2 Latent Heat Recovery

The latent heat recovery concept considers a first stage evaporator at which heat from an external source is applied. The feed is evaporated at the respective liquid-vapour interface and the vapour is transferred through the membrane towards the condensation surface. During condensation,

²unless a heat pump is used.

the latent heat is expelled, transferred through an impermeable layer into the following stage and directly causes heating and evaporation of the feed solution from a thin inter-feed channel. In this way, the heat is passed from stage to stage, following the temperature gradient that is applied from the evaporator to the final condenser. In the final condenser, the heat is removed at a low temperature level. The heat that has originally been supplied to the first stage is reused at every stage, so the overall heat recovery efficiency mainly depends on the total number of stages. It is important to note that a certain fraction of the available heat is required for heating up the cold feed solution in the inter-feed channels until it reaches the respective state of evaporation. An MD process that applies latent heat recovery may be considered a membrane-based MED process, also denoted as MEMD. From a thermodynamic point of view, the latent heat recovery concept is considered the superior approach due to the direct local recovery of the latent heat into the following stage. The heat does not require interim storage and circulation in the form of sensible heat, so pumping effort is reduced. A drawback of the concept is increased system complexity to achieve the optimal flow rate and flow distribution within the individual inter-feed channels. Furthermore, the thin inter-feed channels may introduce a higher risk of channel clogging due to fouling and scaling.

The latent heat recovery concept is especially suitable for PGMD and AGMD. These MD configurations feature an impermeable wall that is required for separation of the individual stages.

2.4 Membranes

The main function of the membrane in MD is reliable support for the liquid-vapour interface that needs to be defined and maintained in any MD configuration. The hydrophobic surface property, mechanical stability, thermal stability and chemical stability are therefore the most essential requirements for MD membranes. Since the membrane automatically introduces a mass transfer resistance for the desired transmembrane vapour transfer, the membrane structural properties should offer the highest possible vapour permeability. Consequently, thin layers with high porosity, large pore size and low tortuosity represent favoured structural characteristics resulting in high membrane permeability. However, the definition of an optimal membrane design is constrained by different conflicting requirements. The maximal pore size is limited by the essential non-wetting criterion while the porosity and the membrane thickness need to ensure appropriate mechanical stability. To determine the optimal membrane thickness, further considerations need to include the opposing thermodynamic requirements of high vapour permeability and low conductive heat transfer.

The materials for MD membranes should meet the desired mechanical, thermal and chemical stability requirements combined with low surface tension, low thermal conductivity, low absorptivity with respect to water, appropriate processability and eventually low cost. High grade polymers such as polypropylene (PP), polyvinylidene fluoride (PVDF) or polytetrafluoroethylene (PTFE) are usually considered for MD membranes. These non-polar polymers naturally feature

excellent hydrophobic characteristics with respect to the bi-polar water properties. However, highly hydrophobic surface properties may also be achieved with other materials in combination with surface modification techniques such as hydrophobic surface coating. The hydrophobic nature of a surface may be quantified by a contact angle measurement. For a hydrophobic surface, a water droplet has a contact angle $\theta > 90^\circ$ with respect to the solid surface and larger contact angles indicate greater hydrophobicity. The highly hydrophobic character of an expanded PTFE membrane with respect to tap water is illustrated in Fig. 2.5(a). A reduced contact angle of tap water that has been slightly contaminated with tensides is illustrated in Fig. 2.5(b).

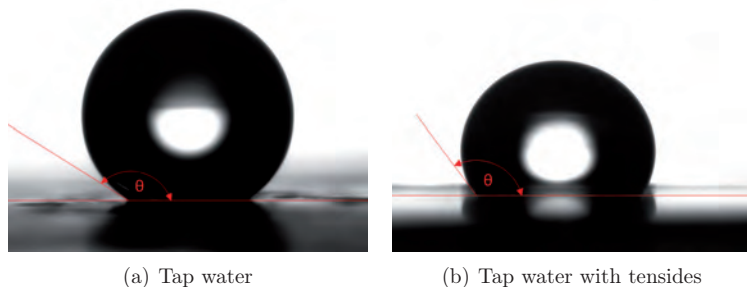


Figure 2.5: Contact angle of water droplets on a micro-porous ePTFE membrane surface

A theoretical evaluation of the expected *LEP* by Eq. 2.2 indicates whether a membrane is suitable for a specific MD application or not. The most application-oriented way to evaluate the suitability of a membrane is experimental evaluation of the *LEP*. This method also allows the evaluation of non-accessible membrane layers that might be covered by additional membrane layers, support structures or fouling layers. An experimental evaluation of the *LEP* with respect to water for various commercially available PP, PVDF and PTFE membranes with different maximal pore sizes is provided in Fig. 2.6(a) [49]. The results clearly validate the inverse dependence of the *LEP* on the maximal pore size, as predicted by Eq. 2.2. It is important to note, that porous membrane structures usually exhibit non-uniform pore geometries. A typical pore size distribution for a commercial capillary PP membrane is provided in Fig. 2.6(b) [49]. In this sample, the maximal pore size is about double the mean pore size. Fundamentally, a narrow pore size distribution is beneficial for MD membranes in order to obtain a high limiting *LEP* for a given mean pore size. The common nominal pore sizes for membranes applied in MD range from $0.02 \mu\text{m}$ to $1.00 \mu\text{m}$, which directly refers to the non-wetting constraint, considering usual pore size distributions and operational pressures. It is important to also include a safety factor, since the *LEP* is expected to reduce over time due to surface deterioration phenomena and effects caused by potential fouling deposition.

Since the suitable membrane pore size is mainly defined by the surface tension of the feed solution, smaller pore systems are principally needed for feed solutions with reduced surface tension. For a given membrane, critical wetting concentrations can be derived for different compounds [13].

The most common membranes are available either as flat sheets or as cylinders. The cylindrical

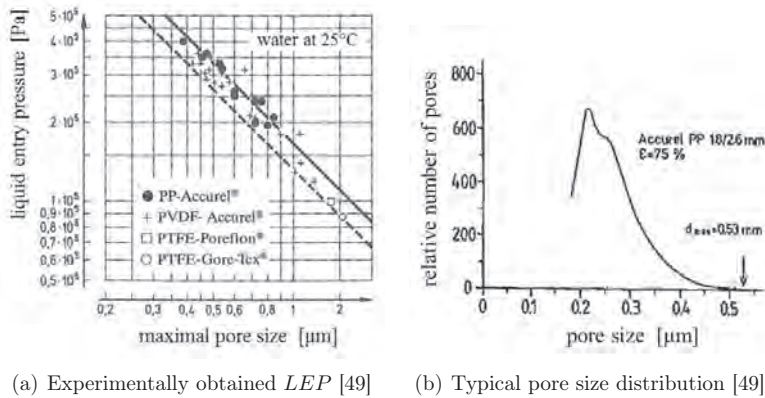


Figure 2.6: Influence of geometrical membrane specifications on the suitability for MD applications.

membranes are further categorised with respect to their diameter into tubular (6 – 25 mm), capillary (400 – 6000 μm) and hollow fibre (80 – 400 μm) membranes [50]. In MD, either flat sheet membranes or capillary membranes are applied.

Different techniques are available for the fabrication of porous membrane structures from polymers. A brief overview of the most relevant membrane fabrication techniques is presented in the following paragraphs, referring to pertinent literature that provides much more detailed descriptions if needed [12, 50, 51].

For phase inversion, the polymers are dissolved in a solvent. Subsequently, the homogeneous solution is cast as a flat sheet membrane or spun to form a capillary membrane. During this process, phase inversion is triggered and the polymer precipitates while the solvent remains liquid and forms the pore system. The phase inversion may either be induced thermally or by a change of the solvent concentration or the addition of a coagulant. The structural membrane characteristics are defined by the concentrations and the control of the phase inversion kinetics. The phase inversion technique may be used for the production of symmetric, asymmetric or multi-layered membranes of PP and PVDF.

Mono-axial or bi-axial stretch forming is a suitable fabrication technique to form highly porous membrane structures from partially crystalline polymer films. The polymer film is then stretched vertically to the directed crystalline regions, triggering micro-cracks that are expanded until the desired pore characteristics are obtained. Stretch forming may be performed in several stages, directions and temperatures. In some processes, solvents are applied for intermediate swelling and drying procedures that help to control the final pore structure. Residual stress within the stretched membranes is reduced by subsequent tempering. Highly sophisticated stretch forming processes are applied for the production of PTFE membranes.

It is important to note that commercial membranes specifically developed for MD applications are not available so far. However, the fundamental technical membrane requirements for MD

membranes are quite similar to those for common microfiltration media, especially with respect to the desired pore geometry. Thus, commercial flat sheet and capillary microfiltration membranes are widely used in the context of MD. A review of various commercially available membranes used in MD, including their structural properties, has been published [51]. All of the listed membranes are symmetric, single hydrophobic layer membranes. The ranges of the presented structural properties are summarised in Tab. 2.1. Even though wide parameter ranges are stated for porosity and mean pore size, most of the applications use membranes with a mean pore size of approximately $0.2\ \mu\text{m}$ and a porosity of 70 to 80%. Most of the flat sheet membranes offer a layer thickness $<100\ \mu\text{m}$, while common capillary membranes are significantly thicker. In order to achieve mechanical stability, the thin flat-sheet membranes are often laminated onto a mechanical support structure. SEM images of commercial PTFE, PP and PVDF membranes suitable for MD are presented in Fig. 2.7.

Table 2.1: Summary of structural properties of commercially available membranes that have been applied in MD [51].

		flat sheet membranes	capillary membranes
thickness	$[\mu\text{m}]$	25 – 140 ^a	35 – 1550
porosity	$[\%]$	34 – 90	35 – 75
mean pore size	$[\mu\text{m}]$	0.02 – 1.00	0.03 – 0.80

^aexcluding mechanical support layer

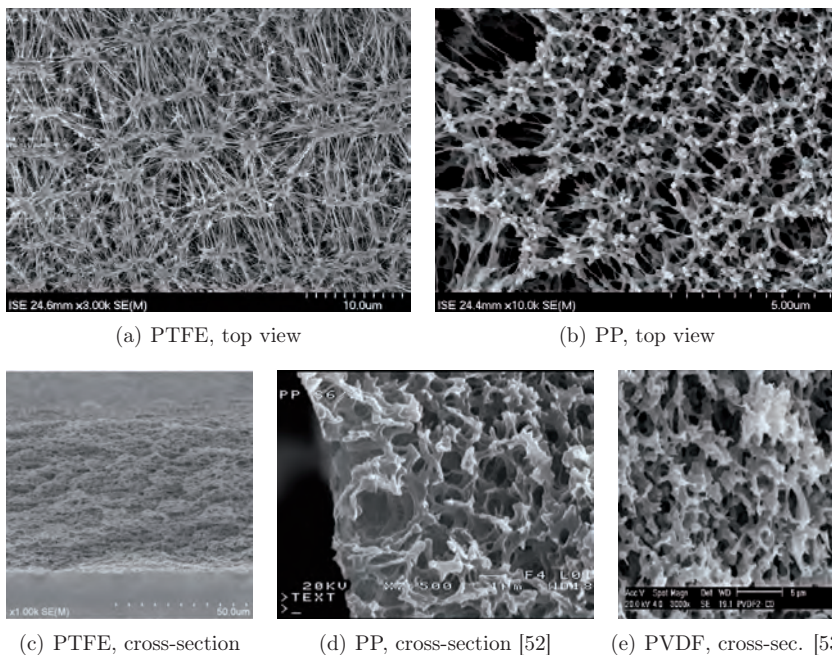


Figure 2.7: Commercially available membrane structures that are commonly applied in MD

The research activity in the field of MD membrane development has increased significantly in recent years. Various, mostly experimental approaches for the identification and preparation of optimised MD membrane structures have been pursued by iteratively making and characterising membranes on a laboratory scale. Current developments specifically address the application of asymmetric membranes, dual-layer or multi-layer membranes, composite membranes and membranes that have been subjected to different surface treatments [51].

An asymmetric membrane, which could consist of two or more functional layers, is characterised by non-uniform structural properties. In asymmetric membranes, the limiting fine porous active layer may be significantly thinner than in symmetric membranes. A sample of an asymmetric capillary dual-layer membrane made of PVDF is presented in Fig. 2.8(a). A fine porous thin outer layer provides a high wetting resistance, while a fingered macro-void inner layer provides effective mechanical support [54]. Further developments include co-polymer composite membranes with highly porous multi-layered pore structures and improved hydrophobicity [55]. An SEM image of a three-layer PVDF-HPF co-polymer capillary membrane is shown in Fig. 2.8(b). Novel co-polymer membranes have been fabricated by using a hydrophilic base polymer and fluorinated surface-modifying macromolecules (SMMs) that migrate towards the membrane surface during membrane formation and render a highly hydrophobic membrane surface. These hydrophobic-hydrophilic membranes are operated with a dry hydrophobic active layer and a wetted macro-void support layer. Enhanced mass transfer due to a thin active top-layer combined with reduced conductive heat losses due to a thick hydrophilic sub-layer has been proposed [56]. The ultra-thin hydrophobic top-layer formed by novel SMMs can be clearly identified on a PES bulk structure in Fig. 2.8(c). Surface treatment of commercial membranes has also been proposed to improve their hydrophobic surface characteristics and fouling resistance. Commercial PP hollow fibre membranes have been coated with a ultra-thin micro-porous fluorosilicone layer by plasma polymerisation [41]. Initial attempts to apply novel PVDF nano-fibre membranes in MD have been made. This promising new generation of membranes prepared by an electrospinning technique is still in the first phase of development but seems to offer much higher hydrophobic characteristics than membranes fabricated by phase inversion [57].

All of these novel membranes are made in the laboratory for scientific purpose, not providing a practical alternative to the adaptation of commercially available membranes with a single hydrophobic layer that were originally optimised and applied in other membrane processes. The experimental and theoretical work within this thesis has concentrated on materials feasible for real application. Consequently a focus is placed on commercially available symmetric membranes consisting on a single hydrophobic layer.

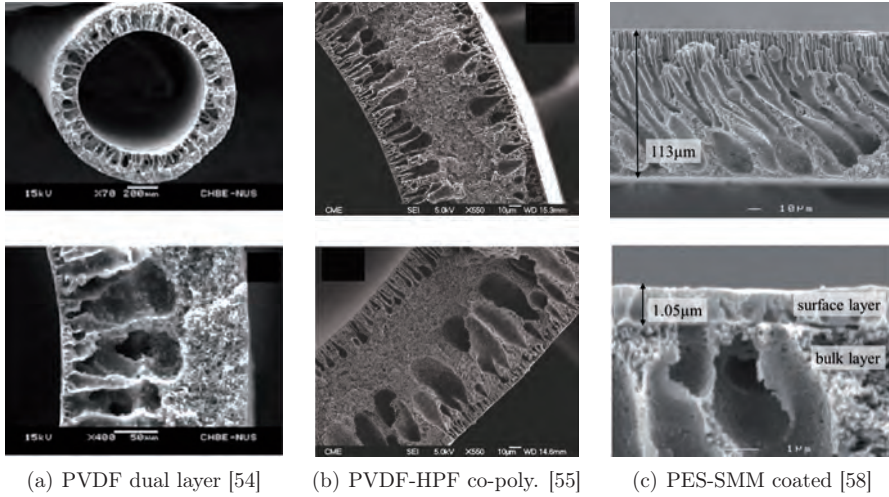


Figure 2.8: Laboratory samples of advanced membrane structures proposed for MD.

2.5 Membrane Modules

The membrane module is defined as a device that integrates the membrane into a functional package including the membrane, the membrane mounting, a housing, flow channels with respective inlets and outlets and mountings. The design of a MD module is always based on one of the basic channel configurations from Figs. 2.2 and 2.3 that have already been introduced and discussed in Sec. 2.2. A summary of the most important technical requirements for the design of MD membrane modules now follows.

The main function of the module is to provide a seal and robust mounting for the membranes and complete separation of the different working fluids. No leakage between the different functional fluid channels is allowed. The flow channels have to be designed so that deflection or rupture of the thin and elastic membrane or film materials is avoided. The materials that are in contact with the working fluids need to provide appropriate chemical resistance, while the whole module needs to provide suitable thermal resistance to withstand the projected operational conditions. The module has to comply with the mechanical and thermal loads applied during assembly and operation. Hydraulic pressure loads may have asymmetric characteristics. Static pressure loads depend on channel height position and pressure loads based on channel flow depend on channel length position. Furthermore, the dynamic behaviour of the pressure loads and thermal expansion during start-up and shut-down phases as well as during non-steady-state operation has to be taken into consideration. Especially for MD modules of reasonable size, thermal expansion is a serious issue, since the MD implies operation with potentially high temperature gradients.

Besides the essential requirements concerning material and stability, an MD membrane module has to achieve a high volumetric packing fraction and high thermodynamic MD process perfor-

mance in terms of flux and energy efficiency. Both requirements are strongly affected by module design parameters such as membrane selection and flow channel geometry. The hydraulic flow velocity, the flow regime and the flow distribution defines heat and mass transfer as well as the hydraulic pressure losses within the flow channels. High heat and mass transfer and low hydraulic pressure loss are opposing requirements that need to be optimised. A homogeneous flow distribution without dead corners is desired. To minimise exergy loss during dynamic operation, the thermal capacity of the module should be fairly low. In order to reduce heat losses to the ambient, either an adapted module channel configuration or thermal insulation has to be considered.

The module design needs to allow adequate air bleeding while the flow channels are being filled and during operation. Operational and maintenance effort may be reduced significantly by preventive module design. Module design may at least partially prevent fouling and scaling, but fouling and scaling always occurs to a certain extent and the channel design should allow flushing and cleaning. Moreover, the module design should allow the membrane to dry out in order to regenerate the essential hydrophobic membrane feature after pore wetting. The maintenance cost are significantly reduced for modules that allow disassembly. Module components that have different lifetimes may be replaced separately e.g. selective or complete membrane replacement without replacing the potentially expensive housing or mechanical framework.

If a low thermal energy demand is of interest, the module design should allow the implementation of an effective heat recovery strategy as introduced in Sec. 2.3, either by fully integrating it into the membrane module or by utilising additional external components. The heat recovery concept may be implemented with a single membrane module or by specifically combining multiple modules. The external piping requirement for the hydraulic integration of the MD module into a system is to be considered in module design. Especially if many modules are connected, aiming for higher system efficiency or higher output capacities, piping could play an important role in the overall system costs. It is obvious that weight and the geometrical dimensions of a single module package should allow module handling.

Eventually the module should offer long lifetime, good recyclability and low cost, which affects material selection as well as issues regarding fabrication and assembly.

2.5.1 Module Design Concepts

A multitude of different membrane modules have been developed, addressing a wide variety of different process requirements throughout membrane technologies. The module designs are categorised with respect to the basic design principle and the membrane type [50]. Considering an MD process, the usual design for capillary membrane modules applied shell-and-tube concepts while the most relevant module designs for flat sheet membranes are plate-and-frame as well as spiral-wound concepts. Schematic illustrations of the different basic design types are presented in Fig. 2.9. Any of the module types may be designed and operated in counter-current flow, co-current flow or cross flow.

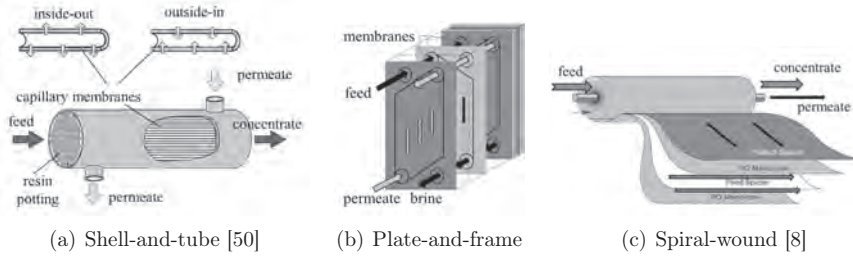


Figure 2.9: Schematic illustration of the different basic module design principles.

Shell-and-tube membrane modules

The shell-and-tube module design principle is usually applied for cylindrical membranes and may consequently be categorised into shell-and-tube modules for tubular, capillary and hollow fibre membranes. The membranes are arranged more or less in parallel and potted with a resin at both face ends. The membrane bundle is integrated into a tubular shell structure, enclosing the fluid channel on the shell-side of the membrane. The single membranes are connected in parallel and the lumen side of the membranes is fed from a head structure. Depending on the module dimensions and the arrangement of the shell side inlets and outlets, the module may be operated in counter-current flow, co-current flow, cross flow or mixed flow mode. Some module designs include baffles in the shell-side fluid channel to achieve a specific flow pattern.

Modules with tubular membranes resist membrane clogging very well, allow efficient cleaning and exhibit low pressure loss. Consequently, these modules are suitable for feeds with high particle content, high fouling potential or high viscosity, such as biological waste waters. Because of the large membrane diameters, mechanical support of the membranes is required and the modules offer a limited volumetric packing fraction that has been proposed to be $<80 \text{ m}^2 \text{ m}^{-3}$ [50].

Modules with capillary membranes allow significantly higher packing fractions due to the smaller membrane diameters. Packing fractions $<1000 \text{ m}^2 \text{ m}^{-3}$ are described in the literature [50]. The capillary membranes feature high geometrical stability and may be used for inside-out or outside-in operation without mechanical support. Due to the small characteristic flow channel diameters, laminar flow regimes hinder effective heat and mass transfer. Random fibre packing leads to flow maldistribution on the shell side of the membranes which is minimised by high packing fractions [59]. The use of braided or twisted membrane bundles and baffles is a concept which has been suggested to achieve uniform flow distribution and enhanced heat and mass transfer [49, 60]. The membranes with small diameters have a high potential for clogging and impede effective membrane cleaning. The feed should therefore have low clogging potential. As a preventive measure, increased pre-treatment or maintenance effort has to be taken into account. It is important to note that membrane replacement concerns an entire membrane bundle rather than single membranes. If the module is designed as an integrated component including the shell-tube and the head structure, the entire module needs to be replaced if the membrane ruptures or clogs up. Shell-and-tube modules with capillary membranes are widely used for microfiltration (MF)

and ultrafiltration (UF), dialysis (DL) and gas permeation (GP) [50].

Shell-and-tube modules with hollow fibre membranes are similar in principle to capillary membrane modules. Volumetric packing fractions of up to $10\,000\text{ m}^2\text{ m}^{-3}$ have been described in the relevant literature [50]. Due to the micro-channel membrane geometry, these modules may only be applied in applications with quite pure feeds. The hollow fibre membrane modules are commonly applied in dialysis (DL) and gas permeation (GP) [50].

The module design with capillary membranes is considered the most promising shell-and-tube design in the context of MD, especially for the design of two-channel configurations as given in DCMD, VMD, SGMD and OMD. It is important to note that the use of capillary membranes introduces fundamental difficulties for the design of the more complex PGMD and AGMD flow channels.

Plate-and-frame membrane modules

The plate-and-frame design principle is used to mount flat sheet membranes within flat frames. The flat flow channels are equipped with channel spacers to mechanically support the thin membrane and film materials. The flow channels are enclosed by stacking potentially similar frames on top of each other. The flow channel width is defined by the width of the single frames and spacers and commonly ranges from 0.5 to 5.0 mm. The key issue for plate-and-frame membrane modules is the connection of the membrane to the frame that is achieved either by sealing gaskets or by welding techniques. At the face ends, the module is closed by end plates that provide mechanical support and the module's inlet and outlet connections. The overall transfer area is adjusted by simply defining the number of frames that are stacked in parallel or series. The different flow channels are fed from central manifolds that are integrated into the frames, allowing co-current flow, counter-current flow or cross-flow design. Based on these design characteristics, the plate-and-frame modules allow easy scale-up with minimal external plumbing. Moreover, the plate-and-frame module concept allows the assembly of different channel configurations based on only a few standard frame components. Thus, there is great potential for automation, modularity and custom configuration of modules. Depending on the stacking technique, disassembly is feasible and either the single membranes or membrane sub-packages may be accessed for analysis, cleaning or replacement. However, plate-and-frame modules cannot compete with shell-and-tube capillary membrane modules in terms of packing fraction. Depending on the width of the single frames, potential packing fractions for plate-and-frame modules are stated to be less than $400\text{ m}^2\text{ m}^{-3}$ [50]. The heat and mass transfer characteristics in the flat flow channels is mainly defined by the channel spacers, which offer great potential for module optimisation. The flat flow channels are quite robust with respect to fouling and clogging.

The plate-and-frame design is widely known from conventional heat exchangers. In membrane technologies, plate-and-frame flat sheet membrane modules are used in microfiltration (MF) and ultrafiltration (UF), electro-dialysis (ED) and pervaporation (PV) [50]. The plate-and-frame

type of modules also represent a suitable module configuration for different MD applications. Not only the simpler two-channel arrangements for DCMD, VMD, SGMD and OMD can be implemented but the more complex channel configurations for PGMD and AGMD are feasible by simple integration of an additional frame layer and corresponding access points.

Spiral-wound membrane modules

In spiral-wound modules, flat sheet membranes are wound around a central tube. The spiral-wound module was originally developed for reverse osmosis (RO), so the conventional design is optimised for the high-pressure membrane process and implements a two-channel cross-flow arrangement as illustrated in Fig. 2.9(c). In this design, the membrane is folded and sealed to form an envelope with one open side. Several of these membrane envelopes are then hydraulically connected to the central manifold and wound around it. The spiral-wound membrane coil is then inserted into a strong cylindrical pressure vessel. The outer surface of the membrane envelopes is on the pressurised feed side and the inside of the envelopes is the low-pressure permeate side. Each side is equipped with a channel spacer. The thin permeate spacer supports the membrane envelope against operational pressure while the thicker feed spacer (0.5 to 1.0 mm) acts as a turbulence promoter to reduce concentration polarisation. The feed is circulated through the module axially from one open end to the other, while the permeate follows the spiral-wound channels formed by the membrane envelopes and collects in the central tubing. Based on the thin flow channels, the common spiral-wound modules exhibit the highest volumetric packing fractions among the flat-sheet membrane modules, reaching values up to $1000 \text{ m}^2 \text{ m}^{-3}$ [50]. However, the thin flow channels introduce high risk with respect to channel clogging and non-optimal conditions for channel cleaning. Extensive pre-treatment may be necessary. In the case of channel clogging or membrane failure, the membrane coils can be replaced while keeping the expensive pressure vessel. Usually multiple spiral coils are arranged in series connection within one pressure vessel.

The conventional spiral-wound module design is widely used in pressurised water treatment. Nowadays RO is operated almost exclusively with this type of modules. The spiral-wound module design is also applied for ultrafiltration (UF) and nanofiltration (NF) [50].

It is obvious that the classic channel configuration in spiral-wound modules is not suitable for MD processes. However, a modified version of the spiral-wound module concept with two symmetric and wider flow channels is applicable in MD two-channel configurations. A modification of the hydraulic inlet and outlet design also allows operation in co-current flow, counter-current flow or mixed flow. The implementation of the more complex three-channel arrangements for PGMD and AGMD is feasible by integration of an additional layer and respective access points. It is important to note that the flow channel widths in MD modules are usually larger than those of classical spiral-wound RO, NF or UF modules. Consequently, the packing fractions that might be achieved in modified spiral-wound MD modules may not exceed those of similar plate-and-frame MD modules.

2.5.2 Performance Parameters for Membrane Distillation Modules

The definition of generic MD module performance parameters allows comparative evaluation of the performance characteristics given for different modules and different operation conditions. Selected parameters for the evaluation of thermodynamic MD module performance are briefly introduced in the following section. It is important to note that a more comprehensive introduction is provided in Sec. 4.1.4.

A flux characterises a area-specific mass transfer rate of a membrane. The average flux of a MD module j_P is evaluated by referring the total permeate output rate \dot{m}_P to the total membrane surface area A_M of the module according to Eq. 2.3.

$$j_P = \frac{\dot{m}_P}{A_M} \quad (2.3)$$

The specific thermal energy consumption q_{HX} represents the amount of thermal energy that is required to produce one ton of product water. The specific thermal energy consumption is evaluated from the thermal power input \dot{Q}_{HX} and the corresponding permeate output rate \dot{m}_P according to Eqs. 2.4.

$$q_{HX} = \frac{\dot{Q}_{HX}}{\dot{m}_P} \quad (2.4)$$

An alternative representation of the specific thermal energy consumption, usually used to evaluate steam-driven thermal desalination systems, is given by the Gained Output Ratio (GOR). It typically indicates how much product water is produced by the latent heat Δh_v of 1 kg of heating steam [6]. However, also in the context of desalination processes that utilise other heat sources than direct steam, the representation of the GOR is applied, using the modified definition according to Eq. 2.5 [51].

$$GOR = \frac{\dot{m}_P \Delta h_v}{\dot{Q}_{heat}} \quad (2.5)$$

The GOR can be interpreted as thermal energy savings with respect to pure ideal evaporation without heat recovery. An MD process without heat recovery is characterised by $GOR < 1$. The GOR can only exceed unity, if heat recovery is introduced. In an example where the GOR is 5, only 20% of the required latent heat has to be provided by an external source.

2.5.3 Commercial Membrane Distillation Module Developments

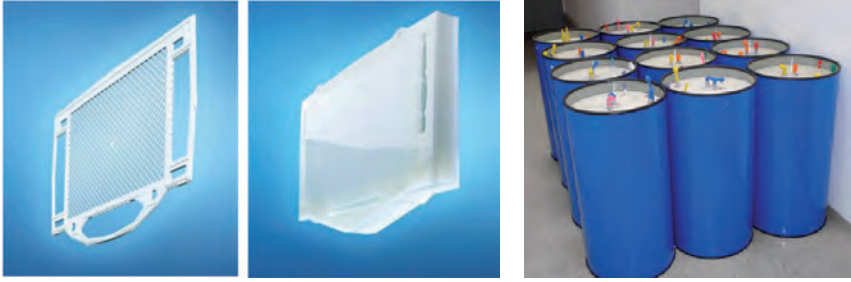
The commercial potential of the MD process was recognised in the early stage of MD development. A first series of patents was filed in the 60's in order to protect the principle process concepts. The MD process was first introduced by a patent in 1963 [61] considering the basic DCMD configuration. A further patent filed in 1967 suggests the use of advanced hydrophobic membrane materials (PE, PP, PVC, PTFE) and introduces an improved process configuration

(PGMD) allowing internal heat recovery by stacking or coiling the flow channels (plate-and-frame, spiral-wound) [47]. In 1968, a patent considers a parallel array of tubular membranes (shell-and-tube) for implementing a process configuration known as SGMD [62]. Also the option of establishing low vapour pressure by means of a vacuum has been suggested (VMD). However, interest in the MD process was lost due to the limited availability of suitable membranes and low flux compared to that of reverse osmosis (RO). In the 80's, MD regained scientific and commercial interest based on the availability of advanced membranes and modules with better characteristics. W.L.Gore & Associates developed and patented a spiral-wound PGMD module that uses highly porous expanded PTFE membranes in 1982 [63]. The module design was introduced as "Gore-Tex Membrane Distillation" [64]. Other activities in full-scale module development were conducted by Akzo which presented experimental studies on large shell-and-tube DCMD modules with capillary PP membranes [49]. The cylindrical module had a channel length of 2.0 m, a diameter of 0.25 m and a membrane area of 50 to 100 m². Operated in the counter-current flow mode, sensible heat recovery in an external heat exchanger was considered. The modules were operated at fluxes from 6 to 50 kg (m² h)⁻¹. However, MD technology has not launched successful commercialisation for economic reasons.

In recent years, MD attracted significantly attention again and many research institutions are currently engaged in scientific work in this field. This is evident due to the increasing number of publications dealing with a variety of topics on MD and related technologies [51]. The companies MemSys, KeppelSeghers, SolarSpring and Scarab Development are pushing the commercialisation of the MD technology with the development of full-scale MD modules. Also Fraunhofer Institute for Solar Energy Systems (ISE) has been working on the development of full-scale MD modules and systems. A review of the recent MD module developments including the corresponding design approach, geometrical module specifications and thermodynamic module performance characteristics has been conducted by the author of this thesis. These approaches, summarised in the following section, may still be considered to be semi-commercial, but some of them seem to be close to successful commercialisation.

Scarab Development offers a semi-commercial AGMD plate-and-frame module based on PTFE membranes. A photograph of the Scarab MD module is provided in Fig. 2.10(c). One module has an active membrane surface area of 2.8 m², consisting of a cassette of 10 injection-moulded frames (63 cm × 73 cm × 1.7 cm) [67]. The air gap width is stated to be about 1.0 mm. Experimental results on the thermodynamic module performance characteristics are available in the literature. At high feed flow rates and operational temperatures of 80 °C, the flux has been reported to be about 9 kg (m² h)⁻¹ at a GOR of 0.9 [67]. A flux of 7 kg (m² h)⁻¹ at a GOR of 0.8 has been reported in a different study [70]. Since the single module does not offer internal heat recovery, a sensible heat recovery concept is suggested that is based on connecting several modules in series [67, 70].

An advanced V-AGMD plate-and-frame module approach is presented by MemSys. PTFE membranes are attached to injection-moulded frames (34 cm × 48 cm) that are illustrated in Fig. 2.10(a). Multiple frames are welded to form cassettes in parallel connection in order to adjust the surface area (0.31 m² to 2.5 m² per cassette) [65]. One integrated module stack consists



(a) Frame and cassette of MemSys V-MEMD mod. [65] (b) SolarSpring PGMD module [66]



(c) Scarab AGMD mod. [67] (d) KeppelSeghers PGMD mod. [68] (e) TNO AGMD mod. [69]

Figure 2.10: Different (semi-)commercial approaches to full-scale MD module development.

of multiple cassettes of different functionality including a steam raiser, 4 to 10 effects (stages) and a final condenser. Due to the similarity of the conceptual design to the conventional MED process, the concept is denoted as V-MEMD. Vacuum is applied to the module stages. Temperature and pressure reduce successively from stage to stage during operation. The module's internal latent heat recovery system offers a GOR from 2.5 to 6.0, depending on the number of stages. The active membrane area varies from 6 to 40 m², respectively [71]. Experimental results for a 4-stage module with 10 m² of membrane have been published by the inventors. For an operation at a heating temperature of 60 °C, the results show an average flux of about 3 kg (m² h)⁻¹ and GOR of about 3. For a two-stage system, a flux of about 9 kg (m² h)⁻¹ has been reported, still achieving a GOR of 1.7 [65]. Fluxes of about 7 kg (m² h)⁻¹ at a GOR of 3.2 have been reported for a module operated at a temperature of 85 °C [68].

The TNO research institute proposed a (V-)AGMD channel arrangement as a so-called “Memstill” concept [72, 73]. The concept was then taken over and improved by KeppelSeghers, switching over to a PGMD design. Bench scale plate-and-frame PGMD modules with different flat-sheet membranes, condenser walls and spacers have been built and characterised (500 cm × 1500 cm) [69]. Large stacked plate-and-frame modules with basic frame dimensions of 1000 cm × 1500 cm and a membrane surface area of 300 m² have been built for full-scale pilot plant testing. A photograph of this industrial scale approach is provided in Fig. 2.10(e). However, due to technical difficulties, the last period of pilot plant testing has been done with smaller modules originating

from improved automated production [69]. Performance results have been reported with fluxes of 3 to 5 kg (m² h)⁻¹ and GOR ranging from 3 to 6 for module operation with deaerated feed water [74]. The frame design allows parallel or series connection of the flow channels in order to define flow channel length for establishing a sensible heat recovery concept if required. Parallel and series module stack configurations with a membrane surface area of 1 × 9 m² and 3 × 3 m² respectively have been experimentally compared. For the series connection of three modules and operation at 80 °C, a flux of 5 kg (m² h)⁻¹ has been achieved at a GOR of 1.8 [75].

A spiral-wound PGMD module that is based on the former patent of Gore [63] has been further developed by the Fraunhofer Institute for Solar Energy Systems (ISE). Besides other module approaches, these prototypes are still being modified, improved and fabricated within different R&D projects, as for the studies reported in this thesis. A batch of modules that have been fabricated for a field test plant is illustrated in Fig. 2.10(b). The official spin-off company SolarSpring is promoting the commercialisation of the spiral-wound modules. The module flow channels (0.3 m to 1.0 m × 3 m to 20 m) equipped with flat-sheet PTFE membranes are spirally coiled, potted at the face ends and enclosed by glass fibre tubing [8, 66]. The module design with the long flow channels is tailored for an internal sensible heat recovery concept, allowing reasonable heat recovery at a low level of complexity. Comprehensive experimental results on the performance specifications have been published by the author of this thesis. For operation at 80 °C without deaeration, a flux of 2.5 kg (m² h)⁻¹ has been achieved at a GOR of 3.3 [66]. With deaeration, a flux of 3.0 kg (m² h)⁻¹ has been achieved at a GOR of 5.2, while at reduced flux, a GOR of 7.2 has been measured [22].

2.6 Advances in Membrane Distillation

Even though MD has not yet launched successful commercialisation, it is considered to be a technology with high potential for the future, offering several advantages compared to established separation technologies.

An MD system is similar in principle to a conventional thermal separation system. Thus, well studied methods of thermodynamic process optimisation for conventional thermal separation processes such as heat recovery strategies could be adopted efficiently to MD applications. The inclusion of membranes for the definition of the liquid-vapour interface introduces a great degree of freedom for geometrical module and flow channel design. Moreover, the entire vapour space is minimised to the volume of the membrane¹, allowing ultimate maximisation of the packing fraction. Unlike conventional thermal separation processes, vapour transport in MD is dominated by diffusive phenomena due to the minimised path length for mass transfer. As a consequence, low-temperature operation is feasible without applying vacuum and advanced separation control could be accessed in multi-component permeation problems by appropriate membrane selection, module design and operation. MD offers superior permeate quality since the membrane prevents

¹In AGMD the vapour space consists of the volume represented by the membrane and the air gap.

any entrainment of feed solution droplets into the product and acts as an effective barrier with respect to particles, bacteria, viruses and any non-volatile compounds. The underlying concept means that higher absolute pressure can be applied on the permeate side in order to ensure high permeate quality even in the case of membrane leakage. In contrast to film evaporators that require certain minimal flow rates to ensure full surface wetting, the liquid-vapour interfacial surface is well defined by the membrane and consequently independent of operational conditions. The membranes ensure permanent channel flooding and eliminate the risk of local dry-out that would reduce performance and promote fouling and scaling. Moreover, the low thermal capacity of the modules and their high robustness against dry-out qualifies the MD approach for dynamic operation, e.g. in combination with a fluctuating renewable energy supply. Due to the modular approach, MD is suitable for the full range of plant capacities, but specific advantages are given for small and medium size systems due to the possibility of implementing effective heat recovery concepts at low level of complexity. Conventional thermal separation systems are usually made of expensive stainless steels or other high-grade metals that are costly to process and still offer only limited corrosion resistance. Membrane modules are commonly manufactured of comparably cheap polymer materials, combining low processing cost and high chemical resistance. Unlike mechanical separation technologies such as RO that need to overcome osmotic pressure, thermal separation technologies offer superior thermodynamic suitability for the treatment of highly concentrated brines. However, the practical implementation in conventional MSF or MED processes is inhibited by issues of corrosion and scaling. MD seems perfectly suited for the treatment of highly concentrated brines since it combines thermodynamic feasibility, high corrosion resistance and a high level of scaling control.

2.7 Potential Fields of Application

The MD separation approach may be applied to any separation problem that is based on evaporation, if the essential non-wetting criterion is observed. MD technology is most commonly categorised with respect to the basic process configuration and channel design, as introduced in Sec. 2.2. Also the method of driving force generation, heat recovery strategy, module design concept or operational state may be referred to for MD technology categorisation. Other categorisation approaches focus on the addressed separation problem rather than on specific design aspects of the MD implementation. It is important to note that MD may be integrated in various ways in order to meet the requirements of different separation problems. In many applications a preferably pure permeate is the valuable product of interest, but in other applications, diluted brines are recycled by concentration or unwanted components are extracted from a valuable solution. Consequently, in MD either the brine, the permeate or both streams could be the desired product. MD is usually considered for the treatment of aqueous solutions with non-volatile compounds such as salts. In this case, only water vapour can pass the membrane and the separation mechanism is categorised as single-component permeation. The rejection rate

is nearly 100% and the permeate consists of water at very high purity, independent of the feed concentration [66]. It is important to note that even though the permeate quality is unaffected by the feed composition, the vapour pressure and consequently the process driving force and flux performance is usually influenced by a dissolved component [66]. If a feed solution contains compounds that are volatile under operational conditions, the porous membrane does not offer a full barrier function for other components in addition to water and multi-component permeation occurs. Different volatile components may either permeate in co-current or in counter-current directions. The separation and consequently the permeate and brine composition is strongly dependent on the respective driving forces and the permeabilities of the different permeating species. The driving forces are defined by the interfacial temperatures and concentrations while the permeabilities refer to the membrane structure, air gap dimensions and the molecular weight of the permeating species. The given dependences may be combined in various ways to adjust the separative behaviour in a multi-component permeation MD application, in order to optimise the process [76].

Based on the specific advantages listed in Sec. 2.6 and the versatility of the process, MD is attributed a high potential in several fields of application. The extraction of a pure valuable permeate from a feed with non-volatile salts may be considered the classical application for MD. Seawater desalination for the production of fresh water has been the most common application considered in MD research and pilot testing [10, 11, 69]. Other desalination applications address the production of ultra-pure water [67, 77]. Also in this thesis, desalination has been chosen as an exemplary application of interest. It is important to note that from a thermodynamic point of view, desalination is representative for any application that considers the extraction of pure water from a feed solution with non-volatile contaminants.

However, MD offers attractive performance for many other fields of application such as food and beverage processing, industrial and municipal waste water treatment, decontamination, resource recovery, medical applications or crystallisation. An indication of the suitability of MD in applications besides desalination may be obtained from the relevant literature. Selected references on representative separation problems have been reviewed.

In the field of food and beverages, MD has been successfully applied for gentle concentration of fruit juices [18]. OMD is considered a suitable configuration due to the operation at low temperatures in order to preserve sensitive aromatic and coloured compounds [78]. SGMD and VMD have been applied for the recovery of volatile fruit juice aroma compounds [79]. Furthermore, aroma-free sucrose solutions have been concentrated with AGMD and DCMD [18, 80, 81]. MD has also been studied in the dairy industry for the concentration of whey and milk, using moderate temperature conditions in order to prevent damage of the sensitive proteins [18, 82].

In the treatment of contaminated water, MD has provided high rejection of arsenic [83], heavy metals [84] and radioactive contaminants [85].

The removal of ammonia from waste water streams has been identified as feasible, but multi-component permeation has to be considered due to the volatile character of the gaseous ammonia

[86]. Industrial waste waters from the dye industry have been successfully concentrated by MD [87]. The treatment of acid solutions represents an attractive application for acid production or recovery as well as for the treatment of specific industrial waste waters. The concentration of acids based on DCMD has been studied for selected compounds. Mineral acids were represented by sulphuric, hydrochloric, phosphoric and nitric acids, while organic acids were represented by citric acid [88]. Further studies on the volatile hydrochloric acid have been presented due to the applicability for regeneration of pickling solutions. The multi-component diffusion of water vapour and hydrochloric acid gas was intensified by salt additives [89, 90]. An AGMD module has been used for the concentration of sulphuric acid, applying a latent heat recovery concept [91]. The concentration of humic acid with DCMD has been experimentally studied, specifically addressing the issue of membrane fouling [92, 93].

Azeotropes such as aqueous hydrochloric acid or formic acid cannot be concentrated beyond their azeotropic point when a conventional evaporation approach is applied. Considering mass transfer that is dominated by diffusive phenomena, individual mass transfer resistances for the different permeating species are defined by the membrane structure and the inert gas in the pore volume or air gap. Depending on the difference in molecule size of the permeating species, different transfer resistances define a selective mass transfer characteristic [76]. Based on a given selectivity, MD allows azeotropic mixtures to be separated, which has been experimentally proven [94, 95].

For the separation of volatile organic compounds (VOCs), MD has been studied with a wide variety of substances. The application may consider waste water treatment, recovery of valuable substances, production of alcohol-free beverages or improvement of fermentation processes in combination with membrane bio-reactors (MBR). The separation of VOCs with MD is based on multi-component permeation. Mostly VMD, SGMD or AGMD configurations have been tested in order to prevent membrane wetting. Based on the increased risk of membrane wetting due to the reduced surface tension of organic mixtures, the feasible concentration for the feed solution is limited for many VOCs [35]. The feasibility of chloroform separation with MD has been verified in a variety of studies, due to its applicability in waste water treatment [96, 97]. SGMD has been applied for the treatment of waste waters containing VOCs as acetone or ethanol [98]. Extraction of aqueous methanol, ethanol, propanol, acetone, ethyl acetate, methyl acetate and methyl *tert*-butyl ether from aqueous solutions has been considered using VMD [36, 99]. The AGMD configuration has been considered for the removal of ethanol [26], propanone [100] and benzene [101].

In medical applications, MD has been tested for the extraction of water from blood plasma [102]. Other studies consider the concentration of valuable extracts from traditional Chinese medicine [103].

Due to the intrinsic suitability of MD for the treatment of highly concentrated brines, MD is attributed a high potential for the treatment of saturated and super-saturated solutions where solutes tend to precipitate. MD membrane crystallisation may play an important role in the vision of implementing an integrated zero liquid discharge (ZLD) concept in the context of seawater desalination or for the recovery of valuable substances from various processes. Crystallisation from supersaturated brine is usually initiated in an external crystalliser [104]. As one example, the integration of MD membrane crystallisation has been identified as potential technology for

the crystallisation from RO brines [105]. The heterogeneous surface of the porous membrane has been recognised to initialise crystallisation, reducing induction time, increasing crystal growth rates and supporting formation of uniform crystals [106].

For resource recovery from industrial waste waters, MD membrane crystallisation has been considered for the extraction of iron salts from etching solutions in the steel industry [107] or the recovery of valuable salts from waste waters in the textile industry [108].

Most of the reviewed applications apart from desalination have only been tested in the laboratory, indicating general feasibility. Hardly any of the studies provide comprehensive concepts for full-scale operation or specific module design suggestions. The lack of energy-related process evaluation and economic feasibility studies indicate the academic status of current research with respect to these applications.

3 Process Analysis

The process analysis chapter provides a comprehensive scientific discussion on the basic behaviour of the membrane distillation process. The focus is placed on a detailed local scale, allowing quantitative evaluation of the principle transfer phenomena, the influence of operation conditions and the role of channel design, incorporating different materials.

A first part covers the theoretical fundamentals and the development of a parametric process model, including the numerical methods for solving the coupled heat and mass transfer equations for the different channel configurations. Subsequently, a section on experimental work provides information on the testing equipment, the testing procedures and the methods for experimental evaluation. A detailed presentation and discussion of the results is provided in the last and most extensive section of this chapter. Experimental results as well as model-based analyses are comprehensively analysed for a variety of scenarios.

The results obtained within this chapter provide the necessary fundamentals for the following chapter that deals with applied module analysis. Many of the presentations are intended to provide a detailed quantitative reference on local phenomena that may be useful for consultation during consideration of the following chapter on modules, that has a broader point of view.

3.1 Fundamentals and Model Development

The following section introduces the fundamentals for thermodynamic modelling of the membrane distillation process. A review and discussion of common modelling approaches is given, referring to pertinent literature. Special attention is given to the phenomenology of heat and mass transfer through porous media, including considerations for multi-layer configurations. Furthermore, issues regarding heat and mass transfer in spacer-filled flow channels are discussed.

The effects of mechanical support structures on membrane performance are identified and a new integrated modelling approach for membranes on backing structures is presented.

3.1.1 Transmembrane Mass Transfer

In membrane distillation, water evaporates at a hot liquid-vapour interface and permeates through a vapour-filled space. The liquid-vapour interface is maintained by a micro-porous hydrophobic membrane that prevents liquid water from entering the vapour-filled space. Different transfer phenomena and driving forces may contribute to the overall mass transfer. The dimensionless Knudsen number Kn , introduced in Eq. 3.1, indicates the nature of the mass transfer phenomena.

$$Kn = \frac{\lambda_{\text{mol}}}{d_M} \quad (3.1)$$

The Knudsen number depends on the mean free path of water molecules λ_{mol} and the characteristic length of the structural boundaries, here the nominal pore size of the membrane d_M .

In the continuum region ($Kn \ll 1$), the mass transport is limited by intermolecular collisions. Viscous flow, driven by a total pressure difference $\Delta\hat{p}$ and ordinary molecular diffusion, driven by a difference in concentration contribute to the total mass transfer. Assuming ideal gas behaviour, the partial vapour pressure difference Δp can be referred to instead of the concentration difference, by applying the ideal gas law. The flux due to viscous flow j_v is then added to the diffusive flux j_d , justified by the fact that there are not any viscous terms in the Stefan-Maxwell equations or diffusive terms in the Navier-Stokes equations [76]. Effective mass transfer coefficients for viscous flow C_v and molecular diffusion $C_{d,\text{mol}}$ are defined to be proportional to the corresponding driving force according to Eq. 3.2.

$$\begin{aligned} j_{(Kn \ll 1)} &= j_{d,\text{mol}} + j_v \\ &= C_{d,\text{mol}} \Delta p + C_v \Delta\hat{p} \end{aligned} \quad (3.2)$$

In the free-molecule region ($Kn \gg 1$), mass transport is limited by collisions with structural boundaries and Knudsen diffusion, driven by a partial pressure difference, is considered to be the dominant diffusive mechanism. A mass transfer coefficient $C_{d,\text{Kn}}$ for Knudsen diffusion is defined, representing the flux proportional to the corresponding driving force.

$$\begin{aligned} j_{(Kn \gg 1)} &= j_{d,\text{Kn}} \\ &= C_{d,\text{Kn}} \Delta p \end{aligned} \quad (3.3)$$

In the transition region ($0.1 < Kn < 10$), superposition of the diffusive mass transfer phenomena is expected. Considering the momentum transferred by the permeating vapour to the membrane wall and to other gas molecules, the momentum balance leads to a total loss based on both mechanisms. This loss in momentum may be interpreted as a loss in partial vapour pressure. A mass transfer resistance is defined for each phenomenon and application of the superposition principle leads to the total mass transfer resistance or the reciprocal mass transfer coefficient, respectively [76]. Consequently, the flux based on diffusive transfer mechanisms j_d is expressed by a combined diffusive mass transfer coefficient C_d . If there is an additional total pressure difference, flux due to viscous flow still needs to be taken into consideration, and the total flux

in the transition region is expressed by Eq. 3.5.

$$\begin{aligned}
 j_{(0.1 < Kn < 10)} &= j_d + j_v \\
 &= C_d \Delta p + C_v \Delta \hat{p} \\
 &= \left[\frac{1}{C_{d,Kn}} + \frac{1}{C_{d,mol}} \right]^{-1} \Delta p + C_v \Delta \hat{p}
 \end{aligned} \tag{3.4}$$

Mass Transfer Through a Membrane

In membrane distillation with a single membrane layer, water evaporates at the membrane interfacial surface on the evaporator side, permeates through the micro-porous membrane structure and condenses at the cold membrane interfacial surface. For the transmembrane water vapour transport, the structural properties of the membrane as well as the presence of air in the membrane pore volume introduce mass transfer resistances. The exact composition of mass transfer phenomena in a given membrane matrix is difficult to analyse. Common membrane modelling approaches are based on the assumption of single cylindrical pores in order to simplify the complex three-dimensional structure of interconnected pores in the membranes. Most authors assume uniform pores and apply models by using a nominal pore size d_M [51]. Some authors take the pore size distribution into account, in order to model a distribution of the different flow regimes in a given membrane structure [109, 110].

Typical Knudsen numbers for membrane distillation conditions are in the range of $0.1 < Kn < 10$, so superposition of the diffusive mass transfer phenomena is expected and Eq. 3.5 needs to be applied for the evaluation of the transmembrane flux j_M . An illustration of the analogous electric circuit for the membrane system is given in Fig. 3.1.

$$\begin{aligned}
 j_M &= j_{M,d} + j_{M,v} \\
 &= C_{M,d}(p_{w,1} - p_{w,0}) + C_{M,v}(\hat{p}_1 - \hat{p}_0) \\
 &= \left[\frac{1}{C_{M,d,Kn}} + \frac{1}{C_{M,d,mol}} \right]^{-1} (p_{w,1} - p_{w,0}) + C_{M,v}(\hat{p}_1 - \hat{p}_0)
 \end{aligned} \tag{3.5}$$

The diffusive part of the transmembrane flux $j_{M,d}$ is proportional to the driving water vapour pressure difference $\Delta p_{w,1-0} = p_{w,1} - p_{w,0}$, where $p_{w,1}$ and $p_{w,0}$ are the water vapour pressures on the hot feed side and the cold permeate side of the membrane, respectively. If the vapour pressure difference is established by means of a temperature difference, the well-known dependence of water vapour pressure on temperature in form of the Antoine equation may be used to determine the individual interfacial vapour pressures [111]. In desalination applications, a reduction of hot feed water vapour pressure by the presence of salt ions has to be taken into account. An empirical correlation for water vapour pressure of sea water is given in the literature [112]. Appropriate

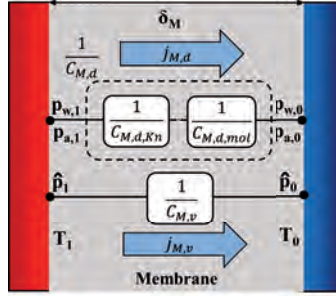


Figure 3.1: Superposition of the different mass transfer resistances in the transition region

correlations are provided in Appendix B. Eq. 3.6 describes the reduced vapour pressure $p_{w,s}$ based on pure water vapour pressure p_w , dependent on sea salt salinity S .

$$p_{w,s} = p_w e^{-2.1609 \cdot 10^{-4} S - 3.5012 \cdot 10^{-7} S^2} \quad (3.6)$$

For salinities $S = 0 - 160 \frac{\text{g}}{\text{kg}}$ and temperatures $T = 0 - 200^\circ\text{C}$ this correlation leads to an error in vapour pressure evaluation of less than 2.5 %.

If the same vapour pressure curve is valid for the evaporator and the condenser fluid, the driving vapour pressure difference can be replaced by the slope of the vapour pressure curve $(\frac{dp}{dT})_{\bar{T}_{1-0}}$ and the interfacial temperature difference ΔT_{0-1} , as follows:

$$j_{M,d} = C_{M,d} \left(\frac{dp}{dT} \right)_{\bar{T}_{1-0}} (T_1 - T_0) \quad (3.7)$$

The slope of the vapour pressure curve is determined by Eq. 3.8, evaluating the Clausius-Clapeyron equation at the mean membrane temperature level \bar{T}_{1-0} .

$$\left(\frac{dp_w}{dT} \right)_{\bar{T}_{1-0}} = \frac{\Delta h_v p_w}{R \bar{T}_{1-0}^2} \quad (3.8)$$

The mean membrane temperature \bar{T}_{1-0} is assumed to be the arithmetic mean temperature of the interfacial temperatures on then evaporator side T_1 and the condenser side T_0 .

$$\bar{T}_{1-0} = 0.5 (T_1 + T_0) \quad (3.9)$$

Eq. 3.7 shows that flux $j_{M,d}$ is proportional to the interfacial temperature difference ΔT_{1-0} . Due to the exponential character of the vapour pressure curve, its slope and therefore flux increases significantly with the membrane mean temperature level \bar{T}_{1-0} .

It has to be taken into account that the vapour pressure curves for the evaporator and the condenser fluid in membrane distillation are usually different, due to a difference in fluid composition. A correction term for the temperature difference may be introduced in order to account for the boiling point elevation due to the solute [113, 114]. Moreover, the validity of Eq. 3.7 is limited by the linear approximation to the exponential vapour pressure curve at membrane

mean temperature \bar{T}_{1-0} and brings restrictions, especially for use in the case of large temperature differences ($\Delta T_{1-0} > 10\text{ K}$) [113]. However, Eq. 3.7 is completely adequate for many theoretical considerations and is often used for the derivation of basic relations and process sensitivities that are not affected by a concentration difference.

Subsequently, the different mass transfer phenomena will be discussed with respect to the specific boundary conditions of membrane distillation processes considering the permeation of a single component. The role of separative effects that are associated with the different transfer phenomena in multi-component diffusion scenarios are discussed elsewhere [76].

At first the transfer phenomena of Knudsen diffusion is analysed. The mass transfer coefficient for the Knudsen diffusion mechanism in a micro-porous membrane structure $C_{M,\text{Kn}}$ is given in Eq. 3.10.

$$C_{M,\text{Kn}} = \frac{2}{6} \frac{M_w}{R \bar{T}_{1-0}} \frac{\varepsilon_M}{\tau_M} \frac{d_M}{\delta_M} \sqrt{\frac{8 R \bar{T}_{1-0}}{\pi M_w}} \quad (3.10)$$

The Knudsen diffusion mechanism is independent of any intermolecular interaction and, for a given species, mainly dependent on the membrane structural parameters. Here, d_M is the nominal pore diameter, referred to as nominal pore size, and δ_M the membrane thickness. The membrane porosity ε_M takes the reduction of the available cross-sectional area for diffusion due to the solid membrane phase into account. The effective path length for diffusion is higher than the actual membrane thickness δ_M , since the vapour needs to wind around the solid membrane phase. The intensity of this effect is strongly dependent on the membrane morphology and is taken into account by the membrane tortuosity factor τ_M . The molecular weight of the permeating water vapour is represented by M_w .

For ordinary molecular diffusion phenomena, a binary mixture of water vapour and air is assumed in the pore volume. In principle, permeation of both species is possible, but the air flux through the membrane is assumed to be many orders of magnitude lower than the vapour flux due to its low solubility in the liquid bulk phases [21, 115]. Consequently, the air in the membrane is considered to be a stagnant film. The air partial pressure in the membrane pore volume is principally dependent on the amount of dissolved air in the water according to Henry's law. In this modelling approach, the air partial pressure in the pore volume is considered to be in equilibrium with the ambient pressure condition (or deaeration pressure condition), since the hydraulic systems in MD applications are usually open to the ambient. The air partial pressure may therefore be derived from the known absolute pressure condition by applying Dalton's law, given in Eq. 3.11.

$$\hat{p} = p_a + p_w \quad (3.11)$$

The air forms a partial pressure gradient in the opposite direction to the water vapour pressure gradient in order to fulfil the condition of Eq. 3.11 everywhere across the membrane. The mass transfer coefficient describing ordinary molecular diffusion $C_{M,\text{d,mol}}$ in a micro-porous membrane

is then defined by Eq. 3.12.

$$C_{M,d,mol} = \frac{M_w}{R \bar{T}_{1-0}} \frac{\varepsilon_M}{\tau_M} \frac{\bar{p}_{1-0}}{\delta_M} \frac{D_{wa}^o}{\bar{p}_{a,1-0,\ln}} \quad (3.12)$$

The molecular diffusion coefficient is independent of pore size, since this phenomenon does not include any interaction with the membrane solid phase. However, the membrane thickness δ_M and the membrane tortuosity τ_M represent the effective path length for diffusion and the membrane porosity ε_M takes the reduction of the available cross-sectional area for diffusion due to the solid membrane phase into account. D_{wa}^o is the ordinary diffusion coefficient of water vapour in air, which is almost independent of the mixing ratio for low total pressures ($0.1 \leq \hat{p} \leq 10$ bar). The Fuller model is used to calculate D_{wa}^o dependent on total pressure \hat{p} and mean membrane temperature \bar{T}_{1-0} [116]. The quantity of air in the pore volume is evaluated by Eq. 3.13, representing the logarithmic mean partial pressure $\bar{p}_{a,1-0,\ln}$ of air in the membrane.

$$\bar{p}_{a,1-0,\ln} = \frac{p_{a,0} - p_{a,1}}{\ln \left(\frac{p_{a,0}}{p_{a,1}} \right)} \quad (3.13)$$

If a uniform total pressure level \hat{p} is assumed throughout the membrane, higher temperatures lead to a higher fraction of water vapour and less air in the pore volume. According to Eqs. 3.11 and 3.12, the molecular diffusion coefficient increases significantly at higher temperature levels [117].

An alternative way to increase the molecular diffusion coefficient is the reduction of the total pressure level in the membrane pore volume. The partial pressure of air and consequently the mass transfer resistance is reduced since the membrane is being partially deaerated. Usually, the liquid streams carry a certain amount of dissolved air to the membrane interface, where an equilibrium with the gas mixture in the pore volume is established. If the dissolved air concentration in the liquid streams changes, the equilibria change and air will be expelled into the membrane pore volume or be removed, respectively. Thus, the presence of air in the membrane pores depends on the amount of dissolved air in the liquid streams and membrane deaeration can be carried out by deaerating those. If the total pressure in the pore volume is still above the respective vapour pressures, a uniform total pressure level ($\Delta \hat{p}_{1-0} = 0$) is formed throughout the membrane, according to Eq. 3.11. If the membrane is evacuated to pressures below the water vapour pressure on the evaporator side, almost no air is left in the pore volume. The residual air accumulates on the condenser side. The local total pressure on the evaporator side is equal to the interfacial water vapour pressure ($\hat{p}_1 = p_{w,1}$), whereas the local total pressure on the condenser side still incorporates a fraction due to air ($\hat{p}_0 = p_{w,0} + p_{a,0}$). A difference in total pressure across the membrane is established ($\Delta \hat{p}_{1-0} > 0$). In this special case, the flux due to viscous flow must be added and a combined Knudsen/molecular diffusion/viscous flow model is applied. Assuming uniform cylindrical pores, the viscous flow permeability of a porous membrane structure may be derived in the form of the Poiseuille flow model [76, 113]. The viscous flow transfer coefficient is given in Eq. 3.14.

$$C_{M,v} = \frac{M}{R \bar{T}_{1-0}} \frac{\varepsilon_M}{\tau_M} \frac{d_M^2}{\delta_M} \frac{\bar{p}_{1-0}}{32\mu_w} \quad (3.14)$$

\bar{p}_{1-0} represents the mean total pressure $\bar{p}_{1-0} = 0.5(\hat{p}_1 + \hat{p}_0)$ in the membrane pore volume, whereas μ_w is the dynamic viscosity of water vapour. The dependence of the dynamic viscosity on temperature is given in property tables [118].

In the limiting case, the membrane is evacuated to pressures equal to or less than the water vapour pressure on the condenser side and consequently, no air is left in the pore volume. The membrane is referred to as fully deaerated. The ordinary diffusion coefficient in Eq. 3.12 tends to infinity and the diffusion through air becomes negligible. The local total pressure on both sides is equal to the local water vapour pressures. The model Eqs. 3.5 reduce to a combined Knudsen/viscous flow model [119], which is specifically attractive for the modelling of the vacuum membrane distillation process. In the typical case, no deaeration is applied and the membrane pore volume will contain a certain amount of air. Due to the uniform total pressure ($\Delta\hat{p}_{1-0} = 0$), no vapour is transferred by viscous phenomena. The model Eqs. 3.5 reduce to the Knudsen/molecular diffusion model that is quite common in membrane distillation modelling [51]. In the absence of a viscous flux, the mass transfer coefficient based on diffusive phenomena may be interpreted as the total membrane mass transfer coefficient $C_{M,d} = C_M$.

In general, exact data on the membrane structure is not available or has high uncertainties. Thus, some authors suggest the use of empirical or semi-empirical methods to determine a total mass transfer coefficient.

The total mass transfer coefficient C_M for a given membrane material can be derived from a set of experimental data, containing flux results at different mean temperature levels obtained at a fixed temperature difference and similar flow rates on the evaporator side and the condenser side. The experiments have to be performed with pure water. The measured data has to be presented according to the specific linear form given in Eq. 3.15 that is derived from the basic heat and mass transfer equations (Eqs. 3.7, 3.20, 3.28, 3.29) [113]. Assumptions that have to be made include a constant value for the total mass transfer coefficient ($C_M = \text{const.}$) as well as equal heat transfer coefficients on the evaporator side and the condenser side ($\alpha_C = \alpha_E = \alpha_{E/C}$) for the complete set of experimentally obtained data. Flux due to viscous flow is not considered by the given representation.

$$\frac{\Delta T_{1-0}}{j_M \Delta h_v} = \left[\frac{1}{C_M \Delta h_v} \left(1 + \frac{\lambda_M^*}{\delta_M} \frac{2}{\alpha_{E/C}} \right) \right] \left(\frac{dp_w}{dT} \right)_{T_{1-0}}^{-1} + \frac{2}{\alpha_{E/C}} \quad (3.15)$$

The intercept of the linear fit yields the heat transfer in the boundary layers $\alpha_{E/C}$ and the slope leads to the mass transfer coefficient C_M . Results obtained by using this ‘‘Linear regression method’’ are reported by several researchers [8, 113, 120–122]. Special attention has to be paid to the fact that the quality of the obtained mass transfer coefficients always depends on the quality of the corresponding heat transfer coefficients obtained. A comparison of the heat transfer results that are identified with the same channel setup but with different membranes or a completely independent experiment should be used to validate the heat transfer results. Moreover, the influence of the different operating conditions in the experiments on the overall mass transfer coefficient, e.g. the influence of the temperature level on air partial pressure, are

not considered and cannot be identified with the given method. However, this method gives a reasonable quantitative indication, especially for comparative studies when the same experimental setup is used for all experiments.

A more detailed, semi-empirical approach is given in Eq. 3.16, which is derived from the mathematical form presented in Eq. 3.5. The membrane structural parameters, the molecular weight of the permeating species and the influencing operating conditions are aggregated into the empirical parameters a , b and d [119].

$$C_M = \left[\frac{1}{a \xi^b} + \frac{\bar{p}_a}{d} \right]^{-1} \quad (3.16)$$

Parameter $\xi = \hat{p} \cdot (\hat{p}_{\text{ref}})^{-1}$ is a dimensionless pressure, a can be interpreted as membrane permeability at reference pressure \hat{p}_{ref} and $0 \leq b \leq 1$ gives an indication of the given flow regime. If b is closer to 1, Knudsen diffusion is considered to be dominant, whereas if b is closer to 0, Poiseuille flow is considered to be the dominant mechanism. Parameters a and b that are identified by gas permeation experiments with different membranes and different gases are provided in the literature [119]. Parameter d may be interpreted as a permeability based on molecular diffusion and was reported to be estimated from membrane specifications [21].

Mass Transfer Through a Combined Membrane and Air Gap

In membrane distillation processes, where an additional air gap is introduced next to the membrane, additional mass transfer resistances need to be considered for process modelling. This air gap is usually two orders of magnitude wider than the membrane layer thickness and dominates the total mass transfer resistance by far. Thus, the membrane properties have little effect on process performance for operation at atmospheric pressure and some authors have neglected the membrane transfer resistance for AGMD process modelling [18, 123, 124]. However, if the membrane has poor structural properties or the air gap resistance is reduced significantly by deaeration, the membrane layer gains in significance and may even predominate. In order to assure model validity over wide range, the total flux through the membrane and air gap j_{M-AG} is modelled using a multi-layer approach. The mass transfer phenomena occurring in the membrane layer are defined by effects in the continuum/free molecule transition region ($0.1 < Kn < 10$), whereas the mass transfer in the air gap is purely in the continuum region ($Kn \ll 1$), since no micro-porous structure is introduced and geometrical boundaries are on the millimetre scale. Consequently, the diffusive mass transfer in the air gap is based on ordinary diffusion phenomenon only.

The resistance due to viscous effects in the air gap is negligible and only the membrane contributes to the combined viscous mass transfer coefficient ($C_{M-AG,v} = C_{M,v}$).

In principle, the mass transfer in the air gap can include an additional term, based on free convection. The dimensionless Rayleigh number Ra , defined in Eq. 3.17, gives an indication whether the diffusive or the convective phenomenon is dominant or a combined mass transfer is

most likely.

$$Ra = \frac{g \alpha_a \Delta T_{1-0} \delta_{AG}^3}{\nu_a \lambda_a} \quad (3.17)$$

Here g is the acceleration due to gravity, ΔT_{1-0} is the interfacial temperature difference, δ_{AG} is the gap width and α_a , ν_a and λ_a are the thermal expansion coefficient, the kinematic viscosity and thermal diffusivity of air, respectively. In a vertical gap, an appreciable convective transfer occurs for high Rayleigh numbers ($Ra \gtrsim 1000$) [125, 126]. Estimations of the Rayleigh number using typical conditions for AGMD ($\delta_{AG} \leq 3$ mm and $\Delta T_{1-0} \leq 40$ K) lead to fairly small values ($Ra < 100$). Additionally, the development of natural convection is inhibited by the air gap spacer filaments and rather high aspect ratios of channel width to channel height. Other researchers performed numerical studies and conclude that the natural convection phenomenon for narrow gaps ($\delta_{AG} < 5$ mm) are negligible [127].

Consequently, if no forced convection is induced, the convective mass transfer in the air gap is negligible and the molecular diffusion resistance through stagnant air $C_{AG,d,mol}^{-1}$ is the only mass transfer resistance that needs to be taken into consideration for the air gap [128, 129]. The additional diffusive resistance is added to the model equations according to the superposition principle.

The total mass transfer through the combined membrane and air gap j_{M-AG} is given in Eq. 3.18. An illustration of the analogous electric circuit for the combined membrane and air gap system is given in Fig. 3.2.

$$\begin{aligned} j_{M-AG} &= j_{M-AG,d} + j_{M-AG,v} \\ &= C_{M-AG,d}(p_{w,1} - p_{w,0}) + C_{M-AG,v}(\hat{p}_1 - \hat{p}_0) \\ &= \left[\frac{1}{C_{M,d,Kn}} + \frac{1}{C_{M,d,mol}} + \frac{1}{C_{AG,d,mol}} \right]^{-1} (p_{w,1} - p_{w,0}) + C_{M,v}(\hat{p}_1 - \hat{p}_0) \end{aligned} \quad (3.18)$$

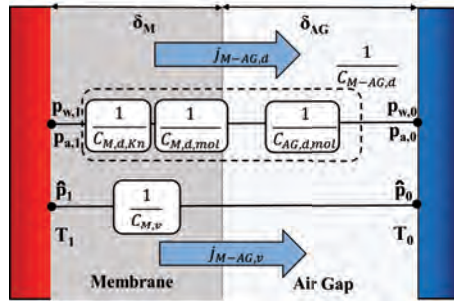


Figure 3.2: Superposition of the mass transfer resistances in a combined membrane and air gap

The mass transfer coefficients associated with the membrane matrix are calculated applying the

definition given in the previous section, assuming that the effective membrane mean temperature is better approximated by the interfacial temperature on the evaporator side than the mean temperature of the vapour space ($\bar{T}_M \approx T_1 \neq \bar{T}_{1-0}$).

The additional mass transfer coefficient due to molecular diffusion in the air gap $C_{AG,d,mol}$ is given in Eq. 3.19.

$$C_{AG,d,mol} = \frac{M_w}{R \bar{T}_{1-0}} \frac{\varepsilon_{AG}}{\delta_{AG}} \frac{\bar{p}_{1-0}}{\bar{p}_{a,1-0,\ln}} \frac{D_{wa}^o}{\quad} \quad (3.19)$$

The air gap thickness δ_{AG} represents the path length for diffusion, whereas the air gap spacer voidage ε_M takes the reduction of the available cross-sectional area for diffusion due to the solid spacer structure into account.

It has been reported, that the “linear regression method” of Eq. 3.15 may be applied in a modified form in order to determine an overall membrane and air gap mass transfer coefficient C_{M-AG} experimentally [130].

3.1.2 Transmembrane Heat Transfer

Heat Transfer Through a Membrane

In membrane distillation processes with a single membrane layer, the total heat transfer through the membrane \dot{q}_M consists of a latent and a conductive part. The latent heat transfer $\dot{q}_{M,l}$ is linked to the transmembrane mass transport j_M by the latent heat of evaporation Δh_v . The conductive heat transfer $\dot{q}_{M,c}$ is directly dependent on its driving interfacial temperature difference ΔT_{0-1} , the effective thermal conductivity of the membrane material λ_M^* and the membrane thickness δ_M .

$$\begin{aligned} \dot{q}_M &= \dot{q}_{M,l} + \dot{q}_{M,c} \\ &= j_M \Delta h_v + \frac{\lambda_M^*}{\delta_M} \Delta T_{1-0} \\ &= k_M \Delta T_{1-0} \end{aligned} \quad (3.20)$$

The dependence of the latent heat of evaporation Δh_v on the temperature is taken into account by an empirical correlation, derived from enthalpy tables for water in the gaseous and liquid phases [118].

$$\Delta h_v = 2501 - 2.30 T - 0.0011 T^2 \quad (3.21)$$

The heat of solution is additionally required to separate the pure product water from the saline feed water. For a sea water concentrate at a salinity of 100 g kg^{-1} , the heat of solution is approximately $\Delta h_s \approx 3 \text{ kJ kg}^{-1}$, which is less than 0.2% compared to the heat of vaporisation and is considered to be negligible [112].

In the absence of viscous flow, j_M in Eq. 3.20 may be replaced by Eq. 3.7, and the integral heat

transfer coefficient of the membrane k_M is described by Eq. 3.22.

$$k_M = C_M \left(\frac{dp}{dT} \right)_{\bar{T}_{1-0}} \Delta h_v + \frac{\lambda_M^*}{\delta_M} \quad (3.22)$$

To estimate the effective thermal conductivity of the porous membrane λ_M^* , usually a combined thermal conductivity for the solid $\lambda_{M(s)}$ and gaseous $\lambda_{M(g)}$ phases is considered, weighted by the material's porosity. In the context of membrane distillation, many authors apply the iso-strain model that considers the solid and the gaseous phase as parallel thermal resistances [21, 122, 131]. An alternative basic model approach is the iso-stress model, that considers the solid and the gaseous phase as serial thermal resistances, consequently leading to lower thermal conductivities. The alternative models that describe the thermal conductivity of composite materials are comparatively evaluated in [132] and compared to measured values taken from [130]. It turned out, that the conductivities calculated by the basic iso-strain model are too high, and the equations resulting in lower values were recommended. Independent examinations suggest the superposition of the iso-stress and the iso-strain model to describe the thermal conductivity in MD membranes [20]. Also in this thesis, the non-woven structure of the membrane solid phase is considered to be non-parallel (see Fig. 2.7) and the iso-strain model has been modified. The modification is based on the idea that the effective path length for conductive heat transport in the solid phase is assumed to be longer than the actual membrane thickness δ_M . To do so, a solid-phase membrane tortuosity factor $\tau_{M(s)} \geq 1$ is introduced into the basic iso-strain model according to Eq. 3.23.

$$\lambda_M^* = \varepsilon_M \lambda_{M(g)} + (1 - \varepsilon_M) \tau_{M(s)}^{-1} \lambda_{M(s)} \quad (3.23)$$

The gaseous phase is composed of water vapour and air and a combined thermal conductivity may be estimated. However, the thermal conductivities are quite similar so that the assumption for the gas phase composition is insignificant and the thermal conductivity of pure species may be assumed [132]. The gaseous phase thermal conductivity is one order of magnitude lower than that of the solid phase polymeric materials. Weighted with a typically high porosity value, the two phases contribute similarly to the total conductive membrane heat transfer.

The heat transferred by conduction is considered to be parasitic, since it does not contribute to mass transfer. The thermal efficiency η_{th} indicates the ratio of latent heat $\dot{q}_{M,l}$ to the total heat \dot{q}_M transferred through the membrane and is defined by Eq. 3.24.

$$\eta_{th} = \frac{\dot{q}_{M,l}}{\dot{q}_M} = \frac{\dot{q}_{M,l}}{\dot{q}_{M,l} + \dot{q}_{M,c}} \quad (3.24)$$

In the absence of viscous flow, the alternative form in Eq. 3.25 can be derived to analyse the thermal efficiency behaviour for different operating conditions by inserting Eq. 3.20 and Eq. 3.22 into Eq. 3.24.

$$\eta_{th} = \frac{C_M \left(\frac{dp}{dT} \right)_{\bar{T}_{1-0}} \Delta h_v}{C_M \left(\frac{dp}{dT} \right)_{\bar{T}_{1-0}} \Delta h_v + \frac{\lambda_M^*}{\delta_M}} \quad (3.25)$$

According to Eq. 3.25, high total mass transfer coefficients C_M result in high thermal efficiencies. Eq. 3.25 is independent of hydrodynamics and temperature differences, since the interfacial temperature difference ΔT_{1-0} has been eliminated. According to the mass transfer coefficient models in Eqs. 3.10 and 3.12 with $C_M \propto \delta_M^{-1}$, the membrane thickness δ_M can be eliminated in Eq. 3.25. Thus thermal efficiency is expected to be independent of membrane thickness as well.

Heat Transfer Through a Combined Membrane and Air Gap

In membrane distillation processes, where an additional air gap is introduced next to the membrane, additional heat transfer resistances need to be considered for process modelling. The heat that is transferred through the membrane and the air gap \dot{q}_{M-AG} is represented by Eq. 3.26 that contains a latent part $\dot{q}_{M-AG,l}$, a conductive part $\dot{q}_{M-AG,c}$ and a part corresponding to radiation exchange across the air gap $\dot{q}_{M-AG,rad}$.

$$\begin{aligned}
 \dot{q}_{M-AG} &= \dot{q}_{M-AG,l} + \dot{q}_{M-AG,c} + \dot{q}_{M-AG,rad} \\
 &= j_{M-AG} \Delta h_v + \left[\frac{\delta_M}{\lambda_M^*} + \frac{\delta_{AG}}{\lambda_{AG}^*} \right]^{-1} \Delta T_{1-0} \\
 &\quad + \frac{\epsilon_{AG} \sigma}{\epsilon_M^{-1} + \epsilon_w^{-1} - 1} (T_1^4 - T_0^4) \\
 &= k_{M-AG} \Delta T_{1-0}
 \end{aligned} \tag{3.26}$$

The latent heat transfer $\dot{q}_{M-AG,l}$ is directly linked to the total flux across the membrane and air gap j_{M-AG} .

The conductive part $\dot{q}_{M-AG,c}$ is modelled with a combined conductive heat transfer resistance of the membrane and the air gap, containing the effective thermal conductivities λ_M^* and λ_{AG}^* and the respective layer thicknesses δ_M and δ_{AG} . The effective thermal conductivity of the membrane λ_M^* was already defined in Eq. 3.23, using a modified iso-strain model. Similarly the effective thermal conductivity of the air gap λ_{AG}^* is defined in Eq. 3.27, taking the thermal conductivity of the spacer solid phase $\lambda_{AG(s)}$ and the gaseous phase $\lambda_{AG(g)}$ into account. If the spacer in the air gap is wetted during operation, additional thermal bridges intensify the conductive heat transfer; furthermore, the thermal connection to the condensation surface is enhanced. These effects are taken into consideration by introducing a third liquid phase into the air gap iso-strain model, depending on its volumetric fraction $x_{AG(l)}$ and the thermal conductivity of water $\lambda_{AG(l)}$.

$$\lambda_{AG}^* = (\epsilon_{AG} - x_{AG(l)}) \lambda_{AG(g)} + (1 - \epsilon_{AG}) \tau_{AG(s)}^{-1} \lambda_{AG(s)} + x_{AG(l)} \lambda_{AG(l)} \tag{3.27}$$

The radiative heat transfer $\dot{q}_{M-AG,rad}$ is described by the Stefan-Boltzmann constant σ , the emissivity of the membrane surface ϵ_M and the film surface of the condensed water ϵ_w . The air gap spacer reduces the effective cross-sectional area for radiation exchange, which is taken into account by the appropriate spacer voidage ϵ_{AG} . Assuming a small difference between the

interfacial membrane temperature on the evaporator side and the membrane surface temperature on the air gap side, compared to the total interfacial temperature difference, the emittance is calculated at temperature T_1 . The radiative heat transfer is usually neglected in common AGMD models [133]. However, rough estimations using a set of parameters that is typical for an AGMD application ($C_{M-AG} = 1.0E^{-7} \text{ kg}(\text{m}^2 \text{ s Pa})^{-1}$; $k_{M-AG,c} = 50 \text{ W}(\text{m}^2\text{K})^{-1}$; $\varepsilon_{AG} = 0.8$) were made, in order to determine the relevance of the radiative heat transfer fraction for the total heat transfer in AGMD processes. Evaluating an operation point at high temperatures ($T_1 = 80^\circ\text{C}$; $T_0 = 70^\circ\text{C}$) results in a radiative heat transfer fraction of approximately 1.4%. For the same scenario at low temperatures ($T_1 = 30^\circ\text{C}$; $T_0 = 20^\circ\text{C}$), the radiative heat transfer fraction is approximately 3.9%. It turns out that radiative heat transfer does generally contribute with low fractions to the overall heat transfer in air gap configurations. However, for special conditions e.g. at low temperatures, the radiative heat transfer contributes appreciably to total heat transfer. Low temperature operation points have some significance in module simulation, specifically when cold zones in full-scale modules are analysed. Thus, radiative heat transfer should be taken into consideration for comprehensive process modelling.

3.1.3 Heat Transfer in the Hydraulic Boundary Layers

In membrane distillation, a temperature gradient towards the membrane needs to be established in order to transfer the required heat for evaporation to the membrane surface. Based on this driving force, heat is transferred from the evaporator bulk stream to the liquid-vapour interface on the evaporator side, passes the vapour space and is then transferred from the liquid-vapour interface into the condenser bulk stream. The basic heat transfer equations for heat transfer in the hydrothermal boundary layers are given in Eqs. 3.28 and 3.29.

$$\dot{q}_E = \alpha_E (T_E - T_1) \quad (3.28)$$

$$\dot{q}_C = \alpha_C (T_0 - T_C) \quad (3.29)$$

α_E and α_C represent the heat transfer coefficients, while $(T_E - T_1)$ and $(T_0 - T_C)$ are the temperature differences from the evaporator bulk stream to the evaporation surface and from the condensation surface to the condenser bulk stream, respectively. Heat transfer in moving fluids consists of conductive and convective heat transfer mechanisms. The Nusselt number Nu is used to describe the heat transfer coefficient α of the hydrothermal boundary layers.

$$\alpha = Nu \frac{\lambda}{d_h} \quad (3.30)$$

In Eq. 3.30, the overall heat transfer is calculated with the fluid's thermal conductivity λ and the hydraulic diameter of the flow channel d_h . The empirical correlations used to describe water's physical properties throughout this thesis are taken from [112]. The correlations include the dependence on temperature and sea salt salinity and may be found in Appendix B. The

dimensionless Nusselt number accounts for the enhancement of the heat transfer by convective phenomena based on turbulences. A common approach for estimating the Nusselt number is given by correlations of the form illustrated in Eq. 3.31.

$$Nu = a Re^b Pr^c \left(\frac{d_h}{L} \right)^d \quad (3.31)$$

Parameters a , b , c and d are parameters that depend on the flow field, while the channel geometry is accounted for by the hydraulic diameter d_h and length of the flow channel L . For laminar flow ($Re_{\text{crit}} \approx 2200 - 3600$), the parameters $a = 1.841$ and $b = c = d = 0.333$ are proposed for heat transfer in a planar gap with fully developed hydrodynamic and thermal boundary layers [134]. Similar values have been proposed in the context of membrane distillation in [135]. Due to the similarity of heat and mass transfer, many Nusselt correlations were originally derived in the context of mass transfer and then adapted to a heat transfer context.

However, the heat transfer correlations that are available for the standard heat transfer problems are usually not applicable for an MD channel set-up. Spacer materials are usually introduced into the gap to define the channel geometry for the flexible film materials and to enhance the convective heat transfer. The entry region for the development of the thermal and hydraulic boundary layers was identified as negligible for spacer-filled channels, since spacer filaments dominate the hydrodynamic conditions and the boundary layers are expected to be fully developed after a few repeated flow cells [136, 137]. Spacer filaments form recirculating vortices in the flow regime ($Re \gtrsim 100$) that increase in size at higher flow rates. Instabilities in the flow regime have been identified for spacer-filled channels at Reynolds numbers about one order of magnitude lower than in empty channels ($Re_{\text{crit}} \approx 180 - 300$) [138, 139]. Different flow regimes within net-type spacers were classified as 'channel flow', where the flow follows the channel formed by two neighbouring spacer rods, gets reflected at the wall and then follows the channel formed by the rods in the second spacer plane, 'corkscrew flow', where the flow passes the spacer filaments like a corkscrew and 'mixing flow', where both phenomena overlap [137]. The lateral fluid movement in channels filled with net-type spacers was identified as being dependent on Reynolds number and it is reported that for $Re \geq 250 - 300$, strong instability breaks up the flow traces [139]. To improve the performance and efficiency of spacer materials, experimental studies and CFD analyses were carried out by several researchers [140–148].

The determination of adequate correlations to describe the hydrodynamic boundary layers has high relevance for the quality of MD modelling results. Various empirical and semi-empirical modelling approaches for laminar and turbulent flow regimes are summarised in the relevant literature [40, 41, 132, 145, 149, 150]. The collections contain a wide range of different mathematical forms, that were originally derived from various scenarios. Many of the presented correlations refer to Eq. 3.31 and its simplified form in Eq. 3.32, assuming $d = 0$.

$$Nu = a Re^b Pr^c \quad (3.32)$$

In the context of water fluid systems, the exponent c in Eqs. 3.31 and 3.32 is typically 0.333. Some approaches take geometrical aspects of spacer design into account [149, 151, 152]. For

spacer-filled channels, the modified form of Eqs. 3.33 and 3.34 is proposed for the prediction of the heat transfer [151, 152]. This correlation was originally derived for mass transfer predictions for the ultra-filtration process with spacer-filled channels.

$$Nu = 0.644 f_S Re^{0.5} Pr^{0.333} \left(\frac{2 d_h}{l_S} \right)^{0.5} \quad (3.33)$$

$$f_S = 1.654 \left(\frac{d_f}{\delta_S} \right)^{-0.039} \varepsilon_S^{0.75} \sin \left(\frac{\phi}{2} \right)^{0.086} \quad (3.34)$$

The correlation includes the hydraulic diameter of the flow channel d_h , the orthogonal distance between the net spacer filaments l_S , the spacer filament diameter d_f , the spacer thickness δ_S , the spacer voidage ε_S and the angle between the spacer filaments ϕ .

However, due to the strong dependence of the hydraulic condition on the usually quite complex geometrical constraints in the spacer-filled flow channels, the validity of any particular Nusselt equation has to be verified carefully for a given scenario. To improve the quality of the results for a specific channel geometry, many authors use basic forms of the heat transfer correlations and identify the respective constants by use of their own experimental data [8, 120, 122, 153].

The Reynolds number Re , defined in Eqs. 3.35, indicates the hydrodynamic condition in the flow channel by using the mean flow velocity \bar{c} , the hydraulic diameter of the respective flow channel d_h and the kinematic fluid viscosity ν .

$$Re = \frac{\bar{c} d_h}{\nu} \quad (3.35)$$

If a spacer is introduced into a flow channel with channel height H and channel/spacer thickness δ_S , the total cross-sectional area in the channel is reduced by the spacer filaments. Introducing the spacer voidage ε_S , Eq. 3.36 gives an estimation for the mean flow velocity \bar{c} in the channel.

$$\bar{c} = \frac{\dot{V}}{A_{\perp}} = \frac{\dot{V}}{H \delta_S \varepsilon_S} \quad (3.36)$$

The hydraulic diameter d_h of a non-circular cross-section is defined as four times the cross-section of the flow channel divided by the wetted circumference. Consequently, the hydraulic diameter for a parallel gap is defined as two times the gap thickness [134]. Considering a spacer-filled channel with a periodically variable cross-section, the use of a generalised formulation is recommended for the derivation of the hydraulic diameter. Eq. 3.37 is based on this generalised form which is defined as four times the volume of the flow channel divided by the wetted surface [154].

$$d_h = \frac{4 \varepsilon_S}{\frac{2}{\delta_S} + (1 - \varepsilon_S) \frac{4}{d_f}} \quad (3.37)$$

The spacer voidage ε_S , the spacer thickness δ_S and the diameter of the spacer filaments d_f are used for the estimation.

The Prandtl number Pr defined in Eq. 3.38 is only dependent on physical fluid properties.

$$Pr = \frac{c_p \mu}{\lambda} \quad (3.38)$$

The thermal capacity c_p , the dynamic viscosity μ and the thermal conductivity λ are introduced. Corresponding empirical correlations may be found in Appendix B.

In all MD configurations, a significant loss in driving force can be attributed to heat transfer in the hydrothermal boundary layers, since the effective interfacial temperature difference is always lower than the bulk temperature difference. The temperature polarisation coefficient θ , defined in Eq. 3.39, represents the ratio of the interfacial temperature difference ΔT_{1-0} to the temperature difference in the bulk streams ΔT_{E-C} .

$$\theta = \frac{\Delta T_{1-0}}{\Delta T_{E-C}} = \frac{T_1 - T_0}{T_E - T_C} \quad (3.39)$$

The temperature polarisation coefficient $0 \leq \theta \leq 1$ provides a quantitative measure to evaluate the effect of driving force reduction due to the heat transfer in the hydrothermal boundary layers. If the temperature polarisation coefficient tends to zero, the process is considered to be limited by the heat transfer in the boundary layers; if the temperature polarisation coefficient tends to unity, the process is limited by mass transfer according to the membrane permeability. A schematic representation of different temperature profiles considering the limiting cases and a balanced temperature polarisation coefficient of $\theta = 0.5$ is provided in Fig. 3.3.

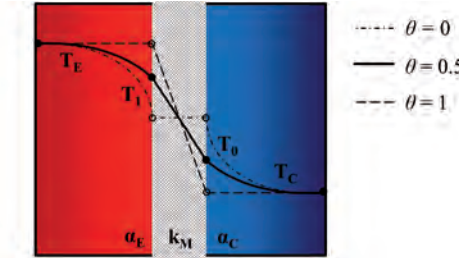


Figure 3.3: Schematic representation of temperature profiles in an MD channel configuration, illustrated for different temperature polarisation coefficients.

The temperature polarisation coefficient θ can also be expressed as a function of the integral heat transfer coefficient of the membrane k_M and the boundary layer heat transfer coefficients α_E and α_C . A detailed derivation of Eq. 3.40 based on Eq. 3.39 is provided in the literature [113].

$$\theta = \left(1 + \frac{k_M}{\left(\frac{1}{\alpha_E} + \frac{1}{\alpha_C} \right)^{-1}} \right)^{-1} \quad (3.40)$$

Substituting the expression for k_M from Eq. 3.22 into Eq. 3.40 shows that temperature polarisation is mainly dependent on membrane properties, temperature level and thermal boundary layers. This substitution is valid for the absence of viscous flow. From Eq. 3.40, a generic phe-

nomenon in membrane distillation becomes apparent. An increase in performance achieved by a higher membrane permeability C_M or higher operating temperatures \bar{T}_{1-0} will lead to high integral membrane heat transfer coefficients k_M and small temperature polarisation coefficients θ . The relative loss in driving force due to heat transfer within the boundary layers increases. The process has a self-restraining character.

3.1.4 Mass Transfer in the Hydraulic Boundary Layers

In membrane distillation, the membrane structure defines the position of the liquid-vapour interface. The evaporation surface is constantly flushed with the feed water by forced convection and water is always available at the evaporation surface during operation. The mass transfer resistances for water from the bulk streams to the interfacial surfaces can therefore be neglected in membrane distillation. However, in feed aqueous solutions, non-volatile solutes such as salts accumulate at the liquid-vapour interface on the feed side, due to the separative effect of the phase change. The specific water flux through the membrane j_w ($= j_M$) is extracted from the feed solution at the membrane surface. The salt ions incorporated in j_s have originally been solved in this feed water at the interfacial salinity S_1 . Consequently, this amount of salt is expelled and accumulates next to the membrane surface. Based on the definition of salinity evaluated at the membrane interfacial surface in Eq. 3.41, Eq. 3.42 can be derived as a source term for the specific flux of salt ions j_s .

$$S_1 = \frac{m_s}{m_s + m_w} \approx \frac{m_s}{m_w} = \frac{\dot{m}_s}{\dot{m}_w} = \frac{j_s}{j_w} \quad (3.41)$$

$$j_{s,\text{source}} \approx j_w S_1 = j_w c_{s,1} \frac{M_s}{\rho_w} \quad (3.42)$$

The molar concentration of the non-volatile solutes next to the liquid-vapour interface $c_{s,1}$ becomes higher than the bulk feed solution in the evaporator channel $c_{s,E}$. A concentration profile is formed. Driven by this concentration gradient, salt ions are transferred from the membrane interface to the feed bulk stream by diffusive and convective mass transfer mechanisms. The specific flux of salt ions $j_{s,1-E}$ transferred from the liquid-vapour interface to the bulk stream is given in Eq. 3.43, introducing the salt mass transfer coefficient on the evaporator side $\beta_{s,E}$.

$$j_{s,1-E} = \beta_{s,E} M_s (c_{s,1} - c_{s,E}) \quad (3.43)$$

Eq. 3.44 describes the mass transfer by the Sherwood number Sh , that indicates the portion of convective transfer with respect to diffusive transfer only.

$$\beta = Sh \frac{D_{sw}^o}{d_h} \quad (3.44)$$

Here, d_h is the characteristic length for diffusion and D_{sw}^o represents the diffusion coefficient of salt in water. A review, presenting diffusion coefficients of ions in water is given in [116]. Based

on the analogy of heat and mass transfer, the Sherwood number is usually calculated by using an empirical correlation of the form given in Eq. 3.45, similar to the correlation used to calculate the Nusselt number.

$$Sh = a Re^b Sc^c \quad (3.45)$$

The parameters a , b and c may be determined by a fit to experimental data or be chosen similarly to those used for the appropriate heat transfer correlation. The hydrodynamic regime is evaluated by the dimensionless Reynolds number Re from Eq. 3.35 and physical parameters affecting mass transfer are introduced by the Schmidt number Sc given in Eq. 3.46.

$$Sc = \frac{\mu}{\rho D_{sw}^o} \quad (3.46)$$

The Schmidt number Sc includes the liquid's dynamic viscosity μ , the liquid's density ρ and the ordinary diffusion coefficient D_{sw}^o .

Assuming a steady-state condition, the salt flux that is transported to the bulk feed stream $j_{s,1-E}$ is equal to the source term at the evaporation surface $j_{s,source}$. Eq. 3.47, derived from Eqs. 3.42 and 3.43, gives an estimation for the interfacial concentration c_1 . A schematic representation of concentration profiles in an MD channel configuration, assuming pure water on the condenser side, is provided in Fig. 3.4.

$$c_{s,1} = c_{s,E} \left(1 - \frac{j_w}{\rho_w \beta_{s,E}} \right)^{-1} \quad (3.47)$$

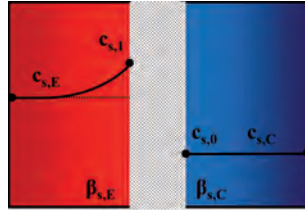


Figure 3.4: Schematic representation of concentration profiles in an MD channel configuration, assuming pure water on the condenser side.

The process driving force in membrane distillation is affected by the feed bulk concentration, as analysed earlier in Sec. 3.1.1. An additional loss in driving force is therefore caused by the higher concentration at the interfacial surface for evaporation. A concentration polarisation coefficient can be defined, representing the ratio of the effective interfacial concentration difference to the bulk stream concentration difference. For solutions containing non-volatile solutes, the permeate side concentration is usually zero, leading to Eq. 3.48, where the concentration polarisation coefficient equals the ratio of the feed side interfacial concentration c_1 to the respective bulk stream concentration c_E .

$$\xi = \frac{\Delta c_{1-0}}{\Delta c_{E-C}} = \frac{c_1 - c_0}{c_E - c_C} = \frac{c_1}{c_E} \quad (3.48)$$

The concentration polarisation coefficient $\xi \geq 1$ gives a quantitative measure for the concentration polarisation phenomenon. It is important to notice that the concentration polarisation

coefficient does not include a direct dependence on salinity level. High transmembrane water flux j_w or poor mass transfer coefficients on the feed side $\beta_{s,E}$ lead to stronger concentration polarisation and higher values for ξ , respectively. The concentration polarisation phenomenon is quantitatively derived and discussed in Sec. 3.4.5, subsequent to comprehensive MD model development.

3.1.5 Integrated Modelling of Membranes on Backing Structures

Many flat sheet membranes used for MD applications are laminated onto an open mechanical support structure, the backing material. Membranes including a support structure are referred to as laminates. The introduction of a backing material leads to significant effects that require consideration for both heat and mass transfer. Depending on the backing position, the membrane area is covered partially either on the evaporator side or on the condenser side, leading to negative effects on process performance. Only a few authors have addressed this topic and published experimental results showing a significant influence of backing materials on flux and thermal efficiency [122, 130, 155, 156]. First approaches to include effects of a backing material into model equations introduce the backing as an homogeneous additional thermal resistance layer next to the membrane [150, 157]. The main effect of this additional resistance layer is a lower membrane interfacial temperature difference that is accompanied by a small change in mean membrane temperature level. Some flux reduction due to the backing is represented by such a “Homogeneous layer approach”, however, it does not show a significant dependence on the backing position. Furthermore, the existing modelling approach is not able to reveal a significant impact of the backing on the thermal efficiency, since the thermal efficiency is not sensitive to a change in temperature difference (see Eq. 3.25). Consequently, the important role of membrane support structures on process performance has not yet been studied sufficiently and especially the theoretical modelling needs some reconsideration.

In order to achieve comprehensive understanding of the nature of the influencing effects, a new and more detailed “Split-path model” for laminates, including effects of the backing structure and its position, is derived within this thesis. The basic idea is to split the total laminate surface area A_L into one fraction $A_{L,B}$, where the membrane surface is covered by the backing and a second fraction $A_{L,M}$, where the membrane surface is open. For clarity, a schematic top view of a scrim type backing with the assignment of the surface fractions is illustrated in Fig. 3.5.

Mathematically, the surface area allocation is represented by Eq. 3.49, where the surface porosity of the backing is used to determine the coverage by the backing material. The surface porosity of the backing is assumed to be equal to the volumetric porosity, the backing voidage ε_B .

$$\begin{aligned} A_L &= A_{L,M} + A_{L,B} \\ &= \varepsilon_B A_L + (1 - \varepsilon_B) A_L \end{aligned} \quad (3.49)$$

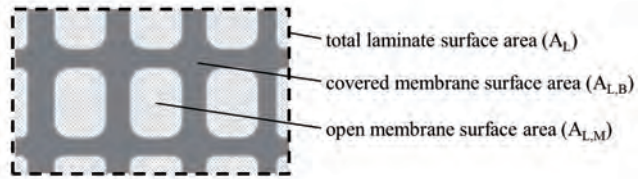


Figure 3.5: Schematic diagram of allocation to open and covered membrane surface area fractions.

Each surface fraction is then considered to be the effective cross-sectional area for an individual transfer path with its individual set of transfer equations. The transfer associated with the total laminate surface is evaluated by the superposition principle.

With this approach, the backing layer is not considered to be homogeneous and the individual transfer phenomena associated with the presence of the backing are modelled more realistically. In this section, the necessary modifications to the heat and mass transfer equations are identified and discussed.

Heat and Mass Transfer Through a Laminate

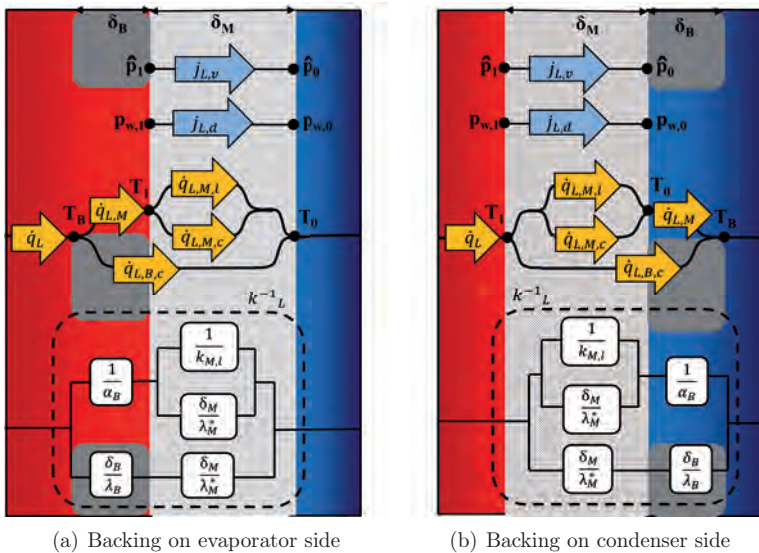


Figure 3.6: “Split-path” approach for a membrane model including support structures.

The phenomenology defining the mass transfer in laminates is quite similar to that of membranes without backing structures and the same basic equations given in the preceding sections are used

in laminate mass transfer modelling. However, some modifications need to be considered. In the common membrane models, the total membrane surface area A_M is considered to be the effective cross-sectional area for transmembrane mass transfer. In these cases, the diffusion paths for the water molecules are typically assumed to be separate and parallel. For the case of disordered diffusion in the asymmetric laminate layers, an assumption must be made for the definition of an effective cross-sectional area for transmembrane mass transfer. In the worst case, only the open surface fraction of the membrane ($A_{L,M} = \varepsilon_B \cdot A_L$) is active and the total laminate surface area is reduced by the complete area that is covered by the backing. In the optimal case, the backing does not have any influence on the effective cross-sectional area and the complete laminate surface area (A_L) is considered the effective cross-sectional area for transmembrane mass transfer. Consequently, a factor accounting for the reduction of the effective cross-sectional area for transmembrane mass transfer needs to be introduced into the common model equations for the mass transfer coefficients. This factor is referred to as the laminate factor f_L ($\varepsilon_B \leq f_L \leq 1$). Furthermore, some of the water molecules diffuse along diagonal paths and therefore cover longer distances from the open evaporator to the open condenser surface. The mean path length for diffusion in the membrane pores is therefore expected to increase. This effect can be accounted for by assuming a greater tortuosity in laminates τ_L than in single membranes ($\tau_L \geq \tau_M$). Modified transfer coefficients for laminates $C_{L,d,mol} (\leq C_{M,d,mol})$, $C_{L,d,Kn} (\leq C_{M,d,Kn})$ and $C_{L,d,v} (\leq C_{M,d,v})$ can be derived by including the laminate factor f_L and the greater laminate tortuosity τ_L in the basic relations for membrane mass transfer coefficients (Eqs. 3.10, 3.12, 3.14). The modified laminate tortuosity and the laminate factor are each assumed to remain equal for all of the transfer phenomena. A discussion of the parametrisation of these specific laminate parameters is continued in the following sections, considering experimentally obtained results. The total flux through a laminate j_L is calculated according to Eq. 3.50.

$$\begin{aligned}
 j_L &= j_{L,d} + j_{L,v} \\
 &= C_{L,d}(p_{w,1} - p_{w,0}) + C_{L,v}(\hat{p}_1 - \hat{p}_0) \\
 &= \left[\frac{1}{C_{L,d,Kn}} + \frac{1}{C_{L,d,mol}} \right]^{-1} (p_{w,1} - p_{w,0}) + C_{L,v}(\hat{p}_1 - \hat{p}_0)
 \end{aligned} \tag{3.50}$$

In order to account for the effect of backing structures on overall heat transfer, latent, conductive, convective and radiative heat transfer phenomena need to be taken into consideration. A rather complex network of thermal resistances is formed by the presence of a backing material. The schematic diagrams including the nomenclature are given in Fig. 3.6. The figures illustrate the channel configurations for a membrane with the backing on the evaporator side and for a membrane with the backing on the condenser side.

The purely conductive heat flow $\dot{q}_{L,B,c}$ is transferred through the cross-sectional area $A_{L,B}$ that is covered by the backing. This path for the heat transfer is represented by a series connection of the conductive thermal resistances of the membrane ($\delta_M \lambda_M^*{}^{-1}$) and the solid part of the backing ($\delta_B \lambda_B^{-1}$). In the open part of the backing, which occupies the cross-sectional area $A_{L,M}$, coupled

heat and mass transfer occurs. The heat flow transferred through this part is labelled with $\dot{q}_{L,M}$, which is then divided into a latent and a conductive fraction $\dot{q}_{L,M,c}$ and $\dot{q}_{L,M,l}$. This path for the heat transfer is represented by a series connection of the heat transfer resistance in the backing pores α_B^{-1} and the conductive and latent heat transfer resistance in the membrane ($\delta_M \lambda_M^*^{-1}$ and $k_{M,l}^{-1}$). If the backing pores are filled with water, conductive and convective heat transfer to the membrane surface occurs. The effective heat transfer in the backing pores is described in Eq. 3.51, where the Nusselt number Nu_B gives the extent of convection, which is expected to increase for higher bulk stream flow rates.

$$\alpha_B = Nu_B \frac{\lambda_w}{\delta_B} \quad (3.51)$$

Based on the resistance circuits in Fig. 3.6, the heat transfer equations have been adjusted in order to account for the main effects of backing structures. The composition of the total heat flow through a laminate \dot{q}_L , is given in Eq. 3.52

$$\begin{aligned} \dot{q}_L &= \dot{q}_{L,M} + \dot{q}_{L,B,c} \\ &= \dot{q}_{L,M,l} + \dot{q}_{L,M,c} + \dot{q}_{L,B,c} \end{aligned} \quad (3.52)$$

Cases are distinguished for the different backing positions. The modified model equations for the single heat flow fractions are given in Tab. 3.1. An integral heat transfer coefficient through the laminate k_L is defined. The nomenclature used is given in Fig. 3.6.

Table 3.1: “Split path” model for single laminates

	Backing on evaporator side	Backing on condenser side
$\dot{q}_L =$	$k_L (T_B - T_0)$	$k_L (T_1 - T_B)$
$\dot{q}_{L,M} =$	$\varepsilon_B \alpha_B (T_B - T_1)$	$\varepsilon_B \alpha_B (T_0 - T_B)$
$\dot{q}_{L,M,l} =$	$j_L \Delta h_v$	$j_L \Delta h_v$
$\dot{q}_{L,M,c} =$	$\varepsilon_B \frac{\lambda_M^*}{\delta_M} (T_1 - T_0)$	$\varepsilon_B \frac{\lambda_M^*}{\delta_M} (T_1 - T_0)$
$\dot{q}_{L,B,c} =$	$(1 - \varepsilon_B) \left[\frac{\delta_M}{\lambda_M^*} + \frac{\delta_B}{\lambda_B} \right]^{-1} (T_B - T_0)$	$(1 - \varepsilon_B) \left[\frac{\delta_M}{\lambda_M^*} + \frac{\delta_B}{\lambda_B} \right]^{-1} (T_1 - T_B)$

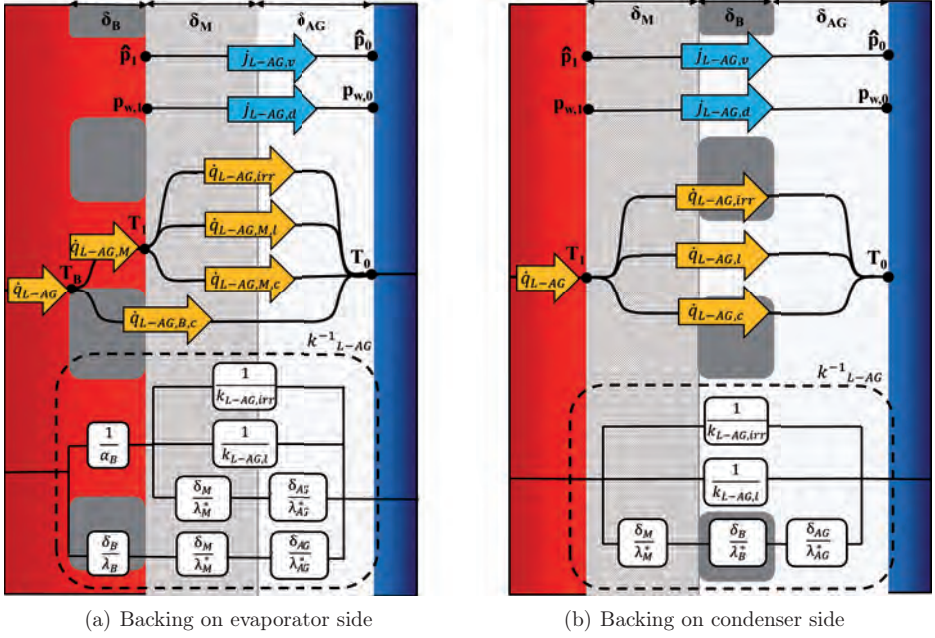


Figure 3.7: Modelling approach for a combined laminate and air gap.

Heat and Mass Transfer Through a Combined Laminate and Air Gap

The mass transfer through a combined laminate and air gap is evaluated according to Eq. 3.53.

$$\begin{aligned}
 j_{L-AG} &= j_{L-AG,d} + j_{L-AG,v} \\
 &= C_{L-AG,d}(p_{w,1} - p_{w,0}) + C_{L-AG,v}(\hat{p}_1 - \hat{p}_0)
 \end{aligned} \tag{3.53}$$

The composition of the combined diffusive laminate and air gap mass transfer coefficient $C_{L-AG,d}$ and the valid set of heat transfer equations depends on the position of the backing.

If the backing faces towards the evaporator channel, the combined diffusive mass transfer coefficient is superposed in Eq. 3.54, according to Eq. 3.18, including the diffusive mass transfer coefficients of the membrane section of the laminate and the air gap section.

$$C_{L-AG,d} = \left[\frac{1}{C_{L,d,Kn}} + \frac{1}{C_{L,d,mol}} + \frac{1}{C_{AG,d,mol}} \right]^{-1} \tag{3.54}$$

Since the resistance due to viscous effects in the air gap section is negligible, only the membrane layer contributes to the combined viscous mass transfer coefficient ($C_{L-AG,v} = C_{L,v}$).

In the case where the backing is facing the evaporator channel, the backing pore volume is filled with liquid, similar to the configuration without an air gap. The “split path” heat transfer model for a single laminate layer is extended for the additional air gap layer by including the effective thermal conductivity of the air gap λ_{AG}^* and the air gap thickness δ_{AG} . The radiative heat flux $\dot{q}_{L-AG,rad}$ from the warm membrane surface on the air gap side to the permeate film is simplified to the transfer equation that was introduced for membranes without backing structures in Eq. 3.26. The total amount of transferred heat is evaluated similar to Eq. 3.52, whereas the modified set of heat transfer equations for the individual fractions is given in Tab. 3.2. An integral heat transfer coefficient through the laminate and air gap k_{L-AG} is defined. The new network of thermal resistances including the nomenclature is illustrated in Fig. 3.7(a).

Table 3.2: “Split path” model for a combined laminate and air gap configuration, with the backing on the evaporator side.

Backing on evaporator side	
$\dot{q}_{L-AG} =$	$k_{L-AG} (T_B - T_0)$
$\dot{q}_{L-AG,M} =$	$\varepsilon_B \alpha_B (T_B - T_1)$
$\dot{q}_{L-AG,M,l} =$	$j_{L-AG} \Delta h_v$
$\dot{q}_{L-AG,M,c} =$	$\varepsilon_B \left[\frac{\delta_M}{\lambda_M^*} + \frac{\delta_{AG}}{\lambda_{AG}^*} \right]^{-1} (T_1 - T_0)$
$\dot{q}_{L-AG,B,c} =$	$(1 - \varepsilon_B) \left[\frac{\delta_M}{\lambda_M^*} + \frac{\delta_B}{\lambda_B^*} + \frac{\delta_{AG}}{\lambda_{AG}^*} \right]^{-1} (T_B - T_0)$
$\dot{q}_{L-AG,rad} =$	$\frac{\varepsilon_{AG} \sigma}{\varepsilon_M^{-1} + \varepsilon_w^{-1} - 1} (T_1^4 - T_0^4)$

If the backing faces towards the air gap, the backing layer adds to the vapour space and needs to be accounted for as an additional transfer resistance. The mass transfer in the backing section is based on the theory for the continuum region ($Kn \ll 1$). Similar mass transfer mechanisms as in the air gap section are assumed. Consequently no Knudsen diffusion occurs, no free convection contributes to the overall mass transfer and viscous flow resistance is neglected.

The combined diffusive laminate and air gap mass transfer coefficient $C_{L-AG,d}$, given in Eq. 3.55, includes three layers: the membrane part of the laminate, the backing part of the laminate and the air gap.

$$C_{L-AG,d} = \left[\frac{1}{C_{L,d,Kn}} + \frac{1}{C_{L,d,mol}} + \frac{1}{C_{B,d,mol}} + \frac{1}{C_{AG,d,mol}} \right]^{-1} \quad (3.55)$$

Since the resistance due to viscous effects in the backing layer is negligible, only the membrane layer contributes to the combined viscous mass transfer coefficient ($C_{L-AG,v} = C_{L,v}$).

Eq. 3.19 is applied to determine $C_{B,d,mol}$ by inserting the backing layer thickness δ_B . The backing voidage ε_B takes the reduction of the available cross-sectional area for diffusion due to the solid backing structure into account. The mean temperature and the partial pressure of air in the backing section are assumed to be equal to the air gap section ($\bar{T}_B \approx \bar{T}_{1-0}$ and $\bar{p}_{B,a,ln} \approx \bar{p}_{1-0,a,ln}$).

To describe the heat transfer through the combined laminate and air gap \dot{q}_{L-AG} in the case of a backing adjacent to the air gap, no complex “Split-path” model needs to be applied. A basic parallel connection of the latent, the conductive and the radiative heat transfer is modelled in Eq. 3.56, similar to the case without backing (see Eq. 3.26). The conductive heat transfer resistance is increased by the backing layer, and a series connection of three homogeneous layers is considered. The total heat transfer resistance k_{L-AG} of the combined laminate and air gap layer is defined. An illustration of the new network of thermal resistances including the nomenclature is given in Fig. 3.7(b).

$$\begin{aligned} \dot{q}_{L-AG} &= j_{L-AG} \Delta h_v + \left[\frac{\delta_M}{\lambda_M^*} + \frac{\delta_B}{\lambda_B^*} + \frac{\delta_{AG}}{\lambda_{AG}^*} \right]^{-1} (T_1 - T_0) \\ &+ \frac{\varepsilon_{AG} \sigma}{\varepsilon_M^{-1} + \varepsilon_w^{-1} - 1} (T_1^4 - T_0^4) \\ &= k_{L-AG} (T_1 - T_0) \end{aligned} \quad (3.56)$$

The effective thermal conductivity of the backing λ_B^* is calculated applying the modified iso-strain model in Eq. 3.57, taking the backing porosity ε_B and the solid phase tortuosity $\tau_{B(s)}$ into account (see Eq. 3.23). No liquid water phase is considered as a thermal bridge, since the backing layer is located in the rather warm section of the vapour space next to the membrane.

$$\lambda_B^* = \varepsilon_B \lambda_{B(g)} + (1 - \varepsilon_B) \tau_{B(s)}^{-1} \lambda_{B(s)} \quad (3.57)$$

The effective thermal conductivities of the membrane part of the laminate λ_M^* and the air gap λ_{AG}^* have already been defined in Eq. 3.23 and Eq. 3.27, respectively.

3.2 Node Models for Theoretical Process Evaluation

In the following section, parametric models are derived for the different channel configurations, representing the common membrane distillation process variants. The models are used to predict the transmembrane vapour flux and heat transfer for a steady-state scenario, based on channel configuration, materials and bulk stream operating conditions. The node models presented here are referred to as one-dimensional models, since homogeneous conditions are assumed along the flow channels. The channels are conceptually divided into a series connection of multiple transfer layers perpendicular to the membrane. Each layer introduces a new set of specific heat and mass transfer properties, according to Sec. 3.1. The walls are considered impermeable and adiabatic. The models were implemented in the C programming language, and the coupled heat and mass transfer equations are solved with an iterative solving algorithm.

3.2.1 Direct Contact Channel Configuration

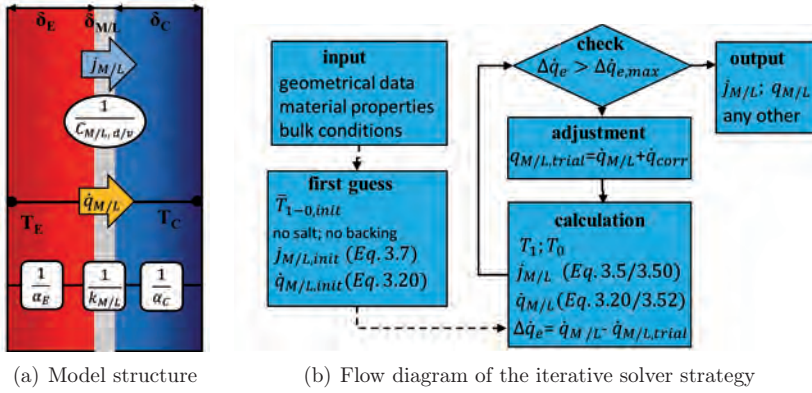


Figure 3.8: Node model for DCMD channel configuration.

A node model for the Direct Contact Membrane Distillation (DCMD) configuration was implemented according to the schematic diagram in Fig. 3.8(a). The mass transfer through the membrane/laminate is given in Eq. 3.5/3.50. The heat transfer in the channel configuration is modelled by a series connection of three layers of thermal resistances:

- resistance from evaporator bulk stream to the membrane/laminate surface (α_E^{-1})
- effective resistance of the membrane/laminate ($k_{M/L}^{-1}$)
- resistance from membrane/laminate surface to the condenser bulk stream (α_C^{-1})

The model equations used for the heat transfer in the boundary layers are Eqs. 3.28 and 3.29. The integral heat transfer resistance in the membrane/laminate is represented by $k_{M/L}$ from Eq. 3.20/Tab. 3.1.

The iterative solving strategy is illustrated in Fig. 3.8(b). At first, the necessary geometrical information about channels, spacers, membrane/laminate and backing as well as material and fluid properties has to be initialised. The evaporator side and condenser side bulk stream flow rates and temperatures, as well as the total pressure level need to be defined. An initial flux result $j_{M/L,init}$ is obtained from Eq. 3.7 by neglecting the feed side salinity, the backing and assuming the membrane/laminate mean temperature to be equal to the arithmetic bulk phase mean temperature $\bar{T}_{1-0,init} = 0.5 (T_E + T_C)$. Then an initial value for the total transferred heat $q_{M/L,init}$ is calculated according to Eq. 3.20, based on the initial flux result. In a next step, the interfacial temperatures and vapour pressures corresponding to $q_{M/L,init}$ are derived and the respective flux $j_{M/L}$ is re-evaluated with Eq. 3.5/3.50. The result is of good quality, since no linearisation is used, feed salinity is taken into account and a more precise value for membrane/laminate mean temperature $\bar{T}_{1-0} = 0.5 (T_1 + T_0)$ is accessible. The new flux result

leads to a new value for the total transferred heat $\dot{q}_{M/L}$ given by Eq. 3.20/3.52. The deviation of the new value for the transferred heat with respect to the initial result that was used for the preceding evaluation of the interfacial temperatures is defined as the thermodynamic error $\Delta\dot{q}_e$.

$$\Delta\dot{q}_e = \dot{q}_{M/L} - \dot{q}_{M/L,init} \quad (3.58)$$

If the error is higher than the user-defined maximal permissible error $\Delta\dot{q}_{e,max}$, the trial result is corrected by a solver term \dot{q}_{corr} that depends on $\Delta\dot{q}_e$ and the number of iterations that have already been done. The solver starts with a large step size to guarantee rapid convergence and then automatically reduces the step size to achieve high accuracy, if necessary. After adjustment of the trial result, the procedure starts over again until the error is lower than the maximal permissible error. This leads to values that satisfy all physical constraints of the coupled heat and mass transfer equations for a DCMD channel configuration. In addition to the flux and transferred heat, any other value of interest is also accessible for further analysis.

3.2.2 Permeate Gap Channel Configuration

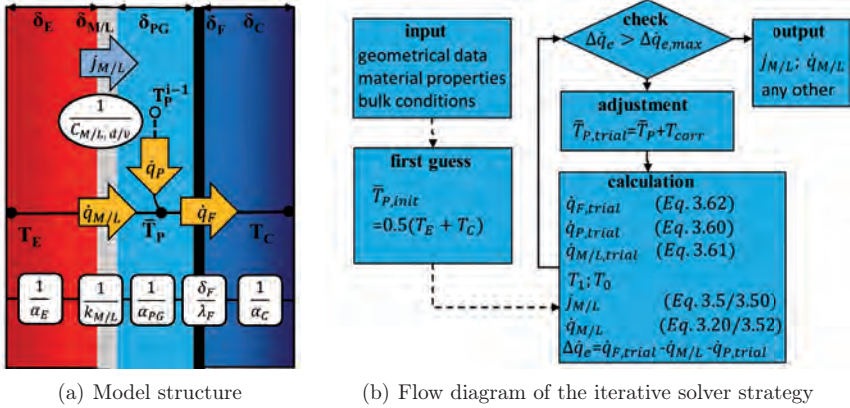


Figure 3.9: Node model for PGMD channel configuration.

In the Permeate Gap Membrane Distillation (PGMD) process, a third channel is introduced by an additional, non-permeable polymeric film. Since the membrane/laminate is in direct contact with water on both sides, the heat and mass transfer models for a DCMD configuration are also valid for the membrane section of the PGMD model.

However, the presence of the permeate gap and the polymeric film material introduces additional heat transfer resistances to the membrane/laminate, that need to be taken into account in PGMD modelling. Thus, the heat transfer in the channel arrangement is modelled by a series connection of five thermal resistance layers, according to Fig. 3.9(a):

- resistance from evaporator bulk stream to the membrane/laminate surface (α_E^{-1})
- effective resistance of the membrane/laminate ($k_{M/L}^{-1}$)
- effective resistance of the permeate gap (k_{PG}^{*-1})
- resistance of the non-permeable polymeric film material ($\delta_F \lambda_F^{-1}$)
- resistance from the film surface to the condenser bulk stream (α_C^{-1})

For the heat transfer in the hydrodynamic boundary layers, Eqs. 3.28 and 3.29 are used.

The heat transfer in the non-permeable polymeric film is purely conductive and is calculated using the film material's thermal conductivity λ_F and the film thickness δ_F .

For the heat transfer in the permeate gap, the solid spacer material allows conductive heat transfer only, whereas the liquid permeate phase allows conductive and convective heat transfer phenomena. The effective heat transfer coefficient for the permeate gap k_{PG}^* is calculated using the permeate spacer voidage ε_{PG} as given in Eq. 3.59.

$$k_{PG}^* = \varepsilon_{PG} Nu_{PG} \frac{\lambda_w}{\delta_{PG}} + (1 - \varepsilon_{PG}) \frac{\lambda_S}{\delta_{PG}} \quad (3.59)$$

The Nusselt number in the permeate gap Nu_{PG} indicates the extent of convective heat transfer in the liquid permeate phase. If the membrane surface is small and the vapour flux is low, the permeate might be considered to be stagnant in the thin gap, the conductive heat transfer mechanism dominates and the Nusselt number in the permeate gap reaches unity. Considering sections with large membrane surface areas, resulting in a relevant permeate flow rate moving towards the permeate channel outlet, significant convection may occur in the permeate channel. In some cases, the fluid in the permeate channel is even forced to flow convectively by a pump. In this case, appropriate correlations to estimate the Nusselt number in the permeate channel need to be chosen. If a permeate flow \dot{m}_P^{i-1} with the temperature T_P^{i-1} and the thermal capacity c_P^{i-1} is moving along the permeate channel into a zone of different temperature \bar{T}_P and thermal capacity c_P , sensible heat \dot{Q}_P is either accepted or ejected by the permeate until the local temperature level is reached. \dot{Q}_P is assigned to the membrane/laminate surface area $A_{M/L}$ of the respective node, in order to gain a specific value \dot{q}_P for the heat flow.

$$\dot{q}_P = \frac{1}{A_{M/L}} \dot{Q}_P = \frac{1}{A_{M/L}} (\dot{m}_P^{i-1} c_P^{i-1} (T_P^{i-1} - T_P) + \dot{m}_P^{i-1} (c_P^{i-1} - c_P) T_P) \quad (3.60)$$

Due to the very thin permeate channels and the very low permeate flow rates, the dynamics of this heat transfer are neglected. However, the term \dot{q}_P in Eq 3.60 enables the model to predict internal recovery of the heat incorporated in the distillate or internal pre-heating of the distillate stream. These effects gain importance in the context of full-scale modules and will be reconsidered in chapter 4.1 on module modelling.

The heat flux through the membrane/laminate $\dot{q}_{M/L}$ and the heat flux through the polymeric film \dot{q}_F are related according to Eq. 3.61.

$$\dot{q}_F = \dot{q}_{M/L} + \dot{q}_P \quad (3.61)$$

If the permeate is considered to be stagnant in the permeate gap, the fraction \dot{q}_P equals zero and no heat is received or rejected by the permeate.

The iterative solving algorithm for the Permeate Gap Membrane Distillation (PGMD) node model, illustrated in Fig. 3.9(b), refers to slightly different constraints than the DCMD algorithm that was presented in the preceding section. As an initial value, the temperature in the centre of the permeate gap is assumed to be equal to the mean bulk stream temperature $\bar{T}_{P,\text{init}} = 0.5 (T_E + T_C)$. Based on this initial estimate, the heat flux $\dot{q}_{F,\text{trial}}$ that is transferred from the centre of the permeate gap through the polymer film into the condenser bulk stream can be evaluated by Eq. 3.62.

$$\dot{q}_F = \left[\frac{1}{2k_{PG}^*} + \frac{\delta_F}{\lambda_F} + \frac{1}{\alpha_C} \right]^{-1} (\bar{T}_P - T_C) \quad (3.62)$$

The heat flux $\dot{q}_{P,\text{trial}}$ that is added to or extracted from the permeate, is known. Consequently, the function in Eq. 3.61 leads to the corresponding value for the heat flux $\dot{q}_{M/L,\text{trial}}$ transferred through the membrane/laminate section. Subsequently, the interfacial temperatures and partial pressures are accessible and the vapour flux $j_{M/L}$ is evaluated according to Eq. 3.5/3.50. Based on this flux result, the corresponding heat flux $\dot{q}_{M/L}$ is recalculated according to Eq. 3.20/3.52. The thermodynamic error $\Delta\dot{q}_e$ is given by the difference determined by Eq. 3.61.

$$\Delta\dot{q}_e = \dot{q}_{F,\text{trial}} - \dot{q}_{M/L} - \dot{q}_{P,\text{trial}} \quad (3.63)$$

If the error is higher than the user-defined maximal permissible error $\Delta\dot{q}_{e,\text{max}}$, the trial is corrected by a solver term that depends on $\Delta\dot{q}_e$ and the number of iterations that have already been done, similar to the solver for the DCMD equations. After adjustment of the result, the procedure is iterated until the error is lower than the maximal permissible error. This leads to values that satisfy all physical constraints of the coupled heat and mass transfer equations for a PGMD channel configuration.

3.2.3 Air Gap Channel Configuration

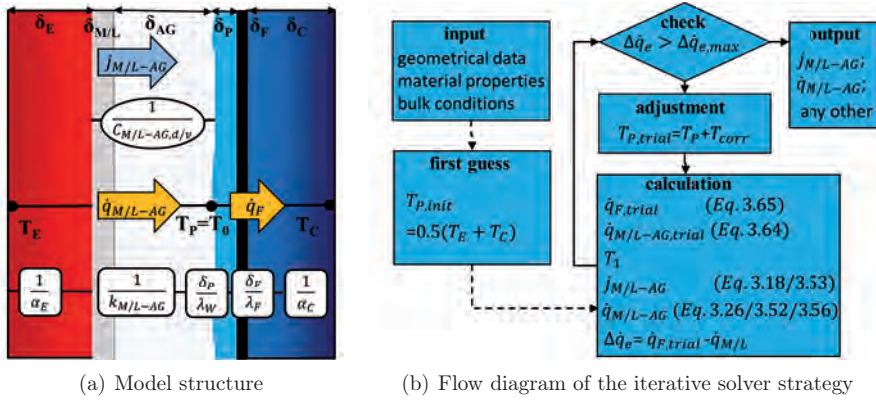


Figure 3.10: Node model for AGMD channel configuration

In Air Gap Membrane Distillation (AGMD) process, a third channel is formed with a non-permeable polymeric film, similar to the PGMD channel configuration. This channel is filled with air and introduces additional heat and mass transfer resistances that need to be considered in AGMD process modelling.

For heat transfer, the model structure consists of a series connection of six thermal resistance layers, according to Fig. 3.10(a):

- resistance from evaporator bulk stream to the membrane/laminate surface (α_E^{-1})
- combined effective resistance of the membrane/laminate and the air gap ($k_{M/L-AG}^{-1}$)
- resistance of the condensate film layer ($\delta_P \lambda_w^{-1}$)
- resistance of the non-permeable polymeric film material ($\delta_F \lambda_F^{-1}$)
- resistance from the film surface to the condenser side bulk stream (α_C^{-1})

For the heat transfer in the hydrodynamic boundary layers, Eqs. 3.28 and 3.29 are used.

Modelling of the condensation sequence is accompanied by high uncertainty. If the condensate is assumed to be a thin homogeneous permeate film layer, convective heat transfer turns out to be negligible and values for the film thickness have been theoretically derived to be in the order of ≈ 0.1 mm [128]. In this case, the heat transfer resistance may be estimated by an approximate permeate film thickness δ_P and the thermal conductivity of water λ_w . Other researchers used special correlations representing the film condensation coefficient [129]. No reports of the use of correlations representing dropwise condensation have been encountered during this review.

The heat transfer in the non-permeable polymer film is purely conductive and is estimated using the film material's thermal conductivity λ_F and the film thickness δ_F .

No heat is internally recovered from the permeate film in Air Gap Membrane Distillation (AGMD), so the total heat flux transferred through the condensate film and the polymer film \dot{q}_F is equal to the heat flux transferred through the membrane/laminate and the air gap $\dot{q}_{M/L-AG}$.

$$\dot{q}_F = \dot{q}_{M/L-AG} \quad (3.64)$$

The iterative algorithm for the AGMD node model, illustrated in Fig. 3.10(b), uses a quite similar solving method to the PGMD algorithm that was presented in the preceding section. As an initial estimate, the cold liquid-vapour interfacial temperature on the permeate film surface $T_P (= T_0)$ is assumed to be equal to the mean bulk stream temperature $\bar{T}_{P,init} = 0.5 (T_E + T_C)$. Based on this assumption, the heat flux $\dot{q}_{F,trial}$ transferred through the permeate film and the polymeric film into the condenser bulk stream can be evaluated with Eq. 3.65.

$$\dot{q}_F = \left[\frac{\delta_P}{\lambda_w} + \frac{\delta_F}{\lambda_F} + \frac{1}{\alpha_C} \right]^{-1} (T_P - T_C) \quad (3.65)$$

The function in Eq. 3.64 leads to the corresponding heat flux $\dot{q}_{M/L-AG,trial}$ that is transferred through the membrane/laminate and air gap section. Subsequently, the interfacial temperatures and partial pressures are known and the vapour flux $j_{M/L-AG}$ is evaluated by Eq. 3.18/3.53. Based on this flux result, the corresponding heat flux $\dot{q}_{M/L-AG}$ is re-evaluated by Eq. 3.26/3.56 or Tab. 3.2. The thermodynamic error $\Delta\dot{q}_e$ is given by the difference determined by Eq. 3.64.

$$\Delta\dot{q}_e = \dot{q}_{F,trial} - \dot{q}_{M/L-AG} \quad (3.66)$$

If the error is higher than the user-defined maximal permissible error $\Delta\dot{q}_{e,max}$, the trial result is corrected by a solver term that depends on $\Delta\dot{q}_e$ and the number of iterations that have already been done, similarly to the solver for the DCMD or PGMD models. After adjustment of the trial result, the procedure is iterated until the error is lower than the maximal permissible error. This leads to values that satisfy all physical constraints of the coupled heat and mass transfer equations for an AGMD channel configuration.

3.3 Experimental Approach

A laboratory-scale test cell was developed for studies of the basic behaviour of membrane distillation processes. This experimental platform is mainly used for membrane characterisation, studies of different MD configurations, parameter identification and model validation. This section gives a detailed description of the test facility, the test cell and the experimental procedures. A supplementary discussion of the expected uncertainties of measurement is provided. The last part of this section introduces the different membrane, laminate, spacer and film materials that are used throughout the experimental parts of this thesis.

3.3.1 Laboratory Cell Design and Test Rig

A multi-purpose test cell for sheet membranes was developed for laboratory-scale experiments. The cell consists of two transparent half-shells made of polycarbonate. The effective area for membrane evaluation is $150 \times 250 \text{ mm}^2$. The main flow channels were milled in the plate material. A set of $37 \times 1 \text{ mm}$ parallel distributor holes guarantees an optimised flow distribution from the integrated inlet and outlet manifolds. The use of different channel spacers and rubber gaskets of the corresponding size allow different channel widths to be configured. The compressibility of the rubber gaskets is taken into account.

A separate channel can be established using an additional, modified gasket, a gap spacer and an impermeable polymeric film between the membrane and the condenser channel. In this way, either permeate gap or air gap configurations can be established. For the permeate gap configuration, the permeate outlet is oriented upwards to guarantee that air is removed from the gap. In the case of an air gap configuration, the permeate outlet is oriented downwards, since the permeate needs to exit the test cell by gravity.

A support frame made of stainless steel and an assembly using a torque wrench assures adequate contact pressure and defined compression for the rubber gaskets. The polycarbonate half-shell structure of 30 mm thickness and a closed, thermally insulating casing minimise thermal losses to the surroundings. The test cell is mounted in an upright position with the outlet manifolds upward to force out any air during operation. Fig. 3.11(a) shows a photograph of one half-shell with the flow distribution manifolds and Fig. 3.11(b) shows a photograph of the mounted test cell without insulation.

The test cell is integrated into a test facility that includes the hydraulic circuits, the controls and the data acquisition. The hydraulic layout of the set-up is shown in Fig. 3.12.

The test facility consists of separate hydraulic loops for the evaporator and condenser. For each loop, the feed water is recirculated from a 10l storage tank (2) by a double-stage centrifugal pump. The evaporator loop is heated by a separate heating loop with an electric heater (6) that can provide up to $1.5 \text{ kW}_{\text{th}}$. The condenser loop is cooled by using the laboratory cooling circuit

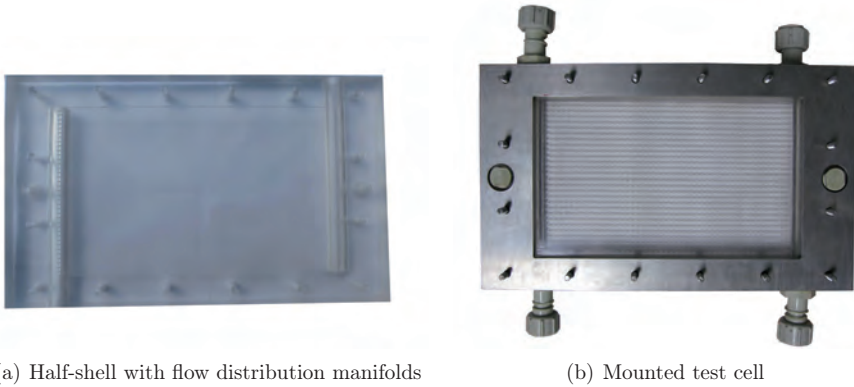


Figure 3.11: Photographs of the membrane test cell.

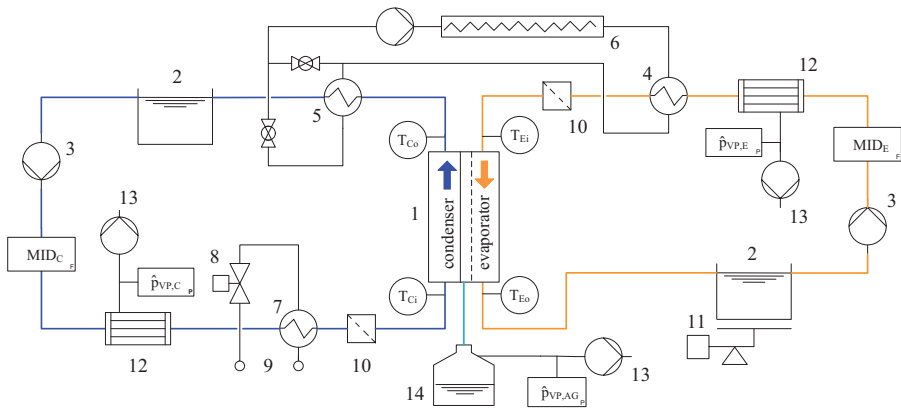


Figure 3.12: Hydraulic layout of the experimental set-up; 1 membrane test cell, 2 feed water tank, 3 feed pump, 4 heat exchanger, 5 auxiliary heat exchanger, 6 electric heater, 7 heat exchanger, 8 motorised valve, 9 laboratory cooling circuit, 10 filter, 11 electronic balance, 12 deaeration module, 13 vacuum pump, 14 permeate tank

(9) and a motorised valve (8) for controlling the cooling power. If needed, the condenser loop can gain heat from a heat exchanger (5), e.g. for high-temperature operation. Mechanical filters (10) with $100\ \mu\text{m}$ pores prevent especially the small internal flow distributor holes of the test cell from being blocked by particles. Commercially available Liqui-Cel membrane contactors from Membrana can optionally be included in both hydraulic loops for in-line water degassing (12). These contactors use polypropylene hollow fibre membranes with a porosity of approximately 25% and a total membrane area of $1.4\ \text{m}^2$. An MZ 2C vacuum pump from Vacuubrand is used to establish the vacuum condition on the lumen side of the hollow fibres. The deaeration modules are present in the hydraulic loops only if needed. For PGMD or AGMD experiments, the permeate is separated into a permeate tank (14). The vacuum pump is optionally used for

AGMD experiments, if the air gap is to be deaerated. All components that are in contact with the testing fluids are made of corrosion-resistant polymer materials. Except of the deaeration equipment, the components allow temperatures up to 95°C. The temperature is limited to approximately 60°C, if the deaeration modules are in use.

Four glass-encapsulated Pt100 temperature sensors are positioned directly at the evaporator inlet T_{Ei} , evaporator outlet T_{Eo} , condenser inlet T_{Ci} and condenser outlet T_{Co} of the test cell. The volumetric flow rates are measured by Krohne Optiflux magnetic inductive flow meters MID_E and MID_C . The weight of the evaporator storage tank is constantly measured with a Kern KB electronic balance. If the deaeration equipment is used, the vacuum conditions are monitored with tecsis3296 absolute pressure sensors $\hat{p}_{VP,E}$ and $\hat{p}_{VP,C}$. All sensor outputs are read in with an Agilent 34970A multiplexer and recorded on a computer.

3.3.2 Testing Conditions and Evaluation of Performance Parameters

Membrane distillation performance depends on a variety of operating conditions. Four independent operating parameters are identified to define the performance for a specific channel configuration: bulk temperature difference, mean temperature level, flow velocities and feed water concentration. If deaeration is applied, deaeration pressure is considered to be a fifth independent parameter that is required for clear definition of a specific operation point. In order to analyse the sensitivity of the process performance to a single operation parameter, the experiments have been performed by varying this specific parameter of interest while keeping the others constant.

Since the temperature difference is directly linked to the process driving force, the experimental results are quite sensitive to the measurement accuracy. Therefore, the temperature difference is controlled directly by referencing the evaporator inlet temperature T_{Ei} and condenser outlet temperature T_{Co} to the proportional-integral (PI) control system, instead of the two inlet temperatures. In this way, the effect of the slight temperature variation along the short flow channels on the effective temperature difference is minimised. The controlled temperatures T_{Ei} and T_{Co} are used to define the nominal mean membrane temperature level \bar{T}_{E-C} for a given operation point. For data analysis, the precise value for the mean temperature level in the test cell is calculated as the arithmetic mean of all main channel inlet and outlet temperatures. The mean flow velocities $\bar{c}_{E/C}$ in the channels are defined by the respective volumetric flow rates $\dot{V}_{E/C}$ that are controlled to be similar for the evaporator and condenser channels for all experiments presented in this work. Tap water is used for most of the experiments and sodium chloride (NaCl) is dissolved in tap water for the experiments on different feed water concentrations. One set of operation conditions with the individual parameter settings for the control system is given as an example in Tab. 3.3.

Table 3.3: Example sets of operation conditions representing the parameter variations in mean temperature, flow velocity and temperature difference, including the individual control parameters.

\bar{T}_{E-C}	ΔT_{E-C}	$\bar{c}_{E/C}$	$T_{Co,set}$	$T_{Ei,set}$	$\dot{V}_{Ei/Ci,set}^a$
[°C]	[K]	[m s ⁻¹]	[°C]	[°C]	[l h ⁻¹]
40	8	0.08	36	44	100
60	8	0.08	56	64	100
80	8	0.08	76	84	100
60	8	0.04	36	44	50
60	8	0.08	56	64	100
60	8	0.12	76	84	150
60	8	0.08	56	64	100
60	12	0.08	54	66	100
60	16	0.08	52	68	100

^aassuming spacer S-320; values dependent on channel width

A new membrane sample was installed, whenever the test cell set-up was changed. All experiments were performed at steady-state operation conditions for at least 5 h. The last 2 h of each experiment are used for further analysis.

To analyse the process performance, the absolute vapour flux J and thermal efficiency η_{th} are evaluated for each experiment. The thermal efficiency can be derived from sensor values obtained in the experiments by using Eq. 3.67.

$$\eta_{th} = \frac{J \Delta h_v}{0.5 \left(\dot{V}_C \rho_C c_{p,C} (T_{Co} - T_{Ci}) + \dot{V}_E \rho_E c_{p,E} (T_{Ei} - T_{Eo}) \right)} \quad (3.67)$$

For the thermo-physical properties of water, the temperature dependence of the latent heat of evaporation Δh_v , the thermal capacity c_p and the density ρ in particular, are taken into account. The arithmetic mean value of the energy balances for the evaporator and condenser channels is used to indirectly assign the heat losses to the surroundings equally to both half-shells. Furthermore, this reduces the uncertainty in evaluating the total transferred heat to a certain extent.

3.3.3 Uncertainty of Measurement and Error Propagation

This section presents a discussion regarding the confidence range of the experimentally obtained results based on the respective uncertainties of measurement, the quality of controls and the propagation of errors. Furthermore, a supplementary discussion and, if available, quantification of additional sources of uncertainties are given.

The individual uncertainties were determined for the temperature, the flow rate and the weight measurements. Regarding the temperatures, high accuracy of the Pt100-sensors (4 wires, class 1/3 B) is guaranteed by an absolute temperature calibration that is performed on a regular basis. The tolerated absolute deviation of the measurements with respect to a DKD-licensed reference sensor is ± 0.05 K. In order to account for a possible drift of the sensors during the period between two calibrations and the fact that the sensors are mounted externally to the test cell, the overall uncertainty of the temperature measurements is assumed to be ± 0.10 K. For the flow meters, a maximal error of $\pm 0.6\%$ was experimentally determined for different flow rates and salinities. A maximal error of ± 1.01 h⁻¹ is taken into consideration, leading to a rather conservative estimation throughout the required range of flow rates. The accuracy of the electronic balance is fundamentally rated as ± 0.05 g. However, a greater uncertainty is introduced by evaporative mass losses from the storage tank to the surroundings, especially at higher operation temperatures. To minimise evaporative mass losses, the storage tank is covered and sealed with a highly flexible polymer film that does not affect the mass measurement. In preliminary PGMD experiments, the mass of the separated distillate was compared to the mass determined by the difference in weight of the evaporator storage tank. An overall uncertainty of approximately ± 5 g h⁻¹ was determined. If the deaeration equipment is used, the overall uncertainty increases to approximately ± 10 g h⁻¹, due to additional evaporative mass losses within the deaeration module.

Subsequent to each experiment, a membrane leakage test was performed by using an aqueous sodium chloride solution at a higher pressure level on the evaporator side and tap water on the permeate side ($\Delta\kappa_{E-C} > 50$ mS cm⁻¹, $\Delta\hat{p}_{E-C} > 0.1$ bar). During the 30 min of leakage testing, the electrical conductivity of the permeate was monitored to assure the mechanical functionality of the membrane sample under test.

A measuring interval of 5 s ensures a large number of data points within the 2 h of interest for evaluating each experiment. The sensor values are derived as arithmetic mean values from the 1440 single data points. The short measurement interval allows the operation parameters to be controlled with high accuracy. Only minimal fluctuations of the controlled parameters are observed. The steady-state stability of the controls is quantified for a standard experiment (Tab. 3.3, line 2), evaluating the 2 h of interest. The standard deviation of the temperature measurements is less than 0.04 K, while the maximal difference from the set point is less than ± 0.10 K. Considering the flow rate measurements, the standard deviation is less than 0.21 h⁻¹, while the maximal difference from the set point is less than ± 1.01 h⁻¹. The error of the arithmetic mean values with respect to the set points are at least one order of magnitude lower than the uncertainty of measurement and therefore considered to be negligible for the temperature as well as the flow rate measurements. The steady-state behaviour of the operation conditions and the resulting flux as well as the test cell's total energy balance are screened for each experiment to ensure correct functioning of the equipment and the validity of the results.

A detailed error analysis has been conducted for the evaluation of the thermal efficiency according

to Eq. 3.67. The Gaussian law of error propagation in Eq. 3.68 describes the probable and the maximal error for a complex parameter of interest $f(z_i)$ that depends on several independent values z_i with their respective individual uncertainties Δz_i .

$$\Delta f(z_i)_{\text{prob}} = \sqrt{\sum_{i>1} \left(\frac{\partial f(z_i)}{\partial z_i} \Delta z_i \right)^2} \quad \Delta f(z_i)_{\text{max}} = \sum_{i>1} \left| \frac{\partial f(z_i)}{\partial z_i} \Delta z_i \right| \quad (3.68)$$

To estimate the overall uncertainty for the thermal efficiency, the individual uncertainties of the respective sensor values are considered as stated above. The probable and maximal uncertainties for the thermal efficiency evaluation have been explicitly evaluated for a set of DCMD, PGMD, AGMD and V-AGMD experiments that covers a wide range of operation conditions. The results presented in Fig. 3.13 correspond to the experiments in Figs. 3.31, 3.33 and 3.34.

It turns out that the uncertainty of the thermal efficiency evaluation is mainly dependent on the temperature differences from the channel inlets to the channel outlets, that needs to be evaluated in Eq. 3.67. This observation indicates the important role of the individual temperature measurements that have by far the largest contribution to the total uncertainty. Especially the AGMD measurements are of low quality, leading to rather high probable errors ranging from 5 – 16%. The uncertainties for the PGMD and V-AGMD configurations are quite similar, ranging from 4 – 9%. For the DCMD operation points, a larger temperature difference is developed, leading to a relatively precise evaluation of the thermal efficiency that is associated with a probable error of 1 – 4%. The measurement uncertainty is not explicitly indicated in the following diagrams to maintain clarity.

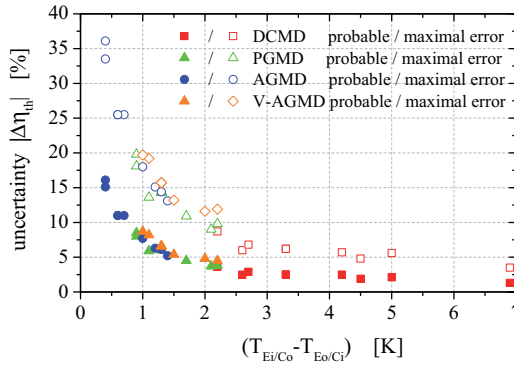


Figure 3.13: Probable and maximal uncertainties in the evaluation of the thermal efficiency estimated for different DCMD, PGMD, AGMD and V-AGMD experiments. The temperature, the flow rate and the flux measurements are taken into consideration for the propagation of errors according to Eq. 3.68.

3.3.4 Materials for Experimental Evaluation

The selection of materials investigated in this thesis focuses on commercially available materials that are used in state-of-the-art MD module design.

A set of commercial membrane products from W. L. Gore & Associates was chosen systematically for experimental evaluation. The membranes have different structural properties, mainly differing in thickness and nominal pore size. All membranes investigated here are made of ePTFE by bi-axial stretch forming. Images of a corresponding membrane structure, made by scanning electronic microscopy (SEM), have already been presented in Figs. 2.7(a) and 2.7(c). All membranes are symmetric single-layer membranes. The technical specifications in Tab. 3.5 were provided by Gore and have to be interpreted as typical or nominal values. Since the listed products represent samples from one "product family", no major differences in other structural parameters are expected.

Many flat sheet membranes used for MD applications are laminated onto an open structure providing mechanical support, the backing material. The products of the lamination process are referred to as laminates. Fig. 3.14 shows a scrim and a non-woven backing structure that were used for the laminates investigated in this work. The approximate specifications for thickness δ_B and volumetric porosity ε_B are given in Tab. 3.4.

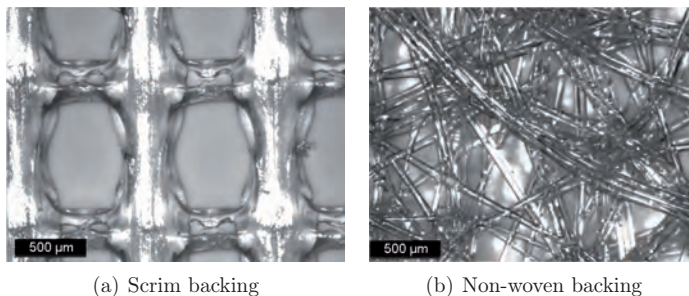


Figure 3.14: Microscopic photographs of different backing structures.

Table 3.4: Specifications for different backing structures.

	reference	material	δ_B [μm]	ε_B [%]
scrim	S	PP	280	50
non-woven	N	PP	200	70

In order to isolate the influence of the membrane parameters, it is necessary to investigate laminates (L) and the corresponding membranes (M) without a backing layer. Thus, the chosen set of samples includes several examples where membranes as well as the corresponding laminates are available. These positions can be identified by a similar reference number (e.g. M-020A and L-020A-S). The reference number itself provides information about the nominal pore size, the

membrane and the backing type. It should be noted that membrane properties may change slightly due to the lamination process.

Table 3.5: Specifications of different membrane materials.

membrane	backing type	d_M [μm]	δ_M [μm]	ε_M [%]
M-005A	none	0.05	23	80
M-020A	none	0.20	70	80
M-020B	none	0.20	30	80
M-045A	none	0.45	98	80
laminate	backing type	d_M [μm]	D^a [μm]	ε_M [%]
L-020A-S	scrim	0.20	350	80
L-020A-N	non-woven	0.20	270	80
L-020B-N	non-woven	0.20	230	80

^amembrane and backing

For the evaporator and the condenser flow channels, two commercially available channel spacers from Tenax and DelStar are used in this work. The spacers (S) are referred to with a reference number that provides information about the spacer thickness. The spacer S-320 has an asymmetric structure consisting of one layer with filaments parallel to the cell edges and one layer with diagonal filaments. The diagonal filaments are oriented towards the active surface, if not indicated otherwise. The spacer S-200 is thinner and has a symmetric structure. Detailed specifications including data on thickness δ_S , porosity which is usually denoted as voidage ε_S and the hydraulic diameter d_h of the spacers are given in Tab. 3.6. A photograph in which the flow direction is indicated by a blue arrow is shown in Fig. 3.15.

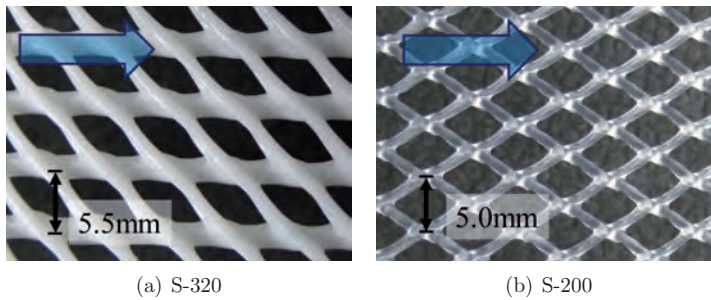


Figure 3.15: Channel spacers used for the evaporator and the condenser flow channel.

For experiments with an additional gap, different channel spacers are used for different gap geometries. In this gap position, the spacer functionality is reduced to defining the geometrical configuration, since the impact of the gap spacer on hydrodynamics is of minor importance.

For setting up the narrow gap in PGMD experiments, commercial polypropylene spacers from DelStar, identified with the reference numbers S-025 and S-050, are used. For setting up wider gaps in AGMD experiments, the S-200 spacer is used. A further variation in gap thickness is achieved by stacking multiple spacers.

Table 3.6: Specifications for different main channel spacers.

reference	position	structure	material	δ_S [mm]	ε_S [%]	d_h^a [mm]
S-320	evaporator/condenser	asymmetric	LDPE	3.20	72	2.2
S-200	evaporator/condenser/air gap	symmetric	PP	2.00	80	1.8
S-050	permeate gap/air gap	symmetric	PP	0.50	80	-
S-025	permeate gap	symmetric	PP	0.25	80	-

^aevaluated with Eq. 3.37

For PGMD and AGMD experiments, a commercially available, impermeable ETFE film from SaintGobain with a nominal thickness of 127 μm is used to separate the permeate channel. This film material is referred to as F-127.

3.4 Results and Model Validation

The materials and the channel configuration used in membrane distillation have a significant effect on process performance and consequently on the overall system efficiency. A comprehensive understanding of the thermodynamic phenomenology is essential in order to ensure optimal material selection and channel design and to develop constructive approaches for process optimisation. A systematic identification and validation of the node model parameters is done successively for the heat transfer in the spacer-filled channels, the membrane structural properties, the backing material and the enhanced gap channel configurations. A separate section is dedicated to each of the main transfer layers, providing experimental and theoretical results as well as a comprehensive supplementary discussion. Subsequent to each section, a brief presentation of selected references from pertinent literature is provided. It should be noted that a comparative quantitative evaluation of results obtained in this thesis and results obtained by others is reasonable only in some cases, since experimental set-ups, materials and operating conditions differ significantly throughout the literature. However, the references allow qualitative comparison, give an overview of specific observations and problems that have been identified elsewhere and provide some further reading on each specific topic.

3.4.1 Spacers - Enhanced Heat Transfer in the Flow Channels

The heat transfer in the flow channel significantly affects the membrane distillation performance. In order to achieve high quality-modelling results for any channel configuration, it is necessary to initially identify the heat transfer for a given channel/spacer geometry depending on the physical fluid properties and the flow velocity.

Determination of Heat Transfer Correlations

In order to obtain a reference for heat transfer in the spacer-filled channel, independent heat transfer measurements have been performed. For these experiments, the test cell was configured in a heat exchanger (HX) mode, using an impermeable polymer film to separate the flow channels. The heat transfer resistance of the film was taken into account during evaluation. A very thin film with a thickness of only $12\ \mu\text{m}$ has been chosen, in order to imitate the flexibility of a membrane material and to minimise the influence of the corresponding heat transfer resistance on the results. The spacer S-320 was placed with the diagonal spacer filaments facing towards the heat transfer layer. One set of experiments was performed without any spacer in the flow channel. In this case, a rigid copper plate with a thickness of $0.5\ \text{mm}$ was used in order to maintain the channel geometry. The flow rate on the warm and the cold sides were set to be equal and the mean temperature was approximately $40\ ^\circ\text{C}$ in all experiments. The individual heat transfer coefficients for each side were derived from the total transferred thermal power and the corresponding temperature difference, assuming equal heat transfer coefficients on both sides. This assumption seems to be reasonable, since the channels were set up symmetrically and the temperatures differed by less than $10\ \text{K}$. The results are presented in Fig. 3.16 as a function of the mean flow velocity, in order to achieve comparability for the different channel geometries. The flow velocities have been determined according to Eq. 3.36, taking the appropriate channel width and spacer voidage into consideration.

The values for the heat transfer increase significantly with flow velocity for all channel configurations, but the beneficial effect becomes smaller at higher flow velocities. A comparison of the results for spacer-filled channels with empty channels underlines the significant enhancement of heat transfer due to the induction of turbulence by spacers. If spacer S-320 is used, the heat transfer at $0.08\ \text{m s}^{-1}$ was determined to be approximately $2900\ \text{W (m}^2\ \text{K)}^{-1}$, which is an increase by a factor of 2.3 with respect to an empty channel configuration. If spacer S-200 is used at the same flow rate, an even higher heat transfer coefficient of approximately $3600\ \text{W (m}^2\ \text{K)}^{-1}$ was observed, which is an increase by a factor of 2.9.

Based on the experimental results, fit parameters for individual Nusselt correlations of the form given in Eq. 3.32 have been derived for each channel configuration. Since the Prandtl number is only dependent on the thermo-physical fluid properties, the exponent c was initially set to 0.333, which is commonly applied for water. The resulting Eqs. 3.69-3.71 are used to generate

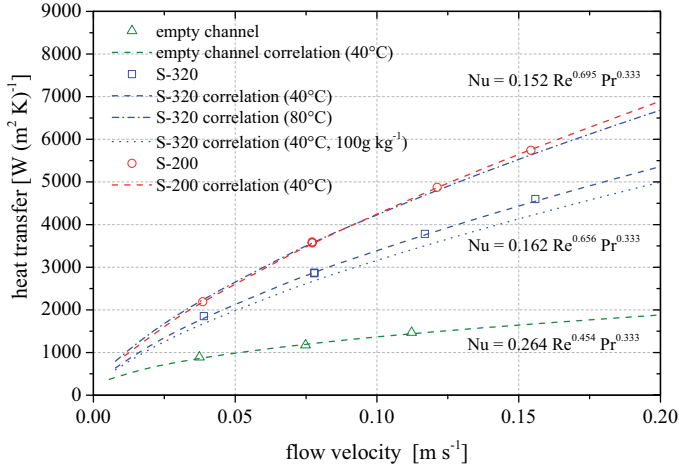


Figure 3.16: Single-side heat transfer coefficient in the flow channels for different feed flow rates. An impermeable polymer film with a thickness of $12 \mu\text{m}$ is used as the heat transfer layer. Testing conditions: $\bar{T}_{E-C} = 40^\circ\text{C}$, HX configuration, tap water.

the respective fit curves presented in Fig. 3.16 by applying Eq. 3.30.

$$\text{empty channel : } a = 0.264 \quad b = 0.454 \quad \Rightarrow \quad Nu = 0.264 Re^{0.454} Pr^{0.333} \quad (3.69)$$

$$\text{spacer S - 320 : } a = 0.162 \quad b = 0.656 \quad \Rightarrow \quad Nu = 0.162 Re^{0.656} Pr^{0.333} \quad (3.70)$$

$$\text{spacer S - 200 : } a = 0.152 \quad b = 0.695 \quad \Rightarrow \quad Nu = 0.152 Re^{0.695} Pr^{0.333} \quad (3.71)$$

The Reynolds and the Prandtl number are dependent on temperature and salinity. These dependencies are therefore influenced by the respective exponents. It should be noted that in the given correlations, the experimentally obtained fit exponent b for the Reynolds number is in the same range as those reported in the literature (Sec. 3.1.3). Consequently, the temperature dependence represented in Eqs. 3.69-3.71 seems to be consistent with the general state-of-the-art theory. To illustrate the quantitative influence of temperature on heat transfer, the correlation obtained for spacer S-320 has been evaluated for 80°C , additionally. The heat transfer result increases by about 25% at the elevated temperature condition. Furthermore, the S-320 correlation has been evaluated at 40°C and a salinity of 100 g kg^{-1} , in order to demonstrate the expected sensitivity of the heat transfer on salt concentration. For the given scenario, the heat transfer value decreases slightly by about 7%.

Validation of the Heat Transfer Correlations

A second set of experiments has been analysed, in order to obtain further validation of the heat transfer correlations in the context of membrane distillation measurements. For this purpose, the test cell was set up in a DCMD configuration using the membrane type M-020A. Measurements with spacers S-320 and S-200 were performed for different feed flow velocities at a mean temperature level of 60 °C and a temperature difference of 8 K. The flow rates were set to be equal on the evaporator and condenser sides. The geometrical channel parameters were chosen according to Tab. 3.6 in order to obtain the nominal flow velocities by applying Eq. 3.30. Due to the flexibility of the membrane, a spacer is necessary to define the channel geometry. Consequently, no useful experiments could be made for an empty channel configuration.

Additionally to the experimental results, model predictions for S-320 and S-200 spacer configurations as well as for a fictional case with an empty flow channel are provided in Fig. 3.17. It should be noted that the set of model parameters for the different channel configurations only differs in the applied heat transfer correlation, which is chosen to be Eq. 3.70 for the configuration with spacer S-320, Eq. 3.71 for the configuration with spacer S-200 and Eq. 3.69 for the fictional empty channel set-up, respectively. A detailed discussion of the choice of model parameters assigned to the membrane is provided in the following section.

A corresponding set of results considering different mean temperature levels is provided in Appendix D.

Flux enhancement with increasing flow velocity can be observed for both spacer geometries. High flow velocities result in large heat transfer coefficients, reduced temperature polarisation (Eq. 3.40) and a larger interfacial temperature difference ΔT_{1-0} . The beneficial effect becomes less pronounced at higher flow velocities, which correlates well with the behaviour of the heat transfer observed in Fig. 3.16. A comparison of the flux results for spacer-filled channels and the flux predicted for an empty channel configuration emphasises the significant role of channel spacers in membrane distillation. Analysing the results for a flow velocity of approximately 0.08 m s^{-1} , the flux increases from $5.5 \text{ kg (m}^2 \text{ h)}^{-1}$ to $11.2 \text{ kg (m}^2 \text{ h)}^{-1}$ for spacer S-320 and to $13.7 \text{ kg (m}^2 \text{ h)}^{-1}$ for the configuration with spacer S-200. Throughout the whole range of flow velocities, the flux results obtained with spacer S-200 are higher than those obtained with the spacer S-320. A good agreement between the model predictions and the experimental results is given. The heat transfer correlations of Eqs. 3.69-3.71, obtained with the independent heat exchanger measurements, still appear to be applicable if a membrane is introduced instead of an impermeable film. Furthermore, the good quantitative agreement indicates that the higher performance for spacer configuration S-200 may be due completely to the respective enhanced of heat transfer.

The thermal efficiency is observed to be in the range from 82 to 85% for the whole set of experiments. These results indicate a low sensitivity of the thermal efficiency with respect to the flow velocity and the spacer geometry, and consequently a low sensitivity to the heat transfer in general. This behaviour was already theoretically derived in Eq. 3.25. The model predicts a

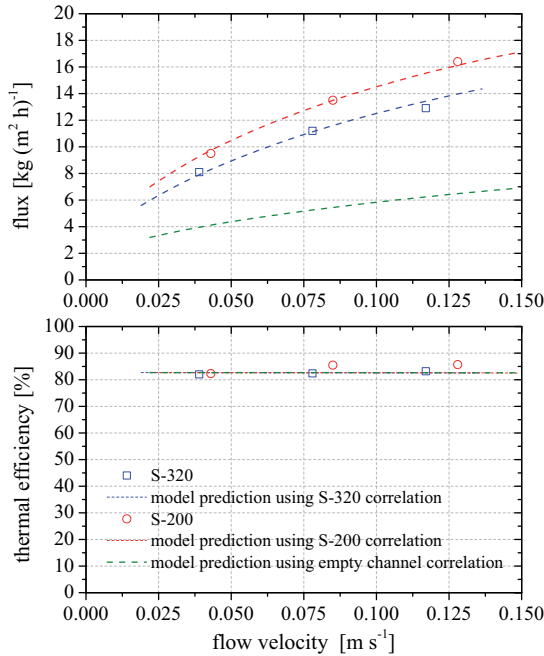


Figure 3.17: Flux measurements using different channel spacers at different feed flow velocities. The model predictions are based on the specific heat transfer correlations for each geometrical spacer/channel configuration. Testing conditions: $\bar{T}_{E-C} = 60^\circ\text{C}$, $\Delta T_{E-C} = 8\text{ K}$, membrane M-020A, DCMD configuration, tap water.

constant efficiency for all flow velocities and channel configurations. The resulting value of 83% is in good quantitative agreement with the experiments.

Further Reading - Selected References on the Role of Heat Transfer and Spacer-filled Flow Channels

Independent studies report constant thermal efficiencies that have been experimentally obtained with a DCMD test cell configuration, operated under constant temperature conditions and flow velocities ranging from $0.06 - 4.5\text{ m s}^{-1}$. The corresponding heat transfer coefficients were estimated to be $1000 - 22\,000\text{ W (m}^2 \text{ K)}^{-1}$. A significant increase in flux is observed for an enhancement of the heat transfer at lower flow velocities, whereas almost no flux enhancement could be achieved at high flow velocities. Additional results are given on the role of spacers concerning DCMD flux, with an empty channel configuration and spacer-filled channels under low flow-rate conditions being compared to a highly turbulent scenario [132]. Experimentally obtained heat transfer coefficients for spacer-filled channels were identified in the range of

4000 – 6000 W (m² K)⁻¹ for flow velocities of approximately 0.2 m s⁻¹. Also in this case, increasing flux and constant thermal efficiency was observed for improved hydrodynamics in the flow channels [121]. Experimental studies on hollow fibre modules and on spacer-filled flat channel membrane modules are presented in [20]. For the operation of the flat sheet configuration at flow velocities from 0.1 – 0.3 m s⁻¹, the heat transfer coefficient was estimated to be 5000 to 15000 W (m² K)⁻¹. The local distribution of heat transfer coefficients in a comparison of four different spacers (including S-320) was studied by means of thermochromic liquid crystals (TLC). The local values ranged from 1000 – 4000 W (m² K)⁻¹ for a given flow condition. A mean heat transfer coefficient was then derived from the local distribution [148]. Further investigations focusing on the influences of the spacer voidage, mesh size and flow attack angle on DCMD flux are presented in [151]. The results are compared to an empty channel configuration, as well. Best results were obtained with spacers providing high flow attack angles, as they had the strongest effect on the induction of turbulences. Similar experimental investigations are presented in [153], including supplementary pressure drop measurements. New innovative spacer geometries with helical, twisted filaments were studied in the context of pressure-driven membrane processes [146].

Regarding the influence of the feed concentration on heat transfer, low sensitivity was identified for salt solutions. For other fluid systems, a change in concentration may have a strong influence on the heat transfer boundary layer. It was shown that for sucrose solutions, the negative influence on performance due to higher concentrations is mainly explained by the effect of a significant change in viscosity on the heat transfer [80].

Depending on the spacer type, hydrodynamic pressure drops from 200 to 700 Pa m⁻¹ were measured for flow velocities of approximately 0.06 m s⁻¹. The study clearly identifies the interdependence of an increased heat transfer and the induced hydrodynamic pressure drop, proposing the definition of a characteristic number as a measure for the spacer efficiency [158]. In the context of ultra-filtration, various pressure drop correlations have been derived for different net-type spacers. The pressure drop was identified to depend strongly on the flow attack angle, increasing by approximately one order of magnitude when the flow attack angle was increased from 45 to 90° [144, 145]. The pressure drop in spiral-wound reverse osmosis modules was experimentally investigated in [154]. For flow velocities ranging from 0.06 to 0.37 m s⁻¹, the corresponding pressure drop was identified to range from 0.03 to 0.7 bar m⁻¹.

3.4.2 Membranes - An Analysis Based on Different Membrane Structures

The membrane is the most sophisticated and most critical component to be selected in membrane distillation. Different membranes offer a wide spectrum of structural properties that are fundamentally suitable for MD. The influence of membrane properties on the process performance and the validation of membrane modelling approaches discussed in the literature has not yet been completely clarified. In this section, the membrane performance is analysed, based on different

membrane structures and operation conditions. The main focus is to achieve comprehensive understanding of the role of the membrane structural properties on performance. A systematic analysis of the experiments gives an indication of the composition of the different mass transfer phenomena, depending on membrane structure and operating conditions. The membranes for experimental evaluation have been selected systematically in order to isolate the role of specific membrane structural parameters. A DCMD set-up was chosen as a suitable configuration for this approach, since the influences which need to be addressed apart from the membrane are minimised. Subsequent to the experimental evaluation, the results are used to derive suitable membrane model parameters as well as to validate the model. An additional discussion refers to a model-based parameter study, considering different operating conditions and membrane structural properties.

Overview of Process Performance for Different Membranes

Fig. 3.18 gives an overview of the experimentally obtained process performance results for all membranes from Tab. 3.5 at mean temperature levels of 40, 60 and 80 °C. Slight deviations of the effective mean temperature levels with respect to the nominal temperature levels are expected, due to the development of small temperature variations along the flow channels. The bulk temperature difference was kept constant at 8 K. The flow velocity was 0.08 m s⁻¹ for all experiments. The main differences between the samples concern the nominal pore diameter and membrane thickness.

All membranes show a significant effect of higher temperature levels on flux. This fundamental behaviour reflects the steeper gradient of the vapour pressure curve at higher temperature levels. However, they do not show the strong exponential behaviour one might expect from the vapour pressure curve. This is due to the fact that the positive effect of a higher flux at higher temperatures is partially compensated by greater temperature polarisation. The exponential dependence of the results is therefore damped. The highest flux values were measured for sample M-020B, reaching 17.8 kg (m² h)⁻¹ at 80 °C. Sample M-005A has the lowest flux performance for all temperature levels, only reaching 14.1 kg (m² h)⁻¹ at 80 °C. Comparing the samples M-020A and M-045A, only slight differences in flux performance are obtained. The obtained flux curves of these samples appear to be more sensitive to the temperature level.

The transferred latent heat increases at higher mean temperatures due to the given proportionality to flux. In contrast to the latent heat, the conductive heat transfer is not directly linked to the mean temperature level. Thus, the thermal efficiency of all samples increases significantly at higher temperatures. Membrane M-005A shows the lowest thermal efficiency of all samples with values of approximately 53 % at 40 °C and 86 % at 80 °C. The best thermal efficiency with values up to 92 % was obtained with membrane M-045A, which has slightly higher values than the membranes M-020A and M-020B.

Due to the large number of samples collated in the overview in Fig. 3.18, no additional model

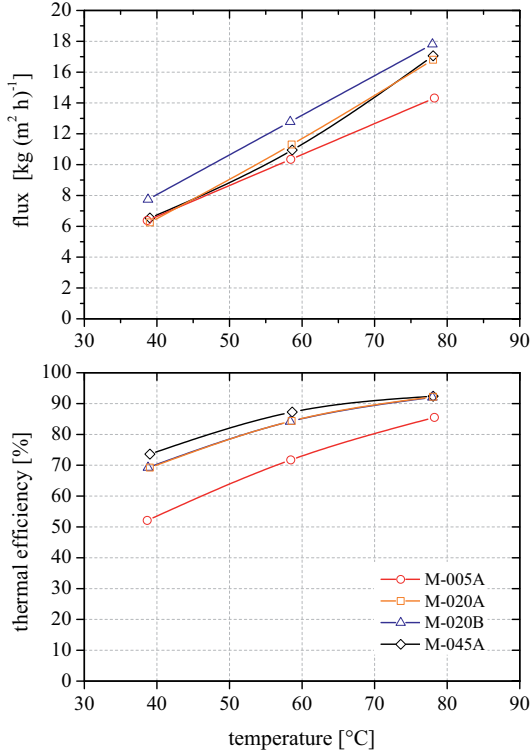


Figure 3.18: Membrane characterisation at different mean temperature levels. Testing conditions: $\Delta T_{E-C} = 8 \text{ K}$, $\bar{c}_{E/C} = 0.08 \text{ m s}^{-1}$, DCMD configuration, channel spacer S-320, tap water.

predictions are given to preserve clarity. A validation of the membrane model and a more detailed analysis, discussing the influence of temperature and the different membrane structural properties with respect to theoretical expectations, are given in the following sections.

Structural Analysis by Means of Membrane Deaeration

The proportions of different mass transfer phenomena in transmembrane vapour transport cannot be measured directly. However, according to the common membrane models, molecular diffusion through stagnant air is one of the major mass transfer resistances in membrane distillation (Eq. 3.12). Furthermore, the amount of air in the membrane pore volume is expected to affect the composition of the mass transfer phenomena significantly. Comparing experimental results obtained with deaerated membranes and results obtained without membrane deaeration may indirectly indicate on the composition of the different mass transfer phenomena. In order to obtain the necessary information, the membrane structures that had previously been used in

Sec. 3.4.2 are used in a second set of experiments. In these experiments, the membranes were deaerated by using deaerated feed water. Preliminary experimental results, demonstrating the feasibility of membrane deaeration by means of feed water deaeration and providing additional information on the deaeration dynamics, have already been published by the author of this thesis [22]. Since the membrane is open to the evaporator and to the condenser flow channel, both streams need to be deaerated to ensure the best possible membrane deaeration. To prevent water vapour from leaving the system through the deaeration equipment, the deaeration pressures were adjusted individually for each experiment. Depending on the temperature level, the deaeration pressure was set to be slightly above the corresponding saturation pressure. The bulk temperature difference was kept constant at 8 K. The flow velocity was 0.08 m s^{-1} for all experiments. Experimental results and model predictions are given in Fig. 3.19 for a temperature level of 40°C and 60°C , respectively. In addition to the absolute results, the relative improvements based on the deaeration effect are indicated. It should be noted that deaeration experiments could not be performed at higher temperature levels, due to material limitations of the deaeration modules. The membrane is assumed to be fully deaerated, if deaeration was applied. The model parametrisation and the theoretical results are discussed in the following section.

Higher process performance is obtained at higher temperature levels. This fundamental behaviour has already been discussed previously.

If the membrane is deaerated, higher performance in flux and thermal efficiency is obtained for all membrane structures and operating conditions. The relative improvements in flux are in the range of +41 to +93 % and in thermal efficiency +9 to +34 %. The experimental results obtained with membranes M-020A, M-020B and M-045A show a significantly higher relative effect of deaeration on flux at 40°C (+65/ + 83/ + 93 %) compared to the relative effect observed at 60°C (+45/ + 53/ + 63 %). According to the expectations stated in Sec. 3.1.2, a lower temperature condition results in a lower water vapour pressure, leading to a higher partial pressure of air in the membrane pore volume. Consequently, the mass transfer resistance due to molecular diffusion has a larger contribution to the total mass transfer resistance and the beneficial effect of deaeration is expected to be more pronounced at lower temperature. The results obtained with membrane M-005A show slightly different behaviour. In this case, the relative effect of deaeration on flux at 40°C (+41 %) is quite similar compared to the relative effect observed at 60°C (+44 %). Due to the small pore size, Knudsen diffusion is expected the dominant transfer phenomena. Since Knudsen diffusion resistance is fundamentally lower at lower temperatures, relative improvements by deaeration appear to be damped.

To clarify the influence of the nominal pore size on process performance, membrane M-005A is compared to M-020B, and M-020A is compared to M-045A. The thin membranes have smaller pores and differ in nominal pore size by a factor 4, while providing a similar membrane thickness of 23-30 μm . Considering these membranes at 40/60 $^\circ\text{C}$, an increasing flux (+21/ + 24 %) and thermal efficiency (+17/ + 33 %) is observed with increasing pore size. If deaeration is applied, the beneficial effect of the pore size on flux appears to be even more distinctive (+42/ + 24 %). The thicker membranes have larger pores and differ in nominal pore size by a factor of 2.3, while providing a similar membrane thickness of 70-98 μm . For these membranes, an rather similar

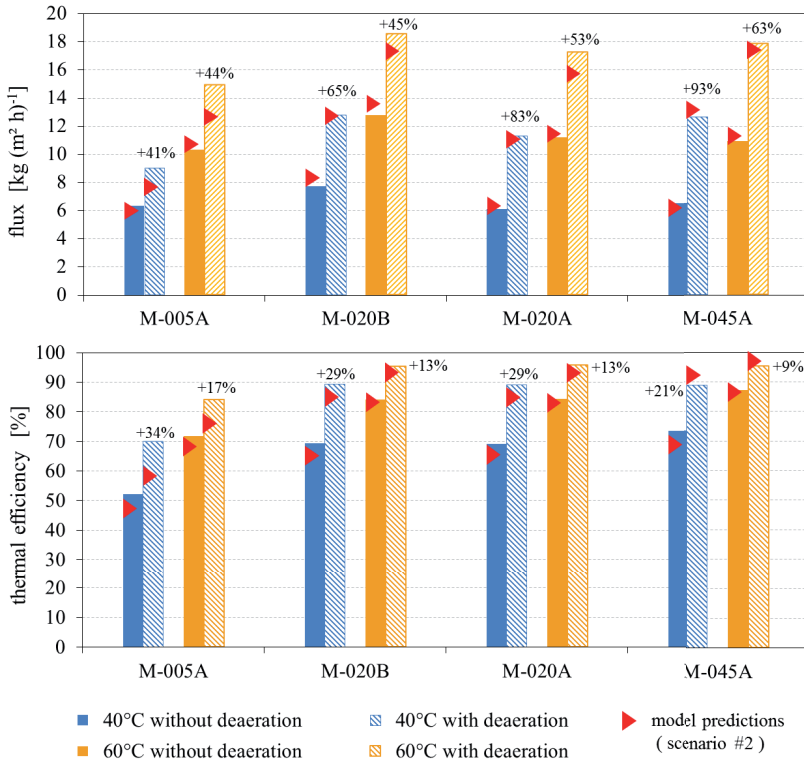


Figure 3.19: Experimental results and model predictions for different membrane structures with and without deaeration. Testing conditions: $\bar{T}_{E-C} = 40/60\text{ }^{\circ}\text{C}$, $\Delta T_{E-C} = 8\text{ K}$, $\bar{c}_{E/C} = 0.08\text{ m s}^{-1}$, channel spacer S-320, DCMD configuration, tap water.

flux performance (+6/ - 2%) and thermal efficiency (+6/ + 3%) is observed with increasing pore size. If deaeration is applied, a weak effect of the pore size on flux performance becomes noticeable (+12/ + 4%).

These general dependencies are in good accordance with the theoretical expectation and may be qualitatively interpreted referring to the combined Knudsen-molecular diffusion mass transfer model (Eqs. 3.10, 3.12). For the membrane with the smallest nominal pore size of $0.05\text{ }\mu\text{m}$, the pores limit the membrane performance significantly, indicating a high contribution of Knudsen diffusion to the overall mass transfer. In this case, the performance may be effectively optimised by the choice of a membrane with larger pore size. According to the experimental results, a sufficient pore size appears to be in the range of $0.2\text{ }\mu\text{m}$. In this case, deaeration strongly affects the overall mass transfer, indicating a strong contribution of the molecular diffusion mechanism on the overall mass transfer. Only limited improvements were achieved, using a membrane with

increased pore size. It turns out that the effect of pore size is less important, if a sufficient pore size is available and deaeration is more effective for membranes with larger pores.

To clarify the influence of the membrane thickness on process performance, membrane M-020A is compared to M-020B. These membranes have a similar nominal pore size of $0.2\ \mu\text{m}$ but vary in thickness by factor 2.3. The thicknesses are 30 and $70\ \mu\text{m}$, respectively. The flux is observed to be higher for the thinner membrane. In these experiments, the flux increased by approximately $1.5\ \text{kg}\ (\text{m}^2\ \text{h})^{-1}$, indicating the higher permeability due to the shorter length for diffusion. According to the membrane model in Eqs. 3.10, 3.12 and 3.14, the membrane thickness affects the mass transfer coefficients inversely. However, while the mass transfer coefficient increases, Eqs. 3.22 and 3.40 predict a decrease in temperature polarisation coefficient resulting in a reduced interfacial temperature difference. The positive effect of a smaller membrane thickness is partially compensated by the negative effect of a smaller resulting driving force. Thus, total flux turns out to be less sensitive to the membrane thickness than one might expect from a basic mass transfer coefficient analysis. The relative effect of deaeration on flux at $40\ ^\circ\text{C}/60\ ^\circ\text{C}$ appears to be higher for the thicker membrane sample (+83%/ +53%) in comparison to the thin sample (+65%/ +45%). For thin membranes with high permeability, the hydrodynamics represent one of the major limiting factors for the overall mass transfer. Thicker membranes are usually less permeable and the membrane itself limits the total mass transfer. Consequently, an improvement of the permeability due to deaeration is more effective for thicker membranes. The thermal efficiency for both membrane samples at $40\ ^\circ\text{C}$ was determined to be equal at 69% for aerated operation and 89% with deaeration. This perfectly meets the expectations, since the thermal efficiency was derived to be independent of the membrane thickness in Eq. 3.25.

Identification and Validation of the Membrane Model Parameters

For the mass transfer model equations presented in Sec. 3.1.1, the structural membrane parameters are required in order to make theoretical performance predictions. The membrane thickness, membrane porosity and membrane pore size may be chosen based on the nominal values given in Tab. 3.5. However, no data on the membrane pore tortuosity is available. Thus, the membrane tortuosity has been identified by minimising the accumulated error over the whole set of data points presented in Sec. 3.4.2. For this purpose, the commercially available optimisation toolbox of MS Excel was used. The tortuosity is assumed to be equal for all membranes, since the material, the fabrication technology and the manufacturer is identical. The optimal result was obtained for a tortuosity value of approximately 1.1, which seems to be a fairly low value, but is still physically reasonable.

The effective thermal conductivity used for all membranes is estimated according to Eq. 3.23 based on a solid-phase tortuosity of 2.0. The thermal conductivity of PTFE is set as $0.25\ \text{W}\ (\text{m}\ \text{K})^{-1}$, whereas the thermal conductivity of the mixture of air and water vapour is set as $0.023\ \text{W}\ (\text{m}\ \text{K})^{-1}$. These assumptions lead to an effective thermal membrane conductivity of $0.0434\ \text{W}\ (\text{m}\ \text{K})^{-1}$. The maximal relative errors of the flux model predictions with respect to the experimental re-

sults throughout Sec. 3.4.2 are summarised in Tab. 3.7, referred to as scenario #1. It turns out that the quantitative results for aerated operation are in good agreement with the experiments. Considering the deaerated condition, the quantitative representation seems to underestimate the role of deaeration. It should be mentioned that the calculations are based on a one-dimensional single pore model with cylindrical pores with geometrical configurations which are assumed to be represented by the nominal membrane parameters. No detailed data on porosity, pore-size distribution or tortuosity is available, since no measurements on the membrane structural parameters could be made for the investigations presented in this thesis. The uncertainty in the membrane structural parameter values and in the rigorous model assumptions itself may explain the deviations.

A visual inspection of the membrane structure presented in Fig. 2.7 gives an impression of the complex three-dimensional structure. This structure consists of a highly interconnected pore volume rather than uniform, cylindrical pores. An assumption of larger pore size might take effects of the pore interconnections into account. Furthermore, visual inspection of the pore dimensions leads to the impression of a larger effective pore size than expected from the nominal value of $0.2 \mu\text{m}$. Considering these arguments, two additional sets of membrane parameters have been derived by assuming a higher effective pore size than specified by the nominal values. In scenario #2 and scenario #3, the pore sizes were assumed to be increased by factors of 1.5 and 2.0. In these cases, the optimiser compensates the effect of larger pore size by higher tortuosities, that were identified to be 1.3 and 1.4, respectively. A detailed summary of the maximal deviations is listed in Tab. 3.7. If larger pore size is assumed, the effect of deaeration on the results is more distinct, so the quality of the results for deaerated operation improves. Due to the higher tortuosity, the quality of the results for the aerated membranes is retained. In all scenarios, the model predictions for membrane M-005A have the lowest quality. However, the qualitative behaviour of the membrane performance with temperature, state of deaeration and membrane structural parameters are described satisfactorily by the model. Scenario #2 was chosen as the best set of parameters that is used throughout this thesis. For this case, the quantitative results of the model predictions are represented in Fig. 3.19 as red markers.

Table 3.7: Maximal errors of the model predictions with respect to the experimental results for different membrane model scenarios.

	scenario #1		scenario #2		scenario #3	
pore size	d_M		$1.5 \cdot d_M$		$2.0 \cdot d_M$	
tortuosity	1.1		1.3		1.4	
	aerated	deaerated	aerated	deaerated	aerated	deaerated
M-005A	-13 %	-26 %	+11 %	-16 %	+17 %	-9 %
M-020B	+8 %	-11 %	+8 %	-7 %	+8 %	+6 %
M-020A	+2 %	-15 %	+2 %	-9 %	+2 %	+5 %
M-045A	+5 %	-6 %	-8 %	+4 %	-10 %	+9 %

To obtain a quantitative reference, the diffusive mass transfer coefficients have been explicitly evaluated according to Eqs. 3.10 and 3.12 for the case of aerated and deaerated operation. The results for different temperature levels are summarised in Tab. 3.8.

For the aerated case, the mass transfer coefficients from Knudsen and molecular diffusion are superposed, whereas the deaerated case is represented by the Knudsen coefficient alone. Naturally, the mass transfer coefficients increase with increasing pore size and with decreasing membrane thickness. Since the Knudsen mechanism is barely influenced by temperature, the mass transfer coefficients for deaerated operation show only low sensitivity to the temperature level. For aerated operation, the superposed mass transfer coefficients show a more pronounced sensitivity to temperature, due to the strong temperature influence on the molecular diffusion resistance. This sensitivity to temperature increases with increasing pore size.

As an additional quantitative reference, the explicit values for the conductive heat transfer coefficients are provided in Tab. 3.8. Based on the assumption of an equal effective thermal conductivity for all membrane samples, the conductive heat transfer coefficients are only dependent on membrane thickness. The conductive heat transfer coefficients are assumed to be independent of temperature and deaeration status.

Table 3.8: Explicit evaluation of the theoretical diffusive mass transfer coefficients (scenario #2) and the conductive heat transfer coefficients for the membrane structures in Tab. 3.5.

	$C_{M,d,aerated}$			$C_{M,d,deaerated}^a$			$\lambda_M^* \delta_M^{-1} b$
	$[10^7 \times \text{kg} (\text{Pa m}^2\text{s})^{-1}]$			$[10^7 \times \text{kg} (\text{Pa m}^2\text{s})^{-1}]$			$[\text{W} (\text{m}^2\text{K})^{-1}]$
	40 °C	60 °C	80 °C	40 °C	60 °C	80 °C	
M-005A	18.6	19.4	21.2	28.1	27.2	26.4	1887
M-020B	28.4	31.8	40.7	86.1	83.5	81.1	1447
M-020A	12.2	13.6	17.5	36.9	35.8	34.7	620
M-045A	10.6	12.4	17.3	59.3	57.5	55.8	443

^apure Knudsen diffusion

^bbased on the assumption of a solid phase membrane tortuosity of $\tau_{M(s)} = 2$

Theoretical Mass Transfer Analysis

In the preceding section, the influence of operating conditions and membrane structural parameters has been discussed, based on experimental results. A focus was placed on the derivation of suitable model parameters. These parameters have been applied in this section to perform a detailed theoretical mass transfer analysis, covering the effects of different operating conditions and different membrane structural parameters. The choice of scenarios and the selected set of model parameters correspond to the experiments presented in Sec. 3.4.2, providing a supplementary and more detailed discussion. The default membrane parameters are based on membrane M-020B. The heat transfer correlation corresponding to spacer S-320 is used, evaluated for a flow velocity of 0.08 m s^{-1} . The default operating conditions are a bulk stream temperature difference of 8 K and a temperature level of 60 °C.

The first sensitivity analysis is performed with respect to operating conditions, covering the influence of temperature and deaeration pressure on flux performance. The results are illustrated

in Fig. 3.20, presenting the flux performance and temperature polarisation coefficient in the top plots and the corresponding detailed analysis of the driving force in the bottom plots.

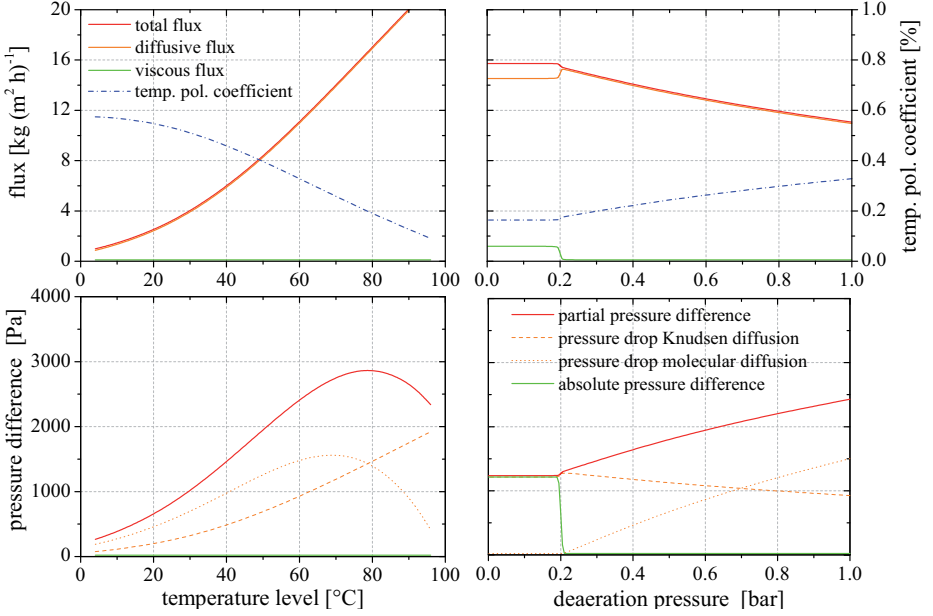


Figure 3.20: A model-based sensitivity analysis, covering the influence of temperature level and the deaeration pressure. The theoretical predictions on flux performance are supported by a detailed analysis of the driving force with respect to the different mass transfer phenomena. Model parameters: $\varepsilon_M = 80\%$; $\delta_M = 70 \mu\text{m}$; $d_M = 0.3 \mu\text{m}$; $\tau_M = 1.3$; $\bar{p}_{1-0} = 1 \text{ bar}$; $\tau_{M,s} = 2$. Operating conditions: $\bar{T}_{E-C} = 60^\circ\text{C}$, $\Delta T_{E-C} = 8 \text{ K}$, $\bar{c}_{E/C} = 0.08 \text{ m s}^{-1}$, $S_{E/C} = 0 \text{ g kg}^{-1}$, channel spacer S-320, DCMD configuration.

If the temperature level increases, the flux increases exponentially. This fundamental behaviour reflects the steeper gradient of the vapour pressure curve at higher temperature levels. However, the positive effect of higher temperatures is partially compensated by higher temperature polarisation due to the increasing amount of heat needed for evaporation on the membrane interface (Eq. 3.40). The exponential form of the flux curve that is observed for temperatures lower than 40°C changes to an almost linear form at higher temperatures. This almost linear form agrees well with the experimental observations presented in Fig. 3.18. The temperature polarisation coefficient is almost 0.6 at low temperature condition, steadily decreasing with increasing temperature and reaching values as low as 0.1 at temperatures close to 100°C . At this temperature, the process is mainly limited by heat transfer, since only 10% of the bulk temperature difference is left to establish the process driving force. The partial pressure difference increases with increasing temperature, showing an exponential behaviour for temperatures lower than 40°C . With increasing temperature, the gradient of the partial pressure difference curve decreases and then becomes negative due to temperature polarisation. A maximum is reached at

approximately 2900 Pa. Due to the superposition of the diffusive mass transfer mechanisms, the partial pressure difference is partitioned into one fraction representing the partial pressure drop based on Knudsen diffusion and one fraction representing the pressure drop of molecular diffusion. At lower temperatures, the vapour pressure is low, leading to a large fraction of air in the membrane pores (Eq. 3.11). For temperatures up to 75 °C, molecular diffusion is the dominant mass transfer mechanism. In the range of 75 – 85 °C, both mass transfer mechanisms contribute equally to the total pressure drop, since the amount of air in the pore volume is decreasing. For temperatures beyond 85 °C, Knudsen diffusion is clearly becoming the dominant mass transfer mechanism. Close to 100 °C, the molecular diffusion mechanism is negligible. Since the presence of air prevents the development of an absolute pressure difference, no viscous flow occurs throughout the whole range of temperatures.

In the sensitivity analysis presented on the right hand side, a variation of the amount of air in the pore volume by means of deaerated feed water is analysed. The deaeration pressure may be interpreted as the absolute pressure level in the pore volume. For lower pressure levels, the flux performance increases, while the increasing amount of transferred heat reduces the temperature polarisation coefficient from 0.32 to 0.17. The partial pressure difference therefore decreases from 2500 Pa to 1250 Pa. The contribution of Knudsen diffusion to the overall mass transfer steadily increases when the deaeration pressure is lowered. This is due to the reduced amount of air in the pore volume, leading to a reduced molecular diffusion resistance. Close to the saturation pressure of approximately 0.2 bar (at 60 °C), the molecular diffusion mechanism becomes negligible. The amount of air that is left in the pore volume is no longer enough to fully balance the vapour pressure gradient. Thus, an absolute pressure difference is established across the membrane, introducing an additional mass transfer due to viscous flow. For deaeration pressures below the saturation pressure, no air is left in the pores and the absolute pressure difference is equal to the partial vapour pressure difference. The flux based on viscous flow appears to be approximately 8 % of the overall flux. In DCMD, the pressure level in the pore volume cannot be reduced to values lower than the respective saturation pressure. Consequently, no change in performance occurs, if the deaeration pressure is further reduced.

The second sensitivity analysis is performed with respect to membrane structural parameters, covering the influence of membrane pore size and membrane thickness on flux performance. The results are illustrated in Fig. 3.21, using the same graphical layout as in Fig. 3.20.

For pore sizes smaller than 0.2 μm , low flux performance is observed. Consequently, the temperature polarisation coefficient is quite high and the partial pressure difference reaches values from 2500 to 5000 Pa. In this case, the process is limited by the membrane mass transfer resistance, dominated by Knudsen diffusion within the small pores. The flux performance increases significantly with increasing pore size, indicating the significant enhancement of the overall mass transfer coefficient. Considering the flux that corresponds to a pore size of 1.0 μm as the final value, 81 % of the potential is already reached for a pore size of 0.2 μm , and 88 % for a pore size of 0.3 μm . This quantitative analysis agrees well with the observations from the experiments in

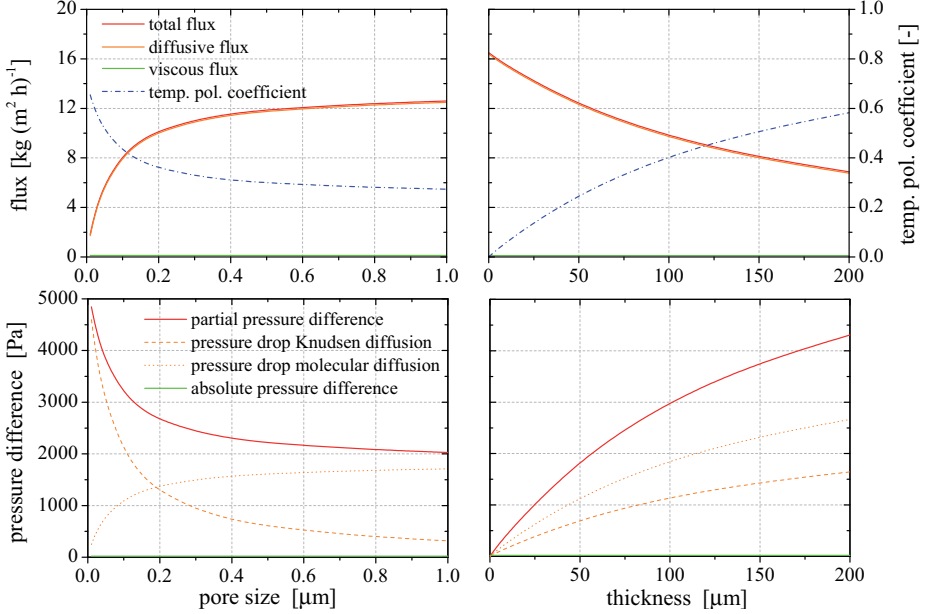


Figure 3.21: A model-based sensitivity analysis, covering the influence of membrane pore size and membrane thickness. The theoretical predictions on flux performance are supported by a detailed analysis of the driving force with respect to the different mass transfer phenomena. Model parameters: $\varepsilon_M = 80\%$; $\delta_M = 70\ \mu\text{m}$; $d_M = 0.3\ \mu\text{m}$; $\tau_M = 1.3$; $\hat{p}_{1-0} = 1\ \text{bar}$; $\tau_{M,s} = 2$. Operating conditions: $\bar{T}_{E-C} = 60\ ^\circ\text{C}$, $\Delta T_{E-C} = 8\ \text{K}$, $\bar{c}_{E/C} = 0.08\ \text{m s}^{-1}$, $S_{E/C} = 0\ \text{g kg}^{-1}$, channel spacer S-320, DCMD configuration.

Sec. 3.4.2. If the pore size is further increased, Knudsen diffusion resistance decreases and molecular diffusion becomes the dominating mass transfer phenomenon. No significant improvement in flux is achieved, since the dominating molecular diffusion is independent of pore size. The presence of air in the membrane pore volume prevents the development of an absolute pressure difference, so no viscous mass transfer is observed.

The performance analysis of membranes with different thicknesses represents a general mass transfer resistance analysis, since the resistance for all mass transfer phenomena is proportional to the membrane thickness. In the limiting case with zero thickness, no mass transfer resistance and consequently no pressure drop is induced by the membrane and the process is limited purely by heat transfer in the boundary layers. Considering very thin membranes with a thickness of less than $40\ \mu\text{m}$, the process is still mainly limited by the heat transfer, indicated by temperature polarisation coefficients of less than 0.2. The flux steadily decreases with increasing membrane thickness. The higher transfer resistance is accompanied by a higher partial pressure drop across the membrane and an increasing temperature polarisation coefficient. The process is limited more and more by the membrane permeability, rather than the heat transfer. The relative proportions of the different mass transfer phenomena are not affected by the membrane thickness,

due to their similar dependence. The presence of air in the membrane pore volume prevents the development of an absolute pressure difference, so no viscous mass transfer is observed.

The Influence of Feed Water Salinity on Membrane Selection

Theoretical and experimental results obtained within this thesis favour the use of thin and highly porous membranes with sufficient pore size, due to their low mass transfer resistance at high thermal efficiency. However, interdependence of operational conditions and material properties introduce difficulties for the derivation of general statements regarding the selection of an optimal membrane. Especially the role of salt on process performance is more complex than one might expect from a simple, one-dimensional analysis. The negative effect of salinity on MD process performance was already predicted due to the influence of the salt ions on water vapour pressure according to Eq. 3.6. For a given scenario, the salt ions reduce the evaporator side vapour pressure and consequently the overall driving force by a certain offset. It is obvious that the sensitivity of the MD performance behaviour depends on the absolute driving force, or the interfacial temperature difference. The salinity effect may be significantly reduced by a deliberate choice of the operating conditions, especially the bulk stream temperature difference and the flow rates. The interdependence of the membrane transfer properties and salinity effects on the process performance characteristics is to be clarified in the following theoretical assessment. The sensitivity analyses on the membrane structural properties of Fig. 3.21 are supplemented by a second dimension, covering the additional effects of feed water salinity. The membrane parameters besides pore size and thickness are those of membrane M-020B. The heat transfer correlation corresponding to spacer S-320 is used, evaluated for a flow velocity of 0.08 m s^{-1} . The default operation conditions are a bulk stream temperature difference of 8 K and a temperature level of $60 \text{ }^\circ\text{C}$. The results on flux performance and thermal efficiency are presented in Fig. 3.22.

For operation at zero salinity, the predicted results for flux and thermal efficiency increase steadily for an improvement of the membrane permeability either by increasing the pore size or by decreasing the thickness. These results have already been discussed in connection with Fig. 3.21. For the use of saline feed water, the flux and the thermal efficiency are reduced for any scenario. The fundamental effect is explained by the salt ions that lower the water vapour pressure and consequently the process driving force according to Eq. 3.6. However, different observations are made on the role of the membrane structural properties considering saline feed water. The performance results obtained by a variation of the pore size are steadily improved with increasing pore size, independently of feed water salinity. The variation of the pore size simply represents an increase of the membrane permeability, without affecting the conductive heat transfer characteristics.

The results obtained by a variation of the membrane thickness change the general trends for saline feed water. It is obvious from the given results that the performance characteristics of

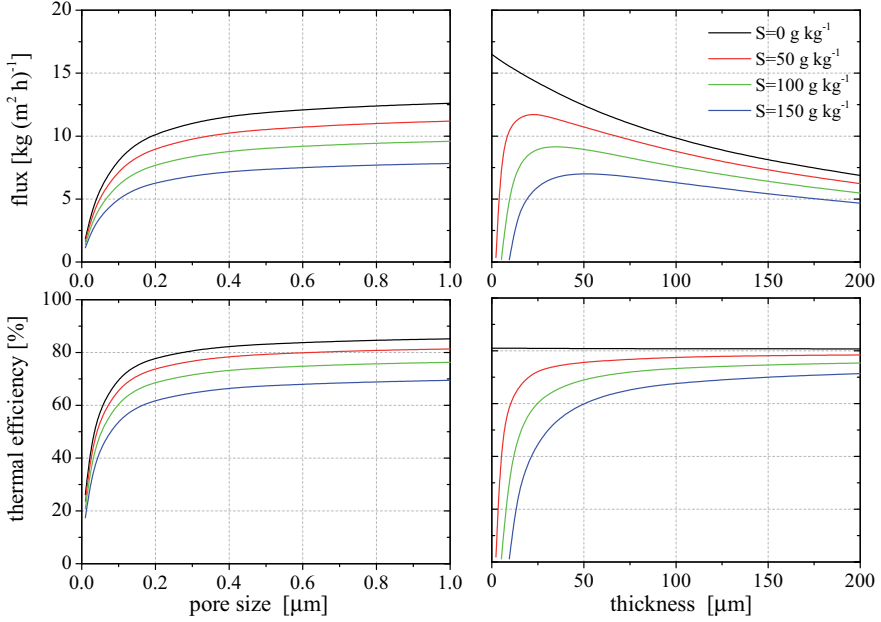


Figure 3.22: A model-based sensitivity analysis, covering the influence of membrane pore size and membrane thickness at different salinities on flux performance and thermal efficiency. Model parameters: $\varepsilon_M = 80\%$; $\delta_M = 70\ \mu\text{m}$; $d_M = 0.3\ \mu\text{m}$; $\tau_M = 1.3$; $\bar{p}_{1-0} = 1\ \text{bar}$; $\tau_{M,s} = 2$. Operating conditions: $\bar{T}_{E-C} = 60\ ^\circ\text{C}$, $\Delta T_{E-C} = 8\ \text{K}$, $\bar{c}_{E/C} = 0.08\ \text{m s}^{-1}$, channel spacer S-320, DCMD configuration.

thin membranes are quite sensitive to the presence of salt ions. Depending on the salinity level, the membranes show an optimal flux performance for a specific thickness. For the given operation conditions and a salinity level of $50\ \text{g kg}^{-1}$, the optimal membrane thickness is expected at $23\ \mu\text{m}$, while the flux at $150\ \text{g kg}^{-1}$ is maximal for a membrane thickness of $50\ \mu\text{m}$. The thermal efficiency is expected to increase steadily with increasing membrane thickness, converging towards a final value for any particular salinity level above zero. Thermal efficiencies for thicker membranes are fundamentally closer to the optimal reference of zero-salinity operation. The complex interdependence of membrane thickness and salinity on process performance is explained as follows: On one hand, a decrease in the membrane thickness does improve the permeability, similar to an increase in pore size. However, the thinner membranes also provide increased conductive heat transfer coefficients. As derived from Eq. 3.25, the improved permeability compensates the increased conductive heat losses and the effective thermal efficiency is independent of membrane thickness at zero salinity. It is important to note that Eq. 3.25 is not valid for saline feed waters (please refer to Eq. 3.7). Other than by the latent heat transfer, the driving temperature difference for the conductive heat loss is not reduced by the salt ions. A decreasing thermal efficiency is observed for thinner membranes, since the increased conductive heat losses cannot be compensated by the latent heat transfer any more.

An optimal membrane selection favours the use of membranes with low mass transfer resistance

at high thermal resistance. It is important to note that a high permeability may be achieved by different approaches. The increase of the membrane porosity, pore size or tortuosity will all lead to improved performance characteristics, while a reduction of the membrane thickness has to be carefully evaluated from a thermodynamic point of view. The optimal membrane thickness for a given scenario has to be derived by taking into consideration the module design, the nominal operating conditions and the salinity level. As a basic principle, the desired membrane thickness is expected to increase with salinity level. In addition to the described thermodynamic requirements, limitations due to the membrane manufacturing process, membrane durability and module design have to be taken into account for membrane optimisation. The topic of optimal membrane selection will be reconsidered in the context of full-scale modules in Sec. 4.3.6.

Further Reading - Selected References on the Role of Membrane Properties and Operating Conditions

Some additional references to experimental work that deals with the influence of membrane structural properties and the influence of different operating conditions on membrane performance are provided in the following section. An investigation of polypropylene hollow fibre membranes with different thickness and porosity is presented in [49]. The hollow fibre membranes are rather thick (150 – 1500 μm) compared to flat sheet membranes. Turbulent flow conditions were chosen for the experiments, so the temperature polarisation is of minor importance and the influence of the membrane structural parameters is quite pronounced. An inverse dependence of the flux on the wall thickness was identified. The general suggestion to use membranes with high porosity is experimentally derived in various experimental studies [49, 159]. Experimental studies on the influence of the nominal pore size (0.10 – 0.45 μm) for flat sheet membranes are presented in [109, 113, 157, 160]. Provided that the pore size is sufficient, the pore size has not been identified as a crucial parameter affecting MD performance in comparison to the membrane porosity and thickness. Due to limitations in the fabrication procedures, porosity and pore size may not be varied independently [159]. If a membrane is deaerated, the role of the pore size was identified to increase, since viscous flow contributes to the mass transfer. The contribution of the viscous flow was theoretically estimated to range from 2 – 27 % for membranes with pore sizes from 0.1 to 1.0 μm . The contribution of viscous flow was identified to increase with temperature [117]. The contribution of viscous flow on overall flux performance could not be clearly verified by independent experiments that apply a temperature difference of 35 K and a mean temperature level of 43 °C and deaerated feed water to the membrane. Despite this, an increasing role of viscous flow at higher temperature levels is predicted, based on theoretical considerations [20]. The principle beneficial effect of membrane deaeration on flux has been addressed by early and recent experimental work that is published in [19, 160]. Extensive experimental and theoretical results on membrane deaeration by means of feed water deaeration have recently been published in [20]. A polypropylene flat sheet membrane with a nominal pore size of 0.1 μm and a hollow fibre membrane with a nominal pore size of 0.2 μm have been investigated in detail. When a

temperature difference of 35 K and a mean temperature level of 43 °C was applied to the flat membrane, the flux increased by approximately 15 % if the water on the permeate side was fully deaerated, 25 % if the fully deaerated water was on the evaporator side and 43 % if fully deaerated water was applied on both sides. For the hollow fibre membrane with a larger pore size, the flux could even be increased by a factor of 2.4. A greater benefit of deaeration was identified for lower temperatures. If membranes are operated at absolute pressures above atmospheric pressure, compaction of the porous structure is expected, depending on the membrane morphology and material. Different influences on structural properties, air pressure level and consequently the permeability and thermal conductivity are predicted in [161]. A 25 % reduction in flux was observed with a PTFE laminate when the total pressure level increased from 1.0 to 1.5 bar, while no influence on flux was observed with an incompressible sample [162]. Contrary to the expectations, no influence on flux was observed in another study, where PTFE membranes were tested at total pressure levels ranging from 1.0 to 1.7 bar [160].

Only a few references have been found on experimental results addressing the effective thermal conductivity of polymeric membranes. Values of approximately $0.04 \text{ W (m}^2 \text{ K)}^{-1}$ for PVDF membranes and values ranging from 0.027 to $0.043 \text{ W (m}^2 \text{ K)}^{-1}$ for PTFE membranes are provided in [81, 130]. A different study refers to these values, expecting a slight increase in the membrane's thermal conductivity with temperature based on the individual material properties [132]. Slightly higher values for PTFE and PVDF membranes were identified and discussed in [121]. A value of $0.046 \text{ W (m}^2 \text{ K)}^{-1}$ was measured for a PP membrane in [113].

The thermal efficiency has been discussed in some studies. Increasing thermal efficiencies from 30 – 60 % were obtained for increasing mean temperature levels of 20 – 35 °C in [121]. The same trends were also obtained in [132], presenting values of 43 – 62 % for mean temperature levels of 30 – 50 °C, respectively. A comparison of the efficiency results at equal temperatures leads to slight differences that may be attributed to different membrane porosities. The beneficial role of membrane deaeration on the thermal efficiency and its independence of membrane thickness was already predicted in [21].

Systematic study of the flux performance dependence on temperature has been done by most of the authors publishing experimental results on MD. However, it should be noted that many of these experiments were performed at a constant condenser inlet temperature and varying evaporator inlet temperatures [20, 49, 132, 150, 159]. In this case, both the mean temperature level and the bulk temperature difference are changed at the same time, leading to a superposition of the effects on flux performance. Consequently, the resulting fluxes usually show a quite pronounced exponential behaviour that is not comparable to the results presented in this thesis. The significant effect of shifting the mean temperature level while raising the bulk stream temperature difference can be observed by a comparative analysis of the results presented in [159], where the evaporator inlet temperature was chosen to be constant, while the condenser inlet temperature is varied in order to increase the driving temperature difference.

The interdependence of the flux performance and the role of the heat transfer in the flow channels is discussed in various studies. Experiments with different membranes using an identical channel configuration led to lower temperature polarisation coefficients for the membranes, providing higher permeability. If the membrane performance for a given membrane was enhanced

by an increase in temperature, the temperature polarisation coefficient was observed to decrease. For highly turbulent flow conditions, the temperature polarisation coefficients were identified in the range of 0.88 – 0.96, whereas at laminar, low-flow conditions, the values were reduced to 0.35 – 0.58 [132]. Other experimental studies addressed the influence of the temperature level on the temperature polarisation coefficients as well as the potential for improving the temperature polarisation coefficients by means of spacers [151, 152, 157]. The results obtained in [109, 113, 132] show a distinctly exponential form of the flux curve with increasing temperature for high flow rates, whereas for low-flow hydrodynamics, the exponential behaviour with temperature appears rather damped. A similar observation of the important role of hydrodynamics on enhanced performance conditions was reported in the context of deaeration [21]. It was concluded that the full benefit of membrane deaeration may only be exploited if the hydrodynamics in the flow channels allow high heat transfer coefficients.

Experimental results regarding the sensitivity of the DCMD process on salinity have been published by several authors. For a temperature difference of 32 K and a mean temperature level of 23 °C, an absolute sensitivity of approximately $0.9 \text{ kg (m}^2 \text{ h)}^{-1}$ per 50 g kg^{-1} NaCl has been observed for salinities ranging from 0 – 240 g kg^{-1} . The relative impact on flux decreases at higher flow rates [135, 163, 164]. Other authors tested aqueous NaCl solutions from 0 – 100 g kg^{-1} , for temperature differences of 30 and 40 K and corresponding mean temperature levels of 35 and 40 °C. An absolute sensitivity of approximately $0.8 \text{ kg (m}^2 \text{ h)}^{-1}$ per 50 g kg^{-1} was identified, with the tendency toward a higher sensitivity for lower salinities and lower flow rates [150]. The impact of salt on DCMD processes was also investigated with Dead Sea salt solutions from 35 – 250 g kg^{-1} . For a temperature difference of 35 K and a mean temperature level of 43 °C, the flux was reduced by approximately 50 %, if the highest salinity is considered. Since the respective modelling results obtained with the standard correlations that describe the effect of salinity on vapour pressure were identified not to be applicable for the high salinity levels, a customised correlation was applied [20]. In the context of high driving forces in an AGMD configuration, low sensitivities of approximately $0.18 \text{ kg (m}^2 \text{ h)}^{-1}$ per 50 g kg^{-1} NaCl have been observed for a temperature difference of 48 K and a mean temperature level of 30 °C [165].

3.4.3 Laminates - Membranes on Backing Structures

Most commercially available flat sheet membranes used in membrane distillation are provided on backing structures, which affect the membrane performance significantly. However, the role of backings structures has not yet been completely clarified. The following sections present the experimental results obtained for the laminates specified in Tab. 3.5. In order to isolate the influence of the mechanical support structures, it is necessary to compare the results obtained for the laminates (L) with the results obtained for the corresponding membranes (M) without a backing layer. Membrane type M-020A was chosen as the reference material for comprehensive experimental evaluation. The main reason is its good process performance and its availability

on a scrim as well as a non-woven backing type, referred to as L-020A-S and L-020A-N. In order to obtain an additional reference, further investigations have been performed with the thinner membrane M-020B and its corresponding laminate L-020B-N. Comparing the results obtained with the same backing type but different membrane thickness gives an indication of the interactive behaviour of membrane structure and backing influence.

Furthermore, the new split-path laminate model that was presented in Sec. 3.1.5 is validated by a comparative evaluation of the experimental results and the corresponding model predictions. The main results that are presented in this section have already been published by the author of this thesis [166].

Influence of a Backing and its Position under Different Operating Conditions

In order to achieve comprehensive understanding of the nature of the influencing effects caused by backing materials, variations in mean temperature level and flow velocity have been studied systematically. For the measurements, membrane type M-020A and its corresponding laminate L-020A-S are used in a standard DCMD test cell configuration with spacer S-320. The backing position is labelled with (BC), if the backing faces the condenser side or with (BE), if it faces the evaporator side. Additional results regarding variations in temperature difference are provided in Appendix E.

Fig. 3.23 shows the effect of the mean temperature level on the membrane performance regarding flux and thermal efficiency. The bulk temperature difference was kept constant at 8 K and the flow rate was set to be 0.08 m s^{-1} on both sides.

The fluxes increase with temperature for the membrane and the laminate samples. The membrane without a support structure (M-020A) shows the highest flux and thermal efficiency at all temperature levels. The results for the pure membrane have already been presented in the previous Sec. 3.4.2. Negative effects induced by the backing material are observed for the laminate for all temperatures. If the backing is orientated towards the evaporator channel (L-020A-S(BE)), the laminate flux reaches only 53 %, 51 % and 55 % of the reference flux from a pure membrane for temperatures of 40 °C, 60 °C, 80 °C, respectively. This correlates quite well with the surface area covered by the scrim backing, which is approximately 50 %. Therefore, it is assumed that the process is limited by the reduced area for evaporation. The complete surface area for condensation is available, ensuring low condensation temperatures and low vapour pressures on the condenser side. The thermal efficiency is reduced by the presence of a backing material throughout the whole range of temperatures. Considering a temperature of 60 °C, the thermal efficiency is reduced from 82 % to 61 %. The negative effect on thermal efficiency is caused by a relative increase of conductive heat losses. These losses still occur over the whole surface area including the covered part, which does not contribute to latent heat transfer.

If the membrane support structure faces the condenser channel (L-020A-S(BC)), 78 %, 65 % and

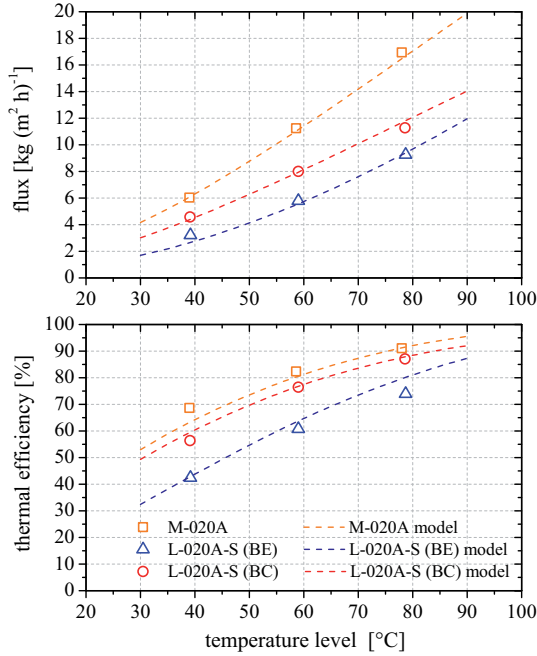


Figure 3.23: Experimental results and model predictions for membrane M-020A and its corresponding laminate L-020A-S for different temperature levels. The backing is oriented towards the evaporator side (BE) and towards the condenser side (BC), respectively. Testing conditions: $\Delta T_{E-C} = 8 \text{ K}$, $\bar{c}_{E/C} = 0.08 \text{ ms}^{-1}$, DCMD configuration, channel spacer S-320 spacer, tap water.

67% of the reference flux is achieved for the different temperatures, respectively. The parasitic effect of the backing is less pronounced. In this configuration, the available surface area for condensation is reduced instead of the surface area for evaporation. Higher local heat flux densities on the condenser side, combined with an additional heat transfer resistance in the backing pores, lead to an increase in condensation temperature, partial vapour pressure and driving force. Here it is assumed that the process is limited by the condenser performance. Also in this configuration, thermal efficiency decreases due to the conductive heat losses that occur over the whole surface area. Considering a temperature of 60°C , the thermal efficiency is reduced from 82% to 74%.

Fig. 3.24 shows the effect of the flow velocity on membrane performance with regard to flux and thermal efficiency. The mean temperature was kept constant at 60°C with a bulk temperature difference of 8 K. The flow velocities were set to be equal on the evaporator and condenser sides.

Flux enhancement with increasing flow velocity can be observed for the membrane and the laminate samples. This fundamental behaviour was already discussed in the context of membranes without backings in Sec. 3.4.1. If the backing faces towards the evaporator channel

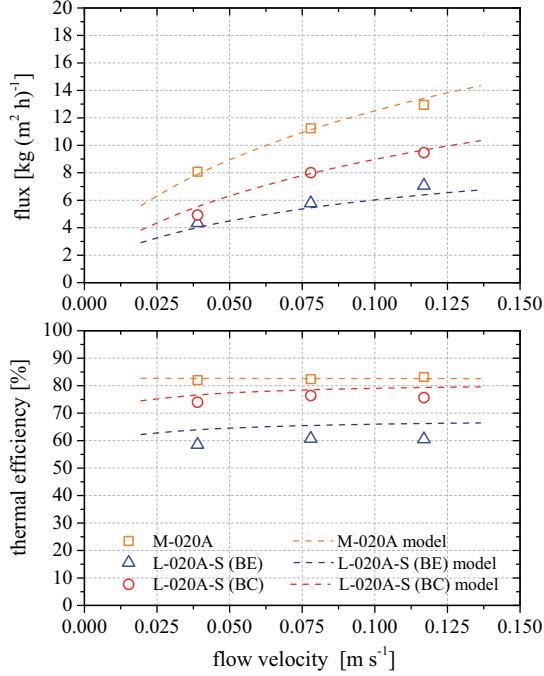


Figure 3.24: Experimental results and model predictions for membrane M-020A and its corresponding laminate L-020A-S for different flow velocities. The backing is oriented towards the evaporator side (BE) and towards the condenser side (BC), respectively. Testing conditions: $\bar{T}_{E-C} = 60^\circ\text{C}$, $\Delta T_{E-C} = 8\text{ K}$, DCMD configuration, channel spacer S-320, tap water

(L-020A-S(BE)), the flux performance of the laminate reaches only 54 %, 51 % and 55 % of the reference flux from a pure membrane for flow velocities of 0.04 m s^{-1} , 0.08 m s^{-1} and 0.12 m s^{-1} , respectively. If the backing is facing towards the condenser channel (L-020A-S(BC)), the negative influence of the backing is less distinctive. Analysing the results, the laminate flux reaches 61 %, 65 % and 73 % of the reference flux through a membrane without a backing structure. The negative effect of the backing appears to be less pronounced at higher flow rates. This observation might be explained by the fact that the heat transfer in the backing pores is an important issue for defining the overall performance of laminates. Since the backing pore volume is filled with water, the corresponding convective heat transfer is expected to increase for higher bulk stream flow velocities.

The thermal efficiency is observed to have a low sensitivity to the flow velocities in the results for the membrane as well as for the corresponding laminate. For the membrane without backing, this fundamental behaviour was already theoretically derived by Eq. 3.25 and experimentally validated in Sec. 3.4.1.

Influence of the Backing Structural Properties on Process Performance

Fig. 3.25 shows the relative impact of different backing structures on the DCMD process. The membranes M-020A and M-020B without backing are taken as references for the respective laminate samples L-020A-S, L-020A-N and L-020B-N. The backing position is labelled with (BC), if the backing faces the condenser side or with (BE), if it faces the evaporator side. The comparison is made at a mean temperature of $60\text{ }^{\circ}\text{C}$, a bulk temperature difference of 8 K and a flow velocity of 0.08 m s^{-1} .

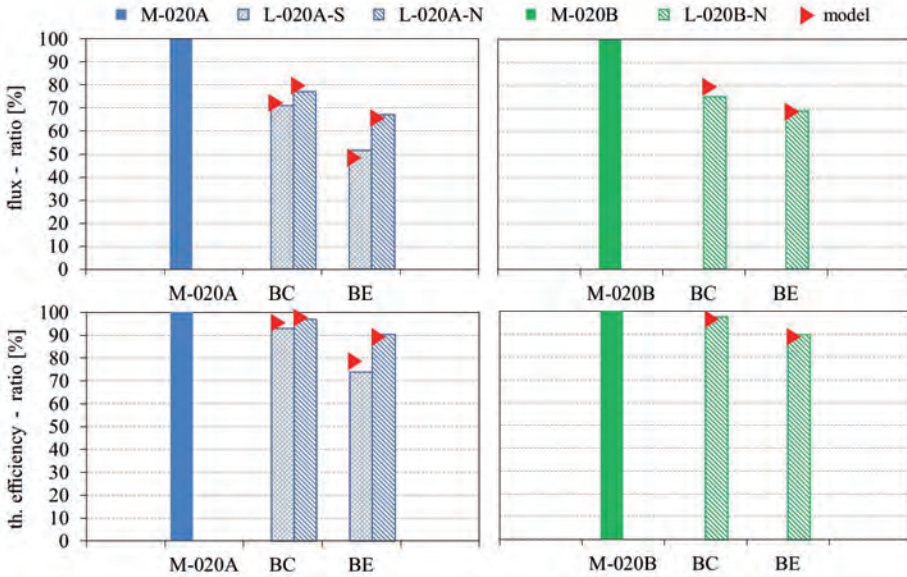


Figure 3.25: Experimental results and model predictions for membranes M-020A and M-020B and their corresponding laminates L-020A-S, L-020A-N and L-020B-N. The backings are oriented towards the evaporator side (BE) and towards the condenser side (BC), respectively. Testing conditions: $\bar{T}_{E-C} = 60\text{ }^{\circ}\text{C}$, $\Delta T_{E-C} = 8\text{ K}$, $\bar{c}_{E/C} = 0.08\text{ m s}^{-1}$, DCMD configuration, channel spacer S-320, tap water.

For both of the investigated backing structures, the flux value is reduced, showing less impact, if the backing is oriented towards the condenser side (BC). For the scrim backing of L-020A-S, only 71 % (BC) and 51 % (BE) of the nominal membrane flux could be achieved, depending on the position. The non-woven type of backing has a smaller effect for both membrane types investigated. Depending on position, the effect was measured to be 77 % (BC) and 67 % (BE) of nominal flux for L-020A-N and 75 % (BC) and 69 % (BE) for L-020B-N.

Analysing the thermal efficiencies of membrane samples M-020A, M-020B and their laminates shows that none of the laminates reaches the efficiency of the corresponding membrane without backing. The best results were measured for laminates supported by a non-woven structure. For

L-020A-N 97% (BC) and 90% (BE), for L-020B-N 98% (BC) and 90% (BE) of the reference value were reached. A stronger reduction of the thermal efficiency is caused by a scrim type of backing. For laminate L-020A-S, the efficiency is reduced to 93% (BC) and 74% (BE). It turns out that the relative influence of the backing structure on thermal efficiency is less than the relative influence on flux.

The impact of a backing appears to be strongly dependent on the backing structural properties but seems to be almost independent of the membrane properties. The influence of the membrane thickness is not affected by the existence of a support layer. The effect of the backing structural properties on the process performance leads to the following analysis: Tab. 3.4 shows higher voidage and thinner material for the non-woven type of backing. Additionally, the non-woven backing has thinner filaments covering the open membrane surface, which might reduce the effective path length for vapour diffusion. Visual inspection of the structures in Fig. 3.14 leads to the assumption, that the non-woven structure allows penetration of water beneath the open filaments to a certain extent. Thus, a larger effective membrane surface area is available. In addition, the heat and mass transfer resistances in the hydraulic boundary layer might be reduced by enhanced convective phenomena inside the backing layer.

Identification and Validation of the Backing Model Parameters

A new integrated membrane and backing model was derived in Sec. 3.1.5. In order to validate the new model approach, model predictions for flux performance and thermal efficiency are compared to each set of experimental results in Figs. 3.23-3.25. Additional validation is provided in Appendix E.

The derivation of the laminate model parameters builds on the heat transfer correlations from Sec. 3.4.1 and the membrane parameters that have been derived in Sec. 3.4.2. The membrane thickness, porosity, mean pore size and solid tortuosity are assumed to remain constant, whereas the tortuosity of the pores is assumed to change due to the significant influence on the diffusion path by the backing ($\tau_L \neq \tau_M$). For the backing model parameters, the basic geometrical specifications are taken from Tab. 3.4. The conductive heat transfer in the backing solid is estimated to be $0.23 \text{ W (m K)}^{-1}$, referring to the thermal conductivity of the polypropylene material. The combined convective and conductive heat transfer in the open backing pores is estimated by a Nusselt correlation, adapting the exponents $b = 0.656$ and $c = 0.333$ from the main flow channel correlation (Eq. 3.70) and a slightly higher factor $a = 0.2$. The hydraulic diameter is assumed to correspond to the backing thickness. The Nusselt numbers in the backing pores take on values of 2.3/3.6/4.7 for flow velocities of 0.04/0.08/0.12 m s^{-1} at 60°C, respectively. The relative dependence of the heat transfer on temperature is equal to that reported for the main flow channels in Sec. 3.4.1, due to the equality of the Nusselt exponents. It should be noted that some uncertainty is associated with this estimation, since the heat transfer in the backing pores is difficult to validate directly by an experiment. However, the main influencing aspects of the bulk stream flow velocity and the fluid properties are accounted for, so the approximation is

considered suitable after indirect experimental validation.

The significant performance difference that results from the position of the backing cannot be explained by effects of heat transfer alone. An important factor capable of describing this difference in position is the laminate factor f_L . The laminate factor was introduced in Sec. 3.1.5 in order to take the effect of the surface coverage on the cross-sectional area for diffusion into account. Assuming the available liquid-vapour interfacial area on the evaporator side to be the limiting factor for mass transfer, the laminate factor is defined using the backing surface porosity, if the backing faces towards the evaporator side ($f_L = \varepsilon_B$). If the backing is facing towards the condenser side, the interfacial area on the evaporator side is not affected ($f_L = 1$).

The modified laminate tortuosities have been determined by means of a parameter identification method. The accumulated errors of the full set of experimental data (Figs. 3.23-3.25 and Appendix E) have been minimised using the MS Excel optimiser software toolbox. Since the laminate tortuosities are expected to depend on the structural design of the backing, the results for the scrim backing and non-woven backing may accommodate different values. The best fitting value for the scrim backing is 1.8, and 1.6 for the non-woven backing. The difference is considered plausible, since the non-woven backing has a higher porosity and smoother distribution of the covered surface sections. The full set of backing model parameters used for all calculations presented in this thesis is documented in Tab. 3.9.

Table 3.9: Membrane and backing parameters used for model predictions.

	d_B / d_h^a [μm]	ε_B [%]	Nu_B^b [-]	τ_L [-]	f_L^c [-]
scrim	280	50	$0.2 Re^{0.656} Pr^{0.333}$	1.8	0.5 / 1
non-woven	200	70	$0.2 Re^{0.656} Pr^{0.333}$	1.6	0.7 / 1

^athe backing thickness is considered to be the backing hydraulic diameter

^bexponents adapted from spacer S-320 Nusselt correlation (Eq. 3.70)

^cfor backing positions BE/BC, based on the open surface area on the evaporator side

The results obtained with the new laminate model predict the general negative influence of the backing structure for all the operating conditions that have been studied. The favoured backing position facing towards the condenser channel is represented by the model. Calculating the mean deviation for flux and thermal efficiency for all experiments presented in this thesis leads to the values 2%/2% for M-020A, 8%/7% for L-020A-S(BE) and 4%/3% for L-020A-S(BC), respectively. A detailed summary of the maximal errors obtained for each set of experiments is given in Tab. 3.10.

The highest relative deviations were obtained for the low-performance operation points, since the general sensitivity to the relative error is quite high in these cases. However, the laminate model turns out to satisfactorily describe the performance dependence of laminates on flux as well as on thermal efficiency, for any variation of the operation parameters.

Analysing the model predictions in Fig. 3.25 demonstrates the applicability of the model with respect to different backing structures. In agreement with the experimentally obtained data, the

Table 3.10: Maximal errors of the model prediction with respect to the experimental results for the different parameter variations.

laminate	$e_{\max}(T_{E-C})$		$e_{\max}(\bar{c}_{E/C})$		$e_{\max}(\Delta T_{E-C})$	
	Fig. 3.23		Fig. 3.24		App. E	
	Δj_M	$\Delta \eta_{th}$	Δj_M	$\Delta \eta_{th}$	Δj_M	$\Delta \eta_{th}$
M-020A	+3%	-5%	+4%	-1%	+5%	-3%
L-020A-S (BE)	-17%	+10%	-9%	+9%	-11%	+4%
L-020A-S (BC)	+7%	+8%	+15%	+5%	-3%	+3%

modelling results show less impact for the non-woven type of backing than for the scrim type backing. The relative error of the model predictions for laminate L-020A-N are $-1\% / -1\%$, if the backing is oriented towards the evaporator channel and $+4\% / < 1\%$ if the backing is oriented towards the condenser channel. Considering the studies of the laminate L-020B-N with the same non-woven backing structure, the relative deviations are $+7\% / -3\%$ if the backing is oriented towards the evaporator channel and $+14\% / -2\%$ if the backing is oriented towards the condenser channel.

Further theoretical and experimental investigations on the fundamentals of mass transfer through partially covered membranes including possible anisotropic effects are needed to verify the assumptions made.

Further Reading - Selected References on the Role of Backing Structures

Detailed experimental studies on a PTFE membrane with a scrim backing were made and published in the framework of a PhD thesis [122]. The specifications of the backing included a thickness of $290 \mu\text{m}$ and a porosity of 60%. An influence of the backing position on flux performance was obtained, but the interpretation of the results remained unclear due to their dependence on experimental procedure. For reasonable stirring rates, a backing position on the condenser side led to a flux reduction of approximately 30%. However, the author interpreted the observations on the basis of the asymmetric test cell design rather than the asymmetric membrane characteristics.

A quite comprehensive experimental study addressing the role of backing structures was published in [157]. Similar PTFE membranes ($30 \mu\text{m}$) with and without backing structures were compared. The investigated backings were positioned on the condenser side (BC) and reduced flux by up to 56%. A non-woven backing structure was identified as the preferred material in comparison to a scrim backing. The authors explained this difference by a higher membrane surface porosity and improved convective heat transfer due to the fine filaments. The estimated backing porosity is stated to be 68% for the non-woven backing and 50% for the scrim backing. An impact of the lamination process on the membrane morphology, thickness in particular, was observed in an SEM analysis of laminate cross-sections. The authors contribute the negative influence of a backing on the membrane performance mainly to reduction of the membrane

porosity and the heat transfer coefficient on the permeate side. The backing is considered as an additional homogeneous thermal resistance layer, according to an approach that was proposed in [150], to account for membranes that are supported by nets on both the evaporator and the condenser sides.

The important role of the backing structural properties is identified experimentally in [155]. In this study, the scrim backing ($127\ \mu\text{m}$) showed less influence on the flux than a non-woven backing ($215\ \mu\text{m}$). However, the performance results do not really provide a direct evaluation of the backing morphology, since a significant difference in backing thickness was present and the PTFE membranes were provided by different manufacturers. No comparison is given with respect to membranes without backing. A backing position on the condenser side (BC) was experimentally derived to be preferable compared to a position on the evaporator side (BE). The differences due to position were quantified to be up to 19%.

The role of different support layers on the flux performance was experimentally investigated in [156]. After peeling the membranes from the backing, the flux increased by 18–148%, depending on the backing structural properties. The impact on flux was identified to be directly dependent on the backing porosity; in addition, the backing thickness is proposed to be one of the important geometrical backing parameters.

3.4.4 Extended Channel Configurations - The Gap Variants

The following section provides a detailed discussion of the specific phenomenology of the PGMD and the AGMD process configuration. The presentation of comprehensive experimental studies clarifies the general performance behaviour with changing operating conditions, the role of backing structures and the influence of the geometrical gap design for PGMD and AGMD. The analysis is accompanied by theoretical considerations and simulation results. Furthermore, the parameters for the modified PGMD and AGMD node models are identified and quantitatively validated by means of experimental results.

The Permeate Gap Configuration

The permeate gap configuration is created by the introduction of a permeate gap next to the condenser side of the membrane. Condensation occurs directly adjacent to the membrane at the liquid-vapour interface on the permeate side. Since the product water is in direct contact with the membrane on the condenser side, the phenomenology in PGMD is similar to the phenomenology in DCMD. However, additional heat transfer resistances are introduced by the permeate gap and the polymer film. In order to study the dependence of PGMD performance on permeate gap design and operating conditions, various test cell experiments have been performed. The experiments have been used to validate the modifications of the heat and mass transfer model

for PGMD presented in Sec. 3.2.2 as well as the corresponding laminate models for a permeate gap configuration in Sec. 3.1.5.

The heat transfer correlations for the main flow channels that were identified in the previous sections remain identical for a permeate gap configuration. Furthermore, the parameters for the membrane and laminate models for DCMD remain valid for the PGMD model, except for one special case that needs to be considered regarding the backing position. If a backing is positioned on the condenser side (BC), the liquid phase in the backing pore volume is considered to be stagnant for the test cell experiments, allowing conductive heat transfer phenomena only. Thus, the Nusselt number within the backing pores is assumed to be unity. If the backing is positioned on the evaporator side (BE), the heat transfer in the backing pores is identical to that in DCMD and the Nusselt correlation from Tab. 3.9 is used. The model parameters for the permeate gap layer are based on geometrical and material specifications of the gap spacer. The gap width and the gap voidage correspond to the permeate gap spacer geometrical parameters given in Tab. 3.6. The thermal conductivity of the polypropylene spacer material is set to be $0.23 \text{ W (m K)}^{-1}$. For the test cell experiments, the liquid phase in the permeate gap is considered to be stagnant, so the respective Nusselt number within the gap is assumed to be unity, similar to the liquid in the backing (BC) void volume. The model parameters describing the polymer film are based on its specifications given in Sec. 3.3.4. The thermal conductivity of the ETFE polymer is set as $0.24 \text{ W (m K)}^{-1}$.

Experimental results and model predictions regarding flux and thermal efficiency for a permeate gap configuration are presented in Fig. 3.26. The experiments were performed for the laminate L-020A-S, with the backing positioned on the condenser (BC) and the evaporator sides (BE), respectively. The test cell was configured using the channel spacer S-320, the gap spacer S-050 and the impermeable film F-127. The bulk temperature difference was kept constant at 12K and the temperature level was set to be 60 °C.

When a PGMD experiment is conducted, a minimal static pressure develops in the permeate gap, since the permeate squeezes out of the test cell. It turned out that the gap width could not be defined as precisely as necessary, if the highly flexible membrane M-020A without a backing was used. However, the expected performance behaviour is provided in the form of model predictions.

The flux results range from 3.2 to 5.2 $\text{kg (m}^2 \text{ h)}^{-1}$ for L-020A-S(BE) and from 3.6 to 4.8 $\text{kg (m}^2 \text{ h)}^{-1}$ for L-020A-S(BC), increasing slightly with the flow velocity. The fluxes appear to be significantly lower than those obtained for the DCMD experiments, due to the additional heat transfer resistance introduced by the permeate gap and the polymer film. The flux performance of the laminate reaches 55 to 72 % with respect to the calculated reference flux for a membrane without backing. In contrast to DCMD, there are quite similar flux results for the different backing positions in PGMD. This is mainly attributed to the additional gap width that is introduced by the backing, if it is positioned on the permeate gap side (BC). Furthermore, the heat transfer in the backing pores is quite low if the backing is positioned in the stagnant permeate (BC), compared to a backing position within the moving fluid in the evaporator channel (BE). This

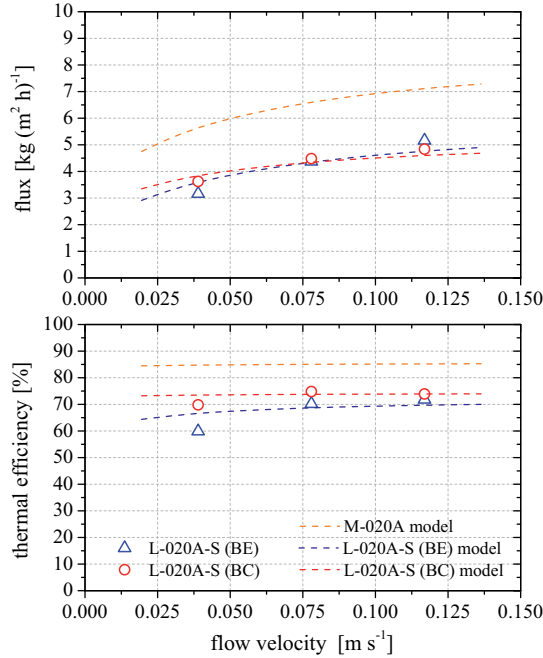


Figure 3.26: Experimental results and model predictions regarding the backing influence on PGMD. Membrane M-020A and its corresponding laminate L-020A-S have been studied for different feed velocities. The backing is positioned on the evaporator side (BE) and the condenser side (BC), respectively. Testing conditions: $\bar{T}_{E-C} = 60\text{ }^{\circ}\text{C}$, $\Delta T_{E-C} = 12\text{ K}$, PGMD configuration, channel spacer S-320, gap spacer S-050, impermeable film F-127, tap water.

effect is clearly indicated by the experimental results and the model predictions. The sensitivity of the flux performance to the flow velocity is low, if the backing is positioned facing the stagnant permeate, since the heat transfer in the backing pore volume is not affected by the channel flow conditions. In the case of a backing facing towards the evaporator channel, the heat transfer in the backing pores is affected by the channel flow conditions and its sensitivity to the flow velocity is slightly higher. The flux curves intercept at approximately 0.08 m s^{-1} .

The thermal efficiency values of 85 % for M-020A and approximately 69 % for L-020A-S(BE) are slightly higher than the results obtained for DCMD. The additional heat transfer resistances in PGMD mainly reduce the temperature difference across the membrane. Since the thermal efficiency is independent of temperature difference, the PGMD results do not differ much from the values obtained for DCMD. However, considering equal bulk stream conditions, the additional heat transfer resistances next to the membrane lead to a slightly increased mean membrane temperature level in PGMD compared to DCMD, thus increasing the thermal efficiency. The thermal efficiency result of 74 %, obtained for L-020A-S(BC), is not directly comparable to the corresponding DCMD results, due to the different heat transfer phenomenology in the backing pores.

The performance predictions of the laminate model, applied in the context of a PGMD channel configuration, quantitatively reflect the phenomenology introduced by the backing material. The maximal and mean deviations of the model predictions that consider a backing position on the condenser channel (BC) are 8 % and 5 % for the flux and 5 % and 2 % for the thermal efficiency. If the backing position faces towards the evaporator channel (BE), the maximal and mean deviations of the model predictions are 16 % and 8 % for the flux and 12 % and 5 % for the thermal efficiency.

The Air Gap Configuration

The air gap configuration is created by the introduction of an air gap next to the condenser side of the membrane. Condensation occurs on an impermeable film material that is cooled by the condenser flow channel. In order to study the dependence of the AGMD performance on air gap design and operating conditions, various test cell experiments were performed. The experiments are used to validate the general heat and mass transfer models for a combined membrane and air gap presented in Sec. 3.1.2 as well as the respective laminate models for an air gap configuration in Sec. 3.1.5.

The heat transfer correlations for the main flow channels and membrane/laminate parameters that were identified in the previous sections remain identical for an air gap configuration. The additional model parameters for the air gap layer are based on geometrical and material specifications of the design materials. Thus, the total gap width (including the condensate film) and the gap voidage correspond to the geometrical parameters of the air gap spacer given in Tab. 3.6. The thermal conductivity of the polypropylene spacer material is set to be $0.23 \text{ W (m K)}^{-1}$. Some assumptions have to be made specifically for the parameters regarding the conductive heat transfer through the air gap. The path length for conductive heat transfer through the spacer solid phase is assumed to be doubled by the tortuous structure, similar to the membrane materials. Moreover, wetting of the air gap spacer is considered to be an additional factor affecting the conductive heat transfer through the gap. The fraction of water that causes a thermal bridge effect is assumed to be 7 % of the gap volume. The small amount of heat transferred by radiation is calculated using emissivity values of 0.85 and 0.95 for the PTFE membrane and the water film, respectively. The condensate film thickness is a parameter which is difficult to determine directly. However, visual observation of the hydrophobic polymer condensation surface shows the formation of almost stationary droplets up to 2 mm in size, rather than a homogeneous film. Furthermore, water accumulates next to the spacer filament positions and the visible portion of water on the condensation surface increases in the direction of gravity. Consequently, the film model includes appreciable simplification of the real physical effects. However, good modelling results were achieved by using a film thickness of 0.75 mm. This value might better be interpreted as a virtual film thickness representing the mean path length for the heat transfer through the liquid phase of the stationary droplets or the liquid phase accumulated next to the spacer

filaments, where the condensation takes place. It should be mentioned that the effective air gap width for heat and mass transfer is determined from the total gap width minus the condensate film layer thickness. The model parameters for the polymer film are based on its specifications given in Sec. 3.3.4. The thermal conductivity of the ETFE polymer is set as 0.24 W (mK)^{-1} .

Experimental results and model predictions regarding flux and thermal efficiency for an air gap configuration are presented in Fig. 3.27. Membrane M-020A and its corresponding laminate L-020A-S have been used. The backing position is labelled with (BC), if the backing faces the condenser side or with (BE), if it faces the evaporator side. The channel configuration is set up using the channel spacer S-320, the gap spacer S-200 and the impermeable film F-127. The bulk temperature difference was kept constant at 12 K and the flow rate was set to be 0.08 m s^{-1} . The air gap is open to the ambient, so the absolute pressure level within the air gap is about 1 bar.

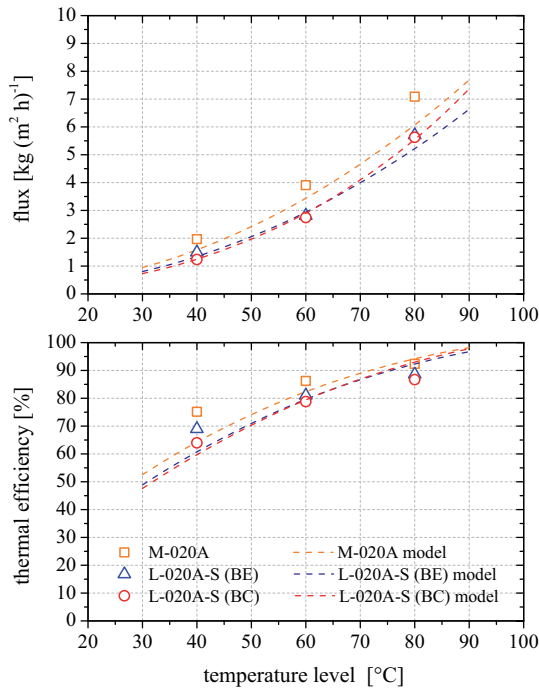


Figure 3.27: Experimental results and model predictions regarding the backing influence on AGMD. Membrane M-020A and its corresponding laminate L-020A-S have been studied for different temperature levels. The backing is positioned on the evaporator side (BE) and the condenser side (BC), respectively. Testing conditions: $\Delta T_{E-C} = 12 \text{ K}$, $\bar{c}_{E/C} = 0.08 \text{ m s}^{-1}$, AGMD configuration, channel spacer S-320, gap spacer S-200, impermeable film F-127, tap water.

The flux and thermal efficiency increase with temperature for the membrane and the laminate samples. The fluxes that are observed from the experiments range from 1.2 to $2.0 \text{ kg (m}^2 \text{ h)}^{-1}$ at $40 \text{ }^\circ\text{C}$ and 5.6 to $7.1 \text{ kg (m}^2 \text{ h)}^{-1}$ at $80 \text{ }^\circ\text{C}$. The general exponential character of the flux curves is

more distinctive in comparison to the curves observed with the DCMD or the PGMD configurations. The air gap introduces a high mass transfer resistance that strongly dominates the AGMD process. At higher temperatures, less air is left in the gap volume, leading to a lower transfer resistance. Since the process is not limited by the bulk heat transfer, only a minimal self-limiting effect due to increased temperature polarisation is expected for higher flux operation points.

The thermal efficiencies are in the range of 64% to 92%, which is quite similar to the results obtained for the DCMD and PGMD configuration. The beneficial effect of the air gap on the conductive heat loss is compensated by its negative effect on flux performance. Furthermore, the general insulating efficiency of the air gap is weakened by thermal bridges, introduced by the solid spacer material and water.

The membrane without a support structure (M-020A) shows the highest flux and thermal efficiency at all temperature levels. Negative effects induced by the backing material are observed for the laminate for all temperatures but appear to be less pronounced in comparison to the DCMD and PGMD variants. If the backing is located toward the evaporator channel (L-020A-S(BE)), the laminate flux reaches 72% of the reference flux and 94% of the reference efficiency from a sole membrane considering a temperature of 60 °C. If the backing faces the condenser channel, the flux reaches 70% and the efficiency reaches 91% of the reference values, respectively. The negative influence of the backing seems to be almost independent of the backing position. Especially the experiments where the backing is located adjacent to the evaporator channel improve in relative performance compared to the negative influence in the DCMD configuration that is presented in Fig. 3.23. This behaviour is explained by the backing influence on the effective air gap width, which dominates the transfer resistance. The air gap width is extended by the backing layer if the backing is positioned towards the condenser channel (BC), whereas the air gap does not include the backing layer, if the backing is located on the side of the evaporator channel (BE).

The AGMD model predictions regarding the membrane without backing underestimate the flux values measured in the experiments. The deviations are in the range of about 15 – 23%. Since the membrane without a backing is quite elastic, the membrane is expected to flex slightly into the volume between the air gap spacer filaments, due to the hydraulic pressure induced by the flow channels. This assumption was confirmed by visual inspection of the membrane during disassembly of the test cell after the experiments. Consequently, the effective gap width between the spacer filaments is slightly lower than the nominal gap width defined by the air gap spacer, leading to higher flux results. Consulting the model, the given deviations would correspond to a change in effective air gap width of approximately 0.5 mm, so the reliability of the experiments turns out to be limited and the model predictions are considered to be plausible despite the deviations. The model predictions regarding the laminates are in good quantitative agreement with the experimentally obtained performance. Especially the independence of the performance behaviour on the backing position is reflected by the laminate model. The maximal and mean deviations of the model for a backing facing the condenser channel (BE) are 5% and 3% for the flux and 8% and 4% for the thermal efficiency. If the backing is located towards the evaporator channel (BE), the maximal and mean deviations are 14% and 7% for the flux and 11% and 6% for the thermal efficiency.

For the AGMD configuration, the air gap is expected to be the dominant mass transfer resistance. This transfer resistance is mainly caused by the air, trapped in the air gap. Consequently, the AGMD performance is enhanced significantly, if the air is removed from the gap. To validate this prediction, experiments have been conducted, successively lowering the absolute pressure level in the air gap by a vacuum pump. If AGMD is operated at subatmospheric pressures ($\hat{p}_{AG} < 1$ bar), the configuration is referred to as Vacuum-enhanced Air Gap Membrane Distillation (V-AGMD). Experimental results and model predictions regarding flux and thermal efficiency are presented in Fig. 3.28. The channel configuration is set up using the laminate L-020A-S(BC), the channel spacer S-320, the gap spacer S-200 and the impermeable film F-127. The bulk temperature difference was kept constant at 12 K and the flow rate was set to be 0.08 m s^{-1} .

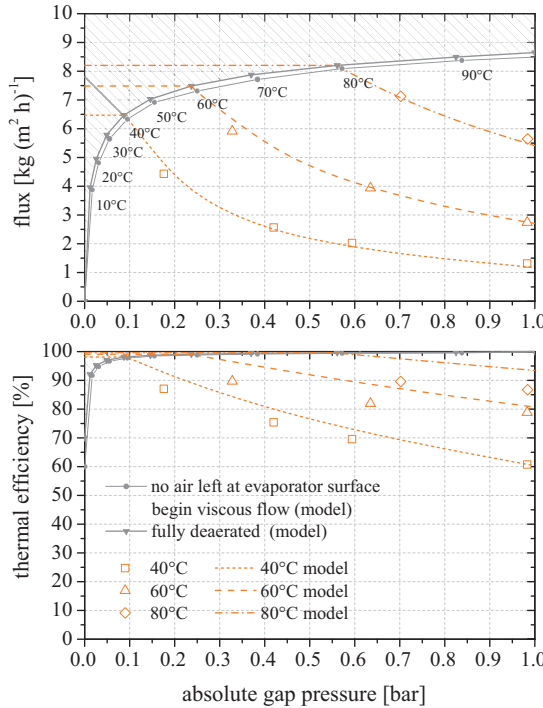


Figure 3.28: Experimental results and model predictions for an AGMD configuration for different absolute gap pressures and temperature levels. Testing conditions: $\Delta T_{E-C} = 12 \text{ K}$, $\bar{c}_{E/C} = 0.8 \text{ m s}^{-1}$, laminate L-020A-S(BC), channel spacer S-320, gap spacer S-200, impermeable film F-127, tap water.

The flux and the thermal efficiency are successively improved if the absolute gap pressure is lowered at any temperature level. At low temperatures, a high fraction of air is present due to the low partial vapour pressure. Consequently, the absolute gap pressure can be lowered significantly and strong performance improvements are achieved. For operation at 40°C , the flux is improved about 238% from $1.3 \text{ kg (m}^2 \text{ h)}^{-1}$ at ambient pressure to $4.4 \text{ kg (m}^2 \text{ h)}^{-1}$ at 0.18 bar. For operation at higher temperatures, the pressure cannot be lowered as much due

to the higher corresponding boiling pressure. Thus the potential for flux enhancement by gap deaeration is limited at higher temperatures. For operation at 60 °C, the flux is improved about 115 % from 2.7 kg (m² h)⁻¹ at ambient pressure to 5.9 kg (m² h)⁻¹ at 0.33 bar. For operation at 80 °C, the flux is improved about 26 % from 5.6 kg (m² h)⁻¹ at ambient pressure to 7.1 kg (m² h)⁻¹ at 0.70 bar. For deaerated operation, the thermal efficiency observed in the experiments reaches values of approximately 90 % for all temperatures.

In principle, the pressure levels could be reduced even further. However, to ensure that the flux performance was not unintentionally influenced by mechanical removal of the water vapour, the absolute pressures were deliberately kept above the respective boiling point. The model predictions give an indication of the performance at lower pressure levels. If the absolute pressure is lower than the vapour pressure on the evaporator side, a total pressure difference is established and the viscous flow phenomenon is introduced. The minimal possible pressure level in air gap membrane distillation is limited by the vapour pressure on the condenser side. If the absolute gap pressure equals the vapour pressure on the condenser side, no air is left and the gap is described as being fully deaerated. The respective thresholds for different temperature conditions were evaluated by means of model predictions and included in the diagram. According to the model predictions, the maximal relative improvements considering a fully deaerated gap are 438 % at 40 °C, 170 % at 60 °C and 49 % at 80 °C.

A reduction to an absolute pressure level below the boiling pressure is possible only if the vapour is extracted mechanically with a strong vacuum pump. This mode would be referred to as Vacuum Membrane Distillation (VMD). The grey hatched area represents the field of pressure conditions that cannot be achieved in Air Gap Membrane Distillation.

The model predictions in Fig. 3.28 are in good agreement with the experimentally obtained data. The maximal and mean deviations of the model are 10 % and 4 % for the flux predictions and 8 % and 6 % for the predictions of the thermal efficiency. It is conspicuous that the model systematically overestimates the thermal efficiencies for the deaerated operating points. The measured efficiency values for deaerated operation do not exceed 90 %, while the model predicts thermal efficiencies of 93 – 97 %, respectively. This deviation is considered to be due to an experimental limitation rather than a fundamental error in the model predictions. It is suspected that in addition to the conductive heat transfer through the active membrane area, minimal heat losses occur due to heat transfer to the ambient and conductive heat transfer associated with the contact area of the cell half-shells next to the active membrane area. The closer the measured thermal efficiency is to the optimal case, the higher is the sensitivity of the result to the almost constant edge effects. It turns out that the measured efficiency values do not exceed the value of 90 %. Improved insulation and a test cell with a larger membrane area would be necessary in order to minimise the edge effects.

In a (V-)AGMD configuration, the vapour diffuses through the membrane and the air gap until it reaches the condensation surface. If a laminate is used and the backing is positioned on the air gap side (BC), the backing introduces an additional mass transfer resistance. In order to analyse the composition of the mass transfer resistances in (V-)AGMD and their dependence on the absolute gap pressure, a model-based pressure drop analysis was conducted. Fig. 3.29 shows the results that correspond to the conditions in Fig. 3.28 at 60 °C.

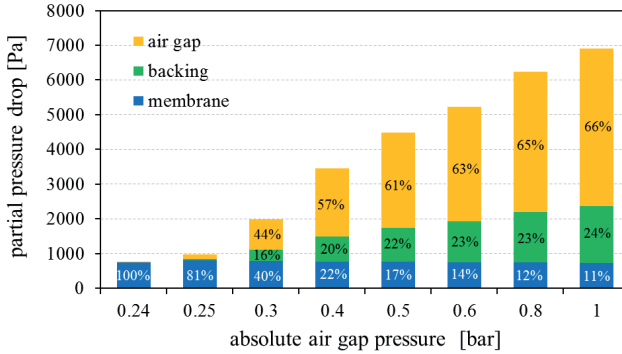


Figure 3.29: Model-based pressure drop analysis for a (V-)AGMD configuration operated at a mean temperature level of 60 °C, a temperature difference of 12 K and different states of deaeration. The model parameters and operating conditions correspond to the results presented in Fig. 3.28.

The highest partial pressure drop of 6910 Pa is detected for operation at ambient pressure, due to the high mass transfer resistance. In this case, only 11 % of the overall partial pressure drop is associated with the membrane, whereas 24 % and 66 % are based on molecular diffusion in the laminate and the air gap, respectively. The partial pressure drop is reduced significantly if the absolute air gap pressure is further reduced. However, the composition of the mass transfer resistances remains almost constant until an absolute pressure level of approximately 0.5 bar is reached. On lowering the pressure level from 0.4 to 0.25 bar, the fraction of the mass transfer resistance associated with the membrane becomes considerably higher. This phenomenon is based on the fact that the Knudsen part of the membrane resistance is independent of pressure level and therefore remains constant, while the molecular diffusion resistance in the laminate and the gap is reduced. In the ideal case at 0.24 bar, where the gap is fully deaerated, no mass transfer resistance is introduced by the backing and the gap layer. 100 % of the pressure drop is due to the membrane Knudsen resistance. Consequently the process performance is independent of the gap width, as long as the pressure drop based on viscous flow is negligible within the air gap. The diffusive mass transfer and conductive heat transfer coefficients have been explicitly evaluated for the AGMD configuration, considering air gap spacer widths from 1 – 3 mm, different operating temperature levels and different states of deaeration. The resulting values are summarised in Tab. 3.11. Due to the high diffusive and thermal resistance of the air gap, the values are low, compared to those presented in Tab. 3.8 for a single membrane in a DCMD configuration. The AGMD mass transfer coefficients increase with temperature due to the changing amount of air in the gap. If air is removed from the gap, a significant increase of the mass transfer coefficients is obvious. If the gap is considered fully deaerated, the Knudsen diffusion resistance in the membrane is the only factor defining the diffusive mass transfer coefficient. This value is independent of gap width and almost equal to those values presented in Tab. 3.8, which were evaluated for membranes instead of a laminate. The laminate's Knudsen coefficient is approximately one order of magnitude higher than the mass transfer coefficient of an aerated

AGMD configuration, indicating the minor role of the membrane structural parameters for an aerated AGMD process. The conductive heat transfer coefficient is independent of temperature and air partial pressure, but depends inversely on the gap width.

Table 3.11: Explicit evaluation of the theoretical coefficients for diffusive mass transfer and conductive heat transfer for the (V-)AGMD configuration with laminate L-020A-S(BC).

$\delta_{S(AG)}$ [mm]	$C_{L-AG,d,aerated}$ [$10^7 \times \text{kg} (\text{Pa m}^2\text{s})^{-1}$]			$C_{L-AG,d,deaerated}^a$ [$10^7 \times \text{kg} (\text{Pa m}^2\text{s})^{-1}$]			$\lambda_{L-AG}^* \delta_{L-AG}^{-1}{}^b$ [$\text{W} (\text{m}^2\text{K})^{-1}$]
	40 °C	60 °C	80 °C	0.7 bar	0.4 bar	≤ 0.2 bar	
1.0	1.9	2.2	3.4	3.4	7.2	25.8	147
2.0	0.9	1.1	1.7	1.6	3.8	25.8	54
3.0	0.6	0.7	1.1	1.1	2.6	25.8	33

^aevaluated for 60 °C; vapour pressure of pure water at 60 °C is approximately 0.2 bar

^bdefined from hot to cold liquid-vapour interface, according to Tab. 3.2

Influence of the Gap Width on Process Performance

The gap design has significant influence on the overall process performance. The gap width is the most crucial gap parameter since it has a strong influence on the thermodynamic behaviour of the corresponding process configuration. Fig. 3.30 presents experimental results and model predictions for a variation in gap width for each of the gap variants, respectively.

The channel configuration is set up using the laminate L-020A-S(BC), the channel spacer S-320 and the impermeable film F-127. The desired gap width is established by using one of the spacers, S-200 or S-050, or a combined stack. The PGMD experiments were performed using narrow gaps in the range of 0.5 – 1.5 mm, whereas the test cell for AGMD and V-AGMD was configured with gaps in the range of 1.0 – 6.0 mm. The temperature level was 60 °C, the bulk temperature difference was kept constant at 12 K and the flow rate was set to be 0.08 m s⁻¹. The absolute pressure level for the V-AGMD configuration was set to 0.33 bar.

The experimentally obtained flux performance is reduced significantly for wider gaps, for all gap variants that have been studied.

For the PGMD configuration, a flux of 4.5 kg (m² h)⁻¹ is obtained for a gap width of 0.5 mm. The heat transfer resistance associated with the gap is higher for wider gaps, so the interfacial temperature difference across the membrane and consequently the flux is reduced to 2.9 kg (m² h)⁻¹ for a gap width of 1.5 mm. The gap width mainly influences the interfacial temperature difference, whereas the temperature level for the membrane remains almost constant. The thermal efficiency of approximately 74% is not affected by the gap width due to its independence of temperature difference (Eq. 3.25 and Appendix E).

For the AGMD configuration, the gap spacer functionality includes the establishment of an air gap, avoiding bridge effects of product water across the open gap. Thus, the minimal feasible

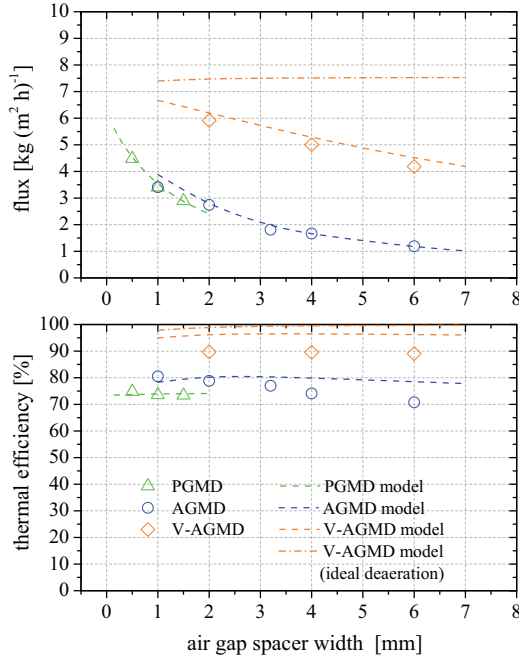


Figure 3.30: Experimental results and model predictions for PGMD, AGMD and V-AGMD configurations for different gap widths. Testing conditions: $\bar{T}_{E-C} = 60\text{ }^{\circ}\text{C}$, $\Delta T_{E-C} = 12\text{ K}$, $\bar{c}_{E/C} = 0.08\text{ m s}^{-1}$, $\hat{p}_{VP,AG}^{VAGMD} = 0.33\text{ bar}$, laminate L-020A-S(BC), channel spacer S-320, gap spacer S-200/S-050, impermeable film F-127, tap water.

gap width is limited, with a lower limit that is assumed to be about 1 mm. The flux result obtained for the AGMD configuration is $3.4\text{ kg (m}^2\text{ h)}^{-1}$ for a gap width of 1 mm. If the gap width is 6 mm, the flux is reduced to $1.2\text{ kg (m}^2\text{ h)}^{-1}$, due to the increased diffusive mass transfer resistance. The thermal efficiency evaluation leads to values of approximately 80%. For larger gap widths, the measured results reduce to 70%. It should be noted that the uncertainty of the efficiency evaluation is high for low-performance operating points (see Fig. 3.13).

If the air gap is partially deaerated, referred to as V-AGMD measurements, the flux increases. This phenomenon has already been discussed previously. If the gap width for the V-AGMD measurements is reduced from 6 mm to 2 mm, the flux increases from $4.2\text{ kg (m}^2\text{ h)}^{-1}$ to $5.9\text{ kg (m}^2\text{ h)}^{-1}$. The sensitivity to the gap width appears to be less pronounced in comparison to the AGMD measurements at ambient pressure, based on the lower fraction of the gap in the overall mass transfer resistance (see Fig. 3.29). The thermal efficiency of approximately 90% was determined to be independent of the gap width, as for the AGMD measurements at ambient pressure. Model predictions of the expected performance characteristics for an air gap that is fully deaerated have been included as supplementary information. For a V-AGMD variant with ideal deaeration, a flux of about $7.5\text{ kg (m}^2\text{ h)}^{-1}$ and a thermal efficiency of about 99% is predicted, independent of

gap width. The performance characteristics are higher compared to the tested V-AGMD configuration with partial deaeration due to the elimination of the molecular diffusion resistance. According to Fig. 3.29, only the Knudsen diffusion resistance of the membrane contributes to the overall mass transfer resistance of the combined laminate and air gap, so performance is almost independent of gap width. A minimal improvement of the performance is observed with increasing gap width, explained by the corresponding increase in thermal resistance.

The model predictions are in good quantitative agreement with the experimentally obtained values. The PGMD predictions show maximal and mean deviations of 2% and 1% for the flux and the thermal efficiency. Considering the model predictions for the AGMD configuration, maximal and mean deviations of 14% and 5% are obtained for the flux and 11% and 6% are obtained for the thermal efficiency. For the V-AGMD model, the maximal and mean deviations are 8% and 6% for the flux and 8% and 8% for the thermal efficiency, respectively. The successive overestimation of the thermal efficiency for V-AGMD has already been discussed previously.

Further Reading - Selected References on the Membrane Distillation Gap Variants

Early experimental studies on AGMD already indicated a rather small effect of membrane structural properties on flux performance [18]. The inverse dependence of flux on the gap width was observed for gap widths ranging from 0.2 to 10 mm. Independent studies confirm this observation for gap widths of 2 – 10 mm [129]. In these experiments, a rather small influence of the hydrodynamics on process performance was observed for Reynolds numbers from 500 to 3500, which were varied separately on the evaporator and the condenser side. A strong exponential dependence of the flux on evaporator temperature was identified from 40 to 70 °C. The corresponding thermal efficiencies were theoretically estimated to increase with temperature from 70 to 90%. A different experimental study on AGMD has been carried out with an aqueous sucrose solution [130]. A proportional correlation between flux and increasing bulk stream temperature difference was observed. A distinct exponential behaviour was identified for increasing mean temperature levels. The flux showed almost linear dependence on the air gap width that was varied from approximately 0.9 to 3.7 mm. Furthermore, a comparison of membranes with and without backing showed lower values for the laminate, but this observation might additionally be caused by a significantly lower membrane porosity. A linear regression method was applied in the context of AGMD, leading to overall membrane-air gap transfer coefficients in the range of 3.3 to 7.0 kg (Pa m² s)⁻¹. Further experimental studies on the treatment of different alcohol aqueous solutions with AGMD have been published by the same authors [25]. Different membranes made of PTFE and PVDF have been used. Considerably higher fluxes were achieved for thin membranes providing high porosity and pore size. A negative effect of a backing on flux performance was quantified with 30% for a given operation point.

A node model representing an AGMD configuration has been developed and validated with external experimental data [128]. The comprehensive theoretical analysis predicts thermal effi-

ciencies of 84 – 95 %, increasing with feed temperature level. Furthermore, low sensitivities were expected with respect to flow velocity ($0.1 - 0.3 \text{ m s}^{-1}$) and salinity ($21 - 53 \text{ g kg}^{-1}$). An analysis of different gap widths from 1 – 5 mm showed an inverse dependence for flux, whereas only a minor impact on thermal efficiency was detected. A model-based sensitivity analysis comparing AGMD and DCMD was published by the same authors [167, 168]. For identical operating conditions, the fluxes predicted for DCMD exceed those predicted for AGMD by more than a factor of 2, whereas the thermal efficiency was predicted to be approximately 8% higher for AGMD. Complementary to the observations in this study, a lower sensitivity with respect to the feed salinity was predicted for the DCMD. A dominating role of the air gap resistance on the overall mass transfer resistance, with a contribution which reduces at higher temperatures, was clearly observed. For DCMD, the hydrodynamics and the membrane resistance contributed similarly to the overall mass transfer resistance. Improvement of the hydrodynamic conditions was identified to be worthwhile, especially for high temperatures due to the corresponding higher performance. An experimental comparison of AGMD and PGMD configuration has been published recently [169]. The experiments were run with a PTFE laminate provided by Gore, a polypropylene condenser film ($70 \mu\text{m}$) and a gap width of approximately 3 mm for each process configuration. The experiments were conducted with artificial sea water at constant condenser inlet temperature, a feed temperature ranging from 50 to 80 °C and flow velocities of $0.1 - 0.3 \text{ m s}^{-1}$. The fluxes obtained with the PGMD configuration were identified to be 20 – 30 % higher than to the AGMD results. If the AGMD configuration was enhanced by a soft vacuum (0.9 bar), the flux increased by approximately 10 %. A greater effect of gap deaeration is predicted, if the pressure could be further reduced. Additionally, the specific thermal energy consumption was quantified. A node model for PGMD and AGMD was partially validated by the experimental data. A systematic underestimation of the AGMD flux was identified and attributed to difficulties caused by elastic gap shrinkage, droplet formation and gap flooding.

Experimental studies on the V-AGMD configuration were conducted with PE hollow fibre membranes with a wall thickness of 90 – 250 μm [27]. The total air gap pressure was set approximately 50 mbar above the corresponding saturated vapour pressure at the evaporator inlet temperature. The experimentally obtained thermal efficiencies of 80 – 90 % did not reach the theoretically predicted values, which range from 92 to 98 %.

3.4.5 A Comparative Evaluation of Different Process Configurations

This section presents a comparative assessment of the different membrane distillation configurations DCMD, PGMD, AGMD and V-AGMD. The test cell experiments for the different configurations are compared at fixed bulk stream conditions, considering systematic parameter variations for each of the characteristic operational parameters, namely the mean temperature, the flow velocity, the temperature difference and the feed salinity.

The materials used for the analysis are identical to those presented in the previous sections.

The basic test cell configuration consists of the laminate L-020A-S that is positioned on the condenser side (BC), the channel spacer S-320 and the impermeable film F-127. The permeate gap is established by using gap spacer S-050, while spacer S-200 is used for setting up the air gap configuration. A temperature level of 60 °C, a bulk temperature difference of 12 K and a flow velocity of 0.08 m s⁻¹ are chosen as the reference operating conditions. For the V-AGMD variant, the total gap pressure is reduced to 0.18/0.33/0.71 bar, depending on the temperature level. It should be noted that the results for the V-AGMD configuration do not reflect the complete performance potential, since the air gap cannot be fully deaerated in the test cell for previously given reasons (Sec. 3.4.4, Fig. 3.28).

For each set of experiments, a detailed analysis of deviations from model predictions for flux and thermal efficiency is provided, including a comparative presentation of the respective model predictions. Prior to the discussions that refer to each different parameter variations individually, a summary of the experimentally obtained average sensitivities with respect to the operating parameters is provided in Tab. 3.12.

Table 3.12: Summary of the experimentally obtained average sensitivities of the MD processes with respect to the operating parameters. The mean sensitivities for flux in [kg (m² h)⁻¹] and thermal efficiency in [%] are given with respect to a defined reference variation Δ .

reference variation configuration	\bar{T}_{E-C} Fig. 3.31 $\Delta = 10$ K		$\bar{c}_{E/C}$ Fig. 3.33 $\Delta = 0.02$ m s ⁻¹		ΔT_{E-C} Fig. 3.34 $\Delta = 10$ K		S_E^a Fig. 3.36 $\Delta = 50$ g kg ⁻¹	
	Δj_M	$\Delta \eta_{th}$	Δj_M	$\Delta \eta_{th}$	Δj_M	$\Delta \eta_{th}$	Δj_M	$\Delta \eta_{th}$
DCMD	2.8	7.1	1.5	0.4	11.1	2.5	1.8	7.5
PGMD	0.6	5.4	0.3	0.9	3.9	4.0	0.9	14.7
AGMD	1.1	6.5	0.1	2.5	2.7	2.1	0.2	1.5
V-AGMD	0.7	0.4	0.4	0.2	7.4	8.7	0.7	3.6

^aevaluated for salinities from 0 – 220 g kg⁻¹

Influence of the Temperature Level on MD Process Performance

The sensitivity analysis with respect to the mean temperature level is presented in Fig. 3.31, including a comparative presentation of the respective model predictions. However, the following quantitative discussion refers to the respective experimental results, while the deviations of the model predictions from the experiments are summarised in Tab. 3.13 at the end of this section. Comparing the different MD configurations, DCMD clearly shows the highest flux performance compared to the gap variants, reaching flux values up to 18.2 kg (m² h)⁻¹ at 80 °C. The maximal values reached for the gap variants are lower due to the additional heat and mass transfer resistances introduced by the gap and the polymer film. The maximal flux performance obtained in the PGMD, AGMD and V-AGMD experiments are 5.4 kg (m² h)⁻¹, 5.6 kg (m² h)⁻¹ and 7.1 kg (m² h)⁻¹, respectively. The fundamental beneficial influence of the higher tempera-

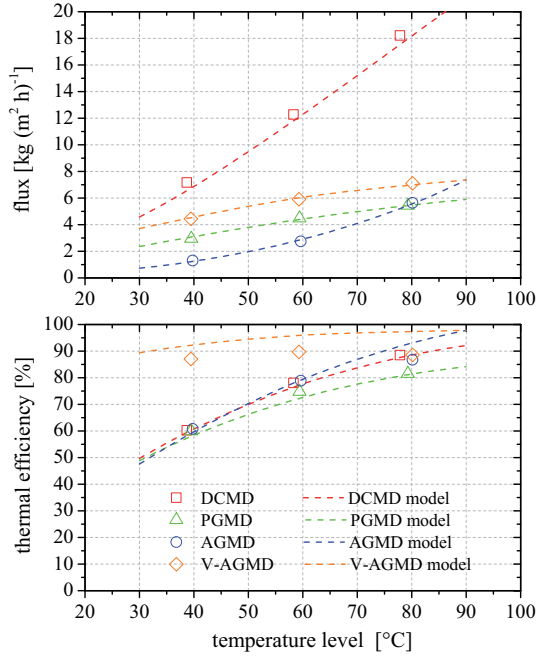


Figure 3.31: Sensitivity analysis with respect to the temperature level, comparing flux and thermal efficiency for DCMD, PGMD, AGMD and V-AGMD configurations. Testing conditions: $\Delta T_{E-C} = 12$ K, $\bar{c}_{E/C} = 0.08$ m s⁻¹, $\hat{p}_{VP,AG}^{VAGMD} = 0.18/0.33/0.71$ bar, laminate L-020A-S(BC), channel spacer S-320, gap spacer S-050/S-200, impermeable film F-127, tap water.

ture level on the flux and thermal efficiency performance is obvious for all MD configurations, but the sensitivity to the temperature level is quite different for the different configurations. The highest sensitivity of $2.8 \text{ kg (m}^2 \text{ h)}^{-1}$ per 10 K at almost linear dependence was obtained for DCMD. The sensitivity of $0.6 \text{ kg (m}^2 \text{ h)}^{-1}$ per 10 K that was achieved for the PGMD configuration, is significantly lower. This is explained by the fact that the membrane heat and mass transfer resistance in DCMD decreases significantly with temperature, while in PGMD, the heat and mass transfer resistance includes the permeate gap and the polymer film resistances that are almost independent of temperature. The AGMD configuration has a sensitivity of approximately $1.1 \text{ kg (m}^2 \text{ h)}^{-1}$ per 10 K, showing an exponential curve due to the changing amount of air defining the dominating air gap mass transfer resistance. If the air gap is partially deaerated, the resulting sensitivity to temperature reduces to $0.7 \text{ kg (m}^2 \text{ h)}^{-1}$ per 10 K. A comparison of the AGMD and the V-AGMD flux results illustrates the beneficial effect of deaeration, which is less pronounced for the high temperature operation points. Consequently, the V-AGMD flux curve has a rather concave shape. Assuming a higher state of deaeration than the one that was experimentally examined, the V-AGMD sensitivity with respect to the temperature level is expected to reduce further (Fig. 3.28).

The thermal efficiencies for DCMD, PGMD and AGMD are quite similar, ranging from 60 % to 80–90 % at 80 °C. The thermal efficiency results obtained for the V-AGMD variant reach values of approximately 90 % throughout the whole range of temperatures. For the V-AGMD configuration, the flux and consequently the latent heat fraction is significantly enhanced, especially for the low-temperature operating points. The enhanced heat transfer additionally lowers the temperature polarisation coefficient and consequently the driving force for the conductive heat transfer.

In order to obtain information on the composition of the thermal resistances within the different material layers, a detailed analysis of the modelling results corresponding to Fig. 3.31 has been conducted. Fig. 3.32 illustrates the drop of temperature associated with the respective material layers for different MD configurations and operation temperatures.

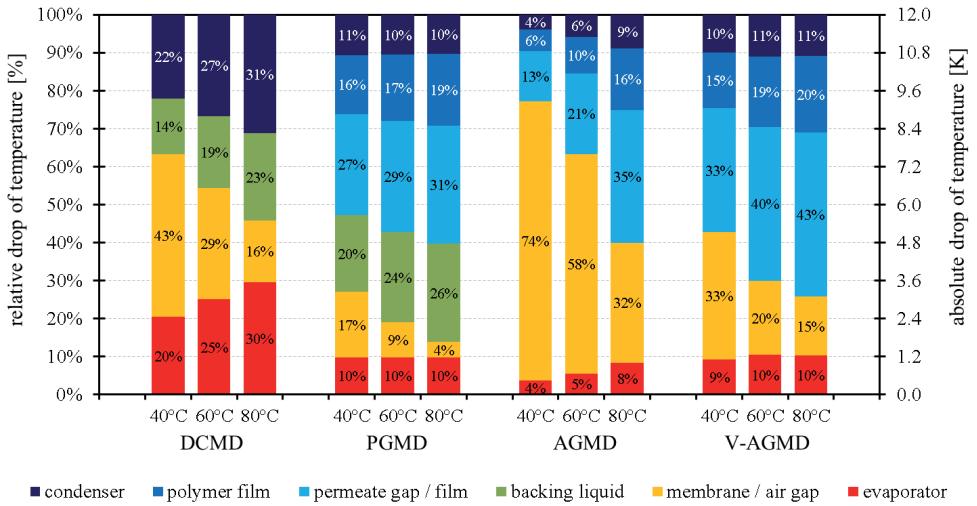


Figure 3.32: Model-based thermal resistance analysis for DCMD, PGMD, AGMD and V-AGMD configurations at different temperature levels. The results correspond to the model predictions that have already been presented in Fig. 3.31.

The membrane/air gap resistance and consequently the fraction of the temperature drop associated with the membrane/air gap decreases with temperature for all MD configurations. As a result, the role of the heat transfer in the bulk streams is gaining significance with temperature level. For the DCMD configuration, the fractions of the evaporator channel, the condenser channel, the membrane and the backing layer are in the same range, whereas the heat transfer in the flow channels is of only minor significance for the gap variants. In PGMD, the additional resistances introduced by the permeate gap and the polymer film account for approximately 30 % and 20 % of the total drop in temperature. Furthermore, the backing layer within the gap (BC) causes a higher temperature drop than in DCMD, since the heat transfer is based on the conductive heat transfer through the stagnant permeate, only. Considering AGMD, the large temperature drop associated with the combined membrane and air gap underlines its dominating

role. The relative fraction of the membrane and air gap reduces from 74% at 40°C to 32% at 80°C, illustrating the strong influence of the temperature level on the molecular diffusion gap resistance. The gap resistance and consequently the respective temperature drop is reduced by lowering the gap pressure in V-AGMD. According to the model, the thermal resistance associated with the liquid permeate on the polymer film induces a rather high temperature drop for the AGMD and V-AGMD process variants. The relative fractions reach values of up to 43%, being higher for V-AGMD.

Influence of Feed Flow Rate on MD Process Performance

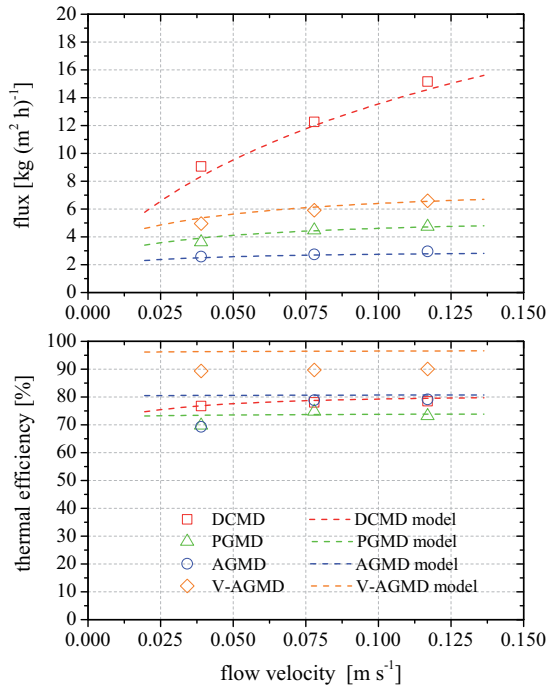


Figure 3.33: Sensitivity analysis with respect to the flow velocity, comparing flux and thermal efficiency for DCMD, PGMD, AGMD and V-AGMD configuration. Testing conditions: $\Delta T_{E-C} = 12$ K, $\bar{T}_{E-C} = 60$ °C, $\hat{p}_{VP,AG}^{VAGMD} = 0.33$ bar, laminate L-020A-S(BC), channel spacer S-320, gap spacer S-050/S-200, impermeable film F-127, tap water.

The sensitivity analysis with respect to the flow velocity is presented in Fig. 3.33, including a comparative presentation of the respective model predictions. However, the following quantitative discussion refers to the respective experimental results, while the deviations of the model predictions from the experiments are summarised in Tab. 3.13 at the end of this section. Comparing the different MD configurations, DCMD clearly shows the highest flux performance com-

pared to the gap variants, reaching flux values up to $15.2 \text{ kg (m}^2 \text{ h)}^{-1}$ at 0.12 m s^{-1} . The maximal values reached for PGMD, AGMD and V-AGMD are $4.7 \text{ kg (m}^2 \text{ h)}^{-1}$, $3.0 \text{ kg (m}^2 \text{ h)}^{-1}$ and $6.6 \text{ kg (m}^2 \text{ h)}^{-1}$, respectively. Although the effect of increasing flow velocity on the flux performance is always positive, the sensitivity is quite different for the different MD configurations. In general, the sensitivity to the flow velocity corresponds to the fraction of the flow channel resistances to the total heat transfer resistance, that was previously analysed in Fig. 3.32. A rather high sensitivity of $1.5 \text{ kg (m}^2 \text{ h)}^{-1}$ per 0.02 m s^{-1} is given for DCMD, due to the high fraction of the bulk streams within the total heat transfer resistance. By introducing a permeate gap resistance, the role of the main channel heat transfer and consequently the sensitivity to the flow velocity is reduced to $0.3 \text{ kg (m}^2 \text{ h)}^{-1}$ per 0.02 m s^{-1} for PGMD. The lowest sensitivity of $0.1 \text{ kg (m}^2 \text{ h)}^{-1}$ per 0.02 m s^{-1} is obtained for the AGMD configuration, affirming the result in Fig. 3.32 that presents the lowest fraction of the flow channels within the total heat transfer resistance for AGMD. If the air gap is partially deaerated, the role of the flow channel heat transfer increases slightly, leading to a sensitivity of approximately $0.4 \text{ kg (m}^2 \text{ h)}^{-1}$ per 0.02 m s^{-1} for the V-AGMD results.

The thermal efficiencies were observed to be almost independent of flow velocity for all MD variants. For DCMD, this general behaviour has already been discussed theoretically (Eq. 3.25) and experimentally (Fig. 3.24). The small systematic offset of the thermal efficiency, comparing the DCMD result of approximately 78% and the PGMD result of approximately 73%, is explained by the backing that is located towards an open flow channel in DCMD and towards the permeate gap with stagnant liquid in PGMD. At low flow velocities, where the convective heat transfer in the backing pores is low also in DCMD, the thermal efficiencies are quite similar. This is indicated by the model predictions, particularly those evaluated at 0.02 m s^{-1} .

Influence of Temperature Difference on MD Process Performance

The sensitivity analysis with respect to the bulk stream temperature difference is presented in Fig. 3.34, including a comparative presentation of the respective model predictions. However, the following quantitative discussion refers to the respective experimental results, while the deviations of the model predictions from the experiments are summarised in Tab. 3.13 at the end of this section. For a temperature difference of up to 25 K, the flux values fall on almost straight lines. For all process configurations, the lines intersect the origin. Since temperature polarisation is not sensitive to temperature difference (Eq. 3.40), this behaviour confirms the proportionality of flux to the driving force. The steepest gradient of $11.1 \text{ kg (m}^2 \text{ h)}^{-1}$ per 10 K is identified for DCMD. The results for the gap variants have smaller gradients, indicating the negative influence of the additional transfer resistances introduced by the gap. Considering a fixed absolute gap pressure level for V-AGMD, the fraction of air within the gap is slightly reduced at higher temperature differences, due to a slight increase of the resulting mean vapour pressure level. Particularly for this case, the flux curve takes on a slightly exponential form. Generally, the accuracy of a linear extrapolation is limited by the validity of linearising the Clausius-Clapeyron

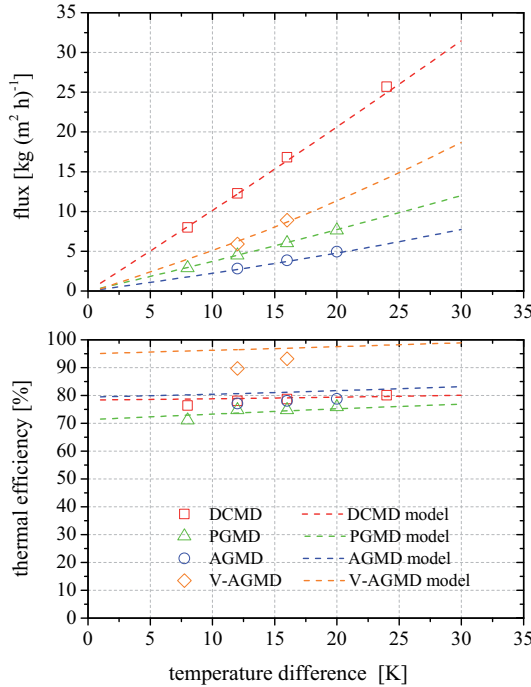


Figure 3.34: Sensitivity analysis with respect to the temperature difference, comparing flux and thermal efficiency for DCMD, PGMD, AGMD and V-AGMD configurations. Testing conditions: $\bar{T}_{E-C} = 60\text{ }^{\circ}\text{C}$, $\bar{c}_{E/C} = 0.08\text{ ms}^{-1}$, $\hat{p}_{VP,AG}^{VAGMD} = 0.33\text{ bar}$, laminate L-020A-S(BC), channel spacer S-320, gap spacer S-050/S-200, impermeable film F-127, tap water.

equation, especially at higher mean temperatures and higher interfacial temperature differences. The experimental results for the thermal efficiencies confirm the values obtained in the previous sensitivity analysis in Fig. 3.33. The thermal efficiencies show a behaviour that is almost independent of temperature difference. For DCMD, this was already expected from the theoretical considerations in Eq. 3.25 and can also be observed for the gap variants.

Influence of Feed Water Salinity on MD Process Performance

The following investigations clarify the role of feed water salinity on process performance. First of all, the effect of concentration polarisation is quantified and discussed on the basis of model predictions. According to Eq. 3.47, concentration polarisation depends on flux and convective mass transfer in the hydraulic boundary layer on the evaporator side. The quantitative effect may be evaluated by considering a DCMD channel arrangement, which has a representative character for all of the channel configurations. The material specifications and the operational conditions

refer to the standard conditions that have already been used throughout the experimental studies. The convective mass transfer coefficient is derived from a feed velocity of 0.08 m s^{-1} and the convective transfer correlation for channel spacer S-320, that was originally introduced as a heat transfer correlation. By considering bulk stream temperature differences from 2 K to 80 K, the effect of concentration polarisation is evaluated for fluxes up to $90 \text{ kg (m}^2 \text{ h)}^{-1}$. The feed water salinity is set to 50 g kg^{-1} . The predicted concentration polarisation coefficients and the reduction of flux performance caused by concentration polarisation are presented in Fig. 3.35.

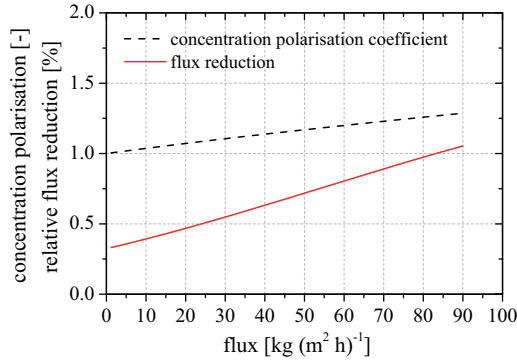


Figure 3.35: Model-based analysis of the concentration polarisation phenomenon under different flux conditions. Flux was varied by considering different bulk stream temperature differences. Testing conditions: $\Delta T_{E-C} = 2 - 80 \text{ K}$, $\bar{T}_{E-C} = 60 \text{ }^\circ\text{C}$, $\bar{c}_{E/C} = 0.08 \text{ m s}^{-1}$, $S_E = 50 \text{ g kg}^{-1}$, DCMD configuration, laminate L-020A-S(BC), channel spacer S-320.

The results involve concentration polarisation coefficients from 1.0 to 1.3 that fundamentally increase with flux. Even though the concentration at the liquid-vapour interface is estimated to be up to 30 % higher than in the bulk stream, the relative effect on flux remains below 1.1 % throughout the full range of fluxes. Due to the low sensitivity of process performance to salinity, especially at high driving force, the relative impact of the increased interfacial salinity turns out to be marginal, even though significant concentration polarisation coefficients are obtained at high-flux operation. The effect of concentration polarisation is considered to be negligible and is not taken into account for in the model predictions within this thesis. This result is in good agreement with studies published by other researchers [135, 163, 170], who also conclude that the phenomenon of concentration polarisation is negligible for typical membrane distillation applications. For a flux of $j_w > 40 \text{ kg (m}^2 \text{ h)}^{-1}$, the effect of concentration polarisation on flux was reported to be approximately 3% [80]. The concentration polarisation coefficient for high-flux operation up to $90 \text{ kg (m}^2 \text{ h)}^{-1}$ has been estimated to be less than 1.15 [20].

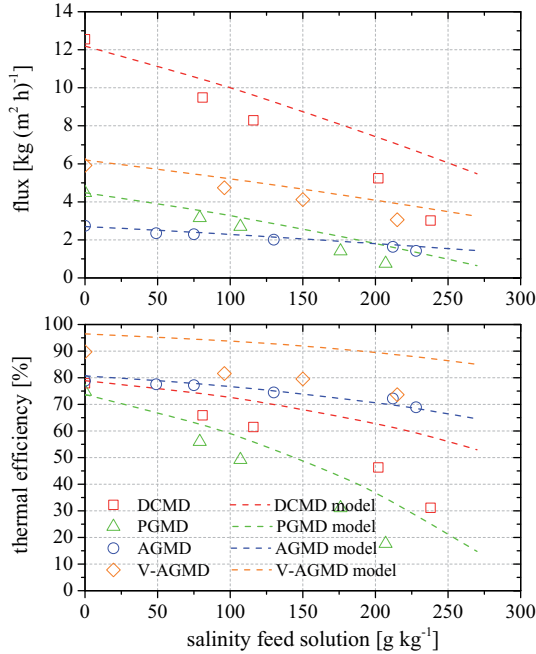


Figure 3.36: Sensitivity analysis with respect to the feed salinity, comparing flux and thermal efficiency for DCMD, PGMD, AGMD and V-AGMD configurations. Testing conditions: $\Delta T_{E-C} = 12$ K, $\bar{T}_{E-C} = 60$ °C, $\bar{c}_{E/C} = 0.08$ m s⁻¹, $\hat{p}_{VP,AG}^{VAGMD} = 0.33$ bar, laminate L-020A-S(BC), channel spacer S-320, gap spacer S-050/S-200, impermeable film F-127, NaCl solutions of different concentrations.

A comparison of the effect of the feed water salinity on the DCMD, PGMD, AGMD and V-AGMD performance is presented in Fig. 3.36, including a comparative presentation of the respective model predictions. However, the following quantitative discussion refers to the respective experimental results, while the deviations of the model predictions from the experiments are summarised in Tab. 3.13 at the end of this section. Sodium chloride (NaCl) solutions of different concentrations have been used to prepare the artificial salt water.

Decreasing fluxes and a drop in thermal efficiency with increasing salinity can be observed for all process configurations. The decrease in flux appears to be almost linear for salinities less than 150 g kg⁻¹ but the sensitivity tends to increase for higher salinities. The basic phenomenon that leads to the negative effect on process performance is the decrease in vapour pressure difference, which results from the decreasing evaporator vapour pressure with increasing concentration of salt ions (Eq. 3.6). Even for the low-flux operating points observed at high salinities, a significant temperature difference between the hot and cold liquid-vapour interfaces causes parasitic conductive heat transfer. Therefore, the thermal efficiency drops significantly at high salinities. The highest flux results have been obtained for the DCMD configuration, ranging from 12.6 kg (m² h)⁻¹ for tap water to 3.0 kg (m² h)⁻¹ at a salinity of 238 g kg⁻¹. It is important to note that the dif-

ferent process configurations differ greatly, considering the sensitivity of the process performance to feed salinity. The DCMD configuration shows the highest sensitivity of $1.8 \text{ kg (m}^2\text{h)}^{-1}$ per 50 g kg^{-1} . For a feed salinity of approximately 200 g kg^{-1} , only 42% of the reference flux with tap water is obtained. Low flux is obtained with PGMD at a similar operation point and only 16% of the tap water reference flux could be achieved at 200 g kg^{-1} . The lowest sensitivity of $0.2 \text{ kg (m}^2\text{h)}^{-1}$ per 50 g kg^{-1} is given for AGMD. In this configuration, still 60% of the tap water reference flux is obtained for a salinity of approximately 210 g kg^{-1} , which is slightly reduced to 52% if the air gap is partially deaerated. In the limiting case, the effect of vapour pressure reduction by salt ions completely outweighs the driving force, resulting in no flux or even in negative flux. From the experimental results in Fig. 3.36, the equilibrium condition for the PGMD configuration is expected at approximately 220 g kg^{-1} . For DCMD, the equilibrium condition is expected at higher salinity of approximately 270 g kg^{-1} . The maximal concentration is fundamentally limited by the maximal solubility of the respective salt, since salt starts to precipitate if the maximal solubility is exceeded.

In general, the effect of a particular feed salinity is to reduce the vapour pressure on the evaporator side and consequently the vapour pressure difference by a certain offset. If MD is operated at a low driving force, as is given for a small interfacial temperature difference, a certain vapour pressure reduction has a high relative impact on the driving force and therefore a strong influence on performance. In the case of a high driving force, which is given for a high interfacial temperature difference, the relative effect of the vapour pressure offset is comparably small. Even though identical bulk stream conditions are considered for the DCMD, PGMD and (V-)AGMD experiments, the interfacial temperature differences are quite different (see Fig. 3.32), which explains their different sensitivity to salinity. In particular, (V-)AGMD features superior characteristics for high salinity operation for the given reasons.

Some discussion is added on the model predictions in Fig. 3.36. The vapour pressure reduction in the model is based on the correlation given in Eq. 3.6, depending on feed salinity. The application of the vapour pressure reduction correlation is suggested for salinities from 0 to 150 g kg^{-1} . In this range, the model gives a reasonable prediction for the negative influence of salt on the different process configurations. Considering a sea salinity level of approximately 34 g kg^{-1} , the deviations of the flux predictions were estimated to be 1%, 4%, 1% and 6% for DCMD, PGMD, AGMD and V-AGMD, respectively. Considering a range up to 150 g kg^{-1} , the different flux errors are quantified to be less than 10%, steadily increasing with salinity. It turns out that the quantitative errors of the specific flux and thermal efficiency predictions increase further for salinities above 150 g kg^{-1} , while the qualitative trends are still represented by the model. Deviations may be explained by differences in salt composition. The correlations describe the physical water properties for sea salt, while the experiments were performed using a pure NaCl solution. Since the molarity of a pure NaCl solution is higher than that of a standard sea-salt composition, a NaCl solution contains more dissolved ions than a sea-salt-based solution at the same salinity (see Appendix C). Thus, the vapour pressure of a pure NaCl solution is expected to be lower than that of a sea-salt solution with the same salinity. If the experimental results were transferred from their NaCl-salinity to their higher corresponding "virtual sea-salt salinity", the systematic deviation from the modelling results would decrease. The use of correlations based on

electrical conductivity instead of salinity would generally lead to better comparability, especially for results obtained with different ionic salt compositions.

It is important to note that the results from Fig. 3.36 strictly refer to the channel configurations and operating conditions considered in the experiments. Even though an appreciable impact of salinity has been identified for the presented conditions, all of the MD configurations offer great potential for the treatment of high-salinity solutions, since the processes could be optimised with respect to high-salinity operation. Higher driving force, which could be achieved by an adapted channel design, reduced temperature polarisation or higher bulk stream temperature differences, fundamentally enhances the process characteristics for the treatment of high-salinity solutions. The impact of the bulk stream temperature difference on the relative effect of salinity on flux performance is illustrated in Fig. 3.37. The results are derived from model predictions that consider feed water with zero salinity and feed water with a salinity of 100 g kg^{-1} .

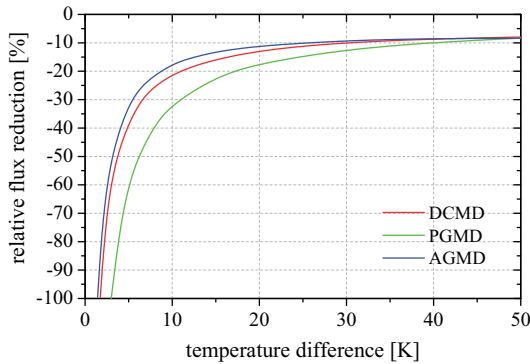


Figure 3.37: Model-based analysis of the flux reduction due to salinity at different bulk temperature differences, considering DCMD, PGMD and AGMD configurations. Flux results obtained with feed water salinities of 0 and 100 g kg^{-1} have been compared. Testing conditions: $\bar{T}_{E-C} = 60^\circ\text{C}$, $\bar{c}_{E/C} = 0.08 \text{ m s}^{-1}$, laminate L-020A-S(BC), channel spacer S-320, gap spacer S-050/S-200, impermeable film F-127.

The results clearly indicate the negative effect of salinity on MD performance for any bulk stream temperature difference. For small temperature differences between 0 and 5 K, the flux performance shows enormous sensitivity to the saline feed water. The higher the bulk stream temperature differences considered, the lower is the influence of salt. For a temperature difference of 10 K, MD already features feasible performance characteristics for the treatment of saline brine, but flux is reduced by 33% for PGMD, 22% for DCMD, 17% for AGMD. As discussed earlier, the different sensitivities of the process configurations are mainly explained by differences in temperature polarisation. For a high bulk stream temperature difference of 40 K, the relative reduction of flux due to the salinity effect is lower than 10% for all of the MD configurations. If higher salinity than 100 g kg^{-1} were considered, the required bulk stream temperature differences for feasible MD operation would increase. It is obvious from the given results that targeted

optimisation of the channel configuration and the operating conditions offers great potential to improve the MD process performance for the treatment of saline feed water. The presented results demonstrate the fundamental phenomena accompanying the salinity effect, which are subsequently applied in the context of module design and optimisation in the following chapters.

Deviations of the Model Predictions from Experimental Results

The mean deviations between the model predictions and the experimental results have been analysed for each parameter variation that has been presented in this section. A detailed summary is given in Tab. 3.13. The derivation of the combined mean deviations throughout all parameter variations for flux and thermal efficiency, leads to values of 4% and 4% for DCMD, 4% and 4% for PGMD, 5% and 5% for AGMD and 6% and 9% for V-AGMD, respectively.

Table 3.13: Summary of the mean percentage deviations to the model predictions with respect to the experimental results for each parameter variation.

configuration	$ \bar{e}(T_{E-C}) $ Fig. 3.31		$ \bar{e}(\bar{c}_{E/C}) $ Fig. 3.33		$ \bar{e}(\Delta T_{E-C}) $ Fig. 3.34		$ \bar{e}(S_E) ^a$ Fig. 3.36	
	Δj_M	$\Delta \eta_{th}$	Δj_M	$\Delta \eta_{th}$	Δj_M	$\Delta \eta_{th}$	Δj_M	$\Delta \eta_{th}$
DCMD	2%	1%	3%	1%	2%	1%	10%	10%
PGMD	2%	1%	4%	3%	1%	1%	10%	11%
AGMD	5%	4%	3%	7%	4%	4%	5%	2%
V-AGMD	3%	8%	5%	8%	4%	6%	10%	13%

^aevaluated for measurements with salinities from 0 – 150 g kg⁻¹

4 Module Analysis

The membrane module is defined to be a device that combines the membrane and other required materials within a functional package.

The following chapter bridges the gap from fundamental scientific research on materials and basic process behaviour to the scale of application. A focus is placed on the derivation of basic methods for qualified interpretation and integration of fundamental knowledge, e.g. from test cell experiments, in the context of full-scale modules. The results from Chapter 3 are applied to develop of a comprehensive full-scale module model that provides a high level of physical detail. Generic module performance parameters are derived in order to allow a comparative quantitative evaluation of different module designs and operational modes. Subsequently, a section on the experimental work provides information on the testing equipment, the testing procedures and the methods for experimental evaluation of different full-scale module prototypes. A detailed presentation and discussion of the results is provided in the last and most extensive section of this chapter. Experimental results as well as model-based analyses are comprehensively evaluated for a variety of scenarios. Besides an analysis of general aspects of MD module operation, the section covers individual aspects concerning the operation of different MD module configurations. The validated module model is then applied to analyse comprehensive studies of the influence of membrane and other material properties on module performance. A quantitative evaluation of fundamental technological limitations is provided by means of extensive parametric field studies.

4.1 Multi-Node Models for Theoretical Module Evaluation

Membrane modules of different size, configuration and design are used in the application of MD processes. The thermodynamic performance is expected to depend mainly on the MD configuration, channel length and channel height rather than on specific effects based on the module type such as spiral-wound or plate-and-frame. From a modelling point of view, a quite generic approach can be used in order to clarify the fundamental potential for the MD technology, independent of the type of module design. For a MD module with flat flow channels, the total active transfer area A_{MD} may be calculated from Eq. 4.1, based on the corresponding specifications in

channel length L and channel height H .

$$A_{\text{MD}} = L \cdot H \cdot z \quad (4.1)$$

Whether the evaporator flow channel has two active sides for heat and mass transfer or one active side and one adiabatic wall, is accounted for by $z \in \{1, 2\}$.

If the flow channels are of reasonable length, the transmembrane heat and mass transfer influence the thermodynamic state of the fluids along the length of the channels. Thus, the assumption of homogeneous conditions along the channels that is made for the evaluation of the one-dimensional single-node models in Sec. 3.2 is not valid when considering flow channels in the context of full-scale membrane modules. In order to account for the local distribution of the operating conditions, the channels are discretised into multiple nodes. Each node represents one segment of the flow channel that is sufficiently small that the assumption of homogeneous conditions and consequently the single-node models from Sec. 3.2 are valid. The nodes are indicated consecutively with indices $1 \leq i \leq n$, where $i = 1$ indicates the position of the evaporator inlet and $i = n$ the position of the evaporator outlet. The specification of the homogeneous flow channel discretisation is given by the total number of nodes n that leads to the effective single node transfer area $A_{\text{M/L}}^i$ by applying Eq. 4.2.

$$A_{\text{M/L}}^i = \frac{A_{\text{MD}}}{n} \quad (4.2)$$

The geometrical channel design and the material parameters are considered constant along the channels so equal parameterisation is given for all nodes. The nodes are thermodynamically linked to each other. The thermodynamic inlet conditions for each node (i), namely the local mass flow rates \dot{m}_{E}^i and \dot{m}_{C}^i , the local salinities S_{E}^i and S_{C}^i and the local temperatures T_{E}^i and T_{C}^i , correspond to the outlet conditions of the preceding node ($i - 1$). The local absolute pressure in the vapour space \hat{p}^i is evaluated individually for each node, depending on the applicable state of deaeration. If the inlet conditions for node (i) are known, the single-node models from Sec. 3.2 are used to calculate the local transmembrane flux $J_{\text{M/L}}^i$ and the local transmembrane heat transfer $\dot{Q}_{\text{M/L}}^i$, taking the local fluid properties into account. The outlet conditions for node (i) are then evaluated by applying the laws of conservation of mass and energy and linked to the inlet conditions of the following node ($i + 1$). This modelling approach is referred to as the multi-node model.

The following sections present different forms of the basic multi-node model that have been implemented. The different model variants are necessary to represent the individual aspects that need to be considered for a DCMD, a PGMD or an AGMD module.

4.1.1 Direct Contact Module Configuration

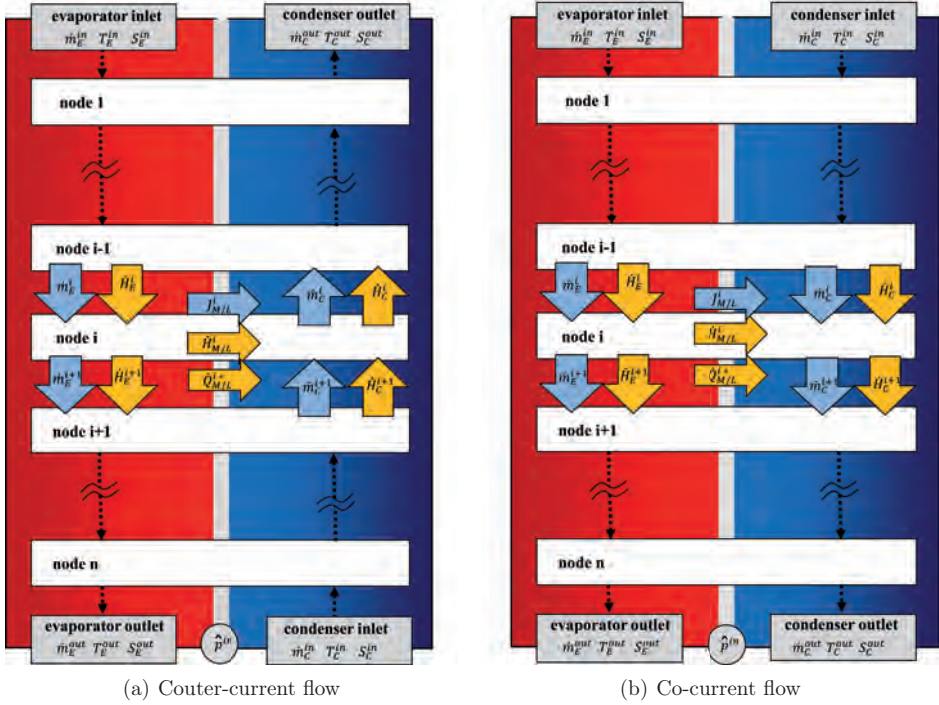


Figure 4.1: Multi-node model for DCMD module analysis - Model structure

A graphical representation of the DCMD multi-node model is given in Fig. 4.1. The grey coloured fields represent the relevant information on the operational conditions that is necessarily passing through the system boundaries into or out of the model. These parameters may be dynamically linked to other hydraulic system components for integrated system simulation. In the usual case of a counter-current operation mode, the inlet and outlet conditions are on opposite sides of the module and the flow direction in the evaporator and the condenser channel differs. Due to its great relevance in common MD applications, the focus of the module analysis within this thesis is on the counter-current operation mode. However, the model is capable of evaluating a co-current flow operation mode, where the inlet and outlet conditions are on the same side of the module and the flow in the evaporator and the condenser channel is in the same direction.

First of all, the local flux is evaluated by means of Eqs. 3.5 or 3.50, taking into account the respective local state of deaeration, which is defined by the absolute pressure input parameter \hat{p}^{in} . To do so, the local absolute pressure \hat{p}^i and the corresponding local partial air pressure \hat{p}_a^i are evaluated, based on the assumption of an ideal pressure distribution along the channel. If the local vapour pressure is equal to or higher than the deaeration pressure, no air is left in that part of the module and the local absolute pressure is defined by the local vapour pressure as given in Eq. 4.3. In the part of the module, where the local vapour pressure is lower than the

deaeration pressure, the residual fraction of air can be evaluated explicitly by locally applying Dalton's law according to Eq. 4.4.

$$\text{for } \hat{p}^{in} \leq p_w^i : \quad \hat{p}^i = p_w^i \quad p_a^i = 0 \quad (4.3)$$

$$\text{for } \hat{p}^{in} > p_w^i : \quad \hat{p}^i = \hat{p}^{in} \quad p_a^i = \hat{p}^i - p_w^i \quad (4.4)$$

The mass balances for the individual channel sides of a DCMD node are given in Eqs. 4.5 and 4.6. The absolute local flux $J_{M/L}^i$, evaluated by means of Eqs. 3.5 or 3.50, is transferred from the evaporator to the condenser channel. The total mass flow in the evaporator channel is reduced by the local flux whereas the mass flow in the condenser channel gains the mass from permeation. In Eq. 4.6, the transferred flux added to the condenser channel is derived with a negative sign in the standard case of counter-current operation, whereas a positive sign would result for co-current operation.

$$\dot{m}_E^{i+1} = \dot{m}_E^i - J_{M/L}^i \quad (4.5)$$

$$\dot{m}_C^{i+1} = \dot{m}_C^i \overset{(+)}{-} J_{M/L}^i \quad (4.6)$$

No salt is transferred through the membrane, so the total mass flow of salt does not change along the flow channels and the local salinities may be evaluated from the mass balances applied for salt. The respective formulations for the evaporator and the condenser channels are given in Eqs. 4.7 and 4.8, respectively.

$$S_E^{i+1} = S_E^{in} \frac{\dot{m}_E^{in}}{\dot{m}_E^{i+1}} \quad (4.7)$$

$$S_C^{i+1} = S_C^{in} \frac{\dot{m}_C^{in}}{\dot{m}_C^{i+1}} \quad (4.8)$$

The enthalpy balances for each individual side of a DCMD node are given in Eqs. 4.9 and 4.10. The local heat flux $\dot{Q}_{M/L}^i$ includes latent and conductive heat transfer from the evaporator to the condenser channel and refers to Eq. 3.20 or Eq. 3.52. The sign in the condenser enthalpy balance (Eq. 4.10) is negative for counter-current and positive for co-current operation.

$$\dot{H}_E^{i+1} = \dot{H}_E^i - \dot{H}_{M/L}^i - \dot{Q}_{M/L}^i \quad (4.9)$$

$$\dot{H}_C^{i+1} = \dot{H}_C^i \overset{(+)}{-} \dot{H}_{M/L}^i \overset{(+)}{-} \dot{Q}_{M/L}^i \quad (4.10)$$

The enthalpies given in Eqs. 4.11 to 4.13 refer to liquid water at a reference temperature of 0 °C, so the temperatures are specified in degrees Celsius.

$$\dot{H}_{E/C}^{i+1} = \dot{m}_{E/C}^{i+1} c_{p,E/C}^{i+1} T_{E/C}^{i+1} \quad (4.11)$$

$$\dot{H}_{E/C}^i = \dot{m}_{E/C}^i c_{p,E/C}^i T_{E/C}^i \quad (4.12)$$

$$\dot{H}_{M/L}^i = J_{M/L}^i c_{p,E}^i T_E^i \quad (4.13)$$

Due to the dependence of the thermal capacity on temperature and salinity, two unknowns are present in Eq. 4.11. Here, the numerical approach features the advantage of reducing the unknowns without committing an energy error in the overall balances. For this purpose, the thermal capacity is considered constant for the derivation of Eq. 4.11, leading to the modified representation in Eq. 4.14. The sensible heat that refers to the change in capacity is accounted for in $\dot{Q}_{M/L}^{i*}$ that includes a capacity compensation from the previous to the present node.

$$\dot{H}_{E/C}^{i+1} = \dot{m}_{E/C}^{i+1} c_{p,E/C}^i T_{E/C}^{i+1} \quad (4.14)$$

$$\dot{Q}_{M/L}^{i*} = \dot{Q}_{M/L}^i + \dot{m}_{E/C}^i (c_{p,E/C}^i - c_{p,E/C}^{i-1}) T_{E/C}^i \quad (4.15)$$

When the enthalpy balances in Eqs. 4.9 and 4.10 are solved with respect to the node outlet temperatures $T_{E/C}^{i+1}$, Eqs. 4.16 and 4.17 are derived to evaluate the temperatures from node to node.

$$T_E^{i+1} = \frac{1}{\dot{m}_E^{i+1} c_{p,E}^i} \left(\dot{H}_E^i - \dot{H}_{M/L}^i - \dot{Q}_{M/L}^{i*} \right) \quad (4.16)$$

$$T_C^{i+1} = \frac{1}{\dot{m}_C^{i+1} c_{p,C}^i} \left(\dot{H}_C^i - \dot{H}_{M/L}^i - \dot{Q}_{M/L}^{i*} \right) \quad (4.17)$$

Based on the local conditions, the local hydraulic pressure losses for the flow channels are estimated by Eqs. 4.18 and 4.19. For the spacer-filled channels, a rather turbulent flow is assumed even for low Reynolds numbers. For turbulent flow, the friction factor ψ is dependent on the Reynolds number and generally described as given in Eqs. 4.18 and 4.19 [134]. Due to the complex three-dimensional geometry of the spacer-filled channels, the coefficients a and b are usually fitted to experimental data [8, 145]. Within this thesis, the coefficients are derived in Sec. 4.3.1.

$$\Delta \hat{p}_E^i = \psi_E \frac{L}{n} \frac{\rho_E}{d_{h,E}} \frac{(c_E^i)^2}{2} \quad \psi_E = a (Re_E^i)^b \quad (4.18)$$

$$\Delta \hat{p}_C^i = \psi_C \frac{L}{n} \frac{\rho_C}{d_{h,C}} \frac{(c_C^i)^2}{2} \quad \psi_C = a (Re_C^i)^b \quad (4.19)$$

For each calculation, the module's total enthalpy balance is evaluated in order to check the validity of the model. This feature gives a reference for debugging during the phase of model implementation and modification. Furthermore, this analytical method of checking the "black-box" model enthalpy balance guarantees that the model does not accidentally behave as energy source or sink in the context of a potential system simulation. The total enthalpy balance of the

DCMD model is given in Eq. 4.20.

$$\dot{H}_E^{in} + \dot{H}_C^{in} = \dot{H}_E^{out} + \dot{H}_C^{out} \quad (4.20)$$

The iterative solving strategy for the DCMD multi-node model is illustrated in Fig. 4.2.

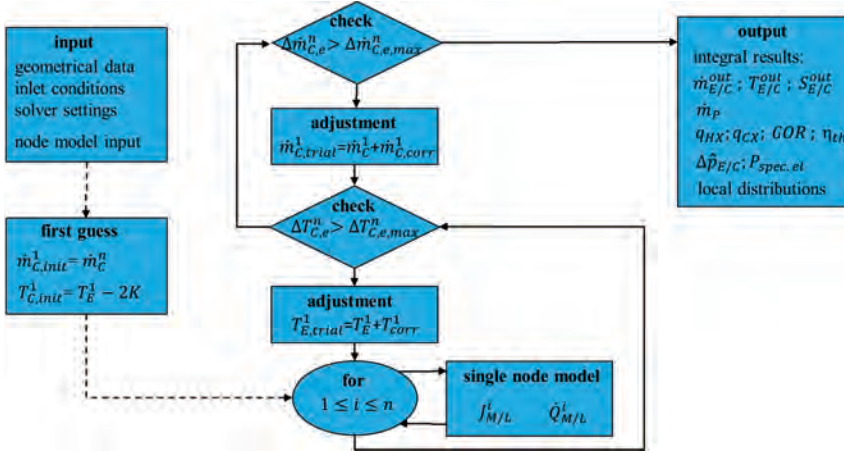


Figure 4.2: DCMD multi-node model - Flow diagram of the iterative solver strategy.

After setting up the numerical solvers, the model has to be initialised with fluid and material properties, geometrical module specifications and thermodynamic inlet conditions for the evaporator and the condenser channels. For the counter-current operation mode, the evaporator inlet conditions are linked to node $i = 1$, whereas the condenser inlet conditions are linked to node $i = n$. The unknown condenser outlet conditions that are required to evaluate node $i = 1$ are initially estimated by an educated guess. The temperature $T_{C,init}^1$ is assumed to be 2K lower than the evaporator inlet temperature. Then the single nodes are solved successively by applying the enthalpy and mass balances from Eqs. 4.5 to 4.17. When the last node $i = n$ is evaluated, the difference $\Delta T_{C,e}^n$ between the calculated condenser temperature and the pre-set inlet condition is calculated with Eq. 4.21.

$$\Delta T_{C,e}^n = T_{C,trial}^n - T_C^{in} \quad (4.21)$$

If the error is higher than the tolerated maximal error $\Delta T_{C,e,max}^n$, the channel evaluation is performed again, based on a corrected starting temperature $T_{C,trial}^1$. The correction term $T_{C,corr}^1$ depends on the actual error $\Delta T_{C,e}^n$ and the number of iterations that have already been completed. The solver starts with a large step size to guarantee rapid convergence and then automatically reduces step size to attain high accuracy, if necessary. The procedure is repeated again until the error is lower than the maximal permissible error.

A second similar iteration loop is implemented to determine the correct condenser outlet mass flow rate \dot{m}_C^1 . The initial guess $\dot{m}_{C,init}^1$ is set equal to the flow rate at the condenser inlet. The

resulting error at node position $i = n$ is defined in Eq. 4.22.

$$\Delta \dot{m}_{C,e}^n = \dot{m}_{C,trial}^n - \dot{m}_C^{in} \quad (4.22)$$

If the error is higher than the tolerated maximal error $\Delta \dot{m}_{C,e,max}^n$, the channel evaluation is performed again, based on a corrected starting mass flow condition $\dot{m}_{C,trial}^1$. Since the rather small mass flow corrections needed do not affect the general solver stability, rapid and reliable convergence is obtained for a correction term $\dot{m}_{C,corr}^1$ that depends only on the actual error $\dot{m}_{C,e}^n$, without the need to change its sensitivity based on the total number of iterations. The procedure is repeated until the error is lower than the maximal permissible error.

For the co-current operation mode, both inlet conditions are linked to node $i = 1$, so the temperature and mass flow conditions are available at the first node $i = 1$ and the module evaluation does not require any channel iteration.

4.1.2 Permeate Gap Module Configuration

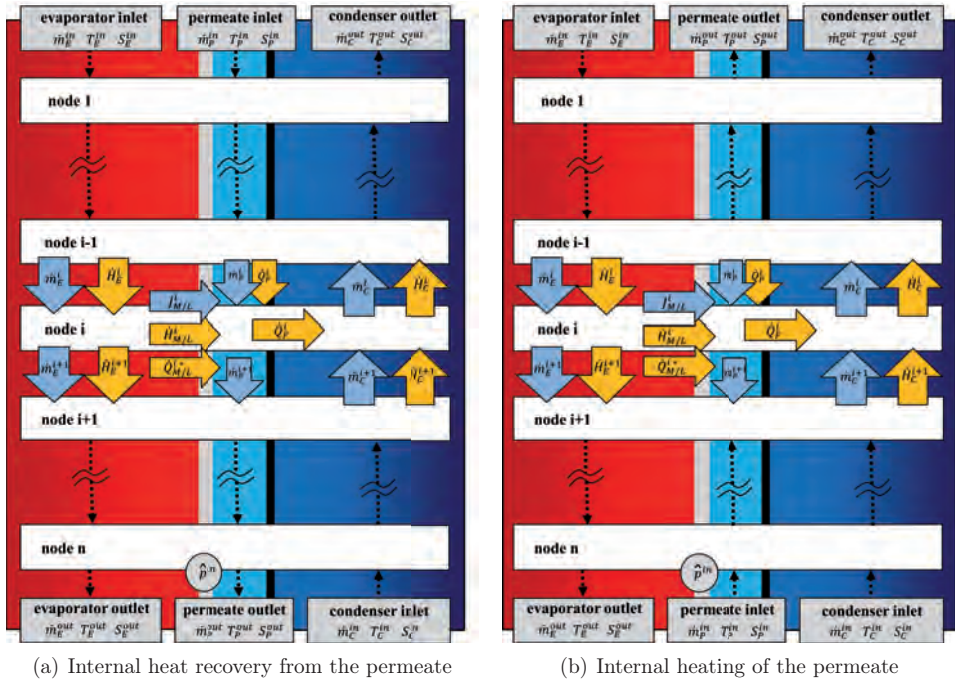


Figure 4.3: Multi-node model for PGMD module analysis - Model structure

A graphical representation of the PGMD multi-node model in counter-current mode is given in Fig. 4.3. The basic scheme of the main flow channels, including the respective inlets and outlets, is similar to the DCMD multi-node model. The additional permeate channel is introduced, including its separate inlet and outlet. In the usual case, the permeate channel does not include channel inlet and the permeate channel inlet conditions are set to zero. If the permeate outlet is set to the cold module side at node position $i = n$, the sensible heat that accompanies with the warm permeate stream is successively recovered to the condenser channel internally. If the permeate outlet is set to the warm module side at node position $i = 1$, the permeate stream successively gains sensible heat from the evaporator while flowing along the permeate channel and is internally heated.

It should be noted that the PGMD model may in principle be used in a co-current flow variant, as well. However, due to its minor relevance and its basic similarity to the DCMD co-current model of Sec. 4.1.1, the PGMD co-current model is not explicitly discussed in this section and no separate graphical representation is provided.

The evaluation of the single nodes is done using the PGMD single-node model from Sec. 3.2.2, taking into account the local state of deaeration by Eqs. 4.3 and 4.4.

The enthalpy and mass balances are slightly modified in order to represent specific aspects of the PGMD channel configuration. The mass balances for the individual channel sides of a PGMD node are given in Eqs. 4.23 and 4.24. The total mass flow of the evaporator channel is reduced by the transmembrane flux, whereas the condenser mass flow does not change along the channel due to the impermeability of the polymer film material. The accumulation of the permeate in the separate permeate channel is represented by the additional mass balance for the permeate channel in Eq. 4.25.

$$\dot{m}_E^{i+1} = \dot{m}_E^i - J_{M/L}^i \quad (4.23)$$

$$\dot{m}_C^{i+1} = \dot{m}_C^i (= \dot{m}_C^{in}) \quad (4.24)$$

$$\dot{m}_P^{i+1} = \dot{m}_P^i + J_{M/L}^i \quad (4.25)$$

The salinities are calculated by the mass balances for the salt species in Eqs. 4.26 to 4.28. For a PGMD module, the salinity in the evaporator changes along the channel due to extraction of the solvent. The salinity in the condenser channel does not change due to the impermeability of the polymer film. If a potential inlet mass flow rate into the permeate channel has a certain salinity (e.g. strip solution), the solution becomes diluted by the gain in mass due to the permeating pure solvent.

$$S_E^{i+1} = S_E^{in} \frac{\dot{m}_E^{in}}{\dot{m}_E^{i+1}} \quad (4.26)$$

$$S_C^{i+1} = S_C^i (= S_C^{in}) \quad (4.27)$$

$$S_P^{i+1} = S_P^{in} \frac{\dot{m}_P^{in}}{\dot{m}_P^{i+1}} \quad (4.28)$$

The mathematical formulations for the local temperatures in Eqs. 4.29 and 4.30 are derived from

the enthalpy balances.

$$T_E^{i+1} = \frac{1}{\dot{m}_E^{i+1} c_{p,E}^i} \left(\dot{H}_E^i - \dot{H}_{M/L}^i - \dot{Q}_{M/L}^{i*} \right) \quad (4.29)$$

$$T_C^{i+1} = \frac{1}{\dot{m}_C^{i+1} c_{p,C}^i} \left(\dot{H}_C^i - \dot{Q}_F^i \right) \quad (4.30)$$

The total amount of heat transferred through the membrane into the permeate channel $\dot{Q}_{M/L}^{i*}$ is evaluated with Eq. 4.15. The total amount of heat transferred from the permeate channel through the polymer film into the condenser channel \dot{Q}_F^i is calculated by Eq. 4.31. Unlike DCMD, the condenser channel in PGMD does not gain the permeating mass, so Eq. 4.30 does not include the enthalpy that is associated with the permeating vapour.

$$\dot{Q}_F^i = \dot{Q}_{M/L}^{i*} + \dot{Q}_P^i \quad (4.31)$$

The sensible heat, accompanied by a change in temperature and thermal capacity of the permeate stream from node to node, is taken into consideration during evaluation of the PGMD single-node model by Eq. 3.60 in Sec. 3.2.2. The total amount of sensible heat from the permeate \dot{Q}_P^i , also given in Eq. 4.32, contains one term associated with the change in temperature and one term associated with a change in thermal capacity.

$$\dot{Q}_P^i = \dot{m}_P^{i-1} c_{p,P}^{i-1} (T_P^{i-1} - T_P^i) + \dot{m}_P^{i-1} (c_{p,P}^{i-1} - c_{p,P}^i) T_P^i \quad (4.32)$$

If the temperature or the thermal capacity in the permeate channel decreases, heat is recovered from the permeate stream into the condenser channel. If the temperature or the capacity of the permeate increases, the thermal energy is transferred from the evaporator channel.

The hydraulic pressure losses in the main flow channels of a PGMD module are estimated similarly to the pressure losses in a DCMD module, as given in Eqs. 4.18 and 4.19.

The total heat balance of the PGMD model is given in Eq. 4.33, which includes the main channel inlet and outlet streams of the condenser and the evaporator channels and the additional permeate channel inlet and outlet streams.

$$\dot{H}_E^{in} + \dot{H}_C^{in} + \dot{H}_P^{in} = \dot{H}_E^{out} + \dot{H}_C^{out} + \dot{H}_P^{out} \quad (4.33)$$

The iterative solving strategy for the PGMD multi-node model is similar to the one illustrated in Fig. 4.2. Analogously to the DCMD channel iteration, the condenser outlet temperature is solved iteratively. Since the mass flow rate in the condenser channel remains constant for the PGMD configuration (Eq. 4.24), no second channel iteration loop is necessary to determine the condenser outlet mass flow rate. In the usual case, the heat from the permeate is internally recovered (Fig. 4.3(a)) and the channel iteration starts at node $i = 1$. If the the permeate is to be internally heated (Fig. 4.3(b)), the iteration starts at node $i = n$, to retain the ability to solve the permeate channel balances in Eqs. 4.25, 4.28 and 4.32 in the forward direction without an additional iteration loop.

4.1.3 Air Gap Module Configuration

A graphical representation of the AGMD multi-node model in the counter-current mode is given in Fig. 4.4. The basic scheme of the main flow channels including their inlets and outlets is similar to the DCMD and PGMD multi-node models. Unlike the PGMD module, the permeate is removed from the air gap gravimetrically. The AGMD model may also be used in a co-current variant, which is not explicitly discussed in this section.

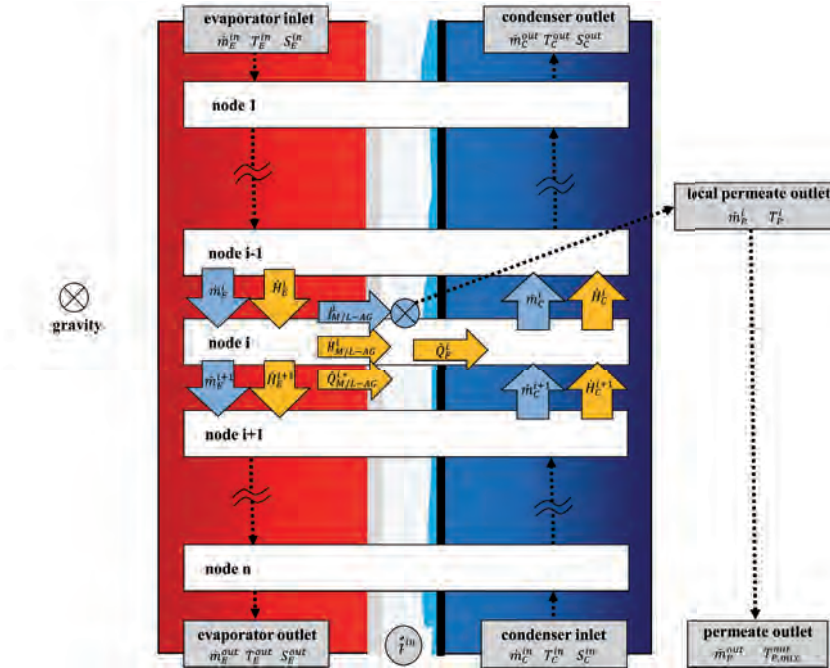


Figure 4.4: Multi-node model for AGMD module analysis - Model structure

The individual nodes are evaluated using the AGMD single-node model from Sec. 3.2.3, taking into account the local state of deaeration by Eqs. 4.3 and 4.4.

The enthalpy and mass balances for the AGMD nodes on the evaporator and the condenser channel sides are similar to those presented for the PGMD configuration. The local mass flow rates are given in Eqs. 4.23 and 4.24, the local salinities are calculated by Eqs. 4.26 and 4.27 and the local temperatures by Eqs. 4.29 and 4.30. The hydraulic pressure losses are estimated by using Eqs. 4.18 and 4.19.

In typical AGMD configurations, the permeate is extracted perpendicular to the main channel flow direction. Consequently, no internal recovery of the sensible heat from the permeate or internal pre-heating of the permeate stream is possible. The enthalpy of the permeate stream that is leaving the AGMD module is determined by Eq. 4.34, which also allows a determination

of the permeate mixing temperature T_P^{out} .

$$\dot{H}_P^{out} = \dot{m}_P^{out} c_{p,P}^{out} T_P^{out} = \sum_{i=1}^n \dot{m}_P^i c_{p,P}^i T_P^i \quad (4.34)$$

The total enthalpy balance of the AGMD model may also be evaluated by Eq. 4.33.

The iterative solving strategy for the AGMD multi-node model is close to that illustrated in Fig. 4.2. Analogously to the DCMD channel iteration, the condenser outlet temperature is solved iteratively. As for the PGMD configuration, the mass flow rate in the condenser channel remains constant for the AGMD configuration and no second channel iteration loop is necessary to determine the condenser outlet mass flow rate.

4.1.4 Evaluation of the Module Performance Parameters

The total permeate output \dot{m}_P is given by Eq. 4.35, representing the sum of all local permeate mass flow rates. Eq. 4.36 defines the total module flux j_P , which represents the specific permeate output with respect to the effective membrane surface area.

$$\dot{m}_P = \sum_{i=1}^n \dot{m}_P^i \quad (4.35)$$

$$j_P = \frac{\dot{m}_P}{A_{M/L}} \quad (4.36)$$

The module recovery ratio R_{Ei} in Eq. 4.37 describes how much product water is extracted from a given amount of feed water that enters the module at the evaporator channel inlet (Ei). Consequently, the module recovery ratio describes the amount of water that is extracted within one passage of the feed water through the evaporator channel. The recovery ratio may alternatively be expressed by the inlet and outlet salinities, derived from the mass balance of the salt. If recirculation is applied, the total system recovery ratio R_R from Eq. 4.38 may be adjusted independently of R_{Ei} by adjusting the amount of raw water for intake, which also affects the brine blow-out. The fraction of the total module input flow rate with respect to the raw water intake is defined as the recirculation factor Z according to Eq. 4.39.

$$R_{Ei} = \frac{\dot{m}_P}{\dot{m}_{Ei}} \quad \left(= 1 - \frac{S_{Ei}}{S_{Eo}} \right) \quad (4.37)$$

$$R_R = \frac{\dot{m}_P}{\dot{m}_R} \quad \left(= 1 - \frac{S_R}{S_B} \right) \quad (4.38)$$

$$Z = \frac{\dot{m}_{Ei}}{\dot{m}_R} \quad \left(= \frac{R_R}{R_{Ei}} \right) \quad (4.39)$$

The thermal power that is consumed in the evaporator channel \dot{Q}_E is equal to the thermal power that is transferred through the membrane/laminate, given in Eq. 4.40. The purely latent fraction is given in Eq. 4.41, leading to the total module thermal efficiency in Eq. 4.42

$$\dot{Q}_E = \sum_{i=1}^n \dot{Q}_{M/L}^i \quad (4.40)$$

$$\dot{Q}_{E,l} = \sum_{i=1}^n J_{M/L}^i \Delta h_v^i \quad (4.41)$$

$$\eta_{th} = \frac{\dot{Q}_{E,l}}{\dot{Q}_E} \quad (4.42)$$

Depending on the process configuration, the module design and the operating conditions, a different heating concept may be preferred to provide the heating power for the module. The cooling concept is then adapted according to the heating concept. It should be noted that depending on the system context, the recirculation strategy and the availability and condition of the raw water, external cooling may be unnecessary and the cooling requirement may be covered by the raw water directly. The simplest variant is direct heating of the evaporator stream without

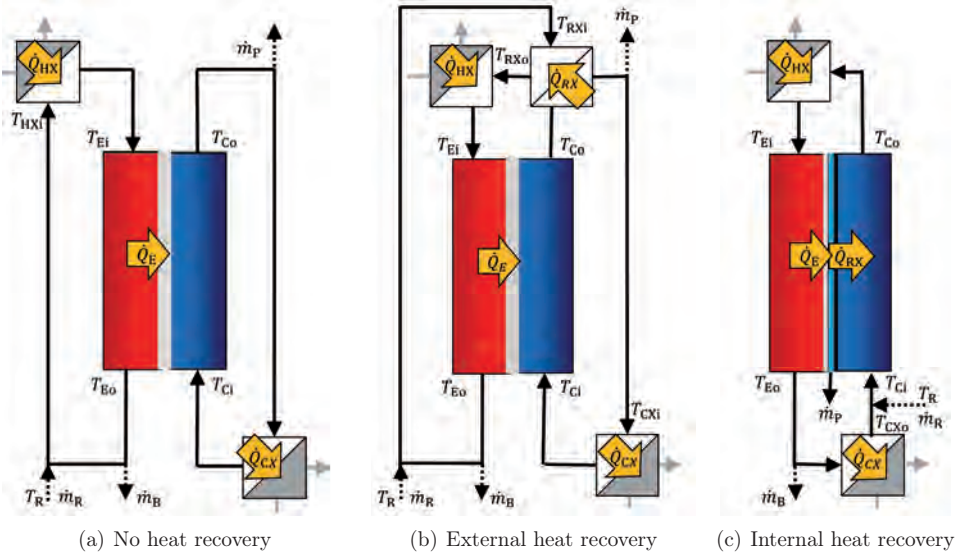


Figure 4.5: Different module heating and cooling concepts.

any recovery (noR) as illustrated in Fig. 4.5(a). In this case, the heating power is calculated with Eq. 4.43. If the influence of the raw water temperature T_R is neglected, the mixing temperature T_{HXi} may be replaced by T_{Eo} . The respective cooling power is defined similarly in Eq. 4.44.

$$\dot{Q}_{HX,noR} = \dot{m}_{Ei} c_{p,Ei} (T_{Ei} - T_{HXi}) \quad (4.43)$$

$$\dot{Q}_{CX, \text{noR}} = \dot{m}_{Ci} c_{p, Ci} (T_{Co} - T_{Ci}) \quad (4.44)$$

If the temperature level at the condenser outlet is higher than the temperature at the evaporator outlet ($T_{Co} > T_{Eo}$), pre-heating of the feed water is fundamentally possible.

A heating concept with external heat recovery (extR) is illustrated in Fig. 4.5(b). In this case, an external recovery heat exchanger (RX) is necessary. The evaluation of the heating and the cooling power for the external heat recovery concept is based on Eqs. 4.45 and 4.46.

$$\dot{Q}_{HX, \text{extR}} = \dot{m}_{Ei} c_{p, Ei} (T_{Ei} - T_{RXo}) \quad (4.45)$$

$$\dot{Q}_{CX, \text{extR}} = \dot{m}_{Ci} c_{p, Ci} (T_{CXi} - T_{Ci}) \quad (4.46)$$

The unknown temperatures T_{RXo} and T_{CXi} are calculated iteratively by using the heat balance of the external recovery heat exchanger given in Eq. 4.47 and the basic transfer equation for heat exchangers in counter-current mode given in Eq. 4.48 [134]. These equations reflect the influence of the heat exchanger transfer performance kA_{RX} on the recovered heat \dot{Q}_{RX} . If the influence of the raw water temperature T_R is neglected, the mixing temperature T_{RXi} and the capacity $c_{p, RXi}$ may be replaced by T_{Eo} and $c_{p, Eo}$, respectively.

$$\dot{m}_{Ei} c_{p, RXi} (T_{RXo} - T_{RXi}) = \dot{m}_{Co} c_{p, Co} (T_{Co} - T_{CXi}) \quad (= \dot{Q}_{RX}) \quad (4.47)$$

$$\dot{Q}_{RX} = kA_{RX} \frac{(T_{RXo} - T_{Co}) - (T_{RXi} - T_{CXi})}{\ln \left(\frac{T_{RXo} - T_{Co}}{T_{RXi} - T_{CXi}} \right)} \quad (4.48)$$

While the heat transfer performance increases, the iterative result converges towards the limiting case, represented by an ideal heat exchanger ($kA_{RX} \rightarrow \infty$). For an ideal heat exchanger, the recovered heat is limited only by the thermal capacities of the flow streams and the inlet temperatures. The limiting inlet temperatures define the corresponding unknown outlet temperature according to Eqs. 4.49-4.51, while the transferred heat is still evaluated by Eq. 4.47.

$$\dot{m}_{Ei} c_{p, RXi} = \dot{m}_{Co} c_{p, Co} \quad \rightarrow \quad T_{Co} = T_{RXo} \ ; \ T_{RXi} = T_{CXi} \quad (4.49)$$

$$\dot{m}_{Ei} c_{p, RXi} > \dot{m}_{Co} c_{p, Co} \quad \rightarrow \quad T_{RXi} = T_{CXi} \quad (4.50)$$

$$\dot{m}_{Ei} c_{p, RXi} < \dot{m}_{Co} c_{p, Co} \quad \rightarrow \quad T_{Co} = T_{RXo} \quad (4.51)$$

In PGMD and AGMD modules, the feed stream may be pre-heated in the condenser channel directly, without using an additional external recovery heat exchanger. The internal heat recovery concept (intR) is illustrated in Fig. 4.5(c). The evaluation of the heating power for the internal heat recovery concept is based on Eq. 4.52. The evaluation of the cooling power is given in Eq. 4.53. If the preceding blow-out (B) and the subsequent raw water mixing (R) are neglected,

the temperature T_{CXo} may be replaced by T_{Ci} and the flow rate \dot{m}_{CXo} is set as \dot{m}_{Eo} .

$$\dot{Q}_{HX,intR} = \dot{m}_{Ei} c_{p,Ei} (T_{Ei} - T_{Co}) \quad (4.52)$$

$$\dot{Q}_{CX,intR} = \dot{m}_{CXo} c_{p,Eo} (T_{Eo} - T_{CXo}) \quad (4.53)$$

The model automatically chooses the optimal heating strategy according to Eqs. 4.54, ensuring a realistic evaluation of the thermal energy requirement. If heat recovery is possible, a internal recovery concept is evaluated for the PGMD and AGMD configurations whereas an external concept is considered for the DCMD module variants. The corresponding definition for the cooling demand is then adjusted according to the heating strategy.

$$\dot{Q}_{HX} = \min(\dot{Q}_{HX,noR}, \dot{Q}_{HX,intR/extR}) \quad (4.54)$$

$$\dot{Q}_{CX} = \text{select}(\dot{Q}_{CX,noR}, \dot{Q}_{CX,intR/extR}) \quad (4.55)$$

The specific thermal energy consumption q_{HX} for heating and q_{CX} for cooling are defined in Eqs. 4.56 and 4.57, representing the respective amount of thermal energy that is required to produce one ton of product water.

$$q_{HX} = \frac{\dot{Q}_{HX}}{\dot{m}_P} \quad (4.56)$$

$$q_{CX} = \frac{\dot{Q}_{CX}}{\dot{m}_P} \quad (4.57)$$

An alternative representation of the thermal energy requirement is given with the Gained Output Ratio (GOR) in Eq. 4.58, representing the thermal energy savings with respect to pure, ideal evaporation. The fundamental definition of the GOR has already been introduced in Sec. 2.5.2.

$$GOR = \frac{\dot{Q}_{E,l}}{\dot{Q}_{HX}} \left(= \frac{\Delta h_v}{q_{HX}} \right) \quad (4.58)$$

The electric power consumption for the hydraulic pumps (HP) is estimated by Eq. 4.59, considering the hydraulic pressure losses in the module channels and the pressure losses in the heat exchangers for heating (HX) and cooling (CX), respectively. For DCMD operation, the pressure loss in the heat exchanger for external heat recovery (RX) is additionally taken into consideration. The pressure loss in the module flow channels is estimated according to Eqs. 4.60, based on the pressure loss correlations from Eqs. 4.18 and 4.19. The pressure loss accompanying each of the heat exchangers is assumed to be 0.15 bar. A total pumping efficiency η_{HP} is introduced for the conversion from electrical to hydraulic energy.

$$P_{HP} = \frac{\dot{V}_{Ei} (\Delta \hat{p}_{Ei-Eo} + \Delta \hat{p}_{HX} + \Delta \hat{p}_{RX})}{\eta_{HP}} + \frac{\dot{V}_{Ci} (\Delta \hat{p}_{Ci-Co} + \Delta \hat{p}_{CX} + \Delta \hat{p}_{RX})}{\eta_{HP}} \quad (4.59)$$

$$\Delta\hat{p}_{Ei-Eo} = \sum_{i=1}^n \Delta\hat{p}_E^i \quad \Delta\hat{p}_{Ci-Co} = \sum_{i=1}^n \Delta\hat{p}_C^i \quad (4.60)$$

If deaeration is applied, the electric power consumption is increased by several additional loads. The most important additional electric load is the vacuum pump (VP). In V-DCMD and V-PGMD, the membrane is indirectly deaerated by means of feed water deaeration with a membrane contactor. The hydraulic pressure loss $\Delta\hat{p}_D$ caused by the feed stream that passes through the deaeration module may be estimated with approximately 0.20 bar. No deaeration module is required for V-AGMD, since the air gap may be directly accessed by the vacuum pump. However, electric energy is required to pump the permeate out of the evacuated permeate chamber. It is important to notice that the flow rate \dot{m}_D that defines the deaeration capacity may be chosen quite differently, depending on the module concept and the recirculation strategy. If no recirculation is applied or if the feed water is ideally not dissolving any air during recirculation, it would be sufficient to estimate the required deaeration capacity based on the aerated raw water stream \dot{m}_R . In the worst case, the recirculated feed stream re-dissolves air until saturation and the required deaeration capacity should be estimated from the full module feed stream \dot{m}_{Ei} . In the model proposed in this thesis, the deaeration effort is estimated by Eq. 4.61, assuming the aeration effort to be mainly dependent on the raw water flow rate, while the additional effort due to re-aeration during recirculation is taken into consideration by a 30% fraction of the module feed flow rate. Further experimental work is required to derive a more precise reference.

$$\dot{m}_D = 0.7 \dot{m}_R + 0.3 \dot{m}_{Ei} \quad (4.61)$$

The overall electric power consumption for the deaeration system may be estimated by Eq. 4.62.

$$P_D = \frac{\dot{V}_{VP} \hat{p}_{VP} \ln\left(\frac{\hat{p}_{amb}}{\hat{p}_{VP}}\right)}{\eta_{VP}} + \underbrace{\frac{\dot{V}_D \Delta\hat{p}_D}{\eta_{HP}}}_{\text{V-DCMD and V-DCMD only}} + \underbrace{\frac{\dot{V}_P \Delta\hat{p}_{amb-VP}}{\eta_{HP}}}_{\text{V-AGMD only}} \quad (4.62)$$

The power consumption for a liquid ring vacuum pump is estimated from isothermal compression of the gas flow from vacuum pressure level \hat{p}_{VP} to ambient pressure \hat{p}_{amb} and a conversion efficiency of η_{VP} . The volumetric gas flow rate \dot{V}_{VP} that is to be removed by the vacuum pump is estimated by Eq. 4.63, including one fraction of air \dot{V}_a and a similar fraction of water vapour $\dot{V}_{w(g)}$ that is carried by the gas flow unintentionally. The derivation of the air flow in Eq. 4.64 is based on the gravimetric concentration of dissolved air x_a in the feed water and the feed flow rate \dot{m}_D . The state of the feed water is considered to be saturated with air, while the saturation conditions of air at different temperatures are derived from experimental data on the saturation condition of nitrogen and oxygen in seawater published in the literature [171]. The molar volume of air at vacuum pressure $v_{a,VP}$ is evaluated from the molar volume of air at ambient pressure $v_{a,amb}$ by applying the ideal gas law. Depending on the deaeration pressure, only a fraction f of the total amount of air carried by the feed stream is to be removed. According to Henry's law, the equilibrium concentration of air in the water is proportional to the partial air pressure, so the fraction of air that is removed from the water is assumed to be similar to the fraction of

pressure reduction with respect to the ambient pressure.

$$\dot{V}_{\text{VP}} = \dot{V}_{\text{a}} + \dot{V}_{\text{w(g)}} \approx 2 \dot{V}_{\text{a}} \quad (4.63)$$

$$\dot{V}_{\text{a}} = f \dot{m}_{\text{D}} x_{\text{a}} \frac{v_{\text{a,VP}}}{M_{\text{a}}} \quad v_{\text{a,VP}} = v_{\text{a,amb}} \frac{\hat{p}_{\text{amb}}}{\hat{p}_{\text{VP}}} \quad f = \frac{\hat{p}_{\text{amb}} - \hat{p}_{\text{VP}}}{\hat{p}_{\text{amb}}} \quad (4.64)$$

The specific electricity consumption is estimated by Eq. 4.65, considering the feed water circulation and the energy demand for deaeration if applied. Several conversion efficiencies for medium-size centrifugal pumps and liquid ring vacuum pumps have been derived from typical technical specifications. Based on this data, a conversion efficiency of $\eta_{\text{FP}} = 50\%$ has been chosen as a suitable parameter for the hydraulic pump and a conversion efficiency of $\eta_{\text{VP}} = 15\%$ is assumed for the vacuum pump.

$$P_{\text{MD,spec}} = \frac{P_{\text{HP}} + P_{\text{D}}}{\dot{m}_{\text{P}}} \quad (4.65)$$

4.1.5 Simulation Settings

Different DCMD, PGMD and AGMD scenarios have been analysed in order to identify a universally valid parameterisation for the numeric solvers.

The accuracy criteria chosen for the different iterative solver loops are summarised in Tab. 4.1. For the single-node iterations, the solvers and the accuracy conditions are based on the specific heat transfer $\dot{q}_{M,L}^i$, ensuring stable properties independently of membrane area and the chosen state of discretisation (see Sec. 3.2). The iteration along the channel determining for the condenser inlet temperature T_{C}^1 is parameterised with an absolute accuracy of 0.001 K, whereas the iteration solving for the condenser inlet mass flow rate \dot{m}_{C}^1 is parameterised with a relative accuracy of 0.01% of the nominal condenser mass flow rate. Each of the criteria has been checked by comparison with simulation results obtained with accuracy criteria with a precision which was set two orders of magnitude higher. The deviations in distillate output and specific thermal energy consumption were negligible ($\ll 0.01\%$). The total energy balance was determined with total error values of less than 1 W, for all scenarios investigated.

Table 4.1: Accuracy criteria for the different iterative solver loops.

parameter	unit	chosen setting	target value
$\Delta \dot{q}_{M/L,e,\max}^i$	[W m ⁻²]	0.01	$J_{M/L}^i, \dot{Q}_{M/L}^i$
$\Delta T_{C,e,\max}^n$	[K]	0.001	T_{C}^1
$\Delta \dot{m}_{C,e,\max}^n$	[%]	0.01	\dot{m}_{C}^1

In order to determine a universally valid strategy for the channel discretisation, an ultra-high

number of nodes ($n = 10.000$) has been considered to be the absolute reference. The determination led to precise results for a discretisation of 10 nodes per meter channel length. Furthermore, the minimal number of nodes has been fixed at $n_{min} = 100$, in order to minimise numerical boundary effects. The numerical error based on the discretisation has been checked for each of the MD configurations, considering channel lengths from 0.7 to 70 m. The deviations with respect to the reference cases are less than 0.4% for the distillate output and less than 0.7% for the specific thermal energy consumption. The influence of the number of nodes on the numerical errors for total distillate output, specific energy consumption and heat balance are illustrated in Fig. 4.6, considering the PGMD scenario with a channel length of 7 m as an example. For this example, the relative deviation is less than 1% for 25 nodes, less than 0.3% for 100 nodes and less than 0.13% for 200 nodes. The thermodynamic error in the total module energy balance is in the range of 0 to 1 W.

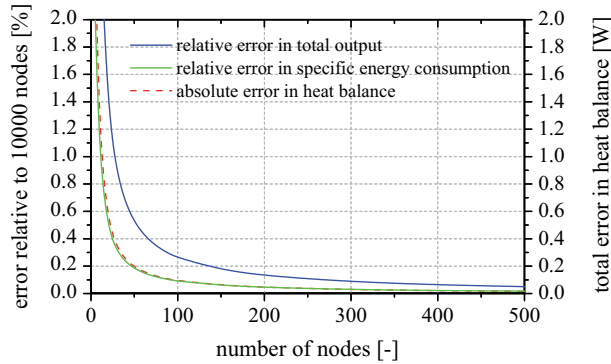


Figure 4.6: Influence of the number of discretisation nodes on the numerical error of the simulation results. The results for the distillate output and the energy consumption are given relative to a scenario that was calculated using 10.000 nodes.

4.2 Experimental Approach

4.2.1 Test Rig for Module Characterisation



Figure 4.7: Photograph of the module test facility.

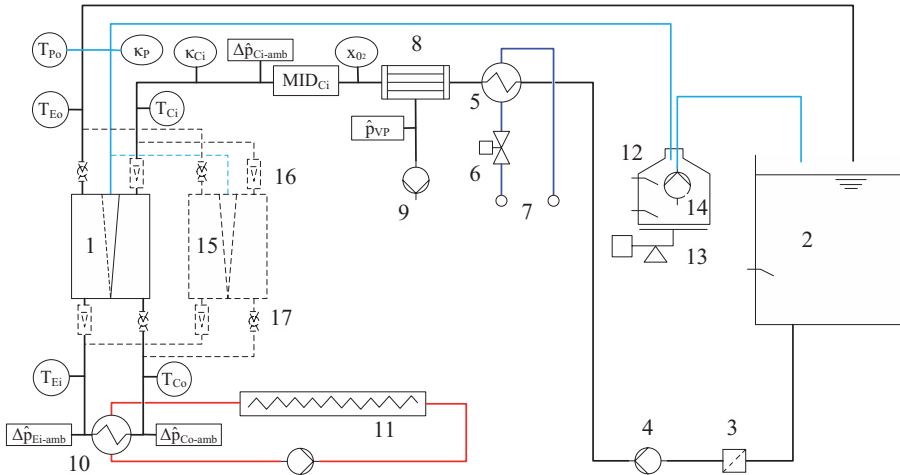


Figure 4.8: Hydraulic layout of the module test facility; 1 MD module, 2 feed water tank, 3 filter, 4 feed pump, 5 heat exchanger for cooling, 6 motor valve, 7 laboratory cooling circuit, 8 deaeration module, 9 vacuum pump, 10 heat exchanger for heating, 11 electric heater, 12 permeate tank, 13 electronic balance, 14 submerged permeate pump, 15 additional module(s) in parallel connection, 16 variable area flow meter, 17 adjustable hydraulic restrictor.

A specialised test facility was developed to characterise the performance of full-scale MD modules. The hydraulic diagram of the test rig in Fig. 4.8 represents the configuration that is used to characterise modules with internal heat recovery (PGMD, AGMD). The feed water is pumped

from a 300l storage tank (2) by a diaphragm pump (4). A 0.5 mm pore-size mechanical filter (3) protects the module against particles. The feed stream is conditioned in a heat exchanger (5). Any required condenser inlet temperature can be set by controlling a motor valve (6), regulating the cooling power provided by the laboratory cooling circuit (7). A commercially available Liqui-Cel membrane contactor from Membrana can optionally be included for in-line feed water degassing (8). This contactor is similar to the one presented in Sec. 3.3.1, using polypropylene hollow fibre membranes with a porosity of approximately 25 % and a total membrane area of 1.4 m². An MZ 2C vacuum pump from Vacuubrand is used to establish the vacuum condition on the lumen side of the hollow fibres. The deaeration module is only present in the hydraulic loop, if needed. After passing through the condenser channel of the MD module (1), the pre-heated feed water gains external heat in a heat exchanger (10). The evaporator inlet temperature is controlled by a 3-phase power switch, regulating an electric heating element (11) in a closed heating circuit. After passing through the module's evaporator channel, the water flows back into the storage tank for recirculation. The separated permeate is temporarily stored in a separate permeate tank (12). If the filling level of the permeate tank exceeds a certain threshold, the permeate is pumped back into the storage tank automatically by a submerged pump (14) in order to avoid an excessive increase of the feed water salinity during operation. Optionally, additional modules may be connected to the test rig in parallel (15). For multi-module measurements, the flow distribution is monitored since each hydraulic line is equipped with a variable area flow meter. The flow distribution may be influenced by adjusting the hydraulic restrictors (17) that are available in each hydraulic line. All components that are in contact with the testing fluids are made of corrosion-resistant materials. The components on the cold side of the module allow temperatures up to 55 °C, whereas the components on the hot side of the module allow temperatures up to 95 °C.

Five glass-encapsulated Pt100 temperature sensors are positioned directly at the evaporator inlet T_{Ei} , evaporator outlet T_{Eo} , condenser inlet T_{Ci} , condenser outlet T_{Co} and the permeate outlet T_{Po} of the MD module. The volumetric feed flow rate is measured by a Krohne Optiflux magnetic inductive flow meter MID_{Ci} at the condenser inlet position. The hydraulic pressure is evaluated relative to the ambient at the condenser inlet $\Delta\hat{p}_{Ci-amb}$, condenser outlet $\Delta\hat{p}_{Co-amb}$ and evaporator inlet $\Delta\hat{p}_{Ei-amb}$ positions with Sensortech KTE300 pressure sensors. If the deaeration equipment is used, the vacuum condition \hat{p}_{VP} is measured by a tecsis3296 absolute pressure sensor and the state of deaeration is monitored by an in-line measurement of the feed stream oxygen saturation x_{O_2} with an WTW OxiCell325 sensor. The feed water electrical conductivity κ_{Ci} and the permeate electrical conductivity are monitored with WTW LRD 325-3 sensors. The weight of the permeate storage tank is constantly measured with a Soehnle Professional electronic balance. All sensor values are read in via an Agilent 34970A multiplexer and stored on a computer.

The hydraulic diagram shown in Fig. 4.8, represents the experimental set-up for characterising modules with internal heat recovery only (PGMD, AGMD, Fig. 4.5(c)). For V-AGMD operation,

the air gap is evacuated through the module's permeate outlets that are connected to a vacuum-seal double-chamber permeate storage tank. The permeate tanks is actively evacuated with a Vacuubrand MZ 2C vacuum pump (see Fig. 3.12). By switching between the two evacuated permeate chambers, continuous operation at sub-atmospheric pressure is possible.

The experimental study of modules without internal heat recovery (DCMD, Fig. 4.5(b)) requires separate fluid loops for the evaporator and the condenser sides. For this purpose, a second test facility of similar design is available and is coupled to the system such that the first test rig captures the full functionality of the evaporator loop and the second test rig captures the full functionality of the condenser loop. The permeate produced during an experiment with a DCMD module is extracted with an overflow in the condenser loop, temporarily stored in one of the permeate storage tanks and then pumped back to the evaporator storage tank, for continuous operation.

4.2.2 Testing Conditions and Evaluation of Performance Parameters

The MD module performance depends on a variety of operating conditions. Four independent operation parameters are identified to define the performance for a given module design: condenser inlet temperature, evaporator inlet temperature, feed flow rate and feed water concentration. If deaeration is applied, the deaeration pressure is considered the fifth independent parameter that is required for clear definition of a specific module operation point. In order to analyse the sensitivity of the process performance to a single operation parameter, the experiments have been performed by varying this specific parameter of interest while keeping the others constant. The evaporator and condenser inlet temperatures $T_{Ei/Ci}$ are regulated by a closed-loop PI control system, that generates precise control values for the motor valve and the power switch for the electric heating device. The feed flow rate \dot{m}_{Ci} is also adjusted by controlling the motor speed of the pump using a closed-loop PI control system. The volumetric sensor feed-back \dot{V}_{Ci} is converted into mass flow information by taking the influence of temperature and salinity on the fluid density into account [112]. Tap water is used for most of the experiments and sea salt originating from the Red Sea, which is commercially available from Seequasal GmbH, is dissolved in tap water for the experiments on different feed water concentrations. The ionic composition of the sea salt is listed in Appendix C.

Before starting with an actual testing procedure, an initial phase is run to preheat and flush the whole system. The fully automated control system is capable of managing the following operational modes for characterisation:

- stationary long-term experiments

- arbitrary sequences of different steady-state operation points
- dynamic characterisation by following pre-defined set-point trajectories
- dynamic characterisation by following set-point trajectories generated dynamically by a coupled simulation (hardware in the loop)

However, all experiments discussed within this thesis were performed under steady-state operating conditions. In order to guarantee steady-state operation, each single experiment runs for at least 2 h, where the last 30 min are used for further analysis. One set of operation conditions is given as an example in Tab. 4.2.

Table 4.2: A set of operation conditions representing a variation in feed flow rate, as an example.

Reference	T_{Ei} [°C]	T_{Ci} [°C]	\dot{m}_{Ei} [kg h ⁻¹]	\dot{m}_{Ci} [kg h ⁻¹]	S_{Ei} [g kg ⁻¹]	S_{Ci} [g kg ⁻¹]	$c_{Ci/Ei}^a$ [m s ⁻¹]
80-25-200-0	80	25	200	200	0	0	0.033
80-25-300-0	80	25	300	300	0	0	0.049
80-25-400-0	80	25	400	400	0	0	0.066
80-25-500-0	80	25	500	500	0	0	0.082

^aconsidering a channel height of 0.7 m and spacer S-320, see prototypes in Tab. 4.3

To analyse the integral module process performance, the performance parameters of interest are derived according to the definitions that have already been applied within the theoretical model discussion in Sec. 4.1.4. Since the definitions for the total output rate (Eq. 4.35), the thermal power consumption of the evaporator channel (Eq. 4.40), the latent part of the transferred thermal power (Eq. 4.41) and the hydraulic pressure loss (Eq. 4.60) contain local values that cannot be accessed experimentally, these definitions are modified into suitable forms for the available experimental data. The total output rate \dot{m}_P is derived from the gradient of the mass signal over time. The thermal power consumption of the evaporator channel is approximated with Eq. 4.66, using a mean value for the mass flow rate $\bar{\dot{m}}_{Ei-Eo}$, in order to account for the small change in evaporator mass flow rate along the channel. A significant part of the total permeate is already produced and extracted within the hot part of the evaporator channel [22]. Thus, a weighting ratio of (1 : 2) is used to approximate the mean flow rate from the inlet and outlet flow rates in Eq. 4.67. In the case of PGMD, the recovered sensible heat from the permeate stream may be experimentally derived from the difference between \dot{Q}_E and \dot{Q}_C .

$$\dot{Q}_E \approx \bar{\dot{m}}_{Ei-Eo} c_{p,Ei} (T_{Ei} - T_{Eo}) \quad (4.66)$$

$$\bar{\dot{m}}_{Ei-Eo} \approx \frac{1}{3}(\dot{m}_{Ei} + 2 \dot{m}_{Eo}) = \dot{m}_{Ei} - \frac{2}{3}\dot{m}_P \quad (4.67)$$

The sole latent part of the transmembrane heat transfer $\dot{Q}_{E,l}$ is estimated by 4.68, using the arithmetic mean value of the latent heat of evaporation $\bar{h}_{v,Ci-Co}$. The dependence of the water's

thermal capacity and latent heat of evaporation on temperature and salinity are taken into account according to the correlations published in [112].

$$\dot{Q}_{E,I} \approx \dot{m}_P \Delta \bar{h}_{v,Ei-Eo} \quad (4.68)$$

The hydraulic pressure loss is evaluated by Eqs. 4.69 and 4.70, not including the pressure loss of the test facility.

$$\Delta \hat{p}_{Ci-Co} = \Delta \hat{p}_{Ci-amb} - \Delta \hat{p}_{Co-amb} \quad (4.69)$$

$$\Delta \hat{p}_{Ei-Eo} = \Delta \hat{p}_{Ei-amb} \quad (4.70)$$

No explicit experimental evaluation of the specific electricity consumption is derived in order to remain independent of the specifications of the laboratory test facility regarding the hydraulic pressure losses and the conversion efficiency of the pumps. These specifications are not considered to be representative for commercial systems, mainly due to their small scale. Moreover, the components were chosen with respect to practical features such as simple and flexible application rather than robustness and efficiency.

4.2.3 Uncertainty of Measurement and Error Propagation

This section provides a discussion regarding the confidence range of the experimentally obtained results, based on the relevant uncertainties of measurement, the quality of controls and the propagation of errors.

The individual uncertainties were determined for the temperature, the flow rate and the weight measurements. Quality comparable to that obtained in Sec. 3.3.3 was found. Regarding the temperatures, high accuracy of the Pt100 sensors (4-wire, class 1/3 B) is guaranteed by an absolute temperature calibration that is performed on a regular basis. The tolerated absolute deviation of the measurements with respect to a DKD-licensed reference sensor is ± 0.05 K. In order to account for a possible drift of the sensors during the period between two calibrations and the fact that the sensors are mounted externally to the module, the overall uncertainty of the temperature measurements is assumed to be ± 0.10 K. For the flow meters, a maximal error of $\pm 0.3\%$ was experimentally determined with different flow rates and salinities. A maximal error of $\pm 2.01 \text{ h}^{-1}$ is taken into consideration, leading to a rather conservative estimation throughout the required range of flow rates. The accuracy of the electronic balance is rated by the manufacturer as ± 1.0 g. Unlike for the test cell experiments, evaporative losses are negligible, since the total output rates of a full-scale module is many orders of magnitude higher than the evaporative losses that are expected. This is explained by the large effective membrane surface area and the low temperatures of the permeate that is extracted from the module. No covering of the permeate tank is required. A quite conservative estimation is made, assuming a maximal error of $\pm 0.05 \text{ l h}^{-1}$. In order to ensure the integrity of the membrane module under test, the electrical

conductivity of the permeate is continuously monitored during the experiments.

A measuring interval of 5 s ensures a large quantity of data points within the 30 min of interest for the evaluation of each experiment. The sensor values are derived as arithmetic mean values from the 360 individual data points. The short measuring interval allows the operation parameters to be controlled with high accuracy. Only minimal fluctuations of the controlled parameters are observed. The steady-state stability of the controls was quantified for a standard experiment (Tab. 4.2, 80-25-300-0) as an example, evaluating the 30 min of interest. The standard deviation of the temperature measurements was less than 0.06 K, while the maximal deviation from the set point is less than ± 0.10 K. Considering the flow rate measurements, the standard deviation is less than 0.71 h^{-1} , while the maximal difference from the set point is less than $\pm 2.0 \text{ kg h}$. The error of the arithmetic mean values with respect to the set points are at least one order of magnitude lower than the uncertainty of measurement and therefore considered negligible for the temperature as well as the flow rate measurements.

The steady-state behaviour of the operating conditions and of the total permeate output rate is screened for each experiment in order to ensure validity of the results. The module's total energy balance is evaluated for each experiment according to Eqs. 4.20 and 4.33 as an additional method to check correct functionality of the testing equipment and the post-processing routines.

A detailed error analysis has been made for the relevant energy performance parameters. The probable and the maximal error are evaluated according to the Gaussian law of error propagation given in Eq. 3.68. A detailed derivation of the propagated uncertainties of measurement for each performance parameter of interest is provided in Appendix F. For estimating the total uncertainties, the individual uncertainties of the respective sensor values are considered as stated above. For the DCMD configuration with external heat recovery, the uncertainty for the temperature T_{RXo} is considered to be 0.1 K, similar to the direct temperature measurements. Furthermore, uncertainties of 1 % are taken into consideration for the empirical fluid property correlations. The probable and the maximal uncertainties for the specific energy demand and the thermal efficiency have been explicitly evaluated for a selected set of DCMD, PGMD, AGMD and V-AGMD experiments that cover a wide range of operating conditions as well as different geometrical module designs. The results are presented in Fig. 4.9.

The resulting uncertainties for the specific energy demand are in the range of $2 - 40 \text{ kWh}_{\text{th}} \text{ t}^{-1}$. The probable error for the most relevant operation points ($< 300 \text{ kWh}_{\text{th}} \text{ t}^{-1}$) range from approximately $2 - 8 \text{ kWh}_{\text{th}} \text{ t}^{-1}$, which represents a relative error of $2 - 4\%$, with lower relative errors for higher energy demands. The absolute uncertainties for the thermal efficiency are in the range of $0.5 - 3.1\%$. The probable error for the relevant operation points ($> 50\%$) ranges from approximately 1 to 1.5% , which represents a relative error of $1.5 - 2\%$, with lower relative errors for higher thermal efficiencies. It turns out that none of the uncertainties shows a relevant difference caused by the process variant. The uncertainty of measurement is not explicitly provided in the following diagrams to retain clarity.

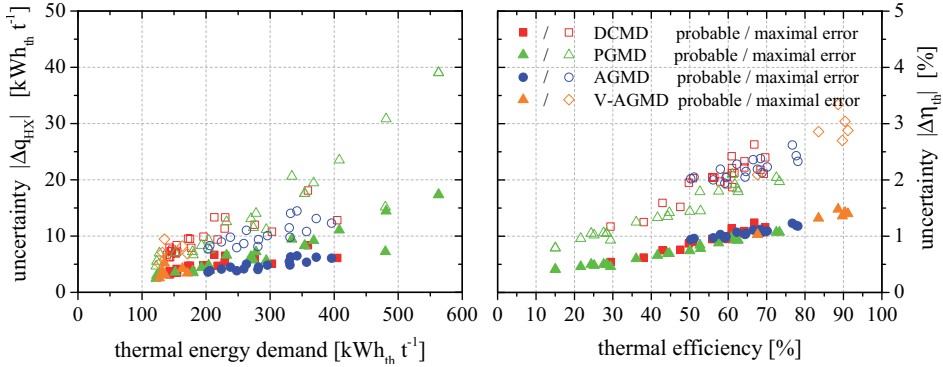


Figure 4.9: Probable and maximal uncertainties in the evaluation of the specific thermal energy demand and the thermal efficiency, estimated for different DCMD, PGMD, AGMD and V-AGMD experiments. The temperature, the flow rate and the output measurements as well as an uncertainty for the fluid property correlations are taken into consideration for the propagation of errors according to Eq. 3.68.

Evaluation of the overall energy balance for a module during standard steady-state experiments ($T_{Ci} = 25^\circ\text{C}$) results in a negative energy error that usually ranges from -50 to $-120 W_{th}$. This energy error consists of one part that is based on the uncertainty of measurement and another part that represents the heat losses to the ambient. Error propagation calculations for the energy balance evaluation show an uncertainty of measurement in the range of approximately 50 to 100 W_{th} , depending on the operating conditions. Fig. 4.10 illustrates the error in the total module energy balance for a selected set of experiments performed with module PGMD-09.8-050-BE (see Tab. 4.3).

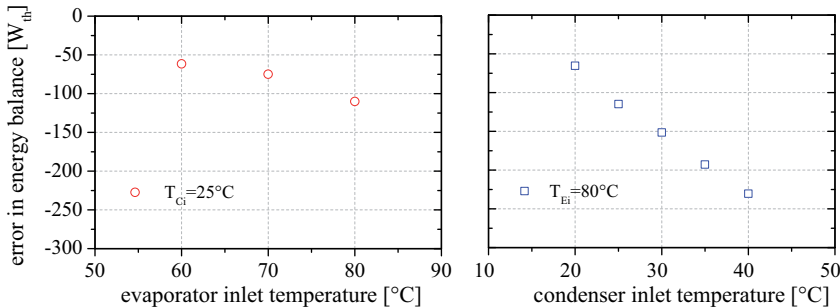


Figure 4.10: Heat losses to the ambient for module PGMD-09.8-050-BE under different temperature conditions.

In the first experiments, the evaporator inlet temperature was constant at 80°C while the condenser inlet temperature was successively increased. If the condenser inlet temperature is close to the room temperature of approximately 20°C , the energy error was determined to be about

$-65 W_{\text{th}}$. If the condenser inlet temperature is increased to 40°C , the energy error increases almost linearly to $-230 W_{\text{th}}$. In a second set of experiments, the evaporator inlet temperature is reduced from 80°C to 60°C for a constant condenser inlet temperature of 25°C . Here, the energy error decreases from $-110 W_{\text{th}}$ to approximately $-60 W_{\text{th}}$.

It turns out that the resulting errors in the total energy balances are of the same order of magnitude as the respective uncertainty of measurement. The quantity of heat loss to the ambient may therefore only be roughly estimated. However, the uncertainty of measurement is expected to represent a rather systematic error within one set of experiments. Thus, the relative differences in the energy error based on the changing temperature conditions may be mainly attributed to heat losses. Based on the given results, approximately $-50 W_{\text{th}}$ to $-100 W_{\text{th}}$ of the heat losses could be assigned to the module's hot face ends. Even though there are steep temperature gradients to the ambient, low sensitivity to the evaporator inlet temperature is observed, due to the low surface fraction and the insulating effect of the rather thick resin potting. The heat losses on the dominant cylindrical outer surface are estimated to be $0 - 150 W_{\text{th}}$, being rather sensitive to the condenser inlet temperature because of the high surface fraction. If the condenser inlet temperature is chosen close to the ambient condition, this part of the heat loss is expected to be negligible. The fraction of the total heat loss compared to the large heat transfer inside the module \dot{Q}_E is less than 2.2% for all results presented in Fig. 4.10 and even less than 0.8% for usual condenser inlet temperatures $\leq 25^\circ\text{C}$.

Based on the given results, the usual error in the overall energy balance is considered to be small and can mainly be assigned to heat losses to the ambient, demonstrating an appropriate system configuration and guaranteeing good quality of the experimental results.

4.2.4 Full-Scale Module Prototypes for Experimental Evaluation

For extensive experimental validation of the multi-node module model approach, various full-scale modules have been designed, fabricated and characterised. The prototype designs are based on the spiral-wound MD module concept that was proposed in 1985 by W.L.Gore & Associates [63]. The spiral-wound module concept has been adopted at the Fraunhofer Institute for Solar Energy Systems (ISE), where tools and fabrication procedures for the production of full-scale prototypes have been developed. A PGMD module design was optimised for integration into autonomous solar systems [8]. Further studies on the associated PGMD module concept, including aspects of module fabrication, characterisation and module performance have already been published by the author of this thesis [22, 66].

A schematic representation of the channel configuration is given in Fig. 4.11. The evaporator and condenser main flow channels each have two active sides. The hot zones of the channels are in the module centre and the cold zones are located toward the module's shell. Therefore, even without module insulation, only minimal heat losses to ambient occur (see Fig. 4.10).

The modules are fabricated using a membrane, a polymer film and different spacer materi-

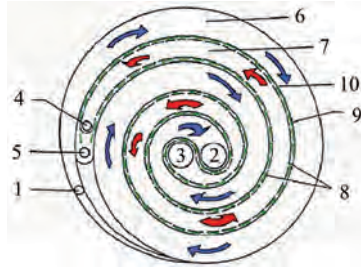


Figure 4.11: Schematic diagram of the spiral-wound module concept; 1 condenser inlet, 2 condenser outlet, 3 evaporator inlet, 4 evaporator outlet, 5 permeate outlet, 6 condenser channel, 7 evaporator channel, 8 permeate channel, 9 hydrophobic membrane, 10 polymer film [66].

als on rolls. The material coils are placed inside the winding machine that is illustrated in Fig. 4.12(a). The layers are aligned with guiding rollers and brought together on a central tube on a motor-driven main spindle. To ensure a well-defined production process, each material spindle is equipped with a controlled magnetic brake, with which the pre-tensioning of each layer can be precisely adjusted. In the flow direction, the flow channels are closed by thermo-mechanical welding of the laminate and the polymer film as shown in Fig. 4.12(d). A top view of the spiral-wound channels including the central tube is given in Fig. 4.12(b). A homogeneous flow distribution over the channel height is induced by the central tube, due to its wide hydraulic diameter compared to the flow channels. The face ends of the spiral coil are closed by a potting process with a resin compound as illustrated in Fig. 4.12(c). The potted coil is pressed into a fibreglass tube and sealed with O-rings. Different module designs with varying materials and geometrical configurations have been fabricated in order to optimise the module performance and robustness. A photograph of two different full-scale module prototypes is given in Fig. 4.12(e).

In the framework of this thesis, a set of full-scale spiral wound modules has been fabricated so that different MD process variants could be evaluated comparatively. Furthermore, different geometrical channel designs have been produced based on the PGMD variant, in order to validate the representation of the different geometrical aspects by the multi-node model. Prototypes with different channel lengths, gap widths and backing positions are available. The geometrical specifications of the different prototypes are listed in Tab. 4.3. The laminate L-020A-S and the polymer film F-127 were chosen for prototype production. The main flow channel and gap spacers are chosen from Tab. 3.6 according to the channel width required. The detailed technical specifications of the different material layers are given in Sec. 3.3.4. It should be noted that the thermodynamic performance characteristics of the different materials have already been theoretically and experimentally analysed in the first part of this thesis (Sec. 3.4).

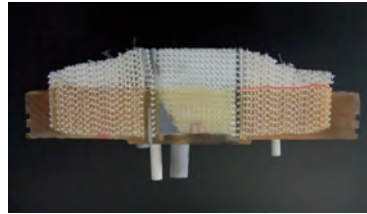
The condenser and evaporator channel inlets are located at the bottom and the outlets are located at the top of the prototypes. Consequently, air is completely removed from the module's flow channels during the filling procedure and during operation. For the PGMD prototypes,



(a) Winding machine with material rolls [66]



(b) Top view of spiral-wound channels [8]



(c) Cross-section of a potted face end



(d) Thermo-mechanical welding bar [8]



(e) Full-scale module prototypes

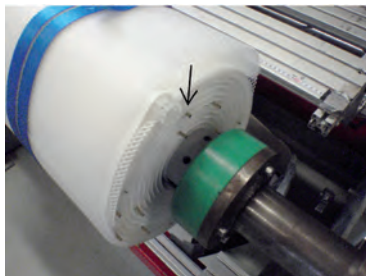
Figure 4.12: Spiral-wound module prototype fabrication.

the permeate outlets are oriented upwards, for the same reason. Usually the permeate outlet is located on the outer perimeter of the coil so that the sensible heat from the permeate is recovered internally. However, some prototypes provide a second opening at a central position for flushing and for experimental studies on an operational mode with internal pre-heating of the permeate. The AGMD prototype provides 12 openings at the bottom of the air gap as illustrated in Fig. 4.13 to allow gravimetric permeate extraction. Furthermore, four openings for pressure sensors are introduced at equal intervals along the channel on the top side of the air gap, in order to monitor the absolute pressure conditions along the air gap during V-AGMD operation.

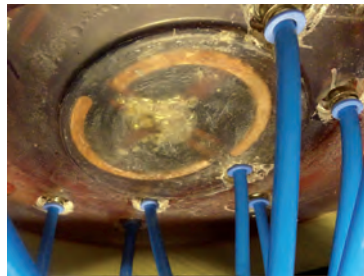
Table 4.3: Geometrical specifications for different spiral-wound MD module prototypes

module	membrane area [m ²]	channel length ^a [m]	channel height [m]	channel width [mm]	gap width [mm]
DCMD-09.8-000-BE	9.8	7.0	0.70	3.20	-
PGMD-09.8-050-BE	9.8	7.0	0.70	3.20	0.50
AGMD-08.7-200-BC	8.7	6.5	0.67	2.00	2.00
PGMD-04.9-050-BE	4.9	3.5	0.70	3.20	0.50
PGMD-09.8-050-BC	9.8	7.0	0.70	3.20	0.50
PGMD-09.8-050B-BE	9.8	7.0	0.70	2.00	0.50
PGMD-14.0-050-BE	14.0	10.0	0.70	3.20	0.50
PGMD-09.1-025-BE	9.1	6.5	0.70	3.20	0.25
PGMD-09.8-100-BE	9.8	7.0	0.70	3.20	1.00

^achannel length refers to each of the main flow channels



(a) Coil with axial permeate outlet tubes



(b) Module base with permeate outlets

Figure 4.13: Photographs of the spiral-wound AGMD module prototype.

4.3 Results and Model Validation

4.3.1 General Aspects of Membrane Distillation Module Operation

The following section presents a discussion of general aspects regarding the operation of MD modules. For any MD configuration, the module performance is generally defined by the operating conditions, the geometrical module design and the thermodynamic properties of the materials used. This section provides a detailed discussion of the general influence of the temperature conditions, the feed flow rate, the feed water salinity and the deaeration conditions on module

performance. Furthermore, general aspects of module channel design and up-scaling concepts are studied. The discussions are illustrated by experimental results and model predictions for PGMD modules with internal heat recovery. It is important to note that the quantitative results explicitly refer to the specific PGMD prototype under discussion and may be quite different for other MD configurations or other prototype specifications. However, the general phenomenology and interpretation are universally valid for each of the MD configurations with internal or external heat recovery. Subsequent sections complete the discussion on MD module analysis by addressing the specific effects accompanying the DCMD, PGMD and AGMD module configurations. Finally, a direct comparison of the different module configurations is provided in Sec. 4.3.5.

General Parametrisation of the Multi-Node Model

The general geometrical parameters of the multi-node models, namely the channel length L , the channel height H , the channel width $\delta_{E/C}$ and the gap width $\delta_{PG/AG}$, are set according to the specifications of the relevant module prototypes, given in Tab. 4.3. The fundamental components of the multi-node models are the corresponding single-node models from Chapter 3, that require a variety of additional model parameters. Since the design materials used for full-scale module fabrication are similar to those considered for the derivation of the single-node models, the nodes in the multi-node model are generally set-up on the basis of the parameterisation presented and validated in the first part of this thesis (e.g. membrane, backing, polymer film, heat transfer correlations etc.). The geometrical parameters of the nodes are assumed to be constant along the flow channels.

The only adjustment that has been made is a general reduction of the effective bulk stream heat transfer coefficients, that were introduced in Sec. 3.4.1. It turned out that the precision of the module model predictions generally improved for all of the process configurations, if the effective heat transfer in the evaporator and the condenser flow channels is reduced by 30%. This reduction was implemented by multiplying the heat transfer correlations in Eqs. 3.70 and 3.71 by a factor of 0.7, leading to the modified Eqs. 4.71 and 4.72.

$$\text{spacer S - 320 :} \quad Nu = 0.113 Re^{0.656} Pr^{0.333} \quad (4.71)$$

$$\text{spacer S - 200 :} \quad Nu = 0.106 Re^{0.695} Pr^{0.333} \quad (4.72)$$

The adaptation of the heat transfer correlations seem reasonable, considering the following argumentation. The multi-node model assumes an ideal counter-current flow channel design. However, unlike for an ideal counter-current flow design that offers symmetric temperature gradients for active heat transfer to both sides, curved flow channels with multiple turns have asymmetric characteristics with respect to the temperature gradients. As a consequence, the effective logarithmic mean temperature difference tends to reduce and a correction factor is recommended

for the thermal design of spiral-wound heat exchangers [172]. The correction factor depends on the total heat transfer coefficient, inner and outer diameters and height of the spiral coil, and the mass flow capacities of the relevant flow streams. The mathematical derivation of the correction factor is provided in Appendix G. According to the cited theory, the recommended correction factors for hypothetical spiral-wound heat exchangers with total heat transfer coefficients of $500 \text{ W (m}^2 \text{ K)}^{-1}$ and geometrical specifications similar to those of the spiral-wound MD module prototypes range from 0.85 to 0.95. These correction factors indicate poorer heat transfer performance in spiral-wound heat exchangers compared to ideal counter-current heat exchangers, which may also apply qualitatively to spiral-wound MD modules.

A further source of heat transfer reduction in the module flow channels compared to the test cell flow channels may be boundary effects in the test cell. Especially turbulence near the test cell inlet region may have contributed to an enhancement of the heat transfer, which would not apply to the heat transfer in a full-scale module flow channel. A reduction of the heat transfer in the module flow channels might also be explained by varying channel width due to operational loads that are applied to the flexible film materials, and non-homogeneous distribution of the flow stream over the channel height, especially in the inlet and outlet regions. Further argumentation may address the asymmetric geometrical configuration of channel spacer S-320, that offers reduced heat transfer coefficients on the channel side with the straight filaments. Unlike the test cell experiments, module operation includes heat transfer through two active sides. The average heat transfer coefficient in the module is therefore expected to be lower than the heat transfer through the diagonal filament side, as measured in the test cell.

The parameterisation of the operating conditions, namely the evaporator and the condenser inlet temperatures $T_{\text{Ei/Ci}}^{\text{in}}$, flow rates $\dot{m}_{\text{Ei/Ci}}^{\text{in}}$ and salinities $S_{\text{Ei/Ci}}^{\text{in}}$, is set according to the desired scenario. For a comparison of model predictions and experimental results, the inlet conditions are set according to the corresponding testing conditions, if not stated otherwise. The absolute pressure input \hat{p}^{in} is set to ambient pressure, if no active deaeration is considered. For the scenarios with active deaeration, the absolute pressure input is set to be the deaeration pressure applied by the vacuum pump.

Pressure Loss Experiments and Parameter Identification

The pumping energy that is needed to overcome the hydraulic pressure loss of the fluid in the flow channels primarily determines the specific electric energy consumption required for module operation. Furthermore, the hydraulic pressure loss introduces limitations regarding the module design and the corresponding permissible operating conditions. In this regard, the membrane's maximal load capacity and the membrane's water entry pressure (WEP) independently limit the maximal pressure loss specifications. Even though the WEP for the given membranes is rated with approximately 4 bar, the maximal local pressure difference from the condenser to the evaporator channels (i.e. $\Delta\hat{p}_{\text{Ci-Eo}}$) should not exceed 1 bar. These specifications result from

practical experience with the investigated spiral-wound modules.

Pressure loss experiments on different spiral-wound channel configurations have been conducted in order to gain information on the existing pressure loss characteristics. Furthermore, the data is applied to derive the empirical parameters used in the pressure loss correlations in Eqs. 4.18 and 4.19. The modules PGMD-04.9-050-BE, PGMD-09.8-050-BE and PGMD-14.0-050-BE provide different channel lengths with 3.5 m, 7.0 m and 10.0 m, while having identical channel widths of 3.2 mm. The module prototype PGMD-9.8-050B-BE has a channel length of 7.0 m but a thinner channel with a width of only 2.0 mm. It should be noted that the channel lengths refer to each of the channels, namely the condenser as well as the evaporator channel. The experiments were conducted with tap water at different mass flow rates to determine the characteristic curves for each of the prototype modules. The characteristic pressure curves in Fig. 4.14 include the accumulated pressure loss of the evaporator and the condenser channels and the respective inlets and outlets, excluding the pressure loss of any external hydraulics.

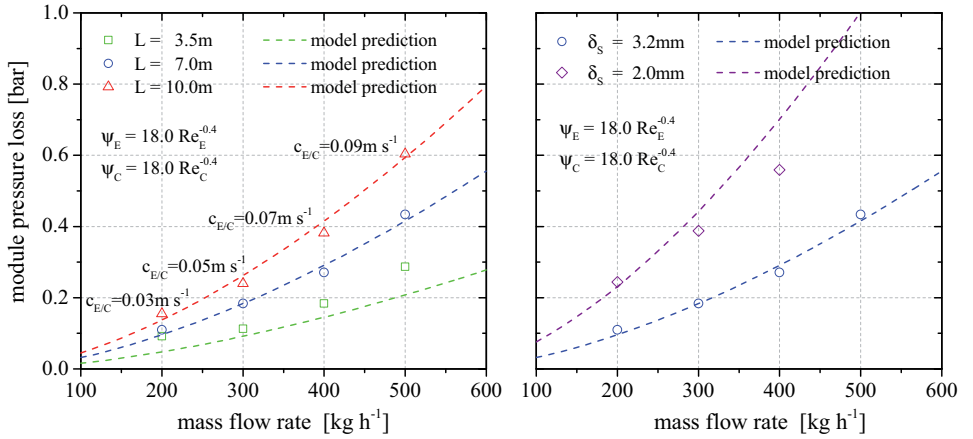


Figure 4.14: Influence of the mass flow rate on the accumulated pressure loss of the evaporator and the condenser channel investigated for different channel lengths and channel widths. The parameters for the empirical model correlation in Eqs. 4.18 and 4.19 have been determined to be $a = 18.0$ and $b = -0.4$. Testing conditions: Modules PGMD-04.9-050-BE, PGMD-09.8-050-BE, PGMD-9.8-050B-BE and PGMD-14.0-050-BE, $T_{Ei} = 80^\circ\text{C}$, $T_{Ci} = 25^\circ\text{C}$, tap water.

The pressure curves of the modules show a characteristic parabolic form, since the pressure loss depends on the flow rate squared (see Eqs. 4.18 and 4.19). For the module with a flow channel length of 7.0 m, the pressure loss increases by 74 mbar for an increase in flow rate from 200 to 300 kg h^{-1} , while an increase by 163 mbar is observed for an increase in flow rate from 400 to 500 kg h^{-1} . Furthermore, the pressure loss clearly increases for the modules with longer flow channels or with thinner flow channel width. Comparing the results obtained for the flow channels of 7.0 and 10.0 m length, both channel length and the pressure loss increase approximately by a factor of 1.4. The pressure loss for the thinner 2.0 mm flow channel is approximately twice

the pressure loss obtained with the 3.2 mm flow channel. In addition to the channel width, this difference may be explained by the difference in spacer geometry.

In spite of the fact that the evaporator and condenser channel designs are similar for each of the tested modules, the experimental results showed a significantly higher pressure loss for the evaporator channels, especially at higher flow rates. Due to the higher absolute pressure level in the condenser channel, the thin film materials may flex into the evaporator channel between the spacer filaments. As a consequence, the effective channel width of the evaporator channel would be reduced compared to the increased condenser channel width. This effect intensifies for higher flow rates and slightly depends on the pressure loss of the external hydraulics between the condenser outlet and the evaporator inlet (i.e. $\Delta\hat{p}_{Co-Ei}$). However, in this thesis, the pressure loss model is only used for a rough estimate of the electricity demand in Eq. 4.59. In this context, only the accumulated module pressure loss is of interest and an equal contribution of both flow channels to the overall pressure loss is assumed for the derivation of the pressure loss model parameters. By applying the MS Excel optimiser toolbox, the model predictions have been fitted to the experimental results. The resulting pressure loss parameters are $a = 18.0$ and $b = -0.4$, leading to the empirical pressure loss correlations given in Eqs. 4.73 and 4.74.

$$\Delta\hat{p}_E = \psi_E \frac{L \rho_E}{d_{h,E}} \frac{(c_E^i)^2}{2} \quad \psi_E = 18.0 Re_E^{-0.4} \quad (4.73)$$

$$\Delta\hat{p}_C = \psi_C \frac{L \rho_C}{d_{h,C}} \frac{(c_C^i)^2}{2} \quad \psi_C = 18.0 Re_E^{-0.4} \quad (4.74)$$

The model predictions reflect the fundamental pressure loss dependence on flow rate and channel design. The mean error of the pressure loss predictions for the modules with a channel length of 7.0 and 10.0 m are 6 and 8 % for a channel width of 3.2 mm and 15 % for a channel width of 2.0 mm. For the prototype with a channel length of only 3.5 m, the pressure loss prediction underestimates the measured values by 29 %. The deviations might be partially explained by the pressure loss introduced by the inlet and outlet pins that is not taken into account in the model predictions. Each of the prototypes are fabricated with identical inlet and outlet pins, so the relative contribution of the inlet and outlets to the overall pressure loss is higher for the prototypes with shorter channel lengths. Furthermore, it has to be recalled that the flow channels in spiral-wound modules follow the spiral geometry. Each of the spiral coils is fabricated with the same central tube, so the average radius of the flow channel is shorter for modules with shorter flow channels. Since the hydrodynamic effects induced by radial forces are not modelled in the pressure loss equation and also the shorter channel radii might partially explain the underestimated model predictions for the prototype with the shortest flow channels. However, the empirical correlations seem to be sufficient for a rough estimation of the electric power consumption.

Influence of Temperature Conditions on Module Performance

To investigate the general influence of temperature conditions on MD module performance, examples of experimental results obtained with prototype PGMD-09.8-050-BE are analysed and discussed. The experiments were conducted with tap water at a feed flow rate of 300 kg h^{-1} . In a first set of experiments, the evaporator inlet temperature was increased from 60 to 80°C at a constant condenser inlet temperature of 25°C . In a second set of experiments, the evaporator inlet temperature was 80°C while the condenser inlet temperature was successively increased from 20 to 40°C . The experimental results as well as model predictions for the permeate output rate, the specific thermal and the specific electric energy consumption are given in Fig. 4.15. The temperature difference measured between the condenser outlet and the evaporator inlet is provided as supplementary information.

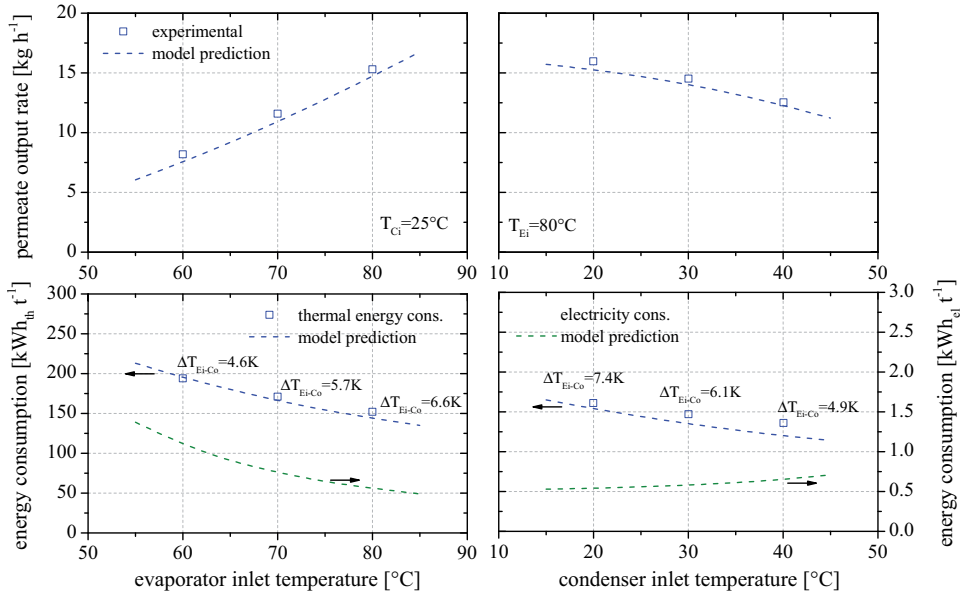


Figure 4.15: Influence of the inlet temperature conditions on the module performance. Testing conditions: Module PGMD-09.8-050-BE, $m_{C_i} = 300 \text{ kg h}^{-1}$, tap water.

If the evaporator inlet temperature was increased from 60 to 80°C , the permeate output rate increased from 8.2 to 15.3 kg h^{-1} , forming a slightly increasing gradient with temperature. Naturally, the positive effect of an increase in evaporator inlet temperature is the increase of the module's mean temperature level and consequently the flux and the thermal efficiency. A second effect is the increasing temperature difference between the evaporator and the condenser channels from 4.6 to 6.6 K , introducing additional driving force for vapour permeation. The significant gain in permeate output rate overcompensates the additional thermal power requirement that depends on the temperature difference (see Eq. 4.52). The specific thermal energy consumption

decreases from 194 to 152 kWh_{th} t⁻¹. Since the pumping power does not change for a constant feed flow rate, the increase in output rate leads to a reduction of the specific electricity demand from 1.11 to 0.56 kWh_{el} t⁻¹. The calculated influence of the evaporator inlet temperature on process performance is in good quantitative agreement with the experimental results. The maximal and mean differences are 8 % and 6 % for the permeate output rate and 5 % and 3 % for the specific thermal energy consumption.

If the condenser inlet temperature is increased from 20 to 40 °C, the permeate output rate reduces from 15.9 to 12.5 kg h⁻¹, even though the module's mean temperature level increases. The positive effect of the increasing mean temperature is outweighed by the reduction of the temperature difference between the evaporator and the condenser channels from 7.4 to 4.9 K, lowering the driving force for permeation. However, the specific thermal energy consumption decreases from 161 to 136 kWh_{th} t⁻¹ due to the lower thermal power requirement and the increased process efficiency for higher mean temperature levels. Since the pumping power does not change for a constant feed flow rate, the decreasing permeate output rate leads to an increase of the specific electricity demand from 0.54 to 0.65 kWh_{el} t⁻¹. The maximal and mean differences between the model predictions and the experimental results are 4 % and 3 % for the permeate output rate and 12 % and 8 % for the specific thermal energy consumption.

From a thermodynamic point of view, the choice of high evaporator inlet temperatures is generally beneficial for the module's performance. However, the exergetic value of the thermal energy and finally the financial costs usually increase with temperature level. Furthermore, the availability of low-grade waste heat sources may attract special interest in MD module operation at low evaporator inlet temperature levels. Usually the MD desalination systems are non-pressurised, limiting the maximum temperature level to 100 °C.

In MD systems that operate without recirculation, the condenser inlet temperature is usually defined by the raw water condition. In systems that operate with recirculation, the condenser inlet temperature may be adjusted, optimising either flux or specific thermal energy consumption. A lower limitation for the condenser inlet temperature is given by the recirculation strategy and the brine cooling concept. It should be remembered that the technical effort for brine cooling increases with the demand for lower temperature levels. This in fact may make MD module operation at higher condenser inlet temperature levels particularly attractive.

Other practical aspects such as the temperature resistance of typical polymer materials or the influence of temperature on scaling or fouling should be taken into consideration during the choice of suitable temperature conditions for MD module operation.

Influence of the Feed Flow Rate on Module Performance

To investigate the general influence of the feed flow rate on MD module performance, examples of experimental results obtained with prototype PGMD-09.8-050-BE are analysed and discussed. The experiments were conducted with tap water with a condenser inlet temperature of 25 °C, an

evaporator inlet temperature of $80\text{ }^{\circ}\text{C}$ and feed flow rates ranging from 200 to 500 kg h^{-1} . The experimental results as well as model predictions for the permeate output rate, the specific thermal and the specific electric energy consumption are given in Fig. 4.16. The temperature difference measured between the condenser outlet and the evaporator inlet is provided as supplementary information.

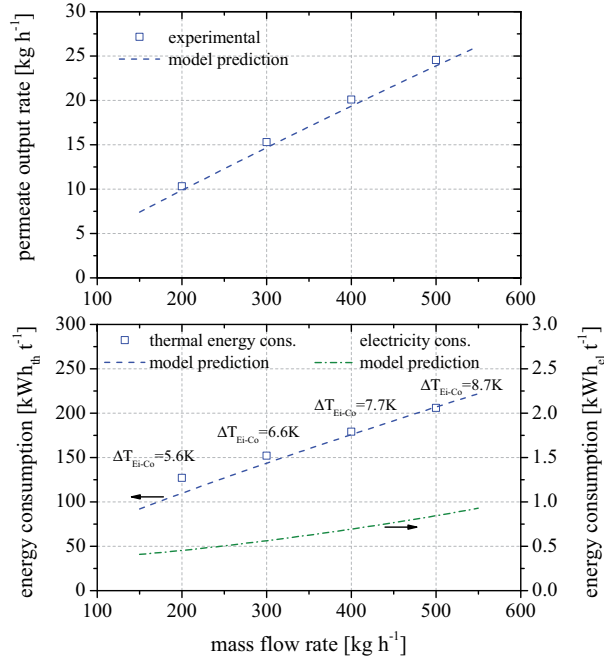


Figure 4.16: Influence of the mass flow rate on the module performance. Testing conditions: Module PGMD-09.8-050-BE, $T_{\text{Ei}} = 80\text{ }^{\circ}\text{C}$, $T_{\text{Ci}} = 25\text{ }^{\circ}\text{C}$, tap water.

The experimentally determined permeate output rates increase significantly with the feed flow rate and range from 10.3 to 24.5 kg h^{-1} . The permeate output rate seems to increase almost proportionally to the feed flow rate, e.g. doubling the feed flow rate from 200 to 400 kg h^{-1} leads to a doubled output rate. Based on the increasing hydraulic pressure loss at higher flow rates, the specific electricity consumption increases from 0.45 to $0.84\text{ kWh}_{\text{el}} \text{t}^{-1}$ with an increasing gradient for feed flow rates from 200 to 500 kg h^{-1} . The specific thermal energy consumption rises with feed flow rate and ranges from 127 to $207\text{ kWh}_{\text{th}} \text{t}^{-1}$. This is explained by the fact that the increasing feed flow rate results in an increased temperature difference across the membrane. In the given case, the temperature difference $\Delta T_{\text{Co-Ei}}$ increases from 5.6 K to 7.7 K , comparing the module operation at 200 and 400 kg h^{-1} . This behaviour is well known from conventional counter-current heat exchangers that show greater temperature differences from the primary to the secondary sides if the respective flow rates are increased. The greater temperature difference in the MD module causes larger local driving forces, and consequently higher local flux and a higher total output rate. Even though the output rate increases proportionally to the feed flow

rate, it cannot fully compensate the increased thermal energy input that depends on feed flow rate and temperature difference (see Eq. 4.52). The predicted influence of the mass flow rate on module performance shows good quantitative agreement with the experimental results. The maximal and mean errors of the model predictions are 4 % and 4 % for the permeate output rate and 14 % and 5 % for the specific thermal energy consumption. Especially for low-flow operation, the predicted energy consumption could not be fully reached by the experimental results. This observation might indicate non-optimal flow distribution for low-flow operation.

It turns out that the choice of flow rate for a given module design is a compromise between permeate output rate and energy efficiency. For a given MD system, the flow rate may be changed with time depending on the actual situation. Smart control systems could be implemented in order to adjust the flow operation based on the availability of energy and the demand for product water. The control systems may even feature predictive functionalities in order to optimise the control strategy.

Influence of the Feed Water Salinity on Module Performance

To investigate the general influence of the feed water salinity on MD module performance, examples of experimental results obtained with prototype PGMD-09.8-050-BE are analysed and discussed. The experiments were conducted with artificial sea water with a condenser inlet temperature of 25 °C, an evaporator inlet temperature of 80 °C and a feed flow rate of 400 kg h⁻¹. Different salt solutions with salinities from 0 to 105 g kg⁻¹ were prepared by dissolving sea salt from Seequasal in tap water. The experimental results as well as model predictions for the permeate output rate, the specific thermal and the specific electric energy consumption are given in Fig. 4.17. The temperature difference measured between the condenser outlet and the evaporator inlet is provided as supplementary information. Extensive experimental work on the quantitative influence of the feed water salinity on the performance of full-scale PGMD modules in the context of various operating conditions has already been published by the author of this thesis [66].

A negative influence of salt on the permeate output rate, the specific thermal energy consumption and the electric energy consumption is observed from the experiments. By using a usual sea water concentration of approximately 35 g kg⁻¹ instead of tap water, the permeate output rate decreases from 20.1 to 16.3 kg h⁻¹. The permeate output rate decreases almost linearly when the feed water salinity is increased. For a salinity level of 105 g kg⁻¹, the permeate output rate is halved with respect to the tap water performance. The temperature difference between the evaporator and the condenser bulk streams slightly increases with salinity, due to the decreased latent heat transfer. Since the thermal capacity of the feed water decreases slightly with increasing salinity, the thermal power input remains almost constant throughout all experiments. Due to the decreasing permeate output rate in the denominator of the equation to evaluate the specific thermal energy consumption, the thermal energy consumption shows exponential behaviour.

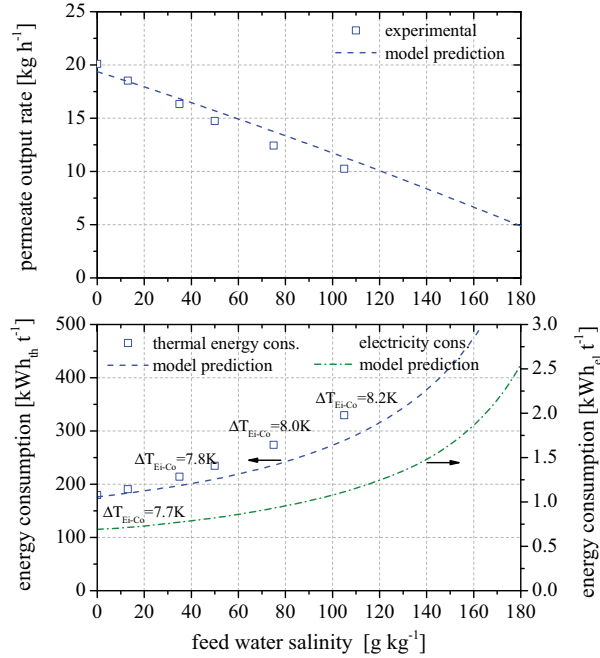


Figure 4.17: Influence of the feed water salinity on the module performance. Testing conditions: Module PGMD-09.8-050-BE, $T_{Ei} = 80^\circ\text{C}$, $T_{Ci} = 25^\circ\text{C}$, $\dot{m}_{Ci} = 400\text{ kg h}^{-1}$, artificial sea water.

By using a usual sea water concentration of approximately 35 g kg^{-1} instead of tap water, the energy consumption increases from 180 to $214\text{ kWh}_{th}\text{ t}^{-1}$. The pressure loss and consequently the required absolute pumping power is almost constant throughout the experiments, so the specific electricity consumption increases with salinity.

The predicted influence of salinity on module performance shows reasonable quantitative agreement with the experimental results. The maximal and mean errors of the model predictions are 11% and 6% for the permeate output rate and 15% and 9% for the specific thermal energy consumption. Especially at high feed water salinities, the predicted energy consumption is lower than the experimental results. Similar deviations have already been observed for the single-node model in Fig. 3.36.

The underlying phenomenon that leads to the negative effect of salinity on process performance is the decrease of the process driving force, which results from the lower evaporator vapour pressure accompanying an increasing concentration of salt ions. Since the vapour pressure for a given salinity is reduced by a specific offset, the corresponding relative influence is strongly dependent on the total driving force. According to the results presented in Fig. 3.37, MD fundamentally shows lower sensitivity to salinity for higher bulk stream temperature differences. For a given module, the temperature difference from the evaporator to the condenser side may be adjusted by the choice of suitable operating conditions, such as higher flow rates. The general recommen-

dition of low-flow operation for intensive heat recovery, that could be derived from Fig. 4.16, may not be applicable for module operation at significant salinity. Considering a given module and feed water salinity, there is an optimal flow rate with regard to energy efficiency, leading to the lowest possible specific energy consumption. For higher feed water salinities, this optimal flow rate increases.

It is important to note that the negative effect of salt on evaporation performance is generally valid, but the driving force and consequently the process sensitivity to salt is determined by the MD configuration, the geometrical module design, the active materials and the operating conditions. Due to the complex interdependence of effects associated with the influence of salt, operating conditions and module design, each individual scenario needs to be evaluated quantitatively. This topic will be addressed in the coming sections.

Influence of Active Deaeration on Module Performance

The beneficial effect of active deaeration on MD performance has already been discussed in detail in Chapter 3.

Deaeration in the context of the DCMD and PGMD variants explicitly refers to the membrane pore volume and may be indirectly implemented by the use of deaerated feed water (see Sec. 3.4.2). Even though the phenomenology of deaeration is identical for the DCMD and PGMD variants, individual constraints require consideration for practical implementation. The operation of a PGMD module introduces specific advantages with respect to deaeration compared to the operation of a DCMD module. Unlike DCMD, only one hydraulic loop has to be deaerated in PGMD, if membrane deaeration is based on feed water deaeration. The membrane is flushed by the feed water only on the evaporator side, while the condenser side of the membrane is hydraulically separated from the cooling fluid by the impermeable film material. Thus, air cannot be expelled into the membrane from the back surface. Extensive experimental work on the fundamental effects of feed water deaeration and its quantitative influence on the performance of full-scale PGMD modules in the context of various operational conditions has already been published by the author of this thesis [22].

In contrast to DCMD and PGMD, deaeration in the context of AGMD refers to the combined membrane and gap volume and may be implemented by direct gap deaeration. Even though the physical effect of deaeration on module performance is similar for all of the MD configurations, a separate discussion of the specific role of direct gap deaeration in AGMD is required, which is provided in Sec. 4.3.4.

In this section, the general influence of membrane deaeration on module performance has been investigated, based on experimental results from prototype PGMD-09.8-050-BE which was operated with and without feed water deaeration. The feed water was deaerated at the maximal capacity of the vacuum pump, achieving a deaeration pressure as low as 0.042 bar. The experiment was conducted with tap water, a condenser inlet temperature of 25 °C, an evaporator inlet

temperature of $80\text{ }^{\circ}\text{C}$ and a feed flow rate of 400 kg h^{-1} . An ideal air pressure distribution is assumed within the module for the model predictions, that have been evaluated for deaeration pressures from atmospheric pressure to full vacuum. Dalton's law is applied to evaluate the local air pressure from the deaeration pressure and the local water vapour pressure. A detailed description on the basic modelling of the pressure distribution is given in Sec. 4.1. In the analysis, a special focus is placed on the role of deaeration with respect to the specific electricity consumption. The power consumption for fluid circulation is estimated by Eq. 4.59 considering the pressure drop in the module flow channels, the heat exchanger and optionally in the deaeration module, while the power consumption for the vacuum pump is derived separately with Eq. 4.63. Two different scenarios have been considered for the evaluation of Eq. 4.61, defining the amount of saturated water that needs to be deaerated. In the first scenario, the water stream for the deaeration module is chosen equal to the module feed flow rate ($Z = 1$), representing the most conservative estimation. In the second scenario, appreciable recirculation is considered ($Z = 10$), which significantly reduces the raw water requirement and the deaeration effort. The experimental results as well as model predictions for the permeate output rate and the specific thermal and electrical energy consumption are given in Fig. 4.18. The temperature difference measured between the condenser outlet and the evaporator inlet is provided as supplementary information.

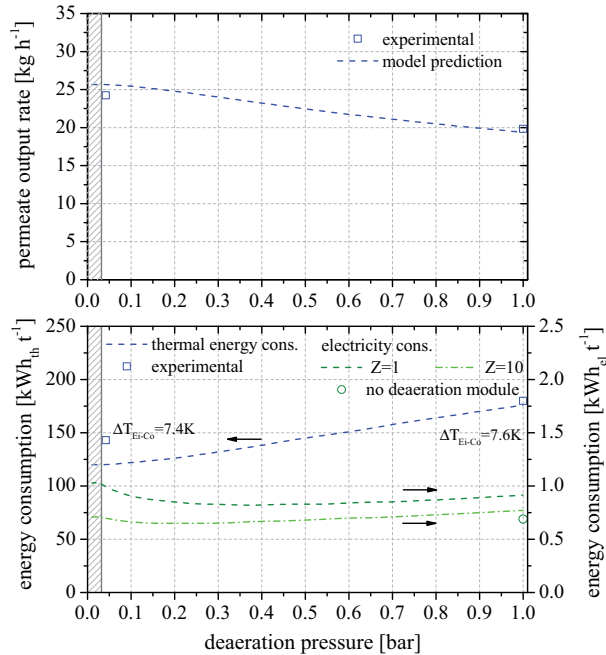


Figure 4.18: Influence of feed water deaeration on the module performance for different deaeration pressures. Testing conditions: Module PGMD-09.8-050-BE, $T_{\text{Ei}} = 80\text{ }^{\circ}\text{C}$, $T_{\text{Ci}} = 25\text{ }^{\circ}\text{C}$, $\dot{m}_{\text{Ci}} = 400\text{ kg h}^{-1}$, tap water.

Without deaeration, the module performance obtained was close to the results that have al-

ready been presented in the previous sections, showing a permeate output rate of 19.8 kg h^{-1} and a specific thermal energy consumption of $180 \text{ kWh}_{\text{th}} \text{ t}^{-1}$. When the deaeration pressure is successively decreased, a steady improvement of the thermodynamic module performance is expected from the model predictions. A lower limit for the deaeration pressure is expected at approximately 0.032 bar, representing the boiling pressure at the given condenser inlet temperature. The pressures below the limiting vapour pressure are indicated by the grey hatched area. The deaeration pressure of 0.042 bar achieved in the experiments is close to the lower limit. In the experiment, the O_2 concentration in the feed water was reduced by approximately 90%. By applying active feed water deaeration, the permeate output rate was increased by 20% to 24.2 kg h^{-1} , even though the bulk stream temperature difference from the evaporator to the condenser channel decreases by 0.2 K. This gives an indication that the total transferred thermal power remains almost constant, while the total thermal efficiency obviously increases due to the higher fraction of latent heat transfer. In the described experiments, the module's overall thermal efficiency increases from 63% to 75% by applying active deaeration. As a consequence, the specific thermal energy consumption reduces by 22%, reaching a value of $143 \text{ kWh}_{\text{th}} \text{ t}^{-1}$. The model predictions reflect the fundamental effect of feed water deaeration. From the model predictions, a performance enhancement of 32% is expected for the permeate output rate and the thermal energy consumption. For deaerated operation, the error of the model prediction is 6% for the permeate output rate and 16% for the specific thermal energy consumption. One reason for the deviation might be a non-ideal deaeration of the membrane pore volume in the experiments, which cannot be directly verified by measurement.

The specific electricity consumption for module operation without deaeration is estimated to be $0.69 \text{ kWh}_{\text{el}} \text{ t}^{-1}$, based on the hydraulic pumps for fluid circulation only. A breakdown of the electricity consumption according to the different load categories is presented in Fig. 4.19. Approximately one half of the electricity consumption is attributed to the pressure loss in the module flow channels, while the rest is evenly distributed among the heat exchangers for heating and cooling. If deaeration is applied, a deaeration module is introduced into the hydraulic loop and causes an additional pressure loss. As a consequence, the electricity consumption raises from 0.69 to $0.92 \text{ kWh}_{\text{el}} \text{ t}^{-1}$, if the entire module feed flow is forced through the deaeration module (refer to Fig. 4.18). When the deaeration pressure is successively reduced, the electricity consumption is composed of the decreasing specific power for fluid circulation and increasing power for air removal. The additional power consumption for the vacuum pump is outweighed by the increasing module performance and a local minimum in the specific electricity consumption curve is expected at a deaeration pressure of approximately 0.35 bar. For lower deaeration pressures, the increasing power consumption of the vacuum pump is not fully compensated by the higher output rate and the specific electricity consumption increases. The specific role of the deaeration equipment for the electricity consumption is clarified in Fig. 4.19, that provides a detailed break-down of the energy consumption for a deaeration pressure of 0.05 bar. A fraction of 47% may be attributed to the deaeration equipment, including the vacuum pump and the pressure drop in the deaeration module. If recirculation is applied, the deaeration power is expected to decrease significantly. One scenario is comparatively analysed in Figs. 4.18 and

4.19, considering a recirculation factor of 10. Since the module feed flow rate remains the same, the electricity consumption associated with the module flow channels and the heat exchangers is not affected by the recirculation factor. However, according to Eq. 4.61, the flow rate that is considered for the deaeration module is significantly lowered from 400 kg h^{-1} to 150 kg h^{-1} , if recirculation is applied. Thus, the electrical load associated with the pressure loss in the deaeration module and the load associated with the air removal is reduced. The specific electricity consumption with deaeration of $0.69 \text{ kWh}_{\text{el}} \text{ t}^{-1}$ turns out to be equal to the energy consumption without deaeration.

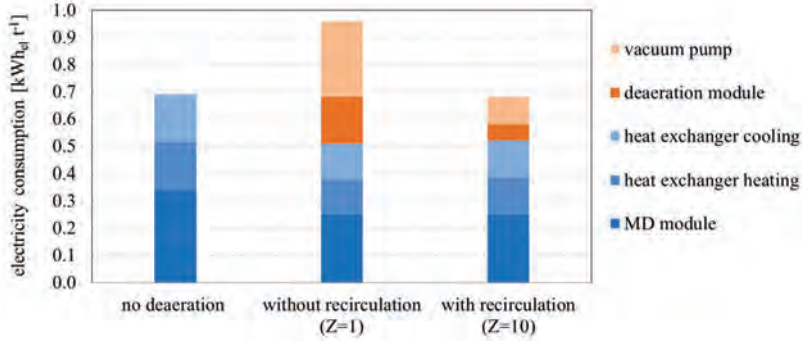


Figure 4.19: Detailed break-down of the electricity consumption for the PGMD process from Fig. 4.18, comparing a scenario without deaeration and two scenarios with a deaeration pressure of 0.05 bar. The flow rate for the deaeration module is 400 kg h^{-1} , if no recirculation is considered and 150 kg h^{-1} if recirculation is considered. General assumptions: $\Delta\hat{p}_{\text{HX}} = 0.15 \text{ bar}$; $\Delta\hat{p}_{\text{CX}} = 0.15 \text{ bar}$; $\Delta\hat{p}_{\text{D}} = 0.20 \text{ bar}$; $\eta_{\text{HP}} = 50 \%$; $\eta_{\text{VP}} = 15 \%$.

As stated earlier, further and more comprehensive results on the topic of deaeration have been published in [22]. The paper presents experimental results on the fundamental possibility to deaerate membranes by deaerating the feed water, on deaeration dynamics and the dependence of the deaeration effects on temperature. The impact of deaeration in different temperature zones of the module is demonstrated by means of a split-module analysis.

The role of the vacuum pump on the overall total electricity demand should be evaluated individually for each scenario, taking system design, deaeration module design, recirculation strategy, operating conditions and pumping efficiencies into consideration. The results presented in this section demonstrate that the deaeration power could be fully compensated and even outweighed by the enhanced thermodynamic module performance. It should be noted that the estimation of the electricity consumption of the vacuum pump in this thesis is based on theoretical considerations. Further and more detailed studies on the actual energy requirements for deaeration are required. This includes experimental evaluation of thermodynamic losses, leakages and the fraction of vapour that passes through the vacuum pump as well as the characterisation of different suitable vacuum pump designs. Especially the assumptions for potential savings by brine recirculation should be subject to some experimental validation and adjustment in future work. Further considerations on the deaeration approach should address the change of the chemical

equilibria in the water that might promote scale formation in the deaeration module, the MD module or other system components.

Improving Heat Recovery: Increasing the Channel Length or Connecting Multiple Modules in Series

To improve the module's capability for heat recovery, the transfer area has to be increased. This may be achieved by simply increasing the channel length for the module. An equivalent thermodynamic effect is achieved by connecting multiple modules in series. An upper limit for the module channel length is given by the mechanical load on the membrane/film materials due to the hydraulic pressure loss. If multiple modules are to be used in series, this limitation may be overcome by designing a system with hydraulic pressure relaxation between the modules.

To investigate the general influence of the flow channel length on MD module performance, experimental results obtained with prototypes PGMD-04.9-050-BE, PGMD-09.8-050-BE and PGMD-14.0-050-BE are analysed and discussed. This set of modules provides channel lengths of 3.5 m, 7.0 m and 10.0 m at a constant channel height of 0.7 m. The experiments were conducted with tap water under identical operating conditions with a condenser inlet temperature of 25 °C, an evaporator inlet temperature of 80 °C and a feed flow rate of 400 kg h⁻¹. The experimental results as well as model predictions for the permeate output rate, the mean flux, the specific thermal energy consumption and the specific electricity consumption are given in Fig. 4.20. The temperature difference measured between the condenser outlet and the evaporator inlet is provided as supplementary information.

The increasing channel length does not have a strong influence on the total permeate output rates, even though the active membrane surface area increases proportionally to the channel length. Comparing the results at 3.5 m and 10.0 m, the permeate output rate increases by only 8.5 % from 19.1 to 20.7 kg h⁻¹, while the membrane surface area is increased by a factor of 2.9. Analysing the results specific to the membrane surface area, the flux reduces from 3.9 to 1.5 kg (m² h)⁻¹ if the channel length is increased from 3.5 m to 10.0 m. The specific thermal energy demand is reduced significantly when the prototypes with longer flow channels are used. The thermal energy consumption was reduced by about 57.1 % from 315 to 135 kWh_{th} t⁻¹ by increasing the channel length from 3.5 m to 10.0 m. The increased channel length results in a smaller temperature difference across the membrane. In the given case, the temperature difference ΔT_{Co-Ei} decreases from 12.9 K to 5.9 K, comparing the modules with channel lengths of 3.5 m and 10.0 m. This behaviour is well known from conventional counter-current heat exchangers, that show small temperature differences from the primary to the secondary sides if sufficient heat transfer area is available. The smaller temperature difference in the MD module reduces the local driving force and consequently the local flux. Eventually, the positive effect of an increased membrane surface area is outweighed by the reduced flux. However, since the required ther-

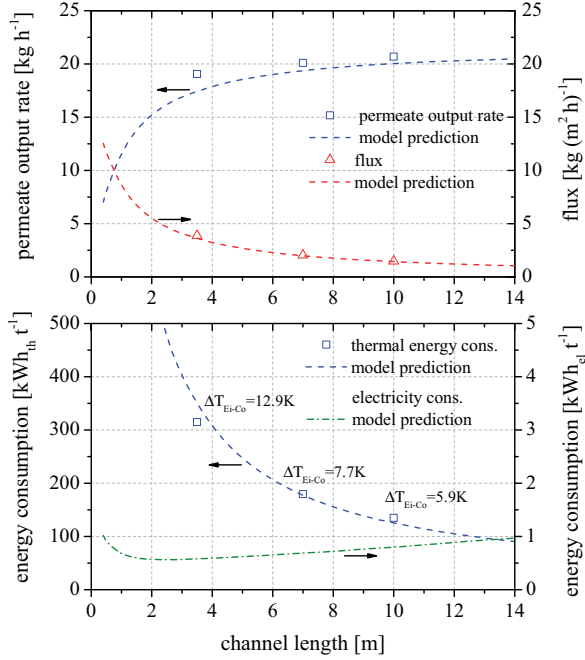


Figure 4.20: Influence of the channel length on the module performance. Testing conditions: Modules PGMD-04.9-050-BE, PGMD-09.8-050-BE and PGMD-14.0-050-BE, $T_{Ei} = 80^\circ\text{C}$, $T_{Ci} = 25^\circ\text{C}$, $\dot{m}_{Ci} = 400\text{ kg h}^{-1}$, tap water.

mal energy demand is proportional to the temperature difference ΔT_{Co-Ei} , the specific thermal energy consumption decreases significantly for modules with longer flow channels. Due to the increasing hydraulic pressure loss for longer flow channels, the specific electricity consumption increases almost linearly from 0.58 to $0.80\text{ kWh}_{el}\text{ t}^{-1}$ for reasonable channel length's from 3.5 to 10 m . For very short flow channels, the output rate decreases significantly, leading to increased electricity consumption.

The influence of the channel length on module performance is represented by the model predictions with good quantitative agreement with the experimental results. The maximal and mean error of the model predictions are 9% and 5% for the permeate output rate and 11% and 7% for the specific thermal energy consumption.

It is obvious from the given results that the channel length (or the optimal number of modules in series) is a crucial parameter determining the conflicting performance parameters, flux and thermal energy demand. One has to decide between a module concept allowing high fluxes or a module concept allowing reasonable heat recovery. The opposing module operating concepts are referred to as high-flux and high-recovery approaches. If maximal fluxes are required from a given scenario, there might not be any heat recovery at all. The definition of the optimal module channel length (or the optimal number of modules in series) is a classic optimisation problem that needs reconsideration for each scenario. It is important to note that salt significantly influ-

ences the performance, especially for high-recovery modules with rather low driving forces. The impression from Fig. 4.20, indicating improved energy efficiency for longer flow channels needs to be reevaluated carefully for saline feed waters. Depending on feed water salinity, the specific thermal energy consumption may even increase for increasing channel lengths. The optimal channel length for a given feed water salinity fundamentally tends towards shorter channels with increasing feed water salinity. An experimental proof of this interdependence has been published by the author of this thesis [66].

An optimal channel length needs to be identified, based on module performance, material costs and costs for thermal and electrical energy. This complex optimisation problem will specifically be addressed in Chapter 5. Subsequent to the conceptual thermodynamic optimisation, the influence of the identified channel length on an economically feasible module design has to be taken into consideration. In terms of fabrication, the spiral-wound module concept is quite advantageous for the production of long flow channels, since the fabrication effort is almost independent of channel length. For producing short flow channels the winding process seems to be quite elaborate and the fabrication procedures for plate-and-frame modules offer advantages.

Up-Scaling the Output Rate:

Increasing the Channel Height or Connecting Multiple Modules in Parallel

To scale up the module output rate, the channel height of the module may be increased. If the flow rate is scaled up proportionally, the permeate output rate increases while the thermodynamic operating conditions and consequently the specific thermal and electrical energy consumption are retained. This up-scaling concept is limited by availability of the materials and the required equipment for module fabrication. Since module flow channels must be oriented vertically for efficient removal of air, high flow channels automatically involve appreciable hydrostatic pressure at the base which pre-loads the materials and may lead to inhomogeneous deformation of the channel form. Moreover, it is anticipated that the homogeneity of the flow distribution over the channel height, which is expected to be non-optimal near the inlets and outlets, is fundamentally improved for an increasing channel length-channel height ratio. Alternatively to the up-scaling concept based on modules with high flow channels, a similar effect is achieved by parallel connection of multiple flow channels or modules. This concept overcomes the limitations due to available materials, fabrication tools or the hydrostatic head. In principle, the up-scaling concept based on module parallel connection is not limited. However, considering the number of modules that might be connected in one branch (one pump, one heat exchanger), a limitation is given by the non-ideal hydraulic parallelisation of multiple flow channels or modules. If multiple modules are hydraulically connected to one inlet manifold, the total inlet flow rates of the evaporator and the condenser channels are split into fractions. After passing through the modules, the split streams are mixed again within the evaporator and the condenser outlet manifolds. The mass flow fractions of the single hydraulic lines depend on the pressure loss characteristics of the module flow channels and the piping. Considering a parallel connection with identical modules

and a well-designed hydraulic layout, a rather homogeneous flow distribution may be possible. However, sub-optimal quality of the module production, the piping and other effects like scale formation may cause non-ideal flow distribution. Two different forms of inhomogeneous flow distribution for modules in parallel connection have been identified. A symmetric inhomogeneity in flow distribution occurs if some modules are operated at higher than nominal flow conditions while other modules are operated at lower than nominal flow conditions. However, each module is operated symmetrically since the flow rates of its own evaporator and condenser channels are equal. This form of inhomogeneity is expected if the hydraulic pressure losses over the different modules or the associated piping are considerably different. If the evaporator and the condenser inlet flow rates of the individual modules differ while the mean flow rates of the modules remain constant, an asymmetric inhomogeneity in flow distribution results. A schematic illustration of different flow distributions is given in Fig. 4.21. For reasons of simplicity, a parallel connection of only two modules is considered, illustrating the general effects that apply also for systems containing more than two modules.

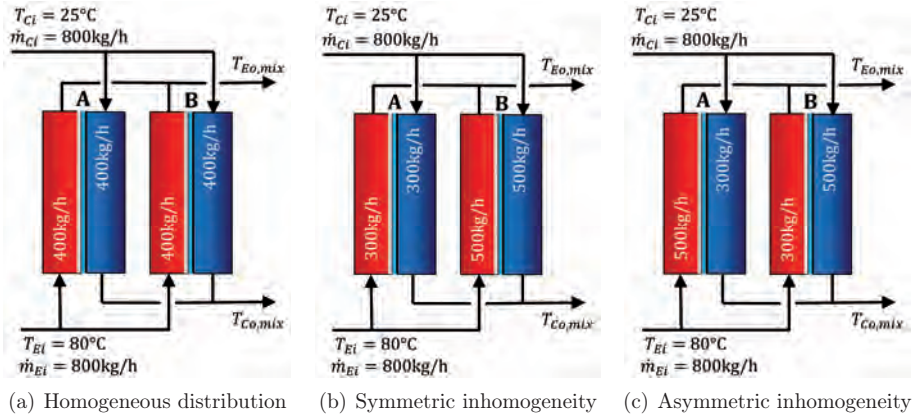


Figure 4.21: Different flow distribution patterns in parallel-connected modules.

In the given example, the evaporator and the condenser inlet streams are rated with 800 kg h^{-1} , determining the nominal inlet flow rate conditions of 400 kg h^{-1} for each of the individual module flow channels. In Fig. 4.21(a), the flow distribution is ideal and both modules are operated at equal (nominal) conditions, symmetrically. An example of symmetric inhomogeneity is given in Fig. 4.21(b), where one module is operated symmetrically with 300 kg h^{-1} while the other module is operated symmetrically with 500 kg h^{-1} . An example of asymmetric inhomogeneity is given in Fig. 4.21(c), where the evaporator and condenser channels of the modules are operated asymmetrically with $500/300 \text{ kg h}^{-1}$ and $300/500 \text{ kg h}^{-1}$, respectively.

A quantitative measure for the inhomogeneity of two modules may be defined, based on characteristic parameters that are derived from each module's mean flow rate in Eq. 4.75 and the asymmetry of individual module operation in Eq. 4.76. Symmetric inhomogeneity is defined in Eq. 4.77 and asymmetric inhomogeneity is defined according to Eq. 4.78. The quantitative inho-

mogeneities for the symmetric and asymmetric cases in Fig. 4.21 are both 200 kg h^{-1} , while the inhomogeneity of the ideal case is rated with 0 kg h^{-1} . In multi-module systems, a combination of symmetric and asymmetric inhomogeneity is most likely.

$$\bar{m}_{\text{Ei-Co}} = \frac{1}{2}(\dot{m}_{\text{Ei}} + \dot{m}_{\text{Co}}) \quad (4.75)$$

$$\Delta\dot{m}_{\text{Ei-Co}} = \dot{m}_{\text{Ei}} - \dot{m}_{\text{Co}} \quad (4.76)$$

$$\text{symmetric inhom. } (\Delta\dot{m}_{\text{Ei-Co}}^{A/B} = 0) : \Delta\bar{m}_{\text{sym}}^{A-B} = \bar{m}_{\text{Ei-Co}}^A - \bar{m}_{\text{Ei-Co}}^B \quad (4.77)$$

$$\text{asymmetric inhom. } (\bar{m}_{\text{Ei-Co}}^A = \bar{m}_{\text{Ei-Co}}^B) : \Delta\bar{m}_{\text{asym}}^{A-B} = \frac{1}{2}(\Delta\dot{m}_{\text{Ei-Co}}^A + \Delta\dot{m}_{\text{Ei-Co}}^B) \quad (4.78)$$

An investigation has been made in order to quantify the influence of non-ideal module parallelisation on module performance. The influences of symmetric inhomogeneities were derived from the experimental and theoretical results that have already been presented in Fig. 4.16. For the experimental characterisation regarding the influence of asymmetric inhomogeneities, four modules ($3 \times \text{PGMD-09.8-050-BE}$, $1 \times \text{PGMD-09.8-050-BC}$)¹ have been chosen as examples. Initially, reference results with guaranteed ideal flow distribution were generated by characterisation of each of the single modules alone. For the multi-module measurements, the modules were mounted in the test rig in parallel connection according to Fig. 4.8. An almost ideal flow distribution was achieved by balancing the pressure losses with hydraulic restrictors. Comparing the mean results of the individual characterisation and the mean results of the multi-module characterisation, the difference in the permeate output rate is 2.4%, whereas the difference in the thermal energy consumption is 3.8%. Based on these results, the flow distribution is expected to be close to the ideal case. Afterwards, asymmetric inhomogeneities in flow distribution were intentionally set to 20, 60 and 100 kg h^{-1} by adjusting the restrictors. All experiments were conducted with a nominal flow rate of 400 kg h^{-1} per module, a condenser inlet temperature of $25 \text{ }^\circ\text{C}$, an evaporator inlet temperature of $80 \text{ }^\circ\text{C}$ and tap water. The experimental results as well as model predictions for the permeate output rate, the specific thermal and the specific electrical energy consumption are given in Fig. 4.22.

Adjusting the flow distribution for the four modules to an optimal flow distribution leads to a higher mean permeate output rate than one might expect from the results presented in Fig. 4.16. One of the modules has a higher performance due to a slightly different design. However, the specific effect due to a slightly different module design is considered to be insignificant for the given investigation, since the main focus is on quantification of the effects due to inhomogeneous flow distribution.

It turns out that the overall module performance is almost independent of symmetric inhomogeneities in flow distribution. When the symmetric inhomogeneity increases from 0 to 200 kg h^{-1} , the mean permeate output rate of the modules decreases by only 0.9%, while the specific thermal

¹Due to the limited availability of modules, one of the four modules differs in its backing position.

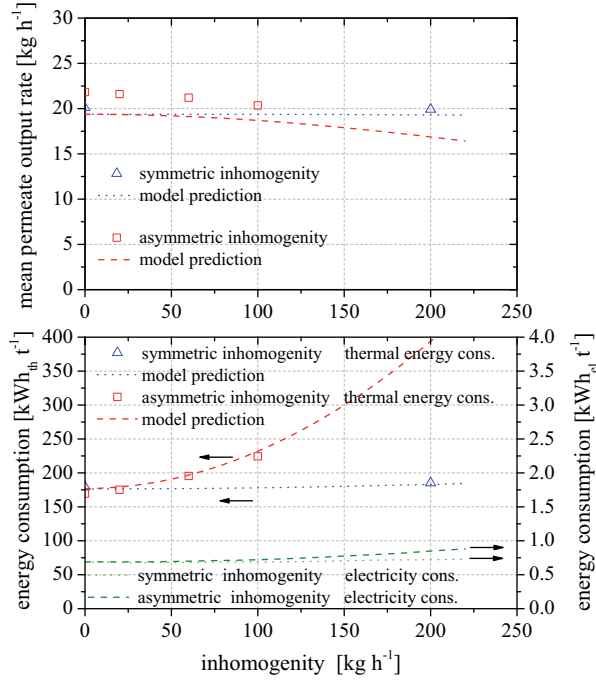


Figure 4.22: Influence of non-ideal module parallelisation based on inhomogeneities in mass flow distribution. Testing conditions: Modules of type PGMD-09.8-050-BE $\dot{m}_{Ci} = 400 \text{ kg h}^{-1}$, $T_{Ei} = 80^\circ\text{C}$, $T_{Ci} = 25^\circ\text{C}$, tap water.

energy consumption increases by 3.2%. The low sensitivity is explained by the fact that disadvantages arising in one module are almost fully compensated by benefits in a second module. This behaviour is also obvious from the almost linear curves in Fig. 4.16. The model predictions reflect the low sensitivity of the module performance to symmetric inhomogeneities. The theoretical results are based on the high quality of the model predictions that have already presented in Fig. 4.16. The predicted increase of 4% in electricity consumption indicates significant sensitivity due to the non-linear behaviour of the pressure loss with flow rate.

Analysing the experimental results obtained for an asymmetric flow distribution of 100 kg h^{-1} , the mean permeate output rate decreases by 6.8%, while the specific thermal energy consumption increases by 32.4% compared to the ideal case. Even higher sensitivities are expected for greater inhomogeneities. The strong effect of asymmetric operation on the thermal energy consumption is mainly explained by the influence on the temperature profiles along the module flow channels. Again the similarity of an MD module and a common heat exchanger is used to interpret the observed thermodynamic behaviour. If the mass flow rates and consequently the mass flow capacities¹ in both flow channels are similar, a rather parallel temperature profile with a constant temperature difference along the flow channels is expected ($\Delta T_{Ei-Co} = \Delta T_{Ci-Eo}$). If the mass

¹mass flow capacity: ($\dot{m} c_p$)

flow capacities in the flow channels differ, an asymmetric temperature profile with a varying temperature difference along the flow channels is expected ($\Delta T_{Ei-Co} \lesssim \Delta T_{Ci-Eo}$). This specific effect is quantitatively evaluated and further discussed in the context of a DCMD module in the following Sec. 4.3.2. Having multiple modules operated asymmetrically in a parallel connection, the different exergy levels of the preheated streams are mixed, reducing the efficiency of the heat recovery. Due to the physical modelling approach, the model predictions reflect the influence of asymmetric operation on the temperature profiles and consequently the corresponding sensitivity of the module performance characteristics with good quantitative agreement. Comparing the predicted and the experimentally obtained permeate output rates, an offset of approximately 10 % is observed. The fact that the offset is almost constant indicates a good representation of the specific effects based on the inhomogeneity. The offset itself is mainly attributed to the inconsistent design of the module prototypes. A very good agreement is given for the predicted specific thermal energy consumption. Here, the experimental results have been reproduced by the model with a maximal and a mean difference of only 3 % and 1 %. The electricity consumption is expected to increase by 27 % due to the reduced permeate output rate and the occurrence of higher flow velocities.

The given results clearly indicate the negative influence of asymmetric operation on the module performance, especially on the internal heat recovery. When designing multi-module systems, special attention has to be paid to the hydraulic layout and the equality of the modules' characteristic pressure curves. Moreover, the flow distribution may be actively balanced by use of static or adjustable hydraulic restrictors. It should be remembered that additional hydraulic pressure losses are induced by the restrictors, which increase the specific electricity consumption. From a technical point of view, an up-scaling of the output rate is considered unlimited, if multiple modules are arranged in separate branches with individual pumps and heat exchangers.

The residual inhomogeneity within an MD multi-module branch eventually limits the potential for arbitrary up-scaling of the branch capacity by parallel connection of further modules. Therefore, the inhomogeneity within an MD module branch or alternatively the reduction of the average module performance characteristics with respect to ideal reference values might be suitable characteristics to compare different hydraulic system concepts, especially with respect to up-scaling.

Improving the Recovery Rate: Adapted Module Design or Feed Water Recirculation

For the basic module concepts presented in this thesis, the necessary thermal energy for evaporation is carried into the module with the evaporator inlet stream. The thermal energy and consequently the permeate output is limited by the sensible heat that is associated with the feed stream. Only 1 % to 8 % of the evaporator inlet mass flow may be extracted as permeate. To overcome the limitation due to the recovery rate, the heating fluid could be hydraulically

separated from the feed stream e.g. by an additional impermeable film layer. In this way, the mass flow rate for the heating stream may be increased independently of the feed flow rate (refer to Sec. 2.2.2).

An alternative way to adjust the system recovery rate independently of the feed flow rate may be achieved by brine recirculation. The following analysis gives an indication of the salinity levels that need to be treated by the module in order to achieve a certain recovery rate. For the given analysis, the module itself is considered to have a module recovery rate of 5%. The resulting module evaporator inlet and outlet salinities presented in Fig. 4.23 were derived from Eqs. 4.37 and 4.38 for raw water salinities of 10, 35, 70 and 100 g kg⁻¹.

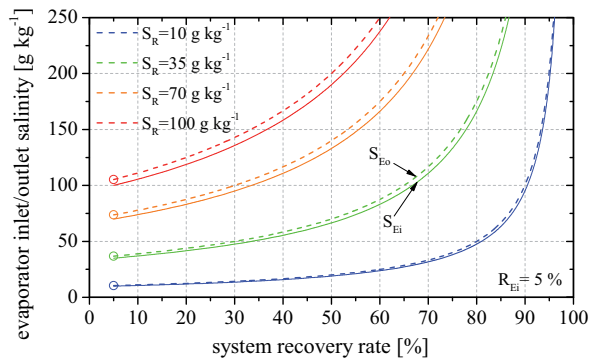


Figure 4.23: Adjustment of the system recovery rate by brine recirculation. Fundamental dependence of the recovery rate on evaporator inlet and outlet salinity for different raw water salinities. The module recovery rate is assumed to be 5%.

The minimum system recovery rate is defined by the module recovery rate of 5%. At this operation point, no brine is recirculated and the evaporator inlet salinity is equal to the raw water salinity. The evaporator outlet concentration is higher than the evaporator inlet concentration based on the extraction of 5% of the input volume flow as pure water. Due to the assumption of a constant module recovery rate, the increase in salinity within the module is higher for higher inlet salinities. Aiming for a system recovery rate of 50%, the brine salinity is twice as high as the raw water salinity. For low raw water salinities, the recovery rate may be significantly increased without reaching high evaporator inlet salinities. Considering brackish water with a salinity of 10 g kg⁻¹, the system recovery rate could be increased from 5% to 80% while the evaporator inlet salinity is still lower than 50 g kg⁻¹.

No separate experimental investigation and model validation on the influence of recirculation on module performance is necessary, since the thermodynamic effects may be referred directly to the influence of salinity on module performance. From a practical point of view, it is important to note that an increasing recovery rate generally raises the probability of scale formation.

4.3.2 Specific Aspects of Direct Contact Module Operation

The general performance characteristics of MD modules have already been clarified in the preceding section, that included a detailed discussion of the basic influences of the temperature conditions, the feed flow rate, the salinity, the state of deaeration and the basic flow channel design. However, besides these general aspects that apply to all of the MD configurations, some important aspects that only apply to specific MD configurations still require clarification. The following section completes the general discussion for DCMD modules, by covering the specific aspects that apply only to DCMD module operation. The associated experimental work has been performed with the spiral-wound prototype DCMD-09.8-000-BE and the model predictions are based on the DCMD multi-node model that was presented earlier in Sec. 4.1.1.

Influence of External Heat Recovery on Direct Contact Module Performance

In contrast to PGMD and AGMD, that apply hydraulic separation of the condenser channel from the permeate, the permeate itself acts as the coolant in DCMD. In order to implement heat recovery in DCMD, heat has to be transferred from the preheated permeate to the feed stream by using an external recovery heat exchanger (RX), as illustrated in Fig. 4.5(b). Especially the evaluation of the thermal energy consumption is dependent on the heat transfer performance of the external recovery heat exchanger, for experimental as well as for simulated results. Consequently, a first step needs to clarify the role of the heat recovery system design on DCMD performance. The methods for such integrated evaluation have already been introduced in Sec. 4.1.4.

The results of the model-based analysis in Fig. 4.24 illustrate the quantitative influence of the external recovery heat exchanger on the thermodynamic performance, taking a module similar to prototype DCMD-09.8-000-BE operated at different mass flow rates as an example. The temperature profiles in the evaporator and the condenser channels are expected to be parallel in the recovery heat exchanger, since the condenser inlet flow rate is adjusted so that the condenser outlet flow rate is set equal to the evaporator inlet flow rate. The results for an ideal heat recovery system ($kA_{RX,ideal} \rightarrow \infty$) are given as an optimal reference. The nomenclature refers to Fig. 4.5(b).

The minimal thermal energy requirement of a DCMD module configuration is achieved when an ideal heat exchanger (RX) is assumed. The most energy-efficient operation with a specific thermal energy consumption of $71 \text{ kWh}_{th} \text{ t}^{-1}$ is expected for the lowest feed flow rate of 200 kg h^{-1} . However, a realistic evaluation of the DCMD energy demand may only be given by assuming a finite transfer performance of the external heat exchanger. The feed stream is preheated from temperature T_{RXi} to temperature T_{RXo} within the external heat exchanger. A limitation for the external heat recovery is given by the performance of the heat exchanger. Based on this limitation, the temperature gain of the feed stream in the recovery heat exchanger $\Delta T_{RXi-RXo}$

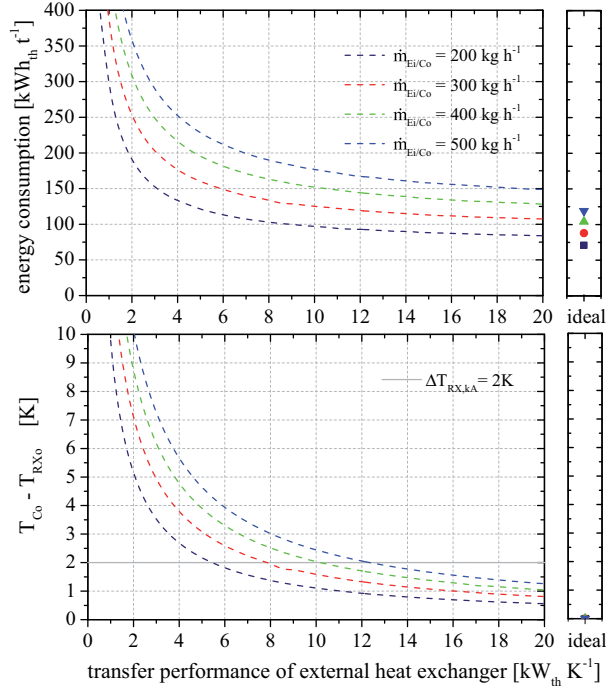


Figure 4.24: Model-based analysis of the influence of a non-ideal external recovery heat exchanger on temperature loss and specific thermal energy consumption for different mass flow rates. Simulation conditions: Module DCMD-09.8-000-BE, $T_{Ei} = 80\text{ }^{\circ}\text{C}$, $T_{Ci} = 25\text{ }^{\circ}\text{C}$, $S_{Ei/Ci} = 0\text{ g kg}^{-1}$.

decreases for higher flow rates and lower transfer performance. Consequently, the required thermal power input \dot{Q}_{HX} (Eq. 4.45) and the specific thermal energy consumption increase with increasing mass flow rates and decreasing transfer performance. The resulting energy consumption converges towards the ideal case, while the heat transfer performance of the external heat exchanger is improved.

The lower plot shows the temperature drop from the hot condenser outlet stream T_{Co} to the feed stream T_{RXo} , based on the limited heat transfer in the external heat exchanger. For an ideal heat exchanger, no temperature drop is associated with the external heat recovery. The lower the limiting transfer performance, the higher the respective drop in temperature. The temperature drop associated with a heat transfer performance of $8\text{ kW}_{th}\text{ K}^{-1}$ at a mass flow rate of 300 kg h^{-1} is 2 K , while the temperature drop could be reduced to 1 K , if the heat transfer performance is chosen to be $16\text{ kW}_{th}\text{ K}^{-1}$. The amount of heat that is available for external heat recovery depends on the mass flow rate, so a higher transfer performance is necessary for higher mass flow rates. In order to retain a temperature drop of 2 K while the mass flow rate is increased from 300 kg h^{-1} to 500 kg h^{-1} , the transfer performance needs to be increased from $8\text{ kW}_{th}\text{ K}^{-1}$ to $12\text{ kW}_{th}\text{ K}^{-1}$. Considering module operation at 300 kg h^{-1} , the temperature drop

of 2 K leads to a specific thermal energy consumption of $135 \text{ kWh}_{\text{th}} \text{ t}^{-1}$, compared to the ideal case of $88 \text{ kWh}_{\text{th}} \text{ t}^{-1}$.

The recovery heat exchanger needs to be chosen carefully, in order to optimise the thermal energy consumption and system costs. For systems with a nominal operation at high flow rates, the preferred heat exchanger size is larger than for low-flow operation systems. The assumption of constant heat transfer performance for the comparison of different operational modes may therefore reflect a rather unlikely case. In order to account for a probable adjustment of the heat exchanger dimensions to the chosen nominal operating conditions, a fixed temperature offset of 2 K is considered by simply modifying the limiting temperatures in Eqs. 4.49-4.51. In each energy-related analysis of DCMD modules presented in this thesis, the chosen temperature offset $\Delta T_{\text{RX,kA}}$ is explicitly indicated. For the module DCMD-09.8-000-BE, the resulting heat exchanger capacities that lead to the defined temperature drop of 2 K can be read from the highlighted intersections in Fig. 4.24.

It turns out that a clear definition of the external heat recovery strategy is necessary for a realistic energy-related analysis of a DCMD configuration with heat recovery. Especially for comparative analyses of different MD variants including DCMD, a detailed discussion of the respective assumptions is essential.

Influence of Asymmetric Operation on Direct Contact Module Performance

For a DCMD module, the inlet conditions for the evaporator and the condenser sides are independent and may be set differently. Thus, asymmetric DCMD operation is possible not only in multi-module systems but also in a single module system. For similar thermal fluid capacities in both flow channels, the difference of the mass flow capacity and consequently the intensity of asymmetric temperature profiles is based on the different mass flow rates only. If the salinity level is different on the evaporator and condenser sides, an additional asymmetry results due to the different thermal fluid capacities.

Since DCMD modules do not have an impermeable film between the evaporator and the condenser channels, the mass flow rate in the evaporator channel decreases while the mass flow rate in the condenser channel increases along the channel. This mass transfer is expected to have significant influence on the DCMD asymmetry and needs to be taken into consideration. For the usual counter-current operation, the asymmetry between the evaporator and condenser sides is constant along the channel and may be expressed by the definition stated in Eq. 4.76 which is transferred to Eq. 4.79.

$$\Delta \dot{m}_{\text{Ei-Co}} = \dot{m}_{\text{Ei}} - (\dot{m}_{\text{Ci}} + \dot{m}_{\text{P}}) \quad (= \Delta \dot{m}_{\text{Eo-Ci}}) \quad (4.79)$$

In order to study the influence of an asymmetric temperature profile in a single DCMD module, a testing series for module DCMD-098-000-BE was defined as given in Tab. 4.4. No salt was used on either the evaporator or the condenser sides, resulting in similar fluid thermal capacities on

both channel sides. The mean inlet mass flow rate was chosen to be 300 kg h^{-1} for each operation point. The quantitative asymmetry according to Eq. 4.79 is provided in the last column. It is obvious from Eq. 4.79 that the equal inlet mass flow rates in scenario #3 do not result in a balanced mass flow difference due to the transmembrane mass transfer. Symmetric operation is expected for scenario #2, where the transmembrane mass transfer is preventively compensated by an adjustment of the inlet mass flow rates. The experimental results as well as the model predictions are presented in Fig. 4.25, showing the permeate output rate, the specific thermal energy consumption, the resulting asymmetry in the temperature profiles and the temperature gain in heat exchanger HX for the different scenarios. For the evaluation of the thermal energy consumption, a temperature drop of 2 K is taken into consideration, accounting for a limited heat transfer in the external heat recovery system.

Table 4.4: Testing conditions for a study on asymmetric DCMD module operation.

Reference	\dot{m}_{Ei} [kg h ⁻¹]	\dot{m}_{Ci} [kg h ⁻¹]	T_{Ei} [°C]	T_{Ci} [°C]	S_{Ei} [g kg ⁻¹]	S_{Ci} [g kg ⁻¹]	$\Delta\dot{m}_{Ei-Co}$ [kg h ⁻¹]
#1	350	250	80	25	0	0	84
#2	308	292	80	25	0	0	0
#3	300	300	80	25	0	0	-16
#4	250	350	80	25	0	0	-116

The permeate output rate was observed to be in the range from 14.2 to 16.3 kg h^{-1} , showing only slight reduction for asymmetric operation. The maximum output rate is experimentally observed for scenario #2, for symmetric operation. Similar results are given by the model predictions, where the maximum output rate of 15.8 kg h^{-1} is observed at a mass flow difference of approximately 30 kg h^{-1} . The maximal and mean differences of the model prediction with respect to the measured permeate output rates are 14% and 7%.

The specific thermal energy consumption increases significantly for asymmetric operation, leading to experimental results from 146 to $405 \text{ kWh}_{th} \text{ t}^{-1}$. It turns out that the corresponding sensitivity is approximately $100 \text{ kWh}_{th} \text{ t}^{-1}$ per mass flow difference of 50 kg h^{-1} . An energy consumption of $177 \text{ kWh}_{th} \text{ t}^{-1}$ was evaluated for scenario #3 with equal inlet mass flow rates. By adjusting the inlet flow rates according to the transmembrane mass transfer of approximately 16 kg h^{-1} in scenario #2, the energy consumption is reduced to $146 \text{ kWh}_{th} \text{ t}^{-1}$. Operation with balanced mass flow rates achieved by flux compensation represents the most efficient operation point for the experiments as well as for the model predictions. The maximal and mean differences of the model prediction from the measured thermal energy consumption are 12% and 6%.

The temperature gain in the heat exchanger HX (ΔT_{Ei-RXo}) that is necessary to heat the feed stream to the requested evaporator inlet temperature of 80°C is provided in the lower plot. A comparison of the temperature gain and the associated specific energy consumption clearly reflects their proportional correlation. Since the evaporator inlet temperature is set constant throughout the study, it is obvious that the highest preheating temperature (T_{RXo}) is achieved for symmetric operation conditions. A higher temperature gain in the heat exchanger HX is necessary for asymmetric operation, due to the inefficient heat recovery in heat exchanger RX.

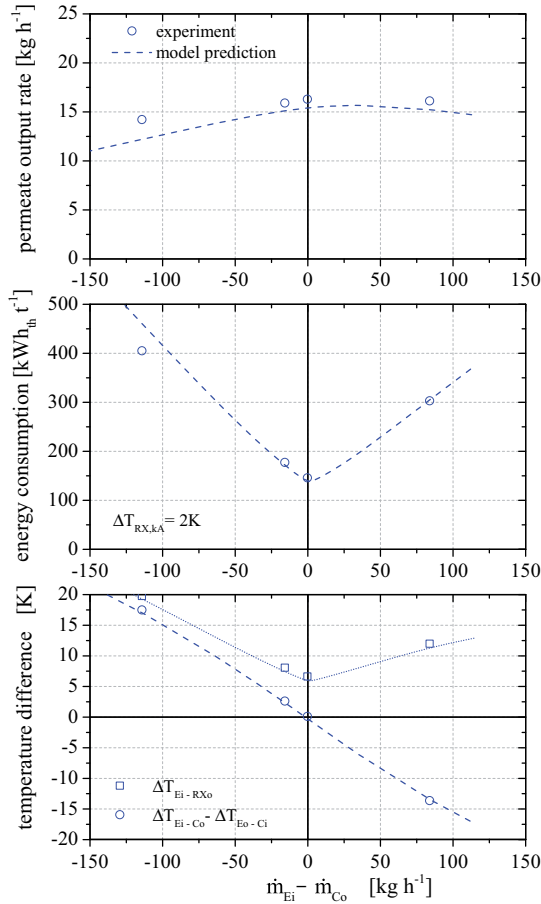


Figure 4.25: Experimental results and model predictions for differing mass flow rates in the evaporator and the condenser channels, at a constant mean mass flow rate of 300 kg h^{-1} . Testing conditions: Module DCMD-09.8-000-BE, $T_{Ei} = 80^\circ\text{C}$, $T_{Ci} = 25^\circ\text{C}$, tap water.

A comparison of the temperature differences between the evaporator and condenser channels on the module's hot side (ΔT_{Ei-Co}) and the cold side (ΔT_{Eo-Ci}) gives an explicit representation of the asymmetry in the temperature profile that result from the differing mass flow rates. The almost linear form of the resulting curve reflects the proportional relation of the temperatures and the mass flow rates. If the mass flow is fully balanced, the curve intersects the origin, reflecting a parallel temperature profile. A comparison of the temperature profiles in scenario #2 and scenario #3 proves the effect of the flux compensation. The influence of asymmetric operation on the temperature profiles is represented by the multi-node model with good quantitative agreement with the experimental results. Comparing the predicted and the measured temperature differences, the absolute error does not exceed 0.8 K .

Based on the given results, mass flow compensation is taken into consideration for the DCMD module studies within this thesis.

4.3.3 Specific Aspects of Permeate Gap Module Operation

Various experimental results and model predictions for PGMD module performance behaviour have already been presented and discussed in Sec. 4.3.1 that covered general influences that apply for all MD configurations. However, some specific aspects regarding the operation of PGMD modules require further clarification, which is provided in the following section.

The model predictions are based on the PGMD multi-node model presented in Sec. 4.1.2. The permeate gap has been parameterised on the basis of the appropriate geometrical specifications according to the validated single-node model parameters from Sec. 3.4.4. The permeate gap is considered to be completely filled with stagnant water, leading to the assumption of purely conductive heat transfer phenomenon through the gap.

Different Modes of Permeate Gap Module Operation

Essentially two different operational modes of the PGMD module are to be compared. In the first mode, the permeate is extracted at the module's outer diameter, which is the cold part of the module. The thermal energy carried by the permeate stream is internally recovered, supplying additional thermal energy for preheating the feed stream. The permeate leaves the module at a low temperature close to the condenser inlet temperature. In the second mode, the permeate is extracted from the centre of the module, which is the hot part of the module. In this case, thermal energy is transferred from the evaporator channel to the permeate channel to preheat the permeate within the module. The permeate leaves the module at a high temperature close to the condenser outlet temperature. For a schematic illustration of the different operational modes, please refer to Fig. 4.3.

To identify the effect of the internal permeate heat recovery or the permeate preheating, experiments and model predictions on both operational modes have been analysed comparatively. The experiments were conducted with a module of type PGMD-09.8-050-BE¹ at a condenser inlet temperature of 25 °C, an evaporator inlet temperature of 80 °C, a feed flow rate of 400 kg h⁻¹ and tap water. A selection of operating parameters are summarised in Tab. 4.5, presenting the experimental results in the upper part of the table and the corresponding values obtained by the model in the lower part of the table.

The main difference between the different operational modes is the outlet temperature of the

¹Nominal specifications similar to PGMD-09.8-050-BE, but the prototype was prepared especially for the given experiments, providing permeate outlets at different channel positions.

Table 4.5: A comparative assessment of different PGMD module operational modes, considering internal heat recovery from the permeate stream and internal preheating of the permeate stream. Testing conditions: Module PGMD-09.8-050-BE, $T_{Ei} = 80^\circ\text{C}$, $T_{Ci} = 25^\circ\text{C}$, $\dot{m}_{Ci} = 400 \text{ kg h}^{-1}$, tap water.

Operation mode	T_P^{out} [$^\circ\text{C}$]	$\Delta T_{Ei-Co} - \Delta T_{Eo-Ci}$ [K]	\dot{m}_P [kg h^{-1}]	q_{HX} [$\text{kWh}_{th} \text{ t}^{-1}$]	\dot{Q}_{HX} [W_{th}]	\dot{Q}_{CX} [W_{th}]
experimental:						
heat recovery	25.4	-0.1	18.6	187	3474	3343
preheating	71.7	2.5	19.9	204	4053	2765
difference	46.3	2.4	1.3	17	579	-578
model predictions:						
heat recovery	28.4	-0.3	19.4	176	3419	3397
preheating	74.9	2.0	19.5	206	4035	2966
difference	46.5	2.3	0.1	30	616	-431

permeate stream, that is cold for the case of internal heat recovery and hot for the permeate preheating mode. Intuitively one might expect the permeate outlet temperature to be roughly in the middle of the respective condenser and the evaporator bulk stream temperatures, as represented by the simulation results. However, the permeate outlet temperatures obtained in the experiments were quite close to the prevailing condenser conditions. The plausibility of this observation is derived from the specific geometrical design of the permeate outlet region in the given prototypes, presented in Fig. 4.11. Before the permeate exits the module, it is thermally conditioned by the condenser fluid, since the last part of the permeate channel is exclusively surrounded by the condenser channel.

For the operational mode with permeate heat recovery, the flow direction of the permeate is from the warm part to the cold part of the module, corresponding to the flow direction within the evaporator channel. Even though the mass flow along the evaporator channel reduces due to transmembrane mass transfer, the flow capacities moving from cold to warm (condenser channel) and those moving from warm to cold (evaporator and permeate channels) are equal and remain constant along the flow channel. Consequently the temperature profiles for the evaporator and condenser channels are naturally parallel for PGMD operation with internal permeate heat recovery ($\Delta T_{Ei-Co} - \Delta T_{Eo-Ci} \approx 0$). For the operational mode with internal permeate preheating, the flow direction of the permeate is from the cold part to the warm part of the module, the same as the flow direction within the condenser channel. The flow capacities moving from cold to warm (condenser and permeate channel) are higher than the flow capacity moving from warm to cold (evaporator channel), comparable to the effects in DCMD operation discussed in Sec. 4.3.2. Consequently, the temperature profile is asymmetric for PGMD operation with internal permeate preheating ($\Delta T_{Ei-Co} - \Delta T_{Eo-Ci} > 0$). Based on the physical modelling of the flow capacity in the permeate gap, the effect of the changing temperature profiles is clearly reflected by the model predictions, showing a deviation of only 0.1 K with respect to the measured value.

The permeate output rate is slightly higher for the operational mode with internal permeate heating. The additional energy demand for the internal permeate heating was identified to be $579 W_{th}$, which increases the specific thermal energy demand by about $17 \text{ kWh}_{th} \text{ t}^{-1}$. However, if the permeate is required at a high temperature level, the advantages of internal preheating become obvious from the following energy analysis. For heating up a permeate stream of 19.9 kg h^{-1} by 46.3 K externally, a thermal power of $1071 W_{th}$ would be required at a high exergy level. For the internal heating concept, only half of the required thermal energy is taken from the high exergy level, increasing the heating demand, while additional thermal energy originates from the low exergy level, reducing the cooling demand. A similar effect may be derived from the model predictions. The thermal energy required for permeate heating is due to the increased heating and the reduced cooling power in roughly similar fractions. It turns out that the modelling approach for the PGMD modules is able to describe the capacitive effects of the permeate channel on the overall module operating characteristics.

The permeate is usually not required at high temperatures. Due to the optimised energy performance of the operational mode with internal heat recovery, this mode is considered to be the standard mode and is used for all the investigations of PGMD modules within this thesis.

Influence of the Permeate Gap Design on Module Performance

One of the main specific aspects in PGMD module design is the geometrical specification of the permeate channel, where the gap width represents the most important design parameter. The influence of the permeate gap width on the module performance was studied by characterising the modules PGMD-09.1-025-BE², PGMD-09.8-050-BE and PGMD-09.8-100-BE, providing different permeate gap widths of 0.25, 0.50 and 1.00 mm, respectively. The experiments were conducted with tap water with a condenser inlet temperature of 25°C , an evaporator inlet temperature of 80°C and a feed flow rate of 400 kg h^{-1} . The experimental results as well as model predictions for the permeate output rate and the specific thermal energy consumption are given in Fig. 4.26. The temperature difference measured between the condenser outlet and the evaporator inlet is provided as supplementary information.

The permeate output rates obtained with the three different prototypes are 19.0, 20.1 and 20.2 kg h^{-1} , showing no significant dependence on the permeate gap width.

The resulting temperature differences increase almost proportionally with the permeate gap width, reflecting the additional heat transfer resistance from the evaporator to the condenser channel based on the permeate gap. While a temperature difference of 7.0 K is obtained for a gap width of 0.25 mm, the temperature difference increases to 8.8 K for a gap width of 1.00 mm. Since no gain in permeate output comes along with the increased temperature difference, the

²Module PGMD-09.1-025-BE has a slightly reduced membrane area because of its reduced channel length compared to the other modules, due to technical difficulties during module production (see Tab. 4.3)

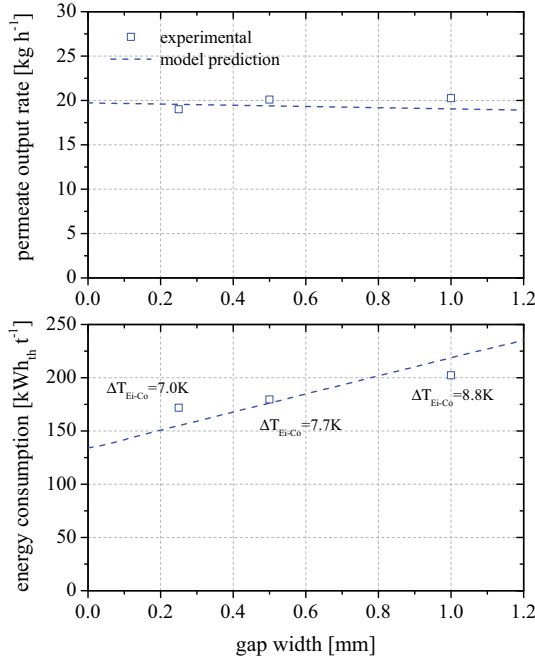


Figure 4.26: Experimental results and model predictions for PGMD modules with different permeate channel gap widths. Testing conditions: Modules PGMD-09.1-025-BE², PGMD-09.8-050-BE, PGMD-09.8-100-BE, $T_{Ei} = 80\text{ }^{\circ}\text{C}$, $T_{Ci} = 25\text{ }^{\circ}\text{C}$, $\dot{m}_{Ci} = 400\text{ kg h}^{-1}$, tap water.

specific thermal energy consumption increases for modules with wider permeate gaps. The minimal specific thermal energy consumption of $172\text{ kWh}_{th}\text{ t}^{-1}$ was obtained for the module with the thinnest gap width of 0.25 mm. For identical operating conditions, the specific thermal energy consumption of the module with a gap width of 1.00 mm is $202\text{ kWh}_{th}\text{ t}^{-1}$. The model fundamentally reflects the influence of the permeate gap width on module performance. The maximal and mean differences between the experimental results and the model predictions are 6% and 4% for the permeate output rate and 10% and 7% for the specific thermal energy consumption. In order to reflect the influence of the permeate gap width alone, an equal channel length for all modules is assumed for the model predictions. Particularly the 10% deviation for the specific thermal energy consumption is therefore mainly attributed to the prototype with slightly reduced channel length rather than to a limited accuracy of the model. If the actual channel length were assumed in the model, the respective deviation would be reduced to 6%.

It turns out that the permeate gap spacer should be chosen as thin as possible in order to obtain thermally efficient PGMD modules. However, a practical limitation is given since the gap width should be wide enough to allow suitable permeate extraction, especially for modules with long permeate channels. If the channel width were chosen too thin, the permeate channel might expand due to the increasing pressure loss, leading to a wider and rather undefined channel

geometry and an increased specific thermal energy consumption.

4.3.4 Specific Aspects of Air Gap Module Operation

The following section completes the discussion of MD module performance for AGMD modules with a separate discussion of the specific aspects regarding the operation of AGMD modules. It is obvious from the results in Sec. 3.4.4 that the air gap significantly influences the performance characteristics of a membrane distillation process, mainly depending on the geometrical design and the pressure conditions. Extensive theoretical and experimental work has been carried out in order to clarify the specific aspects concerning the operation of an AGMD module and the characterisation of different operating conditions. All AGMD experiments were conducted with the same prototype AGMD-08.7-200-BC. The model predictions are based on the AGMD multi-node model presented in Sec. 4.1.2. To parameterise the air gap, the effective gap width was reduced by 10% to 1.8 mm with respect to its nominal width of 2.0 mm, which was defined by the geometrical specifications of the air gap spacer S-200. Unlike in the test cell experiments, the main flow channels in the full-scale module are operated at a considerable pressure caused by the hydraulic pressure loss, mechanically loading the flat sheet laminate and the polymer film. Since the air gap does not induce any back pressure, the flexible sheet materials slightly flex into the air gap. These minimal deformations have been noticed as visible imprints on the sheet materials, observed during visual inspection of the materials after disassembly of the AGMD prototype.

Influence of Evaporator Inlet Temperature on Air Gap Module Performance

Results obtained in a study of the influence of the evaporator inlet temperature are presented in Fig. 4.27. The experiments were conducted with tap water at a constant condenser inlet temperature of 25 °C and a constant flow rate of $\dot{m}_{C_i} = 300 \text{ kg h}^{-1}$. The temperature difference measured between the condenser outlet and the evaporator inlet is provided as supplementary information.

The permeate output rate increases with evaporator inlet temperature, forming an increasing gradient with temperature. The production rate is 5.3 kg h⁻¹ at 50 °C and 17.3 kg h⁻¹ at 80 °C. The beneficial effect of increasing the evaporator inlet temperature is based on an increasing mean temperature level and an increasing temperature difference from the evaporator to the condenser sides. The temperature difference rises from 6.7 K at 50 °C to 12.3 K at 80 °C. Due to the insulating character of the air gap, the temperature differences between the evaporator and the condenser sides and consequently the required thermal power input is rather high, leading to specific thermal energy consumptions of 443 kWh_{th} t⁻¹ at 50 °C and 248 kWh_{th} t⁻¹ at 80 °C.

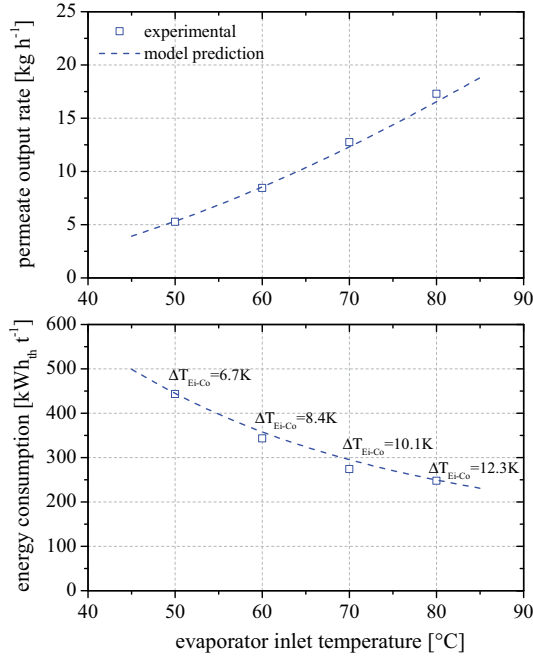


Figure 4.27: Experimental results and model predictions on the influence of the evaporator inlet temperature on AGMD module performance. Testing conditions: Module AGMD-08.7-200-BC, $T_{Ci} = 25\text{ }^{\circ}\text{C}$, $\dot{m}_{Ci} = 300\text{ kg h}^{-1}$, tap water.

The model predictions are in good quantitative agreement with the experimental results. The maximal and mean differences are 4% and 2% for the permeate output rate and 8% and 3% for the specific thermal energy consumption.

It should be noted that the temperature profiles in the evaporator and the condenser channel of the air gap module are not as parallel as observed in the PGMD modules. Depending on the operating conditions, the temperature difference at the cold end of the modules is about 0.5 to 2.0 K less than the temperature difference at the warm end of the module. Since the permeate exits the module locally, the sensible heat from the warm permeate is not recovered and the flow capacity streaming from warm to cold (evaporator channel) is lower than the flow capacity streaming from cold to warm (condenser channel). This effect is also reflected quantitatively by the model predictions.

Influence of Gap Deaeration on Air Gap Module Performance

The test cell experiments in Sec. 3.4.4 already indicated the significant potential for improving the AGMD process performance by actively reducing the pressure in the air gap to below atmospheric pressure for deaeration. However, the test cell experiments represent a specific local

temperature condition that defines the partial vapour pressure and air pressure for any given total pressure. Unlike the test cell experiments, the air gap in the full-scale spiral-wound module involves temperatures that range from condenser inlet to evaporator inlet conditions. Consequently, the pressure conditions along the air gap channel are not explicitly known, if the air gap is actively deaerated during operation. The model is based on the assumption of an ideal pressure distribution along the channel, where the pressure condition is evaluated locally by applying Dalton's law from node to node. A detailed description of the basic modelling of the pressure distribution is given in Sec. 4.1. In order to clarify the potential of air gap deaeration in the context of full-scale AGMD modules, a theoretical and experimental investigation has been conducted. For the experiments, the air gap is actively deaerated by a vacuum pump that was attached to the closed evacuated permeate reservoir. The operating conditions were set to a condenser inlet temperature of 25 °C, a flow rate of 300 kg h⁻¹ and tap water. Evaporator inlet temperatures of 50, 60, 70 and 80 °C were characterised at atmospheric pressure (see Fig. 4.27) while 50, 60 and 80 °C were considered at a deaeration pressure level that is defined by the maximal load of the vacuum pump. For the model predictions, the deaeration pressure was successively reduced from atmospheric pressure to full vacuum. The results regarding the permeate output rate and the specific thermal energy consumption are summarised in Fig. 4.28.

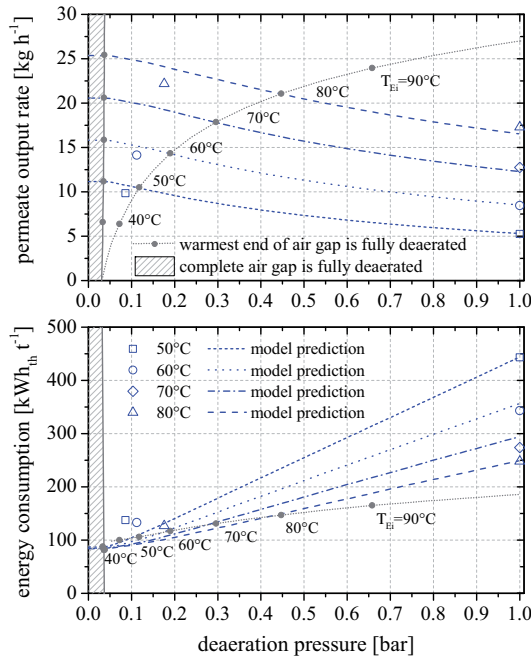


Figure 4.28: Model predictions of the effect of air gap deaeration on (V-)AGMD module performance at different deaeration pressures and different evaporator inlet temperatures. An ideal pressure profile is assumed for the model predictions. Testing conditions: Module AGMD-08.7-200-BC, $T_{Ci} = 25$ °C, $\dot{m}_{Ci} = 300$ kg h⁻¹, tap water.

In order to provide a clear guide to Fig. 4.28, the discussion of the results starts with a detailed interpretation of the model predictions. At atmospheric pressure of approximately 1.0 bar, the results for the different evaporator inlet temperatures are equal to that presented in Fig. 4.27. For AGMD operation with active deaeration, also denoted as vacuum-supported AGMD or V-AGMD operation, the model predictions show a significant effect on permeate output and specific thermal energy consumption. When the curve obtained for an evaporator inlet temperature of 80 °C is analysed as an example, the permeate output rate increases about 53 % from 16.5 kg h⁻¹ at atmospheric pressure to 25.4 kg h⁻¹ at full vacuum. At the same time, the specific thermal energy consumption decreases about 66 % from 249 to 84 kWh_{th} t⁻¹. The electricity consumption for the deaeration is not included in the plot in order to retain clarity. However, the associated model predictions are available. For operation at 80 °C without deaeration, the model predicts a specific electricity consumption of 0.76 kWh_{el} t⁻¹. If a deaeration pressure of 0.05 bar is applied, the electricity consumption is expected to be 0.75 kWh_{el} t⁻¹ for operation without recirculation, indicating complete compensation of the deaeration effort by improved module performance. The electricity consumption may even decrease to 0.62 kWh_{el} t⁻¹, if the deaerated water is recirculated with a recirculation factor of 10. A detailed break down of the electricity consumption into the main consumer loads is provided in Appendix H. The specific differences between the (V-)AGMD deaeration process and that for DCMD and PGMD are the absence of a deaeration module and the need for permeate extraction from the vacuum chamber.

When the deaeration pressure is reduced successively, the fraction of air in the air gap is reduced. Consequently, the diffusive mass transfer resistance is reduced, enhancing flux and process efficiency, especially for the regions of lower temperature (see Fig. 3.28). If the deaeration pressure is lower than atmospheric pressure but still higher than the vapour pressure at the warmest part of the gap², air is still present throughout the entire gap. The module is considered to be partially deaerated. If the deaeration pressure is as low as the vapour pressure at the warmest part of the air gap, no air is left specifically at this position. The warmest part of the air gap is assumed to be fully deaerated while air is still left in the cooler parts of the air gap. This characteristic pressure, explicitly indicated in Fig. 4.28 by the dotted grey line, is obviously dependent on the evaporator inlet temperature. The intersections of the dotted line with the blue curves indicate the respective characteristic pressures for the different evaporator inlet temperature conditions. For 80 °C, this characteristic pressure is observed at approximately 0.45 bar. By further reducing the deaeration pressure (left of dotted grey line), the air gap fraction that is assumed to be fully deaerated increases until the deaeration pressure is as low as the vapour pressure at the coldest part of the air gap³. At this characteristic pressure, which is obviously dependent on the condenser inlet temperature, the entire gap is free of air and the entire gap is assumed to be fully deaerated. This operation point represents the optimal case for module operation, since no transfer resistance is induced by the air gap any more. The respective characteristic pressure is explicitly indicated in Fig. 4.28 with the continuous grey line. For all scenarios presented in Fig. 4.28, the condenser inlet temperature is 25 °C, so the threshold pressure line is found at an almost constant pressure level of approximately 0.03 bar. The aim of applying vacuum to the air

²vapour pressure on the condensation surface at the warm end of the air gap (evaporator inlet position)

³vapour pressure on the condensation surface at the cold end of the air gap (condenser inlet position)

gap in AGMD is the extraction of air, which is not comparable to the aim of actively creating the process driving force by extracting water vapour as in VMD. Consequently, the performance characteristics remain constant when even lower deaeration pressures are applied in the model. This region of deaeration pressures is indicated by the grey hatched area.

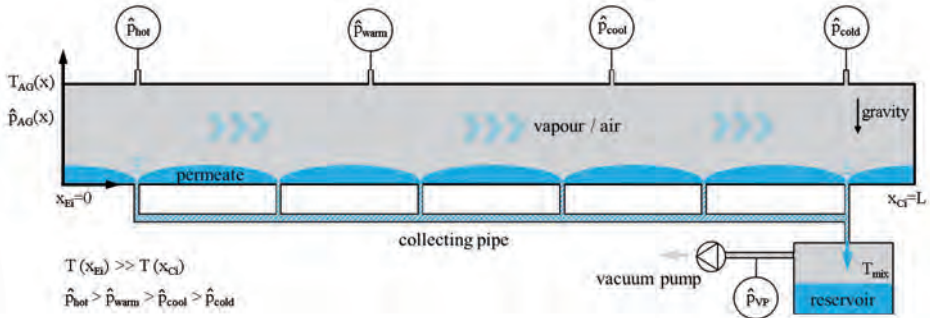


Figure 4.29: Schematic diagram of the air gap in module AGMD-08.7-200-BC, illustrating possible effects during operation with active deaeration.

A schematic diagram of the air gap in module AGMD-08.7-200-BC during operation is given in Fig. 4.29 to aid discussion of the experimental results obtained with deaeration. Here the uniform spacing of the absolute pressure sensors and the permeate outlets are illustrated. The permeate condenses on the film and is then forced to the lower part of the air gap and eventually to the permeate outlets by gravity. The permeate from the different outlets is mixed in a collection pipe and then passed forward into a closed reservoir. The vacuum pump is connected to the reservoir. The red curve represents the expected qualitative form of the temperature and the absolute pressure profiles along the air gap channel.

Like the model predictions, the experimental results in Fig. 4.28 show a significant enhancement of the module performance if vacuum is applied to the air gap. Analysing the experimentally obtained values for an evaporator inlet temperature of 80 °C as an example, the permeate output rate increases about 28 % from 17.3 kg h⁻¹ at atmospheric pressure to 22.2 kg h⁻¹ with deaeration. At the same time, the specific thermal energy consumption decreases about 49 % from 248 to 127 kWh_{th} t⁻¹. It has to be pointed out that the air gap could not be fully deaerated in the experiments. The deaeration pressures that were achieved by operating the vacuum pump at maximal load are 0.178 bar for an evaporator inlet temperature of 80 °C, 0.112 bar for an evaporator inlet temperature of 60 °C and 0.086 bar for an evaporator inlet temperature of 50 °C.

A further analysis of the results obtained with active deaeration is based on Fig. 4.30, where the same values are plotted versus the evaporator inlet temperature. The temperature difference measured between the condenser outlet and the evaporator inlet is provided as supplementary information. An extra diagram gives an indication of the absolute pressure profile during operation, showing the pressures \hat{p}_{hot} , \hat{p}_{warm} , \hat{p}_{cool} and \hat{p}_{cold} that were measured along the channel length L at approximate positions 0.1L, 0.4L, 0.6L and 0.9L. The deaeration pressures assumed for the model predictions range from 0.05 bar for an evaporator inlet temperature of 45 °C to

0.22 bar for an evaporator inlet temperature of 85 °C, according to the vapour pressures that correspond to the permeate mixing temperature in the reservoir. To show the sensitivity of the V-AGMD module performance to a non-ideal pressure profile, two different sets of modelling results are provided in Fig. 4.30. The first set of results was obtained similarly to the prediction in Fig. 4.28, assuming an ideal pressure profile. For the second set of results, the equations are modified such that the local residual air pressure cannot take on values below 0.1 bar, accounting for non-ideal deaeration.

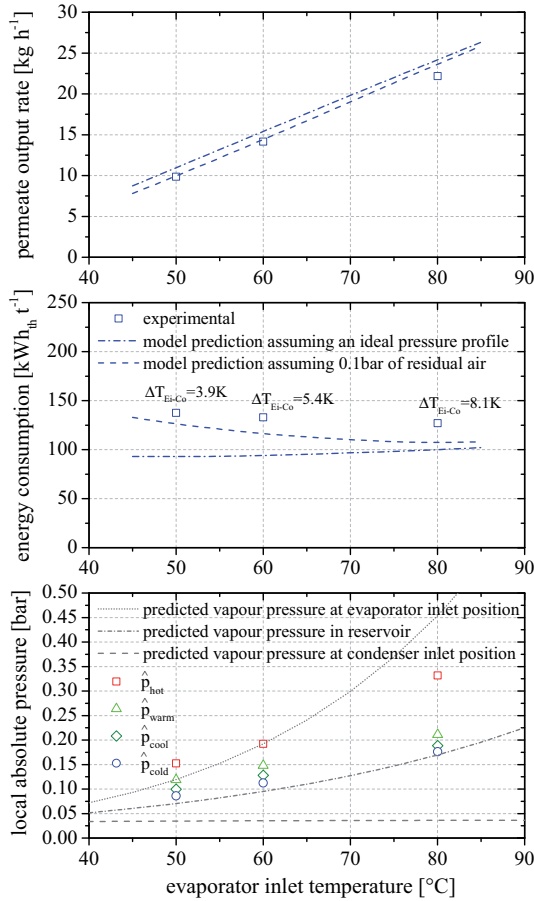


Figure 4.30: Experimental results and model predictions for the influence of the evaporator inlet temperature on V-AGMD module performance and the absolute pressure profile along the air gap. Testing conditions: Module AGMD-08.7-200-BC, $T_{Ei} = 80\text{ }^{\circ}\text{C}$, $T_{Ci} = 25\text{ }^{\circ}\text{C}$, $\dot{m}_{Ci} = 300\text{ kg h}^{-1}$, $\hat{p}_{VP, 50/60/80\text{ }^{\circ}\text{C}} = 0.09/0.11/0.18\text{ bar}$, tap water.

The experimental results for the permeate output rate clearly indicate the well-known positive influence of an increasing evaporator inlet temperature. The output rate increases by a factor

of 2.2 from 9.9 to 22.2 kg h⁻¹ if the evaporator inlet temperature is raised from 50 to 80 °C. The improvement of the permeate rate seems to be almost proportional to the increase in the temperature difference, which is by factor of 2.1. These results indicate rather constant process efficiency, even though the mean temperature in the module differs significantly for the different experiments. A similar statement may be derived from the results obtained for the specific thermal energy consumption, that show low sensitivity to the evaporator inlet temperature. The beneficial effect of increasing the evaporator inlet temperature from 50 to 80 °C is only 10 kWh_{th} t⁻¹. The experiments clearly indicate the major benefit of deaeration, especially for module operation at low temperatures.

As mentioned before, the deaeration pressures did not reach the theoretical minimum that is expected around 0.03 bar, based on the vapour pressure at the condenser inlet position. The minimal pressures that were measured at \hat{p}_{cold} position had values from 0.086 bar to 0.178 bar for evaporator inlet temperatures from 50 to 80 °C. These values are almost equal to the values for \hat{p}_{VP} measured at the vacuum pump and may therefore be referred to as deaeration pressure. In principle, the capacity of the vacuum pump is sufficient to extract all of the air that is released into the air gap from the feed water. However, if the vacuum is as low as the vapour pressure in the reservoir, the vacuum pump starts to carry a significant amount of water vapour instead of pure air. The deaeration pressure is therefore limited to the vapour pressure in the reservoir. For all the experiments represented in Fig. 4.30, the minimal pressures almost match the vapour pressures of the corresponding permeate at the mixing temperature in the reservoir, which has been derived from the model. The higher the local temperatures along the air gap, the higher the corresponding measured absolute pressures that form a steady absolute pressure profile along the air gap. The pressures \hat{p}_{cool} and \hat{p}_{warm} , measured at the central air-gap positions, are only slightly higher than the deaeration pressure, indicating air that is still present in roughly 70 % of the air gap. An appreciable absolute pressure gradient is established in the hot part of the module. The highest pressures \hat{p}_{hot} are measured near the evaporator inlet position. Since the maximal pressure level in the module is expected specifically at the evaporator inlet position, the real maximum is even higher than \hat{p}_{hot} . However, for an evaporator inlet temperature of 50 °C, the measured pressure \hat{p}_{hot} is higher than the simulated value at the evaporator inlet position, indicating the presence of residual air even in the hot part of the module. At least for an evaporator inlet temperature of 80 °C, the pressure \hat{p}_{hot} is significantly lower than the expected pressure at the evaporator inlet position. None of the experimental results reached the values that had been predicted by the model. The model overestimates the permeate output rate by approximately 10 % and the thermal energy consumption by approximately 30 %. This may have different causes. At first, permeate accumulates at the bottom of the air gap, building up until it reaches the nearest permeate outlet for extraction. The fraction of the air gap that is filled with permeate mainly depends on channel width, spacer configuration and design of the permeate outlet. In the given experiments, the distance from one permeate outlet to the next is approximately 1 m, so an appreciable fraction of the air gap is expected to be flooded during operation (see Fig. 4.29). The flooded zones form local PGMD conditions with poor performance characteristics on account of the high parasitic heat losses and the low flux due to the gap width that is 5-10 times wider than usual for a PGMD configuration. A second reason for poorer

experimental performance than the model predictions might be a non-ideal absolute pressure profile that is formed along the air gap channel. Air is continuously released into the air gap from the feed water, especially in the hot part of the module, where the relevant solubility is low. This air streams along the air gap channel from warm to cold, following the absolute pressure gradient, until it is extracted from the air gap through one of the permeate outlets. Based on the air convection, air originating from an upstream location may lower the performance at a downstream location, even though full deaeration would be expected from its local temperatures. Furthermore, water vapour may stream along the air gap, also following the absolute pressure gradient. Unlike the air, the water vapour condenses at the condensation surface, especially if it moves to downstream regions of lower temperature. Depending on the condensation dynamics, vapour convection along the channel may influence the downstream pressures and the downstream temperatures at the condensation location. In the context of vapour and air convection along the air gap, the role of the collecting pipe remains unclear. The collecting pipe may possibly act as a bypass, promoting the homogenisation of the desired pressure profile.

From the model predictions, an appreciable effect of residual air in the gap is derived, especially affecting the specific thermal energy consumption for low-temperature operation. Considering a residual air pressure of 0.1 bar in the gap for the model predictions performed for an evaporator inlet temperature of 50 °C, the difference between the model predictions and the experimental results reduces from 12% to 1% for the permeate output rate and from 32% to 8% for the specific thermal energy consumption. It should be recalled that the results obtained with the V-AGMD single-node model, which is applied in the multi-node module model, already indicate a slight overestimation of the process efficiency in the V-AGMD configuration (see Secs. 3.4.4 and 3.4.5).

Influence of Air-Gap Design on Air Gap Module Performance

One of the main specific aspects in AGMD module design is the geometrical specification of the air gap channel, which significantly influences the thermodynamic (V-)AGMD performance specifications. For the choice of a suitable air-gap channel spacer, a variety of constraints should be considered. The main function of the air-gap spacer is to define the gap width, including mechanical support for the flexible membrane and film materials. The air gap should provide the best possible insulation, so thermal bridges are to be avoided by the choice of gap spacers with high void fractions and low thermal conductivity. Furthermore, the permeate film thickness on the cool impermeable wall may partially be controlled by the air-gap spacer configuration, that should not introduce barriers for the gravimetric permeate down-flow. Since the mass transfer resistance in AGMD is dominated by the air-gap resistance, the air-gap width represents the most crucial parameter for AGMD module design. The basic influence of the gap width on (V-)AGMD process performance has already been assessed by test cell experiments and model predictions that were presented in the fundamental section (Fig. 3.30). Unfortunately, the available set of full-scale module prototypes does not include AGMD modules with different air-gap widths.

However, due to the importance of the gap width parameter in AGMD module design, a model-based analysis has been conducted. The chosen model parameterisation refers to the module design parameters of prototype AGMD-08.7-200-BC, but considers varying air-gap widths that range from 1.0 to 5.0 mm. The operating parameters include non-saline feed water, a condenser inlet temperature of 25 °C, an evaporator inlet temperature of 80 °C and a feed flow rate of 300 kg h⁻¹. The presented results include one set of model predictions that considers AGMD with an aerated air gap, a second set of model predictions that considers V-AGMD with non-ideal gap deaeration addressing the experiments in Fig. 4.30 and a third set of model predictions that considers V-AGMD with ideal gap deaeration. The model results for the permeate output rate and the specific thermal energy consumption are given in Fig. 4.31.

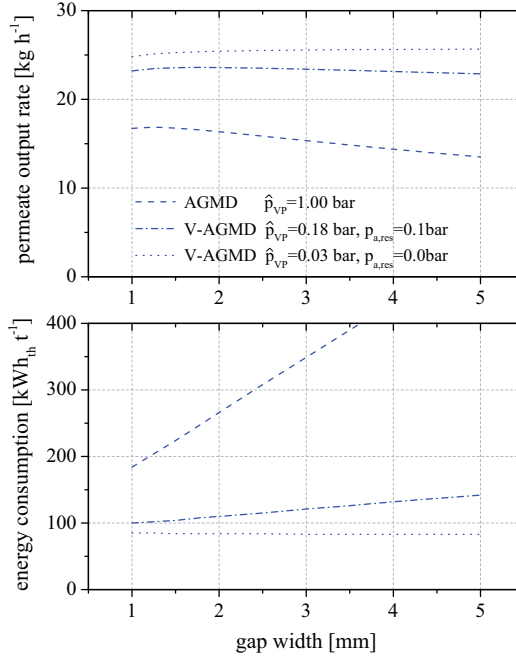


Figure 4.31: Model predictions for AGMD modules with different air-gap widths operated at different states of deaeration. Model parameterisation: Module AGMD-08.7-X-BC, $T_{Ei} = 80\text{ }^{\circ}\text{C}$, $T_{Ci} = 25\text{ }^{\circ}\text{C}$, $\dot{m}_{Ci} = 300\text{ kg h}^{-1}$, tap water.

For the model predictions without gap deaeration, the permeate output rate decreases for increasing gap widths due to the associated increasing mass transfer resistance. Even though the thermal insulation of the air gap steadily improves, a minor effect is observed for the thermal efficiency that ranges from 68 to 73%. Slight improvement of the permeate output rate is observed, if the gap width is increased from 1.0 to about 1.3 mm, which is explained by the slight improvement in thermal efficiency. For wider gaps, the improved thermal insulation cannot compensate the increasing mass transfer resistance. Due to the reduced latent and conductive heat transfer, the temperature difference from the evaporator to the condenser bulk stream and con-

sequently the specific thermal energy consumption substantially increase with gap width. When the gap width is doubled from 2.0 to 4.0 mm, the permeate output rate reduces by 12% from 16.4 to 14.4 kg h⁻¹ while the specific thermal energy consumption increases by 62% from 266 to 431 kWh_{th} t⁻¹.

For the V-AGMD model predictions that consider non-ideal gap deaeration, the mass transfer resistance is significantly reduced compared to a completely aerated case. Like the observations that have already been made in the preceding studies, gap deaeration leads to a higher permeate output rate and reduced thermal energy consumption. If air is removed from the air gap, the sensitivity of the mass transfer resistance and consequently the permeate output rate to the gap width decreases (refer to Fig. 3.29). Due to improved thermal insulation, the thermal efficiency increases from 91 to 95%. When the gap width is doubled from 2.0 to about 4.0 mm, the permeate output rate only decreases by 2% from 23.6 to 23.1 kg h⁻¹ while the specific thermal energy consumption increases by 20% from 110 to 132 kWh_{th} t⁻¹.

For the V-AGMD model predictions that consider ideal gap deaeration, the mass transfer resistance of the gap is independent of the gap width. As a consequence, also the thermodynamic performance is almost independent of gap width and even exhibits slight performance improvements with increasing gap width due to improved thermal insulation. The results for the permeate output rate is about 25.5 kg h⁻¹ and for the specific thermal energy consumption is about 84 kWh_{th} t⁻¹.

4.3.5 A Comparative Evaluation of Different Module Configurations

This section provides a comparative evaluation of the different MD module configurations. The prototypes DCMD-09.8-000-BE, PGMD-09.8-050-BE and AGMD-08.7-200-BC were chosen for the experimental part of the study. Their similar geometrical specifications allow a direct comparison of the DCMD, PGMD, AGMD and V-AGMD process variants for specific operating conditions. Experimental and theoretical sensitivity analyses are conducted on the influence of the evaporator inlet temperature, the mass flow rate and the feed water salinity on thermodynamic module performance. The assessment is based on the default inlet conditions that consist of an evaporator inlet temperature of 80 °C, a condenser inlet temperature of 25 °C, a mass flow rate of 300 kg h⁻¹ and tap water. For the experimental and the model-based evaluation of the DCMD variant, a limited heat transfer performance is assumed for the external heat recovery system, which is taken into account by a constant temperature drop of 2 K (see Sec. 4.3.2 for details). If not stated otherwise, mass flow compensation is considered for the definition of the condenser inlet flow rate in the DCMD experiments and the corresponding model predictions. The condenser inlet mass flow rate is adjusted until the condenser outlet mass flow rate equals the evaporator inlet mass flow rate (see Sec. 4.3.2 for details). For the experimental evaluation of the V-AGMD variant, the deaeration pressure is limited by the vapour pressure in the permeate reservoir. This is taken into account for the associated model predictions, assuming a deaeration

pressure equal to the vapour pressure at permeate mixing temperature. In order to account for a non-ideal pressure profile in the air gap, a local residual air pressure of 0.1 bar is assumed in the V-AGMD model predictions (see Sec. 4.3.4 for details). It should be noted that the V-AGMD results do not represent the optimal mode of operation since there is still significant potential for improvement by reduction of the deaeration pressure (see Fig. 4.28).

Prior to the discussions that refer to the different parameter variations individually, a summary of the experimentally obtained mean sensitivities is provided in Tab. 4.6.

Table 4.6: Summary of the experimentally obtained MD module sensitivities with respect to the different operating parameters. The mean sensitivities for permeate output rate, specific thermal energy consumption and thermal efficiency are given as absolute values with respect to a defined reference variation Δ using the corresponding units [kg h^{-1}], [kWh t^{-1}] and [%].

reference variation	T_{Ei} Fig. 4.32			$\dot{m}_{\text{Ei}/\text{Co}}$ Fig. 4.33			S_{Ei} Fig. 4.34		
	$\Delta = 10 \text{ K}$			$\Delta = 100 \text{ kg h}^{-1}$			$\Delta = 50 \text{ g kg}^{-1}$		
configuration	\dot{m}_{P}	\dot{q}_{HX}	η_{th}	\dot{m}_{P}	\dot{q}_{HX}	η_{th}	\dot{m}_{P}	\dot{q}_{HX}	η_{th}
DCMD	3.8	33.7	5.1	5.1	3.2	0.0	5.4	150.0	19.8
PGMD	3.6	21.4	4.8	4.7	26.4	0.5	4.5	88.8	16.7
AGMD	4.4	47.7	8.6	5.3	39.3	0.7	1.8	31.2	5.5
V-AGMD	4.0	3.1	0.5	n.a.	n.a.	n.a.	1.9	10.5	3.1

Influence of Evaporator Inlet Temperature on Module Performance

In the first comparative sensitivity analysis on DCMD, PGMD, AGMD and V-AGMD, the evaporator inlet temperature was varied from 60 to 80 °C while the other inlet conditions were set to the default values. The deaeration pressures achieved for the V-AGMD experiments are 0.11 bar for an evaporator inlet temperature of 60 °C and 0.18 bar for an evaporator inlet temperature of 80 °C. For the V-AGMD model predictions, the deaeration pressures based on the theoretical permeate mixing temperatures range from 0.08 bar for an evaporator inlet temperature of 55 °C to 0.22 bar for an evaporator inlet temperature of 85 °C (refer to Fig. 4.30 for details). Experimental results and model predictions for the permeate output rate, the specific thermal energy consumption and the overall module thermal efficiency are summarised in Fig. 4.32, including a comparative presentation of the corresponding model predictions. However, the following quantitative discussion refers to the experimental results, while the deviations of the model predictions from the experiments are summarised in Tab. 4.7 at the end of this section.

The beneficial influence of high evaporator inlet temperatures is obvious for all of the process variants. The highest production rate and the lowest thermal energy consumption were obtained with the V-AGMD variant, even though the deaeration pressure could not be reduced to the optimal level. The maximal permeate output rate in the V-AGMD experiments is 22.2 kg h^{-1} ,

than for DCMD or PGMD. The enormous heat transfer resistance of the air gap leads to a large temperature difference between the evaporator and the condenser channels, consequently increasing the heating requirement. The specific thermal energy consumption of the AGMD variant ranges from $343 \text{ kWh}_{\text{th}} \text{ t}^{-1}$ at 60°C to $248 \text{ kWh}_{\text{th}} \text{ t}^{-1}$ at 80°C . In the given scenarios, the energy results obtained for the PGMD variant are quite similar to the DCMD results, ranging from approximately $200 \text{ kWh}_{\text{th}} \text{ t}^{-1}$ at 60°C to $150 \text{ kWh}_{\text{th}} \text{ t}^{-1}$ at 80°C . Since the PGMD channel configuration implies direct contact with water on both sides of the membrane, the PGMD configuration may be considered to be an enhanced DCMD configuration with internal heat recovery. For the given scenarios, the energy performance obtained with the concept of internal heat recovery (PGMD) is comparable to the performance obtained with an external heat recovery concept (DCMD). It should be noted that the DCMD results are strongly dependent on the assumptions made for the performance of the external heat transfer system. Due to appreciable conductive heat losses through the single membrane, the thermal efficiencies obtained for the DCMD and the PGMD variants are lower than the thermal efficiencies in the air-gap variants. Depending on the module mean temperature, the values range from approximately 50 to 60%.

Influence of Feed Flow Rate on Module Performance

In the second comparative sensitivity analysis of DCMD, PGMD, AGMD and V-AGMD, the inlet mass flow rates were varied from 200 to 500 kg h^{-1} while the other inlet conditions were set to the default values. Since the given experimental series has not been explicitly analysed for the V-AGMD measurements, the corresponding result from Fig. 4.32 has been taken to represent the V-AGMD variant at a mass flow rate of 300 kg h^{-1} . The deaeration pressures achieved for this experiment is 0.18 bar, as stated earlier. For the V-AGMD model predictions, the deaeration pressures based on the theoretical permeate mixing temperatures range from 0.16 bar for a mass flow rate of 150 kg h^{-1} to 0.18 bar for a mass flow rate of 550 kg h^{-1} . Experimental results and model predictions for the permeate output rate, the specific thermal energy consumption and the overall module thermal efficiency are summarised in Fig. 4.33, including a comparative presentation of the corresponding model predictions. However, the following quantitative discussion refers to the experimental results, while the deviations of the model predictions from the experiments are summarised in Tab. 4.7 at the end of this section.

The general characteristic increase of the permeate output rate and the specific thermal energy consumption is clearly observed for all of the process variants. The overall thermal efficiency is almost independent of the inlet mass flow rates. The strongest performance characteristic is achieved with the V-AGMD variant. The permeate output rates obtained in the DCMD, PGMD and AGMD variants are quite similar. For a mass flow rate of 300 kg h^{-1} , the specific thermal energy consumption obtained in the DCMD, PGMD and V-AGMD experiments are in the same range from 127 to $152 \text{ kWh}_{\text{th}} \text{ t}^{-1}$. If the mass flow rate is varied, the DCMD

comparatively as an example. For low flow rates, the internal heat recovery system in the PGMD module has sufficient heat transfer area to compete with the relatively small external heat exchanger considered for DCMD. The specific thermal energy consumption for the PGMD module is lower than the specific thermal energy consumption for the DCMD module. For higher flow rates, the external heat transfer area is assumed to increase in DCMD, while the PGMD transfer area remains constant. Thus, the results show lower specific thermal energy consumption for the DCMD module for higher flow rates. The threshold flow rate where both process variants show equal energy consumption mainly depends on the design of the associated heat recovery systems, namely the external heat exchanger for the DCMD process and the permeate-gap design including the polymer film for the PGMD process. If constant external heat transfer performance were considered for the given DCMD results, the sensitivity of the DCMD specific energy consumption would be similar to that obtained for the PGMD variant. Evaluating the values from Fig. 4.24 for an fix heat exchanger size of $8 \text{ kW}_{\text{th}} \text{ K}^{-1}$ as an example, the DCMD specific energy consumption takes on values from approximately 105 to $190 \text{ kWh}_{\text{th}} \text{ t}^{-1}$. It is obvious from the given analysis that a comparison of DCMD and PGMD/AGMD results requires special attention to the assumptions made.

Influence of Feed Water Salinity on Module Performance

In the third comparative sensitivity analysis of DCMD, PGMD, AGMD and V-AGMD the feed water salinity levels were varied from 0 to 210 g kg^{-1} while the other inlet conditions were set to the default values. The salt solutions were prepared by dissolving different amounts of sea salt from the Red Sea in tap water. The deaeration pressures achieved in the experiments range from 0.15 to 0.18 bar, with the lower values for the experiments with higher salinities. For the V-AGMD model predictions, the deaeration pressures based on the theoretical permeate mixing temperatures have a quite narrow range from 0.17 bar to 0.18 bar. Experimental results and model predictions for the permeate output rate, the specific thermal energy consumption and the overall module thermal efficiency are summarised in Fig. 4.34, including a comparative presentation of the corresponding model predictions. However, the following quantitative discussion refers to the experimental results, while the deviations of the model predictions from the experiments are summarised in Tab. 4.7 at the end of this section.

A negative influence of salt on the permeate output rate, the specific energy consumption and the total thermal efficiency is observed for all of the MD process variants. However, the sensitivities to the feed water salinity differ significantly. If the permeate output rates obtained for a salinity level of approximately 50 g kg^{-1} are compared to the tap water measurements, the DCMD and the PGMD output rates decrease by approximately 33 %, while the corresponding AGMD results decrease by only 17 %. Since the permeate output rate is in the denominator of the specific energy equation, all of the specific energy consumption curves steadily increase with an exponential dependence. Again, the AGMD variant shows a quite stable energy consumption for an increase

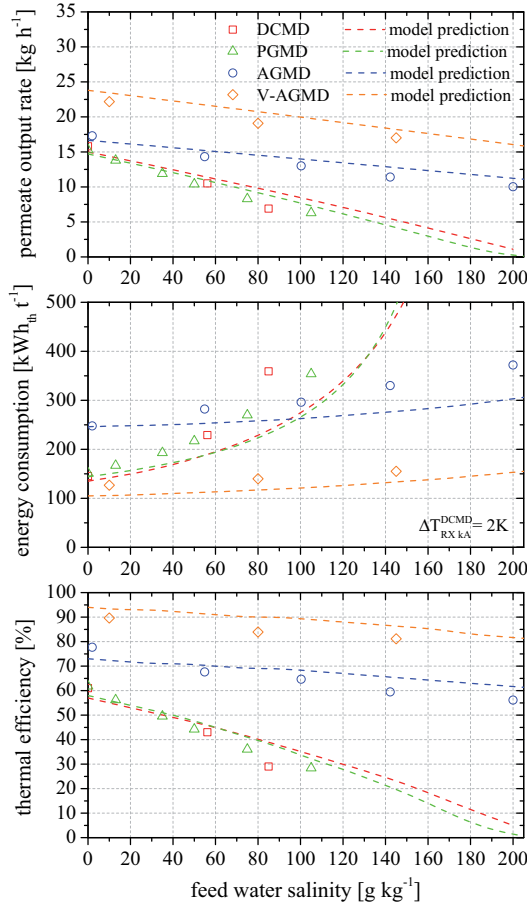


Figure 4.34: Comparative evaluation of experimental results and model predictions of the influence of the feed water salinity on DCMD, PGMD, AGMD and V-AGMD module performance. Testing conditions: Modules DCMD-09.8-000-BE, PGMD-09.8-050-BE, AGMD-08.7-200-BC, $T_{Ei} = 80\text{ }^{\circ}\text{C}$, $T_{Ci} = 25\text{ }^{\circ}\text{C}$, $\dot{m}_{Ei/C0} = 300\text{ kg h}^{-1}$, $\hat{p}_{VP, 10/80/145\text{ g kg}^{-1}}^{\text{VAGMD}} = 0.18/0.16/0.15\text{ bar}$, artificial salt water, tap water on condenser side for the DCMD variant.

in feed water salinity from tap water to approximately 50 g kg^{-1} . The energy consumption only increases by 13% while the energy consumption for the DCMD and the PGMD variant increases by 37% and 30% under comparable conditions.

According to the discussion on the general influence of salinity in Secs. 3.4.2, 3.4.5 and 4.3.1, the basic phenomenon leading to the negative effect of salinity on process performance is the reduced vapour pressure on the evaporator side caused by the presence of salt ions. Since the vapour pressure is reduced by a certain offset, high driving forces and consequently larger interfacial temperature differences generally lower the process sensitivity to salt (refer to Fig. 3.37). This may be clearly derived from the given results. The highest driving force is established with the

AGMD module configuration, due to the large temperature difference between the evaporator and the condenser channels. As a consequence, the performance characteristic of the AGMD process is quite robust with respect to the feed water salinity. The driving force established with the DCMD module is significantly lower. If a DCMD module is operated without salt, the low driving force is compensated by the low mass transfer resistance. During operation with salt water, a strong relative influence of a vapour pressure reduction on the low total driving force is obvious. Even though the bulk stream temperature difference in the PGMD process is greater than in DCMD, the effective interfacial temperature difference across the membrane is comparable, due to the significant temperature drop in the permeate gap. Independently of the vapour pressure driving force, the temperature difference from the evaporator to the condenser channels causes parasitic conductive heat transfer. Therefore, the thermal efficiency drops with increasing salinity for all of the process configurations. Again, different sensitivities are observed when the process configurations are compared. These differences may be directly attributed to the differences in latent heat transfer.

The given results clearly indicate the air-gap variants as the preferred module configurations for treatment of high-salinity solutions. However, for a given module, the temperature difference from the evaporator to the condenser sides and consequently the sensitivity to feed water salinity may be adjusted by the choice of suitable operating conditions. It should be emphasised that the effect of salt on the module performance characteristics is specifically important for the design of high-recovery modules that operate at low temperature differences. For high-flux module concepts, the sensitivity of module performance to feed water salinity is significantly lower for all of the configurations. Depending on the module design and the operational conditions, the influence of salt may even be negligible.

The analysis presented in this section indicates that the influence of salt on the MD module performance depends on the chosen MD configuration, the geometrical module design and the choice of operating conditions and needs to be carefully evaluated for any given scenario. Furthermore, from Fig. 3.22 the membrane is expected to play a major role in adjusting the module's sensitivity to salinity. This topic will be discussed in a subsequent section.

Deviations of the Model Predictions from Experimental Results

The mean differences between the model predictions and the experimental results have been analysed for each parameter variation that has been previously presented in this section. A detailed summary is given in Tab. 4.7. The derivation of the combined mean differences over all parameter variations for permeate output rate, the specific thermal energy consumption and the thermal efficiency leads to values of 9%, 11% and 9% for DCMD, 6%, 10% and 7% for PGMD, 5%, 7% and 6% for AGMD and 6%, 17% and 5% for V-AGMD, respectively. The largest differences are given for the V-AGMD energy consumption, which is mainly attributed to the uncertainty in the experiments, rather than the quality of the model predictions. Furthermore, systematically noticeable differences are identified for the effect of feed water salinity on the

thermal energy demand, especially for high concentrations. A similar finding has already been observed from the single-node models as documented in Tab. 3.13. It is important to notice that the validity of the salt water property correlations is limited to brine salinities lower than 130 – 160 g kg⁻¹. Moreover, some deviation may be explained by differences in salt composition of the salt from Seequasal that originates from the Red Sea and the salt referred to as standard sea salt composition (refer to Appendix C).

The multi-node models are generally able to represent the physical effects of the important operating parameters on MD module performance with good precision and a wide range of validity. The model is considered to be well validated and ready to use in purely model-based analyses that will be presented in the coming sections.

Table 4.7: Summary of the mean differences between the model predictions and the experimental results for each parameter variation.

configuration	$ \bar{e}(T_{Ei}) $ Fig. 4.32			$ \bar{e}(\dot{m}_{Ei/Co}) $ Fig. 4.33			$ \bar{e}(S_{Ei}) $ Fig. 4.34		
	\dot{m}_P	\dot{q}_{HX}	η_{th}	\dot{m}_P	\dot{q}_{HX}	η_{th}	\dot{m}_P	\dot{q}_{HX}	η_{th}
DCMD	3%	4%	7%	5%	9%	6%	17%	20%	16%
PGMD	6%	3%	7%	4%	5%	6%	8%	16%	7%
AGMD	3%	3%	4%	4%	7%	7%	8%	12%	7%
V-AGMD	5%	16%	3%	7%	18%	5%	7%	16%	6%

4.3.6 Selection of an Optimal Membrane

In Sec. 3.4.2, the selection of a suitable membrane was already identified as a complex and critical task, due to the interdependence of membrane thickness, driving force, flux and conductive heat losses, especially for saline feed water. It is obvious from the fundamental results provided in Sec. 3.4.2 that the membrane thickness has to be determined and selected carefully in order to achieve optimal performance characteristics with MD modules. The following section provides methods for appropriate membrane selection taking into account the operating conditions as well as aspects of module design.

At first, a sensitivity analysis has been carried out, covering the interdependent effects of membrane thickness and salinity for each of the four MD configurations, individually. To do so, the module performance is evaluated for salinity levels of 0, 50, 100, 150 and 200 g kg⁻¹ while the membrane thickness has been varied from 20 to 700 μm . The analysis distinguishes between a high-recovery module concept and a high-flux module concept for each of the process configurations. The reference modules, chosen to represent the different MD configurations, have comparable geometrical specifications, which are summarised in Tab. 4.8.

The assessment has been based on default inlet conditions that consist of an evaporator inlet temperature of 80 °C, a condenser inlet temperature of 25 °C and a mass flow rate of 400 kg h⁻¹. For the evaluation of the DCMD variant, a limited heat transfer performance is assumed for the external heat recovery system, which is taken into account by a constant temperature drop

of 2 K (see Sec. 4.3.2 for details). The different mass flow capacities of the evaporator and the condenser channel due to flux and different salinity levels are compensated by mass flow compensation on the condenser side that is taken into account for the DCMD model predictions (see Sec. 4.3.2 for details). The air gap is assumed to have an effective thickness of 1.8 mm instead of the nominal thickness of 2.0 mm, due to deformation of the elastic film layers (see Sec. 4.3.4 for details). The deaeration pressure for the evaluation of the V-AGMD variant is defined to be 0.03 bar, since the air is assumed to be extracted at the coldest spot of the air gap, avoiding the specific experimental limitations from Sec. 4.3.4. The model automatically adjusts the local air pressures according to the prevailing temperature conditions. However, a minimum local air pressure of 0.05 bar still accounts for a non-ideal pressure profile in the air gap (see Sec. 4.3.4 for details).

The reference parameterisation of the node models is derived from channel spacer S-320, laminate L-020A-S, PGMD gap spacer S-025, (V-)AGMD gap spacer S-200 and impermeable film F-127. These materials have already been extensively discussed within this thesis. The results obtained for the permeate output rates and the specific thermal energy consumptions of the DCMD and the PGMD modules are given in Figs. 4.35 and 4.36, whereas the results obtained for AGMD and V-AGMD modules are provided in Appendix I.

Table 4.8: Reference modules used for the comparative assessments of membrane selection and potential for performance improvements by advanced materials

module	membrane area [m ²]	channel length [m]	channel height [m]	channel width [mm]	gap width [mm]
high-recovery concept					
DCMD-09.8-000-BC	9.8	7.0	0.70	3.20	-
PGMD-09.8-025-BC	9.8	7.0	0.70	3.20	0.25
AGMD-09.8-200-BC	9.8	7.0	0.70	3.20	2.00 ^a
high-flux concept					
DCMD-01.4-000-BC	1.4	1.0	0.70	3.20	-
PGMD-01.4-025-BC	1.4	1.0	0.70	3.20	0.25
AGMD-01.4-200-BC	1.4	1.0	0.70	3.20	2.00 ^a

^aan effective thickness of 1.8 mm is used for model parameterisation (see Sec. 4.3.4 for details)

At first the resulting performance characteristics of a DCMD high-recovery module from Fig. 4.35 are analysed. For feed water with zero salinity, the permeate output rate slightly decreases with increasing membrane thickness. This is explained by the reduced membrane permeability, while the thermal efficiency remains almost constant (see Fig. 3.18). The module flux performance decreases with membrane thickness by approximately 0.7 kg h^{-1} per $100 \mu\text{m}$, while the specific thermal energy consumption steadily increases by $30 \text{ kWh}_{\text{th}} \text{ t}^{-1}$ per $100 \mu\text{m}$. Consequently, the membrane thickness should be chosen to be as thin as possible for zero salinity feed water. The model results reflect the negative influence of salt on module performance, leading to a reduced

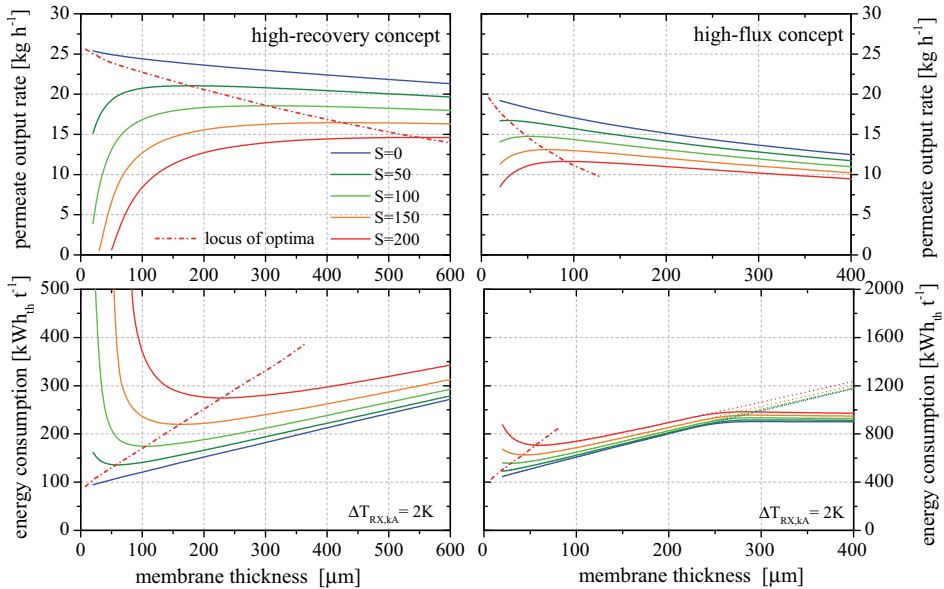


Figure 4.35: A model-based sensitivity analysis, covering the interdependent effects of membrane thickness and salinity on DCMD high-flux and high-recovery modules. Operating conditions: $T_{Ei} = 80\text{ }^{\circ}\text{C}$, $T_{Ci} = 25\text{ }^{\circ}\text{C}$, $\dot{m}_{Ei/Co} = 400\text{ kg h}^{-1}$, $\Delta T_{RX,kA} = 2\text{ K}$; Module: $L = 7.0/1.0\text{ m}$, $H = 0.7\text{ m}$, channel spacer S-320, laminate L-020A-S (BC) (with varying assumed thickness).

permeate output rate and increased energy consumption. Since the effect of salt is sensitive to the membrane thickness, the presence of salt significantly changes the influence of the membrane thickness on the module performance characteristics. The higher the salinity, the thicker the membranes that are required to achieve optimal performance. It is important to note that the optimal membrane thickness for flux is different to the optimal membrane thickness for energy consumption. Considering a salinity level of 100 g kg^{-1} in the given scenario, the optimal output rate is achieved with a $300\text{ }\mu\text{m}$ membrane, while the optimal energy consumption is given for a membrane thickness of $105\text{ }\mu\text{m}$. For ease of analysis, the locus curves of the optimal values are explicitly provided in the plots as red dotted lines. The membrane thickness has a low impact on flux, indicating a membrane thickness close to the corresponding optimal values. However, the design principles for high-recovery modules are probably aiming for optimal energy consumption rather than optimal flux. Thus, a membrane for a high-recovery module is most likely chosen close to the optimal thickness for energy consumption, which is considerably thinner than the value for optimal flux. In this region, the performance characteristics of the module are quite sensitive to the membrane thickness. Especially for thin membranes, a careful quantitative evaluation of the interdependence is recommended. Optimising the given DCMD high-recovery module with respect to heat recovery, the membrane thickness should be chosen between 0 and $230\text{ }\mu\text{m}$ for salinities ranging from 0 to 200 g kg^{-1} . The laminate L-020A-S, which was used in the high-recovery module prototypes, turned out to be suitable for salinity levels of approximately

50 to 100 g kg⁻¹.

Similar trends are found for the influence of the membrane thickness on a DCMD high-flux module, but the sensitivity to membrane thickness at zero salinity is greater. The steady decrease of the module flux performance with membrane thickness is identified to be approximately 1.7 kg h⁻¹ per 100 μm while the steady increase of the specific thermal energy consumption is identified to be approximately 190 kWh_{th} t⁻¹ per 100 μm membrane thickness. As for the high-recovery module, the influence of the membrane thickness on the high-flux module performance changes with the use of saline feed water, and thicker membranes are recommended for increasing salinity. However, for saline feed water, the membrane thickness for optimal performance turns out to be less sensitive to salinity than is observed in the high-recovery modules. It should be noted that the model automatically changes the thermal energy supply strategy from a system configuration with heat recovery (Fig. 4.5(c)) to one with direct heating of the evaporator channel without heat recovery (Fig. 4.5(a)), based on the associated energy consumption. The change of the system configuration leads to the conspicuous turning points near a membrane thickness of 250 μm in the performance curves for thermal energy consumption. The energy consumption that would result without changing the supply strategy are additionally drawn in Fig. 4.35 as dotted lines. However, the energy consumption might not be a parameter of interest for a high-flux module. For the high-flux modules, the membrane selection is most probably motivated by the optimal results regarding flux. It turns out that the optimal membrane thickness for high-flux modules is generally lower than the optimal membrane thickness identified for high-recovery modules. When optimising the given DCMD high-flux module with respect to flux, the membrane thickness should be chosen between 0 and 90 μm for salinities ranging from 0 to 200 g kg⁻¹. Considering the whole range of salinities, the super-sensitive range of membrane thicknesses is identified to be from 0 to 30 μm, which is thinner than the membranes that are usually available for MD applications. Consequently, the membrane selection for high-flux DCMD modules seems to be less critical than that for high-recovery modules. In the context of DCMD high-flux modules, the laminate L-020A-S turns out to be suitable for high salinity levels, whereas the choice of a thinner membrane (e.g. laminate L-020B-S/N) could be considered for moderate salinities of approximately 50 g kg⁻¹.

Since the PGMD configuration may be considered as a DCMD configuration extended by a permeate gap, the heat and mass transfer phenomenology in the membrane is essentially the same. Based on the comparability of the DCMD and the PGMD configuration, the simulation results of PGMD modules presented in Fig. 4.36 show similar interdependent effects of membrane thickness and salinity on module performance. Since the driving force in PGMD modules is significantly reduced by the permeate gap, optimal membranes are thicker and the general sensitivities to the membrane thickness are weaker than the results obtained in the DCMD scenarios. Furthermore, some different characteristics are identified. Unlike the DCMD modules, a specific membrane thickness turns out to be optimal for the PGMD modules, even for zero salinity. This is explained by the poor heat transfer in the backing pore volume that is oriented towards the permeate gap. A reduced membrane thickness increases the membrane permeability, but also its conductive heat transfer resistance. Depending on the heat transfer in the backing pore volume,

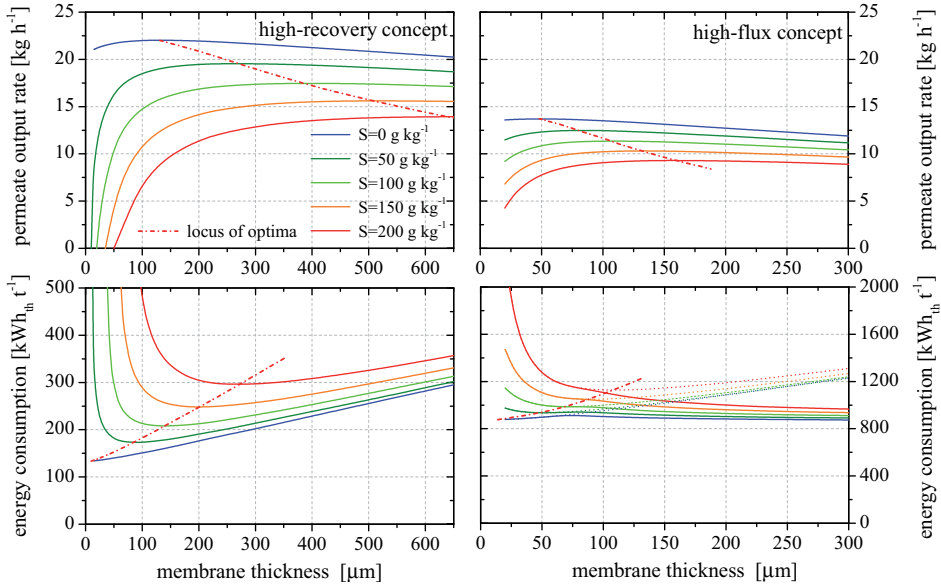


Figure 4.36: A model-based sensitivity analysis, covering the interdependent effects of membrane thickness and salinity on PGMD high-flux and high-recovery modules. Operating conditions: $T_{Ei} = 80^\circ\text{C}$, $T_{Ci} = 25^\circ\text{C}$, $\dot{m}_{Ei}/C_i = 400 \text{ kg h}^{-1}$; Module: $L = 7.0/1.0 \text{ m}$, $H = 0.7 \text{ m}$, channel spacer S-320, laminate L-020A-S (BC) (with varying assumed thickness), gap spacer S-025, impermeable film F-127.

the increased conductive heat transfer in the sections of the membrane that are covered by the backing may not be compensated by the higher membrane permeability. In the case of PGMD modules with the backing positioned towards the permeate channel, the thermal efficiency of the process reduces for thinner laminates. The optimal membrane thickness is defined by the superposition of the opposing effects of the membrane thickness on flux and thermal efficiency. Considering saline feed water, the preferred membrane thickness increases with salinity, similar to the observation made for the DCMD modules. When optimising the given module with respect to heat recovery, the membrane thickness should be chosen between 20 and $270 \mu\text{m}$ for salinities ranging from 0 to 200 g kg^{-1} . The laminate L-020A-S, which has been used in the high-recovery module prototypes, turns out to be suitable for salinity levels ranging from approximately 30 to 60 g kg^{-1} .

As for the DCMD modules, the optimal membrane thickness for high-flux PGMD modules is generally lower than that for the high-recovery PGMD modules. When optimising the given high-flux module with respect to flux, the membrane thickness should be chosen between 50 and $160 \mu\text{m}$ for salinities ranging from 0 to 200 g kg^{-1} . Similar to the observations for the DCMD high-flux modules, the super-sensitive range of membrane thicknesses is identified to be from 0 to $50 \mu\text{m}$, while low sensitivities of the module performance are observed for thicker membranes. The membrane selection for PGMD high-flux modules is therefore considered to be non critical

and the laminate L-020A-S turns out to be suitable for a wide range of salinity levels.

For the sake of completeness, sensitivity analyses on the influence of the membrane thickness on module performance have been conducted for AGMD and V-AGMD configurations, as well. The results are provided in Appendix I. Since the heat and mass transfer characteristics for an AGMD or a V-AGMD configuration are mainly defined by the air gap rather than by the membrane thickness, the influence of the membrane properties on the module performance is of minor importance. However, thicker membranes still reduce the overall permeability of a combined membrane and air gap, leading to a slight reduction of the AG module performance. Unlike for DCMD and PGMD, the effect of the membrane thickness is almost independent of salinity. For any AGMD or V-AGMD scenario, optimal flux and efficiency performance is obtained with membranes that are as thin as possible. The membrane selection for AGMD modules can therefore be limited to consideration of practical aspects only like membrane stability, durability or availability.

The different scenarios covering interdependent effects of membrane thickness and salinity illustrate that the membrane selection process for DCMD and PGMD modules is complex, especially for saline feed water. It is important to note that not only the salinity level but also the operating conditions and aspects of module design need to be taken into consideration for the selection of an optimal membrane. Thus, a comprehensive assessment of the influences of the key operational parameters and selected design parameters on membrane selection has been conducted, taking a PGMD high-recovery module at a feed water salinity of 35 g kg^{-1} as an example. Since the multi-dimensional field of parameters is too large to cover all possible combinations, the analyses aim to derive qualitative trends, creating an awareness of the given interdependence and providing a general method for membrane selection. Due to the similarity of the PGMD and the DCMD configuration, the qualitative results are considered to be valid also for the DCMD configuration. For the analyses on operating conditions, variations in salinity, feed flow rate, temperature difference, mean temperature level and deaeration pressure have been considered. For the analyses on design parameters, variations in heat transfer, permeate gap thickness, channel length, backing porosity and membrane thermal conductivity have been considered. The nominal operational parameters and the model parameterisation are the same as those for the previous analyses. For each scenario, the optimal membrane thickness with respect to the thermal energy consumption was identified by solving the one-dimensional optimisation problem with the generic optimisation program GenOpt[®], which was linked to the MD model (refer to Sec. 5.2.4 for detailed information). The locus curves of the optima are given for each parameter variation in Fig. 4.37.

The trend obtained for a variation of the salinity level is already known from the discussions above. Furthermore, the influence of the channel length on the optimal membrane thickness was already given by the comparison of high-recovery and high-flux modules. Each of the locus curves obtained from the given study is monotonic.

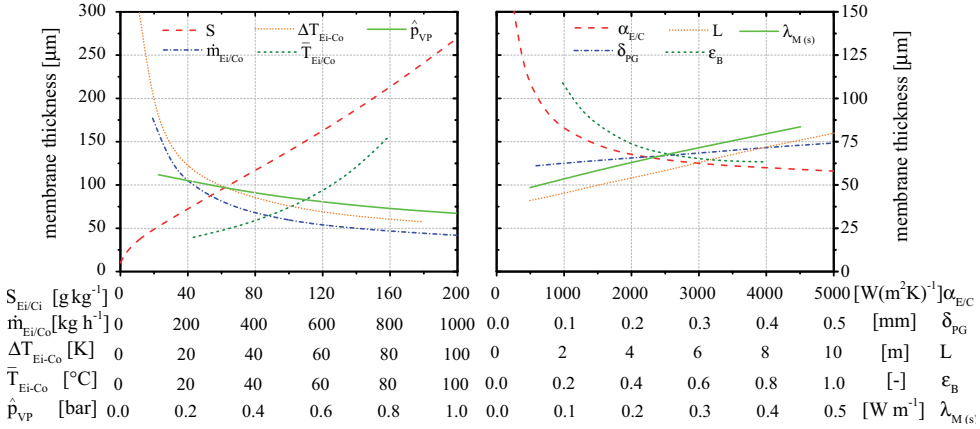


Figure 4.37: Model-based sensitivity analyses, covering the influence of operating conditions and aspects of module design on the optimal membrane thickness with respect to the specific thermal energy consumption. A high recovery PGMD module has been considered as an example. Nominal operating conditions: $S_{Ei/Ci} = 35 \text{ g kg}^{-1}$, $T_{Ei} = 80 \text{ }^{\circ}\text{C}$, $T_{Ci} = 25 \text{ }^{\circ}\text{C}$, $\dot{m}_{Ei/Co} = 400 \text{ kg h}^{-1}$, $\hat{p}_{VP} = 1 \text{ bar}$, Module: $L = 7.0 \text{ m}$, $H = 0.7 \text{ m}$, channel spacer S-320, laminate L-020A-S (BC) (with varying assumed thickness), gap spacer S-025, impermeable film F-127.

A summary of the qualitative trends derived from Fig. 4.37 may be given by the following general statements:

The optimal membrane thickness for saline feed water increases for

- higher feed water salinities
- lower feed flow rates
- smaller temperature differences
- higher mean temperature levels
- lower deaeration pressures
- lower heat transfer coefficients
- thicker permeate gap widths
- longer flow channels
- lower backing porosities
- higher membrane thermal conductivities

All results obtained in this section are conform to the following general statements:

For DCMD and PGMD modules, the optimal membrane for the treatment of feed water without salt may be chosen as thin as is feasible. For the treatment of feed water with a specific salinity, the optimal membrane thickness increases if the interfacial temperature difference is decreased by any change in the operating conditions or in module design. The negative effect of salinity turns out to be more distinct for low driving forces. Therefore, the sensitivity of the optimal membrane thickness to the interfacial temperature difference is expected to increase with salinity level. For AGMD and V-AGMD modules, the optimal membrane thickness is as thin as is feasible, independent of salinity level.

4.3.7 Performance Potential using Advanced Materials

The experimental work that has been done to support the MD analyses and the theoretical model development is based on the specific materials presented in Sec. 3.3.4. The material selection was motivated by the material's thermodynamic properties but also by general availability, minimum order quantity, delivery time, issues concerning fabrication and costs. Some of the materials deployed in the prototype modules may not reflect the best possible choice in terms of thermodynamic performance. Appreciable potential for performance improvement is expected by the introduction of the best design materials that are already commercially available today. Since much research is currently being conducted on the development of new materials for MD, further improvement is expected in the coming years due to the use of advanced materials with thermodynamic properties beyond the current state of the art.

This section provides sensitivity analyses on the quantitative impact that may be achieved by improvements to the different key materials, namely the main channel spacers, the membrane, the backing and the impermeable film. Since the role of a certain material is expected to be different for DCMD, PGMD, AGMD and V-AGMD performance, the analyses were conducted for each of the process variants and evaluated comparatively. Furthermore, the assessment distinguishes between a high-recovery module concept and a high-flux module concept for each of the process configurations. The specifications of the reference modules are summarised in Tab. 4.8. The reference parameterisation of the node models is derived from channel spacer S-320, laminate L-020A-S, PGMD gap spacer S-025, (V-)AGMD gap spacer S-200 and impermeable film F-127, similar to the parameterisation in Sec. 4.3.6. The assessment has been based on the same default inlet conditions as the previous studies that consider an evaporator inlet temperature of 80 °C, a condenser inlet temperature of 25 °C, a mass flow rate of 400 kg h⁻¹ and a salinity of 35 g kg⁻¹. For the DCMD configuration, the limited heat transfer performance for the external heat recovery system as well as a mass flow compensation are taken into consideration. For the (V-)AGMD configuration, the flexibility of the film materials that affect the air-gap width and residual air that presents a lower limit to the air partial pressure in the air gap are taken into account as described in Sec. 4.3.6.

In order to isolate the influence of a specific material, the respective material properties are successively modified in four discrete steps, while the properties of the other materials remain constant at the reference values. The reference parameterisation and the successive parameter modifications are summarised in Tab. 4.9 for the different sensitivity analyses.

Sensitivity analysis #1 is dedicated to potential performance improvements associated with an improvement of the evaporator and the condenser channel spacers. The impact of improved channel spacers is represented by a successive enhancement of the heat transfers by factors of 1.5, 2.0, 4.0 and 10.0. Therefore, the heat transfer correlation in Eq. 4.71, used for the module model predictions, is extended by the factor $f_{\alpha_{E/C}}$. The relative performance improvements predicted for the permeate output rate and specific thermal energy consumption are illustrated in Fig. 4.38. The absolute values for the corresponding reference results are provided as supple-

Table 4.9: Material parameterisation used for the comparative assessment of the potential for performance improvements by advanced materials. The sensitivity analyses are assigned to the key materials of interest as follows: #1 spacer for main flow channels; #2 membrane; #3 backing; #4 impermeable film; #5 combination of selected material improvements.

	parameter	unit	reference	step 1	step 2	step 3	step 4	#5
#1	$f_{\alpha_{E/C}}$	[-]	1.0	1.5	2.0	4.0	10.0	1.5
#2	δ_M	[μm]	70	50	50	50	50	50
	d_M	[μm]	0.2	0.2	40	40	40	0.2
	ε_M	[-]	0.8	0.8	0.8	1.0	1.0	0.8
	$\lambda_M^* \delta_M^{-1}$	[$\text{W}(\text{m}^2\text{K})^{-1}$]	620	620	620	460	1	620
#3	position	[-]	BE	BC	BC	BC	noB	BC
	δ_B	[μm]	280	280	140	70	–	100
	ε_B	[-]	0.5	0.5	0.7	0.9	–	0.8
	τ_L (τ_M)	[-]	1.8	1.8	1.6	1.4	(1.3)	1.5
#4	δ_F	[μm]	127	70	30	10	noF	30

mentary information.

At first, a detailed analysis of the results obtained for the DCMD high recovery configuration is provided as an example and as a guide for reading the corresponding plots. The subsequent discussions focus on the general sensitivities and comparison of the different process configurations rather than on commenting on individual values.

With the materials used in the prototypes from Sec. 4.2.4, the reference values for the DCMD high-recovery configuration are predicted to be 21.6 kg h^{-1} for the permeate output rate and $127 \text{ kWh}_{\text{th}} \text{ t}^{-1}$ for the specific thermal energy consumption. For heat transfer in the main flow channels which is enhanced by factors of 1.5, 2.0, 4.0 and 10.0, the expected improvements of the permeate output rates are 1.5%, 2.3%, 3.6% and 4.3% respectively, while the corresponding reductions of the specific thermal energy consumption are 12.6%, 18.9%, 28.3% and 34.6%. It turns out that improved heat transfer in any high-recovery module configuration mainly leads to a reduction of the specific thermal energy consumption rather than to an improvement of the permeate output rate. The improved heat transfer does fundamentally reduce the thermal energy demand by reducing the temperature polarisation. The bulk stream temperature difference between the evaporator and condenser channels decreases while the interfacial temperature difference and consequently the driving force remain almost constant. The different sensitivities for the different process configurations may principally be attributed to the fraction of the heat transfer in the main flow channels and the overall temperature drop from the evaporator to the condenser bulk streams, which have already been analysed in the context of test cell experiments in Fig. 3.32. The highest sensitivity is obtained for the DCMD variant. The sensitivities for the PGMD and the V-AGMD processes are comparable and the lowest sensitivity is given for the AGMD configuration.

For the high-flux concept, the sensitivities for the different process variants are generally ordered

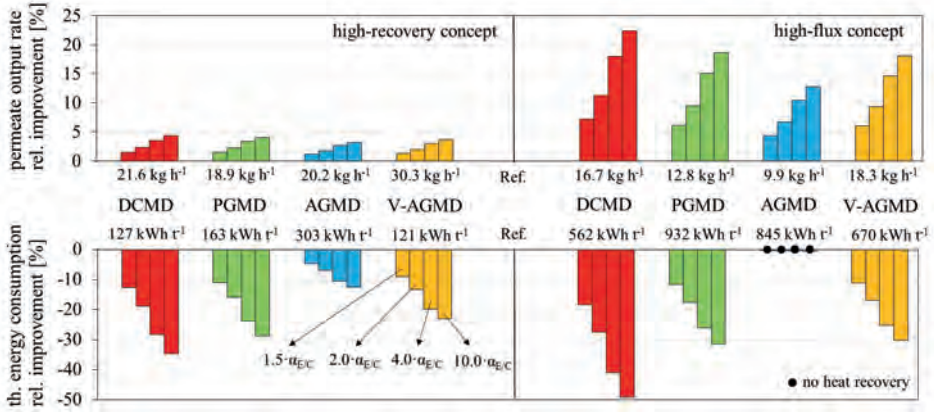


Figure 4.38: Comparative model-based assessment #1 on the potential associated with an improvement of the evaporator and the condenser channel spacers. A successive enhancement of the bulk stream heat transfer coefficient by factors of 1.5, 2.0, 4.0 and 10.0 is considered. The predictions are provided for high-recovery modules and for high-flux modules in DCMD, PGMD, AGMD and V-AGMD configurations. Operating conditions: $T_{Ei} = 80\text{ }^{\circ}\text{C}$, $T_{Ci} = 25\text{ }^{\circ}\text{C}$, $\dot{m}_{Ei/Co} = 400\text{ kg h}^{-1}$, $S_{Ei} = 35\text{ g kg}^{-1}$, $\hat{p}_{VP}^{AGMD} = 0.03\text{ bar}$, $\hat{p}_{a,residual}^{i,VAGMD} = 0.05\text{ bar}$, $\Delta T_{RX,kA}^{DCMD} = 2\text{ K}$; Module: $L = 7.0/1.0\text{ m}$, $H = 0.7\text{ m}$, channel spacer S-320, laminate L-020A-S (BC), gap spacer S-200/S-025, impermeable film F-127.

similarly, but they exhibit significant differences, especially regarding the influence on the permeate output rate. For the high-flux modules, the permeate output rate may be increased by more than 12% for all of the process configurations. For the DCMD variant, a flux improvement of up to 22% is predicted. In contrast to modules with high heat recovery, the improved heat transfer does reduce the bulk stream temperature difference and increase the interfacial temperature difference at the same time. Consequently, the reduced thermal energy consumption for the high-flux concept is accompanied by an enhanced flux performance. It is obvious from the given reference values that high fluxes generally lead to high thermal energy consumptions. However, for applications aiming for high driving forces, the thermal energy consumption may not be the characteristic of greatest interest. According to Eq. 4.54, heat recovery is not reasonable for some of the high-flux scenarios. For these specific scenarios, marked with a black dot, the specific thermal energy consumption is evaluated using Eq. 4.43, based on a direct heating concept. Since the thermal energy consumption for a direct heating concept is independent of the temperature difference between the evaporator and the condenser channels, no improvements based on enhanced heat transfer are predicted for the AGMD configuration in Fig. 4.38.

Sensitivity analysis #2 is dedicated to potential performance improvements associated with an improvement of the membrane. The membrane properties are successively enhanced according to Tab. 4.9. In step one, the membrane thickness is reduced from $70\text{ }\mu\text{m}$ to $50\text{ }\mu\text{m}$, representing a

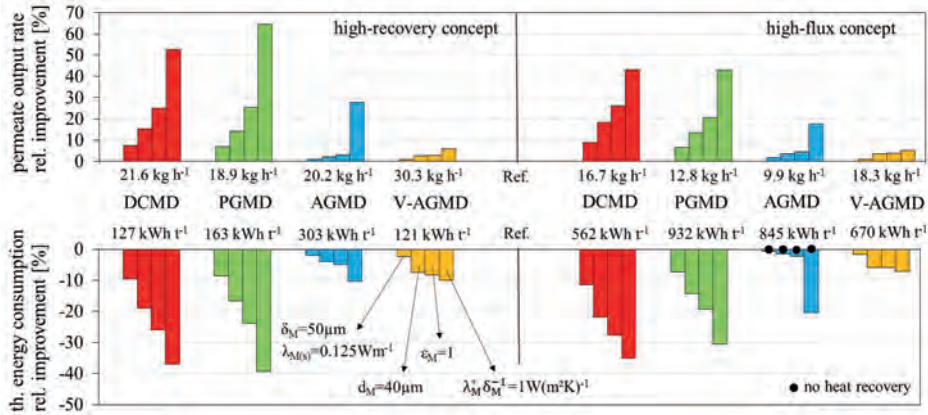


Figure 4.39: Comparative model-based assessment #2 of the potential associated with an improvement of the membrane properties. A successive enhancement of the membrane is considered according to Tab. 4.9. The predictions are provided for high-recovery modules and for high-flux modules in DCM, PGMD, AGMD and V-AGMD configurations. Operating conditions: $T_{Ei} = 80^\circ\text{C}$, $T_{Ci} = 25^\circ\text{C}$, $\dot{m}_{Ei/Co} = 400\text{ kg h}^{-1}$, $S_{Ei} = 35\text{ g kg}^{-1}$, $\hat{p}_{VP}^{\text{VAGMD}} = 0.03\text{ bar}$, $\hat{p}_{a,\text{residual}} = 0.05\text{ bar}$, $\Delta T_{RX,kA}^{\text{DCMD}} = 2\text{ K}$; Module: $L = 7.0/1.0\text{ m}$, $H = 0.7\text{ m}$, channel spacer S-320, laminate L-020A-S (BC), gap spacer S-200/S-025, impermeable film F-127.

general improvement of the membrane permeability by a factor of 1.4. In principle the conductive heat transfer coefficient would increase due to its reciprocal dependence on the membrane thickness. However, in the given scenario the membrane's thermal conductivity is assumed to be reduced so that the membrane's conductive heat transfer coefficient remains constant at a value of $620\text{ W(m}^2\text{K)}^{-1}$. This first step is thermodynamically identical to a scenario that considers any improvement of the membrane permeability by a factor of 1.4 at constant membrane thickness. In the second step, the nominal pore size is increased by more than two orders of magnitude, leading to a negligible Knudsen diffusion resistance. The third step implies a further reduction of the diffusion resistance by an increase of the membrane porosity from 0.8 to 1.0. Since no polymer phase is left for conductive heat transfer, the improved porosity is accompanied by a reduction of the conductive heat transfer coefficient to $460\text{ W(m}^2\text{K)}^{-1}$. In the last step, the membrane is treated as an ideal thermal insulating layer. The relative performance improvements predicted for the permeate output rate and specific thermal energy consumption are presented in Fig. 4.39. The absolute values obtained with reference parameterisation are provided as supplementary information. Due to similar reference conditions, these values are equal to those presented in Fig. 4.39.

The sensitivities of the model predictions with respect to membrane improvements show a similar character for the high-recovery and the high-flux module concepts. Thus, the quantitative discussion is based on the high-recovery module concept as an example.

The given results clearly indicate that an improvement of the membrane permeability without

changing the conductive heat transfer coefficient has a positive effect on all of the process configurations. The permeate output rate and the thermal energy consumption for the DCMD and the PGMD configurations are improved by 7% to 9%. Since the mass transfer resistance of the air-gap variants is mainly defined by the molecular diffusion through the air gap rather than by the membrane structural properties, the role of the membrane is generally of minor thermodynamic relevance. The influence of the improved membrane properties on AGMD and V-AGMD module performance is predicted to be less than 1% for flux and less than 2% for energy consumption. By additionally eliminating the Knudsen diffusion resistance in step 2, further improvements for flux performance and energy consumption are expected for the DCMD and the PGMD high-recovery modules. The improvements amount to 14% to 19%. Again, almost no effect is observed for the air-gap variants. For the V-AGMD configuration, the role of an improved membrane shows a slightly higher effect, since the mass transfer resistance of the gap is strongly reduced by deaeration. A similar statement may be made when an ideal membrane structure with a porosity of 100% is assumed. The predicted flux improvements for DCMD and PGMD are about 25%, while a relative improvement of only 2% to 4% is achieved with the air-gap variants. In the last step, the membrane is considered to be an ideal thermal insulator, leading to 100% thermal efficiency for all of the MD configurations. This scenario is rather unrealistic, but it gives a quantitative reference on the important role of conductive losses in the context of MD modules. The potential for improvements is significant for DCMD and PGMD modules, predicted to be 53% and 65% for the permeate output rate and 37% and 39% for the thermal energy consumption. Unlike for the preceding steps, the air-gap variants show quite different sensitivities. Significant improvements are expected for AGMD, while the sensitivity for V-AGMD is still low. The thermal efficiency achieved with available materials already takes on values >90% for the V-AGMD configuration, while the efficiencies achieved with an AGMD configuration are in the range of 70 to 80% (see Fig. 4.32). Consequently, the ideal insulating layer improves the thermal efficiency for the AGMD, while the V-AGMD variant does not offer significant potential for improvements by insulation.

Sensitivity analysis #3 is dedicated to potential performance improvements associated with an improvement of the backing material. The impact of an improved backing is represented by a successive enhancement of different backing properties according to Tab. 4.9. The parameters associated with the scrim type backing from Tab. 3.4 are used as reference values. In order to clarify the influence of the backing position, backing located towards the evaporator side (BE) is considered to be the reference case, in contrast to the reference cases in the other scenarios. In the first step, the backing position is then changed from the evaporator to the condenser side, so step 1 results in the same reference conditions as the other sensitivity analyses. In step 2, the backing properties are generally improved by reducing the thickness from 280 μm to 140 μm , increasing the porosity from 0.5 to 0.7 and reducing the laminate tortuosity, which is assumed to depend on the backing porosity, from 1.8 to 1.6. In step 3, the backing parameters are improved further by reducing the thickness to 70 μm , increasing the porosity to 0.9 and reducing the laminate tortuosity to 1.4. The last step represents the optimal case of a membrane without backing (noB). The relative performance improvements predicted for the permeate output

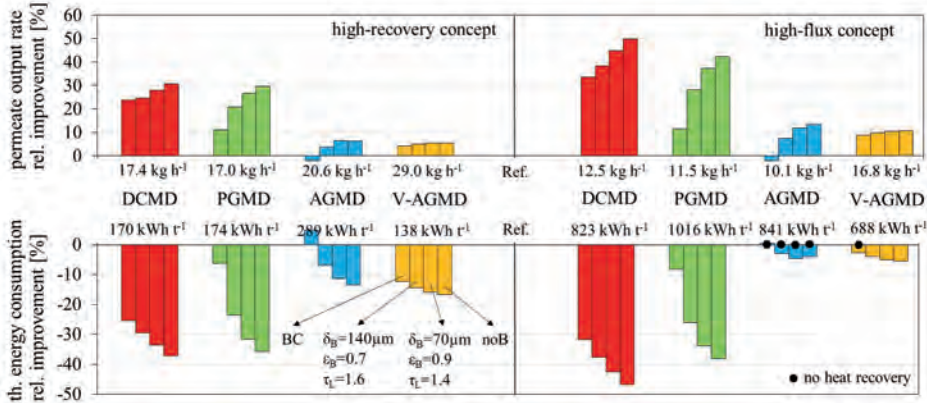


Figure 4.40: Comparative model-based assessment #3 of the potential associated with an improvement of backing properties. A successive change of the backing position and the backing structure is considered according to Tab. 4.9. The predictions are provided for high-recovery modules and for high-flux modules in DCMD, PGMD, AGMD and V-AGMD configurations. Operating conditions: $T_{Ei} = 80\text{ }^{\circ}\text{C}$, $T_{Ci} = 25\text{ }^{\circ}\text{C}$, $\dot{m}_{Ei/Co} = 400\text{ kg h}^{-1}$, $S_{Ei} = 35\text{ g kg}^{-1}$, $\hat{p}_{VP}^{VAGMD} = 0.03\text{ bar}$, $\hat{p}_{a,residual}^{i,VAGMD} = 0.05\text{ bar}$, $\Delta T_{RX,kA}^{DCMD} = 2\text{ K}$; Module: $L = 7.0/1.0\text{ m}$, $H = 0.7\text{ m}$, channel spacer S-320, laminate L-020A-S, gap spacer S-200/S-025, impermeable film F-127.

rate and specific thermal energy consumption are illustrated in Fig. 4.40. The absolute values obtained with the new reference case are provided as supplementary information.

The sensitivities of the model predictions to membrane improvements show a similar character for the high-recovery and the high-flux module concepts. Thus, the quantitative discussion is provided for the high-recovery module concept as an example. As expected from Sec. 3.4.3, significant differences in the performance behaviour are obtained for the different backing positions. The performance predicted for the reference case (BE) is significantly lower than the performance achieved with step 1 (BC), which was taken as the reference case in the other sensitivity analyses. The strongest effect is predicted for the DCMD variant, which shows the flux improved by 24% and the energy consumption reduced by 25%. Even though the fundamental effect of the backing position is similar for the PGMD configuration, the quantitative values of 11% in flux and 6% in thermal energy consumption turn out to be significantly lower. The improvements associated with a backing positioned towards the condenser side are partially offset by the effective permeate gap thickness increasing from 0.25 mm to 0.50 mm due to the backing layer. Furthermore, the heat transfer through the backing pore volume is low if the backing is immersed in the permeate channel. A similar statement may be derived concerning the effect of the backing position on AGMD performance. If the backing is located towards the condenser side, the permeate output rate and the energy consumption are worsened by the backing layer, which increases the distance for diffusion through the air gap. For the V-AGMD configuration, the impact of a wider air gap is low and does not overcompensate the positive effects of a free membrane surface for evapo-

ration. It is obvious from the given results that positioning a backing towards the condenser side is the preferred case and should be considered as the standard design. Analysing the second and third steps, the module performance is enhanced as the backing structural properties are improved. Especially the PGMD and AGMD configurations show appreciable sensitivity to the reduced backing thickness for the given reasons. In the third step, the predicted performance of DCMD and PGMD is improved by 28% for flux and approximately 32% for thermal energy consumption. For the air-gap variants, the predicted improvements are only 6% for flux and approximately 14% for thermal energy consumption. For all of the MD configurations, only minor potential for further improvement is associated with step 4, considering the optimal case without any backing (noB).

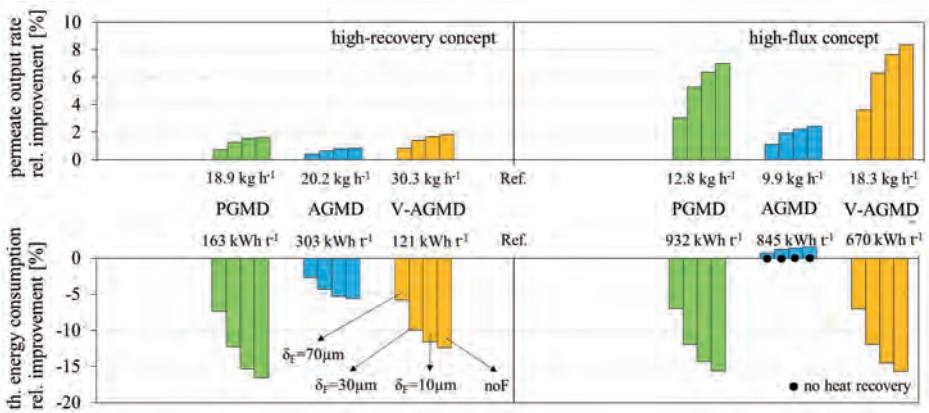


Figure 4.41: Comparative model-based assessment #4 of the potential associated with an improvement of the impermeable film layer. Successive reduction of the film thickness is considered with 127, 70, 30, 10 and 0 μm . The predictions are provided for high-recovery modules and for high-flux modules in PGMD, AGMD and V-AGMD configurations. Operating conditions: $T_{Ei} = 80^\circ\text{C}$, $T_{Ci} = 25^\circ\text{C}$, $\dot{m}_{Ei/Co} = 400\text{ kg h}^{-1}$, $S_{Ei} = 35\text{ g kg}^{-1}$, $\hat{p}_{VAGMD}^{VAGMD} = 0.03\text{ bar}$, $\hat{p}_{a,residual}^{i,VAGMD} = 0.05\text{ bar}$; Module: $L = 7.0/1.0\text{ m}$, $H = 0.7\text{ m}$, channel spacer S-320, laminate L-020A-S (BC), gap spacer S-200/S-025, impermeable film F-127.

Sensitivity analysis #4 is dedicated to potential performance improvements associated with an improvement of the impermeable film. This assessment is relevant only for the PGMD, AGMD and V-AGMD configurations, since no impermeable film is used for the DCMD configuration. The impact of an improved film is represented by a successive reduction of film thickness from the reference value of 127 μm to 70 μm , 30 μm , 10 μm and 0 μm . It is worth mentioning that an equivalent effect would be achieved by enhancing the film material's thermal conductivity instead of the material thickness. The relative performance improvements predicted for the permeate output rate and specific thermal energy consumption are plotted in Fig. 4.40. The absolute values obtained with the reference case are provided as supplementary information. Since the reference parameters are similar to those presented in analyses #1 and #2, the reference performance

values are equal to those presented in Figs. 4.38 and 4.39.

In principle, the influence of the impermeable film is comparable to the influence of the heat transfer coefficient in the main flow channels. The film improvements mainly affect the specific thermal energy consumption rather than the permeate output rate for the high-recovery modules, while the permeate output rate and the energy consumption is affected for high-flux modules. However, the potential for improvement based on the selection of thinner film materials is limited and should not be overestimated. The permeate output for the high-recovery configurations may not be increased by more than 2%. At least the effect on the PGMD and V-AGMD high-flux modules is expected to be in a reasonable range from 6% to 9%. For the AGMD configuration, the improvement of the impermeable film does not have a significant effect on either module concept. The energy consumption for the high-flux AGMD module is even increased due to the influence of the film thickness on the mean air-gap temperature and the direct heating concept without heat recovery. For PGMD and V-AGMD modules, the thermal energy consumption may realistically be reduced by 10% to 12%, by using films with a thickness of 30 μm instead of the reference film material F-127.

Sensitivity analysis #5 considers the evaluation of a combined potential associated with a reasonable improvement for each of the key materials according to the last column in Tab. 4.9. The associated material parameters are modified such that the resulting model predictions reflect the realistic potential for improvement that may be achieved on the medium term. The proposed material properties may partially be achieved by wise material selection even today, or deviate only slightly from the state of the art. In the first step, the heat transfer is assumed to be enhanced by a factor of 1.5. In the second step, the membrane permeability is improved by a reduction of the membrane thickness to 50 μm , while the conductive heat transfer coefficient remains constant at $620 \text{ W}(\text{m}^2\text{K})^{-1}$. This scenario is thermodynamically identical to a scenario that considers any improvement of the membrane permeability by a factor of 1.4 at constant membrane thickness. In the third step, the backing properties are improved to values slightly better than those specified for the non-woven type of backing in Tab. 3.9. The backing thickness is reduced to 100 μm , the backing porosity is increased to 0.8 and the laminate tortuosity is reduced to 1.5. In the last step, the thickness of the impermeable film is reduced to 30 μm . The relative performance improvements predicted for the permeate output rate and specific thermal energy consumption are illustrated in Fig. 4.42. The absolute values obtained with the reference case are provided as supplementary information. Since the reference parameters are similar to those presented in analyses #1, #2 and #4, the reference performance values are equal to those presented in Figs. 4.38, 4.39 and 4.41.

Considering the high-recovery module concept, the expected realistic improvements in permeate output rate and specific thermal energy consumption are 11% and 29% for DCMD, 23% and 50% for PGMD, 11% and 24% for AGMD and 5% and 24% for V-AGMD. For the high-flux module concepts, the expected realistic improvements in permeate output rate and specific thermal energy consumption are 24% and 39% for DCMD, 46% and 51% for PGMD, 22% and 4% for AGMD and 16% and 27% for V-AGMD. As stated in the previous analyses, the performance improvements for the high-recovery modules mainly affect the specific thermal energy

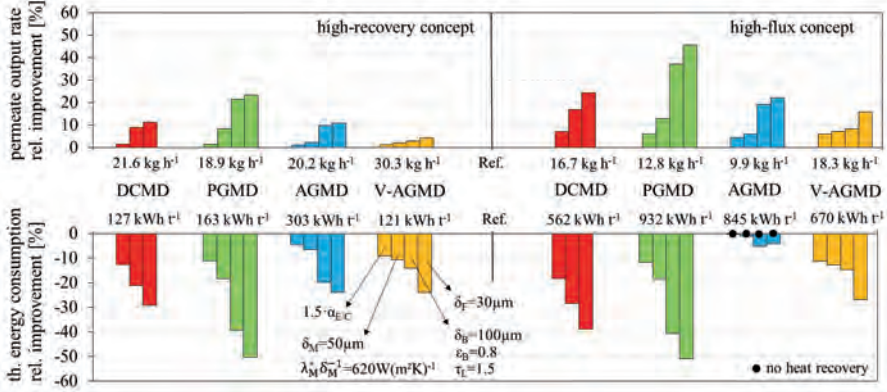


Figure 4.42: Comparative model-based assessment #5 of the combined potential associated with a realistic improvement of the individual materials for the key components. A successive enhancement of the channel spacer, the membrane properties, the backing properties and the film thickness is considered according to Tab. 4.9. The predictions are provided for high-recovery modules and for high-flux modules in DCMD, PGMD, AGMD and V-AGMD configurations. Operating conditions: $T_{Ei} = 80\text{ }^{\circ}\text{C}$, $T_{Ci} = 25\text{ }^{\circ}\text{C}$, $\dot{m}_{Ei/Co} = 400\text{ kg h}^{-1}$, $S_{Ei} = 35\text{ g kg}^{-1}$, $\hat{p}_{VP}^{VAGMD} = 0.03\text{ bar}$, $\hat{p}_{a,residual}^{i,VAGMD} = 0.05\text{ bar}$, $\Delta T_{RX,kA}^{DCMD} = 2\text{ K}$; Module: $L = 7.0/1.0\text{ m}$, $H = 0.7\text{ m}$, channel spacer S-320, laminate L-020A-S (BC), gap spacer S-200/ S-025, impermeable film F-127.

consumption rather than the permeate output rate, while the improvements for the high-flux module concept affect the permeate output rate and the energy consumption. It is obvious, that the availability of suitable laminates will play a significant role in achieving the stated goals. The membrane improvements may be hard to achieve, especially due to limitations based on robustness and durability. Even negative effects on membrane performance could be accepted in the future as a result of procedures like surface coating. However, analysing the important role of the backing structure for DCMD, PGMD and AGMD, the choice and optimisation of suitable backings that might even be integrated into advanced channel spacers, seems a worthwhile focus for further material developments. The promising results for the V-AGMD configuration could be effectively optimised by simply selecting thinner film materials which are already commercially available today.

4.3.8 Parametric Field Studies

The wide variety of MD configurations, geometrical module designs and operational conditions create a broad field of feasible performance characteristics for membrane distillation. Due to the large number of parameters with interdependent influences on the thermodynamic module performance, it does not seem feasible to derive a complete overview of MD performance potential.

Even the quite comprehensive experimental work that has been conducted within the framework of this thesis covers only a narrow window of the possible MD performance characteristics. However, usually some of the conditions such as raw water salinity and available temperature levels are pre-defined by a given project location. In this case, the MD model may be applied for a parametric field study covering a wide range of flow conditions and channel designs. A parametric field study has been set-up for common temperature conditions and sea water salinity as an example, represented by an evaporator inlet temperature of 80 °C, a condenser inlet temperature of 25 °C and a salinity of 35 g kg⁻¹. A focus is placed on the interdependence of permeate output rate, flux and heat recovery for each of the basic process configurations. Thus, the energy input, the transfer area and the channel design have been identified to be the most important parameters to be investigated. The energy input is provided by the sensible heat of the inlet flow streams and is therefore directly linked to the inlet mass flow rates. In real applications, modules with thin flow channels should not be operated at high mass flow rates due to significant hydraulic pressure losses. In order to receive realistic results only, the mass flow rates are derived from flow velocities, which are considered in the range from 0.01 to 0.2 m s⁻¹. However, considering a reasonable flow velocity and a module with long flow channels, the pressure loss may still reach unrealistic values. The results for configurations that cause a hydraulic pressure loss higher than 1.0 bar (evaporator and condenser channels) are therefore filtered out during post-processing. To vary the transfer area, the channel length is varied in a range from 0.5 to 30 m, while keeping the channel height of 0.7 m constant. A variation in channel height seems unnecessary, since it reflects a scale-up/down of the output rate rather than a change in thermodynamic performance behaviour (see Sec. 4.3.1 for details). To cover a wide range of flow channel designs, the channel width is varied from 0.5 to 10 mm, allowing the investigation of a wide range of mass flow rates. A summary of the parameter field is given in Tab. 4.10. By considering all of the parameter combinations, the parametric field study covers 1728 individual scenarios, 576 for each of the MD configurations.

Table 4.10: Summary of the parameters considered for the parametric field studies, covering 576 different scenarios for each considered MD configuration.

parameter	unit	field range
MD configuration		DCMD, PGMD, AGMD
deaeration pressure	[bar]	0.03 , 1.00
flow velocity	[m s ⁻¹]	0.01 , 0.03 , 0.07 , 0.10 , 0.20 , 0.30
channel length	[m]	0.5 , 1.0 , 2.5 , 5.0 , 10.0 , 15.0 , 20.0 , 30.0
channel width	[mm]	0.5 , 1.0 , 2.0 , 3.0 , 5.0 , 7.0 , 10.0

The reference parametrisation of the node models is derived from channel spacer S-320, laminate L-020A-S, PGMD gap spacer S-025, AGMD gap spacer S-200 and impermeable film F-127. However, a moderate improvement of the different key materials is considered, corresponding to sensitivity analysis #5 from Tab. 4.9 (see Fig. 4.42 for details). For the evaluation of the DCMD variant, a limited heat transfer performance is assumed for the external heat recovery system, which is taken into account by a constant temperature drop of 2 K (see Sec. 4.3.2 for details).

Mass flow compensation is considered for the definition of the condenser inlet flow rate in the DCMD model predictions (see Sec. 4.3.2 for details). The air-gap is assumed to have an effective thickness of 1.8 mm instead of the nominal thickness of 2.0 mm, due to deformation of the elastic film layers (see Sec. 4.3.4 for details). For the evaluation of the deaerated operation conditions, a minimum local air pressure of 0.05 bar accounts for non-ideal deaeration of the membrane pore volume or the air gap.

The summarised results obtained for the whole parameter field are given in Fig. 4.43. The mass transfer performance parameters, flux and total output rate, are plotted versus the corresponding heat recovery. To represent the modules' capability for heat recovery, the Gained Output Ratio (GOR) was chosen for reasons of clarity, allowing easier interpretation of the diagrams. It is worth mentioning that the GOR, which fundamental definition is provided in Sec. 2.5.2, is an alternative reciprocal measure for the specific thermal energy consumption and may be transformed directly into the units known from the thermal energy consumption with Eq. 4.58. For orientation, the GOR labels of the x-axis are transformed into a secondary label, representing the heat recovery in the units for the specific thermal energy consumption based on a heat of evaporation of 650 kWh t^{-1} .

The diagrams show the wide variety of performance results that could be achieved with MD. With the given parametric field, the permeate output rates range from 0 to 351 kg h^{-1} and the flux results show values up to $115 \text{ kg (m}^2\text{h)}^{-1}$. The GOR is identified to be from 0.78 to 22. Due to salinity effects, some of the DCMD and PGMD scenarios result in zero output and consequently in zero GOR. It should be noted that the model automatically switches from a heat-recovery concept to a direct-heating concept, if this is beneficial from an energy point of view (see Fig. 4.5). Thus, the lower end GOR results are all based on a direct-heating concept. It is obvious that high fluxes automatically lead to low GOR, confirming the fundamental necessity to decide between a high-flux and a high-recovery module concept. The highest flux result of $115 \text{ kg (m}^2\text{h)}^{-1}$ is obtained with the DCMD configuration, since the DCMD channel design has the lowest total heat and mass transfer resistances. Due to the gap and film resistances, the maximal flux obtained for PGMD is $56 \text{ kg (m}^2\text{h)}^{-1}$ and for AGMD $44 \text{ kg (m}^2\text{h)}^{-1}$. The highest GOR results are achieved with the PGMD configuration. In comparison to AGMD, the heat transfer resistance of the permeate gap is relatively low and the sensible heat from the permeate is recovered. The GOR results obtained for the DCMD configuration only reach values up to 10.8. This major difference to the maximal PGMD result is explained by the model parameterisation that assumes a constant temperature drop of 2 K associated with the external DCMD heat recovery system, while the efficiency of the internal heat recovery in PGMD and AGMD is directly linked to the channel length.

The results obtained for the different MD configurations have also been separated from each other, allowing a more detailed analysis. Fig. 4.44 represents the (V-)DCMD results only, including the results that had been filtered out based on high hydraulic pressure losses. Similar plots, derived for (V-)PGMD and (V-)AGMD, may be found in Appendix J. A comparison

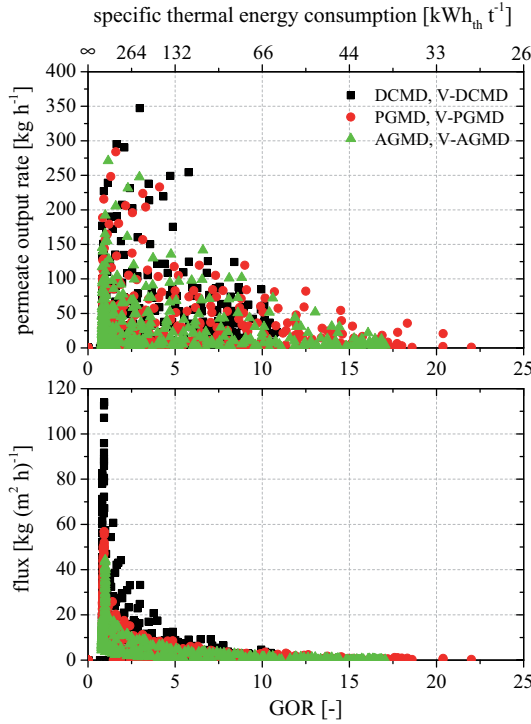


Figure 4.43: Summary of the whole parameter field for (V-)DCMD, (V-)PGMD and (V-)AGMD process configurations based on the conditions stated in Tab. 4.10. The results that include a hydraulic pressure loss higher than 1.0 bar have been filtered out. Constant operating conditions: $T_{Ei} = 80\text{ }^{\circ}\text{C}$, $T_{Ci} = 25\text{ }^{\circ}\text{C}$, $S_{Ei} = 35\text{ g kg}^{-1}$, $S_{Ci}^{\text{DCMD}} = 0\text{ g kg}^{-1}$, $\Delta T_{\text{RX,kA}}^{\text{DCMD}} = 2\text{ K}$, $\hat{p}_{a,\text{residual}} = 0.05\text{ bar}$; Constant module parameter: $H = 0.7\text{ m}$. The material parameterisation covers a realistic improvement of the materials according to scenario #5 from Tab. 4.9 (see Fig. 4.42).

of the maximal values obtained for DCMD and V-DCMD clearly reflects the beneficial effect of membrane deaeration. For the deaerated operating conditions, the field of results is generally shifted towards higher permeate output rates, higher fluxes and higher GOR at the same time. The maximal output rate obtained with deaerated conditions is 351 kg h^{-1} , while a maximum of only 293 kg h^{-1} is predicted without deaeration. The maximal flux reduces from 115 to $83\text{ kg (m}^2\text{ h)}^{-1}$ and the maximal GOR reduces from 10.8 to 9.1, if deaeration is not activated. The filtered scenarios are localised in the area of reasonable GOR rather than for the high-flux scenarios. As expected, the hydraulic pressure loss filter only removes scenarios with appreciable flow channel lengths. It is important to notice that the hydraulic pressure loss filter threshold implicitly defines the maximal channel length and consequently the maximal GOR for a given flow velocity scenario. The field of valid results is therefore strongly dependent on these pressure loss restrictions.

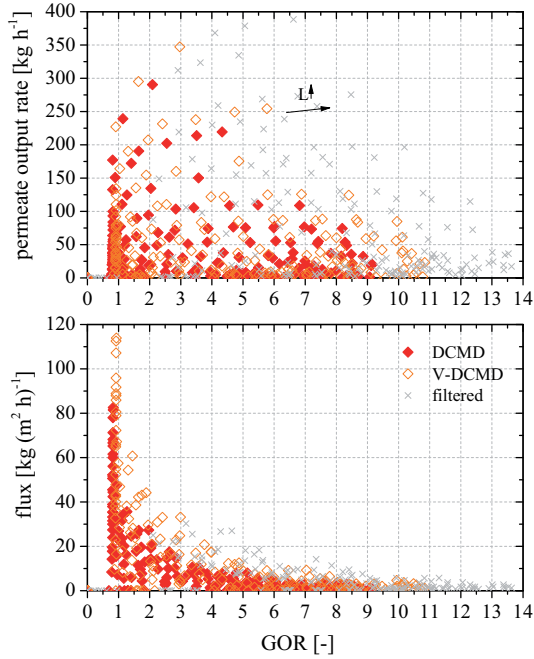


Figure 4.44: Parametric field study on DCMD and V-DCMD process configuration based on the conditions specified in Tab. 4.10. The results that include a hydraulic pressure loss higher than 1.0 bar are filtered out and indicated by grey crosses. Constant operating conditions: $T_{Ei} = 80^\circ\text{C}$, $T_{Ci} = 25^\circ\text{C}$, $S_{Ei} = 35\text{ g kg}^{-1}$, $S_{Ci} = 0\text{ g kg}^{-1}$, $\Delta T_{RX,kA} = 2\text{ K}$, $\hat{p}_{a,\text{residual}} = 0.05\text{ bar}$; Constant module parameter: $H = 0.7\text{ m}$. The material parameterisation covers a realistic improvement of the materials according to scenario #5 from Tab. 4.9 (see Fig. 4.42).

The diagrams in Figs. 4.45 to 4.47 are derived from Fig. 4.43, separately listing the results for DCMD, V-DCMD, PGMD, V-PGMD, AGMD and V-AGMD. A categorisation and colour coding with respect to the flow conditions is included, allowing a convenient and intuitive identification of the general trends. The plots that represent the permeate output rates are categorised with respect to the total mass flow rates. The parametric field includes scenarios with mass flow rates from 9 to 5428 kg h^{-1} that are separated into 9 categories ranging from $0\text{--}150\text{ kg h}^{-1}$ to $3000\text{--}6000\text{ kg h}^{-1}$. The plots that represent the flux results are categorised with respect to the specific mass flow rates, which are derived from the total mass flow rates and the corresponding membrane surface areas. The parametric field includes scenarios with specific mass flow rates from 0.2 to $7755\text{ kg (m}^2\text{ h)}^{-1}$ that are separated into 9 categories ranging from $0\text{--}50\text{ kg (m}^2\text{ h)}^{-1}$ to $3000\text{--}8000\text{ kg (m}^2\text{ h)}^{-1}$. For a clear overview, the scale of the ordinates has partially been chosen to be smaller than the full range of data points that was presented earlier.

For all of the MD configurations, the colour code indicates the strong dependence of the permeate

output rate on the feed flow rate. The higher the feed flow rate, the higher the permeate output rate. The DCMD results are chosen as an example for analysing the results, but the same method of interpretation may also be applied for the results of the (V-)PGMD and (V-)AGMD scenarios. Analysing the DCMD results for feed flow rates from 300-500 kg h⁻¹, the maximal permeate output rate obtained is 23.1 kg h⁻¹, while the maximal output rate increases to 77.1 kg h⁻¹ for feed flow rates from 1000-1500 kg h⁻¹. For short flow channels, a direct-heating concept is considered in the model and the GOR is equal to the total module thermal efficiency. For these short flow-channel scenarios, the output rate increases with channel length due to the increased membrane surface area while the GOR is almost independent of feed flow rate and channel length. For longer channel length, heat recovery is considered and the GOR increases with channel length for a given flow rate. The output rate for any given feed flow rate is limited due to the limited input of thermal energy. The sensitivity of the output rate on channel length decreases for long flow channels (see Fig. 4.20, for details). The maximal GOR are usually found for the scenarios with long flow channels, so the maximal GOR is limited by the pressure loss restriction (see Fig. 4.44). This restriction specifically applies to the scenarios with high flow rates. Since the effect of salinity depends on the driving force and consequently on the specific feed flow rate,

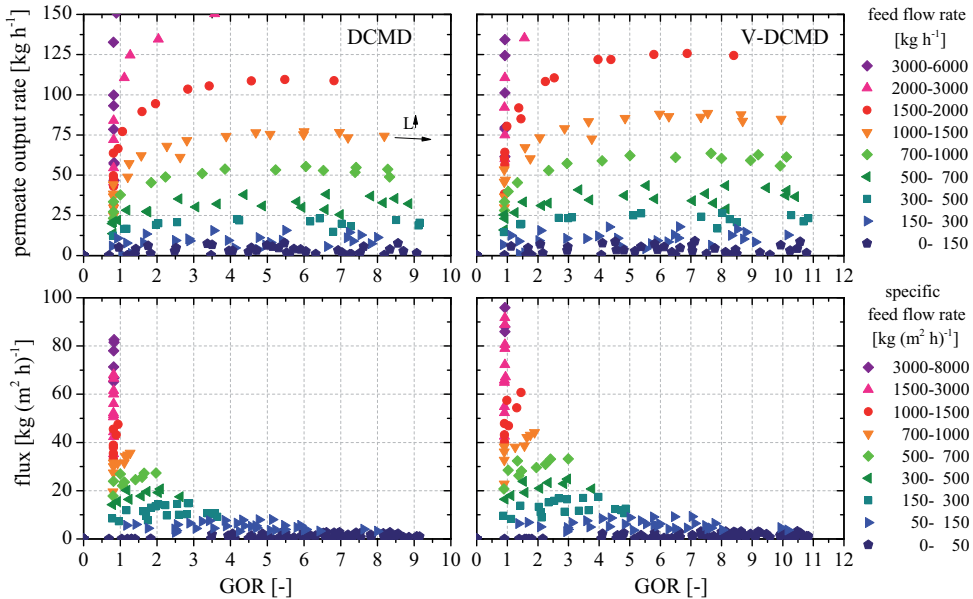


Figure 4.45: Parametric field study on DCMD and V-DCMD configurations based on the conditions stated in Tab. 4.10. The results that include a hydraulic pressure loss higher than 1.0 bar have been filtered out. Constant operating conditions: $T_{Ei} = 80\text{ }^{\circ}\text{C}$, $T_{Ci} = 25\text{ }^{\circ}\text{C}$, $S_{Ei} = 35\text{ g kg}^{-1}$, $S_{Ci} = 0\text{ g kg}^{-1}$, $\Delta T_{RX,kA} = 2\text{ K}$, $\hat{p}_{a,\text{residual}} = 0.05\text{ bar}$; Constant module parameter: $H = 0.7\text{ m}$. The material parameterisation covers a realistic improvement of the materials according to scenario #5 from Tab. 4.9 (see Fig. 4.42).

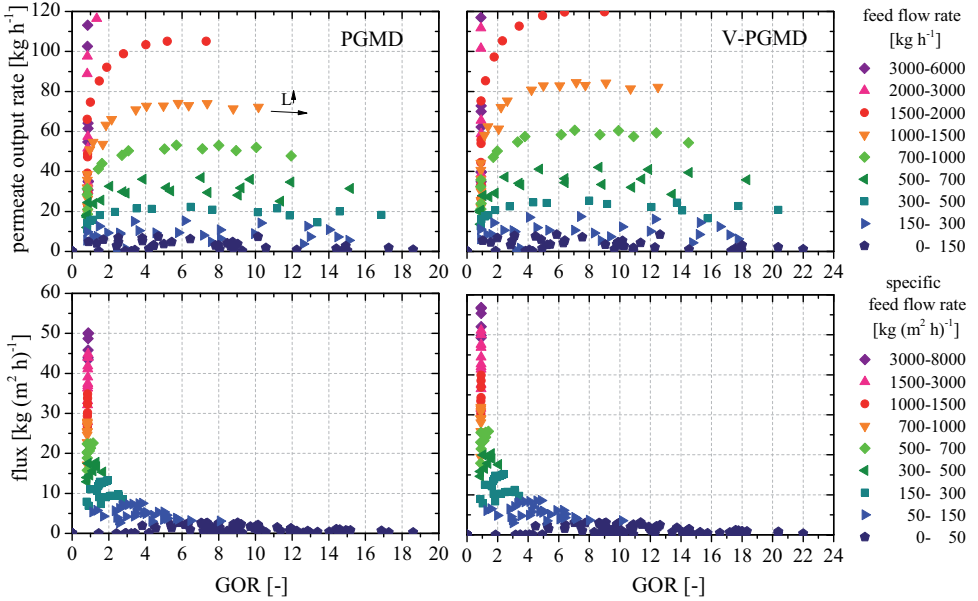


Figure 4.46: Parametric field study on PGMD and V-PGMD configurations based on the conditions stated in Tab. 4.10. The results that include a hydraulic pressure loss higher than 1.0 bar have been filtered out. Constant operating conditions: $T_{Ei} = 80\text{ }^{\circ}\text{C}$, $T_{Ci} = 25\text{ }^{\circ}\text{C}$, $S_{Ei/Ci} = 35\text{ g kg}^{-1}$, $\hat{p}_{a,\text{residual}} = 0.05\text{ bar}$; Constant module parameter: $H = 0.7\text{ m}$. The material parameterisation covers a realistic improvement of the materials according to scenario #5 from Tab. 4.9 (see Fig. 4.42).

the GOR may not fundamentally increase with channel length. For low specific feed flow rates, the effect of salinity changes the basic trends, which is difficult to determine from the given representations. However, in these cases, an increased channel length reduces the output rate and may even reduce the GOR. Some of these data points are identified close to the abscissa, especially for DCMD and PGMD configuration. This effect is expected to intensify for increasing salinity.

The newly defined colour code applied for the flux results illustrates the general dependence of the flux on the specific feed flow rate. For all of the MD configurations, the colour code indicates higher fluxes for the scenarios with higher specific feed flow rates. Again, the DCMD results are chosen as the example for analysing the results. Applying low specific feed flow rates from $50\text{ to }150\text{ kg (m}^2\text{ h)}^{-1}$, the maximal flux is obtained at $8.0\text{ kg (m}^2\text{ h)}^{-1}$, while the maximal flux increases to $27.3\text{ kg (m}^2\text{ h)}^{-1}$ for specific feed flow rates from $500\text{ to }700\text{ kg (m}^2\text{ h)}^{-1}$. It becomes obvious that very high flux results may only be achieved with very high specific feed flow rates. Fluxes higher than $50\text{ kg (m}^2\text{ h)}^{-1}$ are possible, but require specific feed flow rates higher than $1500\text{ kg (m}^2\text{ h)}^{-1}$. In order to achieve systems with high flux and reasonable capacity, significant

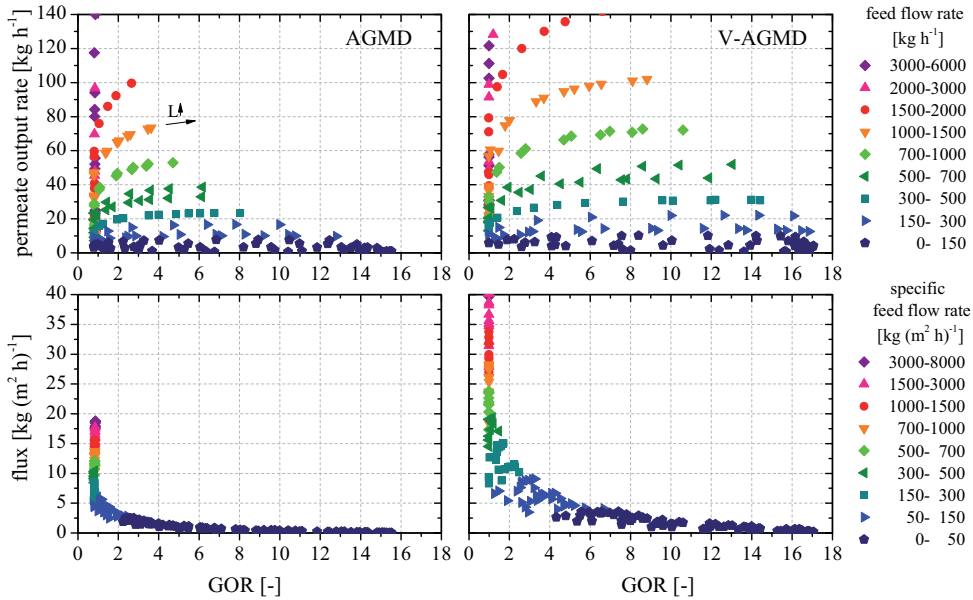


Figure 4.47: Parametric field study on AGMD and V-AGMD process configurations based on the conditions stated in Tab. 4.10. The results that include a hydraulic pressure loss higher than 1.0 bar have been filtered out. Constant operating conditions: $T_{Ei} = 80\text{ }^{\circ}\text{C}$, $T_{Ci} = 25\text{ }^{\circ}\text{C}$, $S_{Ei/Ci} = 35\text{ g kg}^{-1}$, $\hat{p}_{a,\text{residual}} = 0.05\text{ bar}$; Constant module parameter: $H = 0.7\text{ m}$. The material parameterisation covers a realistic improvement of the materials according to scenario #5 from Tab. 4.9 (see Fig. 4.42).

total mass flow rates are required. The derivation of the required feed flow rate for any nominal system capacity may easily be derived from the given representation. Furthermore, the diagram shows the fundamental upper limit of the GOR, depending on the specific feed flow rate. The higher the specific feed flow rate, the lower the capability for heat recovery. Very high GOR of up to 9.2 may be achieved with a DCMD configuration at very low specific feed flow rates, which are represented within the category from 0 to $50\text{ kg (m}^2\text{ h)}^{-1}$. However, in this category, fluxes do not exceed $2.8\text{ kg (m}^2\text{ h)}^{-1}$. For the scenario with the highest GOR, the flux is even lower than $1.0\text{ kg (m}^2\text{ h)}^{-1}$. It is obvious that a large total membrane surface area is required in order to obtain a system with high GOR and reasonable output capacity. The derivation of the required membrane surface area for any nominal system capacity may easily be derived based on the given representation. Considering higher specific feed flow rates from 50 to $150\text{ kg (m}^2\text{ h)}^{-1}$, the maximal GOR is obtained at 8.0, while the maximal GOR decreases to 2.0 for specific feed flow rates from 500 to $700\text{ kg (m}^2\text{ h)}^{-1}$. For specific feed flow rates higher than $700\text{ kg (m}^2\text{ h)}^{-1}$, which is required for fluxes higher than $30\text{ kg (m}^2\text{ h)}^{-1}$, heat recovery is not feasible at all. The influence of the channel width on module performance cannot be derived explicitly from Figs. 4.45 to 4.47. Thus, the variation in channel width is separately plotted and discussed for the DCMD results, considering the feed flow rate category from $1000\text{--}1500\text{ kg h}^{-1}$. The data

points for the given flow rate category include scenarios with channel widths of 3 mm, 7 mm and 10 mm and flow velocities of 0.20 m s^{-1} , 0.10 m s^{-1} and 0.07 m s^{-1} , respectively. The results are represented in Fig. 4.48.

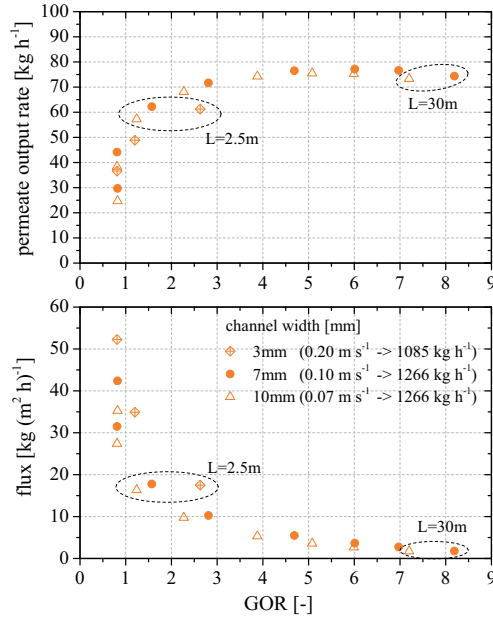


Figure 4.48: Reduced set of DCMD field study results for the mass flow category from 1000 to 1500 kg h^{-1} , extracted from Fig. 4.45.

The data points for a gap width of 7 mm and 10 mm are based on the same feed flow rate of 1266 kg h^{-1} . Considering the representation of the permeate output rate versus GOR for equal feed flow rates, the results almost all fall on a single line. The module performance turns out to be higher for a thinner gap, since the higher flow velocity leads to improved heat transfer. For a high-flux module concept with low GOR, the enhanced heat transfer of the thinner gap improves the output rate and the GOR, while only the GOR is improved for a high-recovery module. Similar results have already been derived from Fig. 4.38. The best heat transfer is given for the highest flow velocity, obtained with a gap width of 3 mm. Comparing the scenarios with heat recovery and equal channel length, especially the GOR is improved significantly by the enhanced heat transfer. However, since the hydraulic pressure loss quadratically increases with flow velocity, the given feed flow rate may not be applied for thin channels longer than 2.5 m, while none of the data points for the thick flow channels are removed by the pressure loss filter.

This section on the parametric field study completes the purely technical part of this thesis, which aimed to identify and analyse suitable MD module concepts. The results involve the combined theoretical and experimental knowledge of materials, channel configurations and operational conditions that was derived throughout the preceding sections. The analysis of the

results from the parametric field study clearly illustrate how thermodynamic module characteristics may effectively be adjusted by adapted flow channel design and appropriate operation. The comprehensive MD model allows precise prediction of the thermodynamic performance for any MD module configuration. However, the thermodynamic model is not capable of evaluating the value of a high GOR, if only minimal output rate may be achieved, or the value of high flux, if the associated process also has enormous thermal energy consumption. It is obvious that an optimal module design depends on the projected scenario and may not be identified by technical considerations alone. The fundamental question that still requires clarification in order to derive a concrete design decision reads as follows: What is the channel design that represents the optimal combination of flux and GOR for a projected scenario? Since a purely thermodynamic method is not capable of combining and weighting the two opposing essential MD performance characteristics represented by flux and thermal energy consumption, economic considerations must be included into the method for conceptual module evaluation. Such an advanced techno-economic approach for MD module evaluation is introduced in the following chapter.

5 Economic Evaluation

For an effective evaluation of the membrane distillation process, technological and economic aspects need to be taken into consideration. Especially the weighting of the opposing essential MD performance characteristics, represented by flux and thermal energy consumption, needs economic considerations for a value to be assigned to the individual demands for transfer area and thermal energy. The water unit costs are considered to be a powerful and comparable measure to identify whether the MD approach is competitive for a certain application. Such universal economic measures may be used as target functions for the evaluation and optimisation of MD module configurations within specific project conditions.

The following chapter provides the derivation and discussion of a new comprehensive cost model for MD desalination projects. The modelling results are analysed in the context of a small reference plant. A comparative evaluation of the expected investment costs for different system configurations is provided. Sensitivity analyses of the water unit costs with respect to different key design parameters are presented, including a discussion of potential suitable design decisions. The results generally include a detailed break down of the water unit costs into the main cost categories. The configuration of an MD plant driven by waste heat is considered in an additional scenario. A method for integrated module and system optimisation is illustrated by assessing five demonstration scenarios.

5.1 Cost Model Development

To evaluate the investment costs, the operational costs and the water unit costs, a detailed cost model is developed specifically for MD applications. The basic model structure is adapted from a generic model structure that was proposed for arbitrary process plants [50]. The common model approach implies the derivation of the overall costs that accumulate within an entire process plant project. The overall project costs are categorised into two main cost categories, the fixed and the variable costs that in turn are broken down into further sub-categories. The existence and relevance of each cost position strongly depends on the technology considered and needs to be evaluated individually. Thus, special attention is given to a differentiated implementation of aspects that specifically apply for the MD technology.

5.1.1 Investment Costs

The investment costs for desalination systems may generally be separated into the following cost categories:

- land cost
- logistics
- civil works and infrastructure
- well supply
- pre-treatment
- desalination unit
- post-treatment
- brine disposal

Investment costs for each of the cost categories are derived separately, taking into account the specific conditions and requirements of a given project.

Methods for a Preliminary Estimation of the Investment Costs

To estimate the investment costs, different fundamental model approaches are introduced in pertinent literature. The most common investment cost models represent simplified methods that rely on actual experience from former projects and the principles of the economy of scales. The most relevant approaches are briefly introduced as follows, including some quantitative references that have been reviewed in literature.

A capacity method is widely used for cost estimations of components, subsystems or complete plants. This method is based on assuming a reduction of the specific costs with increasing capacity. If the reference costs C_{ref} are available for a reference capacity K_{ref} , the absolute costs for any capacity may be estimated by means of a degression coefficient m , according to Eq. 5.1. To represent the specific costs instead of the absolute costs, Eq. 5.1 may be transformed to Eq. 5.2.

$$C = C_{\text{ref}} \left(\frac{K}{K_{\text{ref}}} \right)^m \quad (5.1)$$

$$\frac{C}{K} = \frac{C_{\text{ref}}}{K_{\text{ref}}^m} K^{(m-1)} \quad (5.2)$$

The degression coefficient is usually given in the range of $0.5 \leq m \leq 1.0$. For pumps and heat exchangers, degression coefficients of 0.6 are proposed to represent the cost reduction with in-

creasing power consumption or transfer area, respectively. The cost reductions for tanks and separation columns are proposed with a degression coefficient of 0.7. For complete RO desalination plants with capacities from 4 000 to 200 000 m³ d⁻¹, a degression factor of 0.85 has been derived [50].

A factorial method has been proposed as an alternative method to estimate the investment costs for process plants [173]. This method is used to estimate the overall plant cost C from the costs of the main plant components C_i , which are multiplied with the Lang Factor f_L according to Eq. 5.3.

$$C = f_L \sum_i C_i \quad (5.3)$$

The costs for the actual main plant components need to be derived from the corresponding component specifications, so rather detailed data on the projected plant design and plant operation needs to be available. From an analysis of many process plant projects, a Lang Factor of 3.63 has been derived for usual process plants and 4.74 for complex process plants [50]. The quality of the cost estimation increases, if detailed cost data is available for a specific plant type. A detailed break-down of the Lang Factor into the main cost categories has been derived from data based on several BASF plants. From the listed example, an average Lang Factor of 3.86 has been identified [50].

The definition of a constant Lang Factor does not represent the reduction of costs with increasing plant capacity, even though some of the relevant cost positions do not increase with the plant capacity (e.g. process control). An improved factorial method considering a degression of the Lang Factor f_L with the plant capacity is proposed with the Miller Factor f_M [174]. A general reduction of the Miller Factor with the average cost of the main plant components is shown. An analysis based on BASF plants with investment cost from 0.5 mEUR to 50 mEUR as examples proposes a reduction of the Miller Factor from approximately 5.3 to 3.0, if the average cost of the main components increases from 5 000 EUR to 50 000 EUR [50]. In this example, the reduction of the Miller Factor is approximated by the mathematical form in Eq. 5.4.

$$C = f_M \sum_i C_i = f_{M,\text{ref}} \left(\frac{\bar{C}_K}{\bar{C}_{K,\text{ref}}} \right)^m \sum_i C_i \quad (5.4)$$

In order to derive an example that refers to a membrane system, cost data from ultra-filtration (UF) systems have been analysed by the author of this thesis. For medium-size UF systems, a significant reduction of the specific system costs for components apart from the membrane modules have been identified with increasing plant capacity. A detailed break-down of the system costs is shown for two reference systems [175]. Considering a reference system with a capacity of 15 m³ h⁻¹, almost 90 % of the system costs are attributed to other components than the UF modules and racks, while this fraction reduces to 60 % for a reference system with a capacity of 300 m³ h⁻¹. Assuming that the UF modules and racks are the main components, the total system costs may be estimated by Miller Factors that decrease from approximately 10 to 2.5 for the two reference plants.

Derivation of an Investment Cost Model for MD plants

The principle of estimating the overall system costs to be proportional to the costs associated with the key components seems reasonable for many process plants. For technologies that are fully implemented on a commercial scale, the underlying system design for a given application is well known, allowing high-quality cost estimations to be made by simply applying the capacity model based on experience from previous projects. Considering conventional membrane technologies such as ultra-filtration (UF) or reverse osmosis (RO), the investment costs for the membrane modules and the costs for the rest of the system are directly linked to the plant capacity. In membrane distillation, the investment costs for the membrane modules are not only linked to the plant capacity but also to the intensity of heat recovery, while the costs for the rest of the system depend on plant capacity only. An illuminating example may be given by an analysis of Fig. 4.48, that shows different heat recovery scenarios at similar permeate output capacities. The necessary investment cost for the MD modules is expected to be 12 times higher for a GOR¹ of 6 than for a GOR of approximately 2, based on the significant difference in required membrane area. The system costs apart from the membrane modules are expected to be similar for all the scenarios, due to a comparable flow rate capacity of the system components. The optimal module design with respect to flux and heat recovery may only be determined by an economic evaluation that requires a reasonably accurate representation of the investment costs. It is obvious from the given example that the investment costs for a MD plant are very sensitive to the heat recovery concept and may not be estimated on basis of the plant output capacity alone. Furthermore, the fraction of the investment costs without the costs for membrane modules does not change significantly with the heat recovery concept and should not be estimated proportionally to the module costs by means of a Lang Factor.

A mixed model approach according to Eq. 5.5 has been chosen for to estimate the investment costs for an MD plant. The total investment costs for the MD plant C_I are separated into one fraction implying the costs C_i associated with the specific key components of interest and one fraction C_{rP} implying the cost for the rest of the plant.

$$C_I = \left(\sum_i C_i \right) + C_{rP} \quad (5.5)$$

The cost for the MD modules C_{MD} and the costs for the heat exchangers C_{HX} are considered to be the key component costs for an MD desalination unit. Furthermore, the costs for an UF pre-treatment system C_{UF} as well as optional costs for membrane contactors for deaeration C_D are considered separately in order to identify their specific role from an economic point of view. By including all the separate key cost positions that are used in the investment cost model within this thesis, Eq. 5.5 may be reformulated as Eq. 5.6.

$$C_I = (C_{MD} + C_{HX} + C_{UF} + C_D) + C_{rP} \quad (5.6)$$

¹Gained Output Ratio (GOR), definition in Sec. 2.5.2

It is important to note that each of the key cost categories from Eq. 5.6 is dependent on different capacity measures and needs to be derived as a separate cost function. The capacity measures that define the investment costs for the different main cost categories are listed in Tab. 5.1.

Table 5.1: Capacity measures that define the investment cost for the different categories.

main cost categories		capacity measure	unit	
MD modules	C_{MD}	membrane area	A_{MD}	[m ²]
heat exchangers	C_{HX}	heat transfer capacity	kA_{HX}	[kW K ⁻¹]
deaeration system	C_D	flow rate for deaeration	\dot{m}_D	[kg h ⁻¹]
pre-treatment	C_{UF}	raw water flow rate	\dot{m}_R	[kg h ⁻¹]
remaining plant	C_{rP}	permeate capacity	\dot{m}_P	[t d ⁻¹]

Since the MD technology is not yet fully implemented on the commercial scale, there is no reliable economic data available as a reference for cost estimations. However, detailed experience on the engineering and implementation of different MD pilot plant projects is available at Fraunhofer ISE. Among others, several field test systems have been commissioned within the framework of the EU FP7 project MEDIRAS, which was led by Fraunhofer ISE. In this thesis, the costs associated with specific components of interest, namely the MD modules, the heat exchangers, the deaeration system and the pre-treatment system are estimated with the capacity method from Eq. 5.2 based on pertinent quotations for selected commercial reference components or materials. The investment cost estimation for the remaining plant is also based on the capacity method, while the reference cost is derived from a detailed cost analysis of the MEDIRAS field test systems. The cost function parameters and specifications considered for the different main cost categories are summarised in Tab. 5.2.

The cost estimation for the MD modules is based on the transfer area, that influences material costs and fabrication costs. Reference costs for the PTFE laminate, the spacers and the film material are based on real costs for minimum purchase quantities of approximately 100 m². The reference costs for other design components and fabrication are assumed by the author. The dependence of material costs on the purchase quantity is estimated by a degression coefficient of 0.85, whereas a higher potential for cost reduction with a degression coefficient of 0.7 is expected for other module design components and improved fabrication.

For the heat exchangers, component reference costs are derived from titanium plate-and-frame heat exchangers that have been used in the MEDIRAS field test systems. A reasonable capacity measure for heat exchangers is the heat transfer area or heat transfer capacity. A high fraction of the costs for high-grade titanium heat exchangers is defined by the material costs, so less potential for cost reduction than the values proposed in literature is expected. A degression coefficient of 0.8 is assumed for the heat exchangers.

The costs for a deaeration system differ significantly, depending on whether membrane contactors

Table 5.2: Reference costs and degression coefficients for the main components of a MD desalination unit.

component	specification	ref. capacity	ref. cost	degression
MD modules	PTFE laminate	100 m ²	3 500 EUR	0.85
	spacers, film material	100 m ²	1 000 EUR	0.85
	design components and fabrication	100 m ²	3 500 EUR	0.70
heat exchangers	titanium, plate-and-frame	50 kW K ⁻¹	3 000 EUR	0.80
deaeration system	membrane contactors ^a	50 m ³ h ⁻¹	8 000 EUR	0.80
	liquid ring vacuum pump	50 m ³ h ⁻¹	3 000 EUR	0.80
pre-treatment	complete UF system	10 m ³ h ⁻¹	50 000 EUR	0.70
rest of plant	excluding thermal energy supply and cooling system	10 t d ⁻¹	30 000 EUR	0.60

^aonly V-DCMD and V-PGMD need membrane contactors for deaeration

are needed or not. In V-DCMD and V-PGMD, contactors are required for indirect deaeration of the membrane by means of deaerated feed water. No contactors are required in V-AGMD, since the gap is directly accessible to the vacuum pump. A reasonable capacity measure for the deaeration unit is the water flow stream to be deaerated. It should be noted that for a V-DCMD configuration, deaeration is assumed for both the evaporator and the condenser sides of the membrane. A deaeration unit has been dimensioned according to Eqs. 4.63 and 4.64, assuming the removal of >90 % of dissolved air from a saturated water flow stream of 50 m³ h⁻¹. The reference costs are derived for a suitable liquid ring vacuum pump and a small rack of industrial-scale membrane contactors for deaeration. The degression coefficients for the deaeration modules and the vacuum pump are estimated to be 0.8.

Raw water pre-treatment to a certain extent is expected to be indispensable for any seawater desalination system. The pre-treatment may consist of conventional media filtration, advanced membrane filtration, dosing of chemicals or a combination of these measures. In the presented investment cost model, an ultra-filtration system is assumed for the pre-treatment of the raw water, thus representing an advanced and therefore rather conservative estimation. A reasonable capacity measure for the pre-treatment system is the raw water inlet flow rate that needs to be treated. Reference costs for an UF plant of 10 m³ h⁻¹ filtration capacity and a degression factor of 0.7 are derived from data provided in literature for system capacities from 10 to 1 000 m³ h⁻¹ [175]. The costs include the complete UF system including UF modules, racks, piping, pre-filtration, back flushing, process control etc. Since the UF system is implemented as a sub-system within the MD plant, it seems reasonable to refer to the lower range of the widely varying cost data.

To derive the other investment costs than for the MD modules, the heat exchangers, the deaeration system and the pre-treatment, a detailed cost analysis has been conducted for two field test

systems that were commissioned within the MEDIRAS project in Pantelleria, Italy 2010 and on Gran Canaria, Spain 2011. Both systems are equipped with similar desalination units consisting of 12 membrane modules in parallel, resulting in a total membrane area of 120 m². The technical specifications of the modules are similar to those proposed for prototype PGMD-09.8-050-BE in Tab. 4.3. The maximal capacity of the desalination unit may be rated with approximately $12 \times 35 \text{ kg h}^{-1} \times 24 \text{ h} \approx 10 \text{ m}^3 \text{ d}^{-1}$. Further technical information on the field test systems, including detailed descriptions and hydraulic configurations, have already been published [10]. The overall investment costs of the desalination units are derived to be approximately 60 000 EUR, excluding costs for pre-treatment, solar energy supply, cooling and land cost. A detailed breakdown of the investment costs into different cost sub-categories is given in Fig. 5.1.

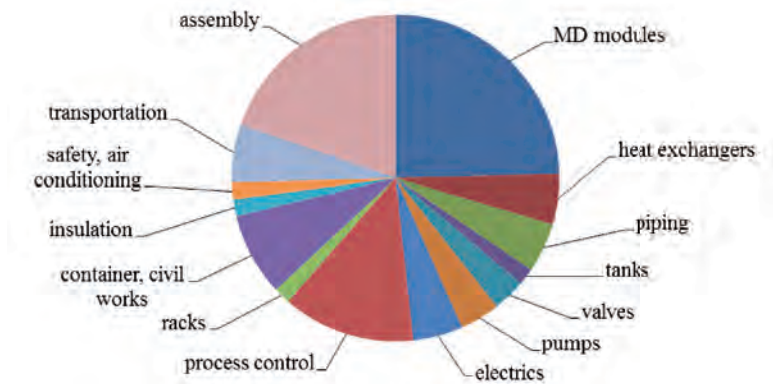


Figure 5.1: Detailed investment cost analysis for the desalination unit of the MD field test systems commissioned in Pantelleria, Italy and on Gran Canaria by Fraunhofer ISE. Maximal output capacity: 10 t d^{-1} , membrane area 120 m². The cost data represents solely the desalination unit, excluding well supply, pre-treatment, solar energy supply system, cooling system and land cost.

If the costs for the MD modules and the heat exchangers are separated from the system costs proposed in Fig. 5.1, the costs for the remaining system may be estimated with 40 000 EUR, leading to specific costs of $4000 \text{ EUR (t d}^{-1})^{-1}$ with respect to the system output capacity. It is important to note, that the data is obtained from a research pilot plant project. Taking into consideration a significant potential for further cost reduction by a careful review of components and suppliers, as well as by optimisation of the assembly procedures, reasonable reference costs for the remaining plant are expected in the range of $3000 \text{ EUR (t d}^{-1})^{-1}$. A reduction of the specific costs with increasing system capacity is considered by applying the capacity model from Eq. 5.2. A degression coefficient of 0.6 has been chosen based on the data for different individual process plant components proposed in the literature [50].

An overview of the specific costs for each of the main cost categories and their dependence on the associated capacity measure is provided in Fig 5.2.

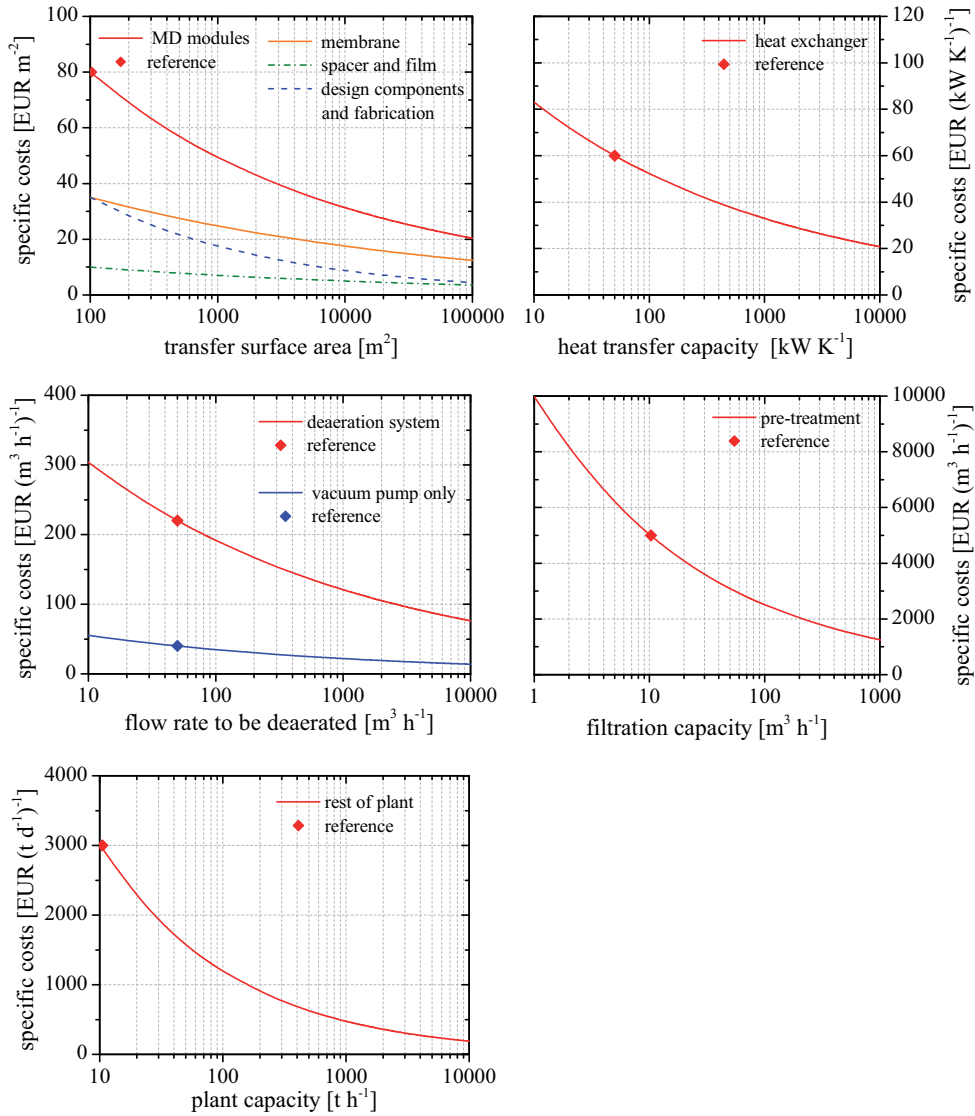


Figure 5.2: Specific costs for the individual main cost categories of an MD desalination unit, depending on the associated capacity measure according to Tab. 5.1. The estimations are based on the capacity method, assuming reference costs according to Tab. 5.2.

5.1.2 Operational Costs

The operational costs combine all cost positions that are necessary for plant operation. The operational costs are separated into fixed operational costs that incur independently of the plant's operational status and variable operational costs that are directly linked to plant operation. The following sections will provide a detailed break-down of the total operational costs into the different cost positions. Furthermore, model equations are derived and discussed for each of the individual cost positions.

Fixed Operational Costs

The fixed operational costs are not directly linked to the plant's operational status and incur independently of permeate production. The main cost categories of the fixed operational costs are listed as follows [50]:

- capital costs
- service and maintenance
- insurance
- module replacement
- personnel
- analysis

The annual costs for the provision of the investment costs a_I , also called capital costs, are calculated by the annuity method in Eq. 5.7 that distributes the investment costs C_I evenly throughout a projected amortisation time n by assuming a fixed interest rate z .

$$a_I = \frac{z(1+z)^n}{(1+z)^n - 1} C_I \quad (5.7)$$

The investment costs are usually funded with capital from external sources and from equity capital. Since the costs for equity capital are usually higher than the costs for capital from external sources, combined costs for capital are to be derived - the weighted average cost of capital (WACC). The WACC depends on factors such as share of equity capital, systematic project risks, potential tax savings and current market situation. A detailed discussion and derivation of the WACC may be found in pertinent literature [176]. For reasons of simplicity, an effective interest rate of 4% is assumed for the proposed cost model. This assumption seems reasonable, since a similar interest rate of 5% is listed for conventional desalination plants in pertinent literature [140]. The amortisation time is assumed to be the economic lifetime of a system, that is not necessarily equal to the actual system lifetime. Different amortisation periods

are usually considered for process technology and buildings and infrastructure. In literature, an amortisation time of 10 years is stated for process technologies and 20 years for buildings and infrastructure [50]. Industrial thermal desalination plants are planned with a lifetime of about 40 years [140]. For RO plants, a lifetime of 25 years has been reviewed [177], whereas the lifetime of UF plants is estimated to be 15 years [175].

Service and maintenance is essential to retain the functionality of a process plant. Functionality checks, sensor calibration and replacement of worn parts are some of the tasks to be done on a regular basis to ensure optimal plant operation and prevent major failures. The annual costs for service and maintenance a_{SM} are usually estimated by referring to the investment costs C_I . A fraction of 3% is proposed for process installations and 1% for buildings and infrastructure [50]. Other authors propose maintenance costs of 2.0 to 2.5% of the investment costs for RO systems [178]. In this thesis the annual costs for service and maintenance are estimated by Eq. 5.8, considering 2.5% of the overall investment, without separating process technology, buildings and infrastructure.

$$a_{SM} = 0.025 C_I \quad (5.8)$$

To minimise the risk for the investment, the plant or selected components may be insured. In this model, the annual costs for insurance a_{In} are estimated by Eq. 5.9, considering 0.5% of the investment costs based on a recommendation from literature [50].

$$a_{In} = 0.005 C_I \quad (5.9)$$

For membrane processes, the life-time of the membrane modules is usually significantly shorter than that of the remaining plant. Since the costs associated with membrane replacement represents an important part of the fixed operational costs, it seems reasonable to consider this cost position separately from the general maintenance position. The annual costs for module replacement a_R depend strongly on the module costs C_{MD} and the lifetime of the membrane modules n_{MD} . In order to achieve a comparable measure for the membrane replacement costs that are incurred at different points in time, the costs for each replacement i in year $0 < i < n_{MD} < n$ need to be transformed into the respective net present value. The total membrane replacement costs within the plant amortisation period are then transferred into annual replacement costs a_{MD} by Eq. 5.10, based on the amortisation time n and the interest rate z , similarly to the capital costs in Eq. 5.7. Since no operational experience in a commercial context is available, it is hard to predict the expected lifetime of MD modules. However, some operational experience is available for a small solar-driven field test system in Gran Canaria that was taken into operation by Fraunhofer ISE in 2005. Results of four-year monitoring have been published, reporting an MD module prototype life cycle of 2 years at full dynamic operation, applying real seawater from a beach well without any pre-treatment [11]. Further field test experience with small MD pilot plants for seawater desalination has been published in [69]. The membrane modules were operated up to 14 months with real, partially problematic seawater that had been pre-treated by particle filters [69]. Taking further developments in membrane robustness and module fabrication

into consideration as well as increased operational experience, more advanced pre-treatment and optimal operating conditions, it seems reasonable to assume the lifetime of the MD modules to be in the same range as that for conventional membrane systems. The expected lifetime of RO membranes from different manufacturers has been reported to be approximately 5 years [179]. Since some of the module parts such as mechanical frames and mounting equipment are expected to be re-usable, the overall MD module replacement costs are assumed to be 80 % of the original MD module investment costs C_{MD} .

$$a_{MD} = \frac{z(1+z)^n}{(1+z)^n - 1} \sum_i \left(\frac{0.8 C_{MD}}{(1+z)^i} \right)^{n_{MD}} \quad (5.10)$$

A similar formulation may be applied to derive the replacement costs for the UF membrane modules. However, some modification is required since the investment costs for the UF pre-treatment system C_{UF} also include other positions than the UF membrane modules. For UF system with capacities of 15, 65 or 300 m³ h⁻¹ only 10, 20 or 40 % of the investment costs C_{UF} are associated with the UF membrane modules [175]. Thus, only 50 % of the investment costs are considered for the estimation of the UF membrane replacement in Eq. 5.11. A life cycle of approximately 8 years is claimed for UF membranes in the context of potable water production in small UF plants [175]. For UF seawater pre-treatment, the lifetime of UF membranes has also been predicted to be in the range from 5 to 10 years [177].

$$a_{UF} = \frac{z(1+z)^n}{(1+z)^n - 1} \sum_i \left(\frac{0.5 C_{UF}}{(1+z)^i} \right)^{n_{UF}} \quad (5.11)$$

Modern desalination plants operate in a fully automated mode. However, there is a minimum personnel requirement for monitoring and minor service activities. The annual personnel costs for RO plants in Spain have been identified to be 1.0 to 1.5 % of the investment costs. A personnel requirement of 4 is specified for the operation of a RO plant with a daily capacity of 3 000 t [178]. For MD plants, the personnel requirement for a plant with a daily capacity of 1 000 t d⁻¹ is assumed to be one operator, changing proportionally to the output rate. The annual labour costs for one operator $a_{L,ref}$ are estimated with 40 000 EUR a⁻¹. The empirical formulation in Eq. 5.12 correlates the overall annual loan costs a_L for an MD plant to the daily permeate capacity.

$$a_L = (0.002 \frac{M_P}{365}) a_{L,ref} \quad (5.12)$$

The annual costs for analysis are not considered separately from the costs for service and maintenance.

Variable Operational Costs

The variable operational costs are directly linked to the permeate production volume. The main cost categories of the variable operational costs are as follows [50]:

- thermal energy
- electricity
- chemicals and additives
- disposal

The basic measure for estimating any variable operational cost position is the operational availability of the plant. A fully automated plant is usually projected for non-stop operation. If some downtime is considered for service and maintenance activities, the operational availability Γ may be estimated with 95 %. If 100 % operational availability is required, a backup system needs to be provided. For systems that rely on a fluctuating energy supply, the availability may strongly depend on the availability of the energy source or the configuration of an energy storage unit. The annual hours of operation t_a are generally given by Eq. 5.13.

$$t_a = \Gamma \frac{8760 h}{a} \quad (5.13)$$

The annual permeate production rate M_P and the annual raw water demand M_R of the plant are defined according to Eq. 5.14.

$$M_P = t_a \dot{m}_P \quad M_R = t_a \dot{m}_R \quad (5.14)$$

The costs for the thermal energy supply are expected to be the most important cost position for a thermally driven desalination process such as MD. The annual costs for thermal energy a_{HX} are derived from the annual permeate production, the specific thermal energy requirement q_{HX} and the specific costs for thermal energy c_{th} according to Eq. 5.15. The annual output capacity and the specific thermal energy demand of the plant depend strongly on module design, heat recovery concept and hydraulic plant layout. Accurate evaluation of the plant performance is available from the detailed thermodynamic module model developed and validated in Chapter 4. The specific costs for thermal energy depend on the energy source, the plant location and specific selling conditions. According to recent statistical data published by the statistical department of the European Commission, EuroStat, the average costs for natural gas for industrial customers in the European Union were around $0.04 \text{ EUR (kWh}_{th})^{-1}$ in 2013 [180]. If waste heat from other thermal processes is available, the unit costs are strongly dependent on its exergy level and potential usability on other processes. The value of waste heat is expected to increase with temperature level. Depending on the project conditions, the unit cost for waste heat may even be negligible. No direct fuel costs are incurred, if a renewable energy supply system such as solar thermal collectors are installed. However, the high investment costs that are associated with the installation of the solar collector field and a suitable storage system need to be amortised according to Eq. 5.7. Overall unit costs of 0.04 to $0.12 \text{ EUR (kWh}_{th})^{-1}$ for the generation of solar-thermal heat for medium-size industrial processes have been published by the European

Solar Thermal Technology Platform (ESTTP) [181].

$$a_{\text{th}} = M_{\text{P}} q_{\text{HX}} c_{\text{th}} \quad (5.15)$$

The annual costs for electricity are derived similarly to the thermal energy costs, depending on annual permeate production, the specific electricity demand of the desalination unit $P_{\text{MD,spec}}$ and the specific costs for electricity c_{el} . Furthermore, the electric power consumption for UF pre-treatment is optionally taken into consideration according to Eq. 5.16, depending on the plant's raw water demand and the specific electricity demand $P_{\text{UF,spec}}$ of the UF system. The annual output capacity and the specific electricity demand of the MD desalination unit depend strongly on module design, hydraulic plant layout, plant operation strategy and electric efficiency of the main consumer loads. A precise evaluation of the plant performance and the corresponding electricity consumption is available from the detailed model developed and validated in Chapter 4. The specific energy demand for UF pre-treatment is assumed to be $0.06 \text{ kWh}_{\text{el}} \text{ t}^{-1}$, based on data for small and medium-size UF systems [175]. An additional term of $0.10 \text{ kWh}_{\text{el}} \text{ t}^{-1}$ is taken into consideration for the raw water supply and miscellaneous consumer loads. The specific costs for electricity depend on the energy source, the plant location and specific selling conditions. According to recent statistical data published by the statistical department of the European Commission, EuroStat, the average costs for electricity for industrial customers in the European Union were around $0.10 \text{ EUR} (\text{kWh}_{\text{el}})^{-1}$ in 2013 [182].

$$a_{\text{el}} = \left(M_{\text{P}} P_{\text{MD,spec}} + M_{\text{R}} (P_{\text{UF,spec}} + P_{\text{supply,spec}}) \right) c_{\text{el}} \quad (5.16)$$

Chemicals and additives are necessary for pre-treatment and membrane cleaning in most of the membrane processes. The costs might vary significantly depending on the raw water quality and pre-treatment concept. For an RO plant, the costs for chemicals have been identified to be approximately 7% of the total life cycle cost [183]. Several authors derived the specific chemical costs to be approximately 0.02 EUR t^{-1} [184]. For better assignability, the specific costs may be referenced to the raw water demand rather than to the product water. Assuming an RO system recovery rate of 50%, the specific chemical costs with respect to the raw water are approximately 0.01 EUR t^{-1} . For the operation of UF membrane systems, the specific costs for chemicals are identified to be approximately 0.01 EUR t^{-1} [175]. No operational experience on MD plant operation is available up to now. MD is claimed to be a very robust membrane process with respect to fouling and scaling when compared to conventional membrane processes, but operational experience and further research will have to validate these statements. In this thesis, the annual costs for chemicals, additives and disposal are assumed to be 0.01 EUR t^{-1} per ton of raw water, according to Eq. 5.17.

$$a_{\text{c}} = M_{\text{R}} c_{\text{c}} \quad (5.17)$$

Specific Operational Costs - The Unit Costs for Water

The specific operational costs are a generally applied measure that refers the total operational costs to the target product. For membrane systems, the target product may either be the permeate or the brine. Considering the production of potable water from saline water without further utilisation of the brine, the permeate is the target product. Consequently, the unit costs for water are defined according to Eq. 5.18.

$$c_w = \frac{\sum_i a_i}{M_P} = \frac{(a_I + a_{SM} + a_{In} + a_{MD} + a_{UF} + a_L)}{M_P} + \frac{(a_{th} + a_{el} + a_c)}{M_P} \quad (5.18)$$

5.2 Results and Discussion

5.2.1 An Analysis of the Investment Costs

The investment costs have been analysed based on the investment cost model introduced in Sec. 5.1.1, considering a reference MD seawater desalination plant according to the specifications in Tab. 5.3.

Table 5.3: Reference MD seawater desalination plant

plant	MD modules		operating conditions
nominal capacity	200 t d ⁻¹	$L = 1/10$ m	$T_{Ei} = 80$ °C
recovery rate	30 %	$H = 0.7$ m	$T_{Ci} = 25$ °C
raw water salinity	35 g kg ⁻¹	improved materials (according to Fig. 4.42)	$\dot{m}_{Ei}^a = 400$ kg h ⁻¹ $\hat{p}_{VP} = 0.05/1.00$ bar

^amass flow compensation assumed on the condenser side for DCMD and V-DCMD

A system recovery rate of 30 %, which can be achieved by recirculating the feed water, is chosen, leading to a brine salinity level of 50 g kg⁻¹ (see Fig. 4.23). The results are evaluated comparatively, considering DCMD, PGMD and AGMD modules with two different channel lengths that reflect a high-flux and a high-recovery module configuration. In order to identify the role of deaeration system costs, the plant investment costs have been evaluated with and without deaeration equipment. A detailed break-down of the expected investment costs for each of the plant configurations is provided in Fig. 5.3.

The investment costs for all of the plant configurations are in the range from 380 000 EUR to 580 000 EUR. The costs for the MD modules vary, depending on the average flux that is achieved in each of the scenarios. In this context, higher costs are always obtained for high-recovery modules than high-flux modules due to the larger membrane surface. Significant costs have been derived for the heat exchangers. For high-flux plant concepts, the heat exchanger costs may even exceed the costs for the MD modules. If the thermal energy demand is reduced by improved heat recovery, the costs for the heat exchangers for heating (HX) and cooling (CX) decrease accordingly (see Fig. 4.5). It is important to note, that the DCMD module configuration presents an exception to this general statement. The heat recovery system for a DCMD system is implemented with additional external heat exchangers (RX) that require an increased heat transfer capacity for enhanced heat recovery. Therefore, total heat exchanger costs in DCMD plants may not decrease significantly for high-recovery concepts. In general, a significant potential for cost reduction is expected for the use of polymer heat exchangers, especially if the heat exchangers are integrated into the modules, so that the heating and/or

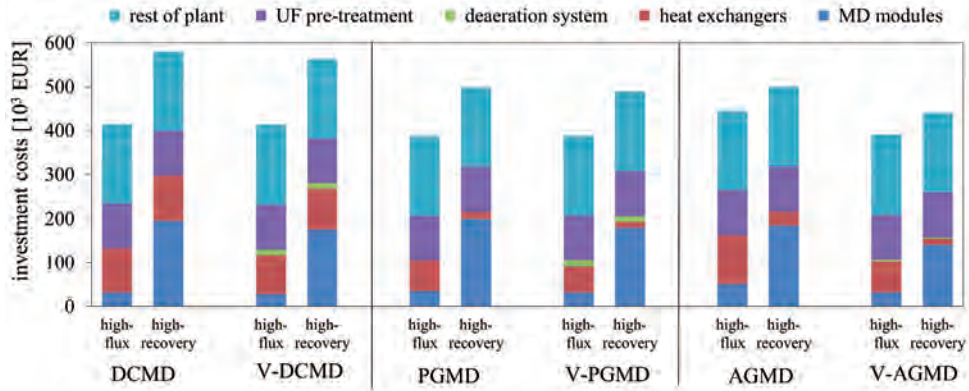


Figure 5.3: Break-down of the investment costs for a reference plant with a daily capacity of 200 t d^{-1} , considering aerated and deaerated conditions for DCMD, PGMD and AGMD high-flux and high-recovery module designs. Detailed system specifications are summarised in Tab. 5.3.

cooling loop may be connected directly to the module. The fraction for the deaeration system within the total investment costs is expected to be in the range from 2% to 4%, if deaeration modules are required (V-DCMD and V-PGMD), while the fraction is less than 1% for the V-AGMD configuration. The absolute investment costs turn out to be even less if a deaeration system is considered, due to the improved thermodynamic system performance for deaerated operation. The fraction of the UF pre-treatment system within the total investment has been estimated to be in the range of 20% to 30%. The absolute costs of the UF pre-treatment and the rest of the plant are the same for all of the scenarios, since identical plant capacity and raw water demand are considered. The raw water demand and consequently the expenses for the pre-treatment system can be reduced for higher recovery rates. However, based on the greater potential for scale formation at higher recovery rates, the resulting pre-treatment effort may also increase. Further investigations have to clarify the required intensity of pre-treatment in the context of MD systems.

5.2.2 A Sensitivity Analysis on the Unit Costs of Water

The unit costs of water have been evaluated by applying the cost model from Sec. 5.1.2 for a reference plant with a daily capacity of 200 t d^{-1} . The reference plant is specified according to Tab. 5.3. The project life cycle is estimated to be 15 years, whereas the MD modules and the UF module life cycles are estimated to be 5 years and 8 years, respectively. The interest rate is taken to be 4%. The specific costs for thermal energy are assumed to be $0.04 \text{ EUR (kWh}_{\text{th}})^{-1}$ and the specific costs for electricity are assumed to be $0.10 \text{ EUR (kWh}_{\text{el}})^{-1}$.

The main focus of the analyses is the presentation of the underlying cost model functionality

and the fundamental relations that are valid for any MD process configuration. Within the assessment, the PGMD and the V-AGMD module variants are considered as case studies. A detailed break-down of the unit water costs into the single cost positions is provided for selected parameter variations, considering a variation of the module channel length, a variation of the module flow rate and a variation of the system recovery rate.

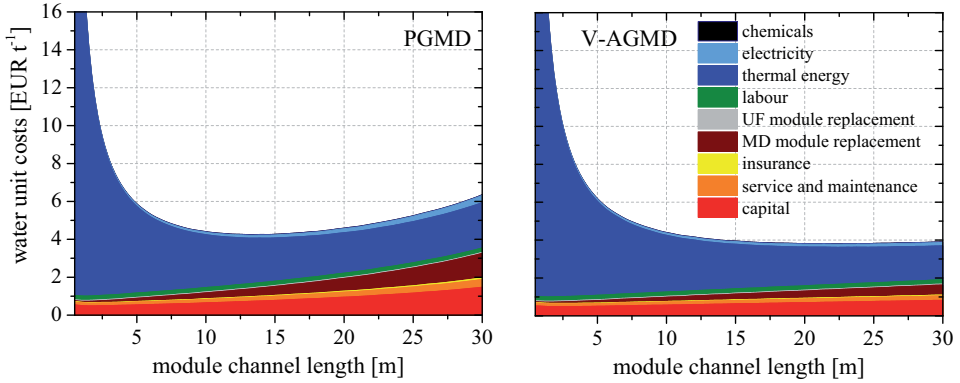


Figure 5.4: Detailed break down of the unit cost for water, considering a reference plant capacity of 200 t d^{-1} . The results are evaluated comparatively for PGMD and V-AGMD modules with different module channel lengths. Detailed system specifications are summarised in Tab. 5.3. Energy costs: $0.04 \text{ EUR (kWh}_{\text{th}})^{-1}$, $0.10 \text{ EUR (kWh}_{\text{el}})^{-1}$. Life cycles: plant 15 a, MD modules 5 a, UF modules 8 a, interest rate 4 %.

A break-down of the unit water costs for a variation of the module channel length from 0.5 m to 30.0 m is illustrated in Fig. 5.4. It is obvious from the given results that the unit costs for water are dominated by the costs for thermal energy, which show a high sensitivity to the module channel length. The costs for the thermal energy relate directly to the specific thermal energy consumption of the modules which is mainly defined by the module channel length (see Fig. 4.20 and Sec. 4.3.8). The costs for the electricity always increase for longer channel lengths due to increased pressure loss, but contribute only about 0.3 % to 7.0 % to the overall water unit costs. The capital costs increase linearly with increasing channel length, since MD module costs are directly linked to the required membrane surface area. This dependence also applies for the MD module replacement costs that represent a significant fraction of the water unit costs if high-recovery modules are considered. The small cost positions for service and maintenance and insurance slightly increase with the channel length due to their dependence on the investment costs. Additional minor fractions of the unit water costs are associated with UF module replacement, labour and chemicals that are also independent of module channel length.

Analysing the water costs for the PGMD module variant, an optimum of 4.25 EUR t^{-1} is identified for a channel length of 13.5 m. For longer flow channels, the increasing MD module costs are not compensated by savings in thermal energy costs. Depending on the process sensitivity to salinity, the thermal energy costs might even increase for long flow channels, which is marginally observed for the PGMD modules with channel lengths from 22 m to 30 m. Considering the same

scenario with V-AGMD modules, the optimal water unit costs of 3.81 EUR t⁻¹ are identified for a channel length of 22 m. The increase in MD module costs (capital and replacement) with channel length is significantly lower for the V-AGMD module variant than for the PGMD module variant due to higher average flux (see Figs. 4.46 and 4.47). Furthermore, the thermal energy consumption and consequently the thermal energy costs turn out to decrease with channel length even for long flow channels. This is explained by the lower sensitivity of the V-AGMD process to salinity.

If a waste-heat driven scenario with free thermal energy is to be considered, Fig. 5.4 might simply be analysed excluding the cost position for thermal energy. In such a scenario, the minimal water unit costs for PGMD and V-AGMD turn out to be around 1 EUR t⁻¹, achieved with module configurations that involve short flow channels.

According to the given analysis, the variation of the module channel length significantly affects the fixed operational costs (capital and MD module replacement costs) as well as the variable operational costs (thermal and electrical energy costs) and might therefore be considered to be one of the most important parameters needing identification by economic optimisation.

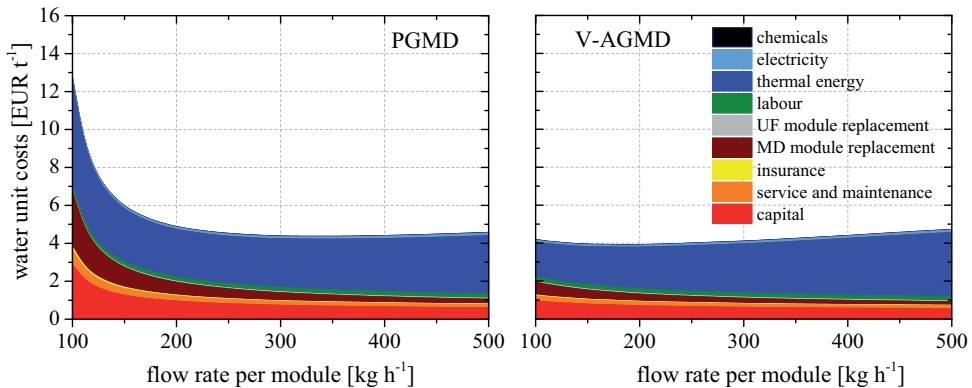


Figure 5.5: Detailed break-down of the unit cost for water, considering a plant capacity of 200 t d⁻¹. The results are evaluated comparatively for PGMD and V-AGMD modules with a channel length of 10 m, operated at different flow rates per module. Detailed system specifications are summarised in Tab. 5.3. Energy costs: 0.04 EUR (kWh_{th})⁻¹, 0.10 EUR (kWh_{el})⁻¹. Life cycles: plant 15 a, MD modules 5 a, UF modules 8 a, interest rate 4%.

A break-down of the unit water costs for a variation of the flow rate per module from 100 kg h⁻¹ to 500 kg h⁻¹ is illustrated in Fig. 5.5. For low-flow operation, a low flux is obtained (see Figs. 4.46 and 4.47), leading to a large membrane area and consequently high capital and MD module replacement costs. This effect is observed for both the PGMD and the V-AGMD variants, but turns out to be much more significant for PGMD. For low-flow rates, the sensitivity of the performance to salinity increases. Especially for PGMD, this effect brings in a significant additional membrane requirement for low-flow operation. The heat recovery decreases for higher module flow rates (see Fig. 4.33), leading to increasing costs for thermal energy with increasing module flow rate. However, depending on the process sensitivity to salinity, the thermal energy

consumption might also increase for lower flow rates. This inverted effect is observed for PGMD modules operated with flow rates from 100 to 250 kg h⁻¹.

For the given plant specifications, the optimal flow rate for the PGMD modules is identified to be 350 kg h⁻¹, leading to water unit costs of 4.36 EUR t⁻¹. Considering the V-AGMD variant, a lower value for the optimal flow rate of 180 kg h⁻¹ is identified, due to reduced membrane area and lower sensitivity to salinity. In this case, the water unit costs are estimated to be 3.92 EUR t⁻¹.

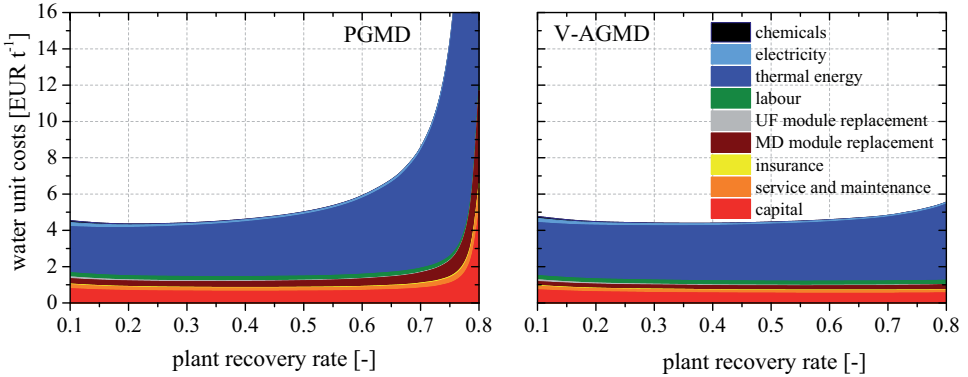


Figure 5.6: Detailed break-down of the unit cost for water, considering a plant capacity of 200 t d⁻¹. The results are evaluated comparatively for PGMD and V-AGMD modules with a channel length of 10 m, operated with different plant recovery rates. Detailed system specifications are summarised in Tab. 5.3. Energy costs: 0.04 EUR (kWh_{th})⁻¹, 0.10 EUR (kWh_{el})⁻¹. Life cycles: plant 15 a, MD modules 5 a, UF modules 8 a, interest rate 4%.

A break-down of the unit water costs for a variation of the plant recovery rate from 10% to 80% is illustrated in Fig. 5.6. Since the plant recovery rate determines the salinity level within the MD system, this sensitivity analysis is fundamentally equivalent to sensitivity analysis with respect to salinity. Considering recovery rates of 20%, 50% and 80%, the brine salinities and consequently the associated module inlet salinities are derived to be 44 g kg⁻¹, 70 g kg⁻¹ and 175 g kg⁻¹, respectively (see Fig. 4.23).

Flux and specific thermal energy consumption become increasingly unfavourable with an increasing recovery rate due to the increasing salinity level (see Fig. 4.17). Increasing costs for MD modules and thermal energy are therefore expected for higher recovery rates. However, the raw water demand and consequently the pre-treatment and deaeration costs (hardware and electricity) as well as the electricity demand for the raw water supply decrease with increasing recovery rate.

The optimal plant recovery rate for PGMD modules is identified to be 20%, whereas a V-AGMD plant may be operated optimally at a higher recovery rate of 35%. The low sensitivity of the V-AGMD process to salinity allows operation with recovery rates up to 80% without a significant impact on the unit water costs, while the ability for high-recovery operation needs to be carefully evaluated for the PGMD process. It is important to note that high-recovery operation

introduces other difficulties, e.g. in the context of scaling and fouling, which have not been taken into consideration in the given analysis.

A separate analysis has been conducted addressing the influence of the external heat recovery system for (V-)DCMD plants on the corresponding water unit costs. It is obvious that the size of the external recovery heat exchanger strongly influences the heat recovery efficiency (refer to Fig. 4.24). Since a larger heat exchanger causes additional investment costs whereas the improved heat recovery causes savings for the thermal energy costs, an economic assessment is necessary to identify the optimal heat exchanger. A break-down of the unit water costs for a variation of the heat exchanger size is illustrated in Fig. 5.7. The heat exchanger size is represented by different temperature losses ($\Delta T_{RX,kA}$) ranging from 0.1 K to 5.0 K corresponding to large and small heat exchangers, respectively. It should be recalled that a fixed temperature loss of 2 K was assumed within the preceding (V-)DCMD studies in this thesis.

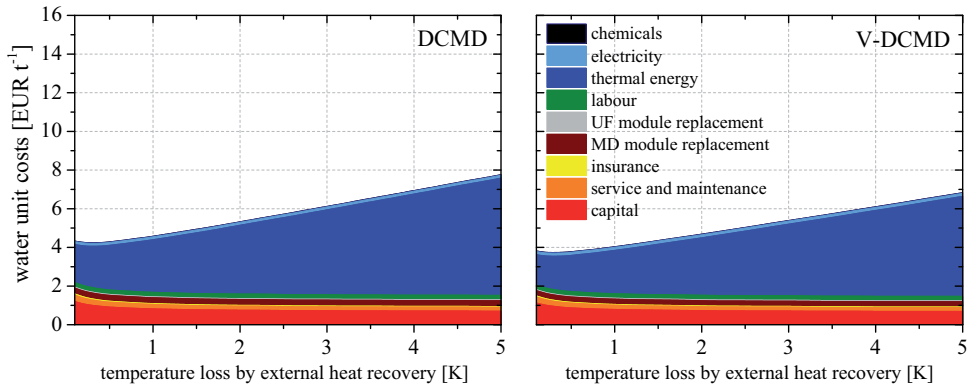


Figure 5.7: Detailed break-down of the unit cost for water, considering a plant capacity of 200 t d^{-1} . The results are evaluated comparatively for DCMD and V-DCMD modules with a channel length of 10 m, considering different temperature losses associated with the external heat recovery system (see Fig. 4.24). Detailed system specifications are summarised in Tab. 5.3.

For the given scenario, the optimal water unit costs are found for a heat recovery system with a temperature loss of only 0.3 K, independently of whether an aerated or a deaerated DCMD configuration is considered. If even lower temperature losses are to be achieved, the investment costs increase significantly due to the associated demand for additional heat transfer surface area. The additional investment cannot be compensated by the reduced thermal energy demand. If greater temperature losses are tolerated, a low sensitivity of the investment costs to the temperature loss is observed. In this region, a minor fraction of the investment costs are caused by the external recovery heat exchangers. The reduced heat exchanger costs cannot compensate the increasing costs for thermal energy that dominate the water unit costs. It is important to note that identification of the optimal size for a recovery heat exchanger is quite sensitive to

the available cost data for the heat exchangers and the proposed cost reductions with increasing scale. Furthermore, other measures that influence the module's thermal energy consumption also affect the optimal dimension of the external heat recovery system. Combined optimisation is therefore recommended.

5.2.3 Design of Waste-Heat Driven Plants

When a waste-heat driven MD desalination plant is to be designed, the available amount of process heat is typically defined by the waste heat source. The plant's output capacity is directly linked to the specific thermal energy consumption of the MD modules and can be adjusted to a target capacity by means of adapted module design. Engines of a ship or diesel generators that are used for the electrification of islands are potential waste-heat sources for small MD plants. In order to illustrate design considerations for such a waste-heat driven MD plant, a heat source that continuously provides thermal power of 1 MW_{th} is considered in the following scenario. In the given example, no costs are incurred for utilisation of the available waste heat. A PGMD system with specifications similar to those stated in Tab. 5.3 are considered in the given example. The system output capacity is varied by adjusting the module's channel lengths from 0.5 to 22 m and consequently the specific thermal energy consumption of the MD modules. A detailed break-down of the water unit costs into the single cost positions is provided in Fig. 5.8.

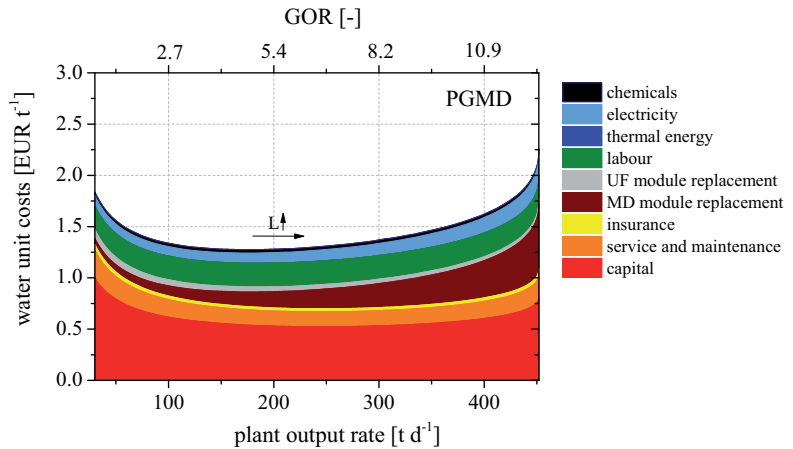


Figure 5.8: Detailed break-down of the unit cost for water for a waste-heat driven desalination plant, considering a continuous waste-heat power of 1 MW_{th} . The results are evaluated for PGMD modules with channel lengths from 0.5 to 22 m. Remaining system specifications are summarised in Tab. 5.3.

With the available thermal power of 1 MW_{th} and the given plant specifications, the total plant output capacity may be adapted from 30 to 460 t d^{-1} , by an adaptation of the thermal en-

ergy consumption of the MD modules. For a module design that involves a GOR² of 5.4, the plant output capacity is 200 t d⁻¹, which increases to a capacity of 300 t d⁻¹ for modules that involve a GOR of 8.2. In the given example, the operational costs range from 1.30 EUR t⁻¹ to 2.30 EUR t⁻¹. If short channel lengths are considered, low GOR lead to low overall output rates that imply high relative capital costs. The relative capital costs decrease for higher output rates due to the increased system capacity. However, as the GOR increases for longer flow channels, the expenses for the MD modules and the associated replacements increase. The lowest unit costs for water are given for a total output capacity of 170 t d⁻¹ that is achieved for modules with a GOR of 4.7 which is based on a channel length of about 4 m. If the channel length is increased further, the GOR and the output capacity increase accordingly, but the water unit costs also increase due to the larger membrane surface area required. As the module's GOR does not further increase for channel lengths beyond 22 m, the output capacity cannot exceed 460 t d⁻¹ within the given specifications.

5.2.4 Techno-Economic Module Optimisation

The preceding sections demonstrate the complexity of finding an optimal design for an MD system. The optimal technical specifications for the MD modules need to be derived based on numerous independent parameters that can be allocated to the following categories:

- material properties
- geometrical parameters
- system conceptual decisions
- operational conditions
- economic constraints.

Due to the large number of independent variables, the specific design parameters may not be identifiable with manual systematic parameter studies. This section provides an advanced method of applying generic parameter optimisation algorithms for the efficient identification of the optimal MD module and system design.

Implementation of a Generic Optimisation Program

GenOpt[®] was identified as a suitable generic parameter optimisation program. In the most general form, GenOpt addresses optimisation problems with an arbitrary set of parametric constraints that describe system performance which is measured by a cost function. GenOpt tries to

²Gained Output Ratio (GOR), definition in Sec. 2.5.2

find a solution for the problem of minimising the cost function. This problem is usually 'solved' by iterative methods, which construct infinite sequences, of progressively better approximations to a 'solution', i.e., a point that satisfies an optimality condition. A variety of algorithms for multi-dimensional parameter optimisation is provided within GenOpt. The algorithms include

- generalised pattern search algorithms (GPS)
- discrete Armijo gradient method
- particle swarm optimisation methods (PSO)
- hybrid GPD-PSO
- simplex algorithm of Nelder and Mead

A detailed description of the different algorithms including their mathematical formulations and their preferential fields of application is provided in the GenOpt documentation [185].

In the given case, the minimal water unit costs characterise the optimal MD module and system configuration that is to be identified. Consequently, a non-analytical cost function (Eq. 5.18) is approximated by an external numerical simulation program, the custom MD model. Within a comprehensive GenOpt benchmark test, the GPS Hookes-Jeeves algorithm was identified as a suitable method for optimising cost functions that are numerically approximated by complex simulation tools [186]. In order to achieve convergent behaviour for such search algorithms that fundamentally require a steady cost function, high precision of the numerical solvers is recommended. In order to reduce the risk of converging at a point that is non-optimum, a multi-start optimisation process has been applied using different sets of initial values and a large initial step size.

For setting up the optimisation problem, the MD model is parametrised based on available specifications derived from a given project scenario, while a user selection of key design parameters is then identified by GenOpt with the objective of achieving minimal water unit costs under given project conditions. A schematic illustration of the parameter optimisation procedure is provided in Fig. 5.9.

After parametrisation of the MD model, GenOpt is configured with the selection of the design parameters to be optimised including their initial points and the corresponding valid parameter ranges. Furthermore, GenOpt is linked to the MD model by defining the simulation start command and the path to the resulting cost function output.

If the optimisation is started, GenOpt calls the MD model and runs the simulation. After evaluating the cost function, the cost value is returned to the optimiser. GenOpt adds this new value to the logged history of the optimisation and derives a new set of parameters by applying the chosen search algorithm. A new simulation is started in order to minimise the cost function step by step. GenOpt provides a graphical on-line representation of the individual parameters and the cost value during the optimisation, as well as a detailed log-file that records information on the cost value, the individual parameters and the simulation time for each intermediate step. If

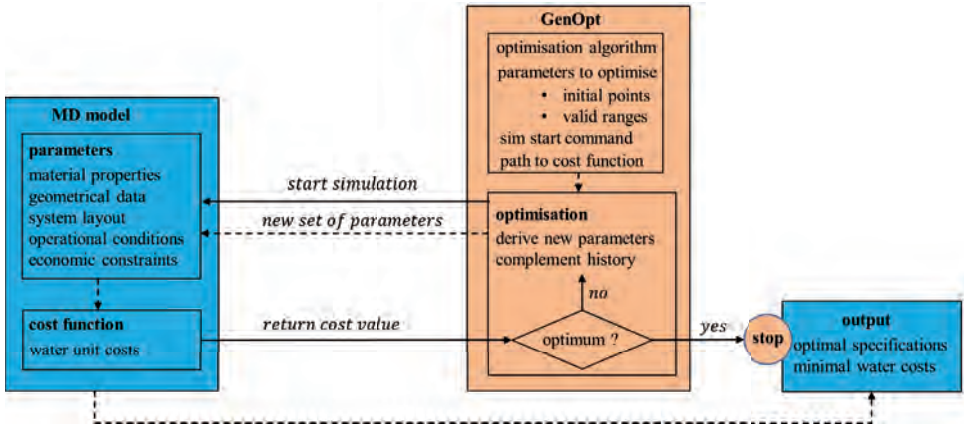


Figure 5.9: Schematic illustration of the parameter optimisation procedure that applies the generic parameter optimisation program GenOpt[®] to the custom MD model.

the actual cost value satisfies the respective constraints that characterise an optimum, the optimisation stops and the optimal set of specifications is provided in the detailed output protocol of the MD model.

The optimisation scenarios that have been investigated within this thesis include 4 or 5 independent variables. GenOpt requires approximately 1 min to run through 100 to 300 iterations to identify the optimal result. It is worth mentioning that the simulation time of the MD model by far dominates the overall duration of an optimisation run.

Demonstration Scenarios

A techno-economic MD module optimisation is performed for five demonstration scenarios that consider the design of a small desalination plant with a daily capacity of 200 t d^{-1} . The scenarios that are listed in Tab. 5.4 cover different specific project conditions defined by available temperature levels, raw water salinities and thermal energy costs.

Scenario #1 might be interpreted as the reference case, considering the treatment of seawater with a medium-grade heat source and thermal energy costs that represent a direct gas-fired power supply or alternatively the costs for solar thermal energy generated by a collector field. In scenario #2, the treatment of a high-salinity brine is considered instead of seawater. This scenario refers to a potential application of MD technology within hybrid membrane systems such as for the treatment of RO brines. In scenario #3, low-priced medium-grade waste heat is utilised for supplying the MD system with thermal energy. Medium-grade waste heat might be available from industrial processes, solar power plants or diesel aggregates (e.g. from generation of electricity on islands, power units on ships etc.). Scenario #4 gives an indication of the optimal

Table 5.4: Demonstration scenarios for techno-economic optimisation of MD modules intended for use in small desalination plants with a daily capacity of 200 t d^{-1} .

scenario	inlet temperatures [°C]	raw water salinity [g kg ⁻¹]	thermal energy cost [EUR (kWh _{th}) ⁻¹]
#1 seawater / medium temperature	25 / 80	35	0.04
#2 concentrate / medium temperature	25 / 80	100	0.04
#3 seawater / medium-grade waste heat	25 / 80	35	0.01
#4 seawater / low-grade waste heat	25 / 50	35	0.005
#5 seawater / medium-grade waste heat	25 / 80	35	0.00

plant design for operation with low-grade waste heat. In order to account for the reduced value of waste heat for lower temperature levels, the costs for the thermal energy in scenario #4 are lower compared to the respective costs considered in scenario #3. High availability is expected for waste heat at low temperatures from arbitrary thermal processes (e.g. cooling systems, air conditioning, electroplating etc.). Scenario #5 addresses operation with medium-grade waste heat of zero cost.

With the exception of the costs for thermal energy, the economic constraints were kept constant for all of the demonstration scenarios. Like the cost-model parameters presented in Sec. 5.2.2, the plant life cycle is estimated to be 15 years, whereas the MD modules and the UF module life cycles are estimated with 5 years and 8 years, respectively. The specific costs for electricity are assumed to be $0.10 \text{ EUR (kWh}_{\text{el}})^{-1}$ and the interest rate is considered to be 4%.

The basic parametrisation of the MD model considers improved materials that have already been introduced in Sec. 4.3.7 (Fig. 4.42) and applied in the analyses from Secs. 4.3.8 to 5.2.2. The MD module channel height has been set to 1.0 m, which represents a reasonable limit for the channel height that might be achieved with typical membrane material dimensions. For deaerated operation conditions, the deaeration pressure and the minimum residual air pressure are assumed to be 0.05 bar. For the (V-)DCMD variant, the mass flow capacities in the evaporator and the condenser channel are balanced out by reducing the mass flow rate in the condenser channel, respectively. The key design parameters that are identified by means of parameter optimisation are the membrane thickness, the module channel length, the flow rate and the plant recovery rate. For the (V-)DCMD variant, the size of the external recovery heat exchanger is additionally identified by the optimiser. A summary of the optimisation parameters including the valid parameter ranges and the associated final accuracies is provided in Tab. 5.5.

As for the parametric field studies in Sec. 4.3.8, high hydraulic pressure losses are expected for parameter combinations that include high flow rates and long flow channels. To prevent the optimiser from including parameter combinations where the mechanical load exceeds a critical

Table 5.5: Variable parameters for techno-economic MD module optimisation.

parameter	symbol	unit	range	minimum step size
membrane thickness	δ_M	[μm]	30 – 200	0.8
channel length	L	[m]	0.5 – 30	0.15
flow rate	\dot{m}	[kg h^{-1}]	100 – 1000	4.2
recovery rate	R_R	[%]	20 – 80	0.3
recovery heat exchanger ^a	$\Delta T_{\text{RX},kA}$	[K]	0.3 – 4.0	0.02

^afor DCMD and V-DCMD only

threshold, a limiting constraint has been implemented. To do so, the cost function has been weighted with high costs, if the combined pressure loss of the evaporator and the condenser channel exceeds the critical value of 1.0 bar.

Identification of the Optimal Plant Design

The optimal module and system specifications have been derived for the different demonstration scenarios from Tab. 5.4, considering the MD module configurations (V-)DCMD, (V-)PGMD and (V-)AGMD separately. A comprehensive compilation of the results is provided in Tabs. 5.6 to 5.10. The documentation includes the set of optimal parameters that was identified by GenOpt, the performance specifications for the MD modules, the water unit costs and a break-down of the water unit costs into fixed and variable operational costs.

In order to gain an impression of the expected volumetric MD system size, the required total MD membrane surface area is clustered into fictive industrial-scale module packages that are introduced in Fig. 5.10. This module concept considers a plate-and-frame design with an effective frame surface area of $2 \times 1 \text{ m}^2$. The required channel length is considered to be realised by series connections of several frames. Basically, multiple frames might be included within one module package in parallel connection in order to scale up the overall output capacity. The maximal module thickness is considered to be 1 m to account for principal limitations imposed by mechanical loads and module handling. The total membrane capacity of one industrial-scale module package depends on the module configuration due to different frame thicknesses. For the considered configurations, the module membrane capacities are specified in Fig. 5.10. The volume-specific membrane areas fit into the range proposed for plate-and-frame MD modules in literature [51]. It is important to note that the given geometrical specifications refer to the effective membrane surface dimensions, so some additional space is required for head structures, frames and end plates.

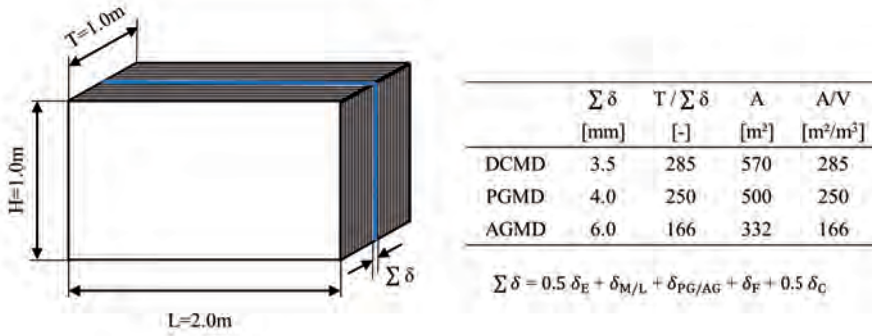


Figure 5.10: Estimated membrane capacities of a fictive industrial-scale module package in plate-and-frame design, considering a different periodic channel layer thickness for DCMD, PGMD and AGMD configurations. Since the specifications refer to effective membrane surface dimensions, some additional space is required for head structures, frames and end plates.

At first, a detailed discussion is provided of the results in Tab. 5.6 that have been obtained for scenario #1. The trends obtained for the optimal membrane thickness meet the expectations from Sec. 4.3.6. The optimal membrane thickness is identified with the minimal value for (V-)AGMD, while thicker membranes are suggested for a (V-)DCMD or (V-)PGMD modules. If the membrane mass transfer resistance is reduced by deaeration, thicker membranes turn out to be optimal due to their improved insulating characteristics. Long flow channels are identified to optimise the heat recovery and reduce thermal energy costs. To optimally balance the con-

Table 5.6: Optimal module configuration for scenario #1 (reference)

		DCMD	V-DCMD	PGMD	V-PGMD	AGMD	V-AGMD
δ_M	[μm]	63	97	120	174	30	30
L	[m]	14.5	14.9	21.3	21.1	28.2	21.2
\dot{m}_{Ei}	[kg h^{-1}]	813	807	611	620	398	568
R_R	[%]	25	29	24	28	28	33
ΔT_{RX}	[K]	0.3	0.3	-	-	-	-
j_M	[$\text{kg}(\text{m}^2\text{h})^{-1}$]	1.6	1.8	0.8	1.0	0.4	1.1
GOR	[-]	14.1	17.9	15.8	19.2	9.2	13.3
n^a	[-]	9	8	21	17	61	24
c_w	[EUR t ⁻¹]	4.01	3.47	3.84	3.31	5.65	3.78
fix.	[%]	47	50	49	52	46	43
var.	[%]	53	50	51	48	54	57

^anumber of industrial-scale module packages according to Fig. 5.10

flicting characteristics of heat recovery and driving force, the specific feed flow rate decreases for the MD configurations with higher total heat transfer resistance. Consequently, longer channel length and lower flow rates are obtained for MD configurations with higher overall heat transfer resistance. For DCMD and PGMD, the optimal channel length and flow rate conditions are almost independent of the status of deaeration, since the membrane thickness has already been adapted as a response to the effect of deaeration. For the AGMD variant, the deaeration status does not affect the membrane thickness and the specific feed flow rate is consequently adapted by the optimiser as a response to the significant difference in transfer resistance. For the plant recovery rate, the optimiser identifies rather low values as being optimal. These results reflect the negative influence of salinity on the thermodynamic module performance, especially for the given high-recovery module concepts. Slightly higher plant recovery rates are obtained for those process configurations that are less sensitive to salinity. Due to the dominant costs for thermal energy, the optimal temperature loss in the external heat recovery system for the DCMD variants is identified with the minimal possible value. These results fulfil the expectation from Fig. 5.7 that considers the same costs for thermal energy as in this scenario.

Based on the energy costs, the resulting module performance characteristics include high GOR and consequently low fluxes. Due to the fixed system capacity for the demonstration scenarios, the flux results directly affect the amount of required membrane surface area, which is reflected by the number of fictive industrial-scale module packages. It is important to note that the industrial-scale module packages include a different amount of membrane surface area, depending on the MD process configuration considered (see Fig. 5.10).

The optimal water unit costs that are obtained for scenario #1 turn out to be similar for all of the process configurations except aerated AGMD, which does not seem to be suitable for the given application. Even though high investment costs are accepted for the high-recovery MD modules, the variable operational costs still amount to approximately 50% of the water unit costs.

The basic argumentation that distinguishes between the different process configurations in scenario #1 is valid also for the other scenarios. Therefore a focus for the analyses of scenarios #2, #3 and #4 is placed on the differing project conditions.

Analysing the results in Tab. 5.7, that were obtained with the high-salinity scenario #2, the optimal membrane thickness turns out to increase significantly for the high-salinity feed water compared to seawater, as predicted in Sec. 4.3.6. The resulting optimal membrane thicknesses for the V-DCMD and the (V-)PGMD configurations are identified to be the maximal values within the valid parameter range. The specific feed flow rates tend to increase based on reduced channel length in order to achieve higher driving forces and consequently lower sensitivity to salinity. If the channel length is reduced, the optimiser is allowed to increase the feed flow rate until it reaches the maximal value that is permitted by the pressure loss restriction. Due to the high raw water salinity, the optimiser identifies the lowest possible recovery rate to be optimal. Similarly to scenario #1, a minimal temperature difference is suggested for the external heat

Table 5.7: Optimal module configuration for scenario #2 (concentrate)

		DCMD	V-DCMD	PGMD	V-PGMD	AGMD	V-AGMD
δ_M	$[\mu\text{m}]$	146	200	200	200	30	30
L	$[\text{m}]$	14.5	14.7	17.9	16.6	25.5	19.7
\dot{m}_{Ei}	$[\text{kg h}^{-1}]$	822	822	670	703	470	623
R_R	$[\%]$	20	20	20	20	20	20
ΔT_{RX}	$[\text{K}]$	0.3	0.3	-	-	-	-
j_M	$[\text{kg}(\text{m}^2\text{h})^{-1}]$	1.3	1.6	0.9	1.1	0.4	1.1
GOR	$[-]$	7.4	9.9	7.4	9.5	6.2	9.6
n^a	$[-]$	11	9	20	15	59	24
c_w	$[\text{EUR t}^{-1}]$	5.86	4.83	5.72	4.78	7.13	4.73
fix.	$[\%]$	34	38	33	36	37	36
var.	$[\%]$	66	62	67	64	63	64

^anumber of industrial-scale module packages according to Fig. 5.10

recovery system based on the high costs for thermal energy.

Also in scenario #2, the resulting module performance characteristics include high GOR and consequently low fluxes. However, due to the strong effect of salinity on the thermodynamic process performance, the GOR is almost 50% lower than for scenario #1. A less conspicuous influence is identified for the (V-)AGMD configuration, due to its low sensitivity to salinity.

The costs for extracting pure water from high-salinity raw water increase by 1.00 to 2.00 EUR t⁻¹, compared to scenario #1 that considers the treatment of seawater. Due to the increased thermal energy consumption, approximately two thirds of the water unit costs are caused by variable operational costs.

Scenario #3 directly reproduces the conditions of scenario #1, but introduces a waste-heat energy supply with low costs for thermal energy. For the results listed in Tab. 5.8, the optimiser identifies modules with reduced flow-channel lengths and consequently less capability for heat recovery, which is a direct response to the reduced thermal energy costs. The suggested flow rates are higher compared to the results of scenario #1, which also shifts the process characteristics from high heat recovery towards an improved output rate. It is worth noting that the reduced channel length also implies a less stringent limitation with respect to hydraulic pressure loss. Due to the higher driving force that accompanies the recommended channel specifications, the optimal membrane thickness decreases slightly compared to the results in scenario #1. Furthermore, the negative effect of salinity decreases and higher recovery rates are suggested. Since the system capability for heat recovery is less important than for scenario #1, slightly reduced size of the external heat exchangers in (V-)DCMD turns out to be optimal.

Even for the low-priced thermal energy in scenario #3, the suggested module characteristics

Table 5.8: Optimal module configuration for scenario #3 (medium-grade waste heat)

		DCMD	V-DCMD	PGMD	V-PGMD	AGMD	V-AGMD
δ_M	$[\mu\text{m}]$	47	74	84	128	30	30
L	$[\text{m}]$	8.7	8.7	10.8	10.7	13.7	11.4
\dot{m}_{Ei}	$[\text{kg h}^{-1}]$	1000	1000	693	695	400	592
R_R	$[\%]$	38	43	37	42	42	48
ΔT_{RX}	$[\text{K}]$	0.8	0.8	-	-	-	-
j_M	$[\text{kg}(\text{m}^2\text{h})^{-1}]$	3.2	3.8	1.8	2.1	0.8	2.0
GOR	$[-]$	8.5	10.5	8.8	10.8	5.7	9.2
n^a	$[-]$	4.5	3.8	9.3	7.8	30.1	12.7
c_w	$[\text{EUR t}^{-1}]$	2.33	2.10	2.23	2.01	3.06	2.08
fix.	$[\%]$	58	61	59	62	58	60
var.	$[\%]$	42	39	41	38	42	40

^anumber of industrial-scale module packages according to Fig. 5.10

include rather high GOR and low flux. However, due to the higher total temperature difference, flux results are significantly higher and GOR are significantly lower than those obtained in scenario #1. The required membrane surface area and consequently the required quantity of industrial scale module packages is halved compared to scenario #1.

The water unit costs decrease significantly if the costs for thermal energy decrease from 0.04 to 0.01 EUR (kWh_{th})⁻¹. Compared to scenario #1, the costs for thermal energy are reduced by a factor of 4 while the required membrane surface area to achieve the target capacity decreases only by a factor of 2, which leads to an increase of the specific fixed cost fraction.

Scenario #4 also refers to a waste-heat energy supply, but here the waste heat is considered at lower temperature levels and lower costs. The corresponding results are listed in Tab. 5.9. The design recommendations obtained from the optimiser account for a low total temperature level and temperature difference as well as the marginal costs that are incurred with low-grade waste heat. In order to maintain a reasonable temperature gradient across the membrane, the channel length is reduced significantly while the feed flow rates are set to similar values as in scenario #3. Since the relative effect of salinity is less pronounced at lower temperatures, the optimiser indicates thinner membranes compared to scenario #3. Based on the low costs for thermal energy, heat recovery is no longer the focus and a slight reduction of the external heat exchanger size is identified for the (V-)DCMD plant configuration.

With the given module specifications, the resulting temperature gradient is similar to the conditions identified in scenario #3. However, less flux is achieved in the given scenario due to the reduced mean temperature level. As a direct consequence, more membrane modules are required

Table 5.9: Optimal module configuration for scenario #4 (low-grade waste heat)

		DCMD	V-DCMD	PGMD	V-PGMD	AGMD	V-AGMD
δ_M	$[\mu\text{m}]$	38	60	66	103	30	30
L	$[\text{m}]$	4.5	4.5	5.4	5.4	7.8	6.1
\dot{m}_{Ei}	$[\text{kg h}^{-1}]$	1000	1000	661	670	368	567
R_R	$[\%]$	31	38	31	37	35	45
ΔT_{RX}	$[\text{K}]$	0.9	0.9	-	-	-	-
j_M	$[\text{kg}(\text{m}^2\text{h})^{-1}]$	2.2	2.9	1.2	1.6	0.4	1.5
GOR	$[-]$	3.2	4.4	3.4	4.8	2.3	5.2
n^a	$[-]$	6.6	5.0	13.9	10.4	56.7	17.1
c_w	$[\text{EUR t}^{-1}]$	3.01	2.51	2.82	2.37	4.18	2.23
fix.	$[\%]$	53	57	57	60	61	63
var.	$[\%]$	47	43	43	40	39	37

^anumber of industrial-scale module packages according to Fig. 5.10

to achieve the target plant capacity. The optimiser favours module characteristics with lower GOR compared to the results obtained in scenario #3, due to the marginal costs associated with thermal energy.

The water unit costs for the low-grade waste heat scenario #4 increase only slightly compared to the results obtained in scenario #3. The difference of the water unit costs for aerated and deaerated operation is more pronounced, indicating the particular benefit of deaeration at low temperatures.

Scenario #5 directly reproduces the conditions of scenarios #1 and #3, but introduces a waste-heat energy supply with zero costs for thermal energy. The corresponding results are listed in Tab. 5.10. With the thermal energy costing nothing, the module concept is optimised towards high-flux performance characteristics in order to reduce total membrane demand. Fundamentally high driving force is obtained with high specific feed-flow rates, so the optimiser identifies short flow channels and high feed flow rates for the given scenario. For operation with a high driving force, the sensitivity to salinity is significantly reduced. Consequently, high plant recovery rates are recommended in order to reduce the raw water demand that defines investment and operational costs for pre-treatment and deaeration. Due to the low sensitivity to salinity, thin membranes are recommended for all of the process configurations.

For the (V-)DCMD configuration, a direct heating concept without an external heat-recovery system is identified to be optimal due to reduced investment costs and reduced pressure loss compared to a variant with external heat recovery. For the AGMD configuration, a direct-heating concept was chosen for purely energy related reasons. If no heat recovery is considered, the GOR

Table 5.10: Optimal module configuration for scenario #5 (free waste heat)

		DCMD	V-DCMD	PGMD	V-PGMD	AGMD	V-AGMD
δ_M	$[\mu\text{m}]$	41	61	48	84	30	30
L	$[\text{m}]$	0.5	0.5	1.4	1.6	0.6	1.6
\dot{m}_{Ei}	$[\text{kg h}^{-1}]$	1000	1000	813	807	564	693
R_R	$[\%]$	77	77	70	72	76	76
ΔT_{RX}	$[\text{K}]$	-	-	-	-	-	-
j_M	$[\text{kg}(\text{m}^2\text{h})^{-1}]$	31	37	11.6	12.4	9.0	11.0
GOR	$[-]$	0.8	0.9	1.4	1.9	0.8	1.8
n^a	$[-]$	0.5	0.4	1.4	1.3	2.8	2.3
c_w	$[\text{EUR t}^{-1}]$	1.00	1.02	1.00	1.00	1.13	0.98
fix	$[\%]$	91	90	91	90	89	91
var.	$[\%]$	9	10	9	10	11	9

^anumber of industrial-scale module packages according to Fig. 5.10

falls below one, which is attributed directly to the thermal efficiency of the process. For the remaining process configurations, minor heat recovery is still considered in order to reduce the costs associated with the heat exchangers for heating and cooling. Due to the high flux results, the overall membrane demand is reduced significantly and only 0.4 to 2.8 industrial-scale module packages are necessary to achieve the planned plant capacity.

The water unit costs are estimated to be around 1.00 EUR t^{-1} , where approximately 90% of the unit costs are allocated to fixed operational costs.

It is obvious from the given results that the optimal choice of key specifications for an MD desalination system may vary significantly with the intended application and the individual project conditions. The new MD cost model may help to identify a suitable plant layout and an appropriately adapted MD module design. Furthermore, the model provides a quantitative measure to evaluate and compare the different basic MD process configurations.

It is important to note that MD technology is not yet implemented on a commercial scale and reliable references on water unit costs from commercial MD projects are not available so far. Thus, the cost model and assumptions cannot yet be validated in practice and the results need to be interpreted as preliminary estimations. However, the fundamental methods and resulting trends are valid, independently of quantitative model validation. The results are considered to be adequate for providing a reasonable approximation to an expected range for the water unit costs and their sensitivities for specific project conditions. The quantitative quality of the results may subsequently be increased by adjustments based on data from future projects.

Further Reading - Selected References on Related Economic Aspects

A reference on economic aspects could be provided by economic assessments carried out by other researchers. Quite differing economic predictions for MD have been derived and published in pertinent literature so far [187], which might mainly be explained by the early state of commercialisation. The results are usually obtained with non-standardised methods and model assumptions. Some authors tend to conservatively rely on experimental experience from mini-scale pilot plant projects, while others publish marvellous economic figures relying on rather optimistic future developments or project conditions. In many cases, a description of the cost model and the associated model assumptions are not transparently discussed or incomplete, so results from pertinent literature are not generally suitable for reference purposes yet. However, some analysis and discussion on economic data has been derived from selected references³.

A transparently described techno-economic cost model on (V-)DCMD seawater desalination with sensible heat recovery has been introduced [20]. The physical model implies a high level of detail and the basic economic model subdivides the total investment costs into membrane cost, heat exchanger cost and other costs. The chosen plant capacity and the assumptions on energy costs for the illustrated example are similar to those applied within this thesis. The water unit costs have been derived to exceed 10 EUR m⁻³ if potential technical improvement is not included and a GOR higher than 10 is considered not to be feasible. If membrane properties are enhanced and membrane costs are reduced based on potential future developments, the water unit costs were predicted to be about 5 EUR m⁻³. In scenarios where waste heat is considered as the thermal energy source, the water unit costs reduce to about 1 EUR m⁻³ due to the reduced membrane requirement and the free thermal energy.

Significantly lower water unit costs have been published by other authors who consider V-AGMD seawater desalination in a fictive plant with a capacity of 100 000 t d⁻¹ [69, 72]. For a fuel-fired process, water unit costs of 0.25 to 0.40 EUR m⁻³ are predicted, while water unit costs for a waste-heat driven process as low as 0.19 to 0.23 EUR m⁻³ have been published. The cost model is quite simple and does not refer to a techno-economic background to estimate the investment costs. The GOR is assumed to be around 10, which might be feasible in principle, but no information is provided on the implementation of the heat recovery concept and the corresponding flux. The thermal energy costs are assumed to be more than one order of magnitude lower than the gas price/solar energy costs considered in this thesis.

Further optimistic economic estimations have been presented for a hypothetical DCMD plant with a capacity of 24 000 t d⁻¹ [188]. The water unit costs are estimated to be 0.40 to 1.00 EUR m⁻³. An average flux of about 6 kg (m² h)⁻¹ was considered for the assessment, while the stated thermal energy consumption correlates to a GOR of about 14 to 17. No detailed discussion of the heat recovery is provided, so it remains unclear how such high GOR values could be achieved with the specified fluxes. The costs for thermal energy are assumed to be about 5 times lower than the gas price/solar energy costs assumed within this thesis, referring to much lower rates

³For convenience of comparison, literature data has been converted to a uniform set of technical or economic measures, if necessary. Assumed currency exchange rate: 1.00 USD \approx 0.72 EUR

for heating steam from co-generation plants.

Autonomous, solar-powered MD systems have been subjected to economic evaluation based on experimental experience with two small pilot plants with a total capacity of 100 and 500 kg d⁻¹ [189]. The pilot plants include similar spiral-wound PGMD modules to those discussed within this thesis. The cost analysis considers the investment costs for the solar thermal collectors and photovoltaic modules in addition to other key cost positions. The estimated water unit costs range from 20 to 26 EUR m⁻³.

Usually the water unit costs for MD are compared to the costs obtained with conventional desalination technologies such as RO, MSF or MED. The economics of conventional desalination plants also mainly depend on system size, site conditions, personnel qualification, energy cost and plant life time.

Industrial-scale thermal desalination plants are typically located next to conventional power plants, utilising low-grade steam extracted from the low-pressure stages of the turbines. The thermal energy costs may then be rated by evaluating the associated loss in electric power generation. A plant power loss of 10 kWh_{el} m⁻³ and unit costs of power loss of 0.03 USD (kWh_{el})⁻¹ are proposed for typical industrial MED and MSF plants [6], leading to significantly lower costs for thermal energy than the costs assumed within this thesis. Also, the costs for electricity are assumed to be lower in the context of industrial-scale desalination. Here, electricity costs of 0.05 USD (kWh_{el})⁻¹ have been mentioned in literature [140]. The energy costs for electrically driven desalination plants may easily be evaluated by directly applying the relevant electricity cost. The unit water costs for industrial-scale MSF, MED or RO desalination plants typically range from 0.40 to 1.10 EUR m⁻³ [6]. It is important to note that the unit water costs for centralised industrial-scale desalination do not include costs for distribution. For smaller systems with capacities of 1 000 m³ d⁻¹, water unit costs take on values clearly above 1.00 EUR m⁻³ [6]. It is obvious that small-scale MD cannot compete with established industrial-scale desalination technology today. Since the cost-model and model assumptions presented within this thesis do not claim validity for industrial-scale application, the potential for MD in industrial-scale processes cannot be evaluated with them. However, due to fundamentally similar thermodynamic limitations, the high potential to optimise the packing fraction and the substantial substitution of high-priced metals with cheap polymers, MD may be able to achieve similar or even lower water unit costs than the classic thermal desalination approaches.

Considering small decentralised plants with a renewable energy supply, also commercialisation of the established desalination technologies is still considered to be in the development and pilot phase. The water unit costs reported on such renewably driven and small plants are significantly higher and vary more widely than those stated for the conventional approaches. Water unit costs of 3.8 to 10 EUR m⁻³ have been reported for 50 m³ d⁻¹ stand-alone PV-RO desalination plants with energy recovery [6]. Estimates on costs for water produced in typically larger wind-powered RO systems range from 2.5 to 10 EUR m⁻³ [190]. MD represents a fundamentally attractive approach for introducing thermal processes with a high GOR into renewable or waste-heat driven desalination systems.

Not only water unit costs but also the water price strongly depends on local conditions. While

the water price in areas abounding in water might be well below 1 EUR m⁻³, the economic value of fresh water is significantly higher in areas with low water availability and insufficient infrastructure. As an example, water is imported to Mallorca by boat during drought, which causes costs of up to 2 EUR m⁻³. Water transfer costs to Greek islands range from 2 to 7 EUR m⁻³. In Aquaba, Jordanian local water costs reach 1.70 EUR m⁻³ [191]. In Cape Verde, the water price is 2.35 to 4.93 EUR m⁻³ [190]. If no water supply structure is available at all, very expensive bottled water is sold at a price, which is often unaffordable for the local population. However, access to water is essential for life and has even been recognised as a human right, so the value of clean fresh water cannot be simply defined in terms of economic numbers.

It may be concluded that the economic feasibility of MD in decentralised desalination is difficult to evaluate due to high uncertainties in the evaluation methods and assumptions, the strong dependence on local conditions and the diffuse technological and economic references currently available for competing desalination approaches. Future development and experience with commercially motivated projects will provide reliable references, eventually defining the role of MD in the desalination market.

It is important to note that MD should not only be considered as technology which is directly competing against the established approaches. MD could also adopt a complementary role within an larger system, such as for the treatment of concentrated brines in RO desalination plants or even for desalination system concepts with zero liquid discharge. However, a successful market launch based on economic feasibility is more likely to be achieved in the context of alternative applications that provide higher product value. This scenario is typically given for applications that aim for very high product water quality or the treatment of highly concentrated brines in the chemical industry.

6 Conclusion

6.1 Summary

Global **desalination** capacities have increased enormously over the past few decades to combat water scarcity in regions with discrepancies between water availability and demand. Currently, the desalination market relies almost exclusively on non-sustainable, industrial-scale processes without providing a solution to prevent the actual water shortage in rural areas. Therefore, the development of small-scale, self-sufficient and environmentally friendly desalination systems is considered to be one of the key challenges to sustainably overcome water scarcity.

Thermally driven Membrane Distillation has been identified as a promising approach for decentralised desalination. However, MD has not been commercialised successfully, still requiring scientific research on material, module and system development. High potential for improvement is associated with adapted membrane module design appropriate to specific project requirements. Comprehensive MD design methods, tools and universal design recommendations are not yet available.

Membrane Distillation (MD) is a thermally driven, membrane-based separation process mainly suitable for the treatment of aqueous feed solutions. A hydrophobic, highly porous membrane separates the feed solution from the permeate. When a vapour pressure gradient is established across the membrane, volatile compounds in the feed solution evaporate and the vapour molecules are forced through the membrane pores from the feed to the permeate sides. Depending on the feed composition, the permeating vapour may consist of a single or multiple components. Seawater does not contain volatile compounds besides water. Seawater desalination can be considered representative for single-component permeation applications.

Several MD process configurations have been developed in order to meet different specific process requirements. This work focuses on the classic MD configurations known as Direct Contact MD, Permeate-Gap MD and Air-Gap MD, which utilise a temperature gradient to establish the process driving force.

In MD processes, an enormous amount of heat is transferred through the membrane, mainly as latent heat but partially also by conductive heat transfer. To reduce the associated thermal energy consumption, heat recovery is typically implemented either by sensible or latent heat recovery concepts.

The main function of the membrane in MD is to reliably support the liquid-vapour interface, which relies on the essential hydrophobic property of the membrane surface. Commercial membranes specifically developed for MD applications are not yet available, so flat-sheet or capillary microfiltration membranes are widely used in the context of MD. In order to fulfil mechanical stability requirements, the thin flat-sheet membranes are commonly laminated onto mechanical support structures. The membrane is incorporated into a membrane module. Either shell-and-tube, plate-and-frame or spiral-wound design concepts are typically considered for MD module design. However, development of MD membrane modules is still in the phase of commercialisation and any one of the concepts might be considered superior in the future.

It is obvious that module optimisation must include fundamental phenomenological aspects, material selection, module concept and design as well as system integration, operational strategy and costs. Comprehensive design methods, tools and universal design guidelines have not been available up to now. The scope of this thesis is to bridge the gap between fundamental research and full-scale module development. A key issue is the thermodynamic evaluation of MD performance rather than practical aspects such as fouling, scaling or pretreatment. The **objective** is the development of a model-based method suitable for comprehensive evaluation and comparison of different MD concepts on a realistic application scale, considering key performance parameters such as output capacity, flux and thermal as well as electricity consumption and subsequently costs.

The desired methods were developed by applying a scientific three-level **approach** that started with analysis of the fundamental MD phenomenology. After that, the scope was widened to full-scale MD modules and finally economic aspects in the context of small MD desalination systems were taken into consideration.

The *Process Analysis* chapter provides the basis for a comprehensive fundamental understanding of thermodynamic MD **phenomenology**, including a qualitative and quantitative discussion of parameters which influence it. The thermodynamic fundamentals include heat and mass transfer through the membrane and through the hydraulic boundary layers in the flow channels. The vapour space includes a mixture of water vapour and stagnant air, which acts as further transfer resistance in addition to the solid membrane structure. Considering typical MD membrane specifications, Knudsen numbers between $0.1 < Kn < 10$ indicate vapour transfer based on combined Knudsen diffusion and molecular diffusion. If the vapour space is fully deaerated, viscous flow phenomena additionally contributes to the overall mass transfer. Transmembrane heat transfer is based on latent and conductive phenomena. The effective thermal membrane conductivity is proposed to be derived from membrane porosity and the tortuosity of the membrane solid phase. Sensible heat transfer was identified to be negligible. If an air gap is introduced, the vapour space is extended accordingly and heat and mass transfer coefficients are derived for a combined membrane and air gap. In contrast to the membrane, wet parts of the air gap introduce thermal bridges and increase the effective thermal conductivity across the air gap. For typical air-gap specifications, Rayleigh numbers $Ra < 100$ indicate the absence of natural convective transfer

phenomena in the air gap. Heat transfer from the flow-channel bulk streams to the respective liquid-vapour interfaces was estimated by generic Nusselt correlations that allow experimental parameter identification. The geometrical specifications of the channel spacers were taken into account in the derivation of channel-dependent parameters such as flow velocity and hydraulic diameter. Due to the transmembrane mass transfer, concentration at the feed-side liquid-vapour interface is higher than in the feed-side bulk stream. This phenomenon, also known as concentration polarisation, can be estimated quantitatively by the presented theory on mass transfer. A new “Split-path model” has been developed, accounting for the effects of a membrane backing on heat and mass transfer. The model refers to technical backing specifications and backing position.

Based on the fundamental transfer equations, parametric models for the prediction of the transmembrane heat and mass transfer under steady-state conditions were derived for DCMD, PGMD and AGMD channel configurations. The so-called **single-node model** represents a one-dimensional approach, in which the channels are divided into a series connection of multiple transfer-resistance layers perpendicular to the membrane. The models were implemented in the C programming language and the coupled heat and mass transfer equations are solved with an iterative algorithm.

Laboratory-scale experiments were carried out for process and material characterisation and experimental model validation. A flat-sheet **membrane test cell** with flow channel dimensions of $150 \times 250 \text{ mm}^2$ was designed. The test cell is integrated into a fully automated test facility that includes two independent hydraulic circuits, controls and data acquisition. The uncertainty of flux measurements has been determined to be $\pm 5 \text{ g h}^{-1}$. The precision of the thermal efficiency measurements is limited by the temperature measurements and ranges from 1 to 16 %, depending on operational conditions and channel configuration.

Different **channel spacers** were characterised for flow velocities from 0.03 to 0.17 ms^{-1} . The heat transfer and flux performance strongly depend on spacer geometry and can be enhanced by a factor of up to 2.9 compared to channels without spacers. Thermal efficiency was shown to be almost independent of spacer geometry and flow rate.

A set of commercially available ePTFE **membranes** was chosen systematically for experimental evaluation. The membranes offer different structural properties, mainly differing in thickness and nominal pore size. The membrane thicknesses range from 23 to $98 \mu\text{m}$ and the nominal pore sizes range from 0.05 to $0.45 \mu\text{m}$, while all of the samples had a porosity of approximately 80 %. The DCMD flux performance was measured to be within 6 and $18 \text{ kg (m}^2 \text{ h)}^{-1}$ and the thermal efficiency was between 50 and 92 %, when a temperature difference of 8 K and temperature levels from 40 to 80°C were applied. Flux results for the different membranes only differed by 2 to $4 \text{ kg (m}^2 \text{ h)}^{-1}$. As expected from theory, thermal efficiency was identified to be independent of membrane thickness. The mass transfer phenomena in the different membranes were analysed by means of membrane deaeration. Flux through the deaerated membranes increased by 41 to 93 % and thermal efficiency by 9 to 34 % compared to the corresponding aerated operation mode. According to theoretically derived predictions, the benefit of membrane deaeration is more pronounced for lower operation temperatures, thicker membranes and membranes with larger pores. The membrane mass transfer coefficients were derived within a range of 11 -

$41 \times 10^{-7} \text{ kg (Pa m}^2\text{s)}^{-1}$ for aerated and $26 - 81 \times 10^{-7} \text{ kg (Pa m}^2\text{s)}^{-1}$ for deaerated operation, depending on membrane structure and temperature. Effective conductive heat transfer coefficients of the membranes were determined theoretically to be between 443 and $1887 \text{ W (m}^2\text{K)}^{-1}$. Optimal membrane selection usually leads to the choice of membranes with low mass transfer resistance combined with high thermal resistance. An increase of the membrane porosity, pore size or a reduction of tortuosity will thus lead to improved performance characteristics, while a reduction of the membrane thickness must be carefully evaluated from a thermodynamic point of view. The results of a theoretical assessment suggest the use of thicker membranes for increased salinity levels. The role of the membrane becomes less significant for when poor hydrodynamics dominate the overall transfer resistance.

Some of the membranes were also investigated as **laminates** with scrim and non-woven types of backing structures. When a backing layer is introduced, a reduction in flux and thermal efficiency can be observed. Only 50 - 80 % of the flux obtained with an non-laminated membrane could be achieved with the laminates, mainly correlating to backing porosity and position. Laminates with non-woven backings performed better than laminates with a scrim type of backing. A backing position towards the condenser side was identified as the preferable configuration.

When a **permeate gap** is introduced next to the membrane, additional heat transfer resistances lead to a significant reduction of flux performance. Flux results of the PGMD experiments ranged between 3.2 and $5.2 \text{ kg (m}^2\text{h)}^{-1}$, when a temperature difference of 12 K and temperature levels from 40 to $80 \text{ }^\circ\text{C}$ were applied. Thermal efficiency results were similar to those observed in DCMD operation. Also in PGMD, the backing led to significant performance reduction, but its orientation did not distinguish the performance results as much as observed in DCMD. Differences can be explained by the fact that the backing increases the overall permeate gap width and faces stagnant instead of convecting water, if positioned towards the permeate channel.

In **air gap** configurations, heat and mass transfer resistances were by far dominated by the air gap, which is about 30 times wider than the membrane. The flux performance ranged between 1.2 and $7.1 \text{ kg (m}^2\text{h)}^{-1}$, when a temperature difference of 12 K and temperature levels from 40 to $80 \text{ }^\circ\text{C}$ were applied. The influence of temperature level is more obvious than for DCMD and PGMD, since mass transfer is mainly limited by pure molecular diffusion in the gap. Due to the poor flux results, improved thermal resistance did not lead to increased thermal efficiency, which was measured to be between 64 and 92 %. The negative influence of the membrane backing in AGMD was less pronounced than in DCMD and PGMD. When the dominating mass transfer resistance of the air gap is reduced by gap deaeration, major performance improvements are achieved, especially at low temperature levels. For operation at $40 \text{ }^\circ\text{C}$, flux increased by 238 % compared to aerated operation. According to the model predictions, the flux increase at complete deaeration could reach up to 438 % at $40 \text{ }^\circ\text{C}$. Since mass transfer resistance improves independently of heat transfer resistance, thermal efficiency rises to about 90 % for any temperature level, indicating the high potential for deaerated AGMD in the context of low-temperature operation. Theoretical model predictions were used to derive a break-down of the overall mass transfer resistance in an AGMD configuration. The mass transfer resistance induced by the membrane only contributed 11 % to the overall transfer resistance for aerated operation. When deaeration is considered, the role of the membrane increases accordingly. The mass transfer coefficients for a

combined laminate and air gap of about 2 mm were derived to be 0.9 to $1.7 \times 10^{-7} \text{ kg (Pa m}^2\text{s)}^{-1}$ for aerated and $26 \times 10^{-7} \text{ kg (Pa m}^2\text{s)}^{-1}$ for deaerated operation. The corresponding thermal conductivity for the combined laminate and air gap was theoretically derived to be $54 \text{ W (m}^2\text{K)}^{-1}$. A **comparative evaluation** of DCMD, PGMD, AGMD and V-AGMD process performance based on fixed bulk stream conditions was presented, considering systematic parameter variations for each of the characteristic operational parameters, namely mean temperature, flow velocity, temperature difference and feed water salinity. The effect of concentration polarisation was estimated to be less than 1.1 % and is therefore considered to be negligible for the applications addressed within this thesis. The effect of salinity was determined to be strongly dependent on operating conditions. The model indicated a generally low impact of salinity for operation with large temperature differences.

The experimental data was compared to the model predictions to demonstrate the **node-model validity**. Combined mean differences for flux and thermal efficiency were identified to be respectively 4 % and 4 % for DCMD, 4 % and 4 % for PGMD, 5 % and 5 % for AGMD and 6 % and 9 % for V-AGMD.

The results from the *Process Analysis* chapter were then applied to develop a comprehensive full-scale MD module model that provides a high level of physical detail. The *Module Analysis* chapter bridges the gap between fundamental scientific research on materials and the thermodynamic process behaviour on the one hand, and the scale of application on the other. A discrete **multi-node model** was implemented in order to account for the local distribution of the operation conditions along the flow channels in full-scale MD modules. The thermodynamic evaluation of each local finite channel element was executed with the validated fundamental single-node models from the preceding chapter, so DCMD, PGMD or AGMD configurations could be evaluated individually. Multiple single nodes were thermodynamically coupled by the appropriate heat and mass balances, allowing the derivation of flow rate, salinity, temperature and pressure profiles along the channels in the flow direction. The profiles of the relevant counter-current flow configuration were solved with an iterative algorithm. Sufficiently fine resolution was proven for a discretisation of 10 nodes per meter of channel length and a minimum of 100 nodes. Generic module performance parameters such as permeate output rate, average flux, recovery rate, thermal efficiency and thermal energy as well as electricity consumption were derived in order to allow different module designs and operational modes to be compared quantitatively.

A **module test rig** was developed to characterise full-scale MD modules for experimental multi-node model validation. The hydraulic components can withstand corrosive feed solutions and operating temperatures up to 90°C . The test infrastructure includes fully automated controls and comprehensive data acquisition. For relevant operating conditions, the probable error for specific thermal energy consumption was estimated to be $3 - 10 \text{ kWh}_{\text{th}} \text{ t}^{-1}$ and $<2\%$ for thermal efficiency. A distinct difference between the uncertainties of the different MD configurations was not identified. From an energy balance, the heat loss to the surroundings was determined to be less than 1 % of the transmembrane heat transfer.

Full-scale spiral-wound **MD module prototypes** with different conceptual, geometrical and material specifications were fabricated, implementing the specifications studied within the *Pro-*

cess Analysis chapter. A set of 9 prototypes included DCMD, PGMD and AGMD modules with membrane surface areas from 4.9 to 14 m². The modules were designed to allow effective sensible heat recovery due to the long flow channels of 3.5 - 10 m.

A comprehensive analysis and discussion of general aspects applying to **MD module operation** was provided. The assessment includes experimental results and model predictions of the key performance parameters for module operation at different temperatures, flow rates, salinities and states of deaeration. Furthermore, the influence of flow channel length on sensible heat recovery and effects of non-ideal flow distribution in parallelised multi-module configurations were evaluated and discussed. Further investigations addressed specific aspects of DCMD, PGMD and AGMD module operation individually. The model predictions all rely on a parametrisation set that was identified in the *Process Analysis* chapter. However, it turned out that the average heat transfer in the full-scale module flow channels is about 30 % lower than the results obtained in lab-scale experiments, which is mainly attributed to the spiral-wound prototype configuration and a non-ideal velocity field in the inlet and outlet regions of the flow channels.

For the operation of **DCMD modules**, the implementation of heat recovery automatically involves an external heat exchanger. The size of the external heat exchanger brings limitations for the DCMD heat recovery capability, since an exergy loss always occurs in heat exchangers of finite size. The exergy loss that must be taken into account for realistic evaluation of DCMD energy consumption is determined by the size of the external heat exchanger and increases with flow rate. If infinite heat exchanger dimensions are considered, the exergy loss of DCMD heat recovery diminishes. To account for a realistic configuration, an exergy loss of 2 K was considered for DCMD performance evaluation throughout this thesis. DCMD heat recovery was identified to be quite sensitive to asymmetric module operation. Even if inlet flow rates on the evaporator and condenser sides were equal, asymmetries in flow rate and temperature profiles were identified, caused by transmembrane mass transfer. This asymmetry already increased thermal energy consumption by about 20 % compared to harmonised operation. Optimal heat recovery was achieved, when the DCMD module was operated with similar mass flow capacities on the evaporator and condenser sides. Mass flow compensation was suggested to compensate effects of transmembrane mass transfer and feed side salinity.

The operation of **PGMD modules** allowed internal heat recovery, since the permeate is separated from the coolant by an impermeable polymer film and feed water can be preheated internally. The impermeable film effectively replaces the external heat exchanger that is required for heat recovery in DCMD operation. However, the additional gap also introduces additional heat transfer resistance which is accompanied with an exergy loss. In order to achieve similar transmembrane driving force, a higher overall bulk stream temperature difference is required. Since the polymer film surface area cannot be defined independently of the membrane area, the exergy loss is mainly determined by the gap and film thicknesses that are to be minimised. For PGMD modules with gap widths from 0.25 to 1.0 mm and a film thickness of 127 μm , the exergy losses were determined within a range of 1.5 to 3.5 K. For energy-saving reasons, the permeate was preferably extracted from the cold end of the module. Thermal energy consumption was reduced by about 10 % compared to an operational mode that considered permeate extraction on the hot side of the module. In the preferable mode, sensible heat was recovered from the

permeate stream and symmetric temperature profiles were established along the flow channels. The operation of **AGMD modules** also allowed internal heat recovery. The air gap introduces additional heat and mass transfer resistance that adds to the vapour space, in contrast to the permeate gap. Due to the additional resistances of a 2.0 mm air gap, the bulk-stream temperature difference of AGMD was observed to be approximately 8 K higher than the results obtained with a similar DCMD module. Higher driving force and higher mass transfer resistance is partially compensated, so the overall output rate differed only slightly from the results obtained with DCMD and PGMD modules. Since stagnant air in the air gap dominates the total mass transfer resistance, high potential for performance improvement can be attributed to gap deaeration. When gap deaeration was considered in the experiments at 80 °C, the permeate output rate increased by 28 % and thermal energy consumption was reduced by 49 %, even though the air gap could not be completely deaerated. The deaeration pressure during this experiment was 176 mbar, limited by the vapour pressure of the mixed warm permeate in the reservoir. An absolute pressure profile along the air gap channel could be maintained during steady-state operation, which was proven by absolute pressure measurements at different locations along the channel. Since deaeration is more effective at lower temperatures, V-AGMD operation offered low energy consumption also at low temperatures. Thermal energy consumption at a temperature level of 50 °C only differed by 7 % to the results for operation at 80 °C. The electricity consumption was estimated to be similar for aerated and deaerated operation, indicating complete compensation of the additional power loads from the deaeration system by enhanced thermodynamic module performance.

A **comparative evaluation** of the performance characteristics of similar DCMD, PGMD, AGMD and V-AGMD modules with 10 m² membrane area was conducted for identical inlet conditions. Systematic parameter variations were considered for the most important operational parameters, namely evaporator inlet temperature, inlet flow rate and feed water salinity. General observations included increased output, reduced energy consumption and higher thermal efficiency with a higher evaporator inlet temperature. For increased feed flow rates, output performance improved but thermal energy consumption also increased due to less effective heat recovery. Thermal efficiency was not affected by the feed flow rate. The output results were very similar for DCMD, PGMD and AGMD and ranged from 8 to 25 kg h⁻¹. Better output performance was obtained for V-AGMD. Thermal energy consumption was measured from 130 to 350 kWh_{th} t⁻¹, being similar for DCMD and PGMD, highest for AGMD and lowest for V-AGMD. The overall thermal efficiency ranged from about 50 to 60 % for DCMD and PGMD, from 60 to 80 % for AGMD and showed almost constant results of 90 % for V-AGMD. The influence of feed-water salinity was tested with artificial feed solutions up to salinities of 200 g kg⁻¹. Even though a negative effect of salinity was observed for all of the process variants, the associated sensitivities were quite different. The lowest sensitivity was obtained for AGMD, followed by V-AGMD, while the highest and similar sensitivities were given for DCMD and PGMD. It was concluded that MD operation with high driving forces, as given for the air-gap configurations, is beneficial for high-salinity operation.

The experimental data was compared to the model predictions to demonstrate the **multi-node model validity**. The mean deviations for the permeate output rate, the specific thermal energy

consumption and the thermal efficiency were identified to be 9%, 11% and 9% for DCMD, 6%, 10% and 7% for PGMD, 5%, 7% and 6% for AGMD and 6%, 17% and 5% for V-AGMD, respectively.

Model-based studies were conducted to clarify the crucial role of **membrane selection** on module performance. The optimal membrane thickness turned out to be strongly dependent on feed-water salinity. For DCMD and PGMD modules, the optimal membrane for the treatment of feed water without salt was identified to be as thin as possible. For the treatment of saline feed water, the recommended membrane thickness increases, while sensitivity changes with module configuration and operating conditions. A comprehensive sensitivity analysis on the interrelation of membrane thickness, salinity level and module configuration was performed, considering DCMD, PGMD and AGMD modules designed either for high flux or for high heat recovery. The salinity levels were varied within the range of 0 to 200 g kg⁻¹. Different optima in membrane thickness were identified, depending on whether output rate or energy consumption was used as the optimisation criterion. For a high-flux DCMD module without heat recovery, the optimal membrane thickness was identified to be within the range from 0 to 90 μm , while optimal membrane thickness increased to 0 to 220 μm for a DCMD module that incorporated significant heat recovery. The optimal membranes for PGMD modules turned out to be slightly thicker. For AGMD modules, the optimal membrane thickness was identified to be as thin as possible, independently of salinity level. Explained by the fact that the negative effect of salinity is more pronounced for low driving forces, it was concluded that the optimal membrane thickness increases if the interfacial temperature difference is lowered by any change in the operating conditions or in module design.

Further sensitivity analyses were presented on the quantitative impact that might be achieved with **advanced materials**. Since the role of certain materials on DCMD, PGMD, AGMD and V-AGMD performance was expected to be different, the analyses were conducted for each of the process variants and evaluated comparatively. Again, the assessment distinguished between a high-recovery module concept and a high-flux module concept. The sensitivity of the module performance to a potential improvement of the channel spacers, the membrane, the backing or the impermeable film was evaluated separately. Subsequently, a combined potential associated with a reasonable improvement for each of the key materials was derived. The relevant material parameters were modified such that the resulting model predictions reflect a realistic potential for improvement that could be achieved on the medium term. The new set of model assumptions considered an improvement of the heat transfer by a factor of 1.5 and the membrane permeability by a factor of 1.4. Additionally, the enhanced model assumptions considered an improved backing structure and a thinner impermeable film. For modules with reasonable heat recovery, the expected performance improvements included a 3 - 23% higher output rate and a 25 - 50% lower energy consumption. For high flux modules, the expected performance improvements included a 3-50% higher output rate.

The last section of the *Module Analysis* chapter presents a comparative **parametric field study** which covers a wide range of module designs and operational parameters. The varied parameters included flow velocities from 0.01 to 0.30 m s⁻¹, channel lengths from 0.5 to 30 m and channel widths from 0.5 to 10 mm. Focus was placed on the interdependence of permeate output rate, flux

and heat recovery, which were comparatively evaluated for DCMD, PGMD and AGMD for aerated and deaerated operation. By considering all of the parameter combinations, the parametric field study covered 1728 individual scenarios, 576 for each of the MD configurations. Scenarios that led to results with high hydraulic pressure loss were filtered out in order to maintain practical feasibility. With the given parametric field, permeate output rates of up to 351 kg h^{-1} were achieved and the flux results showed values of up to $115 \text{ kg (m}^2 \text{ h)}^{-1}$. The GOR¹ reached values of up to 22. Maximum output rates were limited by the pressure loss constraint, especially for scenarios with long flow channels that fundamentally lead to high GOR values. Thus, a high output rate and a high GOR were identified to be conflicting demands. Furthermore, it became obvious that high flux and a high GOR cannot be achieved simultaneously and one has to decide whether a high-flux or high-recovery module concept is preferred. Flux results of up to about 30 kg h^{-1} might still be achieved with a GOR of 2.5, while maximal fluxes decrease to about 10 kg h^{-1} for a GOR of 5 and to about 5 kg h^{-1} for a GOR of 10. The resulting parameter fields for the different MD configurations were subsequently analysed and categorised in detail, supported by colour-coded editing. For all of the MD configurations, the strong dependence of the permeate output rate on feed flow rate could be clearly illustrated by the colour codes. The higher the feed flow rate, the higher the permeate output rate. Furthermore, the general dependence of flux from the area-specific feed flow rate was pointed out. The higher the specific feed flow rate, the higher the predicted flux. The results clearly indicate the role of the most important interdependent parameters that must be defined for any MD project. Moreover, the resulting fields identify the thermodynamic limitations that are implied by MD in general and the different MD configurations in particular. Any MD operational results from elsewhere that are either obtained experimentally or based on model predictions can prospectively be allocated to the relevant result field, allowing generally valid categorisation and comparison.

Technological and economic aspects were taken into consideration for the comprehensive evaluation of the MD process presented in the *Economic Evaluation* chapter. A detailed **cost model** was proposed to estimate the estimation of water unit costs used as an integrative quantitative measure for system comparison and as an optimisation criterion. The widely applied investment cost model was specifically adapted for the evaluation of MD desalination systems. It is important to note that the required membrane surface area and consequently one of the most important cost positions depends not only on the total plant capacity but also on heat recovery specifications, while other key cost components are not affected by the heat recovery specifications. Individual relations were derived and discussed for all of the expected key cost positions such as pre-treatment, deaeration, MD modules, heat exchangers and other system components. Also, the economy of scale was accounted for. Operational costs included financing, energy costs, chemicals, membrane replacement, maintenance, labour and insurance.

The expected **investment costs** were comparatively analysed for different MD configurations and operational strategies in the context of a small reference plant with an overall desalination capacity of 200 t d^{-1} . The expected overall investment costs were derived to be in the range

¹Gained Output Ratio (GOR), definition in Sec. 2.5.2

of 0.38 to 0.58 million EUR. Higher investment costs were associated with the scenarios that considered high heat recovery, due to an increased membrane demand. If a plant configuration without heat recovery was considered, heat exchanger costs exceeded membrane costs. Costs for pretreatment and the rest of the plant were almost independent of MD configuration. Costs estimated for the deaeration system contributed less than 4% to the total system costs.

Sensitivity analyses on the **water unit costs** were performed, again considering a reference plant with a desalination capacity of 200 t d^{-1} . Energy costs were assumed to be $0.04 \text{ EUR (kWh}_{\text{th}})^{-1}$ and $0.10 \text{ EUR (kWh}_{\text{el}})^{-1}$. A plant lifetime of 15 years was assumed, while MD-module replacements once every five years were taken into account. The break-down of the water unit costs clearly indicated an economic optimum for a specific channel length, feed flow rate, recovery rate or heat exchanger size, when evaluated individually. The value and sensitivity of the water unit costs were mainly defined by module costs and costs for thermal energy. The minimum water unit costs then defined the optimal module design specifications, which turned out to be quite different for DCMD, PGMD and AGMD.

The choice of the capacity of **waste-heat driven MD desalination plants** directly refers to the amount of available waste heat and the specific thermal energy consumption of the MD modules. As an illustrative project scenario, a continuous waste-heat source of 1 MW_{th} has been considered. The system output capacity could be varied from 30 to 460 t d^{-1} by an adaptation of the GOR involved with the respective module design. For the projected waste heat scenario, the water unit costs ranged from 1.30 EUR t^{-1} to 2.30 EUR t^{-1} .

An advanced method for integrated module optimisation was proposed in the final section of the thesis. The generic parameter optimisation program GenOpt[®] was linked to the MD model for efficient **techno-economic MD module and system optimisation**. GenOpt optimises arbitrary cost functions, in this case the water unit costs, by generic iterative solving algorithms. Again a desalination plant with a capacity of 200 t d^{-1} was considered as the reference project. Five different scenarios reflect different project conditions regarding available temperatures, feed-water concentration and energy costs. In order to determine optimally customised module configurations and adapted operational conditions for each scenario, the optimiser was allowed to vary the most important design parameters, namely membrane thickness, channel length, feed flow rate, recovery rate and heat exchanger size. A fictive, industrial-scale, plate-and-frame module package with dimensions of $1 \times 1 \times 2 \text{ m}^3$ was used as a reference in order to allow an intuitive impression of the system size. Depending on the MD configuration, one module package contains about 300 to 600 m^2 of membrane surface area, which corresponds to a packing fraction of 150 to $300 \text{ m}^2 \text{ m}^{-3}$. When a temperature level of $80 \text{ }^\circ\text{C}$ was available and seawater was considered as the feed supply, water unit costs ranged from about 3.30 EUR t^{-1} to 5.60 EUR t^{-1} . Deaerated operation resulted in lower water unit costs. About half of the unit water costs were caused by variable operational costs. Due to the high cost associated with thermal energy, the membrane design recommendation tended towards high-recovery modules with a GOR in the range of 9 to 20 and low fluxes that ranged from 0.5 to $2.0 \text{ kg (m}^2 \text{ h)}^{-1}$. The desalination unit consisted of 8 to 60 membrane packages, depending on whether DCMD, PGMD or AGMD was considered. Slightly higher water unit costs were obtained when the feed-water salinity was increased. When medium-grade or low-grade heat was considered, the costs associated with thermal energy are

reduced significantly. In these cases, MD modules with less heat recovery and higher flux are identified to be optimal and the water unit costs decreased to about 2 to 4 EUR t⁻¹. If free waste heat were available, the water unit costs were estimated to be about 1 EUR t⁻¹. The recommended module design tended towards high-flux modules with low GOR values that range between 0.8 and 2.0 and high fluxes that range between 10 and 40 kg (m² h)⁻¹. The desalination unit consists of only 0.5 to 3 membrane packages, depending on whether DCMD, PGMD or AGMD was considered. About 90% of the unit water costs were caused by fixed operational costs. In the high-flux scenario, deaeration operation turned out to be more expensive than aerated operation under some conditions but not all. The optimal choice of key specifications for an MD desalination system varied significantly with the MD configuration and the individual project conditions. The new MD cost model helped to identify optimally customised MD module design and a suitable plant layout. Furthermore, the model provided a quantitative measure for evaluation and comparison of the different MD process configurations.

6.2 Recommendations for Further Research

This thesis provides a comprehensive assessment of thermodynamic MD process and module optimisation including general methods for module adaptation. However, the models and experiments do not include the concept of latent heat recovery, in which thermodynamic and practical limitations still require evaluation and comparative discussion.

The models and methods presented in this thesis may soon be applied within the context of commercially motivated MD projects. Such projects could address either saline water treatment or the separation of other aqueous solutions. The model results still require some re-evaluation and revalidation with data from future projects, especially with respect to the cost model assumptions and potential performance impact based on significant scale-up.

Aspects of dynamic operation are expected to influence the optimal MD process and module design, especially for fluctuating renewable energy supplies. In order to include such aspects, capacitive effects need to be implemented into the model which should then be embedded into a system environment that allows time-dependent simulation. Commercially available simulation tools such as Simulink, TRNSYS or Dymola appear to be suitable for embedding such a new MD type.

Furthermore, experimental and model-based research should clarify the potential role of MD within combined technological separation approaches, such as MD-FO, MD-OMD or MD-RO. The methods presented within this thesis may then be applied to identify the desired MD module design which provides the techno-economic optimum.

This thesis has focussed on a conceptual perspective to derive a thermodynamic understanding of MD and appropriate membrane module design. Practical aspects of module scale-up and module life time have not yet been sufficiently clarified, although limitations in scale-up and module life time significantly affect the economic and practical feasibility of MD. Research and

development on module scale-up specifically addresses aspects of module design and fabrication and is expected to be driven by commercial players. If high-quality module design and fabrication is assumed, the potential module life-time is limited by the membrane life-time. Fundamental research is still required to clarify the mechanisms of membrane deterioration and subsequent membrane wetting in MD, and its dependence on feed composition, fouling, scaling, temperatures and mechanical stress. Such research should include the development of methods to characterise membrane deterioration, including a comparison of membrane deterioration from field test systems and accelerated membrane aging in the laboratory. Such developments are considered essential for the development and application of advanced MD membranes and coatings and the development of membrane regeneration or cleaning procedures.

Further MD research is also required on the mechanisms of solute precipitation that may occur directly on the membrane surface, in the membrane structure or next to the membrane in the flow channels. A detailed understanding of precipitation in MD systems has specific relevance for applications with high potential for scaling and for the development of effective scaling minimisation by appropriately adjusted operation and/or pre-treatment. Reliable control of precipitation is also relevant for the development of MD crystallisers.

Appendix

A Commercial Desalination Technologies

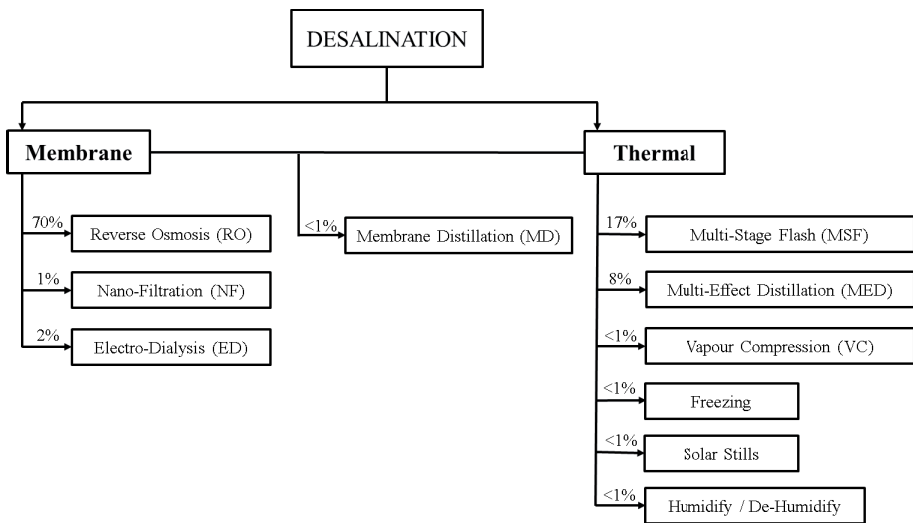


Figure A.1: Desalination technologies classification based on separation process. Illustration adapted from [6].

Desalination technology is most commonly classified with respect to the separation process adapted, as represented in Fig. A.1. Separation may be achieved by thermal or membrane-based processes. Thermal desalination approaches utilise a phase change to separate pure water from the saline feed while rejection of soluble contaminants in membrane-based approaches relies on selective membranes. The membrane distillation (MD) approach is an unusual case, since it represents a thermal separation process that features a membrane and could therefore be classified within both the thermal and the membrane categories. The commercial relevance of the different technologies is indicated in Fig. A.1 by the current share of the desalination market as presented by DesalData [4]. Reverse Osmosis (RO) has by far the greatest market penetration, while classic, thermally driven desalination by the processes of Multi-Stage Flash (MSF) and Multi-Effect Distillation (MED) are still very relevant, especially in the Gulf region. Up to now, other desalination processes have played a minor role in the global desalination market.

However, some of these other approaches contribute significantly to the market for alternative separation applications. The technological approach and key specifications for the most relevant desalination processes are briefly introduced in the following sections, making reference to pertinent literature [140, 192].

The economics of industrial desalination plants mainly depend on system size, site conditions, personnel qualification, energy costs and plant life time. Industrial-scale thermal desalination plants are typically located next to conventional power plants, utilising low-grade steam extracted from the low-pressure stages of the turbines. The thermal energy costs may then be quantified by determining the associated loss in electricity generation. The energy costs for electrically driven desalination plants may easily be evaluated by applying the relevant electricity costs. The unit water costs predicted for industrial-scale MSF, MED and RO desalination plants range from about 0.5 to 2.0 \$ m⁻³.

A.1 Multi-Stage Flash Evaporation

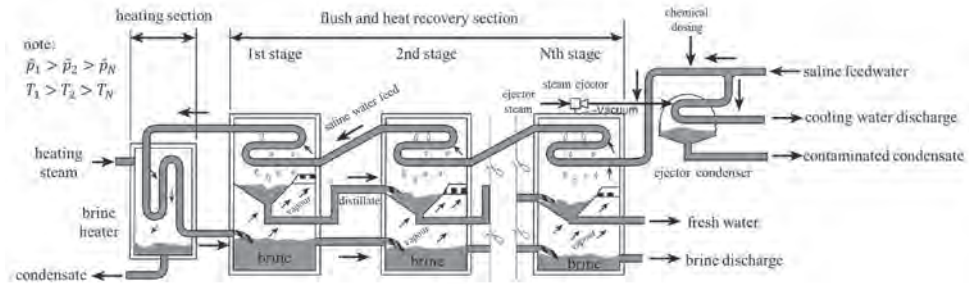


Figure A.2: Schematic diagram of a MSF plant with N stages. Illustration adopted from [192].

Multi-Stage Flash (MSF) is considered to be the classic industrial-scale thermal seawater desalination process. Most MSF plants are operated with steam from co-generation boilers at top brine temperatures around 110 °C. The core element in a MSF system is the flashing chamber, including a brine sump from which flash type evaporation takes place, a horizontal tube bundle condenser and a distillate tray. The entrainment of brine droplets by the flashed-off vapour is prevented by a wire mesh demister, maintaining high distillate quality with salinity values below 10 ppm. Each flashing chamber includes a venting line for the initial evacuation of the chamber and for continuous removal of non-condensable gases carried into the system by the feed stream and by air leaking in from the ambient.

The MSF system, schematically illustrated in Fig. A.2, usually consists of 15 to 25 flashing chambers connected in series. Before feed water is introduced to the core equipment, pretreatment involves coarse filtering, chlorination, deaeration, pH adjustment and/or dosing of antiscalants.

Then, the cold feed water is introduced at the lumen side of the condenser tubes in the last flashing chamber, acting as a coolant for the condenser surface there. The latent heat released during condensation on the shell side of the tubes is recovered within the feed water inside the tubes, accompanied by an increase in feed temperature. The feed is piped through all of the stages until it reaches the maximal pre-heating temperature in the first stage. Subsequently, the temperature of the pre-heated feed is raised to the top brine temperature in the brine heater by applying heating steam. The superheated feed is then released into the brine sump of the first stage that provides lower absolute pressure than the feed vapour pressure. The feed partially flashes until the temperature has decreased. The concentrated feed, also denoted as brine, is then forwarded to the second flashing chamber that is at lower absolute pressure and consequently again provides flashing conditions. It is obvious that temperature and absolute pressure decrease from the first stage towards the last stage. After the brine has passed all flashing stages, it gets disposed from the final stage at a blow-down salinity of 40 to 70 g kg⁻¹, depending on whether brine is partially recirculated or not. Since the warm brine is quite aggressive to the metallic equipment materials, the maximum brine salinity is limited by the maximal tolerable corrosion rate. Also the collected distillate is forwarded from stage to stage until it reaches the fresh water release at the final stage.

The more stages are established, the higher the transfer area and the thermodynamic efficiency of the heat recovery. A reduced thermal energy demand eventually results in reduced operational costs. Since the flashing chambers are made of high-grade metals such as duplex stainless steel, copper-nickel or titanium, significant investment costs are incurred by an increasing number of stages. The GOR² of MSF systems with 20 to 24 stages and top brine temperatures of 110 °C are predicted with numbers of about 8 to 10. Typical specific heat transfer areas for MSF plants range from about 140 to 250 m² (kg s⁻¹)⁻¹, mainly depending on the total number of stages. In MSF, the recovered latent heat that is temporarily stored in the form of sensible heat in the pre-heated feed stream requires significant circulation before actual re-use in the flashing stages. The specific electricity consumption of about 3 to 4 kWh_{el} t⁻¹ associated with MSF desalination is therefore mainly caused by fluid circulation.

The output capacity of commercial MSF units is 30 000 to 75 000 m³ d⁻¹, while a plant project may involve multiple units. The implementation of small MSF plants seems economically unfeasible. During the past decade, only 6 MSF plants with capacities below 500 m³ d⁻¹ have been commissioned, which probably mainly represent demonstration projects [4]. It is important to note, that classic MSF systems appear to be gradually supplanted in the desalination market, indicated by the low number of new installations in recent years [4].

²Thermal energy demand reduction with respect to ideal evaporation. A detailed description of the thermodynamic performance parameters is provided in Sec. 2.5.2

A.2 Multi-Effect Distillation

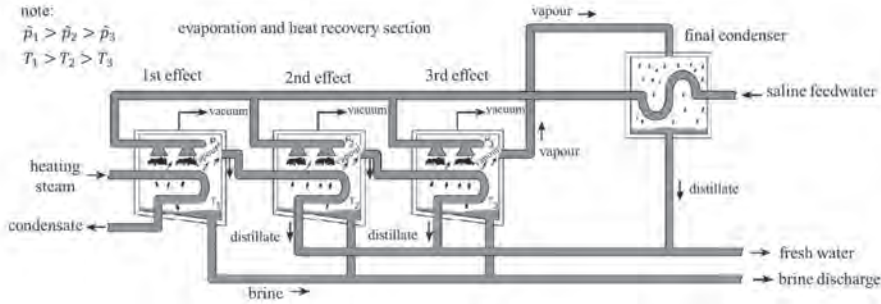


Figure A.3: Schematic diagram of a MED plant, illustrated with 3 effects. Illustration adapted from [192].

Multi-Effect Distillation (MED) is a thermal desalination process that is most commonly operated with steam from co-generation boilers at a medium temperature of about 70 °C. The system usually consists of 8 to 16 effects that are based on horizontal tube falling-film evaporators, as illustrated in Fig. A.3. The motive steam is introduced inside the evaporator tubes of the first effect. Similarly to the MSF process, the feed water is pre-treated by coarse filtering, chlorination, deaeration, pH adjustment and/or dosing of antiscalants before being introduced to the core equipment. Then the feed water is deposited onto the shell side of the evaporator tubes by spray nozzles. As brine wets the outer surface of the warm tubes, it is heated up to its boiling point and then evaporates at constant temperature. The concentration of the brine depends on the amount of feed sprayed onto the evaporator tubes. Brine concentration is typically limited to about 65 g kg⁻¹, to avoid excessive corrosion. Furthermore, a minimum feed flow rate is required to guarantee proper tube wetting, since dry patches would result in high scaling-rate and uneven thermal expansion. The concentrated brine is collected in the sump of the evaporator and is rejected. The vapour from the first effect is passed through a mesh demister to the second effect and condenses within the evaporator tubes of the second effect, releasing the latent heat. The pure fresh water condensate is piped to the plant product water outlet. Since the vapour space within the second effect has a lower temperature and pressure level than the first effect, the released latent heat is directly reused for evaporation on the wetted shell side of the tubes. In the manner described, the latent heat is passed over from effect to effect, each time operating at a lower temperature and pressure level. The vapour of the last effect condenses within a final condenser. Since the final condenser is usually operated with cold feed water, part of the pre-heated condenser outlet stream is branch piped to the spray nozzles in the effects. Non-condensable gases in the vapour space of the effects must be continuously vented to avoid reduction of the net-driving force and a blanket effect of non-condensable gases on the condensation surfaces. To minimise the amount of vapour that escapes from the system and raises the volume flow to be ejected, removal of non-condensable gases is usually located at the coldest spot of the effects and the final condenser.

The thermal energy consumption of MED plants significantly depends on the number of effects. Considering typical MED systems with 8 to 12 effects, a GOR³ of 6 to 8 is achieved. Many industrial MED systems apply Thermal Vapour Compression (TVC) to enhance heat recovery. The latent heat incorporated in the low-temperature steam from the last effect is partially recovered by compressing it with the motive stream in a jet ejector, allowing a subsequent re-injection into the first effect. The GOR of MED systems with 8 to 12 stages is increased to about 12 to 16, if vapour compression is applied. Typical specific heat transfer areas for MED plants with 8 and 12 effects are about 150 and 250 m² (kg s⁻¹)⁻¹, respectively. The specific heat transfer area may be reduced by operation at higher temperatures, but operational temperatures should not exceed 70 °C to limit the rate of scale formation and allow the efficient use of vapour compression. Since the effects are made of high-grade metals such as duplex stainless steel, copper-nickel or titanium, significant investment costs are associated with the transfer area. The thermal energy demand and consequently energy costs decrease with an increasing number of effects, while the required specific heat transfer area and consequently investment costs increase. A major advantage of the MED approach compared to MSF is the reduced pumping demand involved with the latent heat recovery concept, leading to a low electricity consumption of 1.2 to 2.0 kWh_{el} t⁻¹.

The output capacity of commercial MED units is 5 000 to 36 000 m³ d⁻¹, while a plant project may involve multiple units. However, the MED market also includes small units. In recent years, around 50 MED plants with capacities of less than 100 m³ d⁻¹ and 150 MED plants with capacities of less than 500 m³ d⁻¹ have been commissioned annually [4]. The MED approach seems to be attaining predominance on the thermal desalination market, indicated by the significantly higher number of recent installations compared to MSF [4].

Due to the low temperature specifications, the MED process is attributed a high potential for using low-grade waste heat from Concentrated Solar Power plants (CSP). Small MED systems may also be directly driven by solar thermal collectors, but the high thermal system capacity and limited range of valid flow rates limit the applicability of classic MED to dynamic small applications with renewable energy supply.

³Thermal energy demand reduction with respect to ideal evaporation. A detailed description of the thermodynamic performance parameters is provided in Sec. 2.5.2

A.3 Reverse Osmosis

In the Reverse Osmosis (RO) process, separation is based on non-porous membranes that have significantly higher solubility and diffusivity with respect to water molecules than to dissolved salts. The natural osmosis process is countered by artificially applying a high absolute pressure difference from the feed to the permeate side which exceeds the osmotic pressure difference that naturally occurs from the permeate to the feed side. The osmotic pressure of saline feed is proportional to its salinity, so the required pressure for RO increases. The osmotic pressure of seawater is typically around 25 bar. It is obvious that the RO process is technically limited for the treatment of feeds with high salt concentration.

The membrane elements are the key components in RO systems. Polyamide composite membranes are favoured due to their superior water permeability and salt rejection. Different commercial membrane types are available, specifically addressing the requirements of the different pressure-driven desalination applications such as Nano-Filtration (NF), brackish water Reverse Osmosis (BWRO) and sea-water Reverse Osmosis (SWRO). The membranes mainly vary in permeability and salt rejection. The higher the salt rejection, the lower is the water permeability. In today's commercial RO desalination systems, the membranes are almost exclusively configured in spiral-wound membrane elements with an axial length of approximately 1 m. The membrane elements contain 20 to 40 spirally wound membrane envelopes that are hydraulically connected to a central manifold. The outer side of the membrane envelopes is the pressurised feed side and the inner side of the envelopes is the low-pressure permeate side. One coiled membrane element provides a membrane area of about 40 m². Several membrane elements are serially aligned and interconnected within a strong tubular pressure vessel.

Pressurised feed water enters the pressure vessel axially, subsequently passing all membrane elements. While it passes the membrane elements, the flow rate decreases and the concentration increases due to permeate extraction. It is obvious that flux is reduced for subsequent membrane elements, due to increased osmotic pressure. The highly modular design allows easy adaptation of the system capacity by the connection of several pressure vessels in parallel, also denoted a stage. To increase the recovery rate⁴, a number of stages may be connected in series, forming an array of pressure vessels. Usually the number of pressure vessels is reduced from stage to stage, accounting for a reduced flow rate due to permeate extraction. The configuration ratio is the ratio of pressure vessels from one stage to the next. The high-pressure feed and concentrate manifolds are made of stainless steel, while the permeate manifold is most commonly made of PVC due to the low pressure specification.

The feed pressure and the recovery rate mainly define the economics of RO desalination. Due to low salinity in typical NF and BWRO feeds, the required system pressures are 7 to 10 bar and 10 to 20 bar respectively, while systems design considers multi-stage arrays with high recovery rates of 75 to 90 %. The recovery rate is limited by the scaling tendency of the concentrate, even with use of antiscalants. SWRO systems are almost exclusively designed as single-stage units with recovery rates between 45 and 55 %, operated at pressures of 60 to 70 bar. The optimal recovery

⁴The recovery rate is the ratio of extracted permeate to initial feed.

rate is limited by the required pressure level, which has a high impact on energy consumption and investment costs. The flux obtained in SWRO is typically in the range of 20 to 40 kg (m² h)⁻¹. Due to the limited salt rejection of RO membranes, the product water quality of a single-pass RO system is lower than that of thermal desalination processes and typically still contains about 500 ppm of salt.

About 80 % of the electricity consumption in RO systems is caused by the high-pressure pumps. In RO systems of reasonable size, energy from the pressurised concentrate is recovered to the feed by a Pelton Wheel that is attached to the shaft of the high pressure-pump. More recently, isobaric piston pressure exchangers have been considered for energy recovery due to their higher efficiency. The pressure exchangers are suitable also for application in smaller RO systems. According to the efficiency of the energy recovery system and the ratio of feed to concentrate flow rate, the required pumping energy may be reduced by 30 to 50 %. The specific energy consumption for RO plants with a capacity of 55 000 to 325 000 m³ d⁻¹ is stated to be 3.8 to 4.5 kWh_{el} t⁻¹. Small systems may have significantly higher energy consumption due smaller pumps and less efficient or no energy recovery.

Special attention has to be paid to the sensitivity of RO membranes and modules to raw water quality, which defines the scaling and fouling behaviour, cleaning strategy and membrane life time. Before feed water is used for RO desalination, extensive pretreatment is usually applied. Conventional pretreatment involves screens, chlorination, pH adjustment, coagulation/flocculation, media filtration, dechlorination, addition of antiscalants and finally cartridge filtration. Improved RO performance, compactness, reduced requirement of chemicals and improved product water quality is identified for the use of membrane-based MF or UF pretreatment. Future development will show whether membrane-based pretreatment will replace conventional pretreatment in RO systems or not. A major advantage of RO is its modularity, allowing the design of any plant capacity, ranging from less than 1 m³ d⁻¹ to giant plants producing up to 1 000 000 m³ d⁻¹. The special attractivity of RO for small size systems is indicated by a global market share of more than 90 %, considering systems with capacities of less than 1 000 m³ d⁻¹ [4]. RO systems are attributed a high potential for directly applying renewable energy supplies such as wind energy or photovoltaics (PV), but the implementation of stand-alone RO systems is still in the development and piloting phase. The membranes are considered to be sensitive with regard to dynamic operation and must even be replaced after dry-out. Especially if RO is considered with fluctuating renewable energy supplies such as wind energy or photovoltaics (PV), issues regarding energy storage, smart operational strategies and robustness against dynamic operation and down-time outline important fields for future RO research and development.

B Physical Properties of Salt Water

The physical properties of salt water are calculated with empirical correlations from Hömig [112]. The units used for temperature T and salinity S are [°C] and [g kg⁻¹] respectively.

B.1 Density

For temperatures from 10 to 180 °C and for salinities from 0 to 160 g kg⁻¹, the density ρ is calculated according to the following equations [112].

$$\rho = 0.5 a_0 + a_1 Y + a_2 (2 Y^2 - 1) + a_3 (4 Y^3 - 3 Y) \quad [\text{kg dm}^{-3}]$$

with:

$$a_0 = 2.01611 + 0.115313 \sigma + 0.000326 (2 \sigma^2 - 1)$$

$$a_1 = -0.0541 + 0.001571 \sigma - 0.000423 (2 \sigma^2 - 1)$$

$$a_2 = -0.006124 + 0.00174 \sigma - 0.000009 (2 \sigma^2 - 1)$$

$$a_3 = 0.000346 + 0.000087 \sigma - 0.000053 (2 \sigma^2 - 1)$$

and

$$Y = \frac{2 T - 200}{160}$$

$$\sigma = \frac{2 S - 150}{150}$$

B.2 Dynamic Viscosity

For temperatures from 10 to 180 °C and for salinity values from 0 to 130 g kg⁻¹, the dynamic viscosity η is calculated by the following equations (1 000 cP = 1 kg (m s)⁻¹). The maximal error is specified to be 2% [112].

$$\eta = \eta_w \eta_R \quad [\text{cP}]$$

with:

$$\ln \eta_w = -3.79418 + \frac{604.129}{139.18 + T}$$

$$\eta_R = 1 + a_1 S + a_2 S^2$$

and

$$a_1 = 1.474 \cdot 10^{-3} + 1.5 \cdot 10^{-5} T - 3.927 \cdot 10^{-8} T^2$$

$$a_2 = 1.0734 \cdot 10^{-5} - 8.5 \cdot 10^{-8} T + 2.23 \cdot 10^{-10} T^2$$

B.3 Vapour Pressure

For temperatures from 0 to 200 °C and for salinity values from 0 to 160 g kg⁻¹, the vapour pressure p is calculated according to the following equations. The maximal error is specified to be 2.5 % [112].

$$\log \frac{p}{p_w} = -2.1609 \cdot 10^{-4} S - 3.5012 \cdot 10^{-7} S^2 \quad [\text{bar}]$$

The vapour pressure of pure water p_w is estimated from the following equation. p_k represents the critical pressure of water (220.93 bar), while T_k represents the critical temperature of water (647.25 K). The temperatures are expressed in Kelvin [K].

$$\ln \frac{p_w}{p_k} = \frac{T_k}{T} \sum_{i=1}^8 b_i \left(1 - \frac{T}{T_k} \right)^{\frac{i+1}{2}}$$

with the following values for the constants b_1 to b_8 :

$$b_1 = -7.8889166$$

$$b_2 = 2.5514255$$

$$b_3 = -6.7161690$$

$$b_4 = 33.239495$$

$$b_5 = -105.38479$$

$$b_6 = 174.35319$$

$$b_7 = -148.39348$$

$$b_8 = 48.631602$$

B.4 Thermal Capacity

For temperatures from 0 to 180 °C and for salinity values from 0 to 160 g kg⁻¹, the thermal capacity c_p is calculated from the following equations [112]. The maximal error is specified to be 1 %.

$$c_p = A + B T + C T^2 + D T^3 \quad [\text{J (kg K)}^{-1}]$$

and

$$A = 4206.8 - 6.6197 S + 1.2288 \cdot 10^{-2} S^2$$

$$B = -1.1262 + 5.4178 \cdot 10^{-2} S - 2.2719 \cdot 10^{-4} S^2$$

$$C = 1.2026 \cdot 10^{-2} - 5.3566 \cdot 10^{-4} S + 1.8906 \cdot 10^{-6} S^2$$

$$D = 6.8774 \cdot 10^{-7} + 1.5170 \cdot 10^{-6} S - 4.4268 \cdot 10^{-9} S^2$$

B.5 Thermal Conductivity

For temperatures from 10 to 150 °C and for salinity values from 0 to 100 g kg⁻¹, the thermal conductivity λ is calculated from the following equations [112]. However, due to inconsistency with other literature references, the thermal conductivity is considered to be independent of salinity and S is always set to zero [193].

$$\lambda = (A + B T + C T^2) \cdot 10^{-3} \quad [\text{W (m K)}^{-1}]$$

with

$$A = 576.6 - 34.64 CA + 7.286 CA^2$$

$$B = (1526 + 466.2 CA - 226.8 CA^2 + 28.67 CA^3) \cdot 10^{-3}$$

$$C = -(581 + 2055 CA - 991.6 CA^2 + 146.4 CA^3) \cdot 10^{-5}$$

and

$$CA = \frac{28.17 S}{1000 - S}$$

C Ionic Composition of Salt Water

Table C.1: Ionic composition of standard sea salt and sea salt from Seequasal, referring to a standard sea water salinity of about 34.5 g/kg.

element	symbol	standard sea salt [112] [g kg ⁻¹]	Seequasal ^a [g kg ⁻¹]	sodium chloride solution [g kg ⁻¹]
sodium	Na ⁺	10.6	10.2	13.5
potassium	K ⁺	0.4	0.4	-
ammonium	NH ₄ ⁺	-	0.005	-
magnesium	Mg ²⁺	1.3	1.2	-
calcium	Ca ²⁺	0.4	0.4	-
chloride	Cl ⁻	19.0	14.1	21.0
bromide	Br ⁻	0.1	-	-
sulphate	SO ₄ ²⁻	2.7	8.3	-
sum	[g kg ⁻¹]	34.5	34.5	34.5
sum	[mol kg ⁻¹]	1.10	1.00	1.18

^aRed Sea salt commercially available for use in aquaria

D Spacers - Enhanced Heat Transfer in the Flow Channels

Supplementary results on Sec. 3.4.1, regarding the influence of the channel spacer under different operating conditions.

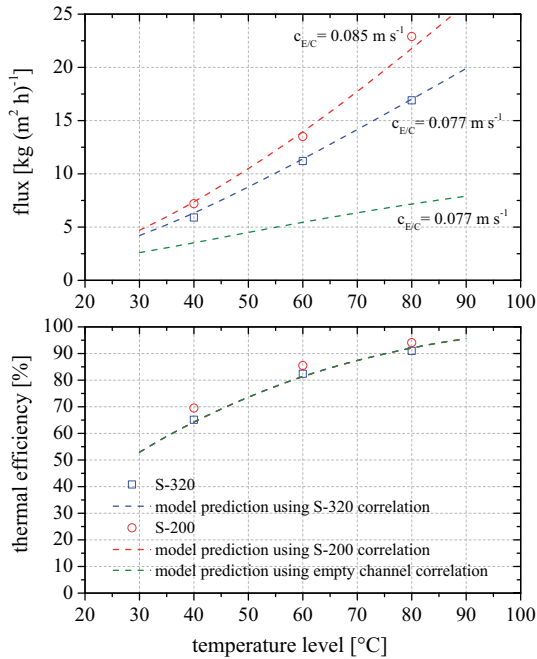


Figure D.1: Flux measurements with different feed flow velocities using different channel spacers. The model predictions are based on the specific heat transfer correlations for each geometrical spacer/channel configuration. Testing conditions: $\bar{c}_{E/C} = 0.08 \text{ m s}^{-1}$, $\Delta T_{E-C} = 8 \text{ K}$, DCMD configuration, tap water.

E Laminates - Membranes on Backing Structures

Supplementary results on Sec. 3.4.3, regarding the influence of membrane backing structures under different operating conditions.

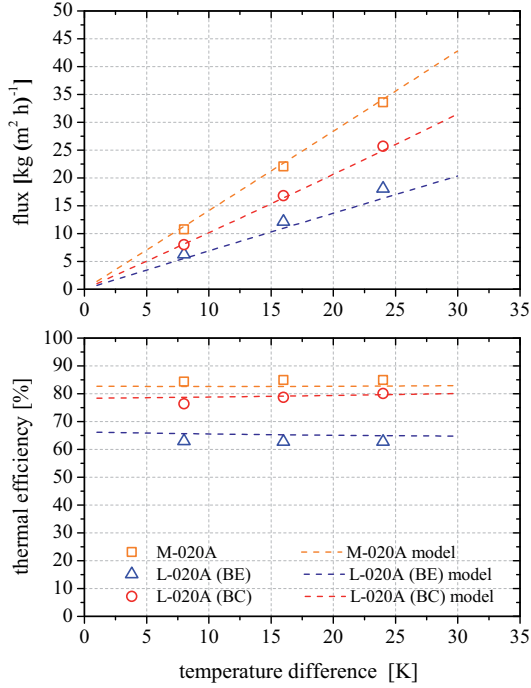


Figure E.1: Experimental results and model predictions for membrane M-020A and its corresponding laminate L-020A-S for different bulk temperature differences. The backing is positioned towards the evaporator side (BE) or towards the condenser side (BC). Testing conditions: $\bar{T}_{E-C} = 60\text{ }^{\circ}\text{C}$, $\bar{c}_{E/C} = 0.08\text{ m s}^{-1}$, DCMD configuration, S-320 spacer, tap water.

F Uncertainty of Measurement and Error Propagation

Derivation of the equations that have been applied to estimate the uncertainty of measurement for module characterisation in Sec. 4.2.3. The derivation is based on Gaussian's law of error propagation given in Eq. 3.68.

$$\begin{aligned}
 \dot{Q}_{\text{HX,extR}} &= \dot{m}_{\text{Ei}} c_{\text{p,Ei}} (T_{\text{Ei}} - T_{\text{RXo}}) & \dot{Q}_{\text{HX,intR}} &= \dot{m}_{\text{Ei}} c_{\text{p,Ei}} (T_{\text{Ei}} - T_{\text{Co}}) \\
 \dot{Q}_{\text{CX,extR}} &= \dot{m}_{\text{Ci}} c_{\text{p,Ci}} (T_{\text{CXi}} - T_{\text{Ci}}) & \dot{Q}_{\text{CX,intR}} &= \dot{m}_{\text{CXo}} c_{\text{p,Eo}} (T_{\text{CXi}} - T_{\text{CXo}}) \\
 \dot{Q}_{\text{E}} &= (\dot{m}_{\text{Ei}} - \frac{2}{3}\dot{m}_{\text{P}}) c_{\text{p,Ei}} (T_{\text{Ei}} - T_{\text{Eo}}) \\
 \dot{Q}_{\text{E,l}} &= \dot{m}_{\text{P}} \Delta \bar{h}_{\text{v,Ei-Eo}} \\
 q_{\text{HX}} &= \frac{\dot{Q}_{\text{HX}}}{\dot{m}_{\text{P}}} & \text{GOR} &= \frac{\dot{Q}_{\text{E,l}}}{\dot{Q}_{\text{HX}}} & \eta_{\text{th}} &= \frac{\dot{Q}_{\text{E,l}}}{\dot{Q}_{\text{E}}}
 \end{aligned}$$

$$\begin{aligned}
 \Delta \dot{Q}_{\text{HX,extR,max}} &= |(c_{\text{p,Ei}} (T_{\text{Ei}} - T_{\text{RXo}})) \Delta \dot{m}_{\text{Ei}}| + |(\dot{m}_{\text{Ei}} (T_{\text{Ei}} - T_{\text{RXo}})) \Delta c_{\text{p,Ei}}| \\
 &+ |(\dot{m}_{\text{Ei}} c_{\text{p,Ei}}) \Delta T_{\text{Ei}}| + |(-\dot{m}_{\text{Ei}} c_{\text{p,Ei}}) \Delta T_{\text{RXo}}|
 \end{aligned}$$

$$\begin{aligned}
 \Delta \dot{Q}_{\text{CX,extR,max}} &= |(c_{\text{p,Ci}} (T_{\text{CXi}} - T_{\text{Ci}})) \Delta \dot{m}_{\text{Ci}}| + |(\dot{m}_{\text{Ci}} (T_{\text{CXi}} - T_{\text{Ci}})) \Delta c_{\text{p,Ci}}| \\
 &+ |(\dot{m}_{\text{Ci}} c_{\text{p,Ci}}) \Delta T_{\text{CXi}}| + |(-\dot{m}_{\text{Ci}} c_{\text{p,Ci}}) \Delta T_{\text{Ci}}|
 \end{aligned}$$

$$\begin{aligned}
 \Delta \dot{Q}_{\text{HX,intR,max}} &= |(c_{\text{p,Ei}} (T_{\text{Ei}} - T_{\text{Co}})) \Delta \dot{m}_{\text{Ei}}| + |(\dot{m}_{\text{Ei}} (T_{\text{Ei}} - T_{\text{Co}})) \Delta c_{\text{p,Ei}}| \\
 &+ |(\dot{m}_{\text{Ei}} c_{\text{p,Ei}}) \Delta T_{\text{Ei}}| + |(-\dot{m}_{\text{Ei}} c_{\text{p,Ei}}) \Delta T_{\text{Co}}|
 \end{aligned}$$

$$\begin{aligned}
 \Delta \dot{Q}_{\text{CX,intR,max}} &= |(c_{\text{p,Eo}} (T_{\text{Eo}} - T_{\text{CXo}})) \Delta \dot{m}_{\text{CXo}}| + |(\dot{m}_{\text{CXo}} (T_{\text{Eo}} - T_{\text{CXo}})) \Delta c_{\text{p,Eo}}| \\
 &+ |(\dot{m}_{\text{CXo}} c_{\text{p,Eo}}) \Delta T_{\text{Eo}}| + |(-\dot{m}_{\text{CXo}} c_{\text{p,Eo}}) \Delta T_{\text{CXo}}|
 \end{aligned}$$

$$\begin{aligned}
 \Delta \dot{Q}_{\text{E,max}} &= |(c_{\text{p,Ei}} (T_{\text{Ei}} - T_{\text{Eo}})) \Delta \dot{m}_{\text{Ei}}| + |(-2/3 c_{\text{p,Ei}} (T_{\text{Ei}} - T_{\text{Eo}})) \Delta \dot{m}_{\text{P}}| \\
 &+ |(\dot{m}_{\text{Ei}} - \frac{2}{3}\dot{m}_{\text{P}}) (T_{\text{Ei}} - T_{\text{Eo}}) \Delta c_{\text{p,Ei}}| + |(\dot{m}_{\text{Ei}} - \frac{2}{3}\dot{m}_{\text{P}}) c_{\text{p,Ei}} \Delta T_{\text{Ei}}| \\
 &+ |-(\dot{m}_{\text{Ei}} - \frac{2}{3}\dot{m}_{\text{P}}) c_{\text{p,Ei}} \Delta T_{\text{Eo}}|
 \end{aligned}$$

$$\Delta \dot{Q}_{E,1,\max} = |\Delta \bar{h}_{v,Ei-Eo} \Delta \dot{m}_P| + |\dot{m}_P \Delta(\Delta \bar{h}_{v,Ei-Eo})|$$

$$\Delta q_{HX,\max} = \left| \frac{1}{\dot{m}_P} \Delta \dot{Q}_{HX,\text{extR},\max} \right| + \left| \frac{\dot{Q}_{HX,\text{extR}}}{\dot{m}_P^2} \Delta \dot{m}_P \right|$$

$$\Delta GOR_{\max} = \left| \frac{1}{\dot{Q}_{HX}} \Delta \dot{Q}_{E,1,\max} \right| + \left| \frac{\dot{Q}_{E,1}}{\dot{Q}_{HX}^2} \Delta \dot{Q}_{HX,\max} \right|$$

$$\Delta \eta_{th,\max} = \left| \frac{1}{\dot{Q}_E} \Delta \dot{Q}_{E,1,\max} \right| + \left| \frac{\dot{Q}_{E,1}}{\dot{Q}_E^2} \Delta \dot{Q}_{E,\max} \right|$$

G General Aspects of Membrane Distillation Module Operation

For the thermal design of counter-current spiral-wound heat exchangers, correction factor F is suggested for the derivation of the log mean temperature difference [172].

$$F = \frac{1}{(1 - (\frac{d_o}{d_i})^2) CN^2} \ln \left(\frac{1 + CN^2}{1 + (\frac{d_o}{d_i} CN)^2} \right) \quad (\text{G.1})$$

$$CN = \frac{k \pi d_o H}{\sqrt{(\dot{m}_1 c_{p,1})(\dot{m}_0 c_{p,0})}} \quad (\text{G.2})$$

Here, d_i is the inner diameter of the spiral coil, d_o is the outer diameter of the spiral coil and H is the height of the spiral coil. The characteristic number CN is derived from the total heat transfer coefficient k , the outer surface area of the spiral apparatus and the geometrical mean value of the mass flow capacities.

H Specific Aspects of Air Gap Module Operation

Supplementary results on Sec. 4.3.4, regarding the influence of membrane backing structures under different operating conditions.

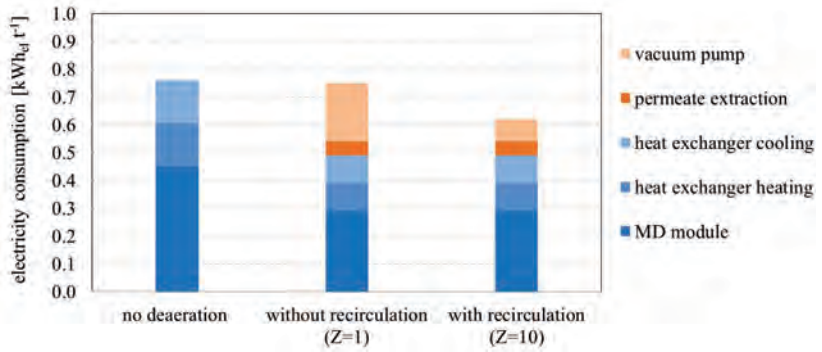


Figure H.1: Detailed break-down of the electricity consumption of the AGMD process from Fig. 4.28, comparing a scenario without deaeration and two scenarios with a deaeration pressure of 0.05 bar. The flow rate for the deaeration module is 300 kg h^{-1} , if no recirculation is considered and 110 kg h^{-1} if recirculation is considered; General assumptions: $\Delta\hat{p}_{\text{HX}} = 0.15 \text{ bar}$; $\Delta\hat{p}_{\text{CX}} = 0.15 \text{ bar}$; $\eta_{\text{HP}} = 50\%$; $\eta_{\text{VP}} = 15\%$.

I Selection of an Optimal Membrane

Supplementary results on Sec. 4.3.6, concerning the selection of an optimal membrane.

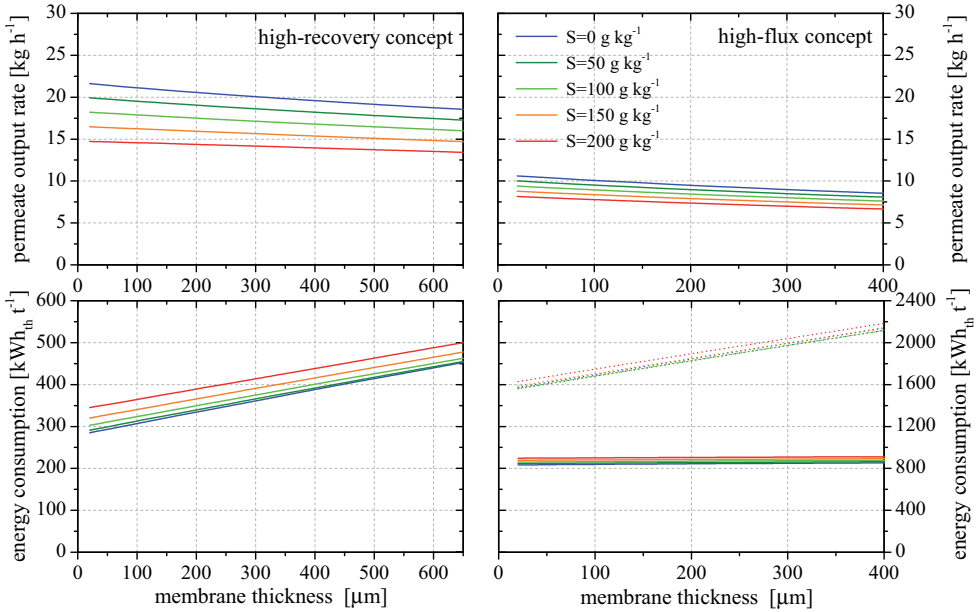


Figure I.1: A model-based sensitivity analysis, covering the interdependent effects of membrane thickness and salinity on AGMD high-flux and high-recovery modules. Operating conditions: $T_{Ei} = 80^\circ\text{C}$, $T_{Ci} = 25^\circ\text{C}$, $\dot{m}_{Ei/Co} = 400 \text{ kg h}^{-1}$; Module: $L = 7.0/1.0 \text{ m}$, $H = 0.7 \text{ m}$, channel spacer S-320, laminate L-020A-S (BC) (with varying assumed thickness), gap spacer S-200, impermeable film F-127.

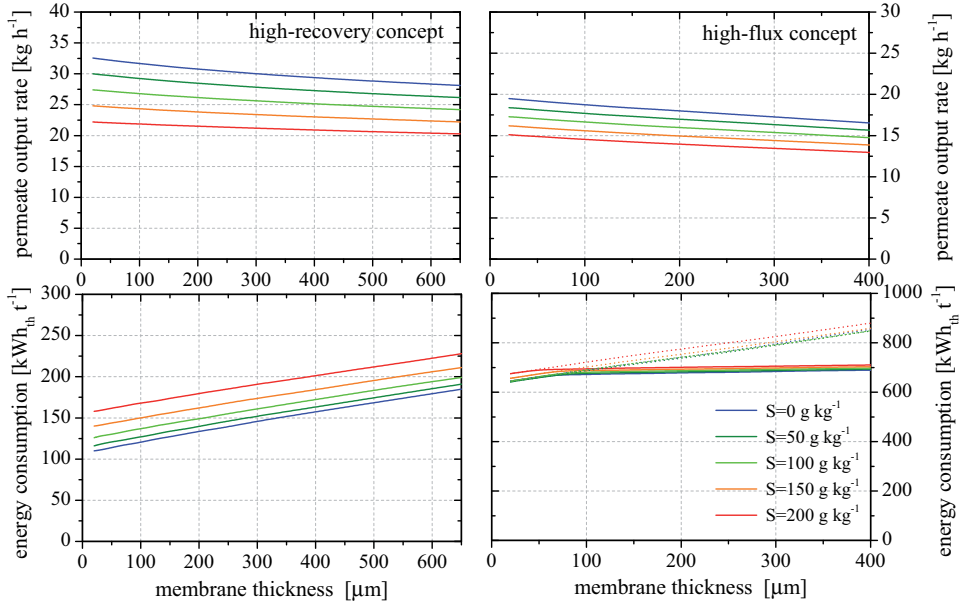


Figure I.2: A model-based sensitivity analysis, covering the interdependent effects of membrane thickness and salinity on V-AGMD high-flux and high-recovery modules. Operating conditions: $T_{Ei} = 80\text{ }^{\circ}\text{C}$, $T_{Ci} = 25\text{ }^{\circ}\text{C}$, $\dot{m}_{Ei/Co} = 400\text{ kg h}^{-1}$, $\hat{p}_{VP} = 0.03\text{ bar}$, $\hat{p}_{a,residual} = 0.05\text{ bar}$; Module: $L = 7.0/1.0\text{ m}$, $H = 0.7\text{ m}$, channel spacer S-320, laminate L-020A-S (BC) (with varying assumed thickness), gap spacer S-200, impermeable film F-127.

J Parametric Field Studies

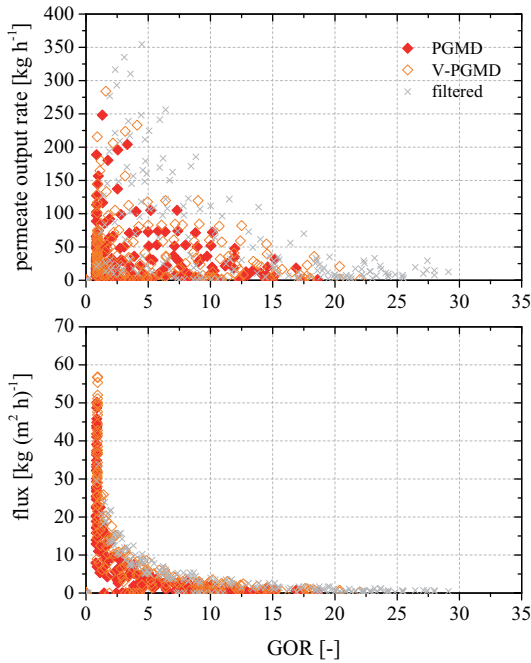


Figure J.1: Parametric field study on PGMD and V-PGMD process configuration based on the conditions stated in Tab. 4.10. The results that are accompanied by a hydraulic pressure loss higher than 1.0 bar have been filtered out. Constant operating conditions: $T_{Ei} = 80^\circ\text{C}$, $T_{Ci} = 25^\circ\text{C}$, $S_{Ei/Ci} = 35\text{ g kg}^{-1}$, $\hat{p}_{a,\text{residual}} = 0.05\text{ bar}$; Constant module parameter: $H = 0.7\text{ m}$, The material parameterisation covers a realistic improvement of the materials according to scenario #5 from Tab. 4.9 (see Fig. 4.42).

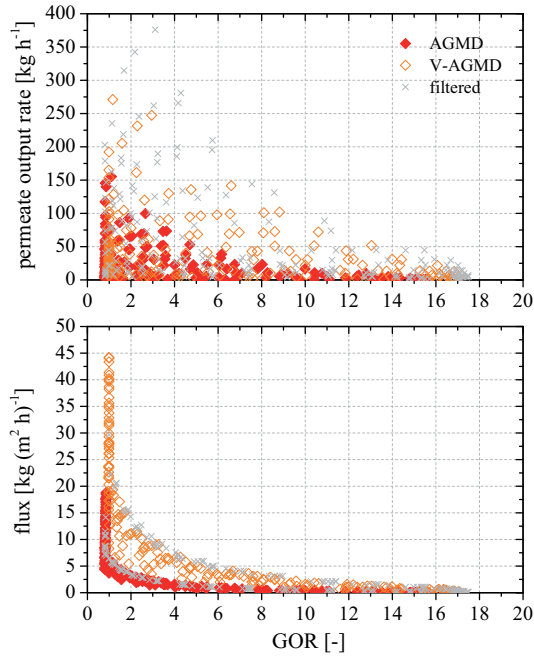


Figure J.2: Parametric field study on AGMD and V-AGMD process configuration based on the conditions stated in Tab. 4.10. The results that are accompanied by a hydraulic pressure loss higher than 1.0 bar have been filtered out. Constant operating conditions: $T_{Ei} = 80\text{ }^{\circ}\text{C}$, $T_{Ci} = 25\text{ }^{\circ}\text{C}$, $S_{Ei/Ci} = 35\text{ g kg}^{-1}$, $\hat{p}_{a,\text{residual}} = 0.05\text{ bar}$; Constant module parameter: $H = 0.7\text{ m}$. The material parameterisation covers a realistic improvement of the materials according to scenario #5 from Tab. 4.9 (see Fig. 4.42).

Nomenclature

Symbols

A	surface area	$[\text{m}^2]$
a	annual operational costs	$[\text{EUR a}^{-1}]$
B	pore factor	$[-]$
C	costs	$[\text{EUR}]$
C	mass transfer coefficient	$[\text{kg}(\text{m}^2 \text{ s Pa})^{-1}]$
c	molar concentration	$[\text{mol l}^{-1}]$
c	specific costs	$[\text{EUR}(\text{kWh})^{-1}]$ $[\text{EUR t}^{-1}]$
c	velocity	$[\text{m s}^{-1}]$
c_p	specific heat capacity	$[\text{J}(\text{kg K})^{-1}]$
d	diameter	$[\text{m}]$
D^o	ordinary diffusion coefficient	$[\text{m s}^{-1}]$
f	factor / fraction	$[-]$
g	gravity	$[\text{kg}(\text{m s}^2)^{-1}]$
GOR	Gained Output Ratio (definition in Sec. 2.5.2)	$[-]$
\dot{H}	enthalpy flow	$[\text{J s}^{-1}]$
H	channel height	$[\text{m}]$
h	specific enthalpy	$[\text{J kg}^{-1}]$
H	enthalpy	$[\text{J}]$
J	absolute mass flux	$[\text{kg s}^{-1}]$
j	specific mass flux	$[\text{kg}(\text{m}^2 \text{ s})^{-1}]$
K	capacity measure	$[\text{a.u.}]$

k	heat transfer coefficient	$[\text{W}(\text{m}^2 \text{K})^{-1}]$
kA	heat transfer performance of a heat exchanger	$[\text{W K}^{-1}]$
Kn	Knudsen number	$[-]$
L	channel length	$[\text{m}]$
\dot{m}	mass flow rate	$[\text{kg s}^{-1}]$
M	daily plant capacity	$[\text{t d}^{-1}]$
M	molar mass	$[\text{kg mol}^{-1}]$
m	degression coefficient	$[-]$
m	mass	$[\text{kg}]$
n	life time	$[\text{a}]$
n	number of nodes	$[-]$
Nu	Nusselt number	$[-]$
\hat{p}	absolute pressure	$[\text{Pa}]$
P	electric power	$[\text{W}]$
p	partial pressure	$[\text{Pa}]$
Pr	Prandtl number	$[-]$
\dot{Q}	absolute heat flux	$[\text{W}]$
\dot{q}	specific heat flux	$[\text{W m}^{-2}]$
Q	absolute heat	$[\text{Ws}]$
q	specific thermal energy consumption	$[\text{kWh t}^{-1}]$
R	recovery rate (definition in Sec. 4.1.4)	$[-]$
R	universal gas constant	$[\text{J}(\text{mol K})^{-1}]$
Ra	Rayleigh number	$[-]$
Re	Reynolds number	$[-]$

Nomenclature

S	salinity	$[\text{g kg}^{-1}]$
Sc	Schmidt number	$[-]$
Sh	Sherwood number	$[-]$
T	temperature	$[\text{°C}]$
t	time	$[\text{s}]$
\dot{V}	volume flow rate	$[\text{m}^3 \text{s}^{-1}]$
V	volume	$[\text{m}^3]$
v	molar volume	$[\text{m}^3 \text{mol}^{-1}]$
x	concentration (air in water)	$[-]$
x	volumetric fraction	$[-]$
Z	circulation factor	$[-]$
z	interest rate	$[\%]$
z	number of active sides in flow channel	$[-]$

Indices

\perp	orthogonal
(g)	gaseous phase
(l)	liquid phase
(s)	solid phase
0	liquid-vapour interface on condenser side
1	liquid-vapour interface on evaporator side
a	air
a	annual
AG	air gap

amb	ambient
asym	asymmetric
B	backing
B	brine
C	condenser
c	chemicals
c	conductive
corr	correction
CX	external heat exchanger for cooling
D	deaeration system
d	diffusive
E	evaporator
e	error
el	electrical
extR	external heat recovery
F	impermeable film
f	filament
FP	feed pump
h	hydraulic
HX	external heat exchanger for heating
I	investment
i	inlet
In	insurance
init	initial

Nomenclature

intR	internal heat recovery
Kn	Knudsen
L	labour
L	laminate
l	latent
L-AG	combined laminate and air gap
ln	logarithmic
M	membrane
M-AG	combined membrane and air gap
max	maximal
MD	membrane distillation module
min	minimal
mol	molecular
noR	no heat recovery
o	outlet
P	permeate
PG	permeate gap
R	raw water
rad	radiative
ref	reference
rP	rest of plant
RX	external heat exchanger for heat recovery
S	spacer
s	salt

s	sensible
SM	service and maintenance
spec	specific
sym	symmetric
th	thermal
UF	ultra-filtration system
v	viscous
VP	vacuum pump
w	water

Greek

α	heat transfer coefficient	$[\text{W}(\text{m}^2 \text{K})^{-1}]$
α	thermal expansion coefficient	$[\text{m K}^{-1}]$
β	mass transfer coefficient	$[\text{m s}^{-1}]$
Δ	difference	$[-]$
δ	thickness	$[\text{m}]$
ϵ	emissivity	$[-]$
η	efficiency	$[\%]$
κ	electrical conductivity	$[\text{mS cm}^{-1}]$
λ	mean free path	$[\text{m}]$
λ	thermal conductivity	$[\text{W}(\text{m K})^{-1}]$
μ	kinematic viscosity	$[\text{m}^2 \text{s}^{-1}]$
ν	dynamic viscosity	$[\text{kg}(\text{m s})^{-1}]$
ϕ	angle between spacer filaments	$[\text{deg}]$

π	ratio of circle's circumference to diameter	[-]
ψ	hydraulic friction factor	[-]
ρ	density	[kg m ⁻³]
σ	Stefan-Boltzmann constant	[W(m ² K ⁴) ⁻¹]
σ	surface tension	[J m ⁻²]
τ	tortuosity	[-]
Θ	temperature polarisation coefficient	[-]
θ	contact angle	[deg]
ε	volumetric porosity/voidage	[-]
Γ	system availability	[%]
ξ	concentration polarisation coefficient	[-]

Literature

Publications

Selected Papers

D. Winter, J. Koschikowski, D. Düver, P. Hertel, U. Beuscher, Evaluation of MD process performance: Effect of backing structures and membrane properties at different operational conditions, *Desalination* 323, Special Issue on Membrane Distillation (2012) 120-133.

D. Winter, J. Koschikowski, S. Ripperger, Desalination using membrane distillation: Flux enhancement by feed water deaeration on spiral-wound modules, *Journal of Membrane Science* 423-424 (2012) 215-224.

D. Winter, J. Koschikowski, D. Düver, Spiral wound modules for membrane distillation: modeling, validation and module optimization, *International Workshop on Membrane Distillation and Related Technologies, Proceedings* (2011).

D. Winter, J. Koschikowski, M. Wieghaus, Desalination using membrane distillation: Experimental studies on full scale spiral wound modules, *Journal of Membrane Science* 375 (2011) 104-112.

Undergraduate and Postgraduate Theses Supervised

J. Braum, Konzeptionierung eines Testmoduls zur experimentellen Untersuchung alternativer Modulkonzepte zur Membrandestillation, Diploma Thesis (2012), Karlsruhe Institut für Technologie.

M. Pergher, Entwicklung und Aufbau eines modularen Teststandsystems zur Vermessung von Entsalzungseinheiten zur Trinkwasseraufbereitung mittels Membrandestillation, Diploma Thesis (2012), Fachhochschule Lübeck.

D. Düver, Experimentelle Untersuchung und Optimierung des Membrandestillationsverfahrens mit einer Flachmembranzelle, Master Thesis (2011), Hochschule für Technik und Wirtschaft Berlin.

C. Sauter, Experimentelle Untersuchung der Membrandestillation mit einer Flachmembranzelle, Diploma Thesis (2011), Karlsruhe Institut für Technologie.

K. Ebert, Entwicklung und Aufbau einer Testzelle fuer die experimentelle Untersuchung verschiedener Membrandestillationsverfahren, Diploma Thesis (2010), Technische Universität Hamburg-Harburg.

M. Katzenmeyer, Experimentelle Untersuchungen zum Harzverguss von Spiralwickelmodulen zur Membrandestillation, Bachelors Thesis (2010), Hochschule Darmstadt.

M. Rolletschek, Aufbau einer Testanlage zur Untersuchung der Parallelisierung von Membrandestillations-Wickelmodulen für die solarthermische Meerwasserentsalzung, Diploma Thesis (2010), Hochschule für Technik und Wirtschaft Berlin.

Bibliography

- [1] United Nations - General Assembly, The human right to water and sanitation A/RES/64/292, 2010.
- [2] World Health Organization and UNICEF, Progress on sanitation and drinking-water, update 2013.
- [3] D. Molden (Ed.), Water for food, water for life - A Comprehensive Assessment of Water Management in Agriculture, International Water Management Institute, 2007.
- [4] [online] DesalData.com, Global Water Intelligence, access in 2014, March 4th.
- [5] V. Gude, N. Nirmalakhandan, S. Deng, Renewable and sustainable approaches for desalination, *Renewable and Sustainable Energy Reviews* 14 (2010) 2641–2654.
- [6] A. Cipollina, G. Micale, L. Rizzuti, *Seawater Desalination - Conventional and Renewable Processes*, Springer Verlag, 2009.
- [7] M. Papapetrou, M. Wiegand, C. Biercamp (Eds.), *ProDes: Roadmap for the Development of Desalination powered by Renewable Energy*, 2010.
- [8] J. Koschikowski, *Entwicklung von energieautark arbeitenden Wasserentsalzungsanlagen auf Basis der Membrandestillation*, Ph.D. thesis, Universität Kassel, 2011.
- [9] F. Banat, N. Jwaieda, M. Rommel, J. Koschikowski, M. Wiegand, Performance evaluation of the large SMADES autonomous desalination solar-driven membrane distillation plant in Aqaba, Jordan, *Desalination* 217 (2006) 17–28.
- [10] R. Schwantes, A. Cipollina, F. Gross, J. Koschikowski, D. Pfeifle, M. Rolletschek, V. Subiela, Membrane distillation: Solar and waste heat driven demonstration plants for desalination, *Desalination* 323 (2013) 93–106.
- [11] R. Raluy, R. Schwantes, V. Subiela, B. Penate, G. Melian, J. R. Betancort, Operational experience of a solar membrane distillation demonstration plant in Pozo Izquierdo-Gran Canaria Island (Spain), *Desalination* 290 (2011) 1–13.
- [12] S. Ripperger, *Mikrofiltration mit Membranen - Grundlagen, Verfahren, Anwendungen*, VHC Verlagsgesellschaft, 1992.

- [13] A. Franken, J. Nolten, M. Mulder, D. Bargeman, C. Smolders, Wetting criteria for the applicability of membrane distillation, *Journal of Membrane Science* 33 (1987) 315–328.
- [14] M. Garcia-Payo, M. Izquierdo-Gil, C. Fernandez-Pineda, Wetting study of hydrophobic membranes via liquid entry pressure measurements with aqueous alcohol solutions, *Journal of Colloid and Interface Science* 230 (2000) 420–431.
- [15] N. Sghaier, M. Prat, S. B. Nasrallah, On the influence of sodium chloride concentration on equilibrium contact angle, *Chemical Engineering Journal* 122 (2006) 47–53.
- [16] R. Tuckermann, Surface tension of aqueous solutions of water-soluble organic and inorganic compounds, *Atmospheric Environment* 41 (2007) 6265–6275.
- [17] C. Gostoli, G. Sarti, Separation of liquid mixtures by membrane distillation, *Journal of Membrane Science* 41 (1989) 211–224.
- [18] S. Kimura, S. Nakao, S. Shimatani, Transport phenomena in membrane distillation, *Journal of Membrane Science* 33 (1987) 285–298.
- [19] K. Schneider, T. van Gassel, Membrandestillation, *Chem.-Ing.-Tech.* 56 (1984) 514–521.
- [20] K. Nikolaus, Trink- und Reinstwassergewinnung mittels Membrandestillation, Ph.D. thesis, Technische Universität Kaiserslautern, Institut für Mechanische Verfahrenstechnik MVT, 2014.
- [21] R. Schofield, A. Fane, C. Fell, Gas and vapour transport through microporous membranes 2. Membrane Distillation, *Journal of Membrane Science* 53 (1990) 173–185.
- [22] D. Winter, J. Koschikowski, S. Ripperger, Desalination using membrane distillation: Flux enhancement by feed water deaeration on spiral-wound modules, *Journal of Membrane Science* 423-424 (2012) 215–224.
- [23] A. Hausmann, P. Sancio, T. Vasiljevic, M. Weeks, M. Duke, Membrane distillation in the dairy industry: process integration and membrane performance, *Proceedings - International Workshop on Membrane Distillation and Related Technologies, Ravello (SA), Italy* (2011) 93–96.
- [24] Integration of membrane distillation into heat paths of industrial processes, *Chemical Engineering Journal* 211-212 (2012) 378–387.

- [25] M. Garcia-Payo, M. Izquierdo-Gil, C. Fernandez-Pineda, Air gap membrane distillation of aqueous alcohol solutions, *Journal of Membrane Science* 169 (2000) 61–80.
- [26] F. Banat, J. Simandl, Membrane distillation for dilute ethanol separation from aqueous streams, *Journal of Membrane Science* 163 (1999) 333–348.
- [27] C. Guijt, G. Meindersma, T. Reith, A. de Haan, Air gap membrane distillation: 2. Model validation and hollow fibre module performance analysis, *Separation and Purification Technology* 43 (2005) 245–255.
- [28] M. Khayet, P. Godino, J. Mengual, Theory and experiments on sweeping gas membrane distillation, *Journal of Membrane Science* 165 (2000) 261–272.
- [29] C. Lee, W. Hong, Effect of operating variables on the flux and selectivity in sweep gas membrane distillation for dilute aqueous isopropanol, *Journal of Membrane Science* 188 (2001) 79–86.
- [30] C. Boi, S. Bandini, G. Sarti, Pollutants removal from wastewaters through membrane distillation, *Desalination* 183 (2005) 383–394.
- [31] M. Khayet, M. Godino, J. Mengual, Possibility of nuclear desalination through various membrane distillation configuration: A comparative study, *International Journal of Nuclear Desalination* 1 (2003) 30–46.
- [32] U. von Stockar, M. Garcia-Payoa-Payo, C. Rivier, I. Marison, Separation of binary mixtures by thermostatic sweeping gas membrane distillation II. Experimental results with aqueous formic acid solutions, *Journal of Membrane Science* 198 (2002) 197–210.
- [33] C. Rivier, M. Garcia-Payoa-Payo, I. Marison, U. von Stockar, Separation of binary mixtures by thermostatic sweeping gas membrane distillation I. Theory and simulations, *Journal of Membrane Science* 201 (2002) 1–16.
- [34] L.-Z. Zhang, Coupled heat and mass transfer in an application-scale cross-flow hollow fiber membrane module for air humidification, *International Journal of Heat and Mass Transfer* 55 (2012) 5861–5869.
- [35] E. Hoffmann, D. Pfenning, E. Philippsen, P. Schwahn, M. Sieber, R. Wehn, D. Woermann, G. Wiedner, Evaporation of alcohol/water mixtures through hydrophobic porous membranes, *Journal of Membrane Science* 34 (1987) 199–206.

- [36] G. Sarti, C. Gostoli, S. Bandini, Extraction of organic components from aqueous streams by vacuum membrane distillation, *Journal of Membrane Science* 80 (1993) 21–33.
- [37] R. Bagger-Jørgensen, A. Meyer, C. Varming, G. Jonsson, Recovery of volatile aroma compounds from black currant juice by vacuum membrane distillation, *Journal of Food Engineering* 64 (2004) 23–31.
- [38] S. Bandini, G. Sarti, Concentration of must through vacuum membrane distillation, *Desalination* 149 (2002) 253–259.
- [39] K. Lawson, D. Lloyd, Membrane distillation I. Module design and performance evaluation using vacuum membrane distillation, *Journal of Membrane Science* 120 (1996) 111–121.
- [40] J. Mengual, M. Khayet, M. Godino, Heat and mass transfer in vacuum membrane distillation, *Heat and Mass Transfer* 47 (2004) 865–875.
- [41] K. K. Sirkar, B. Li, Novel membrane and device for vacuum membrane distillation-based desalination process, *Membrane Science* 257 (2004) 60–75.
- [42] P. Hogan, R. Canning, P. Peterson, R. Johnson, A new option: Osmotic distillation, *Chemical Engineering Process* (1998) 49–61.
- [43] C. Gostoli, Thermal effects in osmotic distillation, *Journal of Membrane Science* 163 (1999) 75–91.
- [44] B. R. Babu, N. Rastogi, K. Raghavarao, Concentration and temperature polarization effects during osmotic membrane distillation, *Journal of Membrane Science* 322 (2008) 146 – 153.
- [45] K. Belafi-Bako, B. Koroknai, Enhanced water flux in fruit juice concentration: Coupled operation of osmotic evaporation and membrane distillation, *Journal of Membrane Science* 269 (2006) 187–193.
- [46] M. Findley, Vaporization through porous membranes, *I&EC Process Design and Development* 6 (1967) 226–230.
- [47] P. Weyl, Recovery of demineralized water from saline waters, US patent No. 3,340,186, 1967.
- [48] Y. Hendrick, Evaporation condensation recovery of a solution component using a vapour permeable wall spaced from a cold wall, US patent No. 3,563,860, 1971.

- [49] K. Schneider, W. Hölz, R. Wollbeck, S. Ripperger, Membranes and modules for transmembrane distillation, *Journal of Membrane Science* 39 (1988) 25–42.
- [50] R. Rautenbach, *Membranverfahren - Grundlagen der Modul- und Anlagenauslegung*, 3. Auflage, Springer, 2007.
- [51] M. Khayet, T. Matsuura (Eds.), *Membrane Distillation*, Elsevier, 2011.
- [52] M. Gryta, Direct contact membrane distillation with crystallization applied to NaCl solutions, *Chemistry Papers* 56 (2002) 14–19.
- [53] M. Nasef, N. Zubir, A. Ismail, M. Khayet, K. Dahlan, H. Saidi, R. Rohani, T. Ngah, N. Sulaiman, PSSA pore-filled PVDF membranes by simultaneous electron beam irradiation: Preparation and transport characteristics of protons and methanol, *Journal of Membrane Science* 268 (2006) 96–108.
- [54] P. Wang, M. Teoh, T.-S. Chung, Morphological architecture of dual-layer hollow fiber for membrane distillation with higher desalination performance, *Water Research* 45 (2011) 5489–5500.
- [55] M. Garcia-Payo, M. Essalhi, M. Khayet, Preparation and characterization of PVDF-HFP copolymer hollow fiber membranes for membrane distillation, *Desalination* 245 (2009) 469–473.
- [56] M. Khayet, J. Mengual, T. Matsuura, Porous hydrophobic/hydrophilic composite membranes: Application in desalination using direct contact membrane distillation, *Journal of Membrane Science* 252 (2005) 101–113.
- [57] C. Feng, K. Khulbe, T. Matsuura, R. Gopal, S. Kaur, S. Ramakrishna, M. Khayet, Production of drinking water from saline water by air-gap membrane distillation using polyvinylidene fluoride nanofiber membrane, *Journal of Membrane Science* 311 (2008) 1–6.
- [58] D. Suk, T. Matsuura, H. Park, Y. Lee, Development of novel surface modified phase inversion membranes having hydrophobic surface-modifying macromolecule (nSMM) for vacuum membrane distillation, *Desalination* 261 (2010) 300–312.
- [59] D. Zhongwei, L. Liying, M. Runyu, Study on the effect of flow maldistribution on the performance of the hollow fiber modules used in membrane distillation, *Journal of Membrane Science* 215 (2003) 11–23.

- [60] M. Teoh, S. Bonyadi, T.-S. Chung, Investigation of different hollow fiber module designs for flux enhancement in the membrane distillation process, *Journal of Membrane Science* 311 (2008) 371–379.
- [61] B. Bondell, Silicone rubber vapour diffusion in saline water distillation, US patent No. 285,032, 1963.
- [62] B. Bondell, Distillation of saline water using silicone rubber membrane, US patent No. 3,361,645, 1968.
- [63] W. Gore, Desalination device and process, US patent No. 4,545,862, 1982.
- [64] W. Gore, Gore-tex membrane distillation, in: 10th Annual Convent Water Supply Improvement Assoc.
- [65] K. Zhao, W. Heinzl, M. Wenzel, S. Büttner, F. Bollen, G. Lange, S. Heinzl, N. Sarda, Experimental study of the Memsys vacuum-multi-effect-membrane-distillation (V-MEMD) module, *Desalination* 323 (2013) 150–160.
- [66] D. Winter, J. Koschikowski, M. Wieghaus, Desalination using membrane distillation: Experimental studies on full scale spiral wound modules, *Journal of Membrane Science* 375 (2011) 104–112.
- [67] A. Kullab, Desalination Using Membrane Distillation - Experimental and Numerical Study, Ph.D. thesis, Royal Institute of Technology, 2011.
- [68] G. Zaragoza, A. Ruiz-Aguirre, D. Alarcón-Padilla, J. Blanco, Analysis of different membrane distillation technologies based on experimental results using solar energy, 1st International Conference on Desalination using Membrane Technology, Sitges, Spain (2013).
- [69] A. Jansen, J. Assink, J. Hanemaaijer, J. van Medevoort, E. van Sonsbeek, Development and pilot testing of full-scale membrane distillation modules for deployment of waste heat, *Desalination* 323 (2013) 55–65.
- [70] E. Guillén-Burrieza, J. Blanco, G. Zaragoza, D. Alarcon, P. Palenzuela, M. Ibarra, W. Gernjak, Experimental analysis of an air gap membrane distillation solar desalination pilot system, *Journal of Membrane Science* 379 (2011) 386–396.
- [71] [online] Homepage memsys clearwater Pte. Ltd. <http://www.memsys.eu/products.html>, access in 2014, feb 18th.

- [72] G. Meindersma, C. Guijt, A. de Haan, Desalination and water recycling by air gap membrane distillation, *Desalination* 187 (2006) 291–301.
- [73] J. Hanemaaijer, J. van Medevoort, A. Jansen, C. Dotremont, E. van Sonsbeek, T. Yuan, L. de Ryck, Memstill membrane distillation - A future desalination technology, *Desalination* 199 (2006) 175–176.
- [74] P. Nijskens, B. Cools, B. Kregerman, Seawater desalination with memstill technology - A sustainable solution for the industry, *Proceedings - International Workshop on Membrane Distillation and Related Technologies*, Ravello (SA), Italy (2011) 83–85.
- [75] E. Burrieza, G. Zaragoza, S. Miralles-Cuevas, J. Blanco, Experimental evaluation of two pilot-scale membrane distillation modules used for solar desalination, *Journal of Membrane Science* 409-410 (2012) 264–275.
- [76] W. Kast, C.-R. Hohenthanner, Mass transfer within the gas-phase of porous media, *International Journal of Heat and Mass Transfer* 43 (2000) 807–823.
- [77] [online] Homepage xzero - The world's purest water for semiconductor industry <http://www.xzero.se>, access in 2014, march 26th.
- [78] P. Onsekizoglu, Production of high quality clarified pomegranate juice concentrate by membrane processes, *Journal of Membrane Science* 442 (2013) 264–271.
- [79] R. Bagger-Jørgensen, A. Meyer, M. Pinelo, C. Varming, G. Jonsson, Recovery of volatile fruit juice aroma compounds by membrane technology: Sweeping gas versus vacuum membrane distillation, *Innovative Food Science & Emerging Technologies* 12 (2011) 388–397.
- [80] R. Schofield, A. Fane, C. Fell, R. Macoun, Factors affecting flux in membrane distillation, *Desalination* 77 (1990) 279–294.
- [81] M. Izquierdo-Gil, M. Garca-Payo, C. Fernandez-Pineda, Direct contact membrane distillation of sugar aqueous solutions, *Separation Science and Technology* 34 (1999) 1773–1801.
- [82] A. Hausmann, P. Sanciolo, T. Vasiljevic, M. Weeks, K. Schroen, S. Gray, M. Duke, Fouling mechanisms of dairy streams during membrane distillation, *Journal of Membrane Science* 441 (2013) 102–111.
- [83] D. Qu, J. Wang, D. Hou, Z. Luan, B. Fan, C. Zhao, Experimental study of arsenic removal by direct contact membrane distillation, *Journal of Hazardous Materials* 163 (2009) 874–879.

- [84] P. Zolotarev, V. Ugrozov, I. Volkina, V. Nikulin, Treatment of waste water for removing heavy metals by membrane distillation, *Journal of Hazardous Materials* 37 (1994) 77–82.
- [85] G. Zakrzewska-Trznadel, M. Harasimowicz, A. Chmielewski, Concentration of radioactive components in liquid low-level radioactive waste by membrane distillation, *Journal of Membrane Science* 163 (1999) 257–264.
- [86] Z. Ding, L. Liu, Z. Li, R. Ma, Z. Yang, Experimental study of ammonia removal from water by membrane distillation (MD): The comparison of three configurations, *Journal of Membrane Science* 286 (2006) 93–103.
- [87] V. Calabro, E. Drioli, F. Matera, Membrane distillation in the textile wastewater treatment, *Desalination* 83 (1991) 209–224.
- [88] M. Tomaszewska, M. Gryta, A. Morawski, Study on the concentration of acids by membrane distillation, *Journal of Membrane Science* 102 (1995) 113–122.
- [89] M. Tomaszewska, M. Gryta, A. Morawski, The influence of salt in solutions on hydrochloric acid recovery by membrane distillation, *Separation and Purification Technology* 14 (1998) 183–188.
- [90] M. Tomaszewska, M. Gryta, A. Morawski, Recovery of hydrochloric acid from metal pickling solutions by membrane distillation, *Separation and Purification Technology* 22–23 (2001) 591–600.
- [91] X. Li, Y. Qin, R. Liu, Y. Zhang, K. Yao, Study on concentration of aqueous sulfuric acid solution by multiple-effect membrane distillation, *Desalination* 307 (2012) 34–41.
- [92] M. Khayet, J. Mengual, Effect of salt concentration during the treatment of humic acid solutions by membrane distillation, *Desalination* 168 (2004) 373–381.
- [93] R. Huo, Z. Gu, K. Zuo, G. Zhao, Preparation and humic acid fouling resistance of poly(vinylidene fluoride)-fabric composite membranes for membrane distillation, *Journal of Applied Polymer Science* 117 (2010) 3651–3658.
- [94] H. Udriot, A. Araque, U. von Stockar, Azeotropic mixtures may be broken by membrane distillation, *The Chemical Engineering Journal and the Biochemical Engineering Journal* 54 (1994) 87–93.

- [95] F. Banat, F. Al-Rub, R. Jumah, M. Shannag, On the effect of inert gases in breaking the formic acid water azeotrope by gas-gap membrane distillation, *Chemical Engineering Journal* 73 (1999) 37–42.
- [96] A. Urriaga, E. Gorri, G. Ruiz, I. Ortiz, Parallelism and differences of pervaporation and vacuum membrane distillation in the removal of VOCs from aqueous streams, *Separation and Purification Technology* 22-23 (2001) 327–337.
- [97] M. Khayet, T. Matsuura, Preparation and characterization of polyvinylidene fluoride membranes for membrane distillation, *Industrial & Engineering Chemistry Research* 40 (24) (2001) 5710–5718.
- [98] C. Boi, S. Bandini, G. Sarti, Pollutants removal from wastewaters through membrane distillation, *Desalination* 183 (2005) 383–394.
- [99] S. Bandini, A. Saavedra, G. Sarti, Vacuum membrane distillation: Experiments and modeling, *AIChE Journal* 43 (1997) 398–408.
- [100] F. Banat, J. Simandl, Membrane distillation for propanone removal from aqueous streams, *Journal of Chemical Technology and Biotechnology* 75 (2000) 168–178.
- [101] F. Banat, J. Simandl, Removal of benzene traces from contaminated water by vacuum membrane distillation, *Chemical Engineering Science* 51 (1996) 1257–1265.
- [102] A. Criscuoli, E. Drioli, A. Capuano, B. Memoli, V. Andreucci, Human plasma ultrafiltrate purification by membrane distillation: Process optimisation and evaluation of its possible application on-line, *Desalination* 147 (2002) 147–148.
- [103] Z. Ding, L. Liu, J. Yu, R. Ma, Z. Yang, Concentrating the extract of traditional chinese medicine by direct contact membrane distillation, *Journal of Membrane Science* 310 (2008) 539–549.
- [104] L. Mariah, C. Buckley, C. Brouckaert, E. Curcio, E. Drioli, D. Jaganyi, D. Ramjugernath, Membrane distillation of concentrated brines - Role of water activities in the evaluation of driving force, *Journal of Membrane Science* 280 (2006) 937–947.
- [105] X. Ji, E. Curcio, S. A. Obaidani, G. D. Profio, E. Fontananova, E. Drioli, Membrane distillation-crystallization of seawater reverse osmosis brines, *Separation and Purification Technology* 71 (2010) 76–82.

- [106] F. Macedonio, E. Drioli, Hydrophobic membranes for salts recovery from desalination plants, *Desalination and Water Treatment* 18 (2010) 224–234.
- [107] K. Karakulski, M. Gryta, A. Morawski, Membrane processes used for separation of effluents from wire productions, *Chemical Papers* 63 (2009) 205–211.
- [108] B. van der Bruggen, E. Curcio, E. Drioli, Process intensification in the textile industry: The role of membrane technology, *Journal of Environmental Management* 73 (2004) 267–274.
- [109] J. Phattaranawik, R. Jiratananon, A. Fane, Effect of pore size distribution and air flux on mass transport in direct contact membrane distillation, *Journal of Membrane Science* 215 (2003) 75–85.
- [110] M. Khayet, M. Godino, J. Mengual, Modelling mass transport through a porous partition: Effect of pore size distribution, *Journal of Non-equilibrium Thermodynamics* 29 (2004) 279–299.
- [111] I. Wichterle, J. Linek, Antoine vapor pressure constants of pure compounds, *Academica*, 1971.
- [112] H. Hömig, *Seawater and Seawater Distillation*, Vulkan-Verlag, 1978.
- [113] R. Schofield, A. Fane, C. Fell, Heat and mass transfer in membrane distillation, *Journal of Membrane Science* 33 (1987) 299–313.
- [114] B. Fabuss, A. Korosi, Boiling point elevations of sea water and its concentrates, *Journal of Chemical and Engineering Data* 11 (1966) 606–609.
- [115] A. Fane, R. Schofield, C. Fell, The efficient use of energy in membrane distillation, *Desalination* 64 (1987) 231–243.
- [116] E. Cussler, *Diffusion - Mass Transfer in Fluid Systems*, Cambridge University Press, 1997.
- [117] L. Martinez, F. Florido-Diaz, A. Hernandez, P. Pradanos, Characterisation of three hydrophobic porous membranes used in membrane distillation: Modelling and evaluation of their water vapour permeabilities, *Journal of Membrane Science* 203 (2002) 15–27.
- [118] R. Perry (Ed.), *Perry's Chemical Engineers' Handbook*, McGraw-Hill, 1997.
- [119] R. Schofield, A. Fane, C. Fell, Gas and vapour transport through microporous membranes: 1. Knudsen-Poiseuille Transition, *Journal of Membrane Science* 53 (1990) 159–171.

- [120] L. Martinez-Diez, M. Vazquez-Gonzalez, F. Florido-Diaz, Study of membrane distillation using channel spacers, *Journal of Membrane Science* 144 (1998) 45–56.
- [121] L. Martinez-Diez, M. Vazquez-Gonzalez, A method to evaluate coefficients affecting flux in membrane distillation, *Journal of Membrane Science* 173 (2000) 225–234.
- [122] U. Dittscher, Untersuchung des Wassertransports über die Gasphase durch eine poröse Membran mit hydrophober Gerüststruktur unter Einfluss einer Temperaturdifferenz, Ph.D. thesis, Universität Köln, 1990.
- [123] M. Chernyshov, G. Meindersma, A. Haan, Modelling temperature and salt concentration distribution in membrane distillation feed channel, *Desalination* 157 (2003) 315–324.
- [124] G. Liu, C. Zhu, C. Cheung, C. Leung, Theoretical and experimental studies on air gap membrane distillation, *Heat and Mass Transfer* 34 (1998) 329–335.
- [125] R. Marek, K. Nitsche (Eds.), *Praxis der Wärmeübertragung*, Hanser Verlag, 2007.
- [126] R. MacGregor, A. Emery, Free convection through vertical plane layers, *Journal of Heat Transfer* (1969) 391–403.
- [127] S. Bouguecha, R. Chouikh, M. Dhahbi, Numerical study of the coupled heat and mass transfer in membrane distillation, *Desalination* 152 (2002) 245–252.
- [128] A. Alklaibi, N. Lior, Transport analysis of air-gap membrane distillation, *Journal of Membrane Science* 255 (2005) 239–253.
- [129] F. Banat, J. Simandl, Desalination by membrane distillation: A parametric study, *Separation Science and Technology* 33 (1998) 201–226.
- [130] M. Izquierdo-Gil, M. Garcia-Payo, C. Fernandez-Pineda, Air gap membrane distillation of sucrose aqueous solutions, *Journal of Membrane Science* 155 (1999) 291 – 307.
- [131] J. Phattaranawik, R. Jiraratananon, Direct contact membrane distillation: Effect of mass transfer on heat transfer, *Journal of Membrane Science* 188 (2001) 137–143.
- [132] J. Phattaranawik, R. Jiraratananon, A. Fane, Heat transport and membrane distillation coefficients in direct contact membrane distillation, *Journal of Membrane Science* 212 (2003) 177–193.

- [133] M. Khayet, Membranes and theoretical modeling of membrane distillation: A review, *Advances in Colloid and Interface Science* (2010).
- [134] VDI-Wärmeatlas, 11.Auflage, Springer, 2013.
- [135] L. Martinez-Diez, M. Vazquez-Gonzalez, Temperature and concentration polarization in membrane distillation of aqueous salt solutions, *Journal of Membrane Science* 156 (1999) 265–273.
- [136] F. Li, W. Meindersma, A. de Haan, T. Reith, Experimental validation of CFD mass transfer simulations in flat channels with non-woven net spacers, *Journal of Membrane Science* 232 (2004) 19–30.
- [137] C. Zimmerer, V. Kottke, Effects of spacer geometry on pressure drop, mass transfer, mixing behavior and residence time distribution, *Desalination* 104 (1996) 129–134.
- [138] I. Kang, H. Chang, The effect of turbulence promoters on mass transfer - Numerical analysis and flow visualization, *International Journal of Heat and Mass Transfer* 25 (1982) 1167–1181.
- [139] P. Feron, G. Solt, The influence of separators on hydrodynamics and mass transfer in narrow cells: Flow visualisation, *Desalination* 84 (1991) 137–152.
- [140] A. Cipollina, A. D. Miceli, J. Koschikowski, G. Micale, L. Rizzuti, CFD simulation of a membrane distillation module channel, *Desalination and Water Treatment* 6 (2009) 177–183.
- [141] M. Chernyshov, A. Haan, G. Meindersma, Comparison of spacers for temperature polarization reduction in air gap membrane distillation, *Desalination* 183 (2005) 363–374.
- [142] F. Li, W. Meindersma, A. de Haan, T. Reith, Optimization of commercial net spacers in spiral wound membrane modules, *Journal of Membrane Science* 208 (2002) 289–302.
- [143] A. D. Costa, A. Fane, Net-type spacers: Effect of configuration on fluid flow path and ultrafiltration flux, *Industrial & Engineering Chemistry Research* 33 (1994) 1645–1851.
- [144] A. D. Costa, A. Fane, D. Wiley, Spacer characterisation and pressure drop modelling in spacer-filled channels for ultrafiltration, *Journal of Membrane Science* 87 (1994) 79–98.
- [145] A. D. Costa, A. Fane, C. Fell, A. Franken, Optimal channel spacer design for ultrafiltration, *Journal of Membrane Science* 62 (1991) 275–291.

- [146] C. Fritzmann, Micro-Structured Spacers for Intensified Membrane Process Performance, Ph.D. thesis, RWTH Aachen, 2012.
- [147] J. Schwinge, P. Neal, D. Wiley, D. Fletcher, A. Fane, Spiral wound modules and spacers: Review and analysis, *Journal of Membrane Science* 242 (2004) 129–153.
- [148] P. Pito, A. Cipollina, G. Micale, M. Ciofalo, A novel TLC based technique for temperature field investigation in MD channel, in: *Proceedings of the International Workshop on Membrane Distillation and Related Technologies*, Ravello (Italy), pp. 9–12.
- [149] E. Drioli, Membrane distillation and related operations - A review, *Separation and Purification Reviews* 34 (2005) 35–86.
- [150] M. Gryta, M. Tomaszewska, A. Morawski, Membrane distillation with laminar flow, *Separation and Purification Reviews* 11 (1996) 93–101.
- [151] J. Phattaranawik, R. Jiratananon, A. Fane, Effects of net-type spacers on heat and mass transfer in direct contact membrane distillation and comparison with ultrafiltration studies, *Journal of Membrane Science* 217 (2003) 193–206.
- [152] J. Phattaranawik, R. Jiratananon, A. Fane, C. Halim, Mass flux enhancement using spacer filled channels in direct contact membrane distillation, *Journal of Membrane Science* 187 (2001) 193–201.
- [153] M. Chernyshov, G. Meindersma, A. de Haan, Comparison of spacers for temperature polarization reduction in air gap membrane distillation, *Desalination* 183 (2005) 363 – 374.
- [154] G. Schock, A. Miquel, Mass transfer and pressure loss in spiral wound modules, *Desalination* 64 (1987) 339–352.
- [155] J. Zhang, N. Dow, M. Duke, E. Ostarcevic, J.-D. Li, S. Gray, Identification of material and physical features of membrane distillation membranes for high performance desalination, *Journal of Membrane Science* 349 (2010) 295–303.
- [156] G. Rao, A. Childress, Direct contact membrane distillation: Effects of membrane pore size distribution and support layer on mass transfer, in: *Proceedings of the International Workshop on Membrane Distillation and Related Technologies*, pp. 27–30.

- [157] S. Adnan, M. Hoang, H. Wang, Z. Xie, Commercial PTFE membranes for membrane distillation application: Effect of microstructure and support material, *Desalination* 284 (2012) 297–308.
- [158] M. Chernyshov, G. Meindersma, A. de Haan, Comparison of spacers for temperature polarization reduction in air gap membrane distillation, *Desalination* 183 (2005) 363–374.
- [159] K. Lawson, D. Lloyd, Membrane distillation II. Direct contact MD, *Journal of Membrane Science* 120 (1996) 123–133.
- [160] T. Cath, V. Adams, A. Childress, Experimental study of desalination using direct contact membrane distillation: A new approach to flux enhancement, *Journal of Membrane Science* 228 (2004) 5–16.
- [161] K. Lawson, M. Hall, D. Lloyd, Compaction of microporous membranes used in membrane distillation: I. Effect on gas permeability, *Journal of Membrane Science* 101 (1995) 99–108.
- [162] J. Zhang, J.-D. Li, S. Gray, Effect of applied pressure on performance of PTFE membrane in DCMD, *Journal of Membrane Science* 369 (2011) 514–525.
- [163] L. Martinez, Comparison of membrane distillation using different feeds, *Desalination* 168 (2004) 359–365.
- [164] L. Martinez, J. Rodriguez-Maroto, On transport resistances in direct contact membrane distillation, *Journal of Membrane Science* 295 (2007) 28–39.
- [165] F. Banat, J. Simandl, Theoretical and experimental study in membrane distillation, *Desalination* 95 (1994) 39–52.
- [166] D. Winter, J. Koschikowski, D. Düver, U. Beuscher, P. Hertel, Evaluation of MD process performance: Effect of backing structures and membrane properties under different operating conditions, *Desalination: Special Issue on Membrane Distillation* 323 (2013) 120–133.
- [167] A. Alklaibi, N. Lior, Comparative study of direct-contact and air-gap membrane distillation processes, *Industrial & Engineering Chemistry Research* 46 (2007) 584–590.
- [168] A. Alklaibi, N. Lior, Heat and mass transfer resistance analysis of membrane distillation, *Journal of Membrane Science* 282 (2006) 362–369.

- [169] A. Cipollina, M. D. Sparti, A. Tamburini, G. Micale, Development of a membrane distillation module for solar energy seawater desalination, *Chemical Engineering Research and Design* 90 (2012) 2101–2121.
- [170] M. Khayet, M. P. Godino, J. I. Mengual, Study of asymmetric polarization in direct contact membrane distillation, *Separation Science and Technology* 39 (2005) 125–147.
- [171] R. Weiss, The solubility of nitrogen, oxygen and argon in water and seawater, *Deep Sea Research and Oceanographic Abstracts* 17 (1970) 721–735.
- [172] T. Bes, Thermal design of spiral heat exchanger, *International Journal of Heat Exchangers* 2 (2001) 59 – 96.
- [173] H. Lang, Simplified approach to preliminary cost estimations, *Chem. Eng.* 55 (1948) 112–113.
- [174] C. Miller, New cost factor - give quick accurate estimations, *Chem. Eng.* 72 (1965) 226–239.
- [175] S. Krause, Ultrafiltration für kleine Trinkwasseraufbereitungsanlagen - Empfehlungen für Planung und Betrieb, Oldenburg Industrieverlag, 2012.
- [176] R. Brealy, S. Myers, F. Allen, *Principles of Corporate Finance*, 8th edition, 2006.
- [177] P. Wolf, S. Siverns, S. Monti, UF membranes for RO desalination pretreatment, *Desalination* 182 (2005) 293–300.
- [178] J. Medina, 20 years evolution of desalination costs in Spain, *International Conference on Desalination Costing* (2004).
- [179] S. Avlonitis, K. Kouroumbas, N. Vlachakis, Energy consumption and membrane replacement cost for seawater RO desalination plants, *Desalination* 157 (2003) 151–158.
- [180] EuroStat, [online] Gas prices for industrial consumers, from 2007 onwards, bi-annual data, access in 2013, Dec 18th.
- [181] G. Stryi-Hipp, W. Weiss, D. Mugnier, P. Dias, *Strategic Research Priorities for Solar Thermal Technology*, 2012.
- [182] EuroStat, [online] Electricity prices for industrial consumers, from 2007 onwards - bi-annual data, access in 2013, Dec 18th.

- [183] P. Côte, S. Siverns, S. Monti, Comparison of membrane-based solutions for water reclamation and desalination, *Desalination* 182 (2005) 251–257.
- [184] C. Fritzmann, J. Löwenberg, T. Wintgens, T. Melin, State-of-the-art of reverse osmosis desalination, *Desalination* 216 (2007) 1–76.
- [185] M. Wetter, GenOpt - Generic Optimization Program, User Manual, Version 3.1.0, Lawrence Berkeley National Laboratories, 2011.
- [186] M. Wetter, J. Wright, A comparison of deterministic and probabilistic optimization algorithms for nonsmooth simulation-based optimization, *Building and Environment* 39 (2004) 989–999.
- [187] M. Khayet, Solar desalination by membrane distillation: Dispersion in energy consumption analysis and water production costs (a review), *Desalination* 308 (2013) 89–101.
- [188] S. Al-Obaidania, E. Curcio, F. Macedonio, G. D. Profio, H. Al-Hinai, E. Drioli, Potential of membrane distillation in seawater desalination: Thermal efficiency, sensitivity study and cost estimation, *Journal of Membrane Science* 323 (2008) 85–98.
- [189] F. Banat, N. Jwaied, Economic evaluation of desalination by small-scale autonomous solar-powered membrane distillation units, *Desalination* 220 (2008) 566–573.
- [190] C. Briceno-Garmendia, D. Benitez, Cape Verde’s infrastructure, a continental perspective, The World Bank (2010).
- [191] E. Tzen, D. Theofiloyianakos, Z. Kologios, Autonomous reverse osmosis units driven by RE sources experiences and lessons learned, *Desalination* 221 (2008) 29–36.
- [192] O. Buross (Ed.), *The ABCs of Desalting*, International Desalination Association, Topsfield, Second Edition, 2001.
- [193] M. Sharqawya, J. Lienhard, S. Zubairb, Thermophysical properties of seawater: A review of existing correlations and data, *Desalination and Water Treatment* 16 (2010) 354–380.

Curriculum Vitae

Name Daniel Winter
Date of birth May 9th, 1983
Place of birth Filderstadt, Germany
Nationality German



Professional Education:

02/2010 - 07/2014 Doctoral research in the field of
“*Membrane Distillation*”
Fraunhofer Institute for Solar Energy Systems (ISE), Germany
Supported by a scholarship of the Reiner Lemoine Stiftung (RLS)

09/2003 - 05/2009 Diploma in Mechanical Engineering
Karlsruhe Institute of Technology (KIT), Germany

1999 - 2002 Technical Gymnasium, Abitur
Gottlieb-Daimler-Schule Sindelfingen, Germany

International Work Experience:

09/2012 Research period, Plataforma Solar de Almería (PSA), Spain
Field of activity: *Research on MED desalination*

12/2005 - 06/2006 Academic Semester in Mechanical Engineering
Purdue University, West Lafayette, Indiana, USA

09/2005 - 12/2005 Professional Internship
LuK USA LLC, Wooster, Ohio, USA
Field of activity: *KAIZEN, Process Optimisation, Quality Management*

Employment Record:

02/2010 - today Junior Scientist
Fraunhofer Institute for Solar Energy Systems (ISE), Germany
Field of activity: *Water Treatment and Separation*

10/2010 - 01/2011 Junior Scientist
PSE AG - projects in solar energy, Germany
Field of activity: *Water Treatment and Separation*

05/2009 - 10/2010 Trainee for scientific research
Fraunhofer Institute for Solar Energy Systems (ISE), Germany
Field of activity: *Water Treatment and Separation*

Acknowledgements

In November 2008, I was offered the chance to join the research group 'Water Treatment and Separation' at the Fraunhofer ISE. The institute and the team corresponded to my own ideals at personal and a professional level. A great spirit, an exciting technological approach and a high measure of multidisciplinary offered a perfect working environment. My decision to join the team turned out to be a long-lasting one and still holds today.

After an initial phase, my professional focus shifted from solar-driven desalination system design towards investigation of the system's core element - the membrane distillation module. In 2010, I started with the scientific analysis of membrane distillation in the framework of a doctorate, from which the present thesis results. During the long journey, I received support, guidance and companionship from many people, to whom I am very grateful.

First of all, I want to express my appreciation to my first supervisor Prof. Siegfried Ripperger from the Technical University of Kaiserslautern. I appreciated his trust and support during all phases of the project. Furthermore, I want to thank Prof. Volker Wittwer for accepting the co-referate and Prof. Hans-Jörg Bart for the chairmanship of the examination committee.

My special thanks go to the Reiner Lemoine Foundation (RLS) that supported me and my scientific project financially with a scholarship. I particularly appreciated the trust and the great degree of freedom the RLS offered to me.

I am very grateful to Joachim Koschikowski, who initiated and led the work on membrane distillation at Fraunhofer ISE. From the beginning, he gave me trust, patience, motivation and substantial support for developing and conducting the scientific studies for my doctorate. I consider it very special to find a great mentor and a good friend at the same time. Another person that contributed greatly to the successful completion of my doctorate is David Düver - my closest colleague for many years. Besides valuable support concerning engineering issues, I am grateful for loyal support during the difficult times when my availability was greatly reduced, either due to my new family situation or due to the finalisation of the thesis. Furthermore, I want to thank the students, Kathrin Ebert, Martin Rolletschek, Mirco Katzenmeyer, Christoph Sauter, David Düver, Marco Pergher and Julia Braun, whose research and results played an important role for the progress of my doctoral studies. Special thanks go to my former colleague Rebecca Schwantes for the support and effort she put into module prototyping. I also want to thank my colleague Florian Gross for all the assistance with my testing facilities regarding electronic design, wiring and troubleshooting. Even though field work and monitoring made no direct contribution to this thesis, I want to thank my hard-working team members and also the members of SolarSpring GmbH for all the experience and impressions I received from joint field projects. This offered me a great opportunity to think out of the box and to carve out the relevant questions for my scientific discussions. Gratitude is also owed to Helen Rose Wilson for the comprehensive proofreading during the finalisation of the thesis.

I want to thank my parents and brothers for all the love and support I have received during my whole life, on which all capabilities and strengths necessary for this project are based.

My greatest thanks are reserved for my wife Myriam and my kids Yuma and Milou. Thank you for all your love, patience, support and tolerance during this long period!

